國立中央大學天文研究所
鹿林天文台年報

2015

No.13

國立中央大學天文研究所 編

目錄

研究論文

工作報告

新聞報導

研究論文

A&A 573, A50 (2015)
DOI: 10.1051/0004-6361/201322906

Astronomy & Astrophysics

Multiwavelength observations of Mrk 501 in 2008⋆

J. Aleksić[1], S. Ansoldi[2], L. A. Antonelli[3], P. Antoranz[4], A. Babic[5], P. Bangale[6], U. Barres de Almeida[6], J. A. Barrio[7], J. Becerra González[8], W. Bednarek[9], K. Berger[8], E. Bernardini[10], A. Biland[11], O. Blanch[1], R. K. Bock[6], S. Bonnefoy[7], G. Bonnoli[3], F. Borracci[6], T. Bretz[12,25], E. Carmona[13], A. Carosi[3], D. Carreto Fidalgo[12], P. Colin[6], E. Colombo[8], J. L. Contreras[7], J. Cortina[1], S. Covino[3], P. Da Vela[4], F. Dazzi[2], A. De Angelis[2], G. De Caneva[10], B. De Lotto[2], C. Delgado Mendez[13], M. Doert[14], A. Domínguez[15,26], D. Dominis Prester[5], D. Dorner[12], M. Doro[16], S. Einecke[14], D. Eisenacher[12], D. Elsaesser[12], E. Farina[17], D. Ferenc[5], M. V. Fonseca[7], L. Font[18], K. Frantzen[14], C. Fruck[6], R. J. García López[8], M. Garczarczyk[10], D. Garrido Terrats[18], M. Gaug[18], G. Giavitto[1], N. Godinović[5], A. González Muñoz[1], S. R. Gozzini[10], A. Hadamek[14], D. Hadasch[19], A. Herrero[8], D. Hildebrand[11], J. Hose[6], D. Hrupec[5], W. Idec[9], V. Kadenius[20], H. Kellermann[6], M. L. Knoetig[11], J. Krause[6], J. Kushida[21], A. La Barbera[3], D. Lelas[5], N. Lewandowska[12], E. Lindfors[20,27], S. Lombardi[3], M. López[7], R. López-Coto[1], A. López-Oramas[1], E. Lorenz[6,†], I. Lozano[7], M. Makariev[22], K. Mallot[10], G. Maneva[22], N. Mankuzhiyil[2], K. Mannheim[12], L. Maraschi[3], B. Marcote[23], M. Mariotti[16], M. Martínez[1], D. Mazin[6], U. Menzel[6], M. Meucci[4], J. M. Miranda[4], R. Mirzoyan[6], A. Moralejo[1], P. Munar-Adrover[23], D. Nakajima[21], A. Niedzwiecki[9], K. Nilsson[20,27], N. Nowak[6], R. Orito[21], A. Overkemping[14], S. Paiano[16], M. Palatiello[2], D. Paneque[6,⋆⋆], R. Paoletti[4], J. M. Paredes[23], X. Paredes-Fortuny[23], S. Partini[4], M. Persic[2,28], F. Prada[15,29], P. G. Prada Moroni[24], E. Prandini[16], S. Preziuso[4], I. Puljak[5], R. Reinthal[20], W. Rhode[14], M. Ribó[23], J. Rico[1], J. Rodriguez Garcia[6], S. Rügamer[12], A. Saggion[16], T. Saito[21], K. Saito[21], M. Salvati[3], K. Satalecka[7], V. Scalzotto[16], V. Scapin[7], C. Schultz[16], T. Schweizer[6], S. N. Shore[24], A. Sillanpää[20], J. Sitarek[1], I. Snidaric[5], D. Sobczynska[9], F. Spanier[12], V. Stamatescu[1], A. Stamerra[3], T. Steinbring[12], J. Storz[12], S. Sun[6], T. Surić[5], L. Takalo[20], F. Tavecchio[3], P. Temnikov[22], T. Terzić[5], D. Tescaro[8], M. Teshima[6], J. Thaele[14], O. Tibolla[12], D. F. Torres[19], T. Toyama[6], A. Treves[17], M. Uellenbeck[14], P. Vogler[11], R. M. Wagner[6,30], F. Zandanel[15,31], R. Zanin[23]
(The MAGIC collaboration)
B. Behera[10], M. Beilicke[32], W. Benbow[33], K. Berger[34], R. Bird[35], A. Bouvier[36], V. Bugaev[32], M. Cerruti[33], X. Chen[37,31], L. Ciupik[38], E. Collins-Hughes[35], W. Cui[39], C. Duke[40], J. Dumm[41], A. Falcone[42], S. Federici[31,37], Q. Feng[39], J. P. Finley[39], L. Fortson[41], A. Furniss[36], N. Galante[33], G. H. Gillanders[43], S. Griffin[44], S. T. Griffiths[45], J. Grube[38], G. Gyuk[38], D. Hanna[44], J. Holder[34], C. A. Johnson[36], P. Kaaret[45], M. Kertzman[46], D. Kieda[47], H. Krawczynski[32], M. J. Lang[43], A. S. Madhavan[48], G. Maier[10], P. Majumdar[49,50], K. Meagher[51], P. Moriarty[52], R. Mukherjee[53], D. Nieto[54], A. O'Faoláin de Bhróithe[35], R. A. Ong[49], A. N. Otte[51], A. Pichel[55], M. Pohl[37,31], A. Popkow[49], H. Prokoph[10], J. Quinn[35], J. Rajotte[44], G. Ratliff[38], L. C. Reyes[56], P. T. Reynolds[57], G. T. Richards[51], E. Roache[33], G. H. Sembroski[39], K. Shahinyan[41], F. Sheidaei[47], A. W. Smith[47], D. Staszak[44], I. Telezhinsky[37,31], M. Theiling[39], J. Tyler[44], A. Varlotta[39], S. Vincent[10], S. P. Wakely[58], T. C. Weekes[33], R. Welsing[10], D. A. Williams[36], A. Zajczyk[32], B. Zitzer[59]
(The VERITAS collaboration)
M. Villata[60], C. M. Raiteri[60], M. Ajello[61], M. Perri[62], H. D. Aller[63], M. F. Aller[63], V. M. Larionov[64,65,66], N. V. Efimova[64,65], T. S. Konstantinova[64], E. N. Kopatskaya[64], W. P. Chen[67], E. Koptelova[67,68], H. Y. Hsiao[67], O. M. Kurtanidze[69,70,79], M. G. Nikolashvili[69], G. N. Kimeridze[69], B. Jordan[71], P. Leto[72], C. S. Buemi[72], C. Trigilio[72], G. Umana[72], A. Lähteenmäki[73,80], E. Nieppola[73,74], M. Tornikoski[73], J. Sainio[20], V. Kadenius[20], M. Giroletti[75], A. Cesarini[76], L. Fuhrmann[77], Yu. A. Kovalev[78], and Y. Y. Kovalev[77,78]

(Affiliations can be found after the references)

Received 24 October 2013 / Accepted 15 July 2014

ABSTRACT

Context. Blazars are variable sources on various timescales over a broad energy range spanning from radio to very high energy (>100 GeV, hereafter VHE). Mrk 501 is one of the brightest blazars at TeV energies and has been extensively studied since its first VHE detection in 1996. However, most of the γ-ray studies performed on Mrk 501 during the past years relate to flaring activity, when the source detection and characterization with the available γ-ray instrumentation was easier to perform.

Aims. Our goal is to characterize the source γ-ray emission in detail, together with the radio-to-X-ray emission, during the non-flaring (low) activity, which is less often studied than the occasional flaring (high) activity.

Methods. We organized a multiwavelength (MW) campaign on Mrk 501 between March and May 2008. This multi-instrument effort included the most sensitive VHE γ-ray instruments in the northern hemisphere, namely the imaging atmospheric Cherenkov telescopes MAGIC and VERITAS, as well as *Swift*, RXTE, the F-GAMMA, GASP-WEBT, and other collaborations and instruments. This provided extensive energy and temporal coverage of Mrk 501 throughout the entire campaign.

Results. Mrk 501 was found to be in a low state of activity during the campaign, with a VHE flux in the range of 10%–20% of the Crab nebula flux. Nevertheless, significant flux variations were detected with various instruments, with a trend of increasing variability with energy and a tentative correlation between the X-ray and VHE fluxes. The broadband spectral energy distribution during the two different emission states of the campaign can be adequately described within the homogeneous one-zone synchrotron self-Compton model, with the (slightly) higher state described by an increase in the electron number density.

Conclusions. The one-zone SSC model can adequately describe the broadband spectral energy distribution of the source during the two months covered by the MW campaign. This agrees with previous studies of the broadband emission of this source during flaring and non-flaring states. We report for the first time a tentative X-ray-to-VHE correlation during such a low VHE activity. Although marginally significant, this positive correlation between X-ray and VHE, which has been reported many times during flaring activity, suggests that the mechanisms that dominate the X-ray/VHE emission during non-flaring-activity are not substantially different from those that are responsible for the emission during flaring activity.

Key words. astroparticle physics – BL Lacertae objects: individual: Mrk 501 – gamma rays: general

⋆ The data for Figs. 2 and 5 are only available at the CDS via anonymous ftp to cdsarc.u-strasbg.fr (130.79.128.5) or via http://cdsarc.u-strasbg.fr/viz-bin/qcat?J/A+A/573/A50

⋆⋆ Corresponding authors: D. Paneque, e-mail: dpaneque@mppmu.mpg.de; K. Satalecka, e-mail: konstancjas@googlemail.com; and N. Mankuzhiyil, e-mail: mankuzhiyil.nijil@gmail.com

† Deceased.

Table 1. List of instruments participating in the multifrequency campaign and used in the compilation of the light curves and SEDs shown in Figs. 2 and 5.

Instrument/Observatory	Energy range covered	Web page
MAGIC	0.31–7.0 TeV	http://wwwmagic.mppmu.mpg.de/
VERITAS	0.32–4.0 TeV	http://veritas.sao.arizona.edu/
Swift/BAT	14–195 keV	http://heasarc.gsfc.nasa.gov/docs/swift/swiftsc.html/
RXTE/PCA	3–20 keV	http://heasarc.gsfc.nasa.gov/docs/xte/rxte.html
Swift/XRT	0.3–10 keV	http://heasarc.gsfc.nasa.gov/docs/swift/swiftsc.html
Swift/UVOT	*V*, *B*, *U*, *UVW1*, *UVM2*, *UVW2*	http://heasarc.gsfc.nasa.gov/docs/swift/swiftsc.html
Abastumani*	*R* band	http://www.oato.inaf.it/blazars/webt/
Crimean*	*R* band	http://www.oato.inaf.it/blazars/webt/
Lulin*	*R* band	http://www.oato.inaf.it/blazars/webt/
Roque de los Muchachos (KVA)*	*R* band	http://www.oato.inaf.it/blazars/webt/
St. Petersburg*	*R* band	http://www.oato.inaf.it/blazars/webt/
Talmassons*	*R* band	http://www.oato.inaf.it/blazars/webt/
Noto	43 GHz	http://www.noto.ira.inaf.it/
Metsähovi *	37 GHz	http://www.metsahovi.fi/
Medicina	8.4 GHz	http://www.med.ira.inaf.it/index_EN.htm
UMRAO*	4.8, 8.0, 14.5 GHz	http://www.oato.inaf.it/blazars/webt/
RATAN-600	2.3, 4.8, 7.7, 11.1, 22.2 GHz	http://www.sao.ru/ratan/
Effelsberg*	2.6, 4.6, 7.8, 10.3, 13.6, 21.7, 31 GHz	http://www.mpifr-bonn.mpg.de/div/effelsberg/index_e.html/

Notes. The instruments with the symbol "*" observed Mrk 501 through the GASP-WEBT program. The energy range shown in Col. 2 is the actual energy range covered during the Mrk 501 observations, and not the nominal energy range of the instrument, which might only be achievable for bright sources and excellent observing conditions. See text for further comments.

1. Introduction

Almost one third of the sources detected at very high energy (>100 GeV, hereafter VHE) are BL Lac objects, that is, active galactic nuclei (AGN) that contain relativistic jets pointing approximately in the direction of the observer. Their spectral energy distribution (SED) shows a continuous emission with two broad peaks: one in the UV-to-soft X-ray band, and a second one in the GeV–TeV range. They display no or only very weak emission lines at optical/UV energies. One of the most interesting aspects of BL Lacs is their flux variability, observed in all frequencies and on different timescales ranging from weeks down to minutes, which is often accompanied by spectral variability.

Mrk 501 is a well-studied nearby (redshift $z = 0.034$) BL Lac that was first detected at TeV energies by the Whipple collaboration in 1996 (Quinn et al. 1996). In the following years it has been observed and detected in VHE γ-rays by many other Cherenkov telescope experiments. During 1997 it showed an exceptionally strong outburst with peak flux levels up to ten times the Crab nebula flux, and flux-doubling timescales down to 0.5 day (Aharonian et al. 1999). Mrk 501 also showed strong flaring activity at X-ray energies during that year. The X-ray spectrum was very hard ($\alpha < 1$, with $F_\nu \propto \nu^{-\alpha}$), with the synchrotron peak found to be at ~100 keV, about 2 orders of magnitude higher than in previous observations (Pian et al. 1998). In the following years, Mrk 501 showed only low γ-ray emission (of about 20–30% of the Crab nebula flux), apart from a few single flares of higher intensity. In 2005, the MAGIC telescope observed Mrk 501 during another high-emission state which, although at a lower flux level than that of 1997, showed flux variations of an order of magnitude and previously not recorded flux-doubling timescales of only few minutes (Albert et al. 2007a).

Mrk 501 has been monitored extensively in X-ray (e.g., Beppo SAX 1996–2001, Massaro et al. 2004) and VHE (e.g., Whipple 1995–1998, Quinn et al. 1999, and HEGRA 1998–1999, Aharonian et al. 2001), and many studies have been conducted a posteriori using these observations (e.g., Gliozzi et al. 2006). With the last-generation Cherenkov telescopes (before the new generation of Cherenkov telescopes started to operate in 2004), coordinated multiwavelength (MW) observations were mostly focused on high VHE activity states (e.g., Krawczynski et al. 2000; Tavecchio et al. 2001), with few campaigns also covering low VHE states (e.g., Kataoka et al. 1999; Sambruna et al. 2000). The data presented here were taken between March 25 and May 16, 2008 during a MW campaign covering radio (Effelsberg, IRAM, Medicina, Metsähovi, Noto, RATAN-600, UMRAO, VLBA), optical (through various observatories within the GASP-WEBT program), UV (*Swift*/UVOT), X-ray (RXTE/PCA, *Swift*/XRT and *Swift*/BAT), and γ-ray (MAGIC, VERITAS) energies. This MW campaign was the first to combine such a broad energy and time coverage with higher VHE sensitivity and was conducted when Mrk 501 was not in a flaring state.

The paper is organized as follows: in Sect. 2 we describe the participating instruments and the data analyses. Sections 3–5 are devoted to the multifrequency variability and correlations. In Sect. 6 we report on the modeling of the SED data within a standard scenario for this source, and in Sect. 7 we discuss the implications of the experimental and modeling results.

2. Details of the campaign: participating instruments and temporal coverage

The list of instruments that participated in the campaign is reported in Table 1. Figure 1 shows the time coverage as a function of the energy range for the instruments and observations used to produce the light curves presented in Fig. 2 and the SEDs shown in Fig. 5.

2.1. Radio instruments

In this campaign, the radio frequencies were covered by various single-dish telescopes: the Effelsberg 100 m radio telescope, the 32 m Medicina radio telescope, the 14 m Metsähovi radio telescope, the 32 m Noto radio telescope, the 26 m University of Michigan Radio Astronomy Observatory (UMRAO), and the 600 m ring radio telescope RATAN-600. Details of the observing strategy and data reduction are given by Fuhrmann et al. (2008); Angelakis et al. (2008, Effelsberg), Teräsranta et al. (1998, Metsähovi), Aller et al. (1985, UMRAO), Venturi et al. (2001, Medicina and Noto), and Kovalev et al. (1999, RATAN-600).

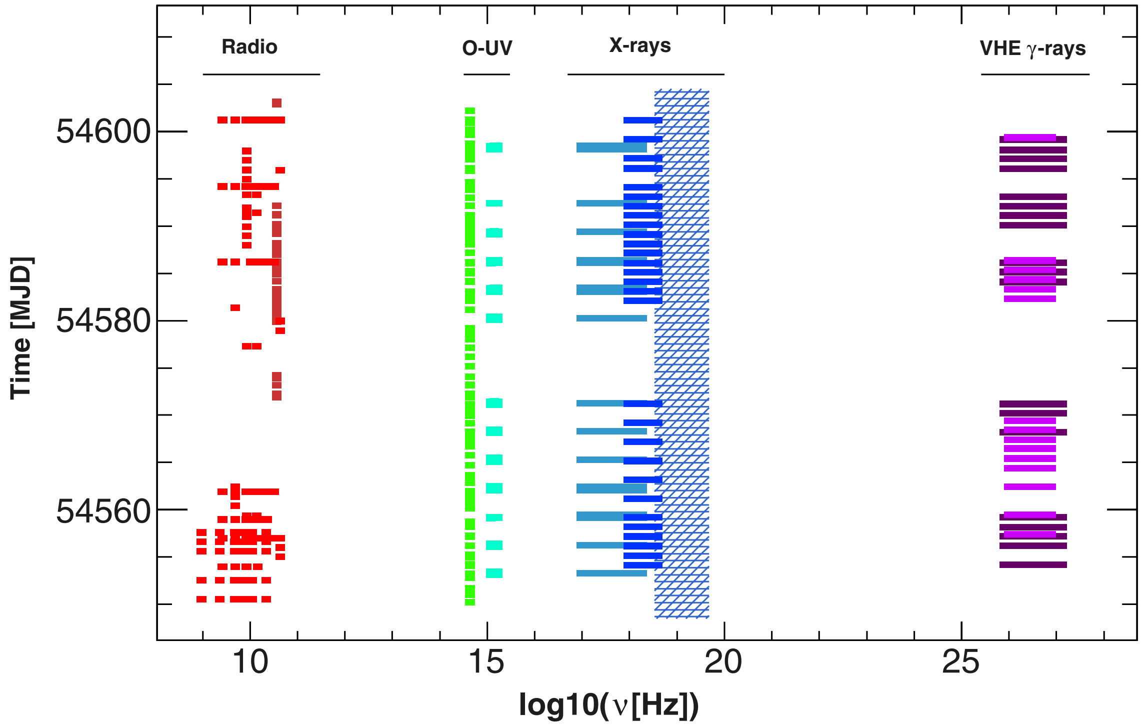

Fig. 1. Time and energy coverage during the multifrequency campaign. For the sake of clarity, the shortest observing time displayed in the plot was set to half a day, and different colors were used to display different energy ranges. The correspondence between energy ranges and instruments is provided in Table 1.

2.2. Optical instruments

The coverage at optical frequencies was provided by various telescopes around the world within the GASP-WEBT program (e.g., Villata et al. 2008, 2009). In particular, the following observatories contributed to this campaign: Abastumani, Lulin, Roque de los Muchachos (KVA), St. Petersburg, Talmassons, and the Crimean observatory. See Table 1 for more details. All the observations were performed at the *R* band, using the calibration stars reported by Villata et al. (1998). The Galactic extinction was corrected for with the coefficients given by Schlegel et al. (1998). The flux was also corrected for the estimated contribution from the host galaxy, 12 mJy for an aperture radius of 7.5 arcsec (Nilsson et al. 2007).

2.3. Swift/UVOT

The *Swift* UltraViolet and Optical Telescope (UVOT; Roming et al. 2005) analysis was performed including all the available observations between MJD 54 553 and 54 599. The instrument cycled through each of the three optical pass bands *V*, *B*, and *U*, and the three ultraviolet pass bands *UVW1*, *UVM2*, and *UVW2*. The observations were performed with exposure times ranging from 50 to 900 s with a typical exposure of 150 s. Data were taken in the *image mode*, where the image is directly accumulated onboard, discarding the photon timing information, and hence reducing the telemetry volume.

The photometry was computed using an aperture of 5 arcsec following the general prescription of Poole et al. (2008), introducing an annulus background region (inner and outer radii 20 and 30 arcsec), and it was corrected for Galactic extinction $E(B-V) = 0.019$ mag (Schlegel et al. 1998) in each spectral band (Fitzpatrick 1999).

Note that for each filter the integrated flux was computed by using the related effective frequency, and not by folding the filter transmission with the source spectrum. This might produce a moderate overestimate of the integrated flux of about 10%. The total systematic uncertainty is estimated to be $\lesssim$18%.

2.4. Swift/XRT

The *Swift* X-ray Telescope (XRT; Burrows et al. 2005) pointed to Mrk 501 18 times in the time interval spaning from MJD 54 553 to 54 599. Each observation was about 1–2 ks long, with a total exposure time of 26 ks. The observations were performed in windowed timing (WT) mode to avoid pile-up, which could be a problem for the typical count rates from Mrk 501, which are about ~5 cps (Stroh & Falcone 2013).

The XRT data set was first processed with the XRTDAS software package (v.2.8.0) developed at the ASI Science Data Center (ASDC) and distributed by HEASARC within the HEASoft package (v. 6.13). Event files were calibrated and cleaned with standard filtering criteria with the *xrtpipeline* task.

The average spectrum was extracted from the summed cleaned event file. Events for the spectral analysis were selected within a circle of 20 pixel (~46 arcsec) radius, which encloses about 80% of the PSF, centered on the source position.

The ancillary response files (ARFs) were generated with the *xrtmkarf* task, applying corrections for the PSF losses and CCD defects using the cumulative exposure map. The latest response matrices (v. 014) available in the *Swift* CALDB[1] were used. Before the spectral fitting, the 0.3–10 keV source energy spectra were binned to ensure a minimum of 20 counts per bin. The spectra were corrected for absorption with a neutral hydrogen column density $N_{\rm H}$ fixed to the Galactic 21 cm value in the direction of the source, namely 1.56×10^{20} cm^{-2} (Kalberla et al. 2005). When calculating the SED data points, the original

[1] The CALDB files are located at http://heasarc.gsfc.nasa.gov/FTP/caldb

spectral data were binned by combining 40 adjacent bins with the XSPEC command *setplot rebin*. The error associated to each binned SED data point was calculated adding in quadrature the errors of the original bins. The X-ray fluxes in the 0.3–10 keV band were retrieved from the log-parabola function fitted to the spectrum using the XSPEC command *flux*.

2.5. RXTE/PCA

The *Rossi* X-ray Timing Explorer (RXTE; Bradt et al. 1993) satellite performed 29 pointings on Mrk 501 during the time interval from MJD 54 554 to 54 601. Each pointing lasted 1.5 ks. The data analysis was performed using the FTOOLS v6.9 and following the procedures and filtering criteria recommended by the RXTE Guest Observer Facility[2] after September 2007. The average net count rate from Mrk 501 was about 5 cps per proportional counter unit (PCU) in the energy range 3–20 keV, with flux variations typically lower than a factor of two. Consequently, the observations were filtered following the conservative procedures for faint sources. For details on the analysis of faint sources with RXTE, see the online Cook Book[3]. In the data analysis, only the first xenon layer of PCU2 was used to increase the quality of the signal. We used the package pcabackest to model the background, the package saextrct to produce spectra for the source and background files and the script pcarsp to produce the response matrix. As with the *Swift*/XRT analysis, here we also used a hydrogen-equivalent column density $N_{\rm H}$ of 1.56×10^{20} cm^{-2} (Kalberla et al. 2005). However, since the PCA bandpass starts at 3 keV, the value used for $N_{\rm H}$ does not significantly affect our results. The RXTE/PCA X-ray fluxes were retrieved from the power-law function fitted to the spectrum using the XSPEC command *flux*.

2.6. Swift/BAT

The *Swift* Burst Alert Telescope (BAT; Barthelmy et al. 2005) analysis results presented in this paper were derived with all the available data during the time interval from MJD 54 548 to 54 604. The seven-day binned fluxes shown in the light curves were determined from the weighted average of the daily fluxes reported in the NASA *Swift*/BAT web page[4]. On the other hand, the spectra for the three time intervals defined in Sect. 3 were produced following the recipes presented by Ajello et al. (2008, 2009b). The uncertainty in the *Swift*/BAT flux/spectra is large because Mrk 501 is a relatively faint X-ray source and is therefore difficult to detect above 15 keV on weekly timescales.

2.7. MAGIC

MAGIC is a system of two 17 m diameter imaging atmospheric Cherenkov telescopes (IACTs), located at the Observatory Roque de los Muchachos, in the Canary island of La Palma (28.8 N, 17.8 W, 2200 m a.s.l.). The system has been operating in stereo mode since 2009 (Aleksić et al. 2011). The observations reported in this manuscript were performed in 2008, hence when MAGIC consisted on a single telescope. The MAGIC-I camera contained 577 pixels and had a field of view of 3.5°. The inner part of the camera (radius ∼1.1°) was equipped with 397 PMTs with a diameter of 0.1° each. The outer part of the camera was equipped with 180 PMTs of 0.2° diameter. MAGIC-I working as a stand-alone instrument was sensitive over an energy range of 50 GeV to 10 TeV with an energy resolution of 20%, an angular PSF of about 0.1° (depending on the event energy) and a sensitivity of 2% the integral flux of the Crab nebula in 50 h of observation (Albert et al. 2008b).

MAGIC observed Mrk 501 during 20 nights between 2008 March 29 and 2008 May 13 (from MJD 54 554 to 54 599). The observations were performed in ON mode, which means that the source is located exactly at the center in the telescope PMT camera. The data were analyzed using the standard MAGIC analysis and reconstruction software MARS (Albert et al. 2008a; Aliu et al. 2009; Zanin et al. 2013). The data surviving the quality cuts amount to a total of 30.4 h. The derived spectrum was unfolded to correct for the effects of the limited energy resolution of the detector and possible bias (Albert et al. 2007b) using the most recent (March 2014) release of the MAGIC unfolding routines, which take into account the distribution of the observations in zenith and azimuth for a correct effective collection area recalculation. The resulting spectrum is characterized by a power-law function with spectral index (-2.42 ± 0.05) and normalization factor (at 1 TeV) of $(7.4 \pm 0.2) \times 10^{-12}$ cm^{-2} s^{-1} TeV^{-1} (see Appendix A). The photon fluxes for the individual observations were computed for a photon index of 2.5, yielding an average flux of about 20% of that of the Crab nebula above 300 GeV, with relatively mild (typically lower than factor 2) flux variations.

2.8. VERITAS

VERITAS is an array of four IACTs, each 12 m in diameter, located at the Fred Lawrence Whipple Observatory in southern Arizona, USA (31.7 N, 110.9 W). Full four-telescope operations began in 2007. All observations presented here were taken with all four telescopes operational, and prior to the relocation of the first telescope within the array layout (Perkins et al. 2009). Each VERITAS camera contains 499 pixels (each with an angular diameter of 0.15°) and has a field of view of 3.5°. VERITAS is sensitive over an energy range of 100 GeV to 30 TeV with an energy resolution of 15%–20% and an angular resolution (68% containment) lower than 0.1° per event.

The VERITAS observations of Mrk 501 presented here were taken on 16 nights between 2008 April 1 and 2008 May 13. After applying quality-selection criteria, the total exposure is 6.2 h live time. Data-quality selection requires clear atmospheric conditions, based on infrared sky temperature measurements, and normal hardware operation. All data were taken during moon-less periods in wobble mode with pointings of 0.5° from the blazar alternating from north, south, east, and west to enable simultaneous background estimation and reduce systematics (Aharonian et al. 2001). Data reduction followed the methods described by Acciari et al. (2008). The spectrum obtained with the full dataset is described by a power-law function with spectral index (-2.47 ± 0.10) and normalization factor (at 1 TeV) of $(9.4 \pm 0.6) \times 10^{-12}$ cm^{-2} s^{-1} TeV^{-1} (see Appendix A). In the calculation of the photon fluxes integrated above 300 GeV for the single VERITAS observations, we used a photon index of 2.5.

3. Light curves

Figure 2 shows the light curves for all of the instruments that participated in the campaign. The five panels from top to bottom

[2] http://www.universe.nasa.gov/xrays/programs/rxte/pca/doc/bkg/bkg-2007-saa/
[3] http://heasarc.gsfc.nasa.gov/docs/xte/recipes/cook_book.html
[4] http://swift.gsfc.nasa.gov/docs/swift/results/transients/

present the light curves grouped into five energy ranges: radio, optical, X-ray, hard X-ray, and VHE.

The multifrequency light curves show little variability; during this campaign there were no outbursts of the magnitude observed in the past for this object (e.g., Krawczynski et al. 2000; Albert et al. 2007a). Around MJD 54 560, there is an increase in the X-rays activity, with a *Swift*/XRT flux (in the energy range 0.3–10 keV) of $\sim 1.3 \times 10^{-10}$ erg cm^{-2} s^{-1} before, and $\sim 1.7 \times 10^{-10}$ erg cm^{-2} s^{-1} after this day. The measured X-ray flux during this campaign is well below $\sim 2.0 \times 10^{-10}$ erg cm^{-2} s^{-1}, which is the average X-ray flux measured with *Swift*/XRT during the time interval of 2004 December 22 through 2012 August 31, which was reported in Stroh & Falcone (2013). In the VHE domain, the γ-ray flux above 300 GeV is mostly below $\sim 2 \times 10^{-11}$ ph cm^{-2} s^{-1} before MJD 54 560, and above $\sim 2 \times 10^{-11}$ ph cm^{-2} s^{-1} after this day. The variability in the multifrequency activity of the source is discussed in Sect. 4, while the correlation among energy bands is reported in Sect. 5.

For the spectral analysis presented in Sect. 6, we divided the data set into three time intervals according to the X-ray flux level (i.e., low/high flux before/after MJD 54 560) and the data gap at most frequencies in the time interval MJD 54 574–54 579 (which is due to the difficulty of observing with IACTs during the nights with moonlight).

4. Variability

We followed the description given by Vaughan et al. (2003) to quantify the flux variability by means of the fractional variability parameter $F_{\rm var}$. To account for the individual flux measurement errors ($\sigma_{\rm err,i}$), the "excess variance" (Edelson et al. 2002) was used as an estimator of the intrinsic source flux variance. This is the variance after subtracting the contribution expected from measurement statistical uncertainties. This analysis does not account for systematic uncertainties. $F_{\rm var}$ was derived for each participating instrument individually, which covered an energy range from radio frequencies at ~8 GHz up to very high energies at ~10 TeV. $F_{\rm var}$ is calculated as

$$F_{\rm var} = \sqrt{\frac{S^2 - \langle\sigma_{\rm err}^2\rangle}{\langle F_\gamma\rangle^2}}, \tag{1}$$

where $\langle F_\gamma\rangle$ denotes the average photon flux, S the standard deviation of the N flux measurements and $\langle\sigma_{\rm err}^2\rangle$ the mean squared error, all determined for a given instrument (energy bin). The uncertainty of $F_{\rm var}$ is estimated according to

$$\Delta F_{\rm var} = \sqrt{F_{\rm var}^2 + err(\sigma_{\rm NXS}^2)} - F_{\rm var}, \tag{2}$$

where $err(\sigma_{\rm NXS}^2)$ is given by Eq. (11) in Vaughan et al. (2003),

$$err(\sigma_{\rm NXS}^2) = \sqrt{\left(\sqrt{\frac{2}{N}}\frac{\langle\sigma_{\rm err}^2\rangle}{\langle F_\gamma\rangle^2}\right)^2 + \left(\sqrt{\frac{\langle\sigma_{\rm err}^2\rangle}{N}}\frac{2F_{\rm var}}{\langle F_\gamma\rangle}\right)^2}. \tag{3}$$

As reported in Sect. 2.2 in Poutanen et al. (2008), this prescription of computing $\Delta F_{\rm var}$ is more appropriate than that given by Eq. (B2) in Vaughan et al. (2003), which is not correct when the error in the excess variance is similar to or larger than the excess variance. For this data set, we found that the prescription from Poutanen et al. (2008), which is used here, leads to $\Delta F_{\rm var}$ that are ~40% smaller than those computed with Eq. (B2) in Vaughan et al. (2003) for the energy bands with the lowest $\frac{F_{\rm var}}{\Delta F_{\rm var}}$, while for most of the data points (energy bands) the errors are only ~20% smaller, and for the data points with the highest $\frac{F_{\rm var}}{\Delta F_{\rm var}}$ they are only few % smaller.

Figure 3 shows the $F_{\rm var}$ values derived for all instruments that participated in the MW campaign. The flux values that were used are displayed in Fig. 2. All flux values correspond to measurements performed on minutes or hour timescales, except for *Swift*/BAT, whose X-ray fluxes correspond to a seven-day integration because of the somewhat moderate sensitivity of this instrument to detect Mrk 501. Consequently, *Swift*/BAT data cannot probe the variability on timescales as short as the other instruments, and hence $F_{\rm var}$ might be underestimated for this instrument. We obtained negative excess variance ($\langle\sigma_{\rm err}^2\rangle$ larger than S^2) for the lowest frequencies of several radio telescopes. A negative excess variance can occur when there is little variability (in comparison with the uncertainty of the flux measurements) and/or when the errors are slightly overestimated. A negative excess variance can be interpreted as no signature for variability in the data of that particular instrument, either because a) there was no variability; or b) the instrument was not sensitive enough to detect it. Figure 3 only shows the fractional variance for instruments with positive excess variance.

At radio frequencies, there is essentially no variability: all bands and instruments show $F_{\rm var}$ close to zero, with the exception of the of RATAN (22 GHz) and Metsähovi (37 GHz), which show $F_{\rm var} \sim 7 \pm 2\%$. A possible reason for this *apparently* significant variability is unaccounted-for errors due to variable weather conditions, which can easily add a random extra fluctuation (day-by-day) of a few percent. However, it is worth mentioning that this flickering behavior has been observed several times with Metsähovi at 37 GHz, for example, in Mrk 501 and also in Mrk 421, while it is rare in other types of blazar objects; hence there is a chance that the measured fractional variability is dominated by a real flickering in the high-frequency radio emission of Mrk 501. More studies on this aspect will be reported elsewhere.

During the 2008 campaign on Mrk 501, we measured variability in the optical, X-ray, and gamma-ray energy bands. The plot also shows some evidence that the observed flux variability increases with energy: in the optical R band (ground-based telescopes) and the three UV filters from *Swift*/UVOT the variability is ~3%, at X-rays it is ~13%, and at VHE it is ~20%, although affected by relatively large error bars (because of the statistical uncertainties in the individual flux measurements).

5. Multifrequency cross-correlations

We used the discrete correlation function (DCF) proposed by Edelson & Krolik (1988) to study the multifrequency cross-correlations between the different energy bands. The DCF quantifies the temporal correlation as a function of the time lag between two light curves, which can give us a deeper insight into the acceleration processes in the source. For example, these time lags may occur as a result of spatially separated emission regions of the individual flux components (as expected, for example, in external inverse Compton models), or may be caused by the energy-dependent cooling time-scales of the emitting electrons.

There are two important properties of the DCF method. First, it can be applied to unevenly sampled data (as in this campaign), meaning that the correlation function is defined only for lags for which the measured data exist, which makes an interpolation of

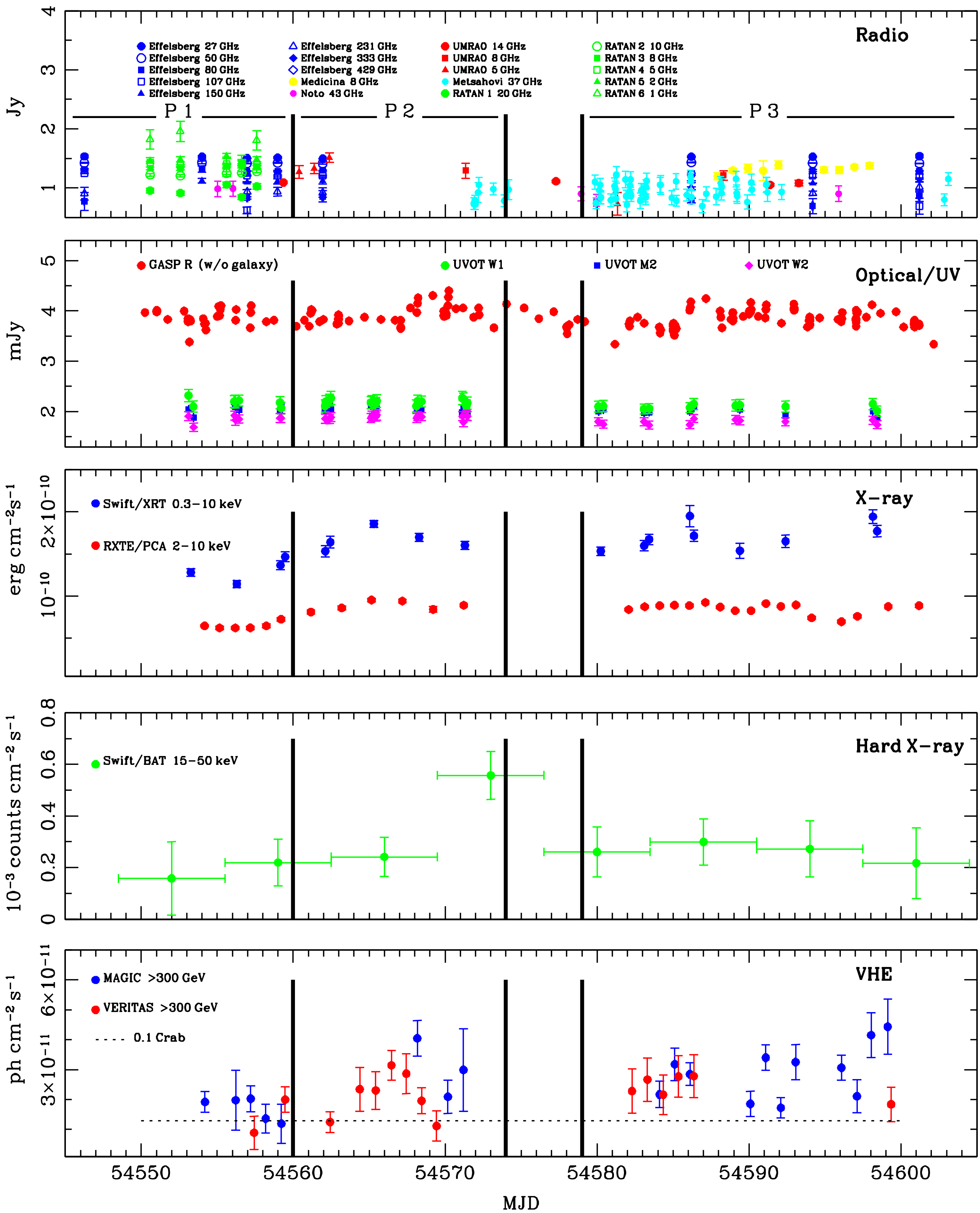

Fig. 2. Multifrequency light curve for Mrk 501 during the entire campaign period. The *panels from top to bottom* show the radio, optical and UV, X-ray, hard X-ray, and VHE γ-ray bands. The thick black vertical lines in all the panels delimit the time intervals corresponding to the three different epochs (P1, P2, and P3) used for the SED model fits in Sect. 6. The horizontal dashed line in the bottom panel depicts 10% of the flux of the Crab nebula above 300 GeV (Albert et al. 2008b).

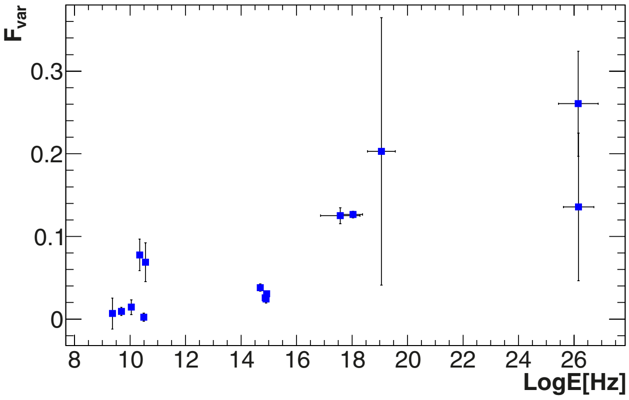

Fig. 3. Fractional variability parameter $F_{\rm var}$ vs. energy covered by the various instruments. $F_{\rm var}$ was derived using the individual single-night flux measurements except for *Swift*/BAT, for which, because of the limited sensitivity, we used data integrated over one week. Vertical bars denote 1σ uncertainties, horizontal bars indicate the approximate energy range covered by the instruments.

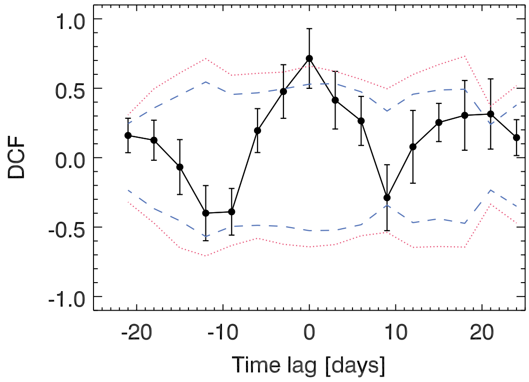

(a) RXTE/PCA vs. *Swift*/XRT

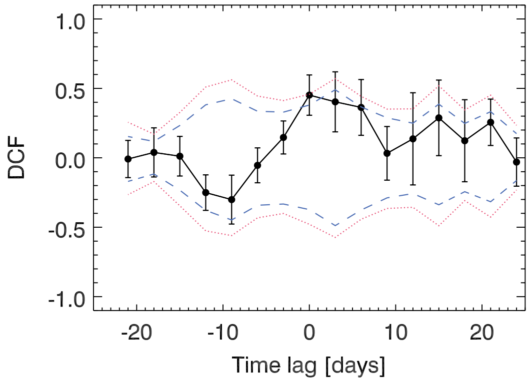

(b) RXTE/PCA vs. MAGIC & VERITAS

Fig. 4. Discrete correlation function for time lags from –21 to +21 days in steps of 3 days. The (black) data points and errors are the DCF values computed according to the prescription given by Edelson & Krolik (1988). The (blue) dashed and the (red) dotted curves depict the 95% and 99% confidence intervals for random correlations resulting from the dedicated Monte Carlo analysis described in Sect. 5.

the data unnecessary. The result is a correlation function that is a set of discrete points binned in time. Second, the errors in the individual flux measurements (which contribute to the dispersion in the flux values) are naturally taken into account. The latter characteristic is a big advantage over the commonly used Pearson correlation function. The main caveat of the DFC method is that the correlation function is not continuous and that care needs to be taken when defining the time bins to achieve a reasonable balance between the required time resolution and accuracy of DCF. Given the many two-day (sometimes three-day) time gaps in the X-ray and VHE observations from this MW campaign (see Figs. 1 and 2), we selected a time bin of three days to compute the DCF with minimal impact of these observational gaps. Moreover, given the relatively low variability reported in Fig. 2, an estimation of DCF would not benefit from a smaller time bin.

Using the data collected in this campaign, we derived the DCF for all different combinations of instruments and energy regions and also for artificially introduced time lags (ranging from –21 to +21 days) between the individual light curves. Significant correlations were found only for the pairs RXTE/PCA – *Swift*/XRT and also (less significant) RXTE/PCA with MAGIC and VERITAS (Figs. 4a and b). In both cases, the highest DCF values are obtained for a zero time lag, with a value of 0.71 ± 0.22 (RXTE/PCA – *Swift*/XRT) and 0.45 ± 0.15 (RXTE/PCA – MAGIC and VERITAS), which implies positive correlations with a significance of 3.2 and 3.0 standard deviations.

As discussed in Uttley et al. (2003), the errors in the DCF computed as prescribed in Edelson & Krolik (1988) might not be appropriate for determining the significance of the DCF when the individual light-curve data points are correlated red-noise data. Depending on the power spectral density (PSD) and the sampling pattern, the significance as calculated by Edelson & Krolik (1988) might therefore overestimate the real significance. To derive an independent estimate of the real significance of the correlation peaks we used the dedicated Monte Carlo approach described below.

First we generated a large set of simulated light curves using the method of Timmer & Koenig (1995) following the prescription of Uttley et al. (2002). As a model for the PSD we assumed a simple power-law shape[5], and generated for each observed light curve and for each PSD model (we varied the PSD slope in the range –1.0 to –2.5 in steps of 0.1) 1000 simulated light curves. The simulated light curves were then resampled using the sampling pattern of the observed light curve. By applying the *psresp* method (Uttley et al. 2002) we tried to determine the best-fitting model for the PSD. This involves the following steps in addition to the light-curve simulation and resampling: the PSD of the observed light curve, as well as the PSD of each simulated light curve, is calculated as the square of the modulus of the discrete Fourier transform of the (mean subtracted) light curve, as prescribed in Uttley et al. (2002). A χ^2 analysis is then used to determine the model that best fits the data. Given the short frequency range, the uneven sampling and the presence of large gaps (particularly in the VHE data), it was not possible to constrain the PSD shape very tightly. The best-fitting models are power laws with indices 1.4 (VHE) and 1.5 (X-rays), however, any power law with an index between 1.0 and 1.9 fits the data reasonably well. The RXTE/PCA light curve is sampled more often and regularly than the other VHE and X-ray light curves, and moreover, Kataoka et al. (2001) found an X-ray PSD slope similar to ours (1.37 ± 0.16) in the frequency range probed here. Therefore we used the simulated RXTE/PCA light curves with a PSD slope

[5] The shape of the PSD from blazars can be typically characterized with a power law $P_\nu \propto \nu^{-\alpha}$ with spectral indices α between 1 and 2 (see Abdo et al. 2010; Chatterjee et al. 2012).

of –1.5 to ascertain the confidence levels in the DCF calculation. We cross-correlated each of the 1000 simulated RXTE/PCA light curves with the observed VHE (MAGIC&VERITAS) and *Swift*/XRT light curves. The 95 and 99% limits of the distribution of simulated RXTE/PCA light curves when correlated with the real VHE and *Swift*/XRT light curves are plotted in Figs. 4a and b as blue dashed and red dotted lines, respectively. The correlation peaks at time lag = 0 are higher than >99% of the simulated data for the DCF for RXTE/PCA correlated with *Swift*/XRT, and ~99% for the simulated data for the DCF for RXTE/PCA with VHE (MAGIC&VERITAS). Given that a 99% confidence level is equivalent to 2.5 standard deviations, this result agrees reasonably well with the significances of ~3 standard deviations estimated from the Edelson & Krolik DCF errors, thus indicating that in this case the red-noise nature and the sampling of the light curve do not have a very strong influence. There are no other peaks or dips in the DCF between VHE and X-rays that appear significant.

The positive correlation in the fluxes from *Swift*/XRT and RXTE/PCA is expected because of the proximity (and overlap) of the energy coverage of these two instruments (see Table 1), while the correlated behavior between RXTE/PCA and MAGIC/VERITAS suggests that the X-ray and VHE emission are co-spatial and produced by the same population of high-energy particles. The correlation between the X-ray and VHE band has been reported many times in the past (e.g., Krawczynski et al. 2000; Tavecchio et al. 2001; Gliozzi et al. 2006; Albert et al. 2007a), but only when Mrk 501 showed flaring VHE activity with VHE fluxes higher than the flux of the Crab nebula. An X-ray/VHE correlation when the source shows a VHE flux below 0.5 Crab has never been shown until now.

6. SED modeling

Using the multifrequency data, we derived time-resolved SEDs for three different periods that were defined according to the observed X-ray flux during this campaign (see Sect. 3). The *Swift*, RXTE, MAGIC, and VERITAS spectral results for the three periods are reported in Appendix A. The X-ray spectral results reported in Tables A.1 and A.2 show that Mrk 501 became brighter and harder in P2/P3 than in P1. The VHE spectra reported in Tables A.3 and A.4 show that the MAGIC and VERITAS spectral results agree with each other within statistical uncertainties (despite the slightly different temporal coverage). The VHE spectral results do not show any significant spectral hardening when going from P1 to P2/P3. This could be due to the low VHE activity of Mrk 501 and the moderate sensitivity that MAGIC and VERITAS had in 2008. In any case, MAGIC measures a VHE spectrum for P2/P3 that is significantly brighter than that measured for P1.

The SED of the inner jet was modeled using a single-zone synchrotron self-Compton (SSC, Tavecchio et al. 1998; Maraschi et al. 2003) model, which is the simplest theoretical framework for the broadband emission of high-synchrotron-peaked BL Lac objects like Mrk 501. To reproduce the double bump shape of the SED, we assumed that the electron energy distribution (EED) can be described by a broken power law, with indices n_1 and n_2, below and above the break ($\gamma_{\rm break}$), $\gamma_{\rm min}$ and $\gamma_{\rm max}$ being the lowest and highest energies, and K the normalization factor. The emission region is assumed to be a spherical plasmon of radius R, filled with a tangled homogeneous magnetic field of amplitude B, and moving with a relativistic Doppler factor δ, such that $\delta = [\Gamma(1 - \beta\cos\theta)]^{-1}$, where $\beta = v/c$, Γ is the bulk Lorentz factor, and θ is the viewing angle with respect to the plasmon velocity.

The SED modeling was performed using a χ^2 minimized fitting algorithm, instead of the commonly used *eyeball* procedure. The algorithm uses the Levenberg-Marquardt method – which interpolates between inverse Hessian method and steepest-descent method. In the fitting procedure, a systematic uncertainty of 15% for optical data sets, 10% for X-ray data sets, and 40% for VHE data sets was added in quadrature to the statistical uncertainty in the differential energy fluxes. The details of the fitting procedure can be found in Mankuzhiyil et al. (2011). We note that the addition in quadrature of the systematic and statistical errors to compute the overall χ^2 is not correct from a strictly statistical point of view. Therefore, the χ^2 was used as a penalty function for the fit, and not as a measure of the true goodness-of-fit. Consequently, even though the fitting algorithm allows us to rapidly converge to a model that describes the data well, the parameter errors provided by the fit are not statistically meaningful, and hence were not used.

The radio emission is produced by low-energy electrons, which can extend over hundreds of pc and even kpc distances, which is many orders of magnitude larger than the typical size of the regions where the blazar emission is produced (~10^{-4}–10^{-1} pc). Given the relatively low angular resolution of the single-dish radio telescopes (in comparison with interferometric radio observations), these instruments measure the total flux density of Mrk 501 integrated over the whole source extension. Consequently, the single-dish radio data were used as upper limits for the blazar emission modeled here. The *Swift*/UVOT data points below 1.0×10^{15} Hz (those in the V, B, U filters) are dominated by the emission from the host galaxy and hence they are considered only as upper limits in the procedure of fitting the SED. The other *Swift*/UVOT data points (those from the filters *UVW1*, *UVM2*, and *UVW2*) were used in the SED model fit. The optical data in the R band from GASP-WEBT were corrected for the host galaxy contribution using the prescriptions from Nilsson et al. (2007), and the VHE data from MAGIC and VERITAS were corrected for the absorption in the extragalactic background light (EBL) using the model from Franceschini et al. (2008). We note that, because of the low redshift of this source, many other prescriptions (e.g., Finke et al. 2010; Domínguez et al. 2011) provide compatible[6] results at energies below 10 TeV.

We noted that the three SEDs can be described with minimal changes in the environment parameters (R, δ, B) and maximum energy of the EED ($\gamma_{\rm max}$). Therefore, we decided to test whether we could explain the modulations of the SED by simply changing the shape and normalization of the EED (K, $n1$, $n2$, $\gamma_{\rm break}$) while keeping all the other model parameters constant. The collected multi-instrument data contain neither high-frequency (>43 GHz) interferometric observations, nor *Fermi*-LAT data and hence it is difficult to constrain the model parameter $\gamma_{\rm min}$. In fact, we noted that a one-zone SSC model can describe the experimental data equally well with $\gamma_{\rm min} = 1$ and $\gamma_{\rm min} = 1000$. Both numbers have been used in the literature, and the multi-instrument data from this campaign cannot be used to distinguish between them. In this work we decided to use $\gamma_{\rm min} = 1000$, which is motivated by two reasons: (i) the preference for a large $\gamma_{\rm min}$ in the one-zone SSC model fits in the Mrk 501 SED reported in Abdo et al. (2011), where the experimental constraints are tighter (because of usage of VLBA and *Fermi* -LAT data); and (ii) the preference for reducing the

[6] At 5 TeV, most models predict an absorption of ~0.4–0.5.

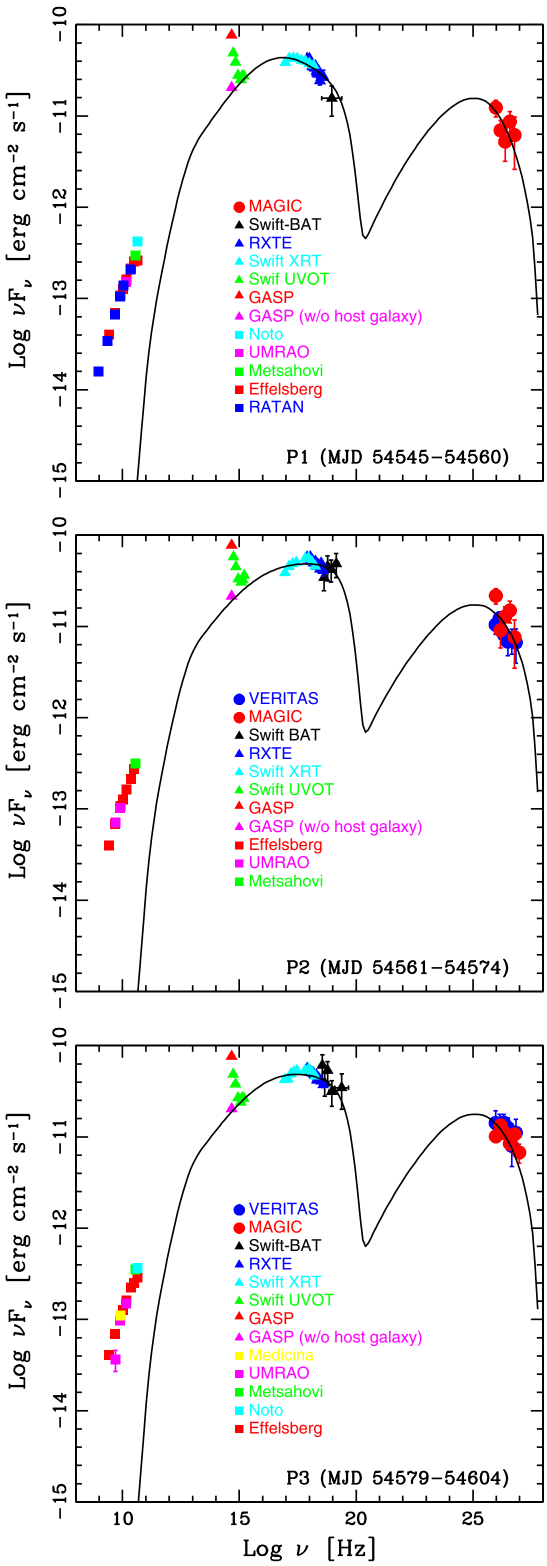

Fig. 5. Spectral energy distributions for Mrk 501 in the three periods described in Sect. 3. The legend reports the correspondence between the instruments and the measured fluxes. Further details about the instruments are given in Sect. 2. The vertical error bars in the data points denote the 1σ statistical uncertainty. The black curve depicts the one-zone SSC model fit described in Sect. 6, with the resulting parameters reported in Table 2.

electron energy density (which largely depends on γ_{min} for soft-electron energy spectra) with respect to the magnetic energy density. We note that even with the choice of $\gamma_{min} = 1000$, the kinetic (electron) energy density resulting from the SED model fit is about two orders of magnitude larger than the magnetic energy density.

The one-zone SSC model fits of the three different periods are shown in Fig. 5. The resulting SED model parameters of the two scenarios are reported in Table 2. The relatively small variations in the broadband SED during this observing campaign can be adequately parameterized with small modifications in the parameters that describe the shape of the EED, namely γ_{break}, n_1, n_2, and K. The one-zone SSC model parameters are determined by the shape of the low-energy bump together with the overall energy flux measured at VHE, and they are not sensitive to exact slope of the VHE spectra. This is mostly due to the relatively large uncertainties in the reported VHE spectra.

7. Discussion

In the SSC framework, the observed flux variability contains information on the dynamics of the underlying population of relativistic electrons. In this context, the general variability trend reported in Fig. 3 suggests that the flux variations are dominated by the high-energy electrons, which have shorter cooling timescales, which causes the higher variability amplitude observed at the highest energies.

Mrk 501 is known for its strong spectral variability at VHE; although these spectral variations typically occur when the source's activity changes substantially, showing a characteristic *harder-when-brighter* behavior (e.g., Aharonian et al. 2001; Albert et al. 2007a; Abdo et al. 2011). During this MW campaign the flux level and flux variability at VHE was low (see Figs. 2 and 3), and neither MAGIC nor VERITAS could detect significant spectral variability during the three temporal periods considered (see Tables A.3 and A.4). This is partially due to the moderate sensitivity of MAGIC and VERITAS back in 2008. On the other hand, in the X-ray domain the instruments *Swift*/XRT and RXTE/PCA have sufficient sensitivity to resolve Mrk 501 very significantly in this very low state, and they both detect a hardening of the spectra when the flux increases from P1 to P2 (see Tables A.1 and A.2); this confirms the *harder-when-brighter* behavior reported previously for this source (e.g., Gliozzi et al. 2006).

The three SEDs from the 2008 multi-instrument campaign can be adequately described with a one-zone SSC model in which the EED is parameterized with two power-law functions (i.e., one break). Such a simple parameterization was not successful in describing the SED from the 2009 multi-instrument campaign, which required an EED described with three power-law functions (Abdo et al. 2011). This difference is related to the reduced instrumental energy coverage of the 2008 observing campaign in comparison to that of 2009. In particular, the SED reported in Abdo et al. (2011) benefitted from 43 GHz VLBA interferometric and 230 GHz SMA observations, as well as from *Fermi*-LAT, which helped substantially to characterize the high-energy (inverse Compton) bump. Therefore, the SEDs shown here have fewer experimental constraints than those shown in Abdo et al. (2011), and this might facilitate the characterization with a simpler theoretical model. In addition, the somewhat higher activity of Mrk 501 during 2009 than in 2008 is also worth mentioning, which might also contribute to this difference in the SED modeling results.

The obtained γ_{break} is ~10 smaller than the γ_{break} expected from synchrotron cooling, which suggests that this break is intrinsic to the injection mechanism. We note that this γ_{break} is

Table 2. Model parameters obtained from the χ^2-minimized SSC fits and the calculated electron energy density values.

Period	$\gamma_{\rm min}$	$\gamma_{\rm break}$	$\gamma_{\rm max}$	n_1	n_2	B [G]	K [cm^{-3}]	R [cm]	δ	Electron energy density [erg cm^{-3}]
P1	1.0×10^3	8.3×10^4	2.8×10^6	2.22	3.43	4.4×10^{-2}	2.1×10^4	9.7×10^{15}	22.8	1.1×10^{-2}
P2	1.0×10^3	4.6×10^4	2.8×10^6	2.23	3.09	4.4×10^{-2}	3.3×10^4	9.7×10^{15}	22.8	1.3×10^{-2}
P3	1.0×10^3	7.3×10^4	2.8×10^6	2.26	3.21	4.4×10^{-2}	3.6×10^4	9.7×10^{15}	22.8	1.3×10^{-2}

comparable (within a factor of two) to the first $\gamma_{\rm break}$ used in Abdo et al. (2011), which was also related to the mechanisms responsible for accelerating the particles[7].

Using the one-zone SSC model curves presented in Sect. 6, we calculated the observed luminosity $L_{\rm obs} = \int_{\nu_{\rm min}}^{\nu_{\rm max}} \nu F(\nu)$ with $\nu_{\rm min} = 10^{11.0}$ and $\nu_{\rm max} = 10^{27.5}$ Hz, and converted it into jet power in radiation, $L_r = L_{\rm obs}/\delta^2$, as prescribed in Celotti & Ghisellini (2008). The radiated jet power for the three epochs were 6.2×10^{41} erg s^{-1}, 7.5×10^{41} erg s^{-1}, and 7.4×10^{41} erg s^{-1} for the periods 1, 2, and 3 respectively; that is, the radiated jet power increased from P 1 to P 2 and remained the same from P 2 to P 3. Given the model parameter values reported in Table 2, the increase in the luminosity of the source is driven by a growth of the electron energy density. In particular, the change from P 1 to P 2 may have been produced by an injection of more electrons. On the other hand, although in P 3 we postulate slightly higher values of K and $\gamma_{\rm break}$ than in P 2, the softening of the electron spectrum (n_2) nullifies the effect, such that the electron energy density, and hence the luminosity, remain constant.

It is worth mentioning that the low X-ray and VHE activity reported in this paper is comparable to the one reported for the MW campaign from 1996 March (Kataoka et al. 1999). In this case, however, we could describe the measured SED using a one-zone SSC with only one break (instead of two) in the EED, and with a better data-model agreement at VHE. The MAGIC and VERITAS spectra, after being corrected for the absorption in the EBL, can be parameterized with a power-law function with index ~2.3, which matches the power-law index predicted by the SSC model well, that is, ~2.3 at 300 GeV and ~2.5 at 1 TeV. On the other hand, the VHE spectra determined with HEGRA data from 1996 March to 1996 August (hence not strictly simultaneous to the 1996 March MW campaign) was parameterized with a power-law function with index 2.5 ± 0.4 above 1.5 TeV, which poorly matched the value of ~3.8 predicted by the SSC model used in Kataoka et al. (1999). Kataoka et al. (1999) also postulated (based on comparisons of the low-activity measured in 1996 with the large flare from 1997) that the variability in the SED of Mrk 501 could be driven by variations in the number of high-energy electrons. Based on the collected broadband SEDs of Mrk 501 from 1997 to 2009, which were characterized with a one-zone SSC scenario, Mankuzhiyil et al. (2012) also suggested that the variability observed in this source is strongly related to the variability in the high-energy portion of the EED.

8. Conclusions

We reported the results from a coordinated multi-instrument observation of the TeV BL Lac Mrk 501 between March and May 2008. This MW campaign was planned regardless of the activity of source to perform an unbiassed (by the high-activity) characterization of the broadband emission.

Mrk 501 was found to be in a relatively low state of activity with a VHE γ-ray flux of about 20% the Crab nebula flux. Nevertheless, significant flux variations were measured in several energy bands, and a trend of variability increasing with energy was also observed. We found a positive correlation between the activity of the source in the X-ray and VHE γ-ray bands. The significance of this correlation was estimated with two independent methods: (i) the prescription given in Edelson & Krolik (1988); and (ii) a tailored Monte Carlo approach based on Uttley et al. (2002). In both cases we found a marginally significant (~3σ) positive correlation with zero time lag. A X-ray to VHE correlation for Mrk 501 has been reported many times in the past during flaring (high) X-ray/VHE activity (e.g., Krawczynski et al. 2000; Tavecchio et al. 2001; Gliozzi et al. 2006; Albert et al. 2007a); but this is the first time that this behavior is reported for such a low X-ray/VHE state. Therefore this result suggests that the mechanisms dominating the X-ray/VHE emission during non-flaring activity do not differ substantially from those that are responsible for the emission during flaring activity.

We also showed that a homogeneous one-zone synchrotron self-Compton model can describe the Mrk 501 SEDs measured during the two slightly different emission states observed during this campaign. The difference between the low (P1) and the slightly higher (P2 and P3) emission states can be adequately modeled by changing the shape of the electron energy distribution. But given the small variations in the broad band SED, other combination of SSC parameter changes may also be able to describe the observations.

Acknowledgements. We are grateful to the referee, who helped us to improve the quality of this manuscript. The authors acknowledge the valuable contribution from Daniel Kranich during the preparation of the multi-instrument observations, as well as in the first steps towards the data reduction and interpretation. We would like to thank the Instituto de Astrofísica de Canarias for the excellent working conditions at the Observatorio del Roque de los Muchachos in La Palma. The support of the German BMBF and MPG, the Italian INFN, the Swiss National Fund SNF, and the Spanish MICINN is gratefully acknowledged. This work was also supported by the CPAN CSD2007-00042 and MultiDark CSD2009-00064 projects of the Spanish Consolider-Ingenio 2010 programme, by grant DO02-353 of the Bulgarian NSF, by grant 127740 of the Academy of Finland, by Projekt 09/176 of the Croatian science Foundation, by the DFG Cluster of Excellence "Origin and Structure of the Universe", by the DFG Collaborative Research Centers SFB823/C4 and SFB876/C3, and by the Polish MNiSzW grant 745/N-HESS-MAGIC/2010/0. This research is supported by grants from the US Department of Energy Office of Science, the US National Science Foundation and the Smithsonian Institution, by NSERC in Canada, by Science Foundation Ireland (SFI 10/RFP/AST2748) and by STFC in the UK. We acknowledge the excellent work of the technical support staff at the *Fred Lawrence Whipple* Observatory and at the collaborating institutions in the construction and operation of the instrument. The St. Petersburg University team acknowledges support from Russian RFBR foundation, grant 12-02-00452. The Abastumani Observatory team acknowledges financial support by the Georgian National Science Foundation through grant GNSF/ST07/180. The Metsähovi team acknowledges the support from the Academy of Finland to our observing projects (numbers 212656, 210338, 121148, and others). The RATAN-600 observations were carried out with financial support of the Ministry of Education and Science of the Russian Federation (contract 14.518.11.7054), partial support from the Russian Foundation for Basic Research (grant 13-02-12103) is also acknowledged. We also acknowledge the use of public data from the *Swift* and RXTE data archive.

[7] The second break in the EED used in Abdo et al. (2011) was related to the synchrotron cooling of the electrons.

Appendix A: X-ray and γ-ray spectra

This section reports the spectral parameters resulting from the fit to the X-ray and γ-ray spectra.

Table A.1. Parameters resulting from the fit with a log-parabola $F(E) = K \cdot (E/\text{keV})^{-\alpha-\beta \cdot \log(E/\text{keV})}$ to the *Swift*/XRT spectra.

Period	K [10^{-2} cm^{-2} s^{-1} keV^{-1}]	α	β	χ^2/n.d.f.
P1	2.65 ± 0.03	2.01 ± 0.01	0.24 ± 0.03	331/308
P2	3.12 ± 0.03	1.85 ± 0.01	0.23 ± 0.02	322/336
P3	3.23 ± 0.03	1.87 ± 0.01	0.26 ± 0.02	409/354

Table A.2. Parameters resulting from the fit with a power law $F(E) = K \cdot (E/\text{keV})^{-\alpha}$ to the RXTE/PCA spectra.

Period	K [10^{-2} cm^{-2} s^{-1} keV^{-1}]	α	χ^2/n.d.f.
P1	4.36 ± 0.21	2.36 ± 0.03	24/19
P2	4.69 ± 0.18	2.19 ± 0.02	18/19
P3	4.78 ± 0.10	2.23 ± 0.01	24/19

Table A.3. Parameters resulting from the fit with a power law $F(E) = K \cdot (E/\text{TeV})^{-\alpha}$ to the measured MAGIC spectra (without correction for the EBL absorption).

Period	K [10^{-12} cm^{-2} s^{-1} TeV^{-1}]	α	χ^2/n.d.f.
P1	5.3 ± 0.5	2.49 ± 0.20	5/3
P2	9.1 ± 0.8	2.44 ± 0.17	5/3
P3	7.7 ± 0.3	2.37 ± 0.05	9/4
All	7.4 ± 0.2	2.42 ± 0.05	2/4

Table A.4. Parameters resulting from the fit with a power law $F(E) = K \cdot (E/\text{TeV})^{-\alpha}$ to the measured VERITAS spectra (without correction for the EBL absorption).

Period	K [10^{-12} cm^{-2} s^{-1} TeV^{-1}]	α	χ^2/n.d.f.
P1	–	–	–
P2	6.0 ± 0.9	2.55 ± 0.22	2/4
P3	8.7 ± 1.5	2.44 ± 0.28	1/4
All	9.4 ± 0.6	2.47 ± 0.10	13/8

References

Abdo, A. A., Ackermann, M., Ajello, M., et al. 2010, ApJ, 722, 520
Abdo, A. A., Ackermann, M., Ajello, M., et al. 2011, ApJ, 727, 129
Acciari, V. A., Beilicke, M., Blaylock, G., et al. 2008, ApJ, 679, 1427
Acciari, V. A., Arlen, T., Aune, T., et al. 2011, ApJ, 729, 2
Aharonian, F., Akhperjanian, A. G., Barrio, J. A., et al. 1999, A&A, 342, 69
Aharonian, F., Akhperjanian, A., Barrio, J., et al. 2001a, A&A, 370, 112
Aharonian, F., Akhperjanian, A., Barrio, J., et al. 2001b, ApJ, 546, 898
Ajello, M., Rau, A., Greiner, J., et al. 2008, ApJ, 673, 96
Ajello, M., Costamante, L., Sambruna, R. M., et al. 2009, ApJ, 699, 603
Albert, J, Aliu, E., Anderhub, H., et al. 2007a, ApJ, 669, 862
Albert, J., Aliu, E., Anderhub, H., et al. 2007b, Nucl. Instr. Meth., 583, A494
Albert, J., Aliu, E., Anderhub, H., et al. 2008a, Nucl. Instr. Meth., 588, A424
Albert, J., Aliu, E., Anderhub, H., et al. 2008b, ApJ, 674, 1037
Aleksić, J., Alvarez, E. A., Antonelli, L. A., et al. 2012, Astropart. Phys., 35, 435
Aliu, E., Anderhub, H., Antonelli, L. A., et al. 2009, Astropart. Phys., 30, 293
Aller, H. D., Aller, M. F., Latimer, G. E., & Hodge, P. E. 1985, ApJS, 59, 513
Angelakis, E., Fuhrmann, L., Marchili, N., Krichbaum, T. P., & Zensus, J. A. 2008, Mem. Soc. Astron. It., 79, 1042
Barthelmy, S. D., Barbier, L. M., Cummings, J. R., et al. 2005, Space Sci. Rev., 120, 143
Bradt, H. V., Rothschild, R. E., & Swank, J. H. 1993, A&AS, 97, 355
Burrows, D. N., Hill, J. E., Nousek, J. A., et al. 2005, Space Sci. Rev., 120, 165
Celotti, A., & Ghisellini, G. 2008, MNRAS, 385, 283
Chatterjee, R., Bailyn, C. D., Bonning, E. W., et al. 2012, ApJ, 749, 191
Domínguez, A., Primack, J. R., Rosario, D. J., et al. 2011, MNRAS, 410, 2556
Edelson, R. A., & Krolik, J. H. 1988, ApJ, 333, 646
Edelson, R., Turner, T. J., Pounds, K., et al. 2002, ApJ, 568, 610
Finke, J. D., Razzaque, S., & Dermer, C. D. 2010, ApJ, 712, 238
Fitzpatrick, E. L. 1999, PASP, 111, 63
Franceschini, A., Rodighiero, G., & Vaccari, M. 2008, A&A, 487, 837
Fuhrmann, L., Krichbaum, T. P., Witzel, A., et al. 2008, A&A, 490, 1019
Fukugita, M., Shimasaku, K., & Ichikawa, T. 1995, PASP, 107, 945
Gehrels, N., Chincarini, G., Giommi, P., et al. 2004, ApJ,611, 1005
Gliozzi, M., Sambruna, R. M., Jung, I., et al. 2006, ApJ, 646, 61
Katarzynski, K., Sol, H., & Kus, A. 2001, A&A, 367, 809
Kataoka, J., Mattox, J. R., Quinn, J., et al. 1999, ApJ, 514, 138
Kataoka, J., Takahashi, T., Wagner, S. J., et al. 2001, ApJ, 560, 659
Kovalev, Y. Y., Nizhelsky, N. A., Kovalev, Y. A., et al. 1999, A&AS, 139, 545
Kovalev, Y. Y., Kellermann, K. I., Lister, M. L., et al. 2005, AJ, 130, 2473
Kalberla, , P. M. W., Burton, W. B., Hartmann, D., et al. 2005, A&A 440, 775
Krawczynski, H., Coppi, P. S., Maccarone, T., & Aharonian, F. A. 2000, A&A, 353, 97
Lobanov, A. P. 2005 [arXiv:astro-ph/0503225]
Mankuzhiyil, N., Ansoldi, S., Persic, M., & Tavecchio, F. 2011, ApJ, 733, 14
Mankuzhiyil, N., Ansoldi, S., Persic, M., et al. 2012, ApJ, 753, 154
Maraschi, L., & Tavecchio, F. 2003, ApJ, 593, 667
Massaro, E. Perri, M., Giommi, P., et al. 2004, A&A, 422, 103
Nilsson, K., Pasanen, M., Takalo, L. O., et al. 2007, A&A, 475, 199
Perkins, J. S., Maier, G., & The VERITAS Collaboration 2009, Proc. Fermi Symp., Washington, D.C., eConf C091122 [arXiv:0912.3841]
Pian, E., Vacanti, G., Tagliaferri, G., et al. 1998, ApJ, 492, L17
Poole, T. S., Breeveld, A. A., Page, M. J., et al. 2008, MNRAS, 383, 627
Poutanen, J., Zdziarski, A. A., & Ibragimov, A. 2008, MNRAS, 389, 1427
Quinn, J., Akerlof, C. W., Biller, S., et al. 1996, ApJ, 456, L83
Quinn, J., Bond, I. H., Boyle, P. J., et al. 1999, ApJ, 518, L693
Roming, P. W. A., Kennedy, T. E., Mason, K. O., et al. 2005, Space Sci. Rev., 120, 95
Sambruna, R. M., Aharonian, F. A., Krawczynski, H., et al. 2000, ApJ, 538, 127
Schlegel, D. J., Finkbeiner, D. P., & Davis, M. 1998, ApJ, 500, 525
Stroh, M. C., & Falcone, A. D. 2013, ApJS, 207, 28
Tavecchio, F., Maraschi, L., & Ghisellini, G. 1998, ApJ, 509, 608
Tavecchio, F., Maraschi, L., Pian, E., et al. 2001, ApJ, 554, 725
Teräsranta, H., Edelson, R., Warwick, R. S., & Uttley, P., et al. 1998, A&AS, 132, 305
Timmer, J., & Koenig, M. 1995, A&A, 300, 707
Uttley, P., McHardy, I. M., & Papadakis, I. E. 2002, MNRAS, 332, 231
Uttley, P., Edelson, R., McHardy, I. M., Peterson, B. M., & Markowitz, A. 2003, ApJ, 584, L53
Vaughan, S., Edelson, R., Warwick, R. S., et al. 2003, MNRAS, 345, 1271
Venturi, T., Dallacasa, D., Orfei, A., et al. 2001, A&A, 379, 755
Villata, M., & Raiteri, C. M. 1999, A&A, 347, 30
Villata, M., Raiteri, C. M., Lanteri, L., Sobrito, G., & Cavallone, M. 1998, A&AS, 130, 305
Villata, M., Raiteri, C. M., Larionov, V. M., et al. 2008, A&A, 481, L79
Villata, M., Raiteri, C. M., Gurwell, M. A., et al. 2009, A&A, 504, L9
Zanin, R., et al. 2013, Proc. 33rd ICRC, Rio de Janeiro, Brasil

[1] IFAE, Edifici Cn., Campus UAB, 08193 Bellaterra, Spain
[2] Università di Udine, and INFN Trieste, 33100 Udine, Italy
[3] INAF National Institute for Astrophysics, 00136 Rome, Italy
[4] Università di Siena, and INFN Pisa, 53100 Siena, Italy
[5] Croatian MAGIC Consortium, Rudjer Boskovic Institute, University of Rijeka and University of Split, 10000 Zagreb, Croatia
[6] Max-Planck-Institut für Physik, 80805 München, Germany
[7] Universidad Complutense, 28040 Madrid, Spain
[8] Inst. de Astrofísica de Canarias, 38200 La Laguna, Tenerife, Spain
[9] University of Lodz, 90236 Lodz, Poland
[10] Deutsches Elektronen-Synchrotron (DESY), 15738 Zeuthen, Germany
[11] ETH Zurich, 8093 Zurich, Switzerland
[12] Universität Würzburg, 97074 Würzburg, Germany
[13] Centro de Investigaciones Energéticas, Medioambientales y Tecnológicas, 28040 Madrid, Spain
[14] Technische Universität Dortmund, 44221 Dortmund, Germany

[15] Inst. de Astrofísica de Andalucía (CSIC), 18080 Granada, Spain
[16] Università di Padova and INFN, 35131 Padova, Italy
[17] Università dell'Insubria, Como, 22100 Como, Italy
[18] Unitat de Física de les Radiacions, Departament de Física, and CERES-IEEC, Universitat Autònoma de Barcelona, 08193 Bellaterra, Spain
[19] Institut de Ciències de l'Espai (IEEC-CSIC), 08193 Bellaterra, Spain
[20] Finnish MAGIC Consortium, Tuorla Observatory, University of Turku and Department of Physics, University of Oulu, 900147 Oulu, Finland
[21] Japanese MAGIC Consortium, Division of Physics and Astronomy, Kyoto University, 606-8501 Kyoto, Japan
[22] Inst. for Nucl. Research and Nucl. Energy, 1784 Sofia, Bulgaria
[23] Universitat de Barcelona (ICC/IEEC), 08028 Barcelona, Spain
[24] Università di Pisa, and INFN Pisa, 56126 Pisa, Italy
[25] Now at École polytechnique fédérale de Lausanne (EPFL), Lausanne, Switzerland
[26] Now at Department of Physics & Astronomy, UC Riverside, CA 92521, USA
[27] Now at Finnish Centre for Astronomy with ESO (FINCA), Turku, Finland
[28] Also at INAF-Trieste
[29] Also at Instituto de Fisica Teorica, UAM/CSIC, 28049 Madrid, Spain
[30] Now at Stockholms universitet, Oskar Klein Centre for Cosmoparticle Physics
[31] Now at GRAPPA Institute, University of Amsterdam, 1098 XH Amsterdam, The Netherlands
[32] Department of Physics, Washington University, St. Louis, MO 63130, USA
[33] Fred Lawrence Whipple Observatory, Harvard-Smithsonian Center for Astrophysics, Amado, AZ 85645, USA
[34] Department of Physics and Astronomy and the Bartol Research Institute, University of Delaware, Newark, DE 19716, USA
[35] School of Physics, University College Dublin, Belfield, Dublin 4, Ireland
[36] Santa Cruz Institute for Particle Physics and Department of Physics, University of California, Santa Cruz, CA 95064, USA
[37] Institute of Physics and Astronomy, University of Potsdam, 14476 Potsdam-Golm, Germany
[38] Astronomy Department, Adler Planetarium and Astronomy Museum, Chicago, IL 60605, USA
[39] Department of Physics, Purdue University, West Lafayette, IN 47907, USA
[40] Department of Physics, Grinnell College, Grinnell, IA 50112-1690, USA
[41] School of Physics and Astronomy, University of Minnesota, Minneapolis, MN 55455, USA
[42] Department of Astronomy and Astrophysics, 525 Davey Lab, Pennsylvania State University, University Park, PA 16802, USA
[43] School of Physics, National University of Ireland Galway, University Road, Galway, Ireland
[44] Physics Department, McGill University, Montreal, QC H3A 2T8, Canada
[45] Department of Physics and Astronomy, University of Iowa, Van Allen Hall, Iowa City, IA 52242, USA
[46] Department of Physics and Astronomy, DePauw University, Greencastle, IN 46135-0037, USA
[47] Department of Physics and Astronomy, University of Utah, Salt Lake City, UT 84112, USA
[48] Department of Physics and Astronomy, Iowa State University, Ames, IA 50011, USA
[49] Department of Physics and Astronomy, University of California, Los Angeles, CA 90095, USA
[50] Saha Institute of Nuclear Physics, 700064 Kolkata, India
[51] School of Physics and Center for Relativistic Astrophysics, Georgia Institute of Technology, 837 State Street NW, Atlanta, GA 30332-0430, USA
[52] Department of Life and Physical Sciences, Galway-Mayo Institute of Technology, Dublin Road, Galway, Ireland
[53] Department of Physics and Astronomy, Barnard College, Columbia University, NY 10027, USA
[54] Physics Department, Columbia University, New York, NY 10027, USA
[55] Instituto de Astronomia y Fisica del Espacio, Casilla de Correo 67 – Sucursal 28, (C1428ZAA) Ciudad Autnoma de Buenos Aires, Argentina
[56] Physics Department, California Polytechnic State University, San Luis Obispo, CA 94307, USA
[57] Department of Applied Physics and Instrumentation, Cork Institute of Technology, Bishopstown, Cork, Ireland
[58] Enrico Fermi Institute, University of Chicago, Chicago, IL 60637, USA
[59] Argonne National Laboratory, 9700 S. Cass Avenue, Argonne, IL 60439, USA
[60] INAF, Osservatorio Astronomico di Torino, 10025 Pino Torinese (TO), Italy
[61] Space Sciences Laboratory, 7 Gauss Way, University of California, Berkeley, CA 94720-7450, USA
[62] ASI-Science Data Center, via del Politecnico, 00133 Rome, Italy
[63] Department of Astronomy, University of Michigan, Ann Arbor, MI 48109-1042, USA
[64] Astron. Inst., St.-Petersburg State Univ., 198504 St. Petersburg, Russia
[65] Pulkovo Observatory, 196140 St. Petersburg, Russia
[66] Isaac Newton Institute of Chile, St.-Petersburg Branch, Russia
[67] Graduate Institute of Astronomy, National Central University, 300 Jhongda Rd., 32001 Jhongli, Taiwan
[68] Moscow M.V. Lomonosov State University, Sternberg Astronomical Institute, Russia
[69] Abastumani Observatory, Mt. Kanobili, 0301 Abastumani, Georgia
[70] Landessternwarte, Zentrum für Astronomie der Universität Heidelberg, Königstuhl 12, 69117 Heidelberg, Germany
[71] School of Cosmic Physics, Dublin Institute For Advanced Studies, Ireland
[72] INAF–Osservatorio Astrofisico di Catania, Italy
[73] Aalto University Metsähovi Radio Observatory Metsähovintie 114, 02540 Kylmälä, Finland
[74] Finnish Centre for Astronomy with ESO (FINCA) University of Turku Väisäläntie 20, 21500 Piikkiö, Finland
[75] INAF Istituto di Radioastronomia, 40129 Bologna, Italy
[76] University of Trento, Department of Physics, 38050 Povo, Trento, Italy
[77] Max-Planck-Institut für Radioastronomie, Auf dem Hügel 69, 53121 Bonn, Germany
[78] Astro Space Center of the Lebedev Physical Institute, 117997 Moscow, Russia
[79] Engelhardt Astronomical Observatory, Kazan Federal University, Tatarstan, Russia
[80] Aalto University Department of Radio Science and Engineering, PO Box 13000, 00076 Aalto, Finland

A&A 578, A22 (2015)
DOI: 10.1051/0004-6361/201424811

Astronomy & Astrophysics

Unprecedented study of the broadband emission of Mrk 421 during flaring activity in March 2010⋆,⋆⋆

J. Aleksić[1], S. Ansoldi[2], L. A. Antonelli[3], P. Antoranz[4], A. Babic[5], P. Bangale[6], U. Barres de Almeida[6,25], J. A. Barrio[7], J. Becerra González[8,26,27], W. Bednarek[9], E. Bernardini[10], B. Biasuzzi[2], A. Biland[11], O. Blanch[1], A. Boller[11], S. Bonnefoy[7], G. Bonnoli[3], F. Borracci[6], T. Bretz[12,28], E. Carmona[13], A. Carosi[3], P. Colin[6], E. Colombo[8], J. L. Contreras[7], J. Cortina[1], S. Covino[3], P. Da Vela[4], F. Dazzi[6], A. De Angelis[2], G. De Caneva[10], B. De Lotto[2], E. de Oña Wilhelmi[14], C. Delgado Mendez[13], D. Dominis Prester[5], D. Dorner[12], M. Doro[15], S. Einecke[16], D. Eisenacher[12], D. Elsaesser[12], M. V. Fonseca[7], L. Font[17], K. Frantzen[16], C. Fruck[6], D. Galindo[18], R. J. García López[8], M. Garczarczyk[10], D. Garrido Terrats[17], M. Gaug[17], N. Godinović[5], A. González Muñoz[1], S. R. Gozzini[10], D. Hadasch[14,29], Y. Hanabata[19], M. Hayashida[19], J. Herrera[8], D. Hildebrand[11], J. Hose[6], D. Hrupec[5], G. Hughes[10], W. Idec[9], V. Kadenius, H. Kellermann[6], M. L. Knoetig[11], K. Kodani[19], Y. Konno[19], J. Krause[6], H. Kubo[19], J. Kushida[19], A. La Barbera[3], D. Lelas[5], N. Lewandowska[12], E. Lindfors[20,30], S. Lombardi[3], M. López[7], R. López-Coto[1], A. López-Oramas[1], E. Lorenz[6], I. Lozano[7], M. Makariev[21], K. Mallot[10], G. Maneva[21], N. Mankuzhiyil[2,31], K. Mannheim[12], L. Maraschi[3], B. Marcote[18], M. Mariotti[15], M. Martínez[1], D. Mazin[6], U. Menzel[6], J. M. Miranda[4], R. Mirzoyan[6], A. Moralejo[1], P. Munar-Adrover[18], D. Nakajima[19], A. Niedzwiecki[9], K. Nilsson[20,30], K. Nishijima[19], K. Noda[6], R. Orito[19], A. Overkemping[16], S. Paiano[15], M. Palatiello[2], D. Paneque[6,⋆⋆⋆], R. Paoletti[4], J. M. Paredes[18], X. Paredes-Fortuny[18], M. Persic[2,⋆⋆⋆⋆], P. G. Prada Moroni[22], E. Prandini[11], I. Puljak[5], R. Reinthal[20], W. Rhode[16], M. Ribó[18], J. Rico[1], J. Rodriguez Garcia[6], S. Rügamer[12], T. Saito[19], K. Saito[19], K. Satalecka[7], V. Scalzotto[15], V. Scapin[7], C. Schultz[15], T. Schweizer[6], S. Sun[6,⋆⋆⋆], S. N. Shore[22], A. Sillanpää[20], J. Sitarek[1], I. Snidaric[5], D. Sobczynska[9], F. Spanier[12], V. Stamatescu[1,32], A. Stamerra[3], T. Steinbring[12], B. Steinke[6], J. Storz[12], M. Strzys[6], L. Takalo[20], H. Takami[19,⋆⋆⋆], F. Tavecchio[3], P. Temnikov[21], T. Terzić[5], D. Tescaro[8], M. Teshima[6], J. Thaele[16], O. Tibolla[12], D. F. Torres[23], T. Toyama[6], A. Treves[24], M. Uellenbeck[16], P. Vogler[11], R. Zanin[18],
(The MAGIC Collaboration)
S. Archambault[33], A. Archer[34], M. Beilicke[34], W. Benbow[35], K. Berger[36], R. Bird[37], J. Biteau[38], J. H. Buckley[34], V. Bugaev[34], M. Cerruti[35], X. Chen[39,10], L. Ciupik[40], E. Collins-Hughes[37], W. Cui[41], J. D. Eisch[42], A. Falcone[43], Q. Feng[41], J. P. Finley[41], P. Fortin[35], L. Fortson[44], A. Furniss[38], N. Galante[35], G. H. Gillanders[45], S. Griffin[33], G. Gyuk[40], N. Håkansson[39], J. Holder[36], C. A. Johnson[38], P. Kaaret[46], P. Kar[47], M. Kertzman[48], D. Kieda[47], M. J. Lang[45], S. McArthur[49], A. McCann[50], K. Meagher[51], J. Millis[52], P. Moriarty[45,53], R. A. Ong[54], A. N. Otte[51], J. S. Perkins[26,27], A. Pichel[55], M. Pohl[39,10], A. Popkow[54], H. Prokoph[10], E. Pueschel[37], K. Ragan[33], L. C. Reyes[56], P. T. Reynolds[57], G. T. Richards[51], E. Roache[35], A. C. Rovero[55], G. H. Sembroski[41], K. Shahinyan[44], D. Staszak[33], I. Telezhinsky[39,10], J. V. Tucci[41], J. Tyler[33], A. Varlotta[41], S. P. Wakely[49], R. Welsing[10], A. Wilhelm[39,10], D. A. Williams[38],
(The VERITAS Collaboration)
S. Buson[15], J. Finke[58], M. Villata[59], C. Raiteri[59], H. D. Aller[60], M. F. Aller[60], A. Cesarini[61], W. P. Chen[62], M. A. Gurwell[63], S. G. Jorstad[64,65], G. N. Kimeridze[67], E. Koptelova[62,66], O. M. Kurtanidze[67,68], S. O. Kurtanidze[67], A. Lähteenmäki[69,70], V. M. Larionov[71,72,73], E. G. Larionova[71], H. C. Lin[62], B. McBreen[37], J. W. Moody[74], D. A. Morozova[71], A. P. Marscher[64], W. Max-Moerbeck[75], M. G. Nikolashvili[67], M. Perri[3,76], A. C. S. Readhead[75], J. L. Richards[41], J. A. Ros[77], A. C. Sadun[78], T. Sakamoto[79], L. A. Sigua[67], P. S. Smith[80], M. Tornikoski[69], I. S. Troitsky[71], A. E. Wehrle[81], and B. Jordan[82]

(Affiliations can be found after the references)

Received 14 August 2014 / Accepted 5 December 2014

ABSTRACT

Context. Because of its proximity, Mrk 421 is one of the best sources on which to study the nature of BL Lac objects. Its proximity allows us to characterize its broadband spectral energy distribution (SED).

Aims. The goal is to better understand the mechanisms responsible for the broadband emission and the temporal evolution of Mrk 421. These mechanisms may also apply to more distant blazars that cannot be studied with the same level of detail.

Methods. A flare occurring in March 2010 was observed for 13 consecutive days (from MJD 55 265 to MJD 55 277) with unprecedented wavelength coverage from radio to very high energy (VHE; $E > 100$ GeV) γ-rays with MAGIC, VERITAS, *Whipple*, *Fermi*-LAT, MAXI, RXTE, *Swift*, GASP-WEBT, and several optical and radio telescopes. We modeled the day-scale SEDs with one-zone and two-zone synchrotron self-Compton (SSC) models, investigated the physical parameters, and evaluated whether the observed broadband SED variability can be associated with variations in the relativistic particle population.

Results. The activity of Mrk 421 initially was high and then slowly decreased during the 13-day period. The flux variability was remarkable at the X-ray and VHE bands, but it was minor or not significant at the other bands. The variability in optical polarization was also minor. These observations revealed an almost linear correlation between the X-ray flux at the 2–10 keV band and the VHE γ-ray flux above 200 GeV, consistent with the γ-rays being produced by inverse-Compton scattering in the Klein-Nishina regime in the framework of SSC models. The one-zone

⋆ Appendices are available in electronic form at http://www.aanda.org

⋆⋆ Multi-wavelength light curves (data in Fig. 1) and broadband spectral energy distributions (the data in Figs. 7, 8a–9f, 12a–13f) are only available at the CDS via anonymous ftp to cdsarc.u-strasbg.fr (130.79.128.5) or via http://cdsarc.u-strasbg.fr/viz-bin/qcat?J/A+A/578/A22

⋆⋆⋆ Corresponding author: David Paneque, e-mail: dpaneque@mpp.mpg.de; Shangyu Sun, e-mail: sysun@mpp.mpg.de; Hajime Takami, e-mail: takami@post.kek.jp

⋆⋆⋆⋆ Also at INAF-Trieste, via Tiepolo Gianbattiste 11, 34131 Trisete.

SSC model can describe the SED of each day for the 13 consecutive days reasonably well, which once more shows the success of this standard theoretical scenario to describe the SEDs of VHE BL Lacs such as Mrk 421. This flaring activity is also very well described by a two-zone SSC model, where one zone is responsible for the quiescent emission, while the other smaller zone, which is spatially separated from the first, contributes to the daily variable emission occurring at X-rays and VHE γ-rays. The second blob is assumed to have a smaller volume and a narrow electron energy distribution with $3 \times 10^4 < \gamma < 6 \times 10^5$, where γ is the Lorentz factor of the electrons. Such a two-zone scenario would naturally lead to the correlated variability at the X-ray and VHE bands without variability at the optical/UV band, as well as to shorter timescales for the variability at the X-ray and VHE bands with respect to the variability at the other bands.

Conclusions. Both the one-zone and the two-zone SSC models can describe the daily SEDs via the variation of only four or five model parameters, under the hypothesis that the variability is associated mostly with the underlying particle population. This shows that the particle acceleration and cooling mechanism that produces the radiating particles might be the main mechanism responsible for the broadband SED variations during the flaring episodes in blazars. The two-zone SSC model provides a better agreement with the observed SED at the narrow peaks of the low- and high-energy bumps during the highest activity, although the reported one-zone SSC model could be further improved by varying the parameters related to the emitting region itself (δ, B and R), in addition to the parameters related to the particle population.

Key words. radiation mechanisms: non-thermal – galaxies: active – BL Lacertae objects: individual: Mrk 421 – gamma rays: galaxies

1. Introduction

Markarian 421 (Mrk 421; RA = $11^{\mathrm{h}}4'27.31''$, Dec = $38°12'31.8''$, J2000) is a BL Lac object that is believed to have a pair of relativistic jets flowing in opposite directions closely aligned to our line of sight. It is also one of the closest (z = 0.031; de Vaucouleurs et al. 1991) and brightest BL Lac objects in the extragalactic X-ray and very high energy (VHE; E > 100 GeV) sky. This object was the first BL Lac object detected by the Energetic Gamma Ray Experiment Telescope (EGRET; Lin et al. 1992) at energies above 100 MeV, and was also the first extragalactic source detected by imaging atmospheric Cherenkov telescopes (IACTs; Punch et al. 1992). Mrk 421 is one of the best-studied BL Lac objects at VHE because it can be detected by modern IACTs within several minutes, and its broadband spectral energy distribution (SED) can be well measured by operating instruments covering energies from radio to VHE. Nearly all the IACTs have measured its VHE γ-ray spectrum (Krennrich et al. 2002; Aharonian et al. 2003, 2002; Okumura et al. 2002; Aharonian et al. 2005; Albert et al. 2007a).

The SED of a blazar is dominated by the emission of the jet components magnified by relativistic beaming. The observed spectrum and polarization indicate that the low-energy bump is synchrotron radiation of electrons in turbulent magnetic fields in the jet. Mrk 421 has a peak frequency of the low-energy bump above 10^{15} Hz, and therefore it is categorized as a high-synchrotron-peaked (HSP) BL Lac object based on the classification criterion presented in Abdo et al. (2010). The peak frequency of the high-energy bump for HSP blazars detected at VHE is usually below 100 GeV[1]. This bump may be interpreted as the inverse-Compton scattering of the same population of electrons off synchrotron photons (synchrotron self-Compton, SSC; Maraschi et al. 1992; Dermer & Schlickeiser 1993; Bloom & Marscher 1996). Alternatively, hadronic models can also explain this bump (e.g., Mannheim 1993; Mücke et al. 2003). Although both leptonic and hadronic models can reproduce the time-averaged broadband SED of Mrk 421 (e.g. Abdo et al. 2011), it is difficult to produce short-time variability (<1 h) with hadronic models, which has been observed in Mrk 421 (e.g. Gaidos et al. 1996). Thus, leptonic models are favored, at least in active states. A recent study on Mrk 421 also supports leptonic models during low blazar activity (Aleksić et al. 2015). In leptonic scenarios, one-zone SSC models with an electron distribution described by one or two power-law functions can typically describe the observed SEDs (e.g., Katarzyński et al. 2003; Błażejowski et al. 2005; Rebillot et al. 2006; Fossati et al. 2008; Horan et al. 2009).

Because Mrk 421 is bright and highly variable, long-term multiwavelength (MW) monitoring campaigns have been organized to intensely study its SED and its temporal evolution from radio to VHE γ-rays. Since 2009, an exceptionally long and dense monitoring of the broadband emission of Mrk 421 has been performed. The results of the 2009 MW campaign, which is related to Mrk 421 during nonflaring (typical) activity, were reported in Abdo et al. (2011). The SED was successfully modeled by both a leptonic and a hadronic model, but the authors commented that the hadronic model required extreme conditions for particle acceleration and confinement. Moreover, the densely sampled SED revealed that the leptonic one-zone SSC model required two breaks in the electron energy distribution (EED) to satisfactorily describe the smooth bumps in the quiescent state SED.

Mrk 421 showed high activity during the entire multi-instrument campaign in 2010. During the period from March 10 (modified Julian day [MJD] 55 265) to March 22 (MJD 55 277), the VHE activity decreased from a high flux ~2 Crab units (c.u.)[2] down to the typical value ~0.5 c.u (Acciari et al. 2014), hence offering the possibility of studying the evolution of the SED during the decay of a flaring event. The extensive MW data collected allow measuring the broadband SED over the largest available fraction of wavelengths with simultaneous observations (mostly within 2–3 h) during 13 consecutive days. The present study is unprecedented for any blazar. The SED and indicated physical parameters in the emission region at different epochs and their temporal evolution have been studied (e.g., Mankuzhiyil et al. 2011; Acciari et al. 2011; Aleksić et al. 2012a), but based on sparse sampling. The observational data for 13 consecutive days provide a first opportunity to directly study the temporal evolution of the SED.

In Sect. 2, we report the observations and data analysis performed with the various instruments. In Sect. 3 we present the observational results on multi-band variability. In Sect. 4, all the broadband SEDs during the flaring activity are characterized within two SSC models and physical parameters in emission regions are derived. In Sect. 5 we discuss the interpretation of the experimental results, and then we summarize this study in Sect. 6. Throughout this paper, the ΛCDM cosmology with H_0 = 71 km s^{-1}, Ω_{M} = 0.27, and Ω_{Λ} = 0.73 is adopted.

[1] See the TeV catalog at http://tevcat.uchicago.edu/

[2] The VHE flux of the Crab nebula between 200 GeV and 10 TeV used in this paper is 2.2×10^{-10} cm^{-2} s^{-1} (Aleksić et al. 2012b).

Table 1. Participating instruments in the campaign on Mrk 421 during 2010 March.

Instrument/Observatory	Energy range covered
MAGIC	0.08–5.0 TeV
VERITAS	0.2–5.0 TeV
Whipple 10-m	0.4–2.0 TeV
Fermi-LAT	0.1–400 GeV
Swift/BAT	14–195 keV
RXTE-PCA	3–32 keV
Swift-XRT	0.3–10 keV
RXTE-ASM	2–10 keV
MAXI	2–10 keV
Swift-UVOT	*UVW1*, *UVM2*, *UVW2*
Abastumani[†]	*R* band
Lulin[†]	*R* band
Roque de los Muchachos (KVA)[†]	*R* band
St. Petersburg[†]	*R* band polarization
Sabadell[†]	*R* band
Goddard Robotic Telescope (GRT)	*R* band
The Remote Observatory for Variable Object Research (ROVOR)	*B*, *R*, *V* bands
New Mexico Skies (NMS)	*R*, *V* bands
Bradford Robotic Telescope (BRT)	*B*, *R*, *V* bands
Perkins	*R* band polarization
Steward	*R* band polarization
Crimean	*R* band polarization
Submillimeter Array (SMA)	225 GHz
Metsähovi Radio Observatory[†]	37 GHz
University of Michigan Radio Astronomy Observatory (UMRAO)[†]	8.0, 14.5 GHz
Owens Valley Radio Observatory (OVRO)	15 GHz

Notes. The energy range shown in Col. 2 is the actual energy range covered during the Mrk 421 observations, and not necessarily the nominal energy range of the instrument, which might only be achievable for bright sources and in excellent observing conditions. [(†)] Through GASP-WEBT program.

2. Observation and data analysis

All instruments that observed Mrk 421 during this campaign are listed in Table 1. The details of observations by each instrument are described below.

2.1. MAGIC

The Major Atmospheric Gamma-ray Imaging Cherenkov (MAGIC) telescope system consists of two 17-meter telescopes that are located on the island of La Palma, 2200 m above sea level. Stereo observation can provide a sensitivity of ~0.008 c.u. above ~300 GeV in 50 h of observation and allows detecting VHE photons between 50 GeV and 50 TeV. A detailed description of the performance of the MAGIC stereo system can be found in Aleksić et al. (2012b).

During this flare, MAGIC made 11 observations, all in stereoscopic mode. The exposure time ranged from ~10 to ~80 min, with the zenith angle ranging from 5 to 30 deg. In total we collected 4.7 h of good-quality data. The MAGIC data presented in this paper were taken in dark conditions and were not affected by bright moonlight. All these observations were conducted in the false-source-tracking (wobble) mode (Fomin et al. 1994): alternatively tracking two positions in the sky that are symmetric with respect to the true source position and 0.4° away from it. The MAGIC data on MJD 55 272 and 55 275 suffered from bad weather and occasional technical problems and were therefore removed from the analysis.

The MAGIC data were analyzed using the MAGIC Standard Analysis Software (MARS; Moralejo et al. 2010). In the analysis routine, signals are first calibrated and then an image-cleaning algorithm that involves the time structure of the shower images, and removes the contribution from the night sky background is applied. Afterward, the shower images are parameterized with an extended set of Hillas parameters (Hillas 1985), and another parameter, hadronness, to reject background showers resulting from charged cosmic rays. The hadronness is determined through a random forest classification (Breiman 2001), which is trained based on shower-image parameters and time information.

Then, all these parameters from the two telescopes are combined to reconstruct the arrival directions and energies of the γ-ray candidate events. The number of signal (excess) events is the number of events around the source position after subtracting the number of background events, which is estimated using the number of events in a source-free region. Flux and a preliminary spectrum are calculated based on this number. Finally, this preliminary spectrum is unfolded to correct for the effect of the limited energy resolution of the detector, as reported in Albert et al. (2007b), which leads to the final (true) observed VHE spectrum of the source.

The systematic uncertainties in the spectral measurements with MAGIC stereo observations are 11% in the normalization factor (at >300 GeV) and 0.15−0.20 in the photon index. The error on the flux does not include uncertainty on the energy scale. The energy scale of the MAGIC telescopes is determined with a precision of about 17% at low energies (E < 100 GeV) and 15% at medium energies (E > 300 GeV). Further details are reported in Aleksić et al. (2012b).

2.2. VERITAS

The Very Energetic Radiation Imaging Telescope Array System (VERITAS) is an array of four imaging atmospheric Cherenkov telescopes 12 m in diameter that are located in southern Arizona (Weekes et al. 2002) and are designed to detect emission from astrophysical objects in the energy range from ∼100 GeV to greater than 30 TeV. VERITAS has an energy resolution of ∼15% and an angular resolution (68% containment) of ∼0.1° per event at 1 TeV. A source with a flux of 0.01 c.u. is detected in ∼25 h of observations, while a 0.05 c.u. source is detected in less than 2 h. The field of view of the VERITAS cameras is 3.5°. For more details on the VERITAS instrument and its imaging atmospheric Cherenkov technique, see Perkins & Maier (2009).

VERITAS monitored Mrk 421 in March 2010 with a 10-min run each day on MJD 55 260, 55 265, 55 267−55 274. Observations were taken near culmination at zenith angles in the range 18°−23° to benefit from the lowest possible energy threshold. All data were taken in wobble mode where the telescopes are pointed away from the source by 0.5° north, south, east, and west to allow for simultaneous background estimation using events from the same field of view.

Before event selection and background subtraction, all shower images are calibrated and cleaned as described in Cogan (2006) and Daniel et al. (2007). Following the calibration and cleaning of the data, the events are parameterized using a moment analysis (Hillas 1985). From this moment analysis, scaled parameters are calculated and used to select the γ-ray-like events (Aharonian et al. 1997; Krawczynski et al. 2006). The event-selection cuts are optimized a priori for a Crab-like source (power-law spectrum photon index $\Gamma = 2.5$ and Crab nebula flux level).

2.3. Whipple 10 m

The *Whipple* 10 m γ-ray telescope was situated at the *Fred Lawrence Whipple* Observatory in southern Arizona. It operated in the 300 GeV to 20 TeV energy range, with a peak response energy (for a Crab-like spectrum) of approximately 400 GeV. The telescope had a 10 m optical reflector with a camera consisting of 379 photomultiplier tubes, covering a field of view of 2.6° (Kildea et al. 2007). The *Whipple* 10-m was decommissioned in July 2011.

The *Whipple* 10 m telescope made ten observations performed in the ON/OFF and TRK (tracking) modes, in which the telescope tracked the source, which was centered in the field of view, for 28 min (ON and TRK runs). The duration of the observations ranged from about one to six hours, with half of the observations more than four hours long. The corresponding OFF run was collected at an offset of 30 min from the source's right ascension for a period of 28 min. The two runs were taken at the same declination over the same range of telescope azimuth and elevation angles. This removed systematic errors that depend on slow changes in the atmosphere. In the TRK mode, only ON runs were taken without corresponding OFF observations, and the background was estimated from events whose major axis points away from the center of the camera (the source position). The data set amounts to 36 h and was analyzed using the University College Dublin analysis package as described in Acciari (2011). The photon fluxes, initially derived in Crab units for energies above 400 GeV, were converted into photon fluxes above 200 GeV using a Crab nebula flux of 2.2×10^{-10} cm^{-2} s^{-1} (Aleksić et al. 2012b). Because the spectrum of Mrk 421 is variable (and sometimes slightly harder or softer than that of the Crab nebula), this conversion could overestimate or underestimate the photon fluxes, but only at the level of ∼10%, which is not critical for the results reported in this paper.

2.4. Fermi-LAT

The *Fermi* Large Area Telescope (LAT) is a γ-ray telescope operating from 20 MeV to more than 300 GeV. The LAT is an array of 4 × 4 identical towers, each one consisting of a tracker (where the photons are pair-converted) and a calorimeter (where the energies of the pair-converted photons are measured). LAT has a large peak effective area (0.8 m^2 for 1 GeV photons), an energy resolution typically better than 10%, and a field of view of about 2.4 sr with an angular resolution (68% containment angle) better than 1° for energies above 1 GeV. Further details on the description of LAT are given in Atwood et al. (2009) and Ackermann et al. (2012). The analyses of the *Fermi*-LAT data were performed here with the ScienceTools software package version v9r32p5. We used the reprocessed *Fermi*-LAT events[3] belonging to the P7REP_SOURCE_V15 class that are located in a circular region of interest (ROI) of 10° radius around Mrk 421, after applying a cut of <52° in the rocking angle, and <100° on the zenith angle to reduce contamination from the γ-rays produced in the upper atmosphere and observed along Earth's limb. The background model used to extract the γ-ray signal includes a Galactic diffuse-emission component and an isotropic component. The model we adopted for the Galactic component is given by the file gll_iem_v05.fit, and the isotropic component, which is the sum of the extragalactic diffuse emission and the residual charged particle background, is parameterized by the file iso_source_v05.txt[4]. The normalizations of the two components in the background model were allowed to vary freely during the spectral-point fitting. The spectral parameters were estimated using the unbinned maximum-likelihood technique (Mattox et al. 1996) in the energy range 300 MeV to 300 GeV. We used the P7REP_SOURCE_V15 instrument response function[5] and took into account all the sources from the second *Fermi*-LAT catalog (2FGL, Nolan et al. 2012) that are located within 15° of Mrk 421. When performing the fit, the spectral parameters of sources within 10° of Mrk 421 were allowed to vary, while those between 10° and 15° were fixed to their values from the 2FGL. When performing the likelihood fit in differential energy bins (spectral bins in the SED), the photon indices of the sources were frozen to the best-fit values obtained from the full spectral analysis.

The sensitivity of *Fermi*-LAT is not good enough to detect Mrk 421 within a few hours, and hence we integrated over two days to have significant detections and to be able to produce γ-ray spectra. Despite the two-day integration window, the number of collected photons above 300 MeV is only about 8 to 15 for each of the two-day intervals. Most of these photons have energies below a few GeV, since photons above 10 GeV are rarely detected from Mrk 421 in a two-day interval. Upper limits at 95% confidence level were calculated for the differential energy bins whenever the maximum-likelihood test statistic (TS)[6] was below 4, or when the detected signal had fewer than two events. The systematic uncertainty in the flux is dominated by the systematic uncertainty in the effective area, which is estimated as 10% below 0.1 GeV, 5% in the energy range between 0.3 GeV and 10 GeV and 10% above 10 GeV(Ackermann et al. 2012).

[3] See http://fermi.gsfc.nasa.gov/ssc/data/analysis/documentation/Pass7REP_usage.html

[4] http://fermi.gsfc.nasa.gov/ssc/data/access/lat/BackgroundModels.html

[5] See http://fermi.gsfc.nasa.gov/ssc/data/analysis/

[6] The maximum-likelihood test statistic TS (Mattox et al. 1996) is defined as TS = $2\Delta \log(\text{likelihood})$ between models with and without a point source at the position of Mrk 421.

The systematic uncertainties are substantially smaller than the statistical uncertainties of the data points in the light curve and spectra.

2.5. X-ray observations

All 11 *Swift*-XRT (Burrows et al. 2005) observations were carried out using the windowed timing (WT) readout mode. The data set was first processed with the XRTDAS software package (v.2.9.3) developed at the ASI Science Data Center (ASDC) and distributed by HEASARC within the HEASoft package (v. 6.15.1)[7]. Event files were calibrated and cleaned with standard filtering criteria with the *xrtpipeline* task using the calibration files available in the *Swift*-XRT CALDB version *20140120*. Events for the spectral analysis were selected within a 20-pixel (~46 arcsec) radius, which encloses about 90% of the PSF, centered on the source position. The background was extracted from a nearby circular region of 40 pixel radius. The ancillary response files were generated with the *xrtmkarf* task applying corrections for PSF losses and CCD defects using the cumulative exposure map. Before the spectral fitting, the 0.3−10 keV source energy spectra were binned to ensure a minimum of 20 counts per bin. The spectra were corrected for absorption with a neutral hydrogen column density fixed to the Galactic 21 cm value in the direction of Mrk 421, namely 1.9×10^{20} cm^{-2} (Kalberla et al. 2005).

The *Rossi* X-ray Timing Explorer (RXTE; Bradt et al. 1993) satellite performed daily pointing observations of Mrk 421 during the time interval from MJD 55 265 to MJD 55 277. The data analysis was performed using `FTOOLS` v6.9 and following the procedures and filtering criteria recommended by the NASA RXTE Guest Observer Facility[8]. The observations were filtered following the conservative procedures for faint sources. Only the first xenon layer of PCU2 was used. We used the package `pcabackest` to model the background and the package `saextrct` to produce spectra for the source and background files and the script[9] `pcarsp` to produce the response matrix. The PCA average spectra above 3 keV were fitted using the XSPEC package using a power-law function with an exponential cutoff (cutoffpl) with the same neutral hydrogen column density as was used in the *Swift*-XRT data analysis. However, since the PCA bandpass starts at 3 keV, the results do not depend strongly on the column density adopted.

We also used data from the all-sky X-ray instruments available in 2010, namely RXTE/ASM, MAXI, and *Swift*/BAT. The data from RXTE/ASM were obtained from the ASM web page[10] and were filtered according to the prescription provided in the ASM web page. The daily fluxes from *Swift*/BAT were gathered from the BAT web page[11] and the daily fluxes from MAXI were retrieved from a dedicated MAXI web page[12].

[7] `http://heasarc.gsfc.nasa.gov/docs/software/lheasoft/download.html`

[8] `http://heasarc.gsfc.nasa.gov/docs/xte/xhp_proc_analysis.html`

[9] The CALDB files are located at `http://heasarc.gsfc.nasa.gov/FTP/caldb`

[10] See `http://xte.mit.edu/ASM_lc.html`

[11] See `http://swift.gsfc.nasa.gov/docs/swift/results/transients/`

[12] See `http://maxi.riken.jp/top/index.php?cid=1&jname=J1104+382`

2.6. Optical and UV observations

The optical fluxes reported in this paper were obtained within the GLAST-AGILE Support Program (GASP) within the Whole Earth Blazar Telescope (WEBT; e.g. Villata et al. 2008, 2009), with various optical telescopes around the globe. Additionally, many observations were performed with the Perkins, Rovor, New Mexico Skies, and the Bradford telescopes. Optical polarization measurements are also included from the Steward, Crimean, and St Petersburg observatories. All the instruments use the calibration stars reported in Villata et al. (1998) for calibration, and the Galactic extinction was corrected with the reddening corrections given in Schlegel et al. (1998). The flux from the host galaxy (which is significant only below $\nu \sim 10^{15}$ Hz) was estimated using the flux values across the *R* band from Nilsson et al. (2007) and the colors reported in Fukugita et al. (1995), and then subtracted from the measured flux.

The *Swift* Ultraviolet/Optical Telescope (UVOT; Roming et al. 2005) obtained data cycling through each of the three ultraviolet pass bands, *UVW1*, *UVM2*, and *UVW2* with central wavelengths of 260 nm, 220 nm, and 193 nm, respectively. The photometry was computed using a 5 arcsec source region around Mrk 421 using a custom UVOT pipeline that performs the calibrations presented in Poole et al. (2008). Moreover, the custom pipeline also allows for separate, observation-by-observation, corrections for astrometric misalignments (Acciari et al. 2011). The flux measurements obtained were corrected for Galactic extinction with E_{B-V} = 0.015 mag (Schlegel et al. 1998) at each spectral band (Fitzpatrick 1999). The contribution of the host galaxy to the UV fluxes is negligible and hence not considered.

2.7. Radio observations

The radio data reported in this manuscript were taken with the 14 m Metsähovi Radio Observatory at 37 GHz, the 40 m Owens Valley Radio Observatory (OVRO) telescope at 15 GHz, and the 26 m University of Michigan Radio Astronomy Observatory (UMRAO) at 14.5 GHz. Details of the observing strategy and data reduction are given by Teraesranta et al. (1998, Metsähovi), Richards et al. (2011, OVRO), and Aller et al. (1985, UMRAO). The 225 GHz (1.3 mm) light curve was obtained at the Submillimeter Array (SMA) near the summit of Mauna Kea (Hawaii). During the period covered in this work, Mrk 421 was observed as part of a dedicated program to follow sources on the *Fermi*-LAT Monitored Source List (PI: A. Wehrle). Observations of available LAT sources were made periodically for several minutes, and the measured source signal strength was calibrated against known standards, typically solar system objects (Titan, Uranus, Neptune, or Callisto).

Mrk 421 is a point-like and unresolved source for these three single-dish radio instruments and for SMA, which means that the measured fluxes are the flux densities integrated over the full source extension, and hence should be considered as upper limits in the SED model fits reported in this paper. However, it is worth noting that the radio flux of Mrk 421 resolved with the VLBA for a region of $1{-}2 \times 10^{17}$ cm (hence comparable to the size of the blazar emission) is a very large part of the radio flux measured with the single-dish radio instruments (see Abdo et al. 2011), and thus it is reasonable to assume that the blazar emission contributes substantially to the radio flux measured by single-dish radio telescopes such as Metsähovi, OVRO, and UMRAO. Moreover, there are several works reporting a correlation between radio and GeV emission in blazars as a population (see e.g. Ackermann et al. 2011), which implies that at least a fraction of the radio emission is connected to the gamma-ray (blazar) emission. The 225 GHz observations from SMA connect the bottom (radio) to the peak (optical/X-rays) of the synchrotron (low-energy) bump of the SED, and hence it is also expected to be strongly dominated by the blazar emission of the source. Therefore, it seems reasonable to adjust the theoretical model in such a way that the predicted energy flux for the millimeter band is close to the SMA measurement, and the predicted energy flux for the radio band is not too far below the measurements performed by the single-dish instruments.

3. Multiband variability

In this section, we present the experimental results derived from the MW campaign observations described in Sect. 2. Figure 1 shows the multiband light curves during the decline observed between 2010 March 10 (MJD 55 265) and 2010 March 22 (MJD 55 277). In the top left panel, the VHE band includes nine observations from MAGIC, nine from VERITAS, and ten from *Whipple*.

The flux above 200 GeV decreases roughly steadily with time. Before MJD 55 272 the fluxes are ~1−2 c.u., while on subsequent days they are below 1 c.u., showing that only the decay (perhaps including the peak) of the flare was observed with the VHE γ-ray instruments in 2010 March. It is worth noting that the VHE flux measured with MAGIC for MJD 55 268 is roughly 50% lower than that measured with VERITAS for that day: 2.1 ± 0.3 vs. 4.0 ± 0.6 in units of 10^{-10} cm^{-2} s^{-1}. Taking into account the measured errors, these fluxes are different by three to four standard deviations. This might result (at least partially) from systematics related to the instruments or observations during that night, but it might also be due to intra-night variability over the MAGIC and VERITAS observation windows, which are about seven hours apart.

The photon flux above 300 MeV (measured by *Fermi*-LAT in two-day long time intervals) does not show any significant variability. A fit with a constant line gives a flux level of $(6.8 \pm 0.9) \times 10^{-8}$ cm^{-2} s^{-1}, with $\chi^2/\mathrm{ndf} = 2.5/6$, which is similar to the mean flux of $\sim 7.2 \times 10^{-8}$ cm^{-2} s^{-1} observed during the first 1.5 yr of *Fermi* operation, from 2008 August to 2010 March (Abdo et al. 2011).

The variability at the X-ray band as measured with RXTE, *Swift* and MAXI is high, with light curves that resemble those at VHE. The *Swift*-XRT energy flux at the band 0.3−10 keV decreases from $\sim 2.2 \times 10^{-9}$ erg cm^{-2} s^{-1} down to $\sim 0.8 \times 10^{-9}$ erg cm^{-2} s^{-1}. The low X-ray fluxes measured during this 13-day period are comparable to the mean 0.3−10 keV X-ray flux of $\sim 0.9 \times 10^{-9}$ erg cm^{-2} s^{-1}, measured during the first seven years of *Swift* operation, from 2005 to 2012 (Stroh & Falcone 2013).

At UV and optical frequencies, the variability is also rather small, in contrast to the VHE and X-ray bands. The emission at the UV and optical bands is variable. For instance, a constant fit yields χ^2/ndf of 174/11 and 144/60 for the UVOT-UVM2 and GASP/*R* band, respectively. Hence Mrk 421 showed some activity at these bands, although it is substantially weaker than that shown at VHE and X-rays. The optical flux at the *R* band measured during this 13-day period is ~16 mJy (~24 mJy if the host galaxy is included), which is comparable to the typical flux of ~25 mJy measured during the first eight years of the Tuorla blazar monitoring program, from 2003 to 2011[13].

Optical polarization measurements are also reported in Fig. 1. The errors on these observations are smaller than 0.1% and 3° for the polarization degree and the electric vector polarization angle and are therefore too small to be visible in the plot. The collected data do not show any flare in the polarization degree or high rotation in the electric vector polarization angle as is observed during the flaring activities in other blazars (e.g. Marscher et al. 2008). There are some small variations in the polarization degree and angle, however, but such random fluctuations are common and expected due to continuous noise processes and not by singular events (see Marscher 2014).

In the radio bands, there were only seven observations during this period, which were performed at frequencies from 14 GHz to 225 GHz. All of them reported a flux of about 0.4−0.5 Jy. We did not find significant variability in any of these single-dish radio observations, which are ≲1 h long. The radio fluxes measured during this 13-day period are comparable to the typical 15 GHz radio flux of ~0.45 mJy measured during the first three years of the OVRO monitoring program, from 2008 to 2011 (Richards et al. 2013).

To quantify the overall variability during these 13 consecutive days, we followed the method provided in Vaughan et al. (2003). The fractional variability F_{var} at each energy band is computed as

$$F_{\mathrm{var}} = \sqrt{\frac{S^2 - \langle \sigma_{\mathrm{err}}^2 \rangle}{\langle F \rangle^2}} \tag{1}$$

where $\langle F \rangle$ is the mean photon flux, S is the standard deviation of the N flux points, and $\langle \sigma_{\mathrm{err}}^2 \rangle$ is the mean-squared error. The error in F_{var} is calculated according to the prescription in Sect. 2.2 of Poutanen et al. (2008),

$$\sigma_{F_{\mathrm{var}}} = \sqrt{F_{\mathrm{var}}^2 + \sqrt{\frac{2\langle \sigma_{\mathrm{err}}^2 \rangle^2}{N \langle F \rangle^4} + \frac{4 \langle \sigma_{\mathrm{err}}^2 \rangle F_{\mathrm{var}}^2}{N \langle F \rangle^2}}} - F_{\mathrm{var}}. \tag{2}$$

This prescription is more precise than the method used in Vaughan et al. (2003) when the σ_{err} is comparable to or larger than S.

The F_{var} values derived from the light curves in Fig. 1 are plotted in Fig. 2. The values of F_{var} are plotted only for instruments with $S^2 > \sigma_{\mathrm{err}}^2$. When there is no variability detectable with the sensivity of the instrument, $S^2 < \sigma_{\mathrm{err}}^2$ might occur (as is the case for *Fermi*-LAT).

The F_{var} is highest at the X-ray band. The values of F_{var} measured by *Swift*-XRT and RXTE-PCA agree well at the 2−10 keV band. We note that *Swift*-XRT shows a higher F_{var} at the 2−10 keV band than at the 0.3−2 keV band. The uncertainty in the F_{var} values at these two bands is small because the measured X-ray flux variations are very large in comparison to the flux uncertainties (which are smaller than 1%), and that makes the difference in the measured variability very significant. This difference cannot be attributed to different temporal coverage, as they were observed with the same instrument (and hence the same time).

To study this difference, we calculated the normalized deviations of the fluxes, $F_{\mathrm{dev}} = (F - \langle F \rangle) / \langle F \rangle$ computed with the *Swift*-XRT light curves at both energy bands (0.3−2 keV and 2−10 keV). Figure 3 shows that the absolute values of F_{dev}, $|F_{\mathrm{dev}}|$, at the 2−10 keV band are always higher than those at the 0.3−2 keV band. This shows that the flux at the 2−10 keV band is intrinsically more variable than at the 0.3−2 keV band across the whole temporal range, and hence that the higher F_{var}

[13] http://users.utu.fi/kani/1m/Mkn_421_jy.html

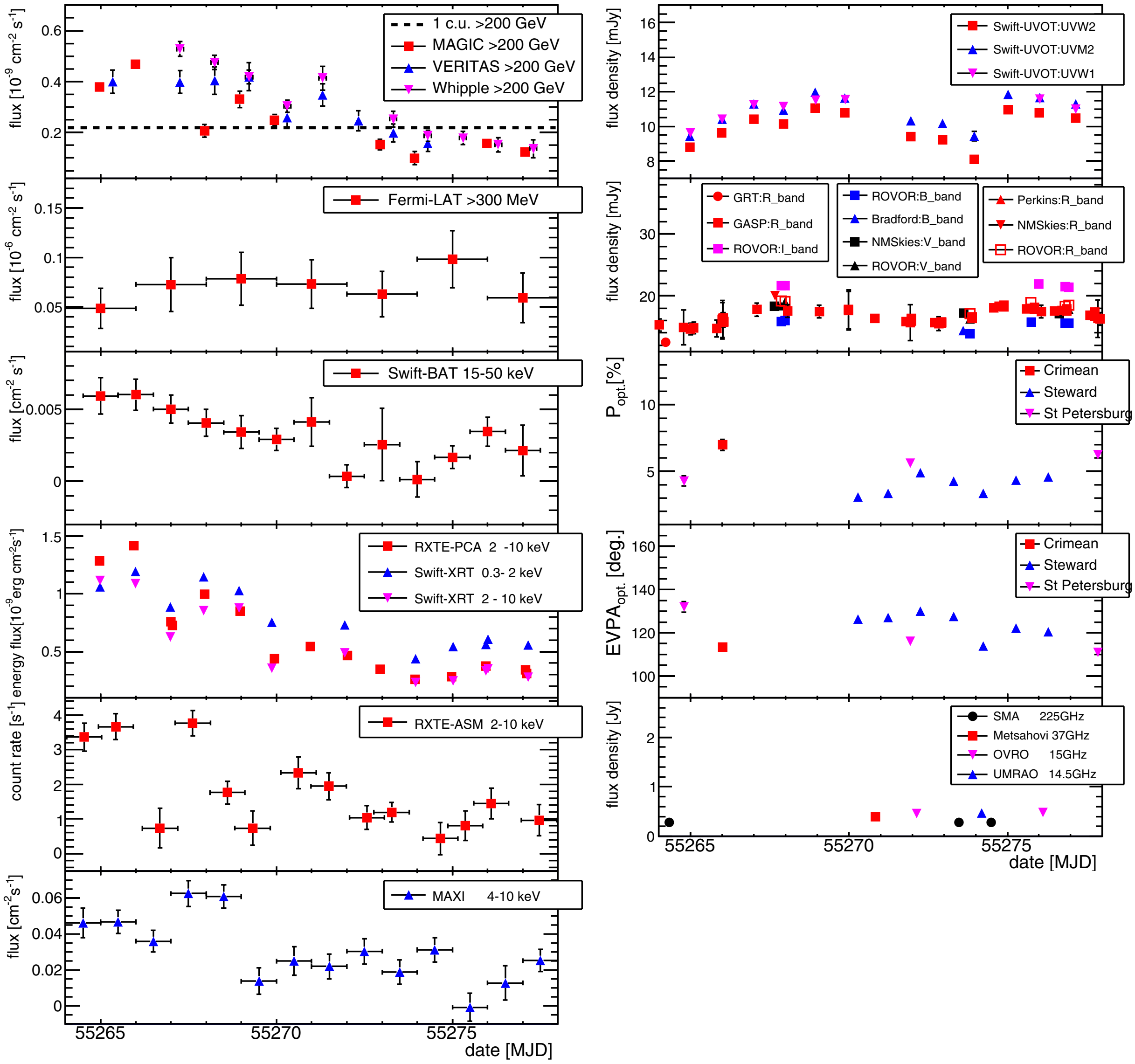

Fig. 1. Light curves of Mrk 421 between MJD 55 264 and 55 278, from VHE to radio (including optical polarization). The *Whipple* data were converted into fluxes above 200 GeV, and the host galaxy contribution was subtracted from the reported optical fluxes. $P_{\rm opt}$ and EVPA$_{\rm opt}$ stand for the polarization degree and the electric vector polarization angle. For details, see text in Sect. 3.

is not due to one or a few observations, but rather dominated by a higher overall relative dispersion at the 2–10 keV flux values during the 13 consecutive days.

The $F_{\rm var}$ at VHE γ-rays is similar to that at X-rays. The flux points from VERITAS and *Whipple* are more concentrated around their mean values, which yield slightly lower $F_{\rm var}$ than that of MAGIC. In conclusion, both VHE γ-rays and X-rays show higher variability than the flux at the other bands, which is additional evidence that they have a closer relation to each other, as reported in several other Mrk 421 flaring episodes (e.g. Maraschi et al. 1999).

To better understand the relation between X-rays and VHE γ-rays, we examined the correlation between the X-ray energy flux at the 0.3–2 keV and 2–10 keV bands and the VHE γ-ray energy flux above 200 GeV. For this exercise we used the X-ray fluxes from *Swift* and RXTE and the VHE fluxes from MAGIC and VERITAS. The VHE photon fluxes given in [cm^{-2} s^{-1}] were converted into energy fluxes reported in [erg cm^{-2} s^{-1}] using a power-law spectrum with index 2.5 above 200 GeV[14]. The top panel in Fig. 4 shows the VHE γ-ray flux vs. X-ray flux at the 0.3–2 keV band, and the resulting fits with a linear ($F_{\rm VHE} = k \cdot F_{\rm X\text{-}ray}$) and a quadratic ($F_{\rm VHE} = k \cdot F^2_{\rm X\text{-}ray}$) function. For the fits we used only MAGIC data, which are the VHE observations taken simultaneously or almost simultaneously with the X-ray observations (see Appendix A for details on simultaneity of the observations). The middle and bottom panels of Fig. 4 also show the X-ray flux vs. VHE-γ-ray flux, but using the X-ray flux at the 2–10 keV band measured with *Swift* and RXTE. Neither a linear nor a quadratic function describes the data perfectly. However, for the 2–10 keV energy range, the VHE to X-ray flux closely follows a linear trend, which it is clearly not the case for the 0.3–2 keV energy range. The physical interpretation of these results is discussed in Sect. 5.

[14] The spectral shape of the VHE emission of Mrk 421 did vary during the 13-day period considered here. Including these spectral variations would shift some of the reported γ-ray energy fluxes by ~10–15%, which we considered not essential for this study.

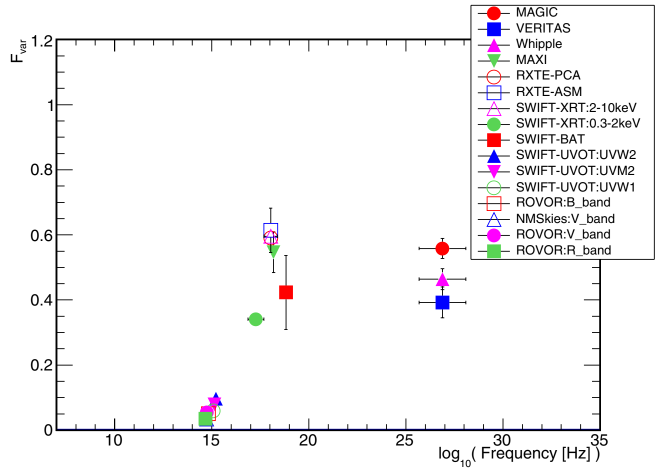

Fig. 2. Fractional variability F_{var} as a function of frequency.

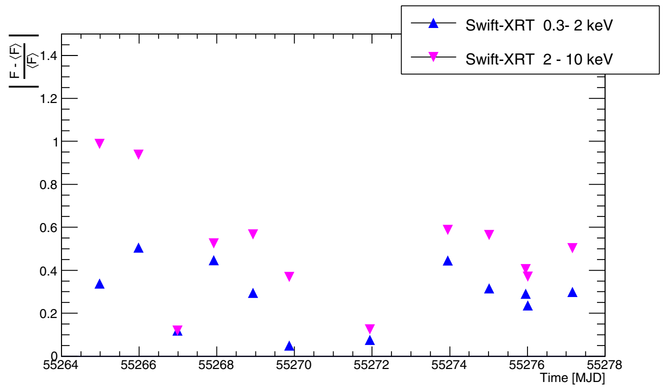

Fig. 3. Temporal evolution of the absolute value of the normalized deviation of the *Swift*-XRT flux, F_{dev}. See text for further details.

4. Temporal evolution of the broadband spectral energy distribution

To study this flaring activity, we built 13 successive simultaneous broadband SEDs for 13 consecutive days. We study these SEDs within one-zone and two-zone SSC scenarios in Sects. 4.1 and 4.2. The characteristics of the MW data are described in Appendix B. Specifically, we investigate whether the temporal evolution of the EED in SSC models can explain the observed variations in the SED during the 13-day period, and hence we try to fix (to their quiescent values) the model parameters related to the environment, namely the blob radius (R), magnetic field (B), and Doppler factor (δ). We cannot exclude that other model realizations with a different set of model parameters (e.g., changing the environment parameters, or varying more model parameters) can also provide a satisfactory description of the broadband SEDs, but in this paper we wish to vary as few model parameters as possible to most directly study the evolution of the EED, which is the part of the model directly connected to the particle acceleration and cooling mechanisms.

We applied steady-state SSC models instead of time-dependent models to the SEDs of each day and estimated physical parameters in the emission regions, which gives us an estimate of the temporal evolution of these physical parameters. Time-dependent models, as developed by Krawczynski et al. (e.g. 2002), Chen et al. (e.g. 2011), are a direct way to derive the physical properties of the emission regions, but they

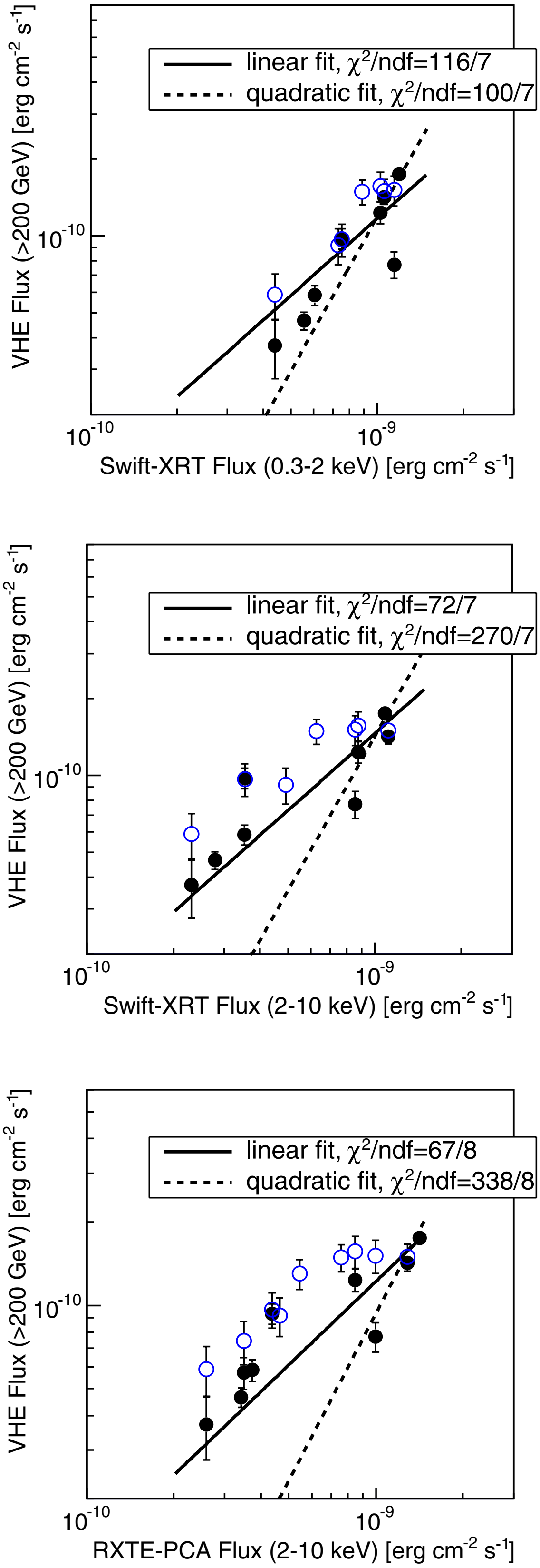

Fig. 4. Correlation between VHE γ-ray flux (MAGIC, black solid circles, and VERITAS, blue empty circles) and X-ray fluxes. *Top*: X-ray flux at the 0.3–2 keV band measured with *Swift*-XRT. *Middle*: X-ray flux at the 2–10 keV band measured with *Swift*-XRT. *Bottom*: X-ray flux at the 2–10 keV band measured with RXTE-PCA. The lines show the fits with linear and quadratic functions. Only MAGIC data points were used for the fits to ensure VHE-X-ray simultaneity (see Appendix A).

include many detailed processes, such as synchrotron or inverse-Compton cooling of electrons, adiabatic cooling of electrons due to the expansion of an emission blob, and the injection of relativistic electrons and its time evolution, and therefore are very complex and have an arbitrarily large number of degrees of freedom. The snapshot approach with steady-state SSC models allows us to observe the time evolution of basic physical parameters averaged over a day in the blobs independently of the difficulty associated with time-dependent models. The time evolution of the averaged basic parameters observed in this study reflects physical mechanisms that are not considered explicitly, but gives us hints about them. A caveat of this approach is that the SEDs are observationally determined from short (about one hour) observations distributed over a relatively long (13 day) period of time, and hence we cannot exclude that some of the SEDs relate to short-lived active states that do not necessarily fit in the scheme of a slowly varying activity phase.

Given the known multiband variability in the emission of Mrk 421 (and blazars in general), we paid special attention to organize observations that were as close in time as possible (see Appendix A for the simultaneity of the observations). The observations performed with MAGIC, RXTE, and *Swift* were scheduled many weeks in advance, which resulted in actual observations occurring always within temporal windows of less than two hours. The observations with VERITAS/*Whipple* were triggered by the high activity detected in 2010 March, and performed typically about seven hours after MAGIC observations because VERITAS and *Whipple* are located at a different longitude from that of MAGIC. At radio frequencies we have only seven observations during this period, but we neither expected nor detected variability at radio during these short (a few days) timescales. Based upon these observations, we show in Appendix B.13 consecutive days of SEDs. Each SED is characterized with a one-zone and a two-zone SSC model as described in the following two subsections.

The peak luminosities and peak frequencies of the low- and high-energy bumps shift during high activity. In general, the peak frequency and peak luminosity decrease as the flare decays. In addition to the migration in the SED peak positions, the shapes of these SED bumps change. The X-ray and γ-ray bumps of the SEDs from MJD 55 265 and 55 266, when Mrk 421 emitted the highest flux, are narrow, and they widen as the flare decays. A quantitative evaluation of the widening of the two SED bumps is reported in Sect. 5.

4.1. SED modeling: one-zone SSC model

In this SSC model, we assume that emission comes from a single, spherical and homogeneous region in the jet, which is moving relativistically toward us. The one-zone SSC model describes most of the SEDs of high-frequency-peaked BL Lac objects with the fewest parameters, and hence it is the most widely adopted. The emission from radio to X-ray results from synchrotron radiation of electrons inside a blob of comoving radius R, with a Doppler factor δ. In this emission blob, there is a randomly oriented magnetic field with uniform strength B. The γ-ray emission is produced by inverse-Compton scattering of the synchrotron photons with the same population of electrons that produce them. We used the numerical code of the SSC model described in Takami (2011). The algorithm implemented in this code allows us to very quickly determine the parameters that accurately describe the SED.

The one-zone homogeneous SSC scenario with an EED described with a broken power-law function (seven free parameters plus the two parameters defining the edges of the EED) can be formally constrained from the seven characteristic observables that can be obtained from the multi-instrument data covering the two SED bumps, namely the spectral indices below and above the synchrotron peak, the peak frequencies and luminosities of the synchrotron and inverse-Compton bumps, and the variability timescale (Tavecchio et al. 1998). However, in reality, the collected data do not allow us to determine these seven parameters with very good precision (particularly for the variability timescale and the peak frequency of the inverse-Compton bump), which implies some degeneracy in the seven (+two) model parameters, which unavoidably necessitates making some approximations or assumptions.

In previous works related to Mrk 421, it was common to use only one or two power-law functions (that is, zero or one break) to describe the EED. However, such a simple model cannot adequately describe the broadband SED from the campaign organized in 2009, when Mrk 421 was in its typical nonflaring VHE state (Abdo et al. 2011). The SED from this paper was better sampled (more instruments with higher sensitivity) than those reported previously, and an additional break (two additional parameters) was required to properly describe the shape of the measured synchrotron bump (from 1 eV to 100 keV), together with the full inverse-Compton bump (from 100 MeV to 10 TeV). Given the similar energy coverage and activity of the source during many days of the 13-day period considered here, we also used three power-law functions (i.e., two breaks) to parameterize the EED:

$$\frac{\mathrm{d}n_\mathrm{e}}{\mathrm{d}\gamma_\mathrm{e}} = \begin{cases} n_\mathrm{e}\gamma_\mathrm{e}^{-s_1} & \text{if } \gamma_{\min} < \gamma_\mathrm{e} \leq \gamma_{\mathrm{br1}} \\ n_\mathrm{e}\gamma_\mathrm{e}^{-s_2}\gamma_{\mathrm{br1}}^{s_2-s_1} & \text{if } \gamma_{\mathrm{br1}} < \gamma_\mathrm{e} \leq \gamma_{\mathrm{br2}} \\ n_\mathrm{e}\gamma_\mathrm{e}^{-s_3}\mathrm{e}^{-\gamma_\mathrm{e}/\gamma_{\max}}\gamma_{\mathrm{br1}}^{s_2-s_1}\gamma_{\mathrm{br2}}^{s_3-s_2}\mathrm{e}^{\gamma_{\mathrm{br2}}/\gamma_{\max}} & \text{if } \gamma_\mathrm{e} > \gamma_{\mathrm{br2}}. \end{cases} \tag{3}$$

where n_e is the number density of electrons, γ_e is the Lorentz factor of the electrons, $\gamma_{\min}$ and $\gamma_{\max}$ define the range of γ_e, s_1, s_2 and s_3 are the indices of the power-law functions, and γ_{br1} and γ_{br2} are the Lorentz factors where the power-law indices change. In total, this model has two more free parameters than the model with a broken power-law EED. The SEDs from the days with highest activity can be described with an EED with only one break, but for the nonflaring activity, we need to use an EED with two breaks. The requirement for a more complex parameterization of the EED in the recent works might be due to the better energy coverage (more instruments involved in the campaigns), and better sensitivity to cover the γ-ray bump. Future observations of Mrk 421 during nonflaring states with as good or better energy coverage will reveal whether the two-break EED is always needed, or whether this is something that was required only to describe the 2009 and 2010 data.

Despite the extensive MW data collected in this campaign, there is still some degeneracy in the choice of the eleven parameter values required to adjust the SED model to the observational data. Given the similarities between the SEDs of the last few days and the SED reported in Abdo et al. (2011), we used the SED model parameter values from Abdo et al. (2011) as a reference for the choice of SSC parameters to describe the 2010 March broadband observations. In particular, we wish to test whether the temporal evolution of the EED can explain the observed variations in the SED during the 13-day period, and hence we fixed $\gamma_{\min}$, $\gamma_{\max}$ and the model parameters related to the environment R, B, and δ to the values reported in Abdo et al. (2011). The value of the Doppler factor, 21, is higher than the value inferred from VLBA measurements of the blob movement

Table 2. Integral flux above 200 GeV and parameters of the one-zone SSC model.

Date [MJD]	MAGIC flux [10^{-10} cm^{-2} s^{-1}]	VERITAS flux [10^{-10} cm^{-2} s^{-1}]	*Whipple* flux [10^{-10} cm^{-2} s^{-1}]	$\gamma_{\rm br1}$ [10^4]	$\gamma_{\rm br2}$ [10^5]	s_1	s_2	$n_{\rm e}$ [10^3 cm^{-3}]
55 265	3.8 ± 0.2	4.0 ± 0.5		60.	6.0	2.23	2.23	1.14
55 266	4.7 ± 0.2			66.	6.6	2.23	2.23	1.16
55 267		4.0 ± 0.5	5.3 ± 0.3	16.	6.0	2.23	2.70	1.10
55 268	2.1 ± 0.3	4.0 ± 0.6	4.8 ± 0.3	16.	6.0	2.20	2.70	0.90
55 269	3.3 ± 0.3	4.2 ± 0.6	4.2 ± 0.3	12.	7.0	2.20	2.70	0.95
55 270	2.3 ± 0.2	2.6 ± 0.4	3.0 ± 0.2	8.0	3.9	2.20	2.70	0.90
55 271		3.5 ± 0.4	4.1 ± 0.5	9.0	5.0	2.20	2.70	0.90
55 272		2.5 ± 0.4		5.0	4.0	2.20	2.50	0.90
55 273	1.5 ± 0.2	2.0 ± 0.4	2.5 ± 0.3	6.0	3.9	2.20	2.70	0.90
55 274	1.0 ± 0.3	1.6 ± 0.3	1.9 ± 0.2	3.5	3.9	2.20	2.70	0.90
55 275			1.8 ± 0.3	5.0	3.9	2.20	2.70	0.85
55 276	1.6 ± 0.2		1.5 ± 0.3	5.7	3.9	2.20	2.70	0.90
55 277	1.2 ± 0.1		1.4 ± 0.4	8.0	3.9	2.20	2.70	0.70

Notes. VERITAS and *Whipple* fluxes were measured around seven hours after the MAGIC observations. The model parameters that were kept constant during the 13-day period are the following ones: $\gamma_{\rm min} = 8 \times 10^2$; $\gamma_{\rm max} = 1 \times 10^8$; $s_3 = 4.70$; $B = 38$ mG; $\log(R[{\rm cm}]) = 16.72$; $\delta = 21$.

in Piner et al. (2010). This is a common circumstance for VHE sources, which has been dubbed the "bulk Lorentz factor crisis", and requires the radio and TeV emission to be produced in regions with different Lorentz factors (Georganopoulos & Kazanas 2003; Ghisellini et al. 2005; Henri & Saugé 2006). During the adjustment of the model to the measured SED, the VHE and X-ray data provide the primary constraint because the variability is highest in these two energy bands.

The model parameters inferred from the observed SEDs (shown in Appendix B) are reported in Table 2. Only one break in the EED (instead of two) is sufficient to describe the narrow SED bumps on MJD 55 265 and 55 266, while two breaks are necessary to properly describe the wider X-ray and γ-ray bumps from MJD 55 267 to MJD 55 277, when Mrk 421 shows a somewhat lower X-ray and VHE activity. The changes in the SED during the flaring activity are dominated by the parameters, $n_{\rm e}$, $\gamma_{\rm br1}$, and $\gamma_{\rm br2}$: lower activity can be parameterized with a lower $n_{\rm e}$ and a decrease in the values of the two break Lorentz factors in the EED. The spectral index s_2 is equal to 2.5 for MJD 55 272, while $s_2 = 2.7$ for the adjacent days. The X-ray bump for MJD 55 272 (see Fig. 3a) is rather narrow, and therefore s_2, which affects the SED slope of the lower energy side of the bump, needs to be closer to s_1 to properly describe the data.

Given the values of the blob radius and Doppler factor used here, the shortest time of the flux variation $t_{\rm min} = (1+z)R/\beta c\delta$ is about one day. This value is reasonable, given the flux variations measured during the March flaring activity (see Fig. 1), but it would not be consistent with the potential intra-night variability that might have occurred in MJD 55 268, as hinted by the disagreement in the VHE fluxes measured by MAGIC and VERITAS. The predicted radiative cooling break by synchrotron radiation[15], $\gamma_{\rm c} = 6\pi m_{\rm e}c^2/(\sigma_{\rm T}B^2R)$, where $m_{\rm e}$ is the electron mass and $\sigma_{\rm T}$ is the Thomson cross-section, is 3.2×10^5 in this model. This formula is derived by equating the timescale of synchrotron radiation to the timescale of electrons staying in the blob $\sim R/c$, on the assumption that the timescale of adiabatic cooling is much longer than that of synchrotron cooling. This assumption is reasonable because R is fixed in this study. The $\gamma_{\rm br2}$ values in the model range from 3.9×10^5 to 7.0×10^5, which is comparable to $\gamma_{\rm c}$, hence suggesting that the second break in the EED might be related to the synchrotron cooling break. Thus, the decrease of $\gamma_{\rm br2}$ and the weak dependence on $n_{\rm e}$ implies that the end of a flare is dominated by cooling. However, the change in the power-law index does not match the canonical change expected from synchrotron cooling, $\Delta s = 1$, which is similar to the situation reported in Abdo et al. (2011). The result that s_3 is softer than expected can be explained by inhomogeneity of the emission blob, or by a weakening of the electron injection.

In general, the agreement between the one-zone SSC model and the observational data is quite acceptable, which shows one more the success of the one-zone SSC model in describing the SEDs of blazars. However, there are several problems. At the low-energy end of the VHE spectra, the model is slightly higher than the data for the SEDs from MJD 55 265, 55 266, 55 268, 55 269, and 55 273; and the model also goes slightly beyond the data in the X-ray bump for MJD 55 265 and 55 266. We cannot exclude that these data-model mismatches arise from the requirement that the EED is the only mechanism responsible for the blazar variability. For instance, if in addition to changing the model parameters related to the EED, the parameters B, R and δ were varied as well, the relative position of the synchrotron and SSC peak could be modified, possibly achieving better agreement with the data.

Overall, the temporal evolution of the broadband SEDs can be described by changes in the EED, keeping $\gamma_{\rm min}$, $\gamma_{\rm max}$, and the model parameters related to the environment (blob radius, magnetic field, and the Doppler factor) constant at the values reported in Abdo et al. (2011). Figures 5a and b depict the one-zone SSC model curves and the parameterized EEDs for the 13 consecutive days. We can divide the whole activity into three periods: MJD 55 265–55 266 (period 1), MJD 55 268–55 271 (period 2), and MJD 55272-55277 (period 3), which correspond to a VHE flux of ∼2 c.u., ∼1.5 c.u., and ∼0.5 c.u., respectively. The EEDs of period 1 have one break, while those of period 2 and 3 have two breaks. Moreover, the EEDs of period 1 have a higher electron number density ($n_{\rm e}$) than those of periods 2 and 3. Figure 5b shows that the greatest variability occurs above the first break ($\gamma_{\rm br1}$) in the EED.

4.2. SED modeling: two-zone SSC model

The one-zone SSC model curves reported in the previous section describe the overall temporal evolution of the low- and

[15] In HBLs like Mrk 421, the cooling of the electrons is expected to be dominated by the synchrotron emission.

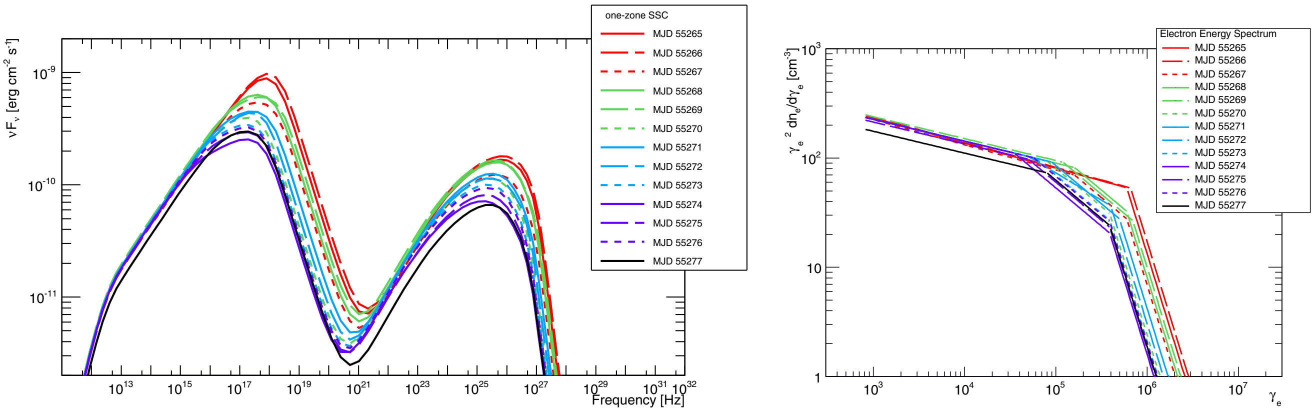

(a) SEDs. (b) EEDs.

Fig. 5. One-zone SSC model curves and the related EEDs used to describe the measured SEDs during the 13-day flaring activity. The parameter values are given in Table 2.

high-energy bumps of the SED during this flaring activity reasonably well. However, we cannot ignore the model-data mismatches mentioned in the last section. This was our main motivation for trying a model with two distinct blobs: one producing the steady emission, the other producing the temporal evolution of the SED, which is evident primarily at the X-ray and VHE γ-ray bands. The two blobs are assumed to be separated by a long distance and the individual radiation fields do not interact with each other. We call these the quiescent blob and the flaring blob. The quiescent blob is described with the parameter values from the one-zone SSC model reported in Table 2 for MJD 55 274, which is the SED with the lowest activity among the 13 consecutive days. While the EED of the quiescent-state blob is described by three power-law functions, we employ only two power-law functions to describe the EED of the flaring blob:

$$\frac{dn_e}{d\gamma_e} = \begin{cases} n_e \gamma_e^{-s_1} & \text{if } \gamma_{\min} < \gamma_e \leq \gamma_{\mathrm{br1}} \\ n_e \gamma_e^{-s_2} \gamma_{\mathrm{br1}}^{s_2 - s_1} & \text{if } \gamma_{\mathrm{br1}} < \gamma_e < \gamma_{\max} \end{cases} \tag{4}$$

where n_e is the electron number density, γ_e is the Lorentz factor of the electrons, $\gamma_{\min}$ and $\gamma_{\max}$ define the range of γ_e, s_1 and s_2 are the indices of the power-law function, and γ_{br1} is the Lorentz factor where the power-law index changes.

In the overall process of adjusting the model to the 13 measured SEDs, we used a flaring blob size R about one order of magnitude smaller than the quiescent blob, which naturally allows faster variability. The size of the blob was kept constant, while the other parameters were allowed to change to describe the characteristics of the flare evolution.

Figure 6 depicts the two-zone model curve adjusted to the broadband SED from MJD 55 265. It is worth noting that the contribution from the flaring blob is relevant only at the X-ray and VHE bands. The model curves related to the remaining 12 consecutive SEDs are shown in Figs. B.4 and B.5, and Table 3 reports the two-zone SSC model parameters that adequately describe the measured SEDs. Except for the magnetic field, which decreases during the decay of the flare, the other model parameters related to the environment remain constant. The changes occur in the three model parameters n_e, $\gamma_{\min}$, and γ_{br1}, while s_1, s_2, $\gamma_{\max}$ can be kept constant for all the 13 SEDs. With this two-zone SSC model, the shortest variability timescale $t_{\min}$ is about one hour, which is comparable to the length of our single-instrument observations, during which we did not measure significant variability. This shortest variability timescale would be consistent

Table 3. Parameters for the flaring blob in the two-zone SSC model.

Date [MJD]	$\gamma_{\min}$ [10^4]	γ_{br1} [10^5]	n_e [10^3 cm^{-3}]	B [mG]
55 265	3.0	3.0	5.0	105
55 266	3.0	3.0	6.0	100
55 267	2.5	1.1	5.9	100
55 268	5.3	1.8	5.6	100
55 269	3.0	2.3	5.2	90
55 270	3.5	0.8	6.0	75
55 271	3.5	1.2	6.5	75
55 272	3.5	2.0	3.0	75
55 273	3.5	0.5	4.0	75
55 274	–	–	–	–
55 275	3.5	0.5	5.0	60
55 276	3.5	1.0	3.0	60
55 277	3.5	0.8	2.5	60

Notes. The model parameters that were kept constant during the 13-day period are the following ones: $\gamma_{\max} = 6 \times 10^5$; $s_1 = 2.0$; $s_2 = 3.0$; $\log(R[\mathrm{cm}]) = 15.51$; $\delta = 35$. The quiescent blob is parameterized with the parameter values from the one-zone SSC model reported in Table 2 for MJD 55 274. We refer to Table 2 for the γ-ray flux above 200 GeV measured with MAGIC, VERITAS and *Whipple*.

with the potential intra-night VHE variability on MJD 55 268. The predicted synchrotron cooling break γ_c for the flaring blob is 7×10^5 for MJD 55 265. For this day, the parameter γ_{br1} for the flaring blob is 3×10^5, with a change in the EED power-law index of 1, which is the canonical change for synchrotron cooling. During the following three days $\gamma_c/\gamma_{\mathrm{br1}} \lesssim 8$, and after MJD 55 269 $\gamma_c/\gamma_{\mathrm{br1}}$ is much larger, which means that the break in the EED of the flaring blob is intrinsic to the acceleration mechanism, and cannot be directly related to the synchrotron cooling during these days.

The flaring blob is characterized by an EED with a very high $\gamma_{\min}$ ($>3 \times 10^4$), which means that it lacks low-energy electrons, and so does not contribute to the radio/optical emission. This is necessary for improving (with respect to the one-zone SSC model from Sect. 4.1) the description of the very narrow peaks at the X-ray and the γ-ray bumps occurring on some days (e.g. MJD 55 265 and 55 266).

Figures 7a and b depict the two-zone SSC model curves and the parameterized EEDs for the 13 consecutive days. In this case, by construction, all the SED variations occur at the X-ray and the

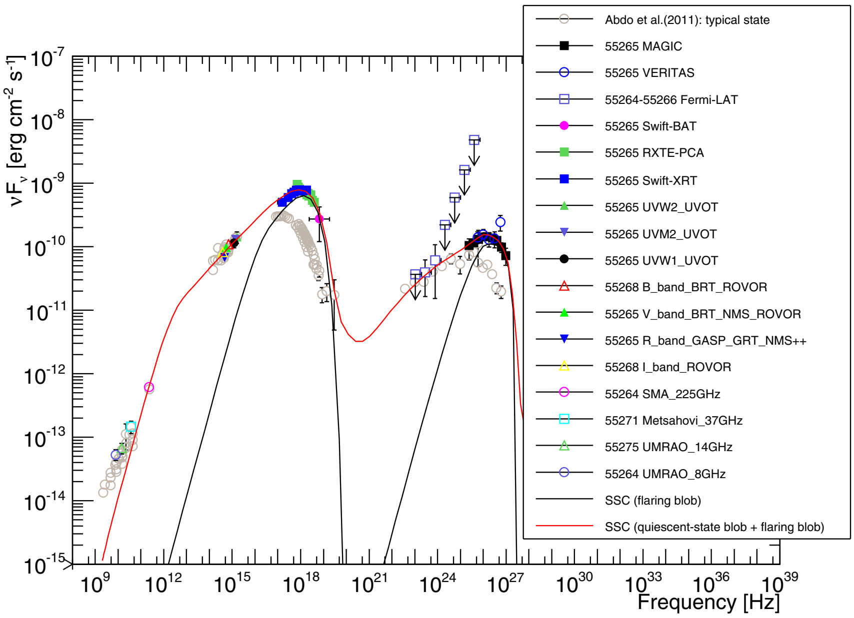

Fig. 6. Largely simultaneous broadband SED of Mrk 421 on MJD 55 265. The correspondence between markers and instruments is given in the legend. The full names of the instruments can be found in Table 1. Because of space limitations, R-band instruments other than GASP, GRT, and NMS are denoted with the symbol "++". Whenever a simultaneous observation is not available, the fluxes from the closest date are reported, and their observation time in MJD is reported next to the instrument name in the legend. The red curve depicts the two-zone SSC model matching the SED data, while the black line shows the contribution of the flaring blob. The gray circles depict the averaged SED from the 2009 MW campaign reported in Abdo et al. (2011), which is a good representation of the nonflaring (typical) SED of Mrk 421.

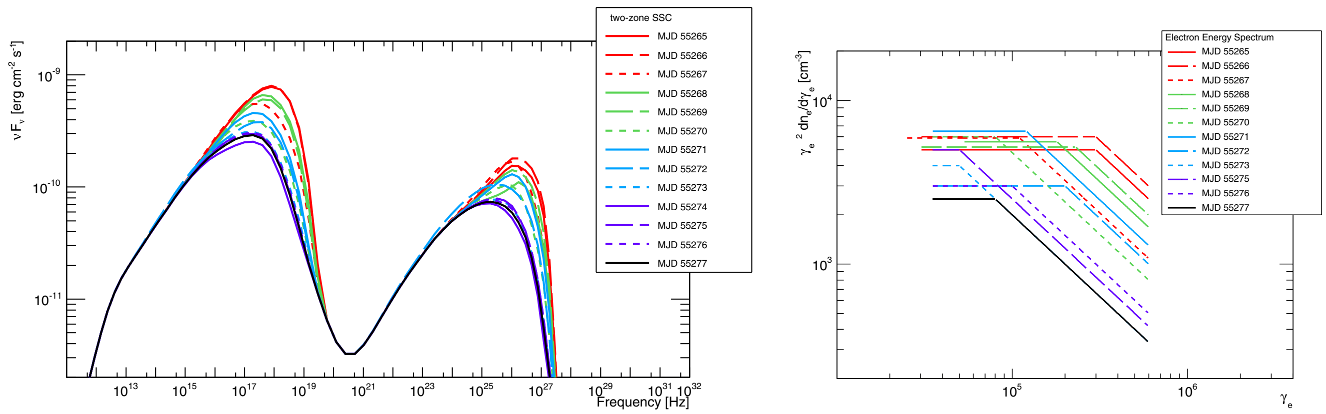

(a) SEDs.

(b) EEDs.

Fig. 7. Two-zone SSC model curves (sum of the emission from the quiescent and the flaring blobs) and the related EEDs from the flaring blob used to describe the measured SEDs during the 13-day flaring activity. The parameter values are given in Table 3.

VHE bands, and the SED peaks are narrower than those from the one-zone SSC scenario. Overall, the decay of the flaring activity is dominated by a reduction in n_{e} and γ_{br1}. The magnetic field also varies with time (not shown in this plot, see Table 3); lower activity is related to lower values of B.

The two-zone SSC model is described by 20 parameters, the one-zone SSC model by 11. However, after fixing the parameters of the quiescent-state blob, we only needed to change the values of four parameters (γ_{min}, γ_{br1}, n_{e}, and B) in the flaring blob, while in the one-zone SSC model we had to change five parameters (γ_{br1}, γ_{br2}, s_1, s_2, n_{e}) to describe the SEDs during these 13 consecutive days (see Sect. 4.1). Therefore, once the parameters of the quiescent blob are fixed, the two-zone SSC model describes the measured temporal evolution of the broadband SED with one free parameter less than the one-zone SSC model.

5. Discussion

The broadband SEDs during this flaring episode, resolved on timescales of one day, allows for an unprecedented characterization of the time evolution of the radio to γ-ray emission of Mrk 421. We find that both the one-zone SSC and the two- zone SSC models can describe the daily SEDs by varying five and four model parameters, mostly related to the EED. This shows that the particle acceleration and cooling mechanism producing the EED could be the main mechanism responsible for the broadband SED variations during the flaring episodes in blazars.

In this theoretical framework, the two-zone SSC model provides better data-model agreement at the peaks of the low- and high-energy SED bumps. Additionally, the two-zone SSC scenario presented here naturally provides shorter timescales (one hour vs. one day) for variability at the X-ray and VHE bands, as the correlated variability at X-ray and VHE bands without any variation at the optical and radio bands. Because low-energy electrons are absent, the peak frequency of the γ-ray bump becomes sensitive to γ_{min} as a result of the strong Klein-Nishina effect, which provides a rather independent channel to adjust the γ-ray bump for the flaring state. On the other hand, the X-ray bump is more sensitive to the magnetic field and γ_{br1}. Hence this phenomenological scenario of two distinct zones (quiescent+flaring) allows for more flexibility in the locations and shapes of the two bumps than in the one-zone SSC model, while still varying fewer parameters. This was particularly useful to adequately describe the evolution of the width of the two SED bumps. We can quantify this effect by computing the widths of the bumps as the full width at half maximum (FWHM) in the logarithmic scale, $\log(\nu_2/\nu_1)$, where ν_1 and ν_2 are the frequencies at which the energy flux is half of that at the peak position. The widths of the SED bumps for the 13 consecutive days are reported in Table 4, showing that both the synchrotron and inverse-Compton peak widths increase from $\log(\nu_2/\nu_1) \sim 2$ to $\log(\nu_2/\nu_1) \sim 3$ during the decay of the flare, which means that the width of the two bumps (in logarithmic scale) is about 50% greater during the nonflaring (low) activity.

The additional flexibility of the two-zone SSC model helps to improve the agreement of the model SEDs with the data from MJD 55 265, 55 266, 55 268, 55 269, and 55 273. The largest data-model differences occur for the first two days, which are the days with the highest activity and the narrowest low- and high-energy bumps. Figures 8a and b compare the data-model agreement for these two days. Note the better agreement of the two-zone SSC model curves with the X-ray data points and, especially, the γ-ray data points. The agreement can be quantified using χ^2 on the broadband SEDs, after excluding the radio data, which are considered as upper limits for the models. In total, we have 50 and 51 data points for MJD 55 265 and MJD 55 266, respectively. With a one-zone SSC model we obtain a χ^2 of 4.0×10^3 for MJD 55 265 and 3.6×10^3 for MJD 55 266, while we obtain 1.2×10^3 for MJD 55 265 and 0.7×10^3 for MJD 55 266 with the two-zone SSC model, which shows that the agreement of the model with the data is better for the latter theoretical scenario. An F-test on the obtained χ^2 values, and assuming conservatively that the one-zone model has 11 free parameters and the two-zone model has 20 free parameters (hence not considering that many of these parameters are kept constant) rejects the one-zone model in favor of the two-zone model for the given set of model parameters with a p-value lower than 10^{-5}. If one considers that many model parameters are kept constant, the rejection of the reported one-zone model in favor of the reported two-zone model would be even clearer. The reduced χ^2 for all cases is well above 1, which shows that none of the models describe the observations perfectly well. Both models oversimplify the complexity in the blazar jets, and hence we do not intend to explain the data at the percent level.

It is worth noting that the EED of the flaring blob is constrained to a very narrow range of energies, namely $\gamma_{\rm min}-\gamma_{\rm max} \sim 3\times10^4-6\times10^5$. One theoretical possibility to produce such a narrow EED is stochastic particle acceleration via scattering by magnetic inhomogeneities in the jet, namely second-order Fermi acceleration (e.g., Stawarz & Petrosian 2008; Lefa et al. 2011; Asano et al. 2014). The spectrum in this model is localized around a characteristic Lorentz factor $\gamma_{\rm ch}$ determined by the power spectrum of magnetic turbulence q and the cooling timescale of electrons, with a shape proportional to $\gamma_{\rm e}^2 \exp\left[-(\gamma_{\rm e}/\gamma_{\rm ch})^{3-q}\right]$ (e.g., Schlickeiser 1985). Such a spectrum can realize the narrow peaks of synchrotron radiation and inverse-Compton scattering that we measured for Mrk 421 during the 2010 March flare.

The treatment made with the one- and two-zone homogeneous SSC models is a simplification of the problem. For instance, relativistic travel within a jet can change the properties of a blob (e.g. expansion of the size R of the emitting region, and decrease in the magnetic field B). This issue has been discussed

Table 4. Peak positions and widths of the synchrotron and inverse-Compton bumps derived from the two-zone SSC model parameters reported in Table 3.

Date	$\nu^{\rm syn}_{\rm peak}$	$(\nu F_\nu)^{\rm syn}_{\rm peak}$	$\nu^{\rm syn}_1$	$\nu^{\rm syn}_2$	$\mathrm{Log}(\nu^{\rm syn}_2/\nu^{\rm syn}_1)$	$\nu^{\rm ic}_{\rm peak}$	$(\nu F_\nu)^{\rm ic}_{\rm peak}$	$\nu^{\rm ic}_1$	$\nu^{\rm ic}_2$	$\mathrm{Log}(\nu^{\rm ic}_2/\nu^{\rm ic}_1)$
–	$[10^{17}]$	$[10^{-10}]$	$[10^{15}]$	$[10^{18}]$	–	$[10^{25}]$	$[10^{-11}]$	$[10^{23}]$	$[10^{26}]$	–
[MJD]	[Hz]	[erg cm^{-2} s^{-1}]	[Hz]	[Hz]	–	[Hz]	[erg cm^{-2} s^{-1}]	[Hz]	[Hz]	–
55 265	8.1	7.9	34.	6.1	2.3	10.	15.	60.	9.5	2.2
55 266	8.1	8.0	34.	5.9	2.2	10.	18.	94.	9.9	2.0
55 267	4.0	5.5	11.	3.3	2.5	10.	17.	56.	5.1	2.0
55 268	4.0	6.6	30.	4.5	2.2	17.	11.	16.	7.3	2.7
55 269	4.0	6.1	1.9	4.5	2.4	10.	14.	42.	7.8	2.3
55 270	2.0	3.9	5.7	2.3	2.6	6.0	10.	11.	4.3	2.6
55 271	2.0	4.6	9.0	2.6	2.5	1.0	13.	30.	5.4	2.3
55 272	4.0	3.8	4.9	2.8	2.8	3.4	11.	7.4	4.5	2.8
55 273	2.0	3.1	3.1	1.9	2.8	1.9	7.7	3.9	3.0	2.9
55 274	2.0	2.5	1.8	1.6	2.9	1.9	7.1	3.0	2.4	2.9
55 275	2.0	3.0	2.8	1.8	2.8	3.4	7.9	4.2	3.0	2.9
55 276	2.0	3.1	3.1	1.8	2.8	1.9	7.5	3.6	3.2	2.9
55 277	2.0	2.9	2.7	1.7	2.8	1.9	7.4	3.4	2.8	2.9

Notes. $\nu^{\rm syn}_{\rm peak}$: the peak frequency of the synchrotron bump; $(\nu F_\nu)^{\rm syn}_{\rm peak}$: the peak energy flux of the synchrotron bump; $\nu^{\rm ic}_{\rm peak}$: the peak frequency of the inverse-Compton bump; $(\nu F_\nu)^{\rm ic}_{\rm peak}$: the peak energy flux of the inverse-Compton bump. For each bump in the SED, the value of $(\nu F_\nu)_{\rm peak}/2$ determines the two frequencies (ν_1 and ν_2) that are used to quantify the width of the bump in the logarithmic scale $\log(\nu_2/\nu_1)$.

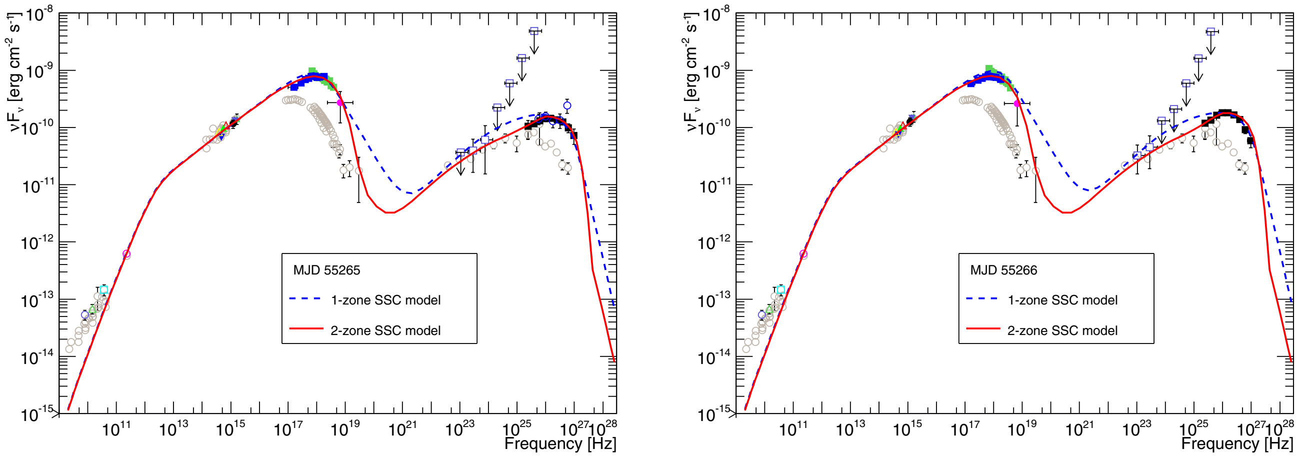

(a) MJD 55 265.

(b) MJD 55 266.

Fig. 8. Broadband SEDs from MJD 55 265 and 55 266 (the two days with the highest activity) with the one-zone and two-zone model curves described in Sects. 4.2 and 4.3. We refer to Figs. B.1 and 2a for details of the data points.

in several papers (e.g. Tagliaferri et al. 2008, for the case of 1ES 1959+650). The fact that we can explain the temporal evolution of the SED during 13 consecutive days without changing the model parameters related to the environment could be interpreted as meaning that the blazar emission region is not traveling relativistically, but rather is stationary in one or several regions of the jet where there is a standing shock. Such standing shocks could be produced, for instance, by recollimation in the jet, and the particles would be accelerated as the jet flows or the superluminal knots cross it (Komissarov & Falle 1997; Sokolov et al. 2004; Marscher 2014). The Lorentz factor of the plasma, as it flows through the standing shock, would be the Lorentz factor that would lead to the Doppler factor (depending on the angle) used in the model.

This MW campaign reveals that the correlation between the X-ray flux at the 2−10 keV band and the VHE γ-ray flux above 200 GeV shows an approximately linear trend (see Fig. 4 middle and bottom panels), while the correlation between X-ray flux at the 0.3-2 keV band and the VHE γ-ray flux is equally close to both a linear and quadratic trend (see Fig. 4 top panel). This is an interesting result because the 0.3−2 keV band reports the synchrotron emission below or at the low-energy (synchrotron) peak of the SED, while the 2−10 keV band reports the emission at or above the low-energy peak. During the Mrk 421 flaring activity observed in 2001, it was also noted that the VHE-to-X-ray (above 2 keV) correlation was linear when considering day timescales, but the correlation was quadratic when considering few-hour long variability (see Fossati et al. 2008). A quadratic (or more-than-quadratic) correlation between X-ray and VHE γ-ray fluxes in the decaying phase is hard to explain with conventional SSC models (Katarzyński et al. 2005). During the flaring activity observed in 2010 March, we do not detect any significant intra-night variability, which might be due to the shorter (about one hour) duration of the observations (in comparison to the many-hour long observations reported in Fossati et al. 2008), or perhaps due to the lower X-ray and VHE activity (in contrast to that of 2001).

The almost linear correlation at 2−10 keV X-rays can be explained as follows: In the framework of the one-zone SSC model, the SED peaks at γ-ray frequencies are produced by the smaller cross-section in the Klein-Nishina regime, rather than by the breaks $\gamma_{\rm br,1/2}$ in the EED. Therefore, the γ-ray emission with energies above the SED peak energy is affected by the lower Klein-Nishina cross-section and is dominated by inverse-Compton scattering off infrared-to-optical photons. Since these target photons are produced by the synchrotron radiation of electrons with a Lorentz factor well below $\gamma_{\rm br1}$, whose density is almost constant during this decaying phase (see Fig. 5b), the density of target photons is almost constant. Thus, the change in the number density of electrons above $\gamma_{\rm br2}$ is directly reflected in the γ-ray flux, resulting in the almost linear correlation between X-ray and γ-ray fluxes. A similar mechanism also works in the two-zone SSC model in each blob. In a flaring blob, γ-ray SED peaks originate from the Klein-Nishina effect. Therefore, γ-rays with energies above the SED peak result from inverse-Compton scattering of electrons off photons below the SED peak at the X-ray band as well as in the one-zone SSC model. Thus, the almost linear relation is realized in both the quiescent and flaring blobs, and hence it is also realized in the total spectra.

The correlation between X-rays and γ-rays was analyzed with a great level of detail in Katarzyński et al. (2005), where the evolution of several quantities such as the number density of electrons, magnetic fields, and the size of the emission region, are simply parameterized to study their contribution to the index of the correlation. Evolution of the emission region volume is a possibility to naturally explain the reduction of the electron number density in the emission region. In the results presented here we fixed the size R to properly study the evolution of the electron spectrum with the steady SSC models at each moment. Further studies of the temporal broadband emission evolution involving such additional parameters will be performed elsewhere.

The SED model results described in Sects. 4.1 and 4.2 allow for an estimate of several physical properties of Mrk 421 during the flaring activity from 2010 March: the total electron number density $N_{\rm e}$, mean electron Lorentz factor $\langle\gamma_{\rm e}\rangle$, the jet power carried by electrons $L_{\rm e}$, the jet power carried by the magnetic field $L_{\rm B}$, the ratio of comoving electron and magnetic field energy densities $U'_{\rm e}/U'_{\rm B} = L_{\rm e}/L_{\rm B}$, the synchrotron luminosity $L_{\rm syn}$ (integrated from $10^{9.5}$ Hz to $10^{20.5}$ Hz), the inverse-Compton luminosity $L_{\rm IC}$ (integrated from $10^{20.5}$ Hz to 10^{28} Hz), and the total photon luminosity from the SSC model $L_{\rm ph} = L_{\rm syn} + L_{\rm IC}$. We can also compute the jet power carried by protons $L_{\rm p}$ assuming one proton per electron ($N_{\rm p} = N_{\rm e}$). The total jet power is $L_{\rm jet} = L_{\rm p} + L_{\rm e} + L_{\rm B}$. We follow the prescriptions given in Celotti & Ghisellini (2008). Specifically, the following formulae are used:

$$N_{\mathrm{e}} = \int_{\gamma_{\min}}^{\gamma_{\max}} \frac{\mathrm{d}n_{\mathrm{e}}}{\mathrm{d}\gamma_{\mathrm{e}}} \mathrm{d}\gamma_{\mathrm{e}}, \tag{5}$$

$$\langle\gamma_{\mathrm{e}}\rangle = \frac{\int_{\gamma_{\min}}^{\gamma_{\max}} \gamma_{\mathrm{e}} \frac{\mathrm{d}n_{\mathrm{e}}}{\mathrm{d}\gamma_{\mathrm{e}}} \mathrm{d}\gamma_{\mathrm{e}}}{N_{\mathrm{e}}}, \tag{6}$$

$$L_{\mathrm{e}} = \pi R^2 \Gamma^2 \beta c N_{\mathrm{e}} \langle\gamma_{\mathrm{e}}\rangle m_{\mathrm{e}} c^2, \tag{7}$$

$$L_{\mathrm{p}} = \pi R^2 \Gamma^2 \beta c N_{\mathrm{e}} m_{\mathrm{p}} c^2, \tag{8}$$

$$L_{\mathrm{B}} = \frac{1}{8} R^2 \Gamma^2 \beta c B^2, \tag{9}$$

$$L_{\mathrm{ph}} = \int \frac{\pi D_{\mathrm{L}}^2 F_\nu}{\Gamma^2} \frac{(1+z)\mathrm{d}\nu}{\delta}, \tag{10}$$

where $\Gamma \sim \delta$, $\beta = \frac{v}{c} = \sqrt{1 - \frac{1}{\Gamma^2}} \sim 1 - \frac{1}{2\Gamma^2}$, $D_{\mathrm{L}} = 134$ Mpc. In the jet power calculation, only one side is considered, differently to what was done in Finke et al. (2008), who used a two-sided jet. The details of these quantities derived with the SSC model parameters are tabulated in Appendix C.

In both the one-zone and two-zone model, the electron luminosity L_{e} and magnetic luminosity L_{B} are more than one order of magnitude away from equipartition, which was reported in Abdo et al. (2011), Mankuzhiyil et al. (2011), Aleksić et al. (2012a). In addition, we found that the ratio $L_{\mathrm{e}}/L_{\mathrm{B}}$ does not vary much during the 13-day period considered here.

In the two-zone model, the total power $L_{\mathrm{p}} + L_{\mathrm{e}} + L_{\mathrm{B}}$ of the flaring blob is about one order of magnitude smaller than that of the quiescent-state blob ($\sim 10^{43}$ erg s^{-1} vs. $\sim 10^{44}$ erg s^{-1}) even though $\langle\gamma_{\mathrm{e}}\rangle$ is 20−30 times higher. This is caused by the smaller size of the flaring blob, in spite of its stronger magnetic field and higher electron density. Nevertheless, the flaring blob is responsible for about half of the photon luminosity $L_{\mathrm{ph}}(=L_{\mathrm{syn}} + L_{\mathrm{IC}})$ of the quiescent-state blob during the highest X-ray/VHE γ-ray activity. This indicates that the radiative efficiency of electrons is high in the flaring blob as a result of the strong magnetic field B and high electron number density n_{e}. Since the contribution of the flaring blob to the total photon luminosity decreases with the decline of the X-ray/VHE activity, the total photon luminosity in the two-zone model does not change substantially during the 13-day period with the VHE flux going from ~2 c.u. down to ~0.5 c.u., remaining at about $(3{-}5) \times 10^{42}$ erg s^{-1}. On the other hand, the variation of the total photon luminosity in the one-zone model is from 9×10^{42} erg s^{-1} to 3×10^{42} erg s^{-1}, and hence, in terms of jet energetics, the production of the measured X-ray/VHE flaring activity is more demanding in the one-zone scenario than in the two-zone scenario.

6. Conclusion

We have reported the MW observations of the decaying phase of a Mrk 421 flare from 2010 March, and characterized it with two leptonic scenarios: a one-zone SSC model, and a two-zone SSC model where one zone is responsible for the quiescent emission, while the other (smaller) zone, which is spatially separated from the former one, contributes to the daily-variable emission occurring mostly at X-rays and VHE γ-rays. We found that flux variability is noticeable at the X-ray and VHE γ-ray bands, while it is minor or not significant in the other bands. These observations revealed an almost linear correlation between the X-ray flux at the 2−10 keV band and the VHE γ-ray flux above 200 GeV, consistent with the γ-rays being produced by inverse-Compton scattering in the Klein-Nishina regime in the framework of SSC models.

The broadband SEDs during this flaring episode, resolved on timescales of one day, allowed for an unprecedented characterization of the time evolution of the radio to γ-ray emission of Mrk 421. Such a detailed study has not been performed on Mrk 421 or any other blazar before. Both the one-zone SSC and the two-zone SSC models can describe the daily SEDs via the variation of only five and four model parameters respectively, under the hypothesis that the variability is associated mostly with the underlying particle population. This shows that blazar variability might be dominated by the acceleration and cooling mechanisms that produce the EED. For both cases (one-zone and two-zone SSC models), an EED parameterized by two power-law functions is sufficient to describe the emission during the very high states (MJD 55 265 and 55 266), but an EED with three power-law functions is needed during the somewhat lower blazar activity.

We also found that the two-zone SSC model describes the measured SED data at the peaks of the low- and high-energy bumps better, although the reported one-zone SSC model could be further improved by the variation of the parameters related to the emitting region itself, in addition to the parameters related to the particle population. The two-zone SSC scenario presented here naturally provides shorter timescales (one hour vs. one day) for variability at the X-ray and VHE bands, as well as lack of correlation between the radio/optical/GeV emission and the variability in the X-ray/VHE bands. Within this two-zone SSC scenario, the EED of the flaring blob is constrained to a very narrow range of energies, namely $\gamma_{\min}{-}\gamma_{\max} \sim 3 \times 10^4{-}6 \times 10^5$, which could be produced through stochastic particle acceleration via scattering by magnetic inhomogeneities in the jet.

Acknowledgements. The authors thank the anonymous referee for providing a very detailed and constructive list of remarks that helped us to improve the manuscript. The MAGIC collaboration would like to thank the Instituto de Astrofísica de Canarias for the excellent working conditions at the Observatorio del Roque de los Muchachos in La Palma. The financial support of the German BMBF and MPG, the Italian INFN and INAF, the Swiss National Fund SNF, the ERDF under the Spanish MINECO, and the Japanese JSPS and MEXT is gratefully acknowledged. This work was also supported by the Centro de Excelencia Severo Ochoa SEV-2012-0234, CPAN CSD2007-00042, and MultiDark CSD2009-00064 projects of the Spanish Consolider-Ingenio 2010 programme, by grant 268740 of the Academy of Finland, by the Croatian Science Foundation (HrZZ) Project 09/176 and the University of Rijeka Project 13.12.1.3.02, by the DFG Collaborative Research Centers SFB823/C4 and SFB876/C3, and by the Polish MNiSzW grant 745/N-HESS-MAGIC/2010/0. The VERITAS collaboration acknowledges supports from the grants from the US Department of Energy Office of Science, the US National Science Foundation and the Smithsonian Institution, by NSERC in Canada, by Science Foundation Ireland (SFI 10/RFP/AST2748) and by STFC in the UK. We acknowledge the excellent work of the technical support staff at the *Fred Lawrence Whipple* Observatory and at the collaborating institutions in the construction and operation of the instrument. The *Fermi*-LAT collaboration acknowledges generous ongoing support from a number of agencies and institutes that have supported both the development and the operation of the LAT as well as scientific data analysis. These include the National Aeronautics and Space Administration and the Department of Energy in the United States, the Commissariat à l'Énergie Atomique and the Centre National de la Recherche Scientifique/Institut National de Physique Nucléaire et de Physique des Particules in France, the Agenzia Spaziale Italiana and the Istituto Nazionale di Fisica Nucleare in Italy, the Ministry of Education, Culture, Sports, Science and Technology (MEXT), High Energy Accelerator Research Organization (KEK) and Japan Aerospace Exploration Agency (JAXA) in Japan, and the K. A. Wallenberg Foundation, the Swedish Research Council and the Swedish National Space Board in Sweden. Additional support for science analysis during the operations phase is gratefully acknowledged from the Istituto Nazionale di Astrofisica in Italy and the Centre National d'Études Spatiales in France. The research at Boston University was funded in part by NASA Fermi Guest Investigator grant NNX11AQ03G. The Submillimeter Array is a joint project between the Smithsonian Astrophysical Observatory and the Academia Sinica Institute of Astronomy and Astrophysics and is funded by the Smithsonian Institution and the Academia Sinica. The OVRO 40-m monitoring program is supported in part by NASA grants NNX08AW31G and NNX11A043G, and

NSF grants AST-0808050 and AST-1109911. The Metsähovi team acknowledges the support from the Academy of Finland to our observing projects (numbers 212656, 210338, 121148, and others). This work was partly supported by Russian RFBR grant 12-02-00452 and St.Petersburg University research grants 6.0.163.2010, 6.38.71.2012. The Abastumani Observatory team acknowledges financial support by the Georgian National Science Foundation through grant GNSF/ST07/4-180 and by the Shota Rustaveli National Science Foundation through the grant FR/577/6-320/13. We acknowledge the use of public data from the *Swift* and RXTE data archive.

References

Abdo, A. A., Ackermann, M., Agudo, I., et al. 2010, ApJ, 716, 30
Abdo, A. A., Ackermann, M., Ajello, M., et al. 2011, ApJ, 736, 131
Abdo, A. A., Abeysekara, A. U., Allen, B. T., et al. 2014, ApJ, 782, 110
Acciari, V., 2011, Ph.D. Thesis, Galway-Mayo Institute of Technology http://veritas.sao.arizona.edu/documents/Theses/Acciari_Thesis.pdf
Acciari, V. A., Aliu, E., Aune, T., et al. 2009, ApJ, 703, 169
Acciari, V. A., Aliu, E., Arlen, T., et al. 2011, ApJ, 738, 25
Acciari, V. A., Arlen, T., Aune, T., et al. 2014, Astropart. Phys., 54, 1
Ackermann, M., Ajello, M., Allafort, A., et al. 2011, ApJ, 741, 30
Ackermann, M., Ajello, M., Albert, A., et al. 2012, ApJS, 203, 4
Aharonian, F. A., Hofmann, W., Konopelko, A. K., & Völk, H. J. 1997, Astropart. Phys., 6, 343
Aharonian, F., Akhperjanian, A., Beilicke, M., et al. 2002, A&A, 393, 89
Aharonian, F., Akhperjanian, A., Beilicke, M., et al. 2003, A&A, 410, 813
Aharonian, F., Akhperjanian, A. G., Aye, K.-M., et al. 2005, A&A, 437, 95
Albert, J., Aliu, E., Anderhub, H., et al. 2007a, ApJ, 663, 125
Albert, J., Aliu, E., Anderhub, H., et al. 2007b, Nucl. Instrum. Methods Phys. Res. A, 583, 494
Aller, H. D., Aller, M. F., Latimer, G. E., & Hodge, P. E. 1985, ApJS, 59, 513
Aleksić, J., Alvarez, E. A., Antonelli, L. A., et al. 2012a, A&A, 542, A100
Aleksić, J., Alvarez, E. A., Antonelli, L. A., et al. 2012b, Astropart. Phys., 35, 435
Aleksić, J., Ansoldi, S., Antonelli, L. A., et al. 2015, A&A, 576, A128
Asano, K., Takahara, F., Kusunose, M., Toma, K., & Kakuwa, J. 2014, ApJ, 780, 64
Atwood, W. B., Abdo, A. A., Ackermann, M., et al. 2009, ApJ, 697, 1071
Błażejowski, M., Blaylock, G., Bond, I. H., et al. 2005, ApJ, 630, 130
Bloom, S. D., & Marscher, A. P. 1996, ApJ, 461, 657
Boone, L. M., Hinton, J. A., Bramel, D., et al. 2002, ApJ, 579, L5
Bradt, H. V., Rothschild, R. E., & Swank, J. H. 1993, A&AS, 97, 355
Breiman, L. 2011, Machine Learning, 45, 5
Brinkmann, W., Papadakis, I. E., Raeth, C., Mimica, P., & Haberl, F. 2005, A&A, 443, 397
Burrows, D. N., Hill, J. E., Nousek, J. A., et al. 2005, Space Sci. Rev., 120, 165
Celotti, A., & Ghisellini, G. 2008, MNRAS, 385, 283
Chen, X., Fossati, G., Liang, E. P., & Böttcher, M. 2011, MNRAS, 416, 2368
Cogan, P. 2006, Ph.D. Thesis, School of Physics, University College Dublin
Daniel, M. K., et al. 2007, Proc. 30th International Cosmic Ray Conf., eds. R. Caballero, et al. (Mexico City, Mexico: Universidad Nacional Autónoma de México), 3, 1325
Dermer, C. D., & Schlickeiser, R. 1993, ApJ, 416, 458
de Vaucouleurs, G., de Vaucouleurs, A., Corwin, H. G., Jr., et al. 1991, Third Reference Catalogue of Bright Galaxies, Vol. 1−3 (Berlin, Heidelberg, New York: Springer-Verlag)
Domínguez, A., Primack, J. R., Rosario, D. J., et al. 2011, MNRAS, 410, 2556
Edelson, R., Turner, T. J., Pounds, K., et al. 2002, ApJ, 568, 610
Finke, J. D., Dermer, C. D., & Böttcher, M. 2008, ApJ, 686, 181
Finke, J. D., Razzaque, S., & Dermer, C. D. 2010, ApJ, 712, 238
Fitzpatrick, E. L. 1999, PASP, 111, 63
Fomin, V. P., Fennell, S., Lamb, R. C., et al. 1994, Astropart. Phys., 2, 151
Fossati, G., Buckley, J. H., Bond, I. H., et al. 2008, ApJ, 677, 906
Franceschini, A., Rodighiero, G., & Vaccari, M. 2008, A&A, 487, 837
Fukugita, M., Shimasaku, K., & Ichikawa, T. 1995, PASP, 107, 945
Gaidos, J. A., Akerlof, C. W., Biller, S., et al. 1996, Nature, 383, 319
Georganopoulos, M., & Kazanas, D. 2003, ApJ, 594, L27
Ghisellini, G., Tavecchio, F., & Chiaberge, M. 2005, A&A, 432, 401
Henri, G., & Saugé, L. 2006, ApJ, 640, 185
Hillas, A. M. 1985, Proc. 19th International Cosmic Ray Conf., San Diego, USA, 3, 445
Horan, D., Acciari, V. A., Bradbury, S. M., et al. 2009, ApJ, 695, 596
Kalberla, P. M. W., Burton, W. B., Hartmann, D., et al. 2005, A&A, 440, 775
Katarzyński, K., Sol, H., & Kus, A. 2003, A&A, 410, 101
Katarzyński, K., Ghisellini, G., Tavecchio, et al. 2005, A&A, 433, 479
Kildea, J., Atkins, R. W., Badran, H. M., et al. 2007, Astropart. Phys., 28, 182
Kneiske, T. M., Bretz, T., Mannheim, K., & Hartmann, D. H. 2004, A&A, 413, 807
Komissarov, S. S., & Falle, S. A. E. G. 1997, MNRAS, 288, 833
Krawczynski, H., Coppi, P. S., & Aharonian, F. 2002, MNRAS, 336, 721
Krawczynski, H., Carter-Lewis, D. A., Duke, C., et al. 2006, Astropart. Phys., 25, 380
Krennrich, F., Bond, I. H., Bradbury, S. M., et al. 2002, ApJ, 575, L9
Lefa, E., Rieger, F. M., & Aharonian, F. 2011, ApJ, 740, 64
Lin, Y. C., Bertsch, D. L., Chiang, J., et al. 1992, ApJ, 401, L61
Mannheim, K. 1993, A&A, 269, 67
Maraschi, L., Ghisellini, G., & Celotti, A. 1992, ApJ, 397, L5
Maraschi, L., Fossati, G., Tavecchio, F., et al. 1999, ApJ, 526, L81
Marscher, A. P. 2014, ApJ, 780, 87
Marscher, A. P., Jorstad, S. G., D'Arcangelo, F. D., et al. 2008, Nature, 452, 966
Mankuzhiyil, N., Ansoldi, S., Persic, M., & Tavecchio, F. 2011, ApJ, 733, 14
Mattox, J. R., Bertsch, D. L., Chiang, J., et al. 1996, ApJ, 461, 396
Moralejo, R. A., Gaug, M., Carmona, E., et al. 2010, Astrophys. Source Code Lib., 11004
Mücke, A., Protheroe, R. J., Engel, R., Rachen, J. P., & Stanev, T. 2003, Astropart. Phys., 18, 593
Nandra, K., George, I. M., Mushotzky, R. F., Turner, T. J., & Yaqoob, T. 1997, ApJ, 476, 70
Nilsson, K., Pasanen, M., Takalo, L. O., et al. 2007, A&A, 475, 199
Nolan, P. L., Abdo, A. A., Ackermann, M., et al. 2012, ApJS, 199, 31
Okumura, K., Asahara, A., Bicknell, G. V., et al. 2002, ApJ, 579, L9
Perkins, J. & Mayer, G. 2009, eConf Proc. C091122 [arXiv:astro-ph:0912.3841]
Piner, B. G., Pant, N., & Edwards, P. G. 2010, ApJ, 723, 1150
Poole, T. S., Breeveld, A. A., Page, M. J., et al. 2008, MNRAS, 383, 627
Poutanen, J., Zdziarski, A. A., & Ibragimov, A. 2008, MNRAS, 389, 1427
Punch, M., Akerlof, C. W., Cawley, M. F., et al. 1992, Nature, 358, 477
Rebillot, P. F., Badran, H. M., Blaylock, G., et al. 2006, ApJ, 641, 740
Richards, J. L., Max-Moerbeck, W., Pavlidou, V., et al. 2011, ApJS, 194, 29
Richards, J. L., Hovatta, T., Lister, M. L., et al. 2013, Eur. Phys. J. Web Conf., 61, 04010
Roming, P. W. A., Kennedy, T. E., Mason, K. O., et al. 2005, Space Sci. Rev., 120, 95
Schlegel, D. J., Finkbeiner, D. P., & Davis, M. 1998, ApJ, 500, 525
Schlickeiser, R. 1985, A&A, 143, 431
Sokolov, A., Marscher, A. P., & McHardy, I. M. 2004, ApJ, 613, 725
Stawarz, L., & Petrosian, V. 2008, ApJ, 681, 1725
Stroh, M. C., & Falcone, A. D. 2013, ApJS, 207, 28
Tagliaferri, G., Foschini, L., Ghisellini, G., et al. 2008, ApJ, 679, 1029
Takami 2011, MNRAS, 413, 1845
Tavecchio, F., Maraschi, L., & Ghisellini, G. 1998, ApJ, 509, 608
Teraesranta, H., Tornikoski, M., Mujunen, A., et al. 1998, A&AS, 132, 305
Tramacere, A., Massaro, F., & Cavaliere, A. 2007, A&A, 466, 521
Tramacere, A., Giommi, P., Perri, M., Verrecchia, F., & Tosti, G. 2009, A&A, 501, 879
Vaughan, S., Edelson, R., Warwick, R. S., & Uttley, P. 2003, MNRAS, 345, 1271
Villata, M., Raiteri, C. M., Lanteri, L., Sobrito, G., & Cavallone, M. 1998, A&AS, 130, 305
Villata, M., Raiteri, C. M., Larionov, V. M., et al. 2008, A&A, 481, L79
Villata, M., Raiteri, C. M., Gurwell, M. A., et al. 2009, A&A, 504, L9
Weekes, T. C., Badran, H., Biller, S. D., et al. 2002, Astropart. Phys., 17, 221

[1] IFAE, Campus UAB, 08193 Bellaterra, Spain
[2] Università di Udine, and INFN Trieste, 33100 Udine, Italy
[3] INAF National Institute for Astrophysics, 00136 Rome, Italy
[4] Università di Siena, and INFN Pisa, 53100 Siena, Italy
[5] Croatian MAGIC Consortium, Rudjer Boskovic Institute, University of Rijeka and University of Split, 10000 Zagreb, Croatia
[6] Max-Planck-Institut für Physik, 80805 München, Germany
[7] Universidad Complutense, 28040 Madrid, Spain
[8] Inst. de Astrofísica de Canarias, 38200 La Laguna, Tenerife, Spain
[9] University of Łódź, 90236 Lodz, Poland
[10] Deutsches Elektronen-Synchrotron (DESY), 15738 Zeuthen, Germany
[11] ETH Zurich, 8093 Zurich, Switzerland
[12] Universität Würzburg, 97074 Würzburg, Germany
[13] Centro de Investigaciones Energéticas, Medioambientales y Tecnológicas, 28040 Madrid, Spain
[14] Institute of Space Sciences, 08193 Barcelona, Spain
[15] Università di Padova and INFN, 35131 Padova, Italy
[16] Technische Universität Dortmund, 44221 Dortmund, Germany
[17] Unitat de Física de les Radiacions, Departament de Física, and CERES-IEEC, Universitat Autònoma de Barcelona, 08193 Bellaterra, Spain

[18] Universitat de Barcelona, ICC, IEEC-UB, 08028 Barcelona, Spain
[19] Japanese MAGIC Consortium, Division of Physics and Astronomy, Kyoto University, 277-8582 Chiba, Kashiwa, Japan
[20] Finnish MAGIC Consortium, Tuorla Observatory, University of Turku and Department of Physics, University of Oulu, 90014 Oulu, Finland
[21] Inst. for Nucl. Research and Nucl. Energy, 1784 Sofia, Bulgaria
[22] Università di Pisa, and INFN Pisa, 56126 Pisa, Italy
[23] ICREA and Institute of Space Sciences, 08193 Barcelona, Spain
[24] Università dell'Insubria and INFN Milano Bicocca, Como, 22100 Como, Italy
[25] Now at: Centro Brasileiro de Pesquisas Físicas (CBPF/MCTI), R. Dr. Xavier Sigaud, 150 – Urca, 22290-180 Rio de Janeiro – RJ, Brazil
[26] NASA Goddard Space Flight Center, Greenbelt, MD 20771, USA
[27] Department of Physics and Department of Astronomy, University of Maryland, College Park, MD 20742, USA
[28] Now at: École polytechnique fédérale de Lausanne (EPFL), 1015 Lausanne, Switzerland
[29] Now at: Institut für Astro- und Teilchenphysik, Leopold-Franzens-Universität Innsbruck, 6020 Innsbruck, Austria
[30] Now at: Finnish Centre for Astronomy with ESO (FINCA), 20100 Turku, Finland
[31] Now at: Astrophysics Science Division, Bhabha Atomic Research Centre, 400085 Mumbai, India
[32] Now at: School of Chemistry & Physics, University of Adelaide, 5005 Adelaide, Australia
[33] Physics Department, McGill University, Montreal, QC H3A 2T8, Canada
[34] Department of Physics, Washington University, St. Louis, MO 63130, USA
[35] Fred Lawrence Whipple Observatory, Harvard-Smithsonian Center for Astrophysics, Amado, AZ 85645, USA
[36] Department of Physics and Astronomy and the Bartol Research Institute, University of Delaware, Newark, DE 19716, USA
[37] School of Physics, University College Dublin, Belfield, Dublin 4, Ireland
[38] Santa Cruz Institute for Particle Physics and Department of Physics, University of California, Santa Cruz, CA 95064, USA
[39] Institute of Physics and Astronomy, University of Potsdam, 14476 Potsdam-Golm, Germany
[40] Astronomy Department, Adler Planetarium and Astronomy Museum, Chicago, IL 60605, USA
[41] Department of Physics and Astronomy, Purdue University, West Lafayette, IN 47907, USA
[42] Department of Physics and Astronomy, Iowa State University, Ames, IA 50011, USA
[43] Department of Astronomy and Astrophysics, 525 Davey Lab, Pennsylvania State University, University Park, PA 16802, USA
[44] School of Physics and Astronomy, University of Minnesota, Minneapolis, MN 55455, USA
[45] School of Physics, National University of Ireland Galway, University Road, Galway, Ireland
[46] Department of Physics and Astronomy, University of Iowa, Van Allen Hall, Iowa City, IA 52242, USA
[47] Department of Physics and Astronomy, University of Utah, Salt Lake City, UT 84112, USA
[48] Department of Physics and Astronomy, DePauw University, Greencastle, IN 46135-0037, USA
[49] Enrico Fermi Institute, University of Chicago, Chicago, IL 60637, USA
[50] Kavli Institute for Cosmological Physics, University of Chicago, Chicago, IL 60637, USA
[51] School of Physics and Center for Relativistic Astrophysics, Georgia Institute of Technology, 837 State Street NW, Atlanta, GA 30332-0430, USA
[52] Department of Physics, Anderson University, 1100 East 5th Street, Anderson, IN 46012, USA
[53] Department of Life and Physical Sciences, Galway-Mayo Institute of Technology, Dublin Road, Galway, Ireland
[54] Department of Physics and Astronomy, University of California, Los Angeles, CA 90095, USA
[55] Instituto de Astronomia y Fisica del Espacio, Casilla de Correo 67 – Sucursal 28, (C1428ZAA) Ciudad Autònoma de Buenos Aires, Argentina
[56] Physics Department, California Polytechnic State University, San Luis Obispo, CA 94307, USA
[57] Department of Applied Physics and Instrumentation, Cork Institute of Technology, Bishopstown, Cork, Ireland
[58] Space Science Division, Naval Research Laboratory, Washington, DC 20375-5352, USA
[59] INAF, Osservatorio Astronomico di Torino, 10025 Pino Torinese (TO), Italy
[60] Department of Astronomy, University of Michigan, Ann Arbor, MI 48109-1042, USA
[61] Department of Physics, University of Trento, 38050 Povo, Trento, Italy
[62] Graduate Institute of Astronomy, National Central University, 32054 Jhongli, Taiwan
[63] Harvard-Smithsonian Center for Astrophysics, Cambridge, MA 02138, USA
[64] Institute for Astrophysical Research, Boston University, 725 Commonwealth Avenue, Boston, MA 02215, USA
[65] Astronomical Institute, St. Petersburg State University, Universitetskij Pr. 28, Petrodvorets, 198504 St. Petersburg, Russia
[66] Institute of Astronomy, National Tsing Hua University, 101 Guanfu Rd., 30013 Hsinchu, Taiwan
[67] Abastumani Observatory, Mt. Kanobili, 0301 Abastumani, Georgia
[68] Landessternwarte, Zentrum für Astronomie der Universität Heidelberg, Königstuhl 12, 69117 Heidelberg, Germany
[69] Aalto University Metsähovi Radio Observatory, Metsähovintie 114, 02540 Kylmälä, Finland
[70] Aalto University Department of Radio Science and Engineering, PO Box 13000, 00076 Aalto, Finland
[71] Astron. Inst., St.-Petersburg State University, 198504 St. Peetersburg, Russia
[72] Pulkovo Observatory, St.-Petersburg, 198504 St. Peetersburg, Russia
[73] Isaac Newton Institute of Chile, St.-Petersburg Branch, Russia
[74] Department of Physics and Astronomy, Brigham Young University, Provo, UT 84602, USA
[75] Cahill Center for Astronomy and Astrophysics, California Institute of Technology, 1200 E California Blvd, Pasadena, CA 91125, USA
[76] ASI-Science Data Center, via del Politecnico, 00133 Rome, Italy
[77] Agrupació Astronòmica de Sabadell, 08206 Sabadell Barcelona, Spain
[78] Department of Physics, University of Colorado Denver, Denver, Colorado, Co 80217-3364, USA
[79] Department of Physics and Mathematics, College of Science and Engineering, Aoyama Gakuin University, 5-10-1 Fuchinobe, 1105 Chuoku, 252-5258 Sagamihara-shi Kanagawa, Japan
[80] Steward Observatory, University of Arizona, Tucson, AZ 85721, USA
[81] Space Science Institute, Boulder, CO 80301, USA
[82] School of Cosmic Physics, Dublin Institute for Advanced Studies, Belfield, Dublin 2, Ireland

Pages 18 to 26 are available in the electronic edition of the journal at http://www.aanda.org

Appendix A: Simultaneity in the multi-instrument observations

The energy coverage as a function of the time for the daily multi-instrument observations from 2010 March 10 (MJD 55 265) to 2010 March 22 (MJD 55 277) is depicted in Figs. A.1 and A.2, which show that most of the observations used to determine the SEDs reported in Appendix B occur within less than 2 h.

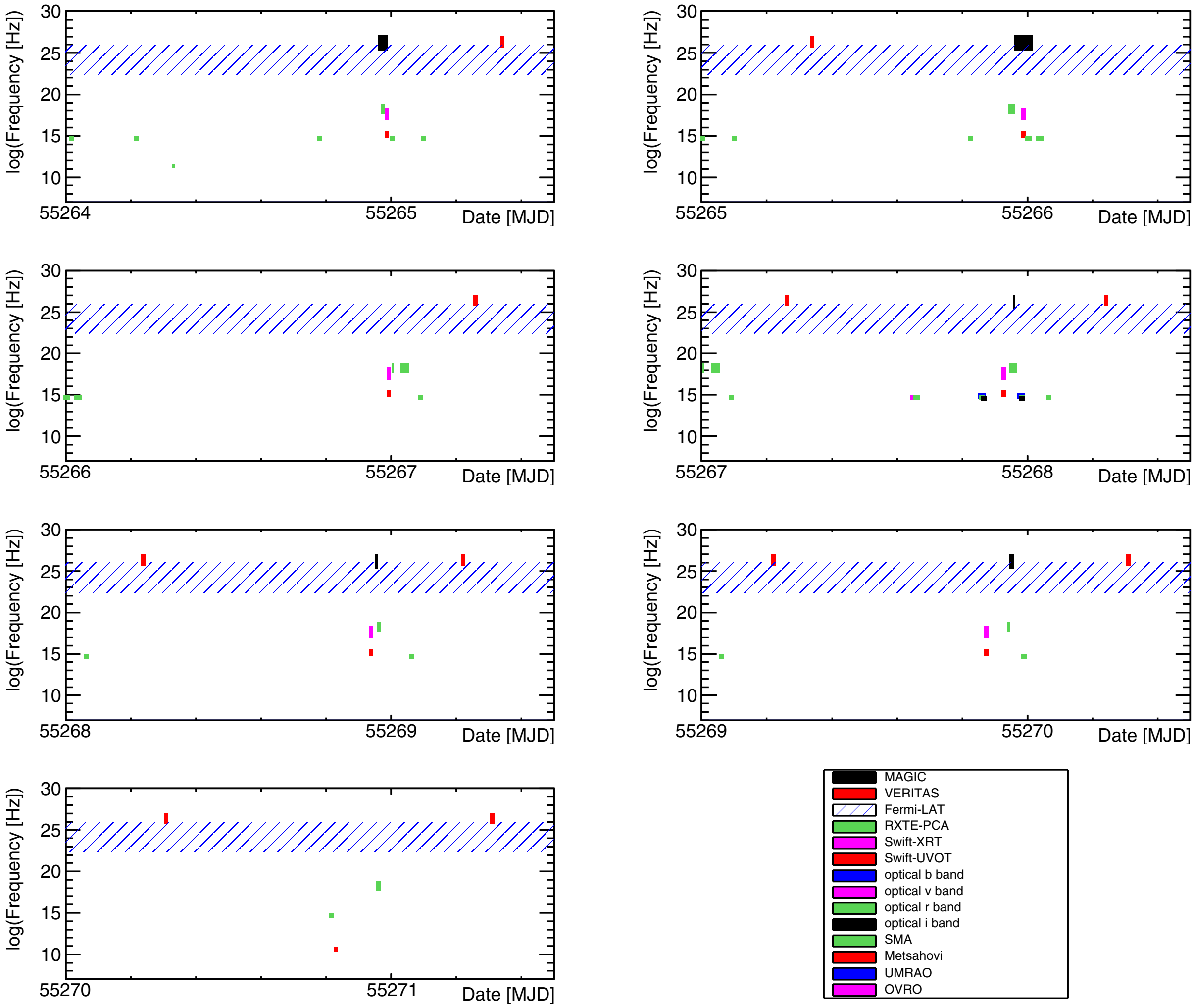

Fig. A.1. Temporal and energy coverage during the flaring activity from 2010 March 10 (MJD 55 265) to 2010 March 16 (MJD 55 271). *Fermi*-LAT data were accumulated during two-day time intervals to ensure significant detections of Mrk 421, and is depicted here with a blue band. For better visibility of the observations at UV, optical, and radio band, where the observation time is usually short and the covered frequency band is narrow, an additional 20 min in time and half a decade in frequency are included when displaying the results. The names of all the optical instruments are listed in Table 1.

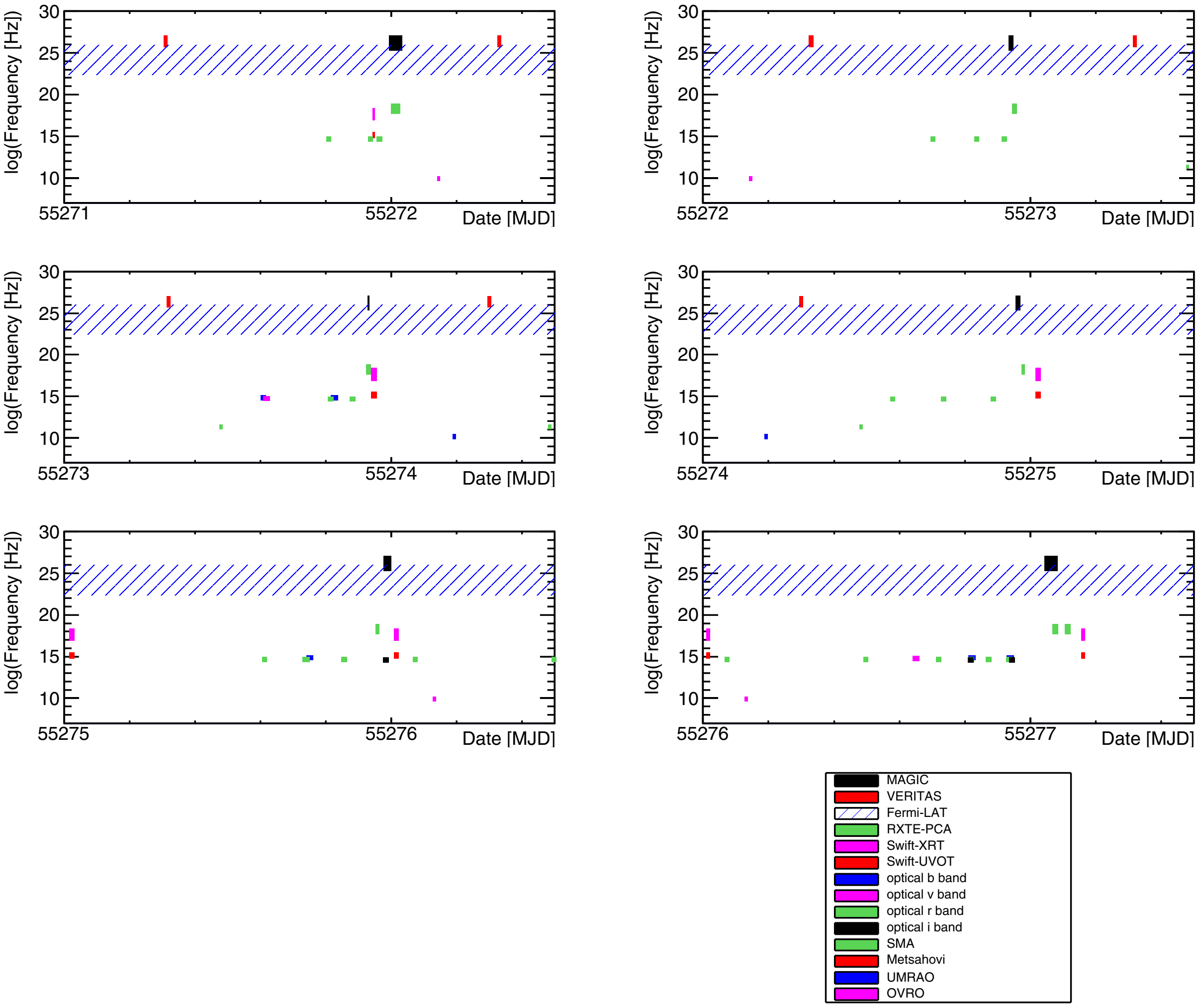

Fig. A.2. Temporal and energy coverage during the flaring activity from 2010 March 17 (MJD 55 272) to 2010 March 22 (MJD 55 277). See the caption of Fig. A.1 for further details.

Appendix B: Broadband SEDs for the 13 consecutive days

The measured SEDs for these 13 consecutive days are shown in Figs. B.1 to B.5 with one-zone SSC model curves (from Figs. B.1 to Fig. B.3) and two-zone SSC model curves (Figs. B.4 and B.5). The SED with a two-zone SSC model curve measured on the first day (MJD 55 265) was shown in Fig. 6 in the main text. For comparison, the average SED from the 2009 MW campaign (Abdo et al. 2011) is shown in all the figures, which is a good representation of the SED of Mrk 421 during its nonflaring (typical) state. The details of the models and the characterization of the SED evolution were discussed in Sects. 4.1 and 4.2 in the main text.

The actual MJD date for each data entry is given in the legend of each figure. For optical bands, the reported SED data points correspond to the averaged values (host-galaxy subtracted) for the specified observing night. As reported in Sect. 3, the variability at the optical band is small and occurs on timescales of several days. Therefore, if there was no instrument observing at a particular optical energy band, then the nearest observation was used, and the corresponding MJD date is described in the legend of the figure.

Although Mrk 421 is cosmologically nearby, at a redshift of 0.03, the absorption of γ-rays by the extragalactic background light (EBL) is not negligible at TeV energies. The VHE spectra are corrected (de-absorbed) with the EBL model provided by Franceschini et al. (2008), where $e^{-\tau_{\gamma\gamma}} = 0.58$ at 4 TeV. At this energy, which is roughly the highest energy bin in the VHE spectra, most models provide $0.5 < e^{-\tau_{\gamma\gamma}} < 0.6$, such as models from Kneiske et al. (2004), Finke et al. (2010), and Domínguez et al. (2011), which means that the results are not sensitive to the particular published EBL model that we selected.

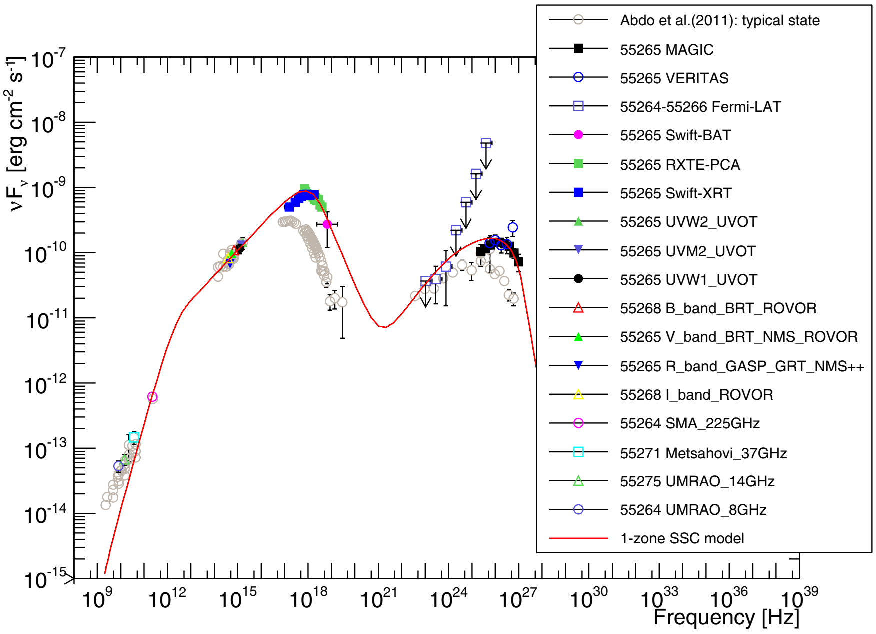

Fig. B.1. Largely simultaneous broadband SED of Mrk 421 on MJD 55 265. The correspondence between markers and instruments is given in the legend. The full names of the instruments can be found in Table 1. Because of space limitations, *R*-band instruments other than GASP, GRT, and NMS are denoted with the symbol "++". Whenever a simultaneous observation is not available, the fluxes from the closest date are reported, and their observation time in MJD is reported next to the instrument name in the legend. The red curve depicts the one-zone SSC model matching the data. The gray circles depict the average SED from the 2009 MW campaign reported in Abdo et al. (2011), which is a good representation of the nonflaring (typical) SED of Mrk 421.

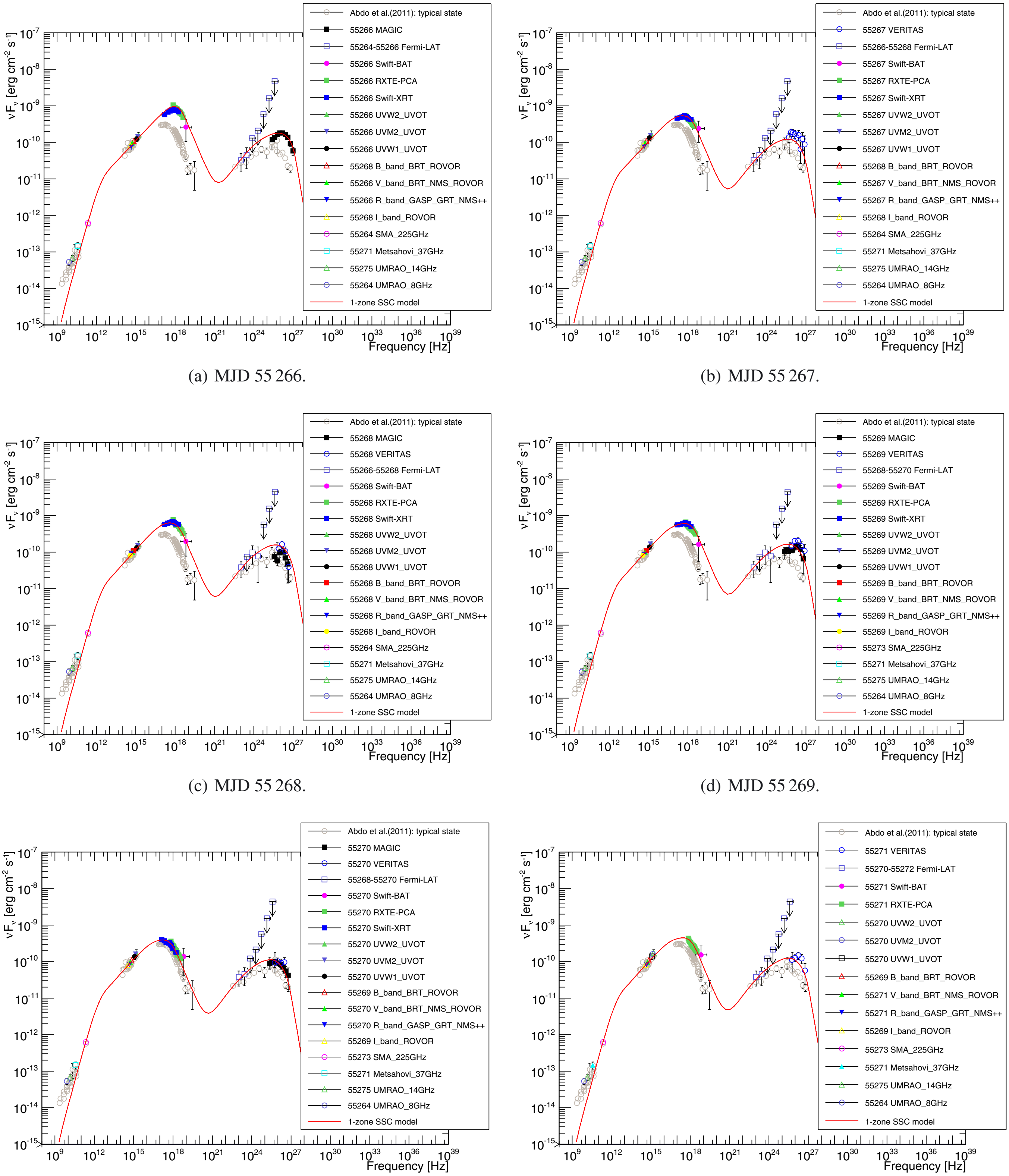

(a) MJD 55 266.

(b) MJD 55 267.

(c) MJD 55 268.

(d) MJD 55 269.

(e) MJD 55 270.

(f) MJD 55 271.

Fig. B.2. Simultaneous broadband SEDs and their one-zone SSC model fits. See caption of Fig. B.1 for further details.

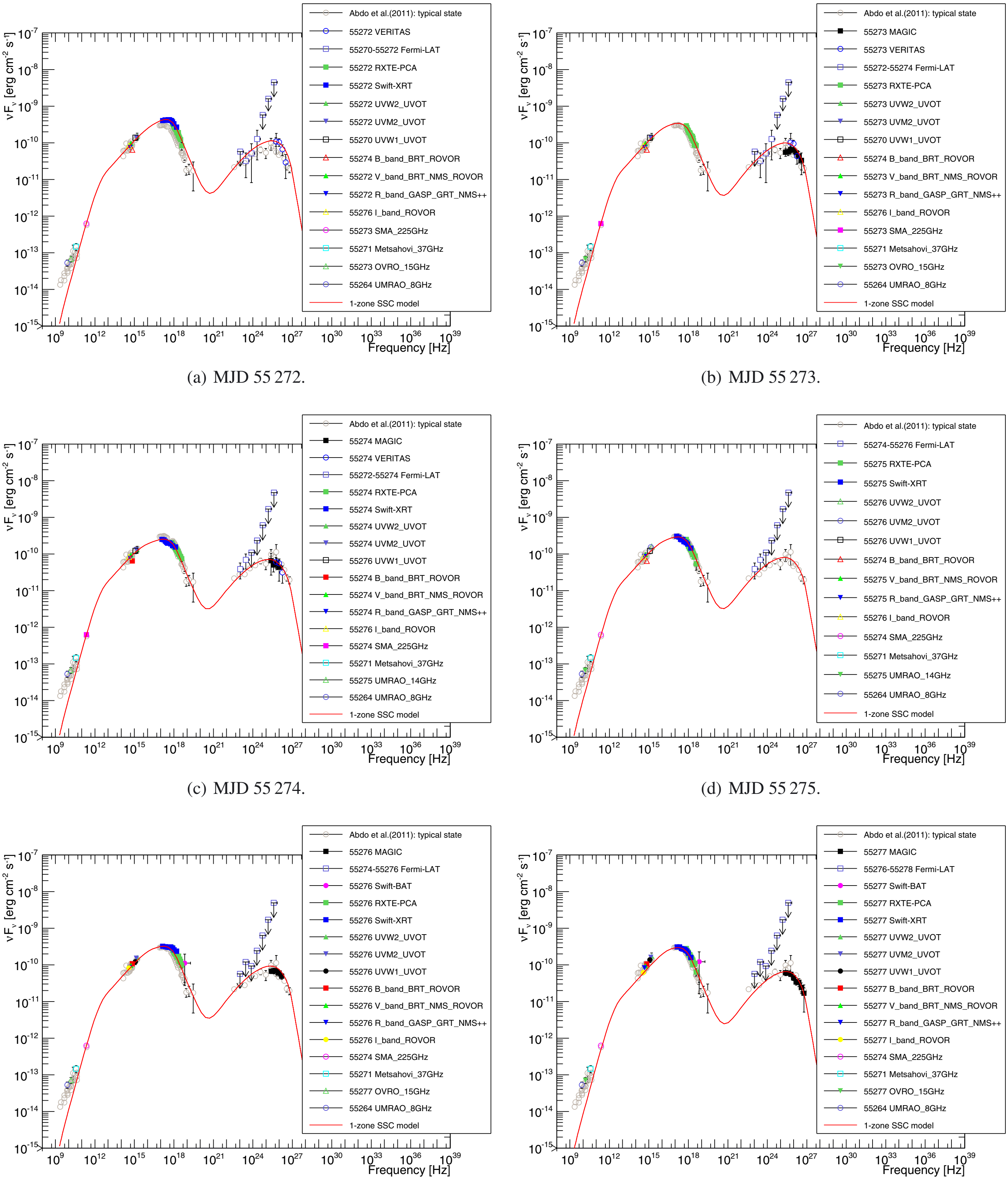

(a) MJD 55 272.

(b) MJD 55 273.

(c) MJD 55 274.

(d) MJD 55 275.

(e) MJD 55 276.

(f) MJD 55 277.

Fig. B.3. Simultaneous broadband SEDs and their one-zone SSC model fits. See caption of Fig. B.1 for further details.

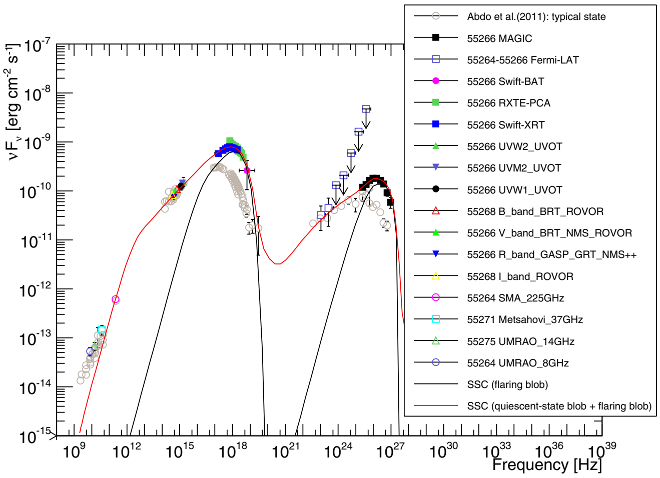

(a) MJD 55 266.

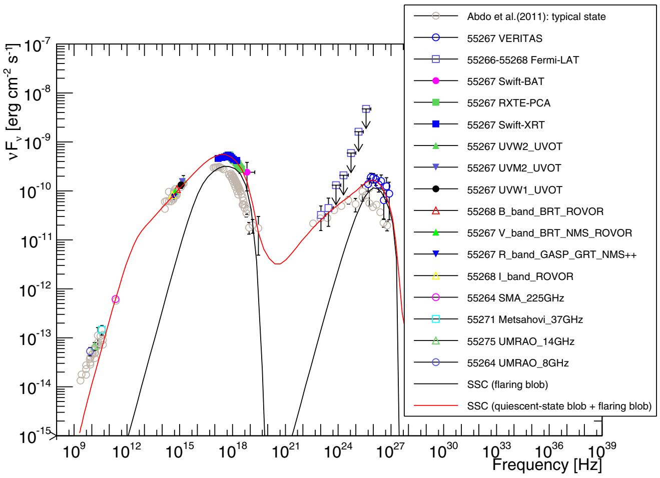

(b) MJD 55 267.

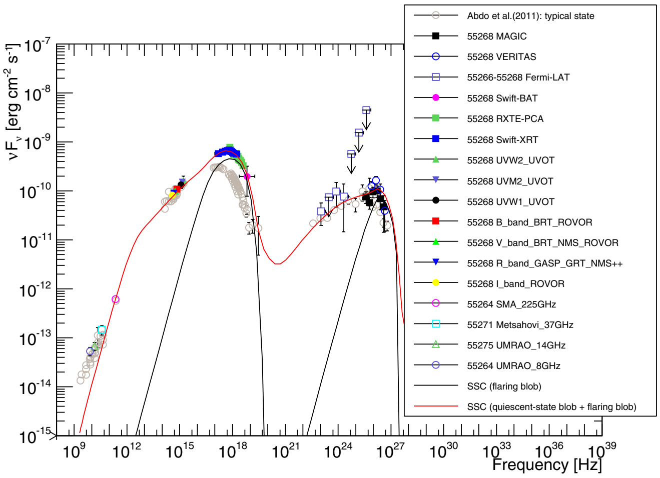

(c) MJD 55 268.

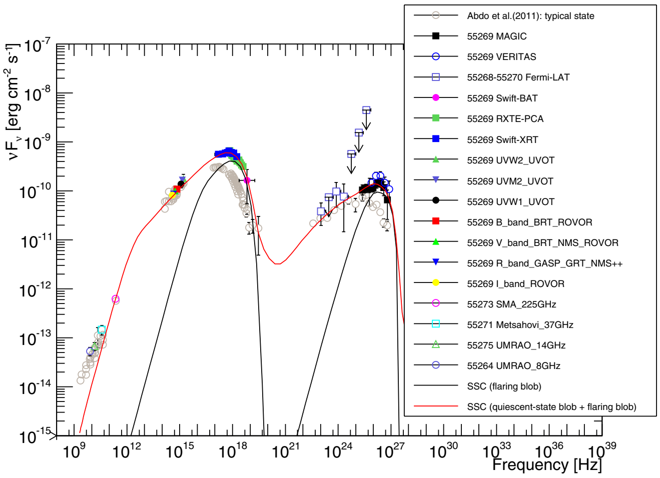

(d) MJD 55 269.

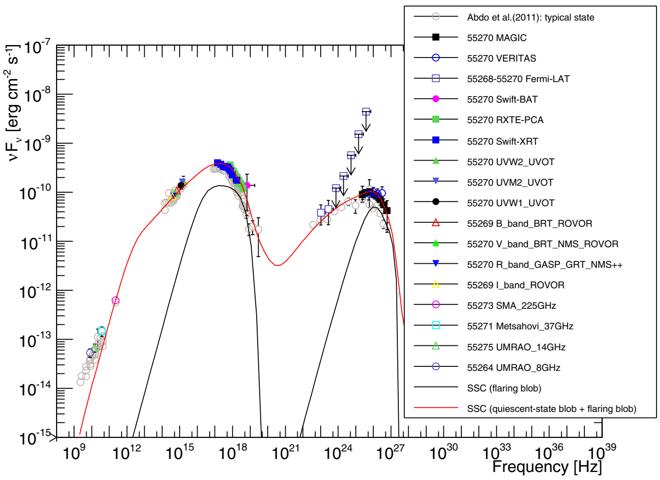

(e) MJD 55 270.

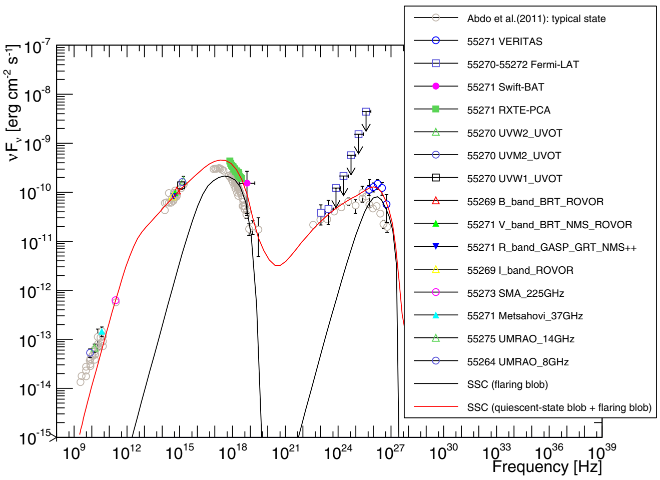

(f) MJD 55 271.

Fig. B.4. Simultaneous broadband SEDs and their two-zone SSC model fits. See caption of Fig. 6 for further details.

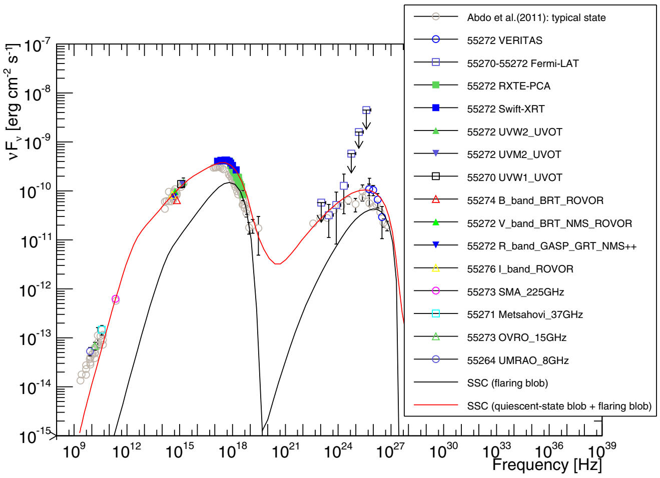

(a) MJD 55 272.

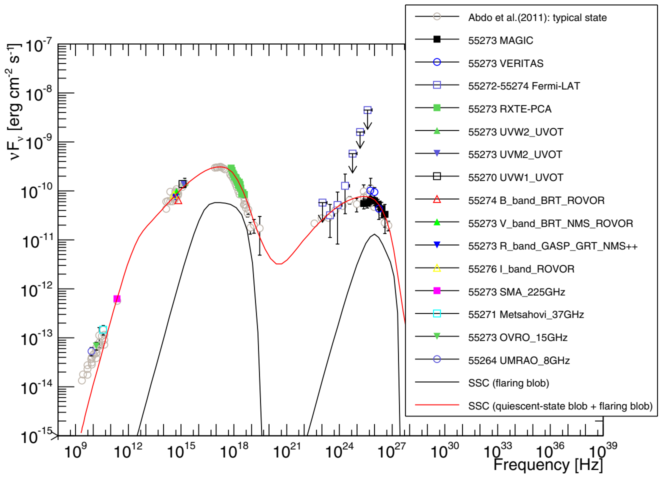

(b) MJD 55 273.

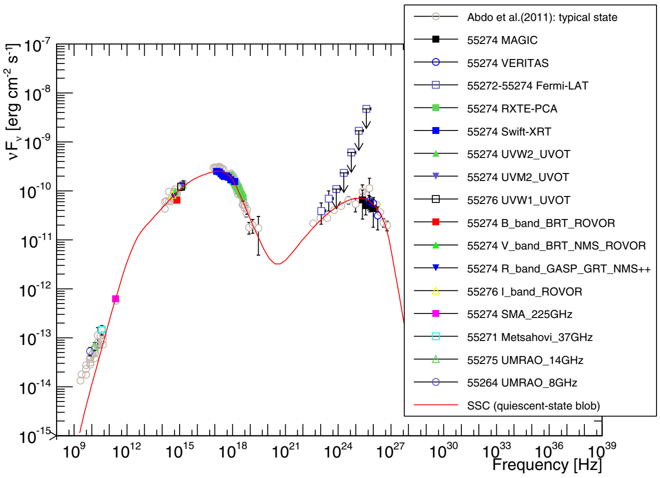

(c) MJD 55 274.

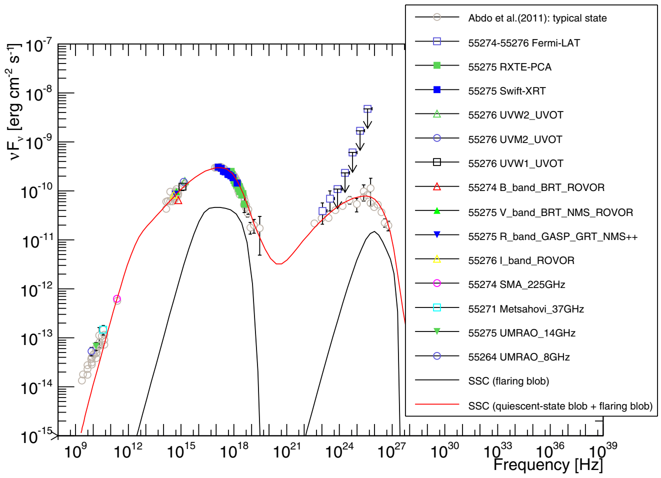

(d) MJD 55 275.

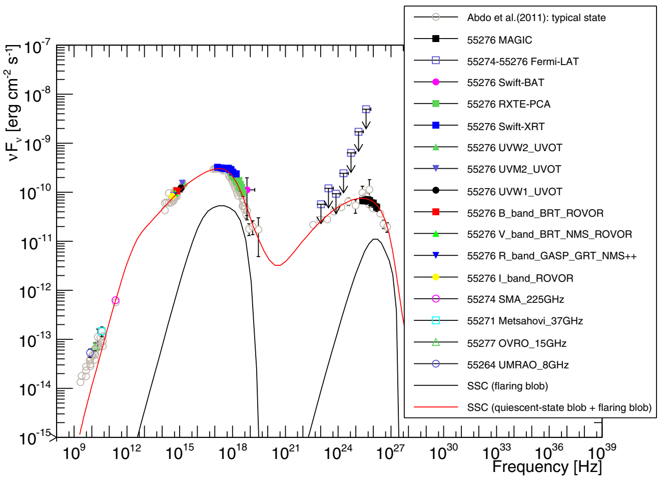

(e) MJD 55 276.

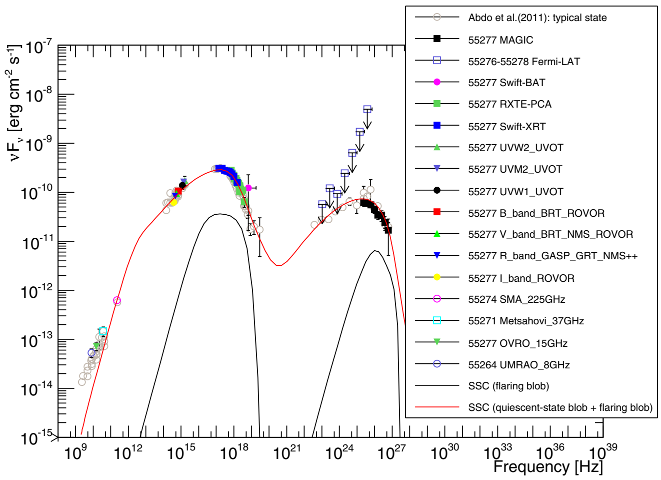

(f) MJD 55 277.

Fig. B.5. Simultaneous broadband SEDs and their two-zone SSC model fits. See caption of Fig. 6 for further details. The emission of the quiescent blob was set to the one describing the SED from MJD 55 274, which is the lowest SED among all the 13 dates considered in this paper. Consequently, there is no flaring blob emission for MJD 55 274.

Appendix C: Physical parameters derived from one-zone and two-zone SSC scenarios

Physical parameters inferred from spectral modeling are tabulated in Table C.1 for the one-zone SSC model and in Table C.2 for the two-zone SSC model. The definition of these quantities are provided by Eqs. (5) to (10).

Table C.1. Jet powers and luminosities derived with the parameters from the one-zone SSC model reported in Table 2.

Date – [MJD]	N_e [10^{-1}] [cm^{-3}]	$\langle\gamma_e\rangle$ [10^3] –	L_e [10^{43}] [$\mathrm{erg\,s^{-1}}$]	L_p [10^{43}] [$\mathrm{erg\,s^{-1}}$]	L_B [10^{42}] [$\mathrm{erg\,s^{-1}}$]	U'_e/U'_B [10^1] –	L_{jet} [10^{44}] [$\mathrm{erg\,s^{-1}}$]	L_{syn} [10^{42}] [$\mathrm{erg\,s^{-1}}$]	L_{IC} [10^{41}] [$\mathrm{erg\,s^{-1}}$]	L_{ph} [10^{42}] [$\mathrm{erg\,s^{-1}}$]
55 265	2.5	3.4	7.8	4.2	6.5	1.2	1.3	6.6	14.	8.1
55 266	2.5	3.4	8.0	4.3	6.5	1.2	1.3	7.2	16.	8.8
55 267	2.4	3.3	7.3	4.0	6.5	1.1	1.2	4.6	11.	5.7
55 268	2.5	3.5	7.9	4.2	6.5	1.2	1.3	5.4	14.	6.7
55 269	2.6	3.4	8.2	4.4	6.5	1.3	1.3	5.5	14.	6.9
55 270	2.5	3.3	7.5	4.1	6.5	1.2	1.2	3.5	9.8	4.5
55 271	2.5	3.4	7.6	4.1	6.5	1.2	1.2	4.0	11.	5.1
55 272	2.5	3.3	7.5	4.1	6.5	1.1	1.2	3.7	10.	4.7
55 273	2.5	3.2	7.3	4.1	6.5	1.1	1.2	3.1	8.7	4.0
55 274	2.5	3.1	7.0	4.1	6.5	1.1	1.2	2.5	6.5	3.1
55 275	2.3	3.2	6.8	3.9	6.5	1.1	1.1	2.8	7.2	3.5
55 276	2.5	3.2	7.3	4.1	6.5	1.1	1.2	3.0	8.2	3.8
55 277	1.9	3.3	5.8	3.2	6.5	.90	.97	2.6	5.7	3.2

Notes. N_e: total electron number density; $\langle\gamma_e\rangle$: mean electron Lorentz factor; L_e: jet power carried by electrons; L_p: the jet power carried by protons; L_B: jet power carried by the magnetic field; U'_e/U'_B: the ratio of comoving electron and magnetic field energy densities; L_{jet}: total jet power; L_{syn}: the synchrotron luminosity; L_{IC}: inverse-Compton luminosity; L_{ph}: total photon luminosity from the SSC model. See the calculation explanation in Sect. 5.

Table C.2. Jet powers and luminosities derived with the parameters from the two-zone SSC model reported in Table 3.

Date	N_e	$\langle\gamma_e\rangle$	L_e	L_p	L_B	U'_e/U'_B	L_{jet}	L_{syn}	L_{IC}	L_{ph}	$^{sum}L_e$	$^{sum}L_p$	$^{sum}L_B$	$^{sum}L_{jet}$	$^{sum}L_{syn}$	$^{sum}L_{IC}$	$^{sum}L_{ph}$
–	$[10^{-1}]$	$[10^4]$	$[10^{43}]$	$[10^{41}]$	$[10^{41}]$	$[10^1]$	$[10^{43}]$	$[10^{41}]$	$[10^{40}]$	$[10^{41}]$	$[10^{43}]$	$[10^{43}]$	$[10^{42}]$	$[10^{44}]$	$[10^{42}]$	$[10^{41}]$	$[10^{42}]$
[MJD]	$[cm^{-3}]$	–	$[erg\ s^{-1}]$	$[erg\ s^{-1}]$	$[erg\ s^{-1}]$	–	$[erg\ s^{-1}]$	$[erg\ s^{-1}]$	$[erg\ s^{-1}]$	$[erg\ s^{-1}]$	$[erg\ s^{-1}]$	$[erg\ s^{-1}]$	$[erg\ s^{-1}]$	$[erg\ s^{-1}]$	$[erg\ s^{-1}]$	$[erg\ s^{-1}]$	$[erg\ s^{-1}]$
the quiescent blob																	
–	2.5	.31	7.0	410	65.	1.1	12.	25.	65.	31.							
the flaring blob											the quiescent blob + the flaring blob						
55 265	1.6	9.0	1.4	2.8	5.3	2.6	1.5	13.	18.	15.	8.4	4.1	7.0	1.3	3.8	8.3	4.6
55 266	1.9	9.0	1.7	3.4	4.8	3.4	1.7	13.	23.	15.	8.7	4.1	7.0	1.4	3.8	8.8	4.6
55 267	2.1	6.5	1.3	3.8	4.8	2.8	1.4	7.9	18.	9.7	8.3	4.1	7.0	1.3	3.3	8.3	4.1
55 268	.89	12.	1.1	1.6	4.8	2.2	1.1	9.5	8.8	10.	8.1	4.1	7.0	1.3	3.4	7.4	4.1
55 269	1.6	8.6	1.4	2.9	3.9	3.5	1.4	8.7	15.	10.	8.4	4.1	6.9	1.3	3.4	8.0	4.1
55 270	1.3	7.6	1.0	2.4	2.7	3.7	1.1	3.4	7.3	4.2	8.0	4.1	6.8	1.3	2.8	7.2	3.5
55 271	1.6	8.4	1.3	2.9	2.7	4.8	1.4	5.0	12.	6.2	8.3	4.1	6.8	1.3	3.0	7.7	3.7
55 272	.77	9.3	.71	1.4	2.7	2.6	.76	3.5	9.9	4.5	7.7	4.1	6.8	1.3	2.8	7.5	3.5
55 273	.74	6.9	.50	1.3	2.7	1.9	.54	1.5	1.9	1.7	7.5	4.1	6.8	1.3	2.7	6.7	3.3
55 274	–	–	–	–	–	–	–	–	–	–	7.0	4.1	6.5	1.2	2.5	6.5	3.1
55 275	.93	6.9	.63	1.7	1.7	3.6	.66	1.2	2.2	1.5	7.6	4.1	6.7	1.3	2.6	6.7	3.2
55 276	.70	8.0	.56	1.3	1.7	3.2	.59	1.3	1.7	1.5	7.6	4.1	6.7	1.3	2.6	6.7	3.2
55 277	.56	7.6	.42	1.0	1.7	2.4	.45	.92	.95	1.0	7.4	4.1	6.7	1.2	2.6	6.6	3.2

Notes. N_e: total electron number density; $\langle\gamma_e\rangle$: mean electron Lorentz factor; L_e: jet power carried by electrons; L_p: jet power carried by protons; L_B: jet power carried by the magnetic field; U'_e/U'_B: ratio of comoving electron and magnetic field energy densities; L_{jet}: total jet power; L_{syn}: synchrotron luminosity; L_{IC}: inverse-Compton luminosity; L_{ph}: total photon luminosity from the SSC model. See the calculation explanation in Sect. 5. The quantities with the ^{sum} superscript report the sums of the quantities from the quiescent and the flaring blob.

A&A 576, A126 (2015)
DOI: 10.1051/0004-6361/201424216

Astronomy & Astrophysics

The 2009 multiwavelength campaign on Mrk 421: Variability and correlation studies⋆,⋆⋆

J. Aleksić[1], S. Ansoldi[2], L. A. Antonelli[3], P. Antoranz[4], A. Babic[5], P. Bangale[6], U. Barres de Almeida[6], J. A. Barrio[7], J. Becerra González[8], W. Bednarek[9], K. Berger[8], E. Bernardini[10], A. Biland[11], O. Blanch[1], R. K. Bock[6], S. Bonnefoy[7], G. Bonnoli[3], F. Borracci[6], T. Bretz[12,25], E. Carmona[13], A. Carosi[3], D. Carreto Fidalgo[12], P. Colin[6], E. Colombo[8], J. L. Contreras[7], J. Cortina[1], S. Covino[3], P. Da Vela[4], F. Dazzi[2], A. De Angelis[2], G. De Caneva[10], B. De Lotto[2], C. Delgado Mendez[13], M. Doert[14], A. Domínguez[15,26], D. Dominis Prester[5], D. Dorner[12], M. Doro[16], S. Einecke[14], D. Eisenacher[12], D. Elsaesser[12], E. Farina[17], D. Ferenc[5], M. V. Fonseca[7], L. Font[18], K. Frantzen[14], C. Fruck[6], R. J. García López[8], M. Garczarczyk[10], D. Garrido Terrats[18], M. Gaug[18], G. Giavitto[1], N. Godinović[5], A. González Muñoz[1], S. R. Gozzini[10], A. Hadamek[14], D. Hadasch[19], A. Herrero[8], D. Hildebrand[11], J. Hose[6], D. Hrupec[5], W. Idec[9], V. Kadenius[20], H. Kellermann[6], M. L. Knoetig[11], J. Krause[6], J. Kushida[21], A. La Barbera[3], D. Lelas[5], N. Lewandowska[12], E. Lindfors[20,27], F. Longo[2], S. Lombardi[3], M. López[7], R. López-Coto[1], A. López-Oramas[1], E. Lorenz[6], I. Lozano[7], M. Makariev[22], K. Mallot[10], G. Maneva[22], N. Mankuzhiyil[2], K. Mannheim[12], L. Maraschi[3], B. Marcote[23], M. Mariotti[16], M. Martínez[1], D. Mazin[6], U. Menzel[6], M. Meucci[4], J. M. Miranda[4], R. Mirzoyan[6], A. Moralejo[1], P. Munar-Adrover[23], D. Nakajima[21], A. Niedzwiecki[9], K. Nilsson[20,27], N. Nowak[6,⋆⋆⋆,30], R. Orito[21], A. Overkemping[14], S. Paiano[16], M. Palatiello[2], D. Paneque[6,⋆⋆⋆], R. Paoletti[4], J. M. Paredes[23], X. Paredes-Fortuny[23], S. Partini[4], M. Persic[2,⋆⋆⋆⋆], F. Prada[15,†], P. G. Prada Moroni[24], E. Prandini[16], S. Preziuso[4], I. Puljak[5], R. Reinthal[20], W. Rhode[14], M. Ribó[23], J. Rico[1], J. Rodriguez Garcia[6], S. Rügamer[12], A. Saggion[16], K. Saito[21], M. Salvati[3], K. Satalecka[7], V. Scalzotto[16], V. Scapin[7], C. Schultz[16], T. Schweizer[6], S. N. Shore[24], A. Sillanpää[20], J. Sitarek[1], I. Snidaric[5], D. Sobczynska[9], F. Spanier[12], V. Stamatescu[1], A. Stamerra[3], T. Steinbring[12], J. Storz[12], S. Sun[6], T. Surić[5], L. Takalo[20], F. Tavecchio[3], P. Temnikov[22], T. Terzić[5], D. Tescaro[8], M. Teshima[6], J. Thaele[14], O. Tibolla[12], D. F. Torres[19], T. Toyama[6], A. Treves[17], M. Uellenbeck[14], P. Vogler[11], R. M. Wagner[6,28], F. Zandanel[15,29], R. Zanin[23],
(The MAGIC collaboration)
S. Archambault[31], B. Behera[10], M. Beilicke[33], W. Benbow[34], R. Bird[35], J. H. Buckley[33], V. Bugaev[33], M. Cerruti[34], X. Chen[36,32], L. Ciupik[37], E. Collins-Hughes[35], W. Cui[38], J. Dumm[39], J. D. Eisch[40], A. Falcone[41], S. Federici[32,36], Q. Feng[38], J. P. Finley[38], H. Fleischhack[10], P. Fortin[57], L. Fortson[39], A. Furniss[42], S. Griffin[31], S. T. Griffiths[43], J. Grube[37], G. Gyuk[37], D. Hanna[31], J. Holder[44], G. Hughes[10], T. B. Humensky[45], C. A. Johnson[42], P. Kaaret[43], M. Kertzman[46], Y. Khassen[35], D. Kieda[47], H. Krawczynski[33], F. Krennrich[40], S. Kumar[44], M. J. Lang[48], G. Maier[10], S. McArthur[49], K. Meagher[50], P. Moriarty[51,48], R. Mukherjee[52], R. A. Ong[53], A. N. Otte[50], N. Park[49], A. Pichel[54], M. Pohl[36,30], A. Popkow[53], H. Prokoph[10], J. Quinn[35], K. Ragan[31], J. Rajotte[31], P. T. Reynolds[55], G. T. Richards[50], E. Roache[34], A. C. Rovero[54], G. H. Sembroski[38], K. Shahinyan[39], D. Staszak[31], I. Telezhinsky[36,32], M. Theiling[38], J. V. Tucci[38], J. Tyler[33], A. Varlotta[38], S. P. Wakely[49], T. C. Weekes[34], A. Weinstein[40], R. Welsing[10], A. Wilhelm[36,32], D. A. Williams[42], B. Zitzer[56],
(The VERITAS collaboration)
M. Villata[58], C. Raiteri[58], H. D. Aller[59], M. F. Aller[59], W. P. Chen[60], B. Jordan[61], E. Koptelova[60,62], O. M. Kurtanidze[63,64], A. Lähteenmäki[65,66], B. McBreen[67], V. M. Larionov[68,69,70], C. S. Lin[60], M. G. Nikolashvili[63], E. Angelakis[71], M. Capalbi[82], A. Carramiñana[72], L. Carrasco[72], P. Cassaro[73], A. Cesarini[74], L. Fuhrmann[71], M. Giroletti[87], T. Hovatta[65,75], T. P. Krichbaum[71], H. A. Krimm[76,77], W. Max-Moerbeck[75], J. W. Moody[79], G. Maccaferri[80], Y. Mori[81], I. Nestoras[71], A. Orlati[80], C. Pace[78], R. Pearson[79], M. Perri[3,82], A. C. S. Readhead[75], J. L. Richards[83], A. C. Sadun[84], T. Sakamoto[85], J. Tammi[65,66], M. Tornikoski[65], Y. Yatsu[81], and A. Zook[86]

(Affiliations can be found after the references)

Received 15 May 2014 / Accepted 16 January 2015

ABSTRACT

Aims. We perform an extensive characterization of the broadband emission of Mrk 421, as well as its temporal evolution, during the non-flaring (low) state. The high brightness and nearby location ($z = 0.031$) of Mrk 421 make it an excellent laboratory to study blazar emission. The goal is to learn about the physical processes responsible for the typical emission of Mrk 421, which might also be extended to other blazars that are located farther away and hence are more difficult to study.

Methods. We performed a 4.5-month multi-instrument campaign on Mrk 421 between January 2009 and June 2009, which included VLBA, F-GAMMA, GASP-WEBT, *Swift*, RXTE, *Fermi*-LAT, MAGIC, and *Whipple*, among other instruments and collaborations. This extensive radio to very-high-energy (VHE; $E > 100$ GeV) γ-ray dataset provides excellent temporal and energy coverage, which allows detailed studies of the evolution of the broadband spectral energy distribution.

Results. Mrk421 was found in its typical (non-flaring) activity state, with a VHE flux of about half that of the Crab Nebula, yet the light curves show significant variability at all wavelengths, the highest variability being in the X-rays. We determined the power spectral densities (PSD) at most wavelengths and found that all PSDs can be described by power-laws without a break, and with indices consistent with pink/red-noise behavior. We observed a harder-when-brighter behavior in the X-ray spectra and measured a positive correlation between VHE and X-ray fluxes with zero time lag. Such characteristics have been reported many times during flaring activity, but here they are reported for the first time in the non-flaring state. We also observed an overall anti-correlation between optical/UV and X-rays extending over the duration of the campaign.

⋆ Appendix A is available in electronic form at http://www.aanda.org

⋆⋆ The complete data set shown in Fig. 1 is only available at the CDS via anonymous ftp to cdsarc.u-strasbg.fr (130.79.128.5) or via http://cdsarc.u-strasbg.fr/viz-bin/qcat?J/A+A/576/A126

⋆⋆⋆ Corresponding authors: Nina Nowak, e-mail: nina.nowak@astro.su.se; David Paneque, e-mail: dpaneque@mppmu.mpg.de.

⋆⋆⋆⋆ Also at INAF-Trieste.

† Also at Instituto de Fisica Teorica, UAM/CSIC, 28049 Madrid, Spain.

Conclusions. The harder-when-brighter behavior in the X-ray spectra and the measured positive X-ray/VHE correlation during the 2009 multi-wavelength campaign suggests that the physical processes dominating the emission during non-flaring states have similarities with those occurring during flaring activity. In particular, this observation supports leptonic scenarios as being responsible for the emission of Mrk 421 during non-flaring activity. Such a temporally extended X-ray/VHE correlation is not driven by any single flaring event, and hence is difficult to explain within the standard hadronic scenarios. The highest variability is observed in the X-ray band, which, within the one-zone synchrotron self-Compton scenario, indicates that the electron energy distribution is most variable at the highest energies.

Key words. BL Lacertae objects: individual: Mrk 421

1. Introduction

Blazars are a class of radio-loud active galactic nuclei (AGN) where the relativistic jet is believed to be closely aligned to our line of sight. They emit radiation over a broad energy range from radio to very high energy γ rays (VHE; $E > 100$ GeV), which is highly variable at all wavelengths. Their spectral energy distributions (SED) are dominated by the jet emission and show two bumps, one at low energies (radio, optical, X-rays) and the other at high energies (X-rays, γ rays, VHE). While the origin of the low-energy bump is presumably synchrotron emission from relativistic electrons, the origin of the high-energy bump is still under debate. To constrain current theoretical models for broadband blazar emission, simultaneous observations of those objects over the whole wavelength range and over a long period are needed. It is important to perform observations at typical[1] or even lower states in order to have a baseline to which other (flaring) states can be compared, as distinct physical processes might play a role when the source is flaring. Weak blazars in a low state are particularly poorly studied in γ rays because of the difficulty to detect them at these energies with current instrumentation. In addition, most multi-wavelength programs are triggered when a source is flaring, and not when it is in low state.

The high-energy peaked BL Lac object (HBL) Mrk 421 was the first extragalactic object discovered at VHE (Punch et al. 1992). It is one of the brightest extragalactic X-ray/VHE objects, and because of its proximity ($z = 0.031$) the absorption by the extragalactic background light (EBL) is low (Albert et al. 2007). Mrk 421 has been well-studied during phases of high activity, but simultaneous broadband observations in a low state, covering both energy bumps, were missing until recently.

Starting in 2009, a multi-wavelength (from radio to VHE), multi-instrument program was organized to monitor the broadband emission of Mrk 421. The scientific goal was to collect a complete, unbiased and simultaneous multi-wavelength dataset to test current theoretical models of broadband blazar emission. In this paper we analyze the temporal variability of Mrk 421 in all wavelengths during the 4.5-month observation period in 2009. During the entire period, Mrk 421 did not show any major flaring activity (e.g., Aleksić et al. 2012; Fortson et al. 2012; Fossati et al. 2008; Gaidos et al. 1996; Mankuzhiyil et al. 2011). The multi-wavelength dataset is used to enhance our understanding of the origin of the high-energy emission of blazars beyond the usually observed flaring states. The underlying physical mechanisms responsible for the acceleration of particles in jets are compared with those observed during flares. This paper can be understood as a sequel to Abdo et al. (2011b; Paper I), where the SED of the Mrk 421 2009 data was analyzed.

This paper is organized as follows: Sect. 2 introduces the participating instruments and the multi-wavelength data. The analysis of the variability in each waveband is presented in Sect. 3. Cross-correlations and periodic behavior are examined in Sects. 4 and 5, and finally in Sect. 6 we summarize and discuss our results.

2. The 2009 multi-wavelength campaign

The duration of the 2009 campaign on Mrk 421 was 4.5 months from 2009 January 19 (MJD 54 850) to 2009 June 1 (MJD 54 983). 29 instruments participated in the campaign. The intended sampling was one observation per instrument every two days, whenever weather, technical and observational limitations allowed[2]. The list of participating instruments and the time coverage as a function of energy range are shown in Table 2 and in Fig. 6 of Paper I. The schedule of the observations can be found online[3]. The individual datasets and the data reduction are presented in detail in Sect. 5 of Paper I and will therefore not be introduced again in this paper. Besides the datasets reported in Paper I, this paper also reports VHE data from 115 h of dedicated Mrk 421 observations with the *Whipple* 10-m telescope (operated by the VERITAS collaboration). These data are essential for the excellent temporal coverage in the VHE for this campaign. Details on the light curve presented here can be found in Pichel (2009) with the general *Whipple* analysis technique described in Horan et al. (2007) and Acciari et al. (2014). The frequencies/wavelengths covered by the campaign are radio (2.6–225 GHz), near-infrared (J, H and K), optical (B, V, g, R and I), UV (*Swift*/UVOT W1, W2 and M2), X-ray (0.3–195 keV), high-energy (HE) γ rays (0.1–400 GeV) and VHE (0.08–5.0 TeV).

Results on the broadband SED as well as a detailed discussion of the SED modeling can be found in Paper I. It is the most detailed SED collected simultaneously for Mrk 421 during its typical activity state and the first time where the high-energy component is completely covered by simultaneous observations from the *Fermi*-LAT and the VHE instrument MAGIC. This allowed the characterization of the typical SED of Mrk 421 with unprecedented detail. In Paper I, the SED could be modeled reasonably well using either a one-zone synchrotron self-Compton (SSC) model having two breaks in the electron spectrum, or a hadronic (synchrotron proton blazar, SPB) model. In order to distinguish between these two scenarios, one must look at the multi-wavelength variability. One- and multizone SSC models predict a positive correlation between X-ray and VHE flux variations (e.g., Graff et al. 2008), as they are produced by the same electron population. In the SPB models of

[1] We use the term "typical" instead of "quiescent", to describe a state that is neither exceptionally high/flaring, nor at the lowest possible level. Even though the term "quiescent" has been used in the past to denote non-flaring activity in Mrk 421 and other blazars, we note that the term quiescent refers to the lowest possible emission, which is actually unknown, and hence not suitable in this context.

[2] E.g., for imaging air Cherenkov telescopes (IACTs) like MAGIC or *Whipple*, observations during moonlight are only possible to a very limited extent, resulting in regular gaps of ∼10 days in the VHE light curves.

[3] https://confluence.slac.stanford.edu/display/GLAMCOG/Campaign+on+Mrk421+(Jan+2009+to+May+2009)

Paper I, a strict correlation between those two bands is neither generally expected nor excluded, but can appear when electrons and protons are accelerated together. Furthermore, the one-zone SSC model of Paper I predicts a correlation between low-energy γ rays from *Fermi*-LAT with millimeter (from SMA) and optical frequencies, something which would be hard to incorporate in the SPB model, as the radiation is produced at different sites.

In the following sections we will first characterize the flux variability in all wavebands and then have a detailed look at the cross-correlation functions between light curves of different bands, primarily at X-rays vs. VHE and optical vs. X-rays, HE and VHE correlations, but also at all other combinations as they might reveal something interesting.

3. Variability

3.1. Light curves

Figure 1 shows the light curves from radio to VHE. No substantial (larger than a factor of 2) flaring activity happened during the campaign; however, some level of variability is present in all energy bands. In the radio band the variability is least pronounced. A significant level of variability is present in the near-infrared (NIR), optical and UV accompanied by an overall increase in flux with time. At X-ray, HE and VHE there is also considerable variability, and only a small overall downward trend in the overall X-ray and VHE flux with time is observed. The X-ray flux variations are stronger on average than the variations in the other wavebands, but still much weaker than the maximum values historically registered for the X-ray and VHE bands (Balokovic et al. 2013; Cortina & Holder 2013).

3.2. Fractional variability

In order to quantify and characterize the variability at different energy bands, we calculated the fractional variability

$$F_{\rm var} = \sqrt{\frac{S^2 - \left\langle \sigma_{\rm err}^2 \right\rangle}{\langle x \rangle^2}}, \tag{1}$$

i.e., the excess variance normalized by the flux, according to Vaughan et al. (2003), where S is the standard deviation of the N flux measurements, $\left\langle \sigma_{\rm err}^2 \right\rangle$ is the mean squared error and $\langle x \rangle^2$ is the square of the average photon flux. We estimate the uncertainty of $F_{\rm var}$ according to Poutanen et al. (2008),

$$\Delta F_{\rm var} = \sqrt{F_{\rm var}^2 + {\rm err}(\sigma_{\rm NXS}^2)} - F_{\rm var}, \tag{2}$$

where ${\rm err}(\sigma_{\rm NXS}^2)$ is given by Eq. (11) in Vaughan et al. (2003):

$${\rm err}(\sigma_{\rm NXS}^2) = \sqrt{\left(\sqrt{\frac{2}{N}}\frac{\left\langle \sigma_{\rm err}^2 \right\rangle}{\langle x \rangle^2}\right)^2 + \left(\sqrt{\frac{\left\langle \sigma_{\rm err}^2 \right\rangle}{N}}\frac{2F_{\rm var}}{\langle x \rangle}\right)^2}. \tag{3}$$

This prescription to calculate the uncertainties is more appropriate than Eq. (B2) in Vaughan et al. (2003) for light curves that have an error in the excess variance comparable to or larger than the excess variance. This is, however, not the case for most light curves in our sample, as $\Delta F_{\rm var}$ according to Poutanen et al. (2008) is less than 5% smaller compared to Eq. (B2) in Vaughan et al. (2003). For the *Fermi*-LAT, and *Swift*/BAT light curves, the difference is ≈10%.

The $F_{\rm var}$ values and errors for the different energy bands (instruments) are shown in Fig. 2. As already noticed when looking at the light curves, Mrk 421 shows little variability in radio, and low but significant variability in all other wavebands with the largest variability in X-rays. We note that in the 2–10 keV band it is intrinsically more variable than in the 0.3–2 keV band, a characteristic which has been recently reported for Mrk 421 during high X-ray and VHE activity (Aleksić et al. 2015b)

Because of the instrument sensitivity, the *Fermi*-LAT, *Swift*/BAT and RXTE/ASM data are binned into 3- and 7-day bins (instead of 1-day bins) and therefore, the variability on smaller timescales is not probed, so $F_{\rm var}$ might be underestimated. When rebinning the RXTE/PCA light curve (sampled every ~2 days) into 7-day bins, $F_{\rm var}$ decreases by ~15% and agrees with $F_{\rm var}$ for RXTE/ASM within the errors. The *Swift*/XRT light curves are irregularly sampled. There were measurements every ~7 days during the early part of the campaign but there are also large gaps and a period of sub-daily observations. Rebinning the *Swift*/XRT light curves into 1- and 7-day bins does not change $F_{\rm var}$ by more than a few percent and all values agree within the errors.

The results reported in Fig. 2 are not affected by the temporal binning or the uneven sampling of the light curves and hence can be considered as characteristic of Mrk 421 during the multiwavelength 2009 campaign (see Appendix A for details).

It is interesting to compare these results with the ones reported recently for Mrk 501 in Doert et al. (2013) and Aleksić et al. (2015a), where the fractional variability increases with energy and is largest at VHE, instead of X-rays. The comparison of these observations indicates that there are fundamental differences in the underlying particle populations, environment, and/or processes producing the broadband radiation in these two archetypical VHE blazars. The higher X-ray variability in Mrk 421 might also be related to the higher synchrotron dominance with respect to the one observed in Mrk 501. According to the broadband SEDs measured for Mrk 501 and Mrk 421 during the typical (non-flaring) activity (Abdo et al. 2011a,b), $\nu F_\nu^{\rm Sync_{peak}} > 2 \times \nu F_\nu^{\rm IC_{peak}}$ for Mrk 501 and $\nu F_\nu^{\rm Sync_{peak}} > 4 \times \nu F_\nu^{\rm IC_{peak}}$ for Mrk 421. These SEDs were parametrized within the one-zone SSC framework in Abdo et al. (2011a,b), using, for Mrk 421, a magnetic field $B \sim 2.5$ times higher than the one used for Mrk 501 (38 mG vs. 15 mG), which naturally produces a synchrotron bump that is relatively higher than the inverse-Compton bump. The higher magnetic field in Mrk 421 may also lead to a higher variability in the X-ray band (with respect to the γ-ray bump) through a faster synchrotron cooling of the high-energy electrons ($\tau_{\rm cool-Sync} \propto 1/B^2$).

3.3. Evolution of the X-ray spectral shape with the X-ray flux

Systematic variations of the X-ray spectral shape are a common phenomenon during blazar flares (e.g. Fossati et al. 2000). A harder-when-brighter behavior is quite typical during flares in blazars, and this characteristic has already been observed in Mrk 421 (e.g. Tramacere et al. 2009). Sometimes one can identify loops in the photon index vs. flux diagram during the course of a flare, which could be related to the dynamics of the system, as reported by Kirk & Mastichiadis (1999) or Rieger et al. (2000). Such behavior was also observed in Mrk 421 during a big flare in 1994 (Takahashi et al. 1996). Here we investigate whether these patterns exist in Mrk 421 during its typical (non-flaring) activity.

The *Swift*/XRT spectrum cannot be fit with a simple power-law because this instrument covers the peak of the synchrotron

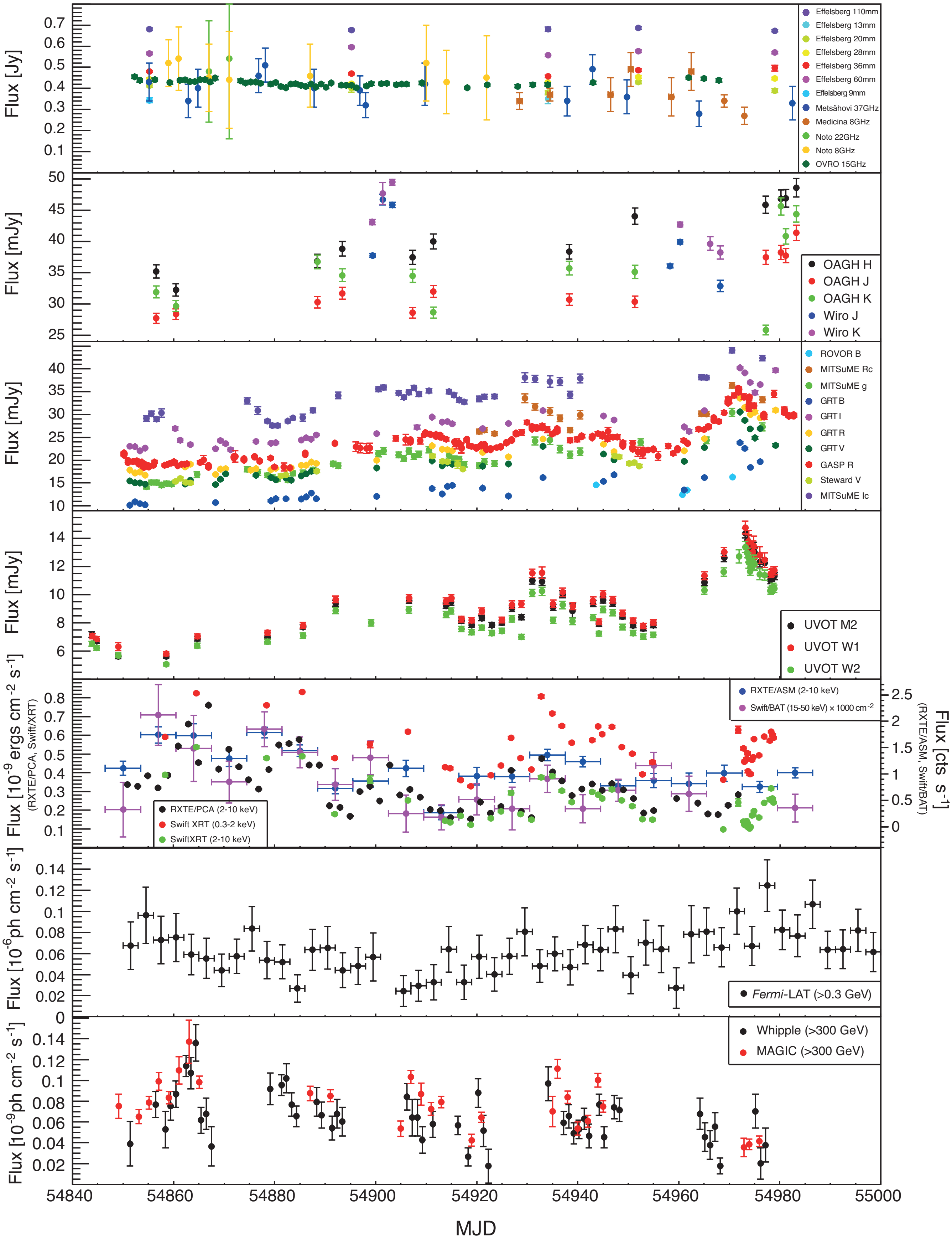

Fig. 1. Light curves of Mrk 421 from radio to VHE from 2009 January 19 (MJD 54 850) to 2009 June 1st (MJD 54 983). Vertical bars denote flux measurement errors, and the horizontal bars denote the time bin widths into which some of the light curves are binned. The *Fermi*-LAT photon fluxes are integrated over a three-day-long time interval. The *Whipple* 10-m data (with an energy threshold of 400 GeV) were converted into fluxes above 300 GeV using a power-law spectrum with index of 2.5.

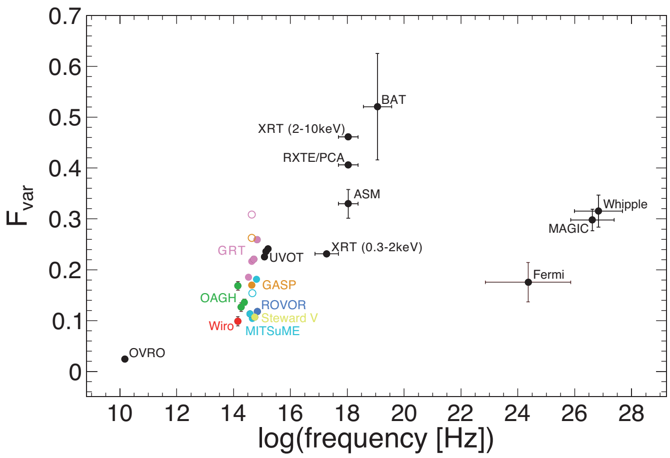

Fig. 2. Fractional variability $F_{\rm var}$ as a function of frequency. Open circles denote $F_{\rm var}$ values in R-band calculated with the host galaxy subtracted as prescribed in Nilsson et al. (2007)

bump, and hence the X-ray spectrum in the 0.3–10 keV band is curved. We can quantify the hardness of the *Swift*/XRT spectra by using the ratio of the X-ray fluxes in the bands 2–10 keV and 0.3–2 keV, and study its evolution with respect to the X-ray flux in the 2–10 keV band. This is shown in the left-hand panel of Fig. 3. The RXTE/PCA spectra, which cover the falling segment of the synchrotron bump (when the source is not flaring), can be fit with a simple power-law function, and hence here we can report the spectral slope vs. the X-ray flux in the 2–10 keV band. This is shown in the in the right-hand panel of Fig. 3. Both *Swift* and RXTE show clearly that the X-ray spectra harden when the X-ray emission increases, and hence we can confirm that the harder-when-brighter behavior also occurs when the source is not flaring. We also investigated the temporal evolution of the plots shown in Fig. 3, looking for loop patterns in the spectral shape-flux plots (clockwise or counter-clockwise) but we did not find any.

3.4. Power density spectrum

Another way to characterize the variability of a given source is the power spectral density (PSD). The PSD quantifies the variability amplitude as a function of Fourier frequency (or timescale) of the variations. The derivation of the PSD is based on the discrete Fourier transform of the light curve under consideration. For blazars, the shape of the PSD is usually a power-law $P_\nu \propto \nu^{-\alpha}$ with spectral index α between 1 and 2 (Abdo et al. 2010; Chatterjee et al. 2012), i.e., there is larger variability at smaller frequencies/longer timescales. This is generally referred to as "red noise". Other features in the PSD, such as breaks or peaks, indicate characteristic timescales or (quasi)-periodic signals.

Calculating the PSD via the discrete Fourier transform is straightforward for light curves that are frequently and regularly sampled over a long period of time. However, in reality, observation time is usually limited and often interrupted by bad weather, object visibility and technical issues, i.e., we are normally dealing with unevenly sampled light curves of limited length that may have large gaps, and this has serious effects on the measured PSD. If the light curve is discretely sampled instead of continuous (which is usually the case as we are dealing with discrete observations or values that are binned over a certain time period), its Fourier transform is convolved with a windowing function, which becomes very complicated when a light curve has an uneven sampling and gaps (Merrifield & McHardy 1994). In addition, light curves of a finite length are affected by red-noise leak, i.e., variability below the smallest frequency (or largest timescale) probed. This variability power leaks into the observed frequency band and changes the observed PSD shape. This effect can manifest as a rise/fall trend throughout the entire interval of the light curve. Likewise, aliasing, i.e., variability power from frequencies larger than the Nyquist frequency, affects the variability in the observed frequency range. The effect of sampling on the study of periodicities will be discussed in Sect. 5.

These effects of the sampling pattern on the PSD can be avoided by using the simulation-based approach of Uttley et al. (2002; PSRESP) to derive the intrinsic PSD of a light curve and its associated uncertainties. We applied this Monte Carlo fitting technique following the prescription given in the appendix of Chatterjee et al. (2008) to all light curves with ~30 or more flux measurements.

First we generated a large set of simulated light curves using the method of Timmer & Koenig (1995). In order to accommodate the problems introduced by the sampling of the light curve, the simulated light curves were about 100 times longer than the measured light curve and then clipped to the required length. This way, they suffer from red-noise leak in the same way as the measured light curve. The simulated light curves also had a much finer sampling than the measured light curve and were then binned to the required binning to include the aliasing effect. Finally, the simulated light curves were resampled with the observed sampling function, so that the windowing function is the same for the measured and the simulated light curves. Poisson noise was added to each simulated light curve to account for observational noise. As a model for the underlying PSD of the simulated light curves we assumed a power-law shape and varied the power-law index α in the range 1.0 to 2.5 in steps of 0.1. We generated 1000 simulated light curves per α value and per measured light curve. We then calculated the PSD for each measured light curve and the 1000 simulated light curves of each model, taking as the PSD the modulus squared of the mean subtracted light curves' discrete Fourier transform between the minimum frequency $\nu_{\rm min} = 1/T$ and the Nyquist frequency $\nu_{\rm Ny} = N/2T$. T is the duration of the light curve. The frequency range covered by our data is approximately 10^{-7}– $\gtrsim 10^{-5.7}$ s^{-1} (corresponding to $\approx$1/120 days^{-1}–$\approx$1/6 days^{-1}), differing somewhat between the light curves depending on the individual length and binning. The light curves were binned into 2–7-day bins, depending on the light curve characteristics. The goodness-of-fit of each PSD model was determined according to the recipe given in the appendix of Chatterjee et al. (2008): The observed χ^2 function

$$\chi^2_{\rm obs} = \sum_{\nu=\nu_{\rm min}}^{\nu_{\rm max}} \frac{\left({\rm PSD_{obs}} - \overline{\rm PSD}_{\rm sim}\right)^2}{(\Delta{\rm PSD_{sim}})^2} \tag{4}$$

from the observed PSD$_{\rm obs}$, the average of the 1000 PSDs from simulated light curves $\overline{\rm PSD}_{\rm sim}$, and the standard deviation ΔPSD$_{\rm sim}$ was compared to the simulated χ^2 distribution

$$\chi^2_{{\rm dist},i} = \sum_{\nu=\nu_{\rm min}}^{\nu_{\rm max}} \frac{\left({\rm PSD}_{{\rm sim},i} - \overline{\rm PSD}_{\rm sim}\right)^2}{(\Delta{\rm PSD_{sim}})^2} \tag{5}$$

calculated from each of the 1000 individual PSDs from simulated light curves PSD$_{{\rm sim},i}$. The success fraction (SuF) is then the fraction of $\chi^2_{{\rm dist},i}$ larger than $\chi^2_{\rm obs}$.

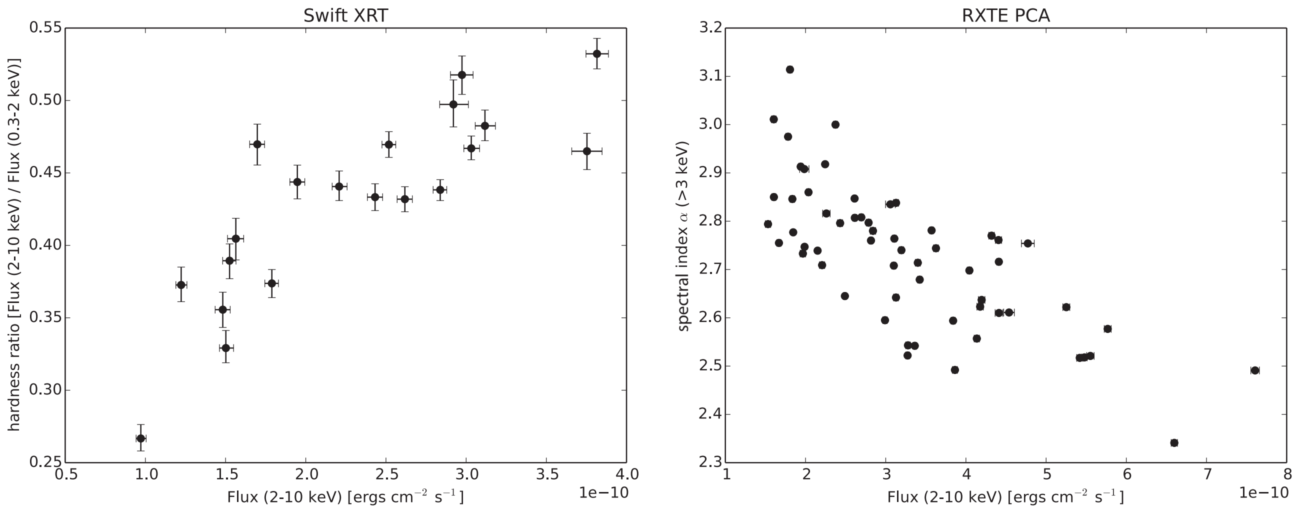

Fig. 3. *Left*: X-ray hardness ratio for the *Swift*/XRT bands 2–10 keV and 0.3–2 keV vs. the X-ray flux in the 2–10 keV band. *Right*: power-law index of RXTE/PCA spectra above 3 keV vs. the X-ray flux in the 2–10 keV band.

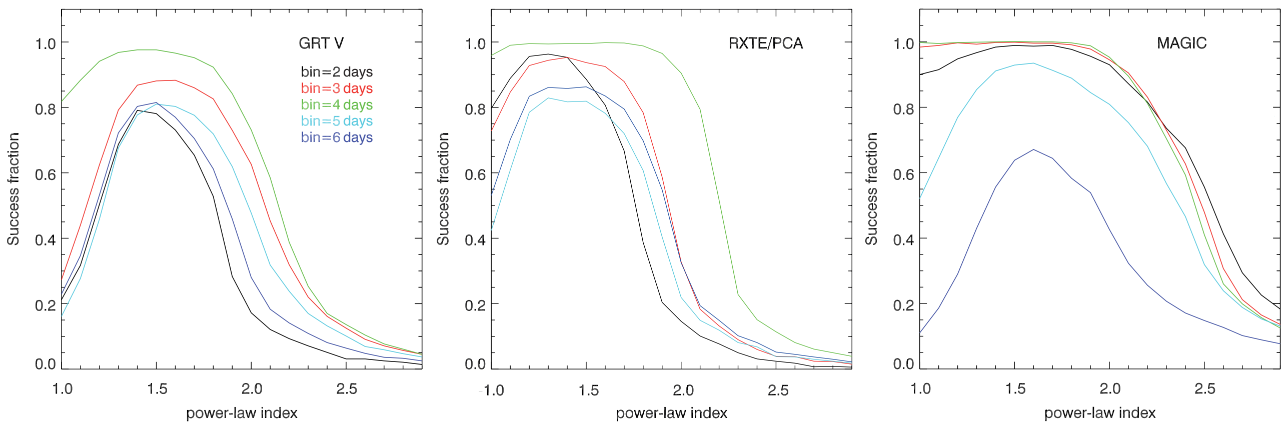

Fig. 4. Success fraction as a function of power-law index α of the PSD for three selected light curves (GRT V band, RXTE/PCA and MAGIC) and a range of light curve binnings (2–6 days) to illustrate the effect of the binning. The location of the maximum does not change significantly with the binning, but there is significant variation in shape, width and amplitude.

Figure 4 shows the SuFs for selected measured light curves and Table 1 gives the best-fit power-law indices α and their uncertainties, calculated as the half width at half maximum (HWHM) of the SuF vs. α curve.

We tried a range of binnings and found that the location of the maximum does not vary systematically with the binning (Fig. 4). The uncertainties, however, depend strongly on the light curve binning and on the logarithmic binning of the PSD (Papadakis & Lawrence 1993). We used light curve bin sizes of a few days (between 2 and 6) and a factor of 1.2 or 1.3 by which the logarithmically spaced frequency bins are separated, in order to reduce the scatter in the PSD points. Sometimes the flux measurements have large uncertainties (mean error non-negligible compared to the variance of the light curve as, e.g., in the case of *Fermi*-LAT) or the light curve has large gaps and/or relatively few data points (e.g., MAGIC). In these cases α is mostly unconstrained. Large gaps or very uneven binning may result in large SuF differences (e.g., MAGIC), or even in changes of the overall shape (e.g., OVRO). In these cases there is no good way to bin the data and obtain a reliable α. If the binning is too small, large gaps are filled with interpolated (probably unrealistic) data in order to calculate the discrete Fourier transform. This results in unwanted changes in the reconstructed PSD and thus in unreliable α values. If the binning is so large that it accomodates also the large gaps such that not too much interpolation is necessary, there are too few data points left and the covered frequency interval becomes too small for a reasonable PSD fit. Unfortunately, the light curves are too short to make analyses based on contiguous parts of a light curve between large gaps.

The maximum of the SuF vs. α curve is generally $\gtrsim$0.8 for all light curves, but we note that for certain binnings the maximum SuF can be significantly lower, or saturate at 1.0. Thus a power-law seems to be a reasonably good fit for all light curves, but as explained above, the fit is restricted by the limited frequency range and by the light curve sampling or gaps. In Table 1 we give the α values where the SuF has a maximum, i.e., the best-fitting power-law indices. As uncertainties we mention only the median HWHM of the distribution of HWHM from different light curve binnings between 2 and 6 days, but please note that this value itself has an uncertainty. In many cases it is not clear why we should prefer one binning over another, so a certain range in SuF shapes is possible. It should be pointed out that these uncertainties in deriving the width of the SuF vs. α curve do not affect the analysis in the following sections, as we always use the best-fitting α, which does not vary with the binning.

The best-fitting PSD models for most light curves are found to be power-laws with indices ~1.3–1.6. There are no big differences between the SuF vs. α curves of different instruments. The

Table 1. Power spectral density (PSD) index α and half-width at half-maximum of the success fraction (SuF) for light curves with more than 30 flux measurements.

Instrument	α^a	*HWHM*
OVRO	2.0	1.2–2.3[b]
GRT *I*	1.5	0.7
MITSuME Ic	1.6	0.7
GASP	1.9	0.5
GRT *R*	1.4	0.8
GRT *V*	1.5	0.5
MITSuME *g*	1.5	0.6
GRT *B*	1.4	1.0
UVOT W1	1.4	0.5
Swift/XRT (0.3–2 keV)	1.5	0.6
Swift/XRT (2–10 keV)	1.4	0.6
RXTE/PCA	1.4	0.6
Fermi-LAT		1.0–2.8[c]
MAGIC	1.6	0.9
Whipple	1.3	0.6

Notes. [(a)] Slope of a power-law $P(\nu) \propto \nu^{-\alpha}$. [(b)] The SuF vs. α curve is asymmetric, thus the PSD of OVRO is not very well constrained. This might be due to the very low variability in radio compared to the other wavelengths. [(c)] The PSD of *Fermi*-LAT is largely unconstrained because of the large flux measurement errors. The SuF is approximately constant and high (>0.8) over a large α range with no clear maximum.

only exceptions are GASP *R* band and OVRO, where the shape is different and α is higher (though still in agreement with the other α values within the uncertainties). A possible explanation might be the small flux error bars and the dense sampling (several values per night, i.e., larger frequency range compared to all other light curves). Without logarithmic binning and with a light curve binning of 1 or 2 days there is a clear maximum at $\alpha = 1.8$.

There is no evidence of a break in the (relatively short) frequency range covered by the multi-wavelength data. Simulated light curves with an underlying broken power-law PSD did not improve the success fraction. The X-ray PSD power-law indices are similar to the ones reported in Kataoka et al. (2001) for the same frequency range. The PSD shape and α are consistent with what was found for blazars by other authors (Chatterjee et al. 2008: X-rays; Abdo et al. 2010: HE γ rays).

4. Cross-correlations

We use the discrete cross-correlation function (DCF) method of Edelson & Krolik (1988) to quantify the correlation of the flux variations between all possible light curve pairs, as long as the light curve has more than 30 flux measurements, i.e., we use the same set of light curves as in Sect. 3.4. This way we can assess correlations between VHE, HE γ rays, X-ray, UV, optical and some radio frequencies.

As a cross-check, we calculate for each light curve pair also the z-transformed cross-correlation function (ZDCF; Alexander 1997). The ZDCF is based on the DCF, but the bin widths of the ZDCF are chosen such that the number of points is the same for each bin, i.e., they are different-sized as opposed to the DCF, where all bins have the same size. In addition, Fisher's z-transform is applied to the cross-correlation coefficients. According to Larsson (2012), the ZDCF is more robust than the DCF for undersampled (w.r.t. the flux variations) light curves. However, for well sampled light curves, the ZDCF has been shown to be consistent with the DCF (e.g., Dietrich et al. 1998; Smith & Vaughan 2007). For this study we used mostly the DCF, as the temporal bin is fixed, so that it also allows us to trivially compare and even combine results from different pairs of instruments. Therefore, we used the ZDCF for verification purposes only.

Two different approaches are used to determine the uncertainties of the DCF. The easiest and fastest way is to simply use the errors given in Edelson & Krolik (1988). However, as discussed in Uttley et al. (2003), these are not appropriate for determining the significance of the DCF when the individual light curve data points are correlated red-noise data. Depending on the PSD and the sampling pattern, the significance as calculated by Edelson & Krolik (1988) might be overestimated. To get a better estimate on the real significance of the correlation peaks we used a Monte Carlo approach, following the description of Arévalo et al. (2009). The Monte Carlo technique is described in detail in Sect. 4.1.

We used a binning of six days for all DCFs because this way different DCFs can be easily compared or, if needed, combined. To make sure that we do not miss correlations or time lags, we always tried a range of binnings, depending on the sampling of the involved light curves.

As the following paragraphs will show, significant correlations are only found between X-rays and VHE. In addition, X-rays and optical light curves seem to follow opposite trends.

4.1. VHE – X-rays

The correlation of the flux variations between the VHE (MAGIC, *Whipple*) and X-ray (RXTE/PCA and *Swift*/XRT 2–10 keV) bands is shown in Fig. 5. The correlations peak at time lag $\Delta t = 0$ and appear to be strongly significant (>5σ), when considering only the errors calculated according to Edelson & Krolik (1988; black error bars). However, as mentioned above, the error bars calculated using Edelson & Krolik (1988) can overestimate the real significance of the correlation. To get a better estimate on the real significance of the correlation peaks we use the following Monte Carlo approach.

For each X-ray light curve we created a set of 1000 simulated light curves in the same way as in Sect. 3.4, using a power-law with the best-fitting slope as determined in Sect. 3.4 from the PSRESP method (see Table 1). The X-ray flux was sampled more often and with smaller statistical errors than the VHE flux, and hence, in order to ascertain the confidence levels in the DCF calculation, it is reasonable to use simulated RXTE/PCA and *Swift*/XRT (2–10 keV) light curves instead of the VHE light curves. We cross-correlated each of the 1000 simulated X-ray light curves with the observed MAGIC and *Whipple* light curves. A power-law spectrum with index 2.5 (Hillas et al. 1998) was used to normalize the integral flux of the *Whipple* 10 m data (with an energy threshold of ~400 GeV) to an integral flux above 300 GeV in order to provide a comparison with MAGIC. We therefore also cross-correlated the original and the simulated X-ray light curves with the combined *Whipple*+MAGIC light curve. From the distribution of 1000 DCFs (i.e., the cross-correlations of the simulated X-ray light curves with the real VHE light curves) we then calculated the 95 and 99% confidence limits, and show them in Fig. 5. For each combination of RXTE/PCA and *Swift*/XRT (2–10 keV) with MAGIC, *Whipple* and *Whipple*+MAGIC the DCF shows a peak at time lag $\Delta t = 0$ with a probability larger than 99%. There are no other peaks or dips in the DCF between VHE and X-rays that appear significant. A positive correlation between X-rays and VHE has been

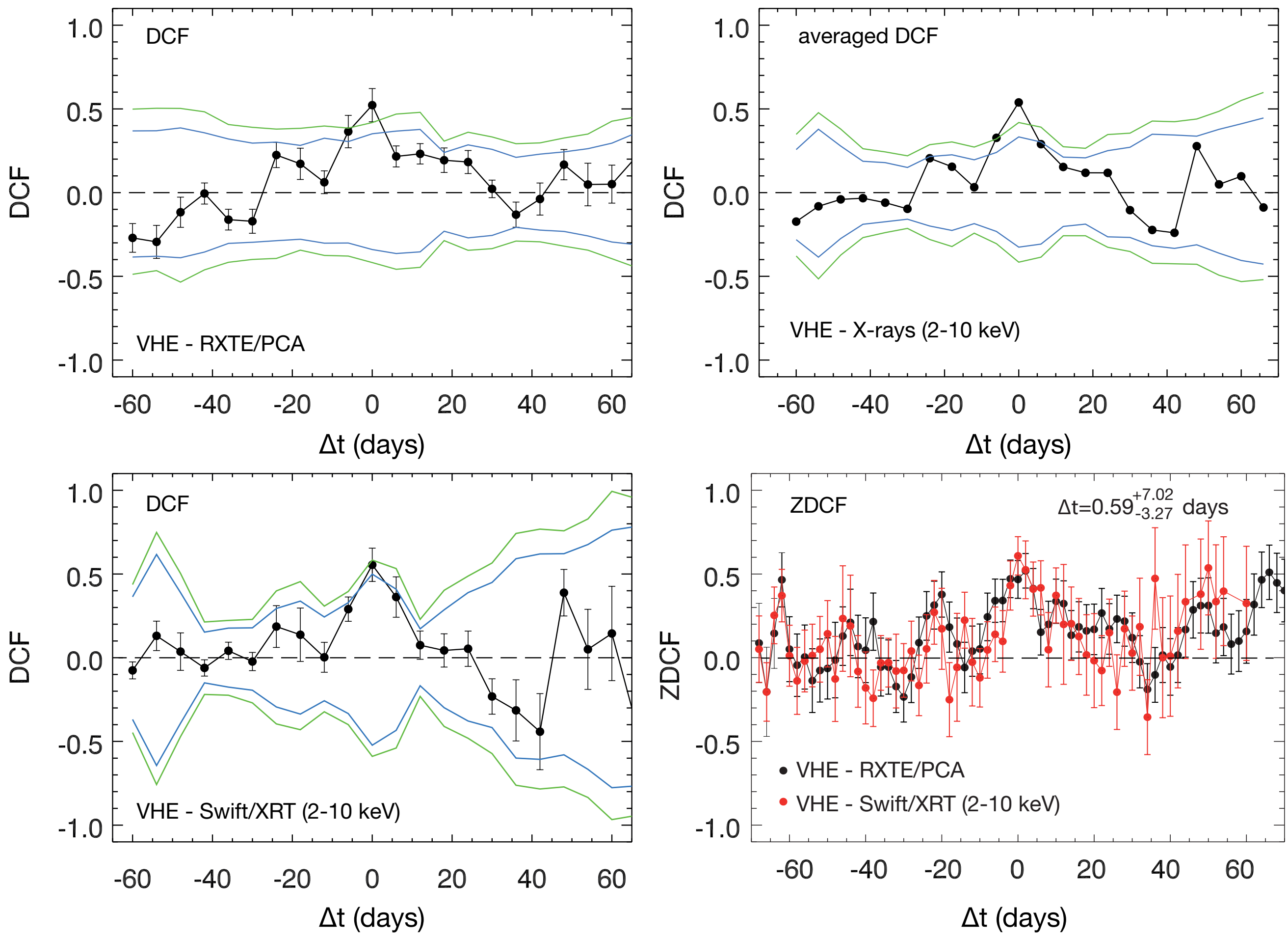

Fig. 5. DCF of the combined *Whipple* and MAGIC (VHE) light curve, correlated with the RXTE/PCA and the *Swift*/XRT (2–10 keV) light curves are shown in the *upper left* and *lower left panels*. The black error bars represent the uncertainties as derived from Edelson & Krolik (1988). The green lines represent the 1% and 99% extremes of the DCF distribution of simulated RXTE/PCA light curves when correlated with the measured VHE light curve. The blue lines represent the 5% and 95% extremes. *Upper right panel*: average of the VHE–RXTE/PCA and VHE–*Swift*/XRT (2–10 keV) DCFs, with the corresponding confidence intervals derived from averaging the DCFs of the simulated light curves. See text for details in the calculation of the average DCFs and contours. *Lower right panel*: z-transformed DCFs.

reported many times during flaring activity (e.g., Fossati et al. 2008), but has never been observed for Mrk 421 in a non-flaring state. Our simulations show that the real significance of the correlation is 3–4σ, indeed confirming that the error bars calculated using Edelson & Krolik (1988) slightly overestimate the significance of the correlation.

We average the DCFs, which has the advantage that spurious features are smoothed out while features present in all DCFs (i.e., those features that are real) are strengthened. This is particularly useful when having many possible combinations and/or marginally significant features like the ones that will be reported in Sect. 4.3. The DCFs were averaged in the following way: for a number of $q+1$ real light curves $A, B_1, \ldots, B_q$ we first calculate all q correlation functions $\mathrm{DCF}(AB_1), \ldots, \mathrm{DCF}(AB_q)$ using a binning of 6 days. Then we calculate the average DCF

$$\overline{\mathrm{DCF}} = \frac{1}{q}\sum_{i=1}^{q}\mathrm{DCF}(AB_i). \tag{6}$$

There is no prescription to combine the uncertainties derived from Edelson & Krolik (1988) for several DCFs, thus no error bars are shown in the upper right panel of Fig. 5. For the determination of the averaged confidence limits we correlate the simulated light curves $a_1, \ldots, a_n$ or $b_{\tilde{q},1}, \ldots, b_{\tilde{q},n}$ ($n = 1000$, $\tilde{q} \in 1, \ldots, q$) with the original light curve $B_{\tilde{q}}$ or A using either

$$\overline{\mathrm{DCF}_{\mathrm{sim},j}} = \frac{1}{q}\sum_{i=1}^{q}\mathrm{DCF}(a_j B_i) \qquad \forall j = 1, \ldots, n \tag{7}$$

or

$$\overline{\mathrm{DCF}_{\mathrm{sim},j}} = \frac{1}{q}\sum_{i=1}^{q}\mathrm{DCF}(A b_{i,j}) \qquad \forall j = 1, \ldots, n. \tag{8}$$

From this distribution of n averaged correlation functions $\overline{\mathrm{DCF}_{\mathrm{sim},j}}$ we then compute the 95 and 99% confidence limits. Whether we use Eqs. (7) or (8) depends on the sampling of the light curves. The sampling and statistical uncertainties of the X-ray light curves are much better than the sampling of the VHE light curves. Therefore the PSD could be better constrained in the X-ray case and hence the confidence limits obtained from correlating the original VHE with simulated X-ray light curves are more reliable than the confidence limits obtained from correlating the original X-ray with simulated VHE light curves. Thus here the light curve A is *Whipple*+MAGIC, the light curves B_i are RXTE/PCA and *Swift*/XRT (2–10 keV) and we use Eq. (8).

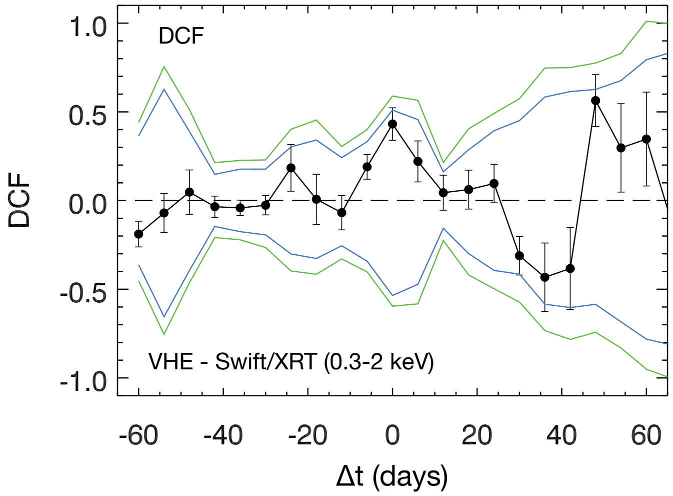

Fig. 6. DCF of the combined *Whipple* and MAGIC ("VHE") light curve, correlated with the *Swift*/XRT (0.3–2 keV) light curve. The black error bars represent the uncertainties as derived from Edelson & Krolik (1988). The green lines represent the 1% and 99% extremes of the DCF distribution of simulated *Swift*/XRT light curves when correlated with the measured VHE light curve. The blue lines represent the 5% and 95% extremes.

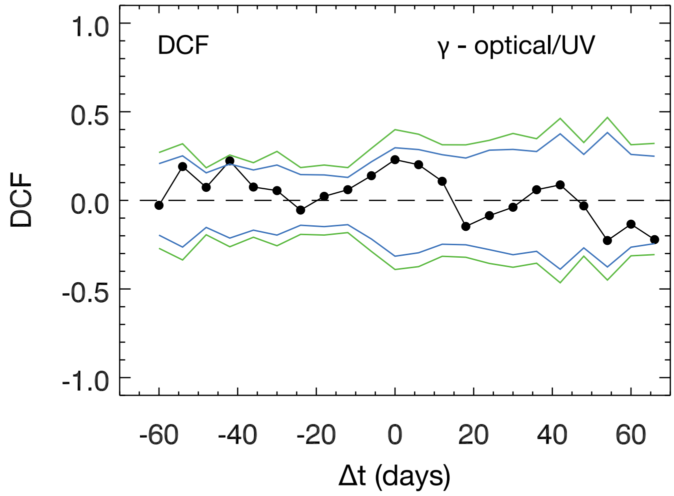

Fig. 7. Average DCF of the *Fermi*-LAT HE γ-ray light curve, correlated with the optical and UV light curves (GASP *R*-band, GRT *BVRI*, MITSuME *g*, MITSuME Ic and UVOT W1), shown in black. The green lines represent the 1% and 99% extremes of the likewise averaged DCF distribution of simulated optical/UV light curves when correlated with the real *Fermi*-LAT light curve. The blue lines represent the 5% and 95% extremes.

The upper right panel of Fig. 5 shows the DCF averaged over the two combinations *Whipple*+MAGIC – RXTE/PCA and *Whipple*+MAGIC – *Swift*/XRT (2–10 keV) and the corresponding confidence limits. There is a clear correlation at time lag $\Delta t = 0$ with a high confidence >99%.

The ZDCFs between the VHE and the X-ray light curves show the same behavior as the corresponding DCFs. However, as the binning is different for each ZDCF (ranging from sub-day scales around time lags $\Delta t \approx 0$ days to a few days at time lags $\Delta t \approx 60$ days), it is not possible to combine them as we did with the DCFs. Rebinning the ZDCFs to even 6-day bins, averaging them subsequently and using the simulated light curves to assess the uncertainties yields almost identical results to the averaged DCF.

Both VHE and X-ray light curves show a weak negative trend with time. To make sure that this trend is not responsible for the correlation, we calculated the (z)DCFs also for the detrended light curves. The difference is marginal. In addition, when comparing X-ray and VHE light curves, one can see that the light curve features nicely agree, i.e., the long-term trend has only a minor contribution to the correlation peak, which is driven by shorter timescale variability.

Figure 6 shows the DCF of the combined *Whipple* and MAGIC light curve, correlated with the *Swift*/XRT (0.3–2 keV) light curve. Although the DCF has a peak at time lag $\Delta t \approx 0$ days which seems to be significant with a confidence level of around 5σ when considering the Edelson & Krolik (1988) errors, the simulations show that this level of correlation is not significant (only $\approx 1.5\sigma$).

4.2. HE γ rays – UV/optical

Figure 7 shows the combined DCF of the *Fermi*-LAT light curve, correlated with optical and UV light curves (using simulated optical and UV light curves to estimate the uncertainties)[4]. There is a peak in the DCF at a time lag $\Delta t = 0$ days, but it is not significant. The uncombined DCFs also show a small peak with a significance $<3\sigma$ or no peak at all when using the Edelson & Krolik (1988) uncertainties. The significance of the small peaks is even lower ($<2\sigma$) when using the uncertainties from simulated data. Larger light curve binsizes would reduce the errors, but also lead to significantly fewer data points, a reduced PSD frequency range, and increased DCF bin sizes. Given the small time window (4.5 month long campaign) under consideration, we cannot improve the DCF quality by rebinning.

4.3. X-rays – UV/optical

We also searched for correlations between the X-ray and UV/optical bands. As done in the previous subsections, we calculated the DCFs for all possible combinations between RXTE/PCA and *Swift*/XRT with *Swift*/UVOT, GASP *R* band, GRT BVRI, MITSuME *g* and MITSuME Ic. The results are shown in panel A of Fig. 8. One feature that is common in almost all DCFs is an anti-correlation at a time lag $\Delta t \approx -20$ to -10 days, i.e., optical/UV variations lead X-ray variations by $\sim$15 days. This feature is significant above 99% and is confirmed by the ZDCF. However, it is not immediately clear what might cause this anti-correlation. The first thing that becomes apparent when looking at the light curves is the long-term trend. The UV/optical light curves show a strong positive trend, while the X-ray light curves show a slight negative trend. Therefore it is not surprising that the DCFs show an overall anti-correlation spread over a large range of time lags. However, this characteristic cannot explain the above-mentioned (anti-)correlations with time lags of 10−20 days.

Hence we detrended the light curves by fitting and subtracting a first-order polynomial to each light curve and recalculated the DCFs and the ZDCFs. They are shown in panel B of Fig. 8 in comparison to the correlations of the original light curves (panel A). In the detrended light curves we find two results: 1) the overall negative correlation spread over most time lags disappears. 2) Some peaks become evident at time lags $\Delta t \approx -36$, -18, $+6$ and $+18$ days (the latter two being absent

[4] In Sect. 3.4 we showed that it is not possible to constrain the PSD of the *Fermi*-LAT light curve because of the large error bars of the light curve data points.

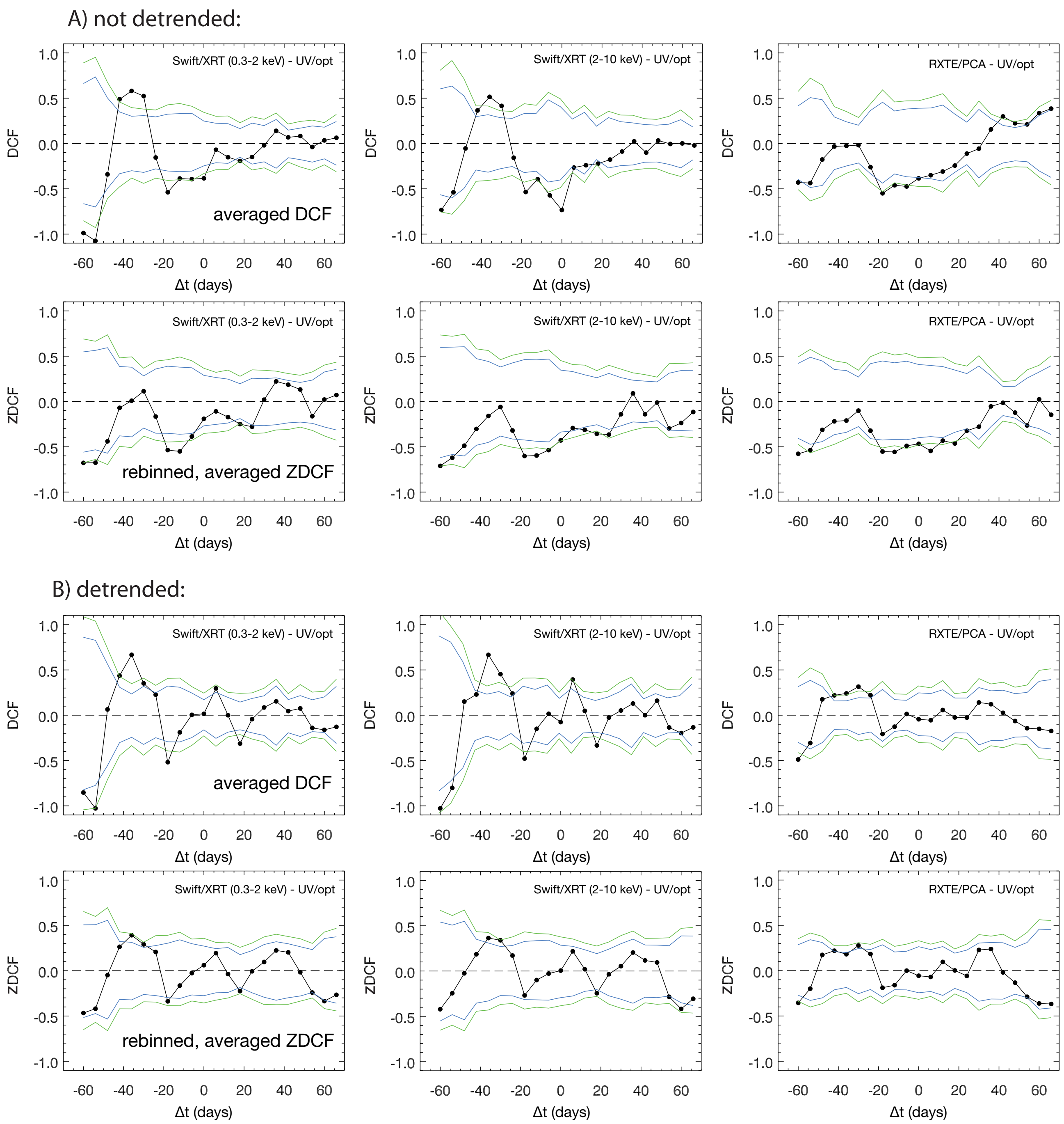

Fig. 8. **a)** DCFs of each X-ray light curve (*Swift*/XRT (0.3–2 keV), *Swift*/XRT (2–10 keV) and RXTE/PCA (2–10 keV)), correlated with several optical and UV light curves, are averaged over all optical to UV bands and shown in black in the upper panel. The green lines represent the 1% and 99% extremes of the likewise averaged DCF distribution of simulated optical/UV light curves when correlated with the observed X-ray light curve. The blue lines represent the 5% and 95% extremes. *Lower panel*: z-transformed DCFs, which were, for the purpose of direct comparison with the DCF, rebinned to the same binning as the DCFs and averaged in the same way. **b)** Same as **a)**, but all light curves have been detrended (as described in 4.3) before correlation.

in the RXTE/PCA – UV/optical DCF). In the ZDCFs these features are generally less pronounced. The presence of such features leads to the suspicion that an underlying quasi-periodic behavior may be responsible for the (anti-)correlations. Indeed there are several local peaks and minima in both the X-ray and UV/optical light curves. In Fig. 9 we illustrate how well these features correlate by overplotting two light curves (*Swift*/XRT (0.3–2 keV) and GASP R band). Both light curves are normalized. The GASP light curve is also rescaled such that both light curves cover approximately the same normalized flux range. In addition, the GASP light curve is shifted in x direction by −36, −18, 6 and 18 days. For time lags where an anti-correlation was detected (−18 and +18 days), we also flipped the GASP light curve about the horizontal axis (such that light curve peaks become troughs and vice versa), such that in each panel of Fig. 9 we should see that both light curves follow the same path whenever there is a real (anti-correlation) present. However, it is obvious from these plots that some, but not all of these features are loosely correlated (as indicated by the low statistical significance of the DCF peaks) and that the limited time window hampers

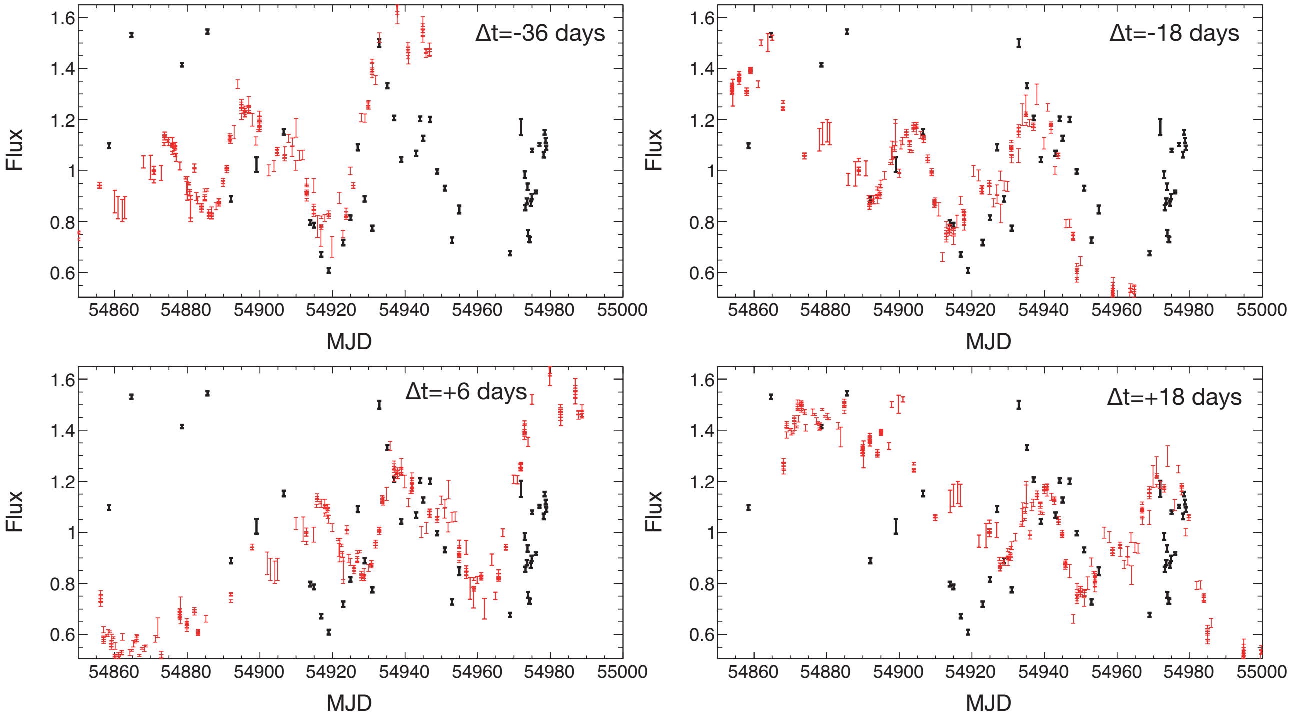

Fig. 9. Example plots to illustrate the correlation between the optical and the X-ray flux variations. All four panels show the normalized *Swift*/XRT (0.3–2 keV) light curve in black. The GASP *R*-band light curve, normalized and rescaled to match the same flux range as the *Swift*/XRT light curve, is overplotted in red with different time lags $\Delta t = -36, -18, +6$, and $+18$ days. In case of anti-correlation ($\Delta t = -18$ and $+18$ days), the GASP light curve is also flipped vertically.

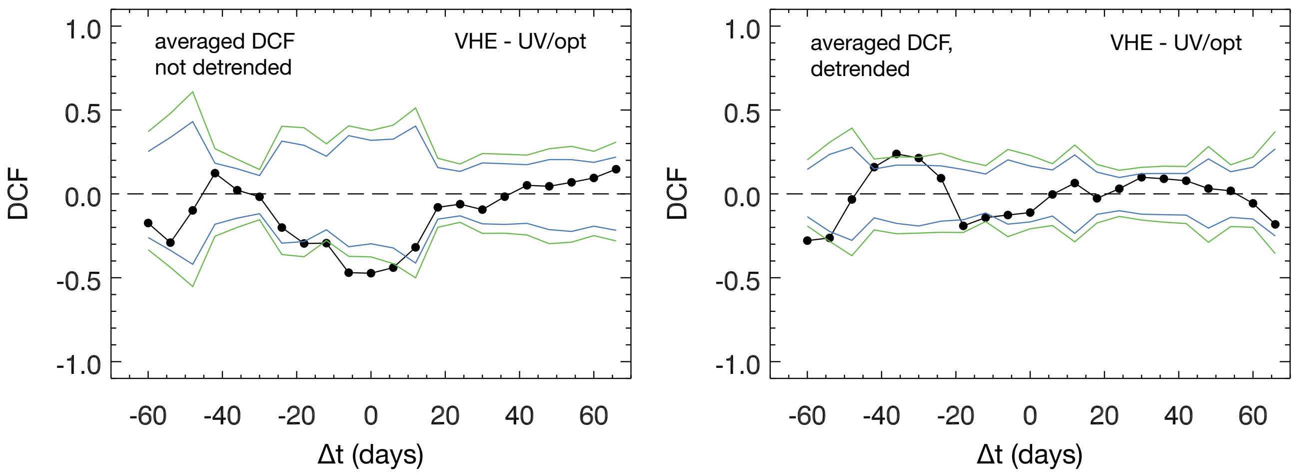

Fig. 10. Average of the DCFs of the combined *Whipple* and MAGIC (VHE) light curve, correlated with several optical and UV light curves, are shown in black in the *left panel*. The green lines represent the 1% and 99% extremes of the likewise averaged DCF distribution of simulated optical/UV light curves when correlated with the observed VHE light curve. The blue lines represent the 5% and 95% extremes. *Right panel*: same as the *left panel*, but all light curves have been detrended (i.e., fitted and subtracted by a first-order polynomial) before correlation.

the ability to detect a convincing correlation. The behavior illustrated in Fig. 9 may well happen just by chance without being caused by an underlying physical mechanism. In Sect. 5 we show that there is no hint of a periodic signal in any of the light curves.

4.4. VHE – optical/UV

The VHE light curves, when correlated with UV and optical light curves, produce a strong negative peak at time lag $\Delta t = 0$ days (Fig. 10), i.e., they are anti-correlated with a probability larger than 99%. However, the optical/UV light curves show a strong positive trend while the VHE light curves show a weak negative trend. After detrending the light curves, the anti-correlation at time lag $\Delta t = 0$ days disappears. Instead, the DCF now shows a similar behavior as the X-ray–optical DCFs (marginally significant anti-correlation at time-lag $\Delta t \approx -18$ days and correlation at ≈ -36 days). This is not surprising given the positive correlation between VHE and X-ray fluxes. More data in the typical state are needed in order to judge whether this behavior is just a chance (anti-)correlation or if it is caused by underlying physical mechanisms.

4.5. Other correlations

All the data in the optical and UV bands vary simultaneously as shown in Fig. 1. The NIR bands seem to be well correlated with the optical and UV bands. However, the number of flux measurements per NIR light curve is too small to calculate a meaningful DCF or ZDCF.

No significant correlations are found between radio or HE γ rays with other wavelengths.

5. Periodicities

5.1. Lomb-Scargle periodogram

Although the Lomb-Scargle periodogram (LSP) is not the best way to determine the PSD for red-noise data (Kastendieck et al. 2011), it is a good way to find periodicities when dealing with unevenly sampled light curves.

A peak in the LSP at a certain time lag can mean that there is a periodicity. However, the sampling also produces peaks, e.g., if there is a flux measurement every 2 days, there will be a strong peak at period $P = 2$ days. Uneven sampling may result in one or more peaks, if at least part of the flux measurements follow an approximately regular observation schedule. The LSPs were determined for periods $\leq L/5 \approx 25$ days, where L is the length of the light curve. To estimate the significance of potential LSP peaks, we also calculated the LSP for 1000 simulated light curves each. The simulated light curves were produced in the same way as in Sect. 3.4 and have the same underlying PSD (estimated above with PSRESP) and the same sampling as the original light curve. From the distribution of LSPs we determined the 95% and 99% confidence limits. We did not find significant LSP peaks in any of the light curves. A peak around $P \approx 18$ days is present in a few optical and X-ray LSPs, but always below 99% confidence level, and in most LSPs even below 95% confidence level.

5.2. Autocorrelation

We use the discrete correlation function (Edelson & Krolik 1988) to calculate the discrete auto-correlation function (DACF) of the variability of Mrk 421 in all observed wave bands. Equally spaced and repeated features in the DACF might be a hint to characteristic timescales and quasi-periodicities. As in the previous sections, we use simulated light curves to estimate the significance of DACF peaks, i.e., the observed light curve is correlated with 1000 simulated light curves. This results in confidence limits that are not symmetric around zero, although the DACF itself is symmetric. The origin of the asymmetry relies on the process used to determine the confidence intervals, which uses 1000 Monte Carlo realizations of one light curve, together with the asymmetry of some of the light curves. This results in different Monte Carlo realizations when the light curve is truncated on the left or on the right (negative or positive time lags), hence yielding different results for the confidence intervals. Consequently, the asymmetry in the confidence intervals is particularly strong where the sampling and variability of the light curve changes significantly with time (e.g., UVOT). Figure 11 shows DACFs for a few representative light curves. There are secondary peaks in some DACFs. However, they are all well below the 95% limit, i.e., they do not appear to be significant. Hence we do not find significant periodicities or characteristic timescales.

6. Discussion of the main observational results

Even though Mrk 421 is known for extreme X-ray and VHE variability, with short and intense flares (e.g. Aleksić et al. 2012; Fossati et al. 2008; Gaidos et al. 1996), the X-ray and VHE activity measured in the 2009 observing campaign was relatively mild, with X-ray/VHE flux variations typically smaller than a factor of 2. The VHE flux of Mrk 421 was also relatively low, with an average flux of about 0.5 times the flux of the Crab Nebula, which is typical for this source (Acciari et al. 2014). Regardless of the low activity, Mrk 421 showed significant variability in the portions of the electromagnetic spectrum where it emits most of its energy power, namely optical/UV, X-rays and HE/VHE γ rays. The optical/X-ray bands bring information from the rising/falling segments of the low-energy bump, while the HE/VHE bands tell us about the rising/falling segment of the high-energy bump. As reported in Sect. 3.2 (see Fig. 2), the highest variability occurs at X-rays ($F_{\rm var} \sim 0.5$), then VHE ($F_{\rm var} \sim 0.3$), and then optical/UV/HE ($F_{\rm var} \sim 0.2$). It is interesting to compare these results with the ones reported recently for Mrk 501 (Aleksić et al. 2015a; Doert et al. 2013), where the fractional variability increases with energy and is largest at VHE, instead of X-rays. The comparison of these two observations indicates that there are fundamental differences in the underlying particle populations and/or processes producing the broadband radiation in these two archetypical VHE blazars. Within the one-zone synchrotron self-Compton scenario, which is commonly used to model the emission of VHE blazars, the X-ray and VHE variability is driven by the dynamics of the population of relativistic electrons through their synchrotron and inverse-Compton emission, respectively. Within this scenario, and for typical model parameters, the ~keV emission is dominated by higher-energy electrons, whereas the ~100 GeV emission is produced by a mixture of lower-energy electrons that inverse-Compton scatter in Thomson regime, and high-energy electrons that inverse-Compton scatter in Klein-Nishina regime (see Paper I). Consequently, the multi-band fractional variability reported in Sect. 3.2 indicates that the population of higher-energy electrons varies more than that at lower energies.

It is worth noticing that the fractional variabilities detected in the energy range 2–10 keV measured by RXTE/PCA, RXTE/ASM and *Swift*/XRT agree reasonably well with a value of 0.4–0.5[5] despite the different observing windows of these three different instruments. On the other hand, the fractional variability measured by *Swift*/XRT in the energy range 0.3–2 keV is ~0.25, which is a factor of 2 lower than the variability detected by *Swift*/XRT in the 2–10 keV energy range. Given that these two observations are performed with the same instrument, the difference in the fractional variability cannot be ascribed to a different observing temporal period that might include or exclude a particular flux variation, and hence the higher variability in the 2–10 keV energy range, in comparison to that in the 0.3–2 keV energy range, is an intrinsic property of Mrk 421 during the 2009 observing campaign, which has also been recently reported for Mrk 421 during high X-ray and VHE activity observed in 2010 (Aleksić et al. 2015b). Because the characteristic synchrotron frequency of relativistic electrons is proportional to the square of the energy of the electrons ($\nu_{\rm c} \propto E_{\rm e}^2$), the higher synchrotron energies will be produced by higher energy electrons, and hence this further supports the theoretical framework of higher variability in the number of higher energy electrons.

[5] As discussed in Sect. 3.2, the somewhat lower value of RXTE/ASM, 0.33+/−0.03, is due to the 7-day integration time, which prevents the detection of variability with temporal scales of days.

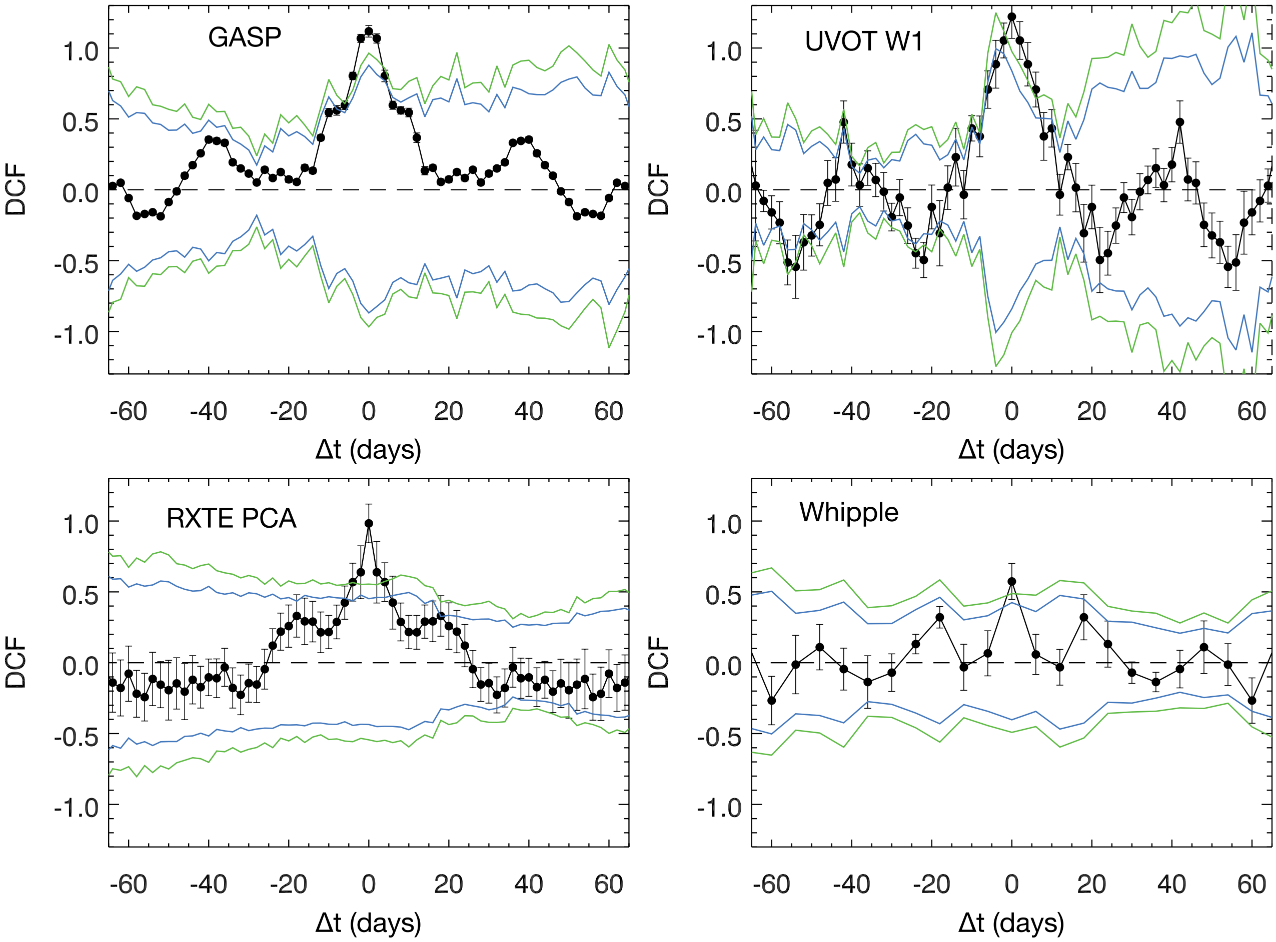

Fig. 11. Discrete auto-correlation function for a few light curves are shown in black. The green lines represent the 1% and 99% extremes of the likewise averaged DACF distribution of simulated light curves when correlated with themselves. The blue lines represent the 5% and 95% extremes.

Given that the high energy electrons are the ones losing their energy fastest ($\tau_{\rm cool} \propto E_{\rm e}^{-1}$), in order to keep the source emitting X-rays, injection (acceleration) of electrons up to the highest energies is needed. We therefore conclude that the injection (acceleration) of high-energy electrons is likely to be the origin of the flux variations in Mrk 421.

From the multi-instrument light curves shown in Fig. 1, it can be seen that, while the variability in X-ray and VHE occurs mostly on ~day timescales, the variability at optical/UV occurs mostly on ~week or even longer timescales[6]. The different variability timescales do not show up in the results reported in Sect. 3.4 (see Table 1). However, this might be the result of the limited sensitivity of the PSD analysis due to the uneven sampling of the light curves, and the rather small range of frequencies sampled (10^{-7}–$\approx 10^{-5.7}$ s^{-1}), which do not provide a long enough lever arm to determine accurately (and ultimately to distinguish) the index of the power-law spectrum of the PSDs from the different energy bands. Therefore, the multi-band light curves and fractional variability show similarities in the X-ray and VHE flux variations, which differ from characteristics of the optical/UV flux variations. This observation is further confirmed by the cross-correlation results reported in Sect. 4, which show a positive correlation with no time lag between the X-ray and VHE emission, but not between the optical/UV and X-ray or VHE. This result indicates that both the X-ray and VHE emissions are co-spatial and produced by the same population of high-energy particles. It is worth noting that, while such a correlation has been reported many times for Mrk 421 during flaring activity (e.g. Fossati et al. 2008), this is the first time that this is observed during a non-flaring (typical) state. Therefore, together with the observed harder-when-brighter behavior in the X-ray spectra, we interpret this experimental observation as evidence that the mechanisms responsible for the X-ray/VHE emission during non-flaring-activity states might not differ substantially from the ones responsible for the emission during flaring-activity states. In particular, the positive X-ray/VHE correlation observed during flaring activity in Mrk 421 and many other blazars has been interpreted by many authors as evidence for leptonic scenarios, and hence against the hadronic scenarios where the X-ray emission and the γ-ray emission are produced by different particle populations and processes. However, with a fine tuning of the parameters, hadronic models are also able to explain single flaring events with an X-ray/VHE correlation with time lag zero (Mastichiadis et al. 2013).

The observations presented here confirm that the relation between X-ray and VHE bands also exists when the source is not flaring. That is, such a relation is persistent over long timescales of at least several months, and does not occur only on single flaring events, and that is much more difficult to explain with hadronic scenarios. Therefore, these observations provide strong evidence supporting leptonic scenarios as responsible for the dominant X-ray/VHE emission from Mrk 421.

[6] Because of the 3-day span and the relatively large statistical uncertainty in the flux points, we cannot evaluate whether short or long timescales dominate the variability in the HE γ-ray band.

Another result that is worth discussing is the overall anti-correlation between the X-ray and optical bands. This anti-correlation spreads over a large range of time lags and hence it is fundamentally different from the one obtained for the X-ray and VHE bands. As we show in Sect. 4, the origin of this overall anti-correlation is the long-term trends of the optical/UV and X-ray activity: while the former increases over time during the observing campaign, the latter decreases. The temporal evolution of the optical and X-ray/VHE bands is complex, and a dedicated correlation analysis over many years will be necessary in order to properly characterize it.

For the 2009 multi-wavelength campaign, we do observe an anti-correlation in the (long-term) temporal evolution between optical/UV and X-rays, and hence it is worth discussing possible theoretical scenarios that might lead to this situation. The first scenario is that the optical/UV and the X-ray/VHE emissions are dominated by the emission from two distinct and unconnected regions with different temporal evolutions of their respective particle populations. In such case, the optical/UV vs. X-ray anti-correlation observed in the 2009 multi-instrument campaign would have occurred by chance, and hence we would also expect to see multi-month time intervals with a positive correlation, or no correlation. A second scenario would be a two-component (high- and low-energy) particle population, in which the low- and high-energy particles have a different but related long-term temporal evolution. A change in the magnetic field intensity while keeping the acceleration timescale constant could lead to the observed optical/UV–X-ray (long-term) anti-correlation. An increase in the magnetization would produce a higher synchrotron emission with a decrease in the energy of the electrons (due to a stronger cooling), which effectively would lead to a higher optical emission with a lower X-ray emission. On the other hand, a lower magnetization would lead to a decrease in the total emitted synchrotron flux, but a higher maximum electron energy, which effectively could lower the optical flux and increase the X-ray flux. In practice, such a scenario would be somewhat similar to the blazar sequence (Ghisellini et al. 1998), with the difference that in the latter scenario the different coolings would relate to different sources instead of different states of the same source. A third scenario could be a global long-term change in the efficiency of the acceleration mechanism that produces the electron energy distribution. Such a change in the global efficiency could shift the entire synchrotron bump to higher/lower energies. For instance, if the acceleration mechanism becomes more efficient to get electrons up to the highest energies at the expense of keeping a lower number of low-energy electrons (i.e., the index of the electron population gets harder), the emission at the rising segment of the synchrotron bump (optical) would decrease, while that on the decreasing segment of the synchrotron bump (X-rays) would increase.

In this study we did not see any correlation between the radio fluxes and those at higher frequencies. However, since the measured radio emission is expected to have large contributions from regions farther away in the jet, it is not surprising to see a non-correlation between radio and optical, X-ray and/or γ-ray energies on timescales of days to weeks. We note, however, that such correlation might be apparent during large flares when the radio emission might be strongly dominated by the same region responsible for the overall broadband emission.

7. Conclusions

We studied the broadband evolution of the SED of Mrk 421 through a 4.5 month long multi-instrument observing campaign in 2009, when the source was in its typical (non-flaring) activity state, with a VHE flux of about half that of the Crab Nebula. Even though the source did not show flaring activity, we could measure significant variability in the energy bands where the emitted power is largest: optical, X-ray, γ rays and VHE. The highest variability occurred in the X-ray band, which, within the standard one-zone SSC scenario, indicates that the high-energy electrons are more variable than the low-energy electrons. We also observed a harder-when-brighter behavior in the X-ray spectra, and found a positive correlation between the X-ray and VHE bands. In the literature one can find many works reporting a positive correlation between the X-ray and VHE fluxes (e.g. Fossati et al. 2008, and references therein) and spectral shape changes with the X-ray flux (e.g. Tramacere et al. 2009), but only when Mrk 421 was showing VHE flaring activity (i.e., VHE flux above the flux of the Crab Nebula). This is the first time that such characteristics are reported for non-flaring activity and suggests that the processess occurring during the flaring activity also occur when the source is in a non-flaring (low) state. In particular, this is a strong argument in favor of leptonic scenarios dominating the broadband emission of Mrk 421 during non-flaring activity, since such a temporally extended X-ray/VHE correlation cannot be explained within the standard hadronic scenarios. Moreover, a negative correlation in the (long-term) temporal evolution of the optical/UV and X-ray bands was also observed. Such a trend could be produced in a region with a particle population where the low- and high-energy particles evolve differently but in a related way, which could be produced by a change in the magnetization of the region while keeping the acceleration timescales constant, or by a global change in the efficiency of the mechanism accelerating the electrons. In any case, even though statistically significant for the 2009 multi-instrument campaign, the current dataset does not allow us to exclude that this optical/X-ray anti-correlation was observed by chance, and hence that the optical and the X-ray bands are produced by distinct and unrelated particle populations that evolve separately. Further multi-instrument observations extending over many years will help to address this question.

Acknowledgements. We would like to thank the referee for the useful comments that helped to improve the manuscript. We also thank Patricia Arévalo for helpful contributions and suggestions. The MAGIC collaboration would like to thank the Instituto de Astrofísica de Canarias for the excellent working conditions at the Observatorio del Roque de los Muchachos in La Palma. The financial support of the German BMBF and MPG, the Italian INFN and INAF, the Swiss National Fund SNF, the ERDF under the Spanish MINECO, and the Japanese JSPS and MEXT is gratefully acknowledged. This work was also supported by the Centro de Excelencia Severo Ochoa SEV-2012-0234, CPAN CSD2007-00042, and MultiDark CSD2009-00064 projects of the Spanish Consolider-Ingenio 2010 programme, by grant 268740 of the Academy of Finland, by the Croatian Science Foundation (HrZZ) Project 09/176 and the University of Rijeka Project 13.12.1.3.02, by the DFG Collaborative Research Centers SFB823/C4 and SFB876/C3, and by the Polish MNiSzW grant 745/N-HESS-MAGIC/2010/0. The VERITAS collaboration acknowledges support from the US Department of Energy, the US National Science Foundation and the Smithsonian Institution, by NSERC in Canada, by Science Foundation Ireland, and by STCF in the UK. We acknowledge the excellent work of the technical support at the FLWO and the collaboration institutions in the construction and operation of the instrument. The *Fermi*-LAT Collaboration acknowledges support from a number of agencies and institutes for both development and the operation of the LAT as well as scientific data analysis. These include NASA and DOE in the United States, CEA/Irfu and IN2P3/CNRS in France, ASI and INFN in Italy, MEXT, KEK, and JAXA in Japan, and the K. A. Wallenberg Foundation, the Swedish Research Council and the National Space Board in Sweden. Additional support from INAF in Italy and CNES in France for science analysis during the operations phase is also gratefully acknowledged. We acknowledge the use of public data from the *Swift* and RXTE data archives. The OVRO 40 m monitoring program is supported in part by NASA grants NNX08AW31G and NNX11A043G, and NSF grants AST-0808050 and AST-1109911. The Metsähovi team acknowledges the support from the Academy of Finland to our observing projects (numbers 212656, 210338, 121148, and others). The Abastumani Observatory team acknowledges financial support by the Shota Rustaveli National Science Foundation through project FR/577/6-320/13. The St. Petersburg University team acknowledges support from the Russian RFBR foundation via grant 09-02-00092. AZT-24 observations are made within an agreement between Pulkovo, Rome and Teramo observatories. This research is partly based on observations with the 100 m telescope of the MPIfR (Max-Planck-Institut fuer Radioastronomie) at Effelsberg, as well as with the Medicina and Noto telescopes operated by INAF–Istituto di Radioastronomia. M. Villata organized the optical-to-radio observations by GASP-WEBT as the president of the collaboration.

References

Abdo, A. A., Ackermann, M., Ajello, M., et al. 2010, ApJ, 722, 520
Abdo, A. A., Ackermann, M., Ajello, M., et al. 2011a, ApJ, 727, 129
Abdo, A. A., Ackermann, M., Ajello, M., et al. 2011b, ApJ, 736, 131
Acciari, V. A., Arlen, T., Aune, T., et al. 2014, Astropart. Phys., 54, 1
Albert, J., Aliu, E., Anderhub, H., et al. 2007, ApJ, 663, 125
Aleksić, J., Alvarez, E. A., Antonelli, L. A., et al. 2012, A&A, 542, A100
Aleksić, J., Ansoldi, S., Antonelli, L. A., et al. 2015a, A&A, 573, A50
Aleksić, J., Ansoldi, S., Antonelli, L. A., et al. 2015b, A&A, in press, DOI: 10.1051/0004-6361/201424811
Alexander, T. 1997, in Astronomical Time Series, eds. D. Maoz, A. Sternberg, & E. M. Leibowitz, Astrophys. Space Sci. Lib., 218, 163
Arévalo, P., Uttley, P., Lira, P., et al. 2009, MNRAS, 397, 2004
Balokovic, M., Furniss, A., Madejski, G., & Harrison, F. 2013, ATel, 4974, 1
Chatterjee, R., Jorstad, S. G., Marscher, A. P., et al. 2008, ApJ, 689, 79
Chatterjee, R., Bailyn, C. D., Bonning, E. W., et al. 2012, ApJ, 749, 191
Cortina, J., & Holder, J. 2013, ATel, 4976, 1
Dietrich, M., Peterson, B. M., Albrecht, P., et al. 1998, ApJS, 115, 185
Doert, M., David Paneque for the MAGIC Collaboration, the VERITAS Collaboration, & the Fermi-LAT Collaboration 2013 [arXiv:1307.8344]
Edelson, R. A., & Krolik, J. H. 1988, ApJ, 333, 646
Fortson, L., VERITAS Collaboration, & Fermi-LAT Collaborators 2012, in AIP Conf. Ser. 1505, eds. F. A. Aharonian, W. Hofmann, & F. M. Rieger, 514
Fossati, G., Celotti, A., Chiaberge, M., et al. 2000, ApJ, 541, 166
Fossati, G., Buckley, J. H., Bond, I. H., et al. 2008, ApJ, 677, 906
Gaidos, J. A., Akerlof, C. W., Biller, S., et al. 1996, Nature, 383, 319
Ghisellini, G., Celotti, A., Fossati, G., Maraschi, L., & Comastri, A. 1998, MNRAS, 301, 451
Graff, P. B., Georganopoulos, M., Perlman, E. S., & Kazanas, D. 2008, ApJ, 689, 68
Hillas, A. M., Akerlof, C. W., Biller, S. D., et al. 1998, ApJ, 503, 744
Horan, D., Atkins, R. W., Badran, H. M., et al. 2007, ApJ, 655, 396
Kastendieck, M. A., Ashley, M. C. B., & Horns, D. 2011, A&A, 531, A123
Kataoka, J., Takahashi, T., Wagner, S. J., et al. 2001, ApJ, 560, 659
Kirk, J. G., & Mastichiadis, A. 1999, Astropart. Phys., 11, 45
Larsson, S. 2012, in Fermi & Jansky 2011: Our Evolving Understanding of AGN
Mankuzhiyil, N., Ansoldi, S., Persic, M., & Tavecchio, F. 2011, ApJ, 733, 14
Mastichiadis, A., Petropoulou, M., & Dimitrakoudis, S. 2013, MNRAS, 434, 2684
Merrifield, M. R., & McHardy, I. M. 1994, MNRAS, 271, 899
Nilsson, K., Pasanen, M., Takalo, L. O., et al. 2007, A&A, 475, 199
Papadakis, I. E., & Lawrence, A. 1993, MNRAS, 261, 612
Pichel, A., for the VERITAS Collaboration 2009 [arXiv:0908.0010]
Poutanen, J., Zdziarski, A. A., & Ibragimov, A. 2008, MNRAS, 389, 1427
Punch, M., Akerlof, C. W., Cawley, M. F., et al. 1992, Nature, 358, 477
Rieger, F. M., Kirk, J. G., & Mastichiadis, A. 2000 [arXiv:astro-ph/0005479]
Smith, R., & Vaughan, S. 2007, MNRAS, 375, 1479
Takahashi, T., Tashiro, M., Madejski, G., et al. 1996, ApJ, 470, L89
Timmer, J., & Koenig, M. 1995, A&A, 300, 707
Tramacere, A., Giommi, P., Perri, M., Verrecchia, F., & Tosti, G. 2009, A&A, 501, 879
Uttley, P., McHardy, I. M., & Papadakis, I. E. 2002, MNRAS, 332, 231
Uttley, P., Edelson, R., McHardy, I. M., Peterson, B. M., & Markowitz, A. 2003, ApJ, 584, L53
Vaughan, S., Edelson, R., Warwick, R. S., & Uttley, P. 2003, MNRAS, 345, 1271

---

[1] IFAE, Edifici Cn., Campus UAB, 08193 Bellaterra, Spain
[2] Università di Udine, and INFN Trieste, 33100 Udine, Italy
[3] INAF National Institute for Astrophysics, 00136 Rome, Italy
[4] Università di Siena, and INFN Pisa, 53100 Siena, Italy
[5] Croatian MAGIC Consortium, Rudjer Boskovic Institute, University of Rijeka and University of Split, 10000 Zagreb, Croatia
[6] Max-Planck-Institut für Physik, 80805 München, Germany
[7] Universidad Complutense, 28040 Madrid, Spain
[8] Inst. de Astrofísica de Canarias, 38200 La Laguna, Tenerife, Spain
[9] University of Lodz, 90236 Lodz, Poland
[10] Deutsches Elektronen-Synchrotron (DESY), 15738 Zeuthen, Germany
[11] ETH Zurich, 8093 Zurich, Switzerland
[12] Universität Würzburg, 97074 Würzburg, Germany
[13] Centro de Investigaciones Energéticas, Medioambientales y Tecnológicas, 28040 Madrid, Spain
[14] Technische Universität Dortmund, 44221 Dortmund, Germany
[15] Inst. de Astrofísica de Andalucía (CSIC), 18080 Granada, Spain
[16] Università di Padova and INFN, 35131 Padova, Italy
[17] Università dell'Insubria, Como, 22100 Como, Italy
[18] Unitat de Física de les Radiacions, Departament de Física, and CERES-IEEC, Universitat Autònoma de Barcelona, 08193 Bellaterra, Spain
[19] Institut de Ciències de l'Espai (IEEC-CSIC), 08193 Bellaterra, Spain
[20] Finnish MAGIC Consortium, Tuorla Observatory, University of Turku and Department of Physics, University of Oulu, 900147 Oulu, Finland
[21] Japanese MAGIC Consortium, Division of Physics and Astronomy, 606-8501 Kyoto University, Japan
[22] Inst. for Nucl. Research and Nucl. Energy, 1784 Sofia, Bulgaria
[23] Universitat de Barcelona (ICC/IEEC), 08028 Barcelona, Spain
[24] Università di Pisa, and INFN Pisa, 56126 Pisa, Italy
[25] Now at École polytechnique fédérale de Lausanne (EPFL), 1015 Lausanne, Switzerland
[26] Now at Department of Physics & Astronomy, UC Riverside, CA 92521, USA
[27] Now at Finnish Centre for Astronomy with ESO (FINCA), Turku, 21500 Piikkiö, Finland
[28] Now at Stockholm University, Fysikum, Oskar Klein Centre, AlbaNova, 106 91 Stockholm, Sweden
[29] Now at GRAPPA Institute, University of Amsterdam, 1098 XH Amsterdam, Netherlands
[30] Now at Stockholm University, Department of Astronomy, Oskar Klein Centre, AlbaNova, 106 91 Stockholm, Sweden
[31] Physics Department, McGill University, Montreal, QC H3A 2T8, Canada
[32] DESY, Platanenallee 6, 15738 Zeuthen, Germany
[33] Department of Physics, Washington University, St. Louis, MO 63130, USA
[34] Fred Lawrence *Whipple* Observatory, Harvard-Smithsonian Center for Astrophysics, Amado, AZ 85645, USA
[35] School of Physics, University College Dublin, Belfield, Dublin 4, Ireland
[36] Institute of Physics and Astronomy, University of Potsdam, 14476 Potsdam-Golm, Germany
[37] Astronomy Department, Adler Planetarium and Astronomy Museum, Chicago, IL 60605, USA
[38] Department of Physics and Astronomy, Purdue University, West Lafayette, IN 47907, USA
[39] School of Physics and Astronomy, University of Minnesota, Minneapolis, MN 55455, USA
[40] Department of Physics and Astronomy, Iowa State University, Ames, IA 50011, USA
[41] Department of Astronomy and Astrophysics, 525 Davey Lab, Pennsylvania State University, University Park, PA 16802, USA
[42] Santa Cruz Institute for Particle Physics and Department of Physics, University of California, Santa Cruz, CA 95064, USA
[43] Department of Physics and Astronomy, University of Iowa, Van Allen Hall, Iowa City, IA 52242, USA
[44] Department of Physics and Astronomy and the Bartol Research Institute, University of Delaware, Newark, DE 19716, USA
[45] Physics Department, Columbia University, New York, NY 10027, USA
[46] Department of Physics and Astronomy, DePauw University, Greencastle, IN 46135-0037, USA

[47] Department of Physics and Astronomy, University of Utah, Salt Lake City, UT 84112, USA
[48] School of Physics, National University of Ireland Galway, University Road, Galway, Ireland
[49] Enrico Fermi Institute, University of Chicago, Chicago, IL 60637, USA
[50] School of Physics and Center for Relativistic Astrophysics, Georgia Institute of Technology, 837 State Street NW, Atlanta, GA 30332-0430, USA
[51] Department of Life and Physical Sciences, Galway-Mayo Institute of Technology, Dublin Road, Galway, Ireland
[52] Department of Physics and Astronomy, Barnard College, Columbia University, NY 10027, USA
[53] Department of Physics and Astronomy, University of California, Los Angeles, CA 90095, USA
[54] Instituto de Astronomia y Fisica del Espacio, Casilla de Correo 67 – Sucursal 28, (C1428ZAA) Ciudad Autonoma de Buenos Aires, 1428 Buenos Aires, Argentina
[55] Department of Applied Physics and Instrumentation, Cork Institute of Technology, Bishopstown, Cork, Ireland
[56] Argonne National Laboratory, 9700 S. Cass Avenue, Argonne, IL 60439, USA
[57] Harvard-Smithsonian Center for Astrophysics, Cambridge, MA 02138, USA
[58] INAF–Osservatorio Astronomico di Torino, 10025 Pino Torinese (TO), Italy
[59] Department of Astronomy, University of Michigan, Ann Arbor, MI 48109-1042, USA
[60] Graduate Institute of Astronomy, National Central University, Jhongli 32054, Taiwan
[61] School of Cosmic Physics, Dublin Institute for Advanced Studies, Dublin, 2, Ireland
[62] Moscow M.V. Lomonosov State University, Sternberg Astronomical Institute, 119992 Moscow, Russia
[63] Abastumani Observatory, Mt. Kanobili, 0301 Abastumani, Georgia
[64] Landessternwarte, Zentrum für Astronomie der Universität Heidelberg, Königstuhl 12, 69117 Heidelberg, Germany
[65] Aalto University Metsähovi Radio Observatory Metsähovintie 114 02540 Kylmälä, Finland
[66] Aalto University Department of Radio Science and Engineering, PO Box 13000, 00076 Aalto, Finland
[67] University College Dublin, Belfield, Dublin 4, Ireland
[68] Isaac Newton Institute of Chile, St. Petersburg Branch, 196140 St. Petersburg, Russia
[69] Pulkovo Observatory, 196140 St. Petersburg, Russia
[70] Astronomical Institute, St. Petersburg State University, 198504 St. Petersburg, Russia
[71] Max-Planck-Institut für Radioastronomie, Auf dem Hügel 69, 53121 Bonn, Germany
[72] Instituto Nacional de Astrofísica, Óptica y Electrónica, Tonantzintla, Puebla 72840, Mexico
[73] INAF Istituto di Radioastronomia, Sezione di Noto, Contrada Renna Bassa, 96017 Noto (SR), Italy
[74] Department of Physics, University of Trento, 38050 Povo, Trento, Italy
[75] Cahill Center for Astronomy and Astrophysics, California Institute of Technology, 1200 E California Blvd, Pasadena, CA 91125, USA
[76] Astro Space Center of the Lebedev Physical Institute, 117997 Moscow, Russia
[77] Center for Research and Exploration in Space Science and Technology (CRESST) and NASA Goddard Space Flight Center, Greenbelt, MD 20771, USA
[78] Indiana University, Department of Astronomy, Swain Hall West 319, Bloomington, IN 47405-7105, USA
[79] Department of Physics and Astronomy, Brigham Young University, Provo, UT 84602, USA
[80] INAF Istituto di Radioastronomia, Stazione Radioastronomica di Medicina, 40059 Medicina (Bologna), Italy
[81] Department of Physics, Tokyo Institute of Technology, Meguro City, Tokyo 152-8551, Japan
[82] ASI-Science Data Center, via del Politecnico, 00133 Rome, Italy
[83] Department of Physics, Purdue University, 525 Northwestern Ave, West Lafayette, IN 47907, USA
[84] Department of Physics, University of Colorado, Denver, CO 80220, USA
[85] Department of Physics and Mathematics, College of Science and 952 Engineering, Aoyama Gakuin University, 5-10-1 Fuchinobe, Chuoku, Sagamihara-shi Kanagawa 252-5258, Japan
[86] Department of Physics and Astronomy, Pomona College, Claremont CA 91711-6312, USA
[87] INAF Istituto di Radioastronomia, 40129 Bologna, Italy

Pages 17 to 18 are available in the electronic edition of the journal at http://www.aanda.org

Appendix A: Reliability of F_{var}

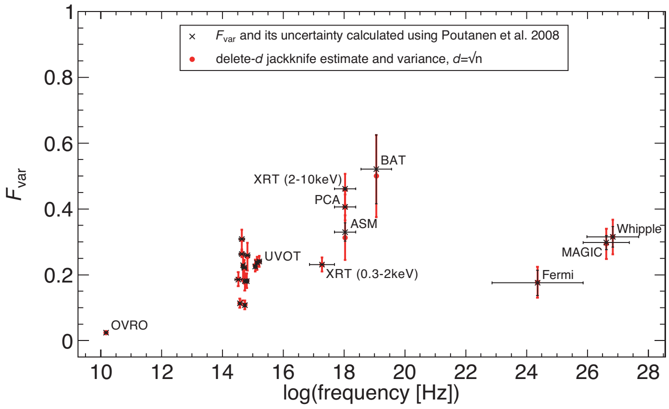

Fig. A.1. Measured fractional variability F_{var} (black) compared with a delete-d jackknife estimate (red) with $d = \sqrt{N}$, for all light curves with a minimum of 15 data points.

Almost all light curves of the campaign are unevenly sampled. The sampling is different for each instrument depending on observation schedule, weather and technical issues. There are often gaps of different lengths in the light curves and each light curve has a different number of data points ranging from a few up to a few hundred. In addition, some light curves are binned into bins of several days because of the limited sensitivity of the corresponding instruments. Therefore we have to assess whether there is an error introduced to F_{var} by the uneven sampling and the binning and how the F_{var} values can be compared. In addition we need to know the minimum number of flux measurements per light curve which are needed to obtain a reliable, unbiased F_{var} value.

To address these questions, we first made a delete-d jackknife analysis, i.e., from each light curve containing N data points, we randomly removed d data points ($1 \leq d \leq N-2$) and calculated F_{var} for this reduced sample of $N-d$ data points. Applying a delete-d jackknife analysis on a time series is formally not correct, as the data are correlated in time (blazar light curves usually show a red-noise behavior). However, our purpose is to create datasets that have statistical properties identical to the real data to demonstrate the impact of gaps and uneven sampling on F_{var}. Figure A.1 shows F_{var} for the jackknife datasets with $d = \sqrt{N}$ in comparison with F_{var} for the original light curves. The F_{var} values do not change significantly. The error bars are larger because of the reduced number of flux values in the jackknife samples. The result does not depend on the particular choice of d, as long as there are sufficient datapoints in the jackknife-samples remaining. Some of the light curves are (almost) regularly sampled, namely *Fermi*-LAT, RXTE/PCA and RXTE/ASM. These are good examples that demonstrate that irregular sampling does not introduce a bias to the F_{var} measurement.

We also varied d between 1 and $N-2$. Figure A.2 shows F_{var} vs. $(N-d)/N$ for selected light curves. As long as $N-d$ is larger than ~5, the measured F_{var} is approximately constant with varying d and in agreement with F_{var} of the original light curve. Likewise, the error bars do not change significantly. Strong deviations from F_{var} of the original light curve occur only, if at all, when $N-d < 10$. No significant deviations are observed at $N-d \geq 20$ for any of the light curves. Thus we conclude that our F_{var} measurement is robust for all light curves with 20 or more flux data points. In our multi-wavelength sample most light curves in the optical, UV, X-rays, HE γ rays and VHE have more than 20 flux data points. In the radio and near-infrared, most light curves do not.

F_{var} is reliable for all but the smallest samples. If after removal of d data points the remaining sample is smaller than about 10, then F_{var} might be over- or underestimated.

We also made a moving-block jackknife test, i.e., we removed blocks of m consecutive measurements. This test is still formally correct when the data are slightly correlated in time, but the drawback is that the number of jackknife samples is much smaller than in case of the delete-d jackknife test. Likewise, it only shows the influence of gaps, not the influence of a random sampling. Figure A.3 shows the test for $m = \sqrt[3]{N}$. As in the case of the delete-d jackknife test, the F_{var} values do not change significantly and the uncertainties are larger.

These conclusions, however, are only valid because the dataset does not have any strong flare and hence it is unaffected by removing points or blocks randomly. Occasional strong flares therefore should be removed before doing an F_{var} analysis of light curves that are otherwise in a typical or low state.

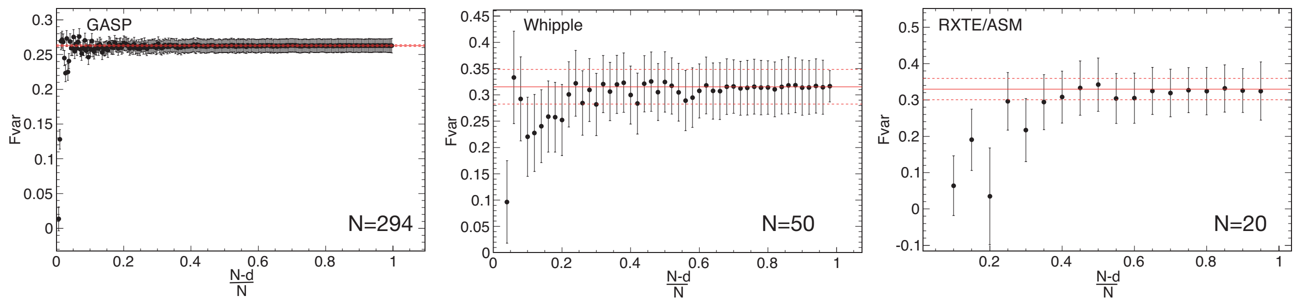

Fig. A.2. Fractional variability F_{var} (red) as a function of $(N - d)/N$ for the jackknife-d samples of selected representative light curves. The measured F_{var} of the original light curve and its error are shown as red horizontal lines. The F_{var} of the jackknife-samples is constant and agrees with the original F_{var} within its errors for all but the largest d (i.e., the smallest jackknife-samples).

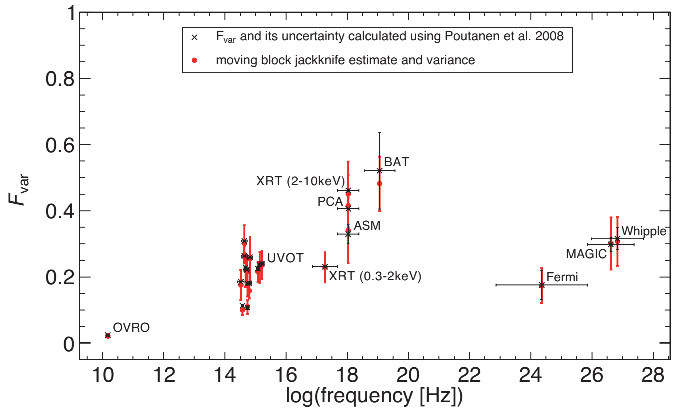

Fig. A.3. Measured fractional variability F_{var} (black) compared with a moving-block jackknife estimate (red), using a blocksize of $m = \sqrt[3]{N}$, for all light curves with a minimum of 15 data points.

The Astronomical Journal, 149:111 (6pp), 2015 March doi:10.1088/0004-6256/149/3/111

FIRST PHOTOMETRIC SOLUTION OF A VERY SHORT PERIOD CONTACT BINARY BELOW THE PERIOD LIMIT

L. Liu[1,2,3], W. P. Chen[4,5], S. B. Qian[1,2,3], R. J. Chuang[6], L. Q. Jiang[1,2,3], C. S. Lin[7], and H. Y. Hsiao[7]
[1] Yunnan Observatories, Chinese Academy of Sciences (CAS), P.O. Box 110, 650011 Kunming, China; LiuL@ynao.ac.cn
[2] Key Laboratory for the Structure and Evolution of Celestial Objects, Chinese Academy of Sciences, 650011 Kunming, China
[3] University of the Chinese Academy of Sciences, Yuquan Road 19#, Sijingshang Block, 100049 Beijing, China
[4] Graduate Institute of Astronomy, National Central University, Taiwan; wchen@astro.ncu.edu.tw
[5] Department of Physics, National Central University, Taiwan
[6] Department of Statistics & Information, Fu-Jen University, Taiwan, ROC.; 032476@mail.fju.edu.tw
[7] Lulin Observatory, National Central University, Taiwan; chishenglinlin@yahoo.com.tw
Received 2014 July 28; accepted 2015 January 22; published 2015 February 26

ABSTRACT

The star 1SWASP J022727.03+115641.7 was reported as a contact binary with a period shorter than the empirical limit of such systems. Our study shows the star not to be variable. Instead, it is the nearby star, 2MASS 02272637+1156494, that exhibits variability. The *BRI* CCD light curves of 2MASS 02272637+1156494 show the system to be a moderate mass ratio ($2.154^{+0.008}_{-0.074}$), and shallow contact ($10.4^{+1.4}_{-1.9}$%) W-type contact binary. The masses, radii, and luminosities of the binary components are, respectively, $M_1 = 0.25^{+0.05}_{-0.01}\,M_\odot$, $M_2 = 0.54^{+0.11}_{-0.04}\,M_\odot$, $R_1 = 0.45^{+0.02}_{-0.01}\,R_\odot$, $R_2 = 0.63^{+0.04}_{-0.02}\,R_\odot$, $L_1 = 0.038^{+0.018}_{-0.005}\,L_\odot$, and $L_2 = 0.071^{+0.037}_{-0.010}\,L_\odot$, with an estimated distance 326^{+127}_{-46} pc. These uncertainties mainly come from the errors of the colors used to estimate the temperature of the primary star. A dark spot was introduced on the massive component in the final solution.

Key words: binaries: close – binaries: eclipsing – stars: evolution – stars: individual (2MASS 02272637+1156494)

1. INTRODUCTION

Contact binaries present a special configuration of stellar interaction for which both components fill their Roche lobes, so the stellar atmospheres are highly distorted. The origin and fate of such systems are of interest in terms of stellar dynamics, and of stellar evolution in comparison to that of single stars. Contact binary systems appear to have an empirical period limit of 0.22 days (Rucinski 1992). The mechanism leading to such a limit is an unsettled issue, commonly attributed to orbital decay (Paczynski 1967; Webbink 1976), or stellar convective instability (Rucinski 1992). Alternatively, the shortest period may be set when a cool contact binary is formed from a detached binary via an angular momentum losing process driven by a magnetized wind. The maximum angular momentum loss rate constrains the minimum time of the primary filling the Roche lobe, and a 0.7 $M_\odot$ primary would reach the Roche lobe overflow in ~13 Gyr, i.e., nearly the age of the universe (Stepien 2006).

A few observational cases, however, have challenged the period limit. For example, the binary system GSC 01387–00475, with a spectral type K4 V–K5 V, has a period of 0.2187 days and a primary mass of 0.638 $M_\odot$ (Rucinski & Pribulla 2008). Jiang et al. (2012) extended the study to model the system and concluded that the mass of the primary cannot be less than 0.63 $M_\odot$, or else the system will merge in a very short time scale via an dynamically unstable mass transfer. The M dwarf contact binary SDSS J001641–000925, with a period of 0.198561 days, has 0.54 ± 0.07 $M_\odot$ for the primary, and 0.34 ± 0.04 $M_\odot$ for the secondary (Davenport et al. 2013). Additional cases include 07d_2_2291 with a period 0.2013 days, and 07a_1_3517 with a period of 0.2143 days (Nefs et al. 2012). The exact period limit of contact binaries, therefore, is still an open issue, and may need revision when more very short period systems are documented.

Here, we report another such system, 2MASS 02272637+1156494, with a period of 0.21095 days. The star lies close to 1SWASP J022727.03+115641.7, which was among the short period binaries found by Norton et al. (2011) using the SuperWASP data. Our study showed that 1SWASP J022727.03+115641.7 in fact is not variable as designated (Norton et al. 2011). Instead, it is 2MASS 02272637+1156494 that displays the variation with the determined period. The misidentification by Norton et al. (2011) must have been because the SuperWASP mission used a small lens (Canon 200 mm *f*/1.8), with a wide 7.8 × 7.8 deg^2 field of view (FOV), so failed to resolve the stars. The 2MASS 02272637+1156494 system is red, with $B = 16.650$ mag, $V = 15.860$ mag, $R = 15.010$ mag (Zacharias et al. 2005), and 2MASS magnitudes of $J = 13.286 \pm 0.024$ mag, $H = 12.641 \pm 0.024$ mag, and $K = 12.476 \pm 0.027$ mag (Cutri et al. 2003). These colors were utilized to derive the effective temperature of the primary component. We present new imaging photometric measurements of the star, with which to characterize this contact binary.

2. NEW CCD IMAGING PHOTOMETRY

The field of 2MASS 02272637+1156494 was observed for three nights (2013 September 7, 9, 11) with the Lulin One-meter Telescope (LOT) of the National Central University in Taiwan, located at 120°52″25 E, 23°28′07″ N, and at an altitude of 2862 m. A PI1340 × 1300 B CCD was used, with the standard *UBVRI* filter set, that gave an effective FOV of about 11.5 × 11.2 arcmin^2 (Kinoshita et al. 2005). For the data reported here, the integration times for the images were 120s in the *BRI* bands.

Figure 1 shows the field of our target star, 2MASS 02272637+1156494. The misidentified variable, 1SWASP J022727.03+115641.7, and another star in the field 2MASS 02273033+1155461, are used as photometric comparisons. The aperture

Table 1
The Original Data of 2MASS 02272637+1156494 Observed in the *BRI* Bands by the LOT Hel. JD 2456500+

Hel.JD	Δ*m*	*Error*	Filter	Hel.JD	Δ*m*	*Error*	Filter	Hel.JD	Δ*m*	*Error*	Filter	Hel.JD	Δ*m*	*Error*	Filter
43.16572	.552	.018	*B*	43.33918	.647	.005	*R*	45.34048	.675	.003	*R*	47.32266	.512	.003	*R*
43.17157	.531	.025	*B*	43.34504	.472	.005	*R*	45.34217	.621	.003	*R*	47.32437	.561	.003	*R*
43.17734	.583	.020	*B*	43.35082	.356	.004	*R*	45.34384	.573	.003	*R*	47.32603	.614	.003	*R*
43.18315	.616	.025	*B*	43.35661	.278	.004	*R*	45.34551	.535	.003	*R*	47.32782	.673	.003	*R*
43.18896	.630	.018	*B*	43.36240	.230	.004	*R*	45.34720	.490	.004	*R*	47.32950	.725	.004	*R*
43.19476	.711	.025	*B*	43.36820	.191	.004	*R*	45.34891	.452	.004	*R*	47.33126	.781	.004	*R*
43.20057	.761	.016	*B*	45.24145	.521	.003	*R*	45.35055	.417	.003	*R*	47.33295	.816	.004	*R*
43.20638	.881	.019	*B*	45.24314	.476	.004	*R*	45.35220	.389	.003	*R*	47.33460	.837	.004	*R*
43.21211	1.036	.019	*B*	45.24486	.436	.004	*R*	45.35392	.369	.003	*R*	47.33631	.831	.004	*R*
43.21788	1.253	.031	*B*	45.24650	.395	.003	*R*	45.35560	.336	.004	*R*	47.33804	.821	.004	*R*
43.22367	1.347	.028	*B*	45.24818	.372	.004	*R*	45.35731	.317	.003	*R*	47.33986	.831	.005	*R*
43.22953	1.227	.022	*B*	45.24983	.339	.003	*R*	45.35895	.295	.003	*R*	47.34160	.807	.005	*R*
43.23531	.974	.024	*B*	45.25151	.315	.003	*R*	45.36064	.275	.003	*R*	47.34325	.764	.005	*R*
43.24109	.843	.024	*B*	45.25320	.301	.003	*R*	45.36229	.265	.003	*R*	47.34493	.721	.003	*R*
43.24846	.751	.018	*B*	45.25485	.276	.003	*R*	45.36395	.252	.003	*R*	47.34658	.661	.003	*R*
43.25428	.741	.024	*B*	45.25654	.261	.003	*R*	45.36562	.238	.003	*R*	47.34833	.606	.004	*R*
43.26013	.643	.014	*B*	45.25819	.249	.004	*R*	45.36727	.225	.004	*R*	47.34998	.556	.003	*R*
43.26593	.583	.021	*B*	45.25988	.238	.003	*R*	45.36899	.221	.004	*R*	47.35172	.504	.003	*R*
43.27176	.593	.013	*B*	45.26153	.227	.004	*R*	45.37063	.206	.004	*R*	47.35336	.466	.005	*R*
43.27759	.558	.018	*B*	45.26319	.216	.003	*R*	45.37230	.194	.004	*R*	47.35507	.425	.003	*R*
43.28344	.578	.014	*B*	45.26485	.204	.004	*R*	45.37396	.180	.005	*R*	47.35677	.391	.003	*R*
43.28919	.597	.022	*B*	45.26652	.192	.003	*R*	45.37566	.175	.007	*R*	47.35854	.357	.003	*R*
43.29505	.648	.018	*B*	45.26819	.187	.004	*R*	47.24876	.430	.004	*R*	47.36034	.326	.004	*R*
43.30086	.718	.023	*B*	45.26987	.171	.003	*R*	47.25047	.404	.003	*R*	47.36203	.310	.004	*R*
43.30796	.800	.015	*B*	45.27152	.158	.003	*R*	47.25222	.369	.003	*R*	47.36370	.292	.004	*R*
43.31384	.956	.019	*B*	45.27318	.161	.003	*R*	47.25400	.349	.004	*R*	47.36538	.271	.004	*R*
43.31968	1.165	.026	*B*	45.27487	.150	.003	*R*	47.25582	.320	.004	*R*	43.16961	−.085	.006	*I*
43.32551	1.349	.025	*B*	45.27654	.143	.003	*R*	47.25753	.297	.003	*R*	43.17538	−.082	.006	*I*
43.33132	1.296	.030	*B*	45.27821	.142	.003	*R*	47.25921	.290	.003	*R*	43.18118	−.061	.004	*I*
43.33721	1.174	.029	*B*	45.27987	.148	.003	*R*	47.26089	.276	.003	*R*	43.18699	−.046	.004	*I*
43.34310	.977	.027	*B*	45.28153	.148	.004	*R*	47.26266	.249	.003	*R*	43.19280	.000	.006	*I*
43.34889	.792	.020	*B*	45.28322	.146	.004	*R*	47.26446	.237	.004	*R*	43.19860	.041	.004	*I*
43.35466	.661	.018	*B*	45.28494	.146	.003	*R*	47.26614	.216	.004	*R*	43.20442	.113	.006	*I*
43.36046	.663	.020	*B*	45.28660	.152	.003	*R*	47.26785	.209	.003	*R*	43.21015	.227	.007	*I*
43.36625	.600	.019	*B*	45.28833	.155	.003	*R*	47.26955	.198	.004	*R*	43.21594	.362	.006	*I*
43.37208	.609	.031	*B*	45.29001	.166	.003	*R*	47.27129	.195	.003	*R*	43.22171	.482	.006	*I*
43.16765	.138	.004	*R*	45.29172	.171	.003	*R*	47.27297	.185	.004	*R*	43.22752	.471	.006	*I*
43.17352	.146	.004	*R*	45.29337	.183	.003	*R*	47.27476	.178	.002	*R*	43.23335	.308	.005	*I*
43.17931	.151	.004	*R*	45.29503	.188	.004	*R*	47.27650	.177	.004	*R*	43.23914	.183	.004	*I*
43.18506	.189	.005	*R*	45.29674	.193	.003	*R*	47.27822	.169	.003	*R*	43.24646	.073	.004	*I*
43.19088	.226	.004	*R*	45.29845	.214	.003	*R*	47.27998	.165	.003	*R*	43.25229	.009	.004	*I*
43.19675	.278	.004	*R*	45.30014	.225	.003	*R*	47.28168	.159	.004	*R*	43.25810	−.028	.004	*I*
43.20249	.343	.005	*R*	45.30181	.233	.003	*R*	47.28341	.164	.003	*R*	43.26398	−.052	.004	*I*
43.20829	.452	.005	*R*	45.30350	.255	.003	*R*	47.28513	.163	.004	*R*	43.26982	−.073	.004	*I*
43.21405	.606	.005	*R*	45.30518	.265	.003	*R*	47.28686	.159	.004	*R*	43.27562	−.074	.006	*I*
43.21984	.764	.005	*R*	45.30688	.278	.003	*R*	47.28858	.173	.004	*R*	43.28146	−.067	.004	*I*
43.22563	.806	.005	*R*	45.30856	.305	.003	*R*	47.29028	.169	.003	*R*	43.28725	−.055	.004	*I*
43.23145	.664	.005	*R*	45.31025	.321	.003	*R*	47.29210	.178	.004	*R*	43.29307	−.021	.004	*I*
43.23725	.510	.005	*R*	45.31196	.348	.003	*R*	47.29374	.184	.003	*R*	43.29891	.015	.005	*I*
43.24456	.368	.004	*R*	45.31362	.371	.003	*R*	47.29542	.189	.003	*R*	43.30470	.060	.004	*I*
43.25039	.294	.005	*R*	45.31532	.406	.003	*R*	47.29712	.198	.003	*R*	43.31185	.175	.005	*I*
43.25624	.250	.004	*R*	45.31701	.442	.003	*R*	47.29879	.210	.003	*R*	43.31771	.317	.005	*I*
43.26210	.200	.004	*R*	45.31867	.478	.003	*R*	47.30053	.218	.003	*R*	43.32350	.479	.005	*I*
43.26790	.180	.004	*R*	45.32035	.514	.003	*R*	47.30222	.230	.003	*R*	43.32933	.509	.006	*I*
43.27377	.170	.004	*R*	45.32203	.561	.003	*R*	47.30387	.240	.003	*R*	43.33522	.452	.005	*I*
43.27957	.160	.004	*R*	45.32373	.606	.003	*R*	47.30554	.257	.003	*R*	43.34110	.289	.006	*I*
43.28538	.179	.005	*R*	45.32539	.653	.004	*R*	47.30733	.268	.003	*R*	43.34691	.167	.007	*I*
43.29116	.213	.004	*R*	45.32708	.708	.003	*R*	47.30903	.282	.003	*R*	43.35271	.073	.004	*I*
43.29699	.250	.004	*R*	45.32874	.753	.003	*R*	47.31077	.306	.003	*R*	43.35850	.005	.004	*I*
43.30280	.302	.005	*R*	45.33041	.787	.003	*R*	47.31245	.322	.003	*R*	43.36428	−.029	.004	*I*
43.30990	.409	.004	*R*	45.33208	.790	.003	*R*	47.31417	.340	.003	*R*	43.37010	−.047	.004	*I*
43.31583	.559	.005	*R*	45.33374	.793	.003	*R*	47.31589	.372	.004	*R*	…	…	…	…
43.32161	.741	.006	*R*	45.33540	.799	.003	*R*	47.31757	.398	.004	*R*	…	…	…	…
43.32744	.838	.004	*R*	45.33711	.776	.003	*R*	47.31922	.438	.003	*R*	…	…	…	…
43.33329	.823	.006	*R*	45.33881	.725	.003	*R*	47.32092	.476	.003	*R*	…	…	…	…

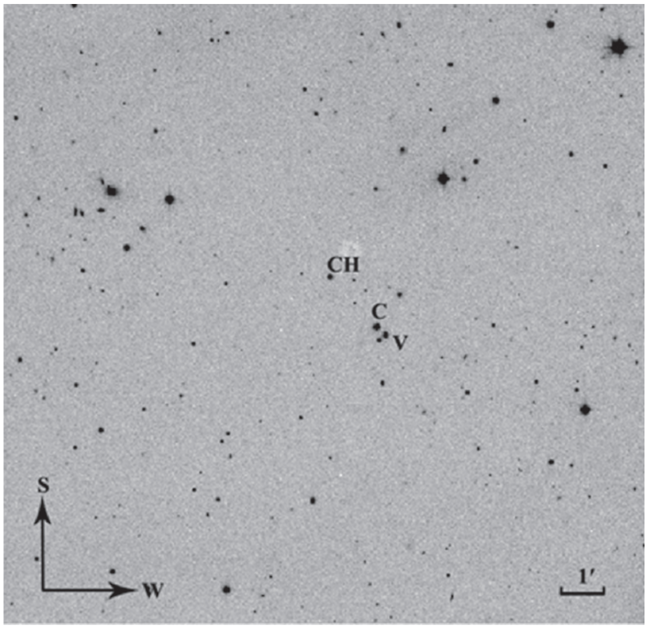

Figure 1. Field around our target, 2MASS 02272637+1156494, marked as V (variable). Also marked are the comparison star (C) 1SWASP J022727.03 +115641.7, and the check star (CH), 2MASS 02273033+1155461.

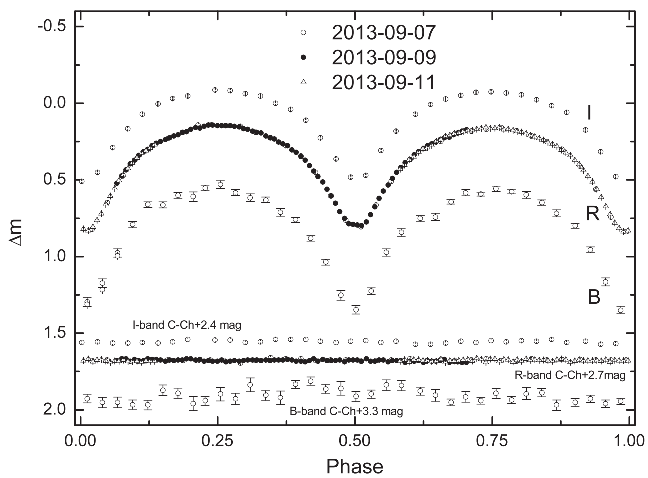

Figure 2. *B*-band light curves of 2MASS 02272637+1156494 taken on 2013 September 7, 9, and 11. The 3 day light curves are phased up smoothly, suggesting little night to-night fluctuations.

photometry package PHOT/IRAF was exercised to reduce the images, with the standard procedure of dark correction and flat-fielding. We chose the size of PHOT very carefully that we make sure the nearby faint star did not be included in the PHOT. The photometric errors depend on several parameters, such as the FWHMPSF, the standard deviation of background in counts, the readout noise, and the specific fitting methods applied. Typical photometric errors of our measurements are less than 0.01 mag. Table 1 summarizes the observations. In deriving the light curves, shown in Figure 2, the phase was calculated with the equation $2456543.3288+0\overset{d}{.}21095 \times E$, where E is the epoch number. As is seen, the light curves taken in three nights phased up smoothly, suggesting little nightly variation. The magnitude differences between the two comparison stars, on the other hand, remained nearly constant,

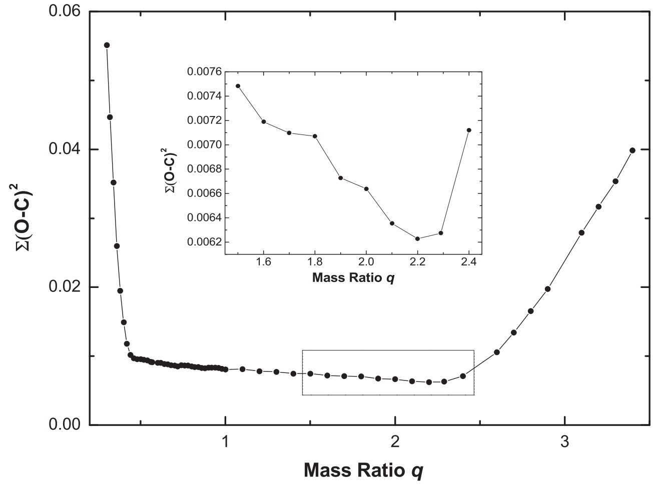

Figure 3. Relationship between the mass ratio q and the fitting residuals. The section from 0.48 to 2.3 is relatively flat, but it meets a valley bottom at 2.2. This is the initial mass ratio q that we have used in the solution.

vindicating the nonvariable nature of 1SWASP J022727.03 +115641.7.

3. PHOTOMETRIC SOLUTIONS

We analyzed the light curves with the 2010 Version of the W-D code (Wilson & Devinney 1971; Wilson 1979, 2008). First, the colors of 2MASS 02272637+1156494 were used to estimated the effective temperature of the primary component (Worthey & Lee 2011). The star has $(V - R) = 0.85$, and given an estimated uncertainty of 0.05 mag (Zacharias et al. 2005), the temperature should range between 3700 and 4100 K. In the solution, we taken a possible temperature value as 3800 K, and we used the temperature range to limit its uncertainty. Thus, we have $T_1 = 3800^{+300}_{-100}$ K. Second, we used the q-search method to get an initial input value of the mass ratio q. The details are: we fixed the mass ratio q at a series of values of 0.1, 0.2, 0.3, etc, then fitted the light curves with the W-D code for each q value, obtaining a series of corresponding fitting residuals, illustrated in Figure 3, and selected the final q value with minimal residuals. The optimal mass ratio thus determined was $q = 2.2$. We then derived the light curves with the temperatures 3700, 4100 K and $q = 2.2$, adopting the bolometric albedo $A_1 = A_2 = 0.5$ (Rucinski 1969) and the gravity-darkening coefficient $g_1 = g_2 = 0.32$ (Lucy 1967), corresponding to the common convective envelope of the binary. The square root limb-darkening coefficients were used (Claret & Gimenez 1990). In our modeling, the adjustable parameters included the mass ratio q, the orbital inclination i, the mean temperature of the secondary, T_2, and the monochromatic luminosity of the primary. The final solution always converged to a contact model. The photometric solutions are summarized in Table 2 and the theoretical light curves thus computed are plotted in Figure 4. The residuals of spot and no-spot fittings were also shown in the bottom of this figure.

We compared the model fit with a starspot to that without. There are eight adjustable parameters for the no-spot model, namely the phase shift, inclination, temperature of the secondary, potential, mass ratio, and the monochromatic luminosity of the primary (L_{1B}, L_{1R} and L_{1I}). For the spot model, there are four additional free parameters, the latitude, longitude, radius and the temperature ratio of the spot. To test if

Table 2
Photometric Solutions for 2MASS 02272637+1156494

Parameters	*BRI*(no-spot) $T_1 = 3800$ K	*BRI*(spot) $T_1 = 3800$ K	*BRI*(no-spot) $T_1 = 3700$ K	*BRI*(spot) $T_1 = 3700$ K	*BRI*(no-spot) $T_1 = 4100$ K	*BRI*(spot) $T_1 = 4100$ K
$g_1 = g_2$	0.32	0.32	0.32	0.32	0.32	0.32
$A_1 = A_2$	0.50	0.50	0.50	0.50	0.50	0.50
$x_{1\text{bolo}}, x_{2\text{bolo}}$	−0.034, −0.034	−0.034, −0.034	−0.057, −0.057	−0.057, −0.057	0.157, 0.157	0.157, 0.157
$y_{1\text{bolo}}, y_{2\text{bolo}}$	0.655, 0.655	0.655, 0.655	0.671, 0.671	0.671, 0.671	0.504, 0.504	0.504, 0.504
x_{1B}, x_{2B}	0.419, 0.519	0.419, 0.519	0.352, 0.452	0.352, 0.452	0.952, 1.052	0.952, 1.052
y_{1B}, y_{2B}	0.780, 0.780	0.780, 0.780	0.859, 0.859	0.859, 0.859	−0.144, −0.144	−0.144, −0.144
x_{1R}, x_{2R}	0.172, 0.172	0.172, 0.172	0.147, 0.147	0.147, 0.147	0.384, 0.384	0.384, 0.384
y_{1R}, y_{2R}	0.559, 0.559	0.559, 0.559	0.568, 0.568	0.568, 0.568	0.316, 0.316	0.316, 0.316
x_{1I}, x_{2I}	−0.021, −0.021	−0.021, −0.021	−0.045, −0.045	−0.045, −0.045	0.177, 0.177	0.177, 0.177
y_{1I}, y_{2I}	0.254, 0.054	0.254, 0.054	0.280, 0.080	0.280, 0.080	0.036, −0.236	0.036, −0.236
T_2	3761 K	3759 K	3664 K	3664 K	4046 K	4041 K
$q = M_2/M_1$	2.154	2.154	2.211	2.080	2.166	2.147
i (°)	82.5	83.0	83.0	82.4	82.5	82.7
$\Omega_1 = \Omega_2$	5.4296	5.4035	5.5108	5.3009	5.4303	5.3852
Ω_{in}	5.4674	5.4674	5.5476	5.3644	5.4846	5.4579
Ω_{out}	4.8521	4.8521	4.9308	4.7648	4.8690	4.8427
$L_1/(L_1 + L_2)(B)$	0.3669	0.3694	0.3594	0.3734	0.3732	0.3789
$L_1/(L_1 + L_2)(R)$	0.3496	0.3517	0.3437	0.3574	0.3515	0.3562
$L_1/(L_1 + L_2)(I)$	0.3345	0.3362	0.3288	0.3422	0.3328	0.3367
r_1 (pole)	0.2972	0.2994	0.2944	0.2991	0.2981	0.3004
r_1 (side)	0.3105	0.3131	0.3076	0.3128	0.3116	0.3143
r_1 (back)	0.3451	0.3493	0.3427	0.3490	0.3473	0.3510
r_2 (pole)	0.4235	0.4256	0.4276	0.4259	0.4253	0.4261
r_2 (side)	0.4511	0.4539	0.4561	0.4542	0.4534	0.4545
r_2 (back)	0.4799	0.4835	0.4849	0.4838	0.4827	0.4845
f	6.2%	10.4%	6.0%	10.6%	8.8%	11.8%
θ (°)	⋯	86.5	⋯	86.5	⋯	86.5
ψ(°)	⋯	269.9	⋯	269.9	⋯	269.9
r_{spot}(°)	⋯	10.2	⋯	10.2	⋯	10.2
T_s/T_*	⋯	0.800	⋯	0.800	⋯	0.800
$\sigma(O - C)^2$	0.008055	0.007463	0.007452	0.006292	0.007465	0.006818

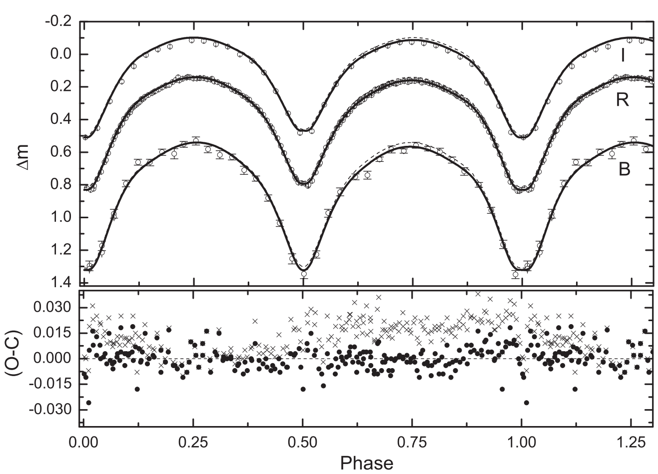

Figure 4. Upper panel is the observed and theoretical light curves in the B, R and I bands of 2MASS 02272637+1156494 with the temperature of 3800 K. A cool spot is adopted to model the presented O'Connell effect of the light curves. The dash lines are the solutions without cool spot. And the lower panel are the residuals of the fittings. The forks denote the (O-C) of no-spot modeling, while the solid cycles denote the (O-C) of spot modeling. The solid cycles are obviously much close to the dash zero line. That means the spot modeling is better, which was agreed with statistical test.

Table 3
Results of Statistical Test and Model Selection Criteria

Temperature (K)	Model	F-statistic ($\alpha = 0.05$) $F(4,204) = 2.415$	AIC
3700	no-spot	206.8	−1760.6
	spot		−2104.2
3800	no-spot	251.0	−1746.8
	spot		−2124.8
4100	no-spot	157.3	−1772.6
	spot		−2070.0

the spot (complete) model fits the 217 observations significantly better than the no-spot (reduced) model, we conducted the F-test and computed the Akaike information criterion (AIC) for three temperatures 3700, 3800, and 4100 K, summarized in Table 3.

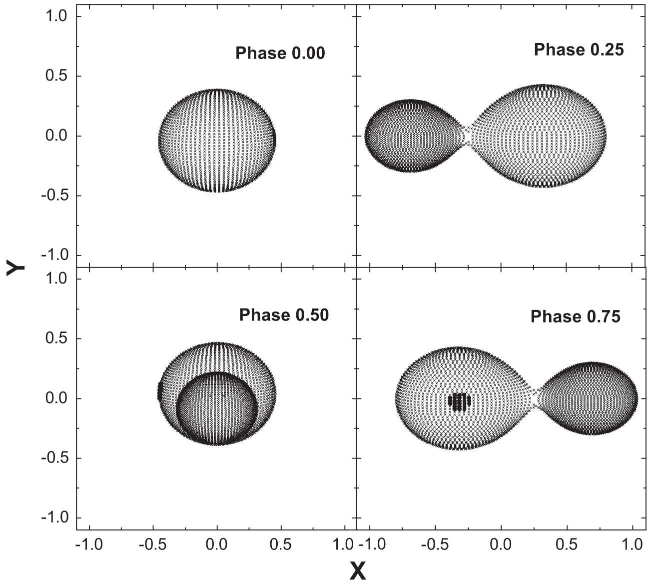

Figure 5. Geometric structure of 2MASS 02272637+1156494 at phase 0.00, 0.25, 0.50 and 0.75. A cool spot can be clear seen in all panels except the 0.25 phase. It is related to the solution with the temperature of 3800 K.

Table 4
Physical Parameters of 2MASS 02272637+1156494

Parameter	Value
T_1(K)	3800^{+300}_{-100}
T_2(K)	3759^{+282}_{-95}
$M_1\,(M_\odot)$	$0.25^{+0.05}_{-0.01}$
$M_2\,(M_\odot)$	$0.54^{+0.11}_{-0.04}$
$R_1\,(R_\odot)$	$0.45^{+0.02}_{-0.01}$
$R_2\,(R_\odot)$	$0.63^{+0.04}_{-0.02}$
$L_1\,(L_\odot)$	$0.038^{+0.018}_{-0.005}$
$L_2\,(L_\odot)$	$0.071^{+0.037}_{-0.010}$
$A\,(R_\odot)$	$1.380^{+0.085}_{-0.030}$
$\log g_1$	$4.54^{+0.03}_{-0.00}$
$\log g_2$	$4.57^{+0.03}_{-0.00}$
$M_{\rm bol1}$	$8.36^{+0.15}_{-0.46}$
$M_{\rm bol2}$	$7.66^{+0.17}_{-0.45}$
$M_{\rm bol_{max}}$	$7.203^{+0.163}_{-0.455}$
BCv.	$-1.091^{+0.257}_{-0.170}$
Distance (pc)	326^{+127}_{-46}

Under the F-test, an addition of four free parameters leads to a critical F-statistic $F_{\alpha=0.05}(4, 204) = 2.415$, whereas the F-statistic for 3700, 3800, and 4100 K is, respectively, 206.84, 251.03, and 157.33, all far exceedingly the critical value, $p < 0.0001$. The null hypothesis (the no-spot model) can be rejected with confidence, hence the model with a starspot is significantly better.

We also computed the AIC to compare the relative quality between the no-spot and spot models. The AIC does not give the goodness of a model but only provides a way to select between models on the basis of the maximum likelihood principle (Akaike et al. 1973). The smaller the AIC value of a model, the better the fit to the data. The AIC value is minimal for the spot model of 3800 K, in agreement with the result of the F-test.

On the basis of the two statistical tests, we conclude that a model with a starspot is favored. The geometrical structure of 2MASS 02272637+1156494 is sketched in Figure 5.

4. DISCUSSION AND CONCLUSIONS

The geometric structure, depicted in Figure 4, shows that 2MASS 02272637+1156494 is a totally eclipsing binary system, so the photometric solution should be relatively reliable. We used the Dartmouth model isochrones (Dotter et al. 2008) to estimate the physical parameters of each component (see Liu et al. 2014a, 2014b, for details), and concluded that 2MASS 02272637+1156494 is a moderate mass-ratio ($2.154^{+0.008}_{-0.074}$), shallow contact ($10.4^{+1.4}_{-1.9}$%) binary, where "shallow" is defined when the contact degree is less than 20%. The light curves are influenced by the O'Connell effect (O'Connell 1951), i.e., an inequality between the two maxima in the light curve of a contact binary, caused by some factors which break the symmetrical structure of a contact binary.

The mass of the primary (more massive component) inferred by the Dartmouth isochrones is 0.54 $M_\odot$ when $T_1 = 3800$ K. The maximum V mag of 2MASS 02272637+1156494 is 15.86 mag, and the bolometric correction at V is $BCv = -1.091$ for 3800 K (Worthey & Lee 2011). Combining the absolute bolometric magnitude derived by the photometric solution, the distance modulus of the system was estimated as 7.203 mag, or at a distance 326 pc. Similarly, if the temperature of the primary is 3700 K, $M_1 = 0.24\,M_\odot$, $M_2 = 0.50\,M_\odot$, $BCv = -1.260$, and the distance would be 280 pc. And if the temperature of the primary is 4100 K, $M_1 = 0.30\,M_\odot$, $M_2 = 0.65\,M_\odot$, $BCv = -0.834$, and the distance would be 453 pc. Hence, the system physical parameters are $M_1 = 0.25^{+0.05}_{-0.01}\,M_\odot$, $M_2 = 0.54^{+0.11}_{-0.04}\,M_\odot$, $R_1 = 0.45^{+0.02}_{-0.01}\,R_\odot$, $R_2 = 0.63^{+0.04}_{-0.02}\,R_\odot$, $L_1 = 0.038^{+0.018}_{-0.005}\,L_\odot$, and $L_2 = 0.071^{+0.037}_{-0.010}\,L_\odot$, and the distance is 326^{+127}_{-46} pc. The parameters and associated uncertainties are given in Table 4. The main source of the uncertainty comes from

Table 5
Comparison of Short-period Contact Binaries

Name	Period (days)	$q = M_2/M_1$	f	Subtype	M_1	M_2	Ref.
GSC 01387–00475	0.2187	0.474	presumed small	⋯	0.638	0.302	(1)
SDSS J001641–000925	0.198561	0.62	18–25%	A	0.34	0.54	(2)
07d_2_2291	0.2013	0.42	7.7%	A	⋯	⋯	(3), (4)
07a_1_3517	0.2143	0.34	9.3%	A	⋯	⋯	(3), (4)
1SWASP J052926.88+461147.5	0.22664218	0.37	20%	A	⋯	⋯	(5), (4)
CC Com	0.22068573	1.9	17%	W	0.378	0.717	(6)
2MASS02272637+1156494	0.21095	2.154	10.4%	W	0.25	0.54	(7), (8)

References.(1) Rucinski & Pribulla 2008, (2) Davenport et al. 2013, (3) Nefs et al. 2012, (4) Qian et al. 2014, (5) Lohr et al. 2013, (6) Kose et al. 2011, (7) Norton et al. 2011, (8) this work.

the distance estimation. Being a shallow system means the system is newly formed, so has experienced little mass transfer. The mass ratio of 2MASS 02272637+1156494, hence, should represent its initial value.

Binnendijk (1970) classified a W UMa-type binary into an A or a W subtype according to the shape of the light curve. In an A-type system, the transit minima are deeper than the occultation ones, indicating a large and hot massive component. Conversely, in a W-type system, the deeper occultation minima reveal a hotter, less massive component star. Qian et al. (2014) reported three contact binaries near or shorter than the period limit. All these systems are moderate mass-ratio, shallow contact binaries, with A-type *RI* light curves. Our target 2MASS 02272637+1156494 share many similar physical parameters with these three systems, yet is a W-type system with the presence of a cool spot. Table 5 summarizes the parameters of these short period systems. Their contact degrees are all less than 20%–25%. We collected from the literature all reported very short period contact binaries with a period near the period limit, listed in Table 5.

The contact binary system we present here, 2MASS 02272637+1156494, adds to the sample of systems that necessitate modification of the empirical period limit. So far, there have been no ultra-short systems found with periods much slower than the limit. The theoretical model to explain the existence of such a limit is still relevant to constrain the formation process of contact binaries.

This work is partly supported by the Chinese Natural Science Foundation (Nos. 11103074, 11133007, and 11325315), by the Science Foundation of Yunnan Province (2012HC011), by the Strategic Priority Research Program "The Emergence of Cosmological Structures" of the Chinese Academy of sciences, Grant No. XDB09010202, and by the West Light Foundation of the Chinese Academy of Sciences. We thank the staff of Lulin Observatory for acquisition and processing of the images used in this study. We also are grateful to the anonymous referee who has offered useful suggestions to improve the paper.

REFERENCES

Akaike, H. 1973, in 2nd Int. Symp. on Information Theory, Information Theory and an Extension of the Maximum Likelihood Principle, ed. B. N. Petrov & F. Csaki (Budapest: Akademiai), 267
Binnendijk, L. 1970, VA, 12, 217
Claret, A., & Gimenez, A. 1990, A&A, 230, 412
Cutri, R. M., Skrutskie, M. F., Van Dyk, S., et al. 2003, The 2MASS All-sky Catalog of Point Sources, yCat., 2246, OC
Davenport, J. R. A., Becker, A. C., West, A. A., et al. 2013, ApJ, 764, 62
Dotter, A., Chaboyer, B., Jevremovic, D., et al. 2008, ApJS, 178, 89
Jiang, D. K., Han, Z. W., Ge, H. W., Yang, L. H., & Li, L. F. 2012, MNRAS, 421, 2769
Kinoshita, D., Chen, C. W., Lin, H. C., et al. 2005, ChJAA, 5, 315
Kose, O., Kalomeni, B., Keskin, V., Ulas, B., & Yakut, K. 2011, AN, 332, 626
Liu, L., Chen, W.-P., Na, W.-W., et al. 2014, NewA, 31, 60
Liu, L., Qian, S. B., & Fernandez Lajus, E. 2014, NewA, 26, 116L
Lohr, M. E., Norton, A. J., Kolb, U. C., et al. 2013, A&A, 549, 86
Lucy, L. B. 1967, ZA, 65, 89
O'Connell, D. J. K. 1951, PRCO, 2, 850
Nefs, S. V., Birklay, J. L., Snellenet, I. A. G., et al. 2012, MNRAS, 425, 950
Norton, A. J., Payne, S. G., Evans, T., et al. 2011, A&A, 528A, 90
Paczynski, B. 1967, AcA, 17, 287
Qian, S. B., Jiang, L. Q., Zhu, L. Y., et al. 2014, CoSka, 43, 290Q
Rucinski, S. M. 1969, AcA, 19, 245
Rucinski, S. M. 1992, AJ, 103, 960
Rucinski, S. M., & Pribulla, T. 2008, MNRAS, 388, 1831
Stepien, K. 2006, AcA, 56, 347
Webbink, R. F. 1976, ApJ, 209, 829
Wilson, R. E. 1979, ApJ, 234, 1054
Wilson, R. E. 2008, ApJ, 672, 575
Wilson, R. E., & Devinney, E. J. 1971, ApJ, 166, 605
Worthey, G., & Lee, H.-C. 2011, ApJS, 193, 1
Zacharias, N., Monet, D. G., Levine, S. E., et al. 2005, yCat, 1297, 0Z

The Astrophysical Journal, 812:65 (22pp), 2015 October 10 doi:10.1088/0004-637X/812/1/65

FIRST *NuSTAR* OBSERVATIONS OF MRK 501 WITHIN A RADIO TO TeV MULTI-INSTRUMENT CAMPAIGN

A. Furniss[1], K. Noda[2], S. Boggs[3], J. Chiang[4], F. Christensen[5], W. Craig[6,7], P. Giommi[8], C. Hailey[9], F. Harisson[10], G. Madejski[4], K. Nalewajko[4], M. Perri[11], D. Stern[12], M. Urry[13], F. Verrecchia[11], W. Zhang[14]
(The NuSTAR Team),
M. L. Ahnen[15], S. Ansoldi[16], L. A. Antonelli[17], P. Antoranz[18], A. Babic[19], B. Banerjee[20], P. Bangale[2], U. Barres de Almeida[2,21], J. A. Barrio[22], J. Becerra González[14,23,24], W. Bednarek[25], E. Bernardini[26,27], B. Biasuzzi[16], A. Biland[15], O. Blanch[28], S. Bonnefoy[22], G. Bonnoli[17], F. Borracci[2], T. Bretz[29,30], E. Carmona[31], A. Carosi[17], A. Chatterjee[20], R. Clavero[23], P. Colin[2], E. Colombo[23], J. L. Contreras[22], J. Cortina[28], S. Covino[17], P. Da Vela[18], F. Dazzi[2], A. De Angelis[32], G. De Caneva[26], B. De Lotto[16], E. de Oña Wilhelmi[33], C. Delgado Mendez[31], F. Di Pierro[17], D. Dominis Prester[19], D. Dorner[29], M. Doro[32], S. Einecke[34], D. Eisenacher Glawion[29], D. Elsaesser[29], A. Fernández-Barral[28], D. Fidalgo[22], M. V. Fonseca[22], L. Font[35], K. Frantzen[34], C. Fruck[2], D. Galindo[36], R. J. García López[23], M. Garczarczyk[26], D. Garrido Terrats[35], M. Gaug[35], P. Giammaria[17], N. Godinović[19], A. González Muñoz[28], D. Guberman[28], Y. Hanabata[37], M. Hayashida[37], J. Herrera[23], J. Hose[2], D. Hrupec[19], G. Hughes[15], W. Idec[25], H. Kellermann[2], K. Kodani[37], Y. Konno[37], H. Kubo[37], J. Kushida[37], A. La Barbera[17], D. Lelas[19], N. Lewandowska[29], E. Lindfors[38], S. Lombardi[17], F. Longo[16], M. López[22], R. López-Coto[28], A. López-Oramas[28], E. Lorenz[2], P. Majumdar[20], M. Makariev[39], K. Mallot[26], G. Maneva[39], M. Manganaro[23], K. Mannheim[29], L. Maraschi[17], B. Marcote[36], M. Mariotti[32], M. Martínez[28], D. Mazin[2], U. Menzel[2], J. M. Miranda[18], R. Mirzoyan[2], A. Moralejo[28], D. Nakajima[37], V. Neustroev[38], A. Niedzwiecki[25], M. Nievas Rosillo[22], K. Nilsson[38,40], K. Nishijima[37], R. Orito[37], A. Overkemping[34], S. Paiano[32], J. Palacio[28], M. Palatiello[16], D. Paneque[2], R. Paoletti[18], J. M. Paredes[36], X. Paredes-Fortuny[36], M. Persic[16,41], J. Poutanen[38], P. G. Prada Moroni[42], E. Prandini[15], I. Puljak[19], R. Reinthal[38], W. Rhode[34], M. Ribó[36], J. Rico[28], J. Rodriguez Garcia[2], T. Saito[37], K. Saito[37], K. Satalecka[22], V. Scapin[22], C. Schultz[32], T. Schweizer[2], S. N. Shore[42], A. Sillanpää[38], J. Sitarek[25], I. Snidaric[19], D. Sobczynska[25], A. Stamerra[17], T. Steinbring[29], M. Strzys[2], L. Takalo[38], H. Takami[37], F. Tavecchio[17], P. Temnikov[39], T. Terzić[19], D. Tescaro[23], M. Teshima[2], J. Thaele[34], D. F. Torres[43], T. Toyama[2], A. Treves[44], V. Verguilov[39], I. Vovk[2], M. Will[23], R. Zanin[36]
(The MAGIC Collaboration),
A. Archer[45], W. Benbow[46], R. Bird[47], J. Biteau[48], V. Bugaev[45], J. V Cardenzana[49], M. Cerruti[46], X. Chen[50,51], L. Ciupik[52], M. P. Connolly[53], W. Cui[54], H. J. Dickinson[49], J. Dumm[55], J. D. Eisch[49], A. Falcone[56], Q. Feng[54], J. P. Finley[54], H. Fleischhack[51], P. Fortin[46], L. Fortson[55], L. Gerard[51], G. H. Gillanders[53], S. Griffin[57], S. T. Griffiths[58], J. Grube[52], G. Gyuk[52], N. Håkansson[50], J. Holder[59], T. B. Humensky[60], C. A. Johnson[48], P. Kaaret[58], M. Kertzman[61], D. Kieda[62], M. Krause[51], F. Krennrich[49], M. J. Lang[53], T. T. Y. Lin[57], G. Maier[51], S. McArthur[63], A. McCann[64], K. Meagher[65], P. Moriarty[53], R. Mukherjee[66], D. Nieto[60], A. O'Faoláin de Bhróithe[51], R. A. Ong[67], N. Park[63], D. Petry[68], M. Pohl[50,51], A. Popkow[67], K. Ragan[62], G. Ratliff[52], L. C. Reyes[69], P. T. Reynolds[70], G. T. Richards[65], E. Roache[46], M. Santander[66], G. H. Sembroski[54], K. Shahinyan[55], D. Staszak[57], I. Telezhinsky[50,51], J. V. Tucci[54], J. Tyler[58], V. V. Vassiliev[67], S. P. Wakely[63], O. M. Weiner[60], A. Weinstein[49], A. Wilhelm[50,51], D. A. Williams[48], B. Zitzer[71]
(The VERITAS Collaboration),
and
O. Vince[76], L. Fuhrmann[72], E. Angelakis[72], V. Karamanavis[72], I. Myserlis[72], T. P. Krichbaum[72], J. A. Zensus[73], H. Ungerechts[73], A. Sievers[73]
(The F-Gamma Consortium), R. Bachev[74], M. Böttcher[75], W. P. Chen[76], G. Damljanovic[77], C. Eswaraiah[76], T. Güver[78], T. Hovatta[10,79], Z. Hughes[48], S. I. Ibryamov[80], M. D. Joner[81], B. Jordan[82], S. G. Jorstad[83,84], M. Joshi[83], J. Kataoka[85], O. M. Kurtanidze[86,87], S. O. Kurtanidze[86], A. Lähteenmäki[79,88], G. Latev[89], H. C. Lin[76], V. M. Larionov[90,91,92], A. A. Mokrushina[90,91], D. A. Morozova[90], M. G. Nikolashvili[86], C. M. Raiteri[93], V. Ramakrishnan[79], A. C. R. Readhead[9], A. C. Sadun[94], L. A. Sigua[86], E. H. Semkov[80], A. Strigachev[74], J. Tammi[79], M. Tornikoski[79], Y. V. Troitskaya[90], I. S. Troitsky[90], and M. Villata[93]

[1] Department of Physics, Stanford University, Stanford, CA 94305, USA; amy.@gmail.com, nodak5@gmail.com, josefa.becerra@nasa.gov
[2] Max-Planck-Institut für Physik, D-80805 München, Germany
[3] Space Science Laboratory, University of California, Berkeley, CA 94720, USA
[4] Kavli Institute for Particle Astrophysics and Cosmology, SLAC National Accelerator Laboratory, Stanford University, Stanford, CA 94305, USA
[5] DTU Space, National Space Institute, Technical University of Denmark, Elektrovej 327, DK-2800 Lyngby, Denmark
[6] Lawrence Livermore National Laboratory, Livermore, CA 94550, USA
[7] Space Science Laboratory, University of California, Berkeley, CA 94720, USA
[8] ASI Science Data Center (ASDC), Italian Space Agency (ASI), Via del Politecnico snc, Rome, Italy
[9] Columbia Astrophysics Laboratory, Columbia University, New York, NY 10027, USA
[10] Cahill Center for Astronomy and Astrophysics, Caltech, Pasadena, CA 91125, USA
[11] INAF-OAR, Via Frascati 33, I-00040 Monte Porzio Catone (RM), Italy
[12] Jet Propulsion Laboratory, California Institute of Technology, Pasadena, CA 91109, USA
[13] Yale Center for Astronomy and Astrophysics, Physics Department, Yale University, P.O. Box 208120, New Haven, CT 06520-8120, USA
[14] NASA Goddard Space Flight Center, Greenbelt, MD 20771, USA

[15] ETH Zurich, CH-8093 Zurich, Switzerland
[16] Università di Udine, and INFN Trieste, I-33100 Udine, Italy
[17] INAF National Institute for Astrophysics, I-00136 Rome, Italy
[18] Università di Siena, and INFN Pisa, I-53100 Siena, Italy
[19] Croatian MAGIC Consortium, Rudjer Boskovic Institute, University of Rijeka and University of Split, HR-10000 Zagreb, Croatia
[20] Saha Institute of Nuclear Physics, 1\AF Bidhannagar, Salt Lake, Sector-1, Kolkata 700064, India
[21] Centro Brasileiro de Pesquisas Físicas (CBPF\MCTI), R. Dr. Xavier Sigaud, 150—Urca, Rio de Janeiro—RJ 22290-180, Brazil
[22] Universidad Complutense, E-28040 Madrid, Spain
[23] Inst. de Astrofísica de Canarias, E-38200 La Laguna, Tenerife, Spain
[24] Department of Physics and Department of Astronomy, University of Maryland, College Park, MD 20742, USA
[25] University of Łódź, PL-90236 Lodz, Poland
[26] Deutsches Elektronen-Synchrotron (DESY), D-15738 Zeuthen, Germany
[27] Humboldt University of Berlin, Istitut für Physik Newtonstr. 15, D-12489 Berlin, Germany
[28] IFAE, Campus UAB, E-08193 Bellaterra, Spain
[29] Universität Würzburg, D-97074 Würzburg, Germany
[30] Ecole polytechnique fédérale de Lausanne (EPFL), Lausanne, Switzerland
[31] Centro de Investigaciones Energéticas, Medioambientales y Tecnológicas, E-28040 Madrid, Spain
[32] Università di Padova and INFN, I-35131 Padova, Italy
[33] Institute of Space Sciences, E-08193 Barcelona, Spain
[34] Technische Universität Dortmund, D-44221 Dortmund, Germany
[35] Unitat de Física de les Radiacions, Departament de Física, and CERES-IEEC, Universitat Autònoma de Barcelona, E-08193 Bellaterra, Spain
[36] Universitat de Barcelona, ICC, IEEC-UB, E-08028 Barcelona, Spain
[37] Japanese MAGIC Consortium, ICRR, The University of Tokyo, Department of Physics and Hakubi Center, Kyoto University, Tokai University, The University of Tokushima, KEK, Japan
[38] Finnish MAGIC Consortium, Tuorla Observatory, University of Turku and Department of Physics, University of Oulu, Finland
[39] Inst. for Nucl. Research and Nucl. Energy, BG-1784 Sofia, Bulgaria
[40] Finnish Centre for Astronomy with ESO (FINCA), Turku, Finland
[41] INAF-Trieste, Italy
[42] Università di Pisa, and INFN Pisa, I-56126 Pisa, Italy
[43] ICREA and Institute of Space Sciences, E-08193 Barcelona, Spain
[44] Università dell'Insubria and INFN Milano Bicocca, Como, I-22100 Como, Italy
[45] Department of Physics, Washington University, St. Louis, MO 63130, USA
[46] Fred Lawrence Whipple Observatory, Harvard-Smithsonian Center for Astrophysics, Amado, AZ 85645, USA
[47] School of Physics, University College Dublin, Belfield, Dublin 4, Ireland
[48] Santa Cruz Institute for Particle Physics and Department of Physics, University of California, Santa Cruz, CA 95064, USA
[49] Department of Physics and Astronomy, Iowa State University, Ames, IA 50011, USA
[50] Institute of Physics and Astronomy, University of Potsdam, D-14476 Potsdam-Golm, Germany
[51] DESY, Platanenallee 6, D-15738 Zeuthen, Germany
[52] Astronomy Department, Adler Planetarium and Astronomy Museum, Chicago, IL 60605, USA
[53] School of Physics, National University of Ireland Galway, University Road, Galway, Ireland
[54] Department of Physics and Astronomy, Purdue University, West Lafayette, IN 47907, USA
[55] School of Physics and Astronomy, University of Minnesota, Minneapolis, MN 55455, USA
[56] Department of Astronomy and Astrophysics, 525 Davey Lab, Pennsylvania State University, University Park, PA 16802, USA
[57] Physics Department, McGill University, Montreal, QC H3A 2T8, Canada
[58] Department of Physics and Astronomy, University of Iowa, Van Allen Hall, Iowa City, IA 52242, USA
[59] Department of Physics and Astronomy and the Bartol Research Institute, University of Delaware, Newark, DE 19716, USA
[60] Physics Department, Columbia University, New York, NY 10027, USA
[61] Department of Physics and Astronomy, DePauw University, Greencastle, IN 46135-0037, USA
[62] Department of Physics and Astronomy, University of Utah, Salt Lake City, UT 84112, USA
[63] Enrico Fermi Institute, University of Chicago, Chicago, IL 60637, USA
[64] Kavli Institute for Cosmological Physics, University of Chicago, Chicago, IL 60637, USA
[65] School of Physics and Center for Relativistic Astrophysics, Georgia Institute of Technology, 837 State Street NW, Atlanta, GA 30332-0430, USA
[66] Department of Physics and Astronomy, Barnard College, Columbia University, NY 10027, USA
[67] Department of Physics and Astronomy, University of California, Los Angeles, CA 90095, USA
[68] Astronomical Observatory, Volgina 7, 11060 Belgrade, Serbia
[69] Physics Department, California Polytechnic State University, San Luis Obispo, CA 94307, USA
[70] Department of Applied Science, Cork Institute of Technology, Bishopstown, Cork, Ireland
[71] Argonne National Laboratory, 9700 S. Cass Avenue, Argonne, IL 60439, USA
[72] Max-Planck-Institut für Radioastronomie, Auf dem Huegel 69, D-53121 Bonn, Germany
[73] Institut de Radio Astronomie Millimétrique, Avenida Divina Pastora 7, Local 20, E-18012 Granada, Spain
[74] Institute of Astronomy, Bulgarian Academy of Sciences, 72 Tsarigradsko shosse Blvd., 1784 Sofia, Bulgaria
[75] Centre for Space Research, Private Bag X6001, North-West University, Potchefstroom Campus, Potchefstroom, 2520, South Africa
[76] Graduate Institute of Astronomy, National Central University, 300 Zhongda Road, Zhongli 32001, Taiwan
[77] Astronomical Observatory, Volgina 7, 11060 Belgrade, Serbia
[78] Istanbul University, Science Faculty, Department of Astronomy and Space Sciences, Beyazí t, 34119, Istanbul, Turkey
[79] Aalto University Metsähovi Radio Observatory, Metsähovintie 114, FI-02540 Kylmälä, Finland
[80] Institute of Astronomy and NAO, Bulgarian Academy of Sciences, 1784 Sofia, Bulgaria
[81] Department of Physics, Brigham Young University Provo, UT, USA
[82] School of Cosmic Physics, Dublin Institute For Advanced Studies, Ireland
[83] Institute for Astrophysical Research, Boston University, 725 Commonwealth Avenue, Boston, MA 02215, USA
[84] Astronomical Institute, St. Petersburg State University, Universitetskij Pr. 28, Petrodvorets, 198504 St. Petersburg, Russia
[85] Research Institute for Science and Engineering, Waseda University, 3-4-1 Okubo, Shinjuku, Tokyo 169-8555, Japan
[86] Abastumani Observatory, Mt. Kanobili, 0301 Abastumani, Georgia
[87] Engelhardt Astronomical Observatory, Kazan Federal University, Tatarstan, Russia
[88] Aalto University Department of Radio Science and Engineering, P.O. BOX 13000, FI-00076 Aalto, Finland
[89] Institute of Astronomy with NAO, BAS, BG-1784, Sofia, Bulgaria

[90] Astron. Inst., St.-Petersburg State Univ., Russia
[91] Pulkovo Observatory, St.-Petersburg, Russia
[92] Isaac Newton Institute of Chile, St.-Petersburg Branch, Chile
[93] INAF, Osservatorio Astronomico di Torino, I-10025 Pino Torinese (TO), Italy
[94] Department of Physics, University of Colorado Denver, Denver, CO, USA
Received 2015 April 22; accepted 2015 September 5; published 2015 October 8

ABSTRACT

We report on simultaneous broadband observations of the TeV-emitting blazar Markarian 501 between 2013 April 1 and August 10, including the first detailed characterization of the synchrotron peak with *Swift* and *NuSTAR*. During the campaign, the nearby BL Lac object was observed in both a quiescent and an elevated state. The broadband campaign includes observations with *NuSTAR*, MAGIC, VERITAS, the *Fermi* Large Area Telescope, *Swift* X-ray Telescope and UV Optical Telescope, various ground-based optical instruments, including the GASP-WEBT program, as well as radio observations by OVRO, Metsähovi, and the F-Gamma consortium. Some of the MAGIC observations were affected by a sand layer from the Saharan desert, and had to be corrected using event-by-event corrections derived with a Light Detection and Ranging (LIDAR) facility. This is the first time that LIDAR information is used to produce a physics result with Cherenkov Telescope data taken during adverse atmospheric conditions, and hence sets a precedent for the current and future ground-based gamma-ray instruments. The *NuSTAR* instrument provides unprecedented sensitivity in hard X-rays, showing the source to display a spectral energy distribution (SED) between 3 and 79 keV consistent with a log-parabolic spectrum and hard X-ray variability on hour timescales. None (of the four extended *NuSTAR* observations) show evidence of the onset of inverse-Compton emission at hard X-ray energies. We apply a single-zone equilibrium synchrotron self-Compton (SSC) model to five simultaneous broadband SEDs. We find that the SSC model can reproduce the observed broadband states through a decrease in the magnetic field strength coinciding with an increase in the luminosity and hardness of the relativistic leptons responsible for the high-energy emission.

Key words: BL Lacertae objects: general – galaxies: individual (Markarian 501) – X-rays: galaxies

1. INTRODUCTION

Markarian 501 (Mrk 501) is a nearby, bright X-ray-emitting blazar at $z = 0.034$, also known to emit very-high-energy (VHE; $E \geqslant 100$ GeV) gamma-ray photons (Quinn et al. 1996). Blazars are among the most extreme astrophysical sources, displaying highly variable emission at nearly every wavelength and timescale probed thus far. These objects are understood to be active galactic nuclei that are powered by accretion onto supermassive black holes and have relativistic jets pointed along the Earth's line of sight (Urry & Padovani 1995). Relativistic charged particles within blazar jets are responsible for the non-thermal spectral energy distribution (SED), which is characterized by two broad peaks in the νF_ν spectral representation. The origin of the lower-energy peak is relatively well understood, resulting from the synchrotron radiation of relativistic leptons in the presence of a tangled magnetic field (Marscher 2008). Within the leptonic paradigm, the higher-energy SED peak is attributed to inverse-Compton up-scattering by the relativistic leptons within the jet of either the synchrotron photons themselves, namely synchrotron self-Compton (SSC) emission (Maraschi et al. 1992), or a photon field external to the jet, namely external Compton emission (e.g., Dermer et al. 1992; Sikora et al. 1994). Alternatively, hadronic models attribute the higher-energy peak of blazar emission to proton synchrotron emission and/or synchrotron emission by secondary leptons produced in p–γ interactions (Bednarek 1993; Aharonian et al. 2002).

Along with the other nearby VHE blazar Mrk 421, Mrk 501 represents one of the most comprehensively studied VHE blazars. The blazar has been the subject of multiple broadband observation campaigns (e.g., Catanese et al. 1997; Kataoka et al. 1999; Petry et al. 2000; Abdo et al. 2011a). Mrk 501 is one of the brightest X-ray sources in the sky, and has been observed by *RXTE* to display significant X-ray variability up to 20 keV (Gliozzi et al. 2006). During a phase of high activity at VHE energies in 1997, this source was also observed by *BeppoSAX* to display unusually hard, correlated X-ray emission up to >100 keV, with a photon index of $\Gamma < 2$ (Pian et al. 1998).

Observations of Mrk 501 have so far lacked sufficient sensitivity at the hard X-ray energies (10–100 keV). Observations at hard X-ray energies provide direct insight into the highest energy particles through detection of synchrotron emission. There is also the possibility for insight into the lower energy particles through the detection of inverse-Compton emission from photon up-scattering by the lower-energy electrons. As a relativistic synchrotron emitter, the falling edge of the synchrotron peak mimics the energy distribution of the emitting particles, allowing the highest energy particles to be directly probed through hard X-ray observations. The energy-dependent cooling timescale can lead to more rapid variability at hard X-ray energies than at soft X-ray energies. Gliozzi et al. (2006) reported independent soft (2–10 keV) and hard (10–20 keV) X-ray variability of Mrk 501 using *RXTE*.

Other hard X-ray observations have previously been performed with *BeppoSAX* (Massaro et al. 2004a) and *Suzaku* HXD (Anderhub et al. 2009). Due to the rapid X-ray variability displayed by blazars such as Mrk 501, the long integration time required for significant detection and spectral reconstruction by the aforementioned X-ray instruments was not ideal for extracting information about hard X-ray variability. Much more sensitive hard X-ray observations of blazars, however, are now possible with *Nuclear Spectroscopic Telescope Array NuSTAR*.

NuSTAR is a hard X-ray (3–79 keV) observatory launched into a low Earth orbit in 2012 June (Harrison et al. 2013). It features the first focusing hard X-ray telescope (XRT) in orbit that allows high sensitivity beyond the 10 keV cutoff shared by all other currently active focusing soft X-ray telescopes. The inherently low background associated with concentrating the X-ray light enables *NuSTAR* to achieve approximately a one-hundred-fold improvement in sensitivity over the collimated and coded-mask instruments that operate in the same spectral range.

NuSTAR observed Mrk 501 four times in 2013 as part of a simultaneous multiwavelength (MWL) campaign, including VHE observations by MAGIC and VERITAS, high-energy (HE; 100 MeV−100 GeV) gamma-ray observations by the *Fermi* Large Area Telescope (LAT), soft X-ray and UV observations with *Swift* X-ray Telescope (XRT) and Ultraviolet Optical Telescope (UVOT), optical observations from a number of ground-based instruments including the GASP-WEBT program, as well as radio observations by the Owens Valley Radio Observatory (OVRO; 15 GHz), Metsähovi (37 GHz), and the F-Gamma monitoring program, providing measurements between 2.64 and 228.39 GHz. The *NuSTAR* observations took place on 2013 April 13, May 8, and July 12 and 13 (MJD 56395, 56420, 56485, and 56486, respectively), with the latter two observations resulting from target of opportunity (ToO) exposures triggered by an elevated state observed by the *Swift* XRT and the MAGIC telescopes.

We use these observations to study the hard X-ray spectral behavior of Mrk 501 in detail over multiple flux states. The *NuSTAR* observations, analysis, and results are detailed in Section 2, with the contemporaneous MWL observations, analysis and results shared in Section 3. After comparing the simultaneous *Swift* XRT and *NuSTAR* observations in Section 4, we investigate variability of the source in Section 5. The MWL SEDs are constructed over the multiple observed states and investigated in terms of a single-zone equilibrium SSC model in Section 6, with discussion and conclusions provided in Section 7.

2. *NuSTAR* OBSERVATIONS AND ANALYSIS

In order to maximize the strictly simultaneous overlap of observations by *NuSTAR* and ground-based VHE observatories during this broadband campaign of Mrk 501, the observations were arranged according to visibility of the blazar at the MAGIC and VERITAS sites. The *NuSTAR* coordinated observations involving both VERITAS and MAGIC were performed on 2013 April 13 and May 8, with the *NuSTAR* ToO observations (initiated by *Swift* and MAGIC) performed on 2013 July 12 and 13. The *NuSTAR* observations typically spanned 10 hr, resulting in 10–30 ks of source exposure after removing periods of orbital non-visibility. The observation details are summarized in Table 1. The data were reduced using the standard `NuSTARDAS` software package[95] `v1.3.1`.

The spectral analysis was performed with `XSPEC`[96] Version 12.7.1. The data were binned to require 20 counts per bin, and fit with three spectral models via χ^2 minimization. The first model applied to the data is a power law

$$A(E)_{\rm PL} = K\left(E/E_0\right)^{-\Gamma}, \quad (1)$$

referred to as the PL model for the remainder of this work, where $F(E)$ is the flux at energy E, Γ is the index, K is the normalization parameter (in units of photons keV^{-1} cm^{-2} s^{-1}) and E_0 is fixed at 10 keV.

Table 1
Summary of the *NuSTAR* Hard X-Ray Observations of Mrk 501

Observation ID	MJD Exposure Range	Exposure (ks)	Number Orbits	Detection Range (keV)
60002024002	56395.1–56395.5	19.7	6	3–60
60002024004	56420.8–56421.5	28.3	10	3–65
60002024006	56485.9–56486.2	11.9	4	3–70
60002024008	56486.8–56487.1	11.4	4	3–70

Note. The observations are sometimes referred to with the last three digits of the observation ID within this work.

The second spectral model applied to the data is a broken power law, referred to as BKNPL model for the remainder of this work. The model is made up of two power-law photon indices, meeting at a break energy $E_{\rm break}$

$$A(E)_{\rm BKNPL} = K\left(E/E_{\rm break}\right)^{-\Gamma_{1,2}} \quad (2)$$

where Γ_1 and Γ_2 represent the photon indices below and above the break energy $E_{\rm break}$, respectively.

The third spectral model applied to the data is a log parabola, referred to as the LP model for the remainder of this work. This model has been suggested to better represent the X-ray spectra of TeV-detected blazars between 0.2 and 100 keV (e.g., Massaro et al. 2004b; Tramacere et al. 2007). This model allows the spectral index to vary as a function of energy according to the expression

$$A(E)_{\rm LP} = K\left(E/E_0\right)^{-\left(\Gamma+\beta\,\log\left(E/E_0\right)\right)}, \quad (3)$$

with a curvature parameter β. The spectral data, model fits, and data-to-model ratios for each *NuSTAR* observation are shown in Figure 1. The spectral fitting results for each model as applied to the *NuSTAR* observations are summarized in Table 2. The errors for each parameter are found using a value of $\Delta\chi^2 = 2.706$, corresponding to a 90% confidence level for one parameter.

For all four *NuSTAR* observations, the X-ray emission of Mrk 501 is best represented with a log parabola. A statistical F-test (Snedecor & Cochran 1989) using the χ^2 and degrees of freedom (dof) of the PL versus LP fit results in F-statistics of 97.8, 129.3, 200.1 and 251.3 for the observations 002, 004, 006, and 008, respectively, corresponding to probabilities of 1.1×10^{-21}, 4.6×10^{-28}, 2.9×10^{-41}, and 7.9×10^{-50} for being consistent with the null PL hypothesis. The broken power-law fit to the second *NuSTAR* observation, ID 004, produces a break energy at the lower limit of the *NuSTAR* sensitivity window, and is interpreted as a failed fit. The other three observations fit the break energy near $E_{\rm break} = 7$ keV, motivating the decision to present the *NuSTAR* flux values in the 3–7 and 7–30 keV bands throughout this work. The upper bound of 30 keV is the typical orbit-timescale detection limit for the Mrk 501 observations.

The *NuSTAR* observations show the blazar to be in a relatively low state for the first two observations, and a relatively high state during the last two observations, with the 3–7 keV integral fluxes derived from the log-parabolic fits 2–4 times higher than found for the first two observations. More specifically, the average 3–7 keV integral flux values (in units

[95] http://heasarc.gsfc.nasa.gov/docs/nustar/analysis/
[96] https://heasarc.gsfc.nasa.gov/xanadu/Xspec/XspecManual.pdf

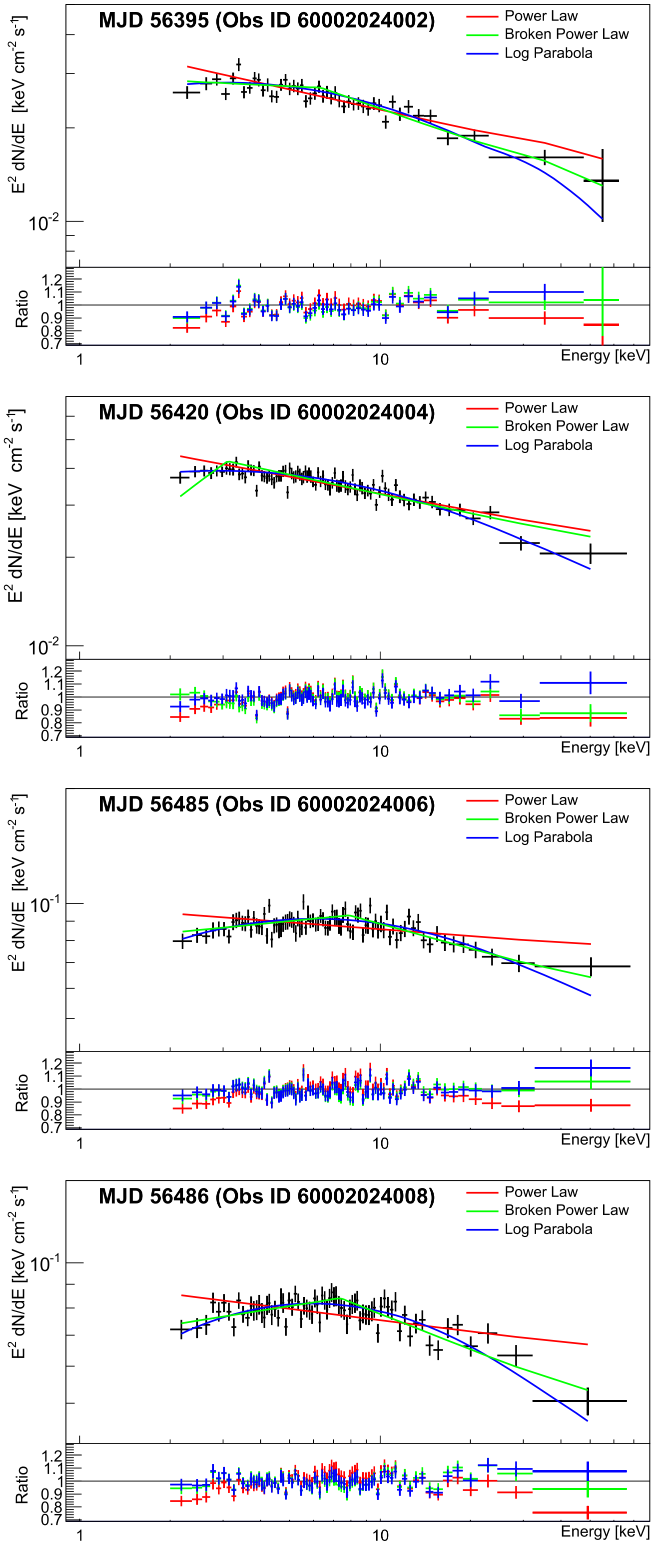

Figure 1. Spectral energy distributions of Mrk 501 derived from the *Nu-STAR* observations, showing the PL (red), BKNPL (green), and LP (blue) models fitted to each observation. The *NuSTAR* observations show significant detection of the blazar up to at least 65 keV in each observation. The data-to-model ratios are shown in the bottom panel of each plot, with the spectral fit parameters summarized in Table 2. Spectra have been rebinned for figure clarity.

of 10^{-11} erg cm^{-2} s^{-1}) were 3.72 ± 0.02 and 5.19 ± 0.02, respectively, for the observations occurring on MJD 56395 and 56420, and 12.08 ± 0.09 and 10.75 ± 0.05, respectively, for the observations starting on MJD 56485 and 56486. In the same flux units, the 7–30 keV integral flux values for the first two observations are similarly 3–4 times lower than the flux states observed in the last two observations (4.81 ± 0.03 and 6.98 ± 0.05 on MJD 56395 and 56420 as compared to 18.6 ± 0.1 and 16.4 ± 0.1 on MJD 56485 and 56486). These integral flux values are summarized in Table 2.

The *NuSTAR* observations extend across multiple occultations by the Earth, and the integral flux and index (Γ) light curves for the orbits of each extended observation are shown in Figure 2. The periods with simultaneous observations with the ground-based TeV instruments of MAGIC and VERITAS are highlighted by gray and brown bands in the upper portion of each light curve. The observations and results from MAGIC and VERITAS for these time periods are summarized in Section 3.1.

The 3–7 and 7–30 keV integral flux values of the first exposure (Observation ID 002) show low variability ($\chi^2 = 7.0$ and 13.4 for 5 dof), while the trend of increasing flux in both the 3–7 and 7–30 keV bands is clear during the second observation (Observation ID 004). The 7–30 keV flux increases from $(5.1 \pm 0.1) \times 10^{-11}$ erg cm^{-2} s^{-1} to $(8.8 \pm 0.1) \times 10^{-11}$ erg cm^{-2} s^{-1} in fewer than 16 hr. The 7–30 keV increases from $(1.7 \pm 0.1) \times 10^{-10}$ erg cm^{-2} s^{-1} to $(2.0 \pm 0.1) \times 10^{-10}$ erg cm^{-2} s^{-1} in fewer than 7 hr on MJD 56485 (Observation ID 006) and significantly decreases from $(1.9 \pm 0.1) \times 10^{-10}$ erg cm^{-2} s^{-1} to $(1.4 \pm 0.1) \times 10^{-10}$ erg cm^{-2} s^{-1}, again in fewer than 7 hr on MJD 56486 (Observation ID 008).

The relation between the log-parabolic photon indices and 7–30 keV flux values resulting from the fits to the *NuSTAR* observations of Mrk 501 are shown for each observation separately in Figure 3. The curvature β was not seen to change significantly from orbit to orbit and therefore was fixed at the average value found for each observation (see Table 2 for values). The count rate light curves show no indications of variability on a timescale of less than an orbit period (∼90 minutes). As observed previously in the X-ray band for Mrk 501 (Kataoka et al. 1999), the source was displaying a harder-when-brighter trend during this campaign. This has also been observed in the past for Mrk 421 (Takahashi et al. 1996).

3. BROADBAND OBSERVATIONS

3.1. VHE Gamma-rays

3.1.1. MAGIC

MAGIC is a VHE instrument composed of two imaging atmospheric Cherenkov telescopes (IACTs) with mirror diameters of 17 m, located at 2200 m above sea level at the Roque de Los Muchachos Observatory on La Palma, Canary Islands, Spain. The energy threshold of the system is 50 GeV and it reaches an integral sensitivity of 0.66% of the Crab Nebula flux above 220 GeV with a 50-hr observation (Aleksić et al. 2015a).

MAGIC observed Mrk 501 in 2013 from April 9 (MJD 56391) to August 10 (MJD 56514). On July 11 (MJD 56484), ToO observations were triggered by the high count rate of ∼15 counts s^{-1} observed by *Swift* XRT (see Section 3.3). The flaring state was observed intensively for five consecutive nights until July 15 (MJD 56488). After that the observations continued with a lower cadence until August 10.

Table 2
NuSTAR Spectral Fit Summary, with Integral Flux Values (in Units of $\times 10^{-11}$ erg cm^{-2} s^{-1}) Derived From the Log-parabolic Fits

	Power law		Broken Power law				Log Parabola				
Obs. ID	Index Γ	PL χ^2/dof	Index Γ_1	Index Γ_2	E_{break} (keV)	BKNPL χ^2/dof	Index Γ	Curvature β	LP χ^2/dof	3–7 keV Flux	7–30 keV Flux
002	2.216 $\pm$ 0.009	831/700	2.04 $\pm$ 0.03	2.34 $\pm$ 0.02	6.3 $\pm$ 0.4	747/698	2.290 $\pm$ 0.010	0.26 $\pm$ 0.03	729/699	3.72 $\pm$ 0.02	4.81 $\pm$ 0.03
004	2.191 $\pm$ 0.006	1204/889	1.25 $\pm$ 0.20	2.21 $\pm$ 0.01	3.1 $\pm$ 0.1	1211/887	2.250 $\pm$ 0.008	0.21 $\pm$ 0.02	1051/888	5.19 $\pm$ 0.02	6.98 $\pm$ 0.05
006	2.060 $\pm$ 0.006	1246/924	1.92 $\pm$ 0.02	2.22 $\pm$ 0.02	7.9 $\pm$ 0.4	1057/922	2.115 $\pm$ 0.008	0.24 $\pm$ 0.02	1024/923	12.08 $\pm$ 0.09	18.6 $\pm$ 0.1
008	2.081 $\pm$ 0.007	1152/863	1.90 $\pm$ 0.02	2.25 $\pm$ 0.02	7.4 $\pm$ 0.3	914/861	2.149 $\pm$ 0.008	0.32 $\pm$ 0.02	892/862	10.75 $\pm$ 0.05	16.4 $\pm$ 0.1

Notes. Data, models, and ratios, are shown in Figure 1. The indices of the LP fits are derived at 10 keV. The errors for each parameter are found using a value of $\Delta\chi^2 = 2.706$, corresponding to a 90% confidence level for a parameter. Observation IDs are shortened by removing the first 60002024 identifier in column one.

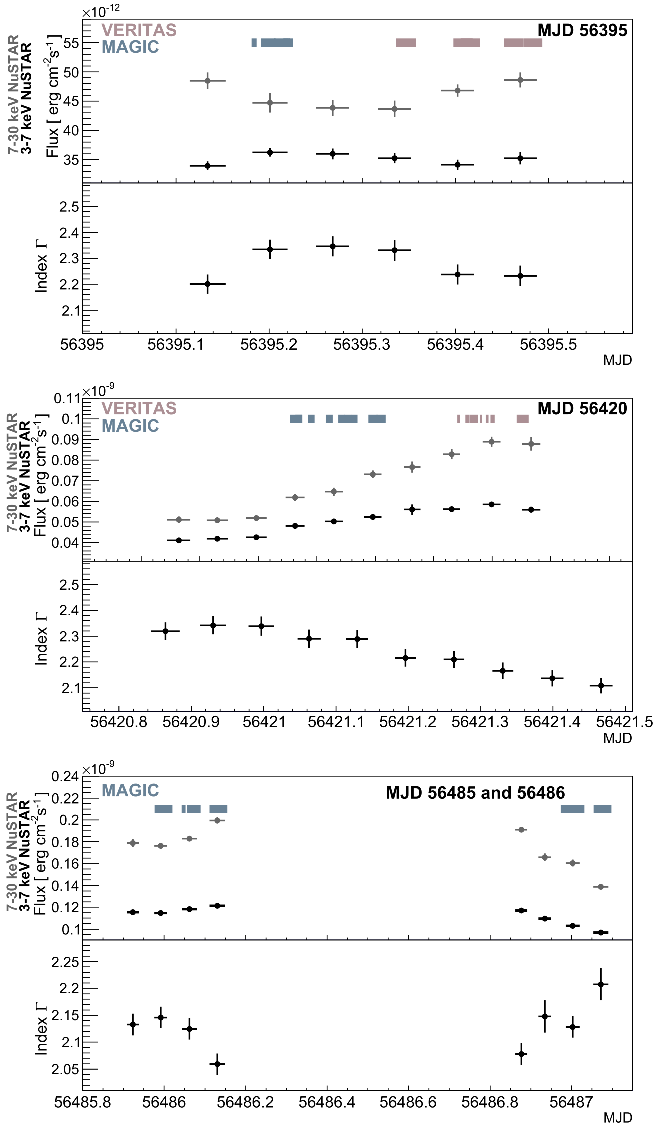

Figure 2. *NuSTAR* orbit-binned light curves, with 3–7 keV (black) and 7–30 keV (gray) integral flux values (top panel of each plot) and the log-parabolic indices (Γ, lower panel) with the curvature parameters (β) fixed to the value found for the full *NuSTAR* exposure. The third and fourth observations are shown in the third plot. The periods where simultaneous quality-selected observations with MAGIC and VERITAS occurred are highlighted in the top panel of each plot with color coded bands. We note that the vertical axes are set differently for each observation to allow a clear view of the orbit-to-orbit variability and that the light curve for the full campaign is shown in Figure 5.

The source was observed during 17 nights, collecting a total of 22 hr of data with zenith angles between 10° and 60°. Only five hours survived the standard quality cuts for regular MAGIC data analysis because many observations were taken during the presence of a Saharan sand–dust layer in the atmosphere known as "Calima." As we explain below, using the Light Detection and Ranging (LIDAR) information we could recover 10 of the 17 hr which would have been rejected otherwise. The telescopes were operated in the so-called wobble mode (Fomin et al. 1994), where the pointing direction is changed every 20 (or 15) minutes among 2 (or 4) positions with an offset of 0°.4 from the source position.

All the data were analyzed following the standard procedure (Aleksić et al. 2012) using the MAGIC Analysis and Reconstruction Software (MARS; Zanin et al. 2013). An

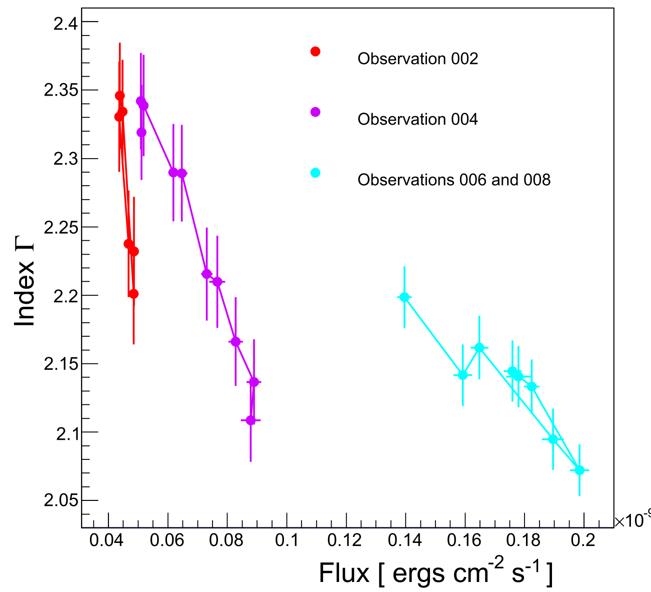

Figure 3. Log-parabolic fit index Γ at 10 keV vs. the 7–30 keV integral flux for *NuSTAR*, binned by orbit. The first exposure is shown in red, the second in violet, and the last two in cyan, with solid lines meant to guide the eye along the parameter evolution over the full observations. In all three cases, the spectrum hardens when the intensity increases; in the fourth observation, the spectrum then softens as the intensity decreases.

image cleaning was applied based on information of signal amplitude and timing of each pixel, and the shower images were parametrized using the Hillas parameters (Hillas 1985). For the reconstruction of the gamma-ray direction and the gamma-hadron separation, the random forest method is applied using the image parameters and the stereoscopic parameters. (Albert et al. 2008; Aleksić et al. 2010). The energy reconstruction utilizes look-up tables. The analysis steps were confirmed independently with data from the Crab Nebula and dedicated Monte Carlo simulations of gamma-ray showers.

A fraction of the data set (10.4 of 15.1 hr, specifically the observations between MJD 56485 and MJD 56514) was affected by "Calima," a Saharan sand–dust layer in the atmosphere. A correction within the framework of the MARS software is applied to account for the absorption due to Calima using LIDAR measurements taken simultaneously with the MAGIC observations (Fruck et al. 2013). The correction was carried out in two steps. Due to the dust attenuation during Calima, the estimated energy is shifted toward low energies, and thus is corrected event by event, as the first step. Then, to account for the shift of the energy estimation, a correction to the collection area is applied as a second step, due to the energy dependence in the collection area. The atmospheric transmission values for this method were obtained from the temporally closest LIDAR measurement. During the observations affected by Calima the atmospheric transmission ranged from 85% down to 60%, being relatively stable within a timescale of one day, which is a typical feature of a Calima layer (unlike a cloudy sky). The precision on the energy correction is estimated to be around 5% of the attenuation (40%–15%), which corresponds to <2% of the estimated energy, at most. After the Calima correction, the energy threshold increases inversely proportional to the transmission value. This correction method was tested independently on a Crab Nebula data set observed under similarly hazy weather conditions (Fruck & Gaug 2015). Details of the method can be found in Fruck

Table 3
MAGIC and VERITAS Observations, Analysis, and Spectral Fit Summary for *NuSTAR*-simultaneous Observations

Exposure Start MJD	Exposure Stop MJD	Exposure Length (hr)	Instrument	Zenith Angle (deg)	Detection Significance (σ)	Power-law Index	Integral Flux > 200 GeV ($\times 10^{-11}$ ph cm^{-2} s^{-1})	χ^2	dof
56395.179	56395.223	1.0	MAGIC	10–14	7.8	2.50 ± 0.24	2.39 ± 0.44	0.58	6
56395.336	56395.493	2.5	VERITAS	15–35	8.3	3.1 ± 0.4	1.85 ± 0.38	0.76	5
56421.142	56421.209	1.1	MAGIC	12–28	12.5	2.24 ± 0.08	5.08 ± 0.54	15.5	13
56421.340	56421.462	1.0	VERITAS	20–32	14.7	2.25 ± 0.15	4.45 ± 0.61	6.9	9
56485.972	56486.014	1.0	MAGIC	12–24	20.4	2.19 ± 0.07	20.8 ± 1.2	10.0	12
56486.039	56486.083	1.0	MAGIC	28–43	20.7	2.39 ± 0.08	25.2 ± 1.3	26.5	10
56486.106	56486.148	1.0	MAGIC	48–60	14.3	2.71 ± 0.12	*32.4 ± 2.0*	11.9	11
56485.972	**56486.148**	2.9	MAGIC	12–60	32.3	2.28 ± 0.04	24.3 ± 0.8	24.1	15
56486.966	56487.022	1.3	MAGIC	12–27	25.2	2.37 ± 0.06	24.9 ± 1.1	20.3	12
56487.050	56487.091	0.9	MAGIC	33–46	18.5	2.23 ± 0.09	17.8 ± 1.0	14.5	11
56486.966	**56487.091**	2.2	MAGIC	12–46	31.8	2.31 ± 0.05	20.9 ± 0.7	30.4	12

Notes. Observations occurring on the same day are grouped with horizontal lines. Daily average values of MAGIC observations are shown in bold, below the results for each observation occurring on that day. Statistical (1σ) error bars are provided for the power-law indices and the integral fluxes. The flux value between MJD 56486.106 and 56486.148 (shown in italics) is estimated with fitting parameters due to an energy threshold above 200 GeV. The significance of the observed gamma-ray signals is computed according to Equation (17) in Li & Ma (1983).

(2015). This is the first time an event-by-event atmospheric correction is applied to MAGIC data.

The analysis results of the MAGIC data taken during good weather conditions have a systematic uncertainty in the flux normalization and in the energy scale. For both of them, the component changing run-by-run is estimated to be ~11% using Crab Nebula observations (Aleksić et al. 2015a). It is attributed mainly to the atmospheric transmission of the Cherenkov light, which can change on a daily basis (even during so-called good weather conditions) and the mirror reflectivity, which can change also on a daily basis due to the deposition of dust. The atmospheric correction applied in the analysis of the data taken during Calima increases this run-by-run systematic error from 11% to 15% due to the uncertainty in the correction. Since the systematic uncertainty can be different according to the atmospheric correction,we have added 15% or 11% (with or without the atmospheric correction) to the statistical errors of the flux in quadrature for the evaluation of flux variability.

The summary of the MAGIC analysis results for observations occurring simultaneously with *NuSTAR* is provided in Table 3. The derived spectra are shown in Figure 4, where the spectral points are drawn with statistical errors only. The resultant flux values above 200 GeV range from $(2.39 \pm 0.51) \times 10^{-11}$ ph cm^{-2} s^{-1} (0.11 Crab Nebula flux) on MJD 56395 to $(5.52 \pm 0.87) \times 10^{-10}$ ph cm^{-2} s^{-1} (2.5 times the Crab Nebula flux) on MJD 56484. As seen in the overall light curve (top panel of Figure 5, shown again only with statistical errors), MAGIC observations indicate a significant variability around MJD 56484. A hint of intra-night variability was observed on MJD 56486 and 56487 simultaneously with the *NuSTAR* observations, as shown in the zoomed-in light curve (top panel of Figure 6). During these two nights the VHE emission is consistent with a constant flux, resulting in a χ^2/dof of 7.3/4 (12% probability) with the inclusion of the systematic error. Without accounting for the additional systematic error, the constant fit to the flux results in a χ^2/dof of 57/4.

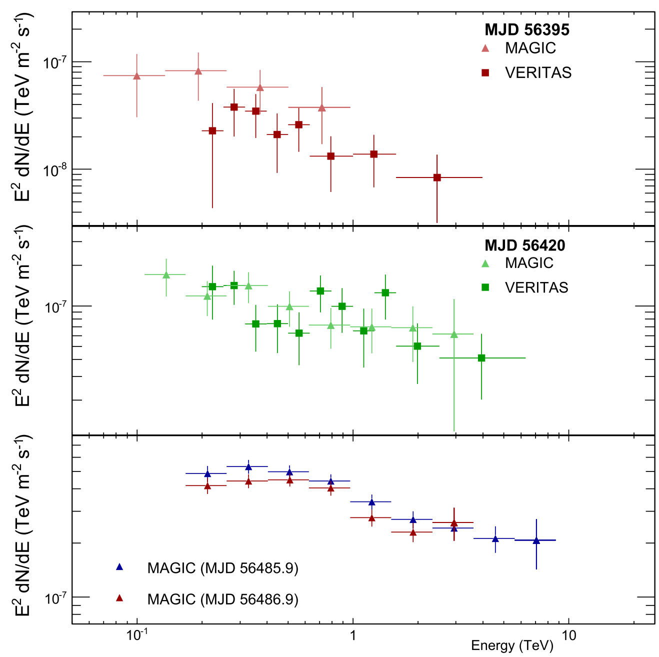

Figure 4. MAGIC and VERITAS spectra averaged over epochs with simultaneous *NuSTAR* exposures. The power-law spectral fitting parameters for the VHE data are summarized in Table 3. Only statistical (1σ) error bars are shown for each of the spectral points.

3.1.2. VERITAS

VERITAS is a VHE instrument comprised of four 12-m IACTs and is sensitive to gamma-rays between ~100 GeV and ~30 TeV (Holder et al. 2006; Kieda 2013). This instrument can detect 1% Crab Nebula flux in under 25 hr. VERITAS observed Mrk 501 fourteen times between 2013 April 7 (MJD 56389) and 2013 June 18 (MJD 56461), with 2.5 and 1.0 hr quality-selected exposures occurring simultaneously with *NuSTAR* on MJD 56395 and MJD 56421, respectively. On days without simultaneous *NuSTAR* observations, the exposure times ranged between 0.5 and 1.5 hr. The observations occurring

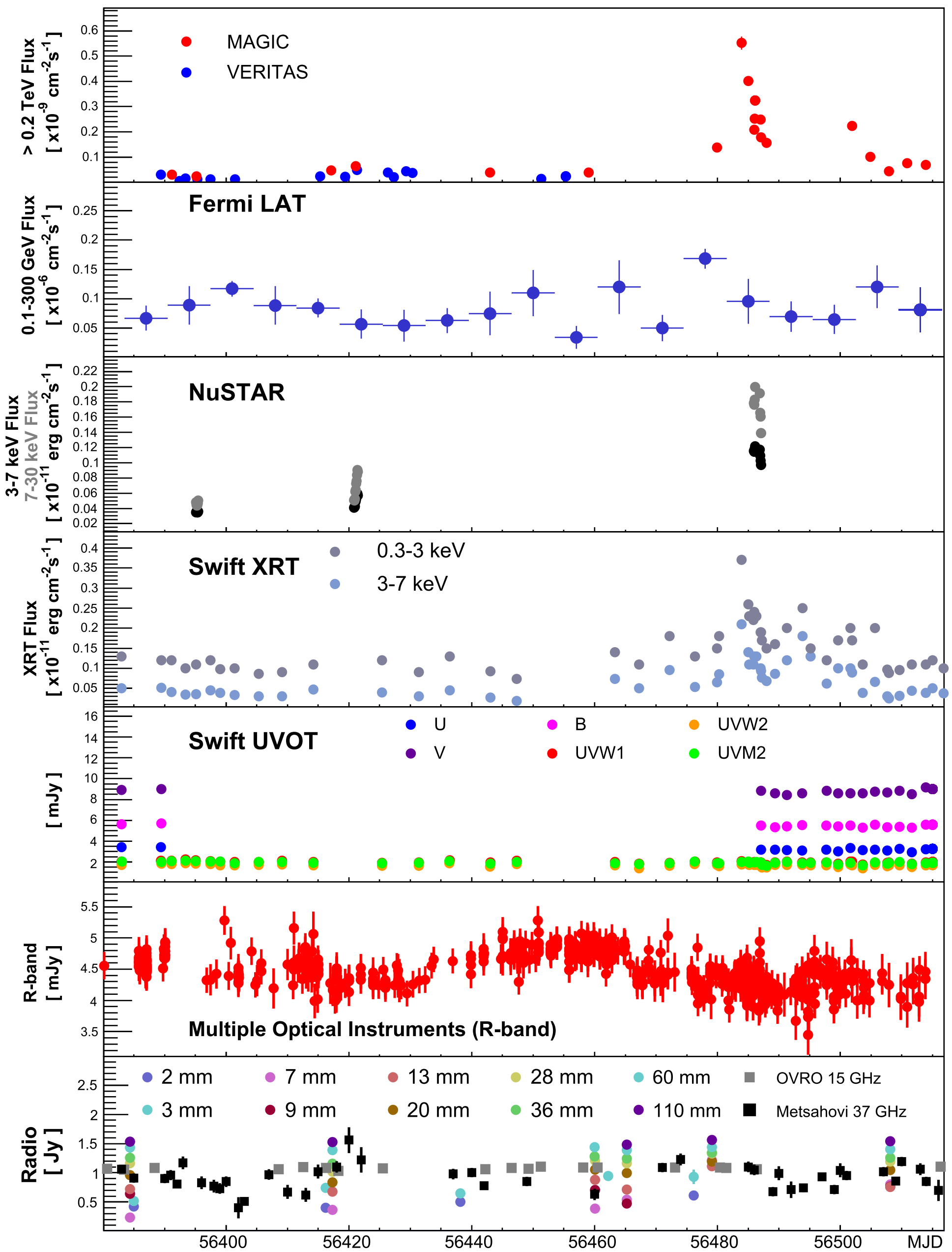

Figure 5. Broadband light curves of Mrk 501 from MJD 56380 to 56520. The VHE data are shown with statistical error bars only. Optical data are corrected as described in Section 3.4. All radio light curve points for 2–110 mm are provided by the F-Gamma consortium.

simultaneously with *NuSTAR* are summarized in Table 3. Due to an annual, ∼2 month long monsoon season in southern Arizona where VERITAS is located, no VERITAS observations were possible for this campaign after 2013 June 18.

The VERITAS observations were taken with 0°.5 offset in each of the four cardinal directions to enable simultaneous background estimation (Fomin et al. 1994). Events were reconstructed following the procedure outlined in Acciari et al. (2008a). The recorded shower images were parameterized by their principal moments, giving an efficient suppression of the far more abundant cosmic-ray background. Cuts were applied to the mean scaled width, mean scaled length, apparent altitude of the maximum Cherenkov emission (shower maximum), and θ, the angular distance between the position of Mrk 501 and the reconstructed origin of the event. The results were independently reproduced with two analysis packages (Cogan 2008; Prokoph 2013). The uncertainty on the energy calibration of VERITAS is estimated at 20%. Additionally, the systematic uncertainty on the spectral index is estimated at 0.2, appearing to be relatively independent of the source slope (Madhavan 2013).

A differential power law is fit to the data ($dN/dE \propto E^{-\Gamma}$) to characterize the VHE spectrum of the source. VERITAS observed Mrk 501 to vary by no more than a factor of three in flux throughout the observations, with the integral flux ranging from $(1.85 \pm 0.38) \times 10^{-11}$ ph cm^{-2} s^{-1} above 200 GeV (8% Crab Nebula flux above the same threshold) on MJD 56395 to $(4.45 \pm 0.61) \times 10^{-11}$ ph cm^{-2} s^{-1} (20% Crab Nebula flux) on MJD 56421. The source displayed low spectral variability, ranging between $\Gamma = 3.1 \pm 0.4$ in the low flux state to

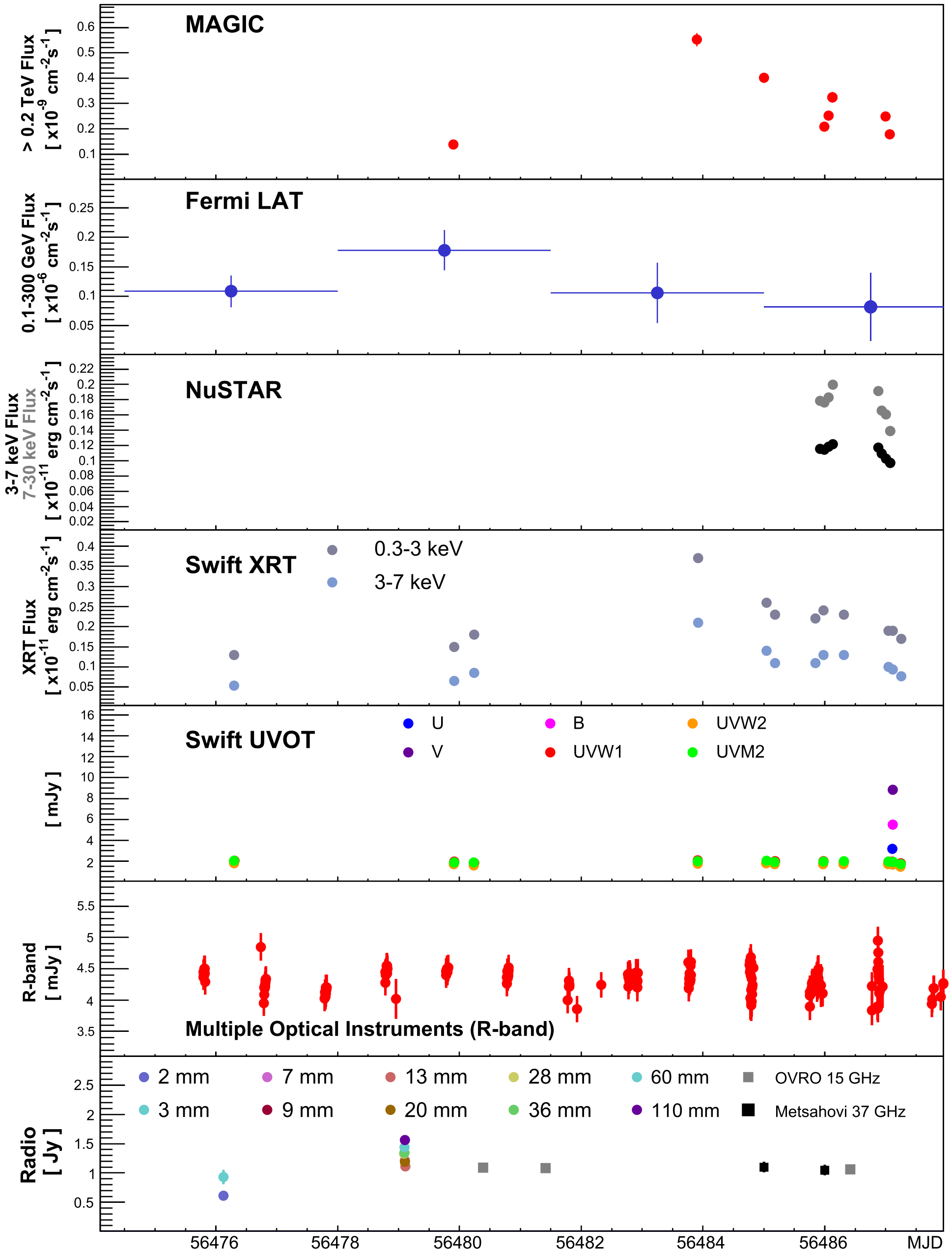

Figure 6. Broadband light curve zoomed in to the period of the elevated X-ray and VHE gamma-ray state.

$\Gamma = 2.19 \pm 0.07$ in the higher flux state. The observation and analysis results are summarized in Table 3 (for *NuSTAR* simultaneous observations only), with the VHE spectra of the *NuSTAR* simultaneous observations shown in Figure 4. Day-to-day uncertainties in flux calculations that might be introduced by different atmospheric conditions (even under strictly good weather conditions) are not included in Table 3 and are estimated at less than 10%.

3.1.3. VHE Results

The full light curve of VHE observations from MAGIC and VERITAS is shown in Figure 5, with a zoom into the period of elevated flux in Figure 6. The flux values are shown with statistical errors only. The MAGIC and VERITAS observations of Mrk 501 in 2013 show the source in states which are consistent with the range of states observed in the past. The observations of VERITAS, occurring primarily in the beginning of the campaign, detected the source in a 5%–10% Crab state, in agreement with the early MAGIC observations. Later on in the campaign, MAGIC observed a flux elevated state of order ~2.5 times the Crab flux.

3.2. HE Gamma-rays

Fermi LAT is a pair-conversion telescope sensitive to photons between 30 MeV and several hundred GeV (Atwood et al. 2009). Spectral analysis was completed for two periods contemporaneous with the *NuSTAR* observations using the unbinned maximum-likelihood method implemented in the LAT `ScienceTools` software package version `v9r31p1`, which is available from the *Fermi* Science Support Center. The LAT data between MJD 56381 and MJD 56424 was used for comparison with the first two *NuSTAR* exposures, while MJD

56471–56499 was used for *NuSTAR* exposures occurring during the elevated state.

"Source" class events with energies above 100 MeV within a 12° radius of Mrk 501 with zenith angles $<100°$ and detected while the spacecraft was at a $<52°$ rocking angle were used for this analysis. All sources within the region of interest from the second *Fermi* LAT catalog (2FGL, Nolan et al. 2012) are included in the model. With indices held fixed, the normalizations of the components were allowed to vary freely during the spectral fitting, which was performed using the instrument response functions `P7REP_SOURCE_V15`. The Galactic diffuse emission and an isotropic component, which is the sum of the extragalactic diffuse gamma-ray emission and the residual charged particle background, were modeled using the recommended files.[97] The flux values were computed using an unbinned maximum likelihood analysis while fixing the spectral indices for the sources within the region of interest. The systematic uncertainty of the LAT effective area is estimated as 10% below 100 MeV and decreasing linearly in Log(E) to 5% between 316 MeV and 10 GeV.[98]

The light curve for LAT observations of Mrk 501 was computed between MJD 56380 and 56520 in week-long bins (second panel from the top in Figure 5) and 3.5-day bins between MJD 56474 and 56488 (second panel from top of Figure 6). Single day-binned light curve was also investigated, but no day within the time period provided a significant detection. More specifically, no day provided a test statistic (Mattox et al. 1996) of greater than 9.

During the first epoch (MJD 56381–56424), the spectral analysis of the LAT data shows the blazar had an integral flux of $F_{0.1-100\mathrm{GeV}} = (5.3 \pm 4.4) \times 10^{-8}\ \mathrm{ph\ cm^{-2}\ s^{-1}}$, and an index of $\Gamma = 2.0 \pm 0.3$. Analysis of the second epoch (MJD 56471–56499) results in an integral flux of $F_{0.1-100\mathrm{GeV}} = (6.5 \pm 2.1) \times 10^{-8}\ \mathrm{ph\ cm^{-2}\ s^{-1}}$ and index of $\Gamma = 1.7 \pm 0.1$. These values are consistent with the average flux and index values calculated over the first 24 months of the science phase of the LAT mission and reported in the 2FGL catalog ($F_{0.1-100\mathrm{GeV}} = (4.8 \pm 1.9) \times 10^{-8}\ \mathrm{ph\ cm^{-2}\ s^{-1}}$ and $\Gamma = 1.74 \pm 0.03$; Nolan et al. 2012).

3.3. *Swift* X-Ray and UV Telescope Observations

The XRT onboard *Swift* (Gehrels et al. 2004) is a focusing X-ray telescope sensitive to photons with energies between 0.3 and 10 keV. The *Swift* satellite observed Mrk 501 59 times between 2013 January 1 and September 5 (MJD 56293–56540). All XRT observations were carried out using the Windowed Timing readout mode. The data set was first processed with the XRTDAS software package (v.2.9.0) developed at the ASI Science Data Center and distributed by HEASARC within the HEASoft package (v. 6.13). Event files were calibrated and cleaned with standard filtering criteria with the *xrtpipeline* task using the calibration files as available in the *Swift* CALDB version 20140120.

The spectrum from each observation was extracted from the summed and cleaned event file. Events for the spectral analysis were selected within a circle of 20 pixel (~46″) radius, which encloses about 80% of the *Swift* XRT point-spread function (PSF), centered on the source position. The background was extracted from a nearby circular region of 40 pixel radius. The ancillary response files were generated with the *xrtmkarf* task, applying corrections for PSF losses and CCD defects using the cumulative exposure map. The latest response matrices (v.014) available in the *Swift* CALDB were used. Before the spectral fitting, the 0.3–10 keV source energy spectra were binned to ensure a minimum of 20 counts per bin.

The data were fit with an absorbed power-law model, with index Γ, as well as an absorbed log-parabolic model, where in both cases the neutral hydrogen column density was set at $1.55 \times 10^{20}\ \mathrm{cm^{-2}}$, taken from Kalberla et al. (2005). The summary of the XRT observations and spectral analysis results are provided in Table 4. The light curve of the observations, including 0.3–3 and 3–7 keV integral flux bands, is shown in Figure 5, with a zoom into the period of elevated flux in Figure 6. The 3–7 keV band is not traditionally quoted for *Swift* XRT data, but is motivated by direct comparison to the 3–7 keV band computed for the *NuSTAR* observations.

Mrk 501 displays a relatively steady flux state until after MJD 56480, when the flux increases to $(38.3 \pm 1.5) \times 10^{-11}\ \mathrm{erg\ cm^{-2}\ s^{-1}}$ on MJD 56483 (corresponding to the day with the XRT count rate of 15 $\mathrm{counts\ s^{-1}}$ which triggered MAGIC and *NuSTAR* observations). This high X-ray state was followed by a general drop in flux, continuing through the last XRT observation included in this work (2013 September 1; MJD 56540).

The power-law fitted indices and 3–7 keV flux derived from the power-law fits are plotted in Figure 7 for all 59 observations. The source clearly displays the harder-when-brighter trend found previously in other TeV blazars, such as Mrk 421 (Takahashi et al. 1996). This behavior is similar to that displayed in the hard X-ray band 7–30 keV observed by *NuSTAR* and shown in Figure 3. Notably, the photon indices in the soft X-ray band are systematically harder than those observed by *NuSTAR* in the 7–30 keV band. The spectral index observed by *Swift* XRT (Γ, determined at 1 keV) ranges between 1.4 and 2.2 (Figure 7) while the *NuSTAR* index, determined at 10 keV, ranges from 2.1 to 2.4 (Figure 3).

Additionally, UV/optical observations were collected with the UVOT onboard *Swift*. These observations were carried out using the "filter of the day," i.e., one of the six lenticular filters (*V, B, U, UVW1, UVM2*, and *UVW2*), unless otherwise specified in the ToO request, so images are not always available for all filters. There are 50 observations included in this Mrk 501 campaign, 18 of which included exposures in all filters while the remaining 32 observations contain UV imaging only.

For each filter observation, we performed aperture photometry analysis using the standard UVOT software distributed within the HEAsoft 6.10.0 package and the calibration included in the latest release of CALDB. Counts were extracted from apertures of 5″ radius for all filters and converted to fluxes using the standard zero points from Poole et al. (2008). The flux values were then de-reddened using the value of $E(B-V) = 0.017$ (Schafly & Finkbeiner 2011) with $A_\lambda/E(B-V)$ ratios calculated for UVOT filters using the mean Galactic interstellar extinction curve from Fitzpatrick (1999). No variability was detected to occur within single exposures in any filter. The processing results were verified, checking for possible contamination from nearby objects falling within the background apertures.

[97] The files used were `gll_iem_v05_rev1.fit` for the Galactic diffuse and `iso_source_v05.txt` for the isotropic diffuse component, both available at http://fermi.gsfc.nasa.gov/ssc/data/access/lat/BackgroundModels.html

[98] http://fermi.gsfc.nasa.gov/ssc/data/analysis/LAT_caveats.html

Table 4
Swift XRT Observations and Analysis Results for *NuSTAR*-simultaneous Periods

Observation ID	Date (MJD)	Exp (s)	Flux 2–10 keV	Flux 0.5–2 keV	Flux 3–7 keV	Flux 0.3–3 keV	Index Γ	χ^2/dof	Γ LP	β LP	χ^2/dof
00080176001	56395.06	9636.0	6.9 ± 0.1	6.41 ± 0.06	3.6 ± 0.1	11.0 ± 0.1	2.05 ± 0.01	403.5/416	2.06 ± 0.02	−0.02 ± 0.04	402.6/415
00091745001	56485.84	250.7	21.1 ± 1.7	12.7 ± 0.4	10.9 ± 0.9	22.3 ± 0.7	1.77 ± 0.05	108.1/94	1.74 ± 0.08	0.10 ± 0.16	107.0/93
00030793235	56485.98	709.1	24.3 ± 1.1	14.6 ± 0.2	13.1 ± 0.9	24.1 ± 0.4	1.77 ± 0.03	228.7/222	1.75 ± 0.05	0.03 ± 0.09	227.6/221
00030793236	56486.31	1002.0	24.0 ± 0.7	14.1 ± 0.3	13.4 ± 0.6	23.4 ± 0.4	1.73 ± 0.03	291.6/270	1.68 ± 0.04	0.13 ± 0.08	285.1/269
00030793237	56487.04	949.5	19.1 ± 0.9	12.0 ± 0.2	10.4 ± 0.4	18.9 ± 0.3	1.76 ± 0.03	229.9/237	1.73 ± 0.05	0.07 ± 0.08	228.9/236

Notes. Integral flux values are calculated according to the PL model, and are provided in $\times 10^{-11}$ erg cm^{-2} s^{-1} units. The errors for each parameter are found using a value of $\Delta\chi^2 = 2.706$, corresponding to a 90% confidence level for a parameter.

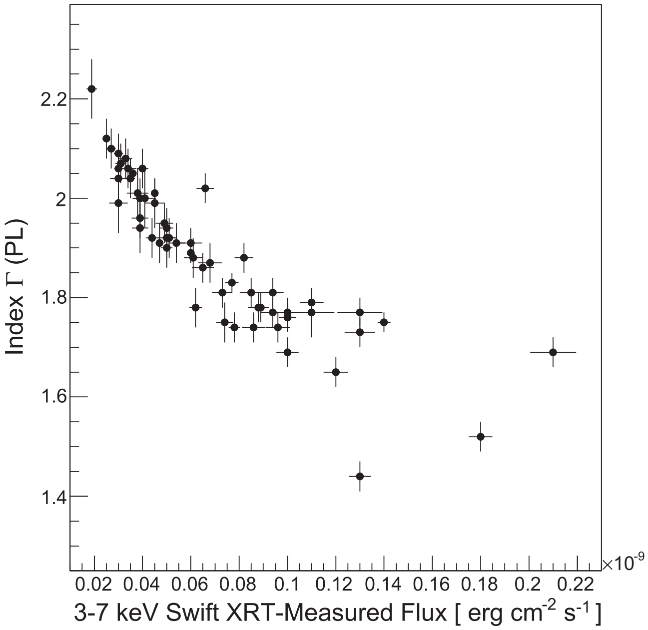

Figure 7. Power-law index vs. 3–7 keV flux values fit to the *Swift* XRT observations of Mrk 501.

3.4. Optical

Temporal coverage at optical frequencies was provided by various telescopes around the world, including the GASP-WEBT program (e.g., Villata et al. 2008, 2009). In particular, we report observations performed in the *R*-band from the following observatories: Crimean, Roque de los Muchachos (KVA), Lulin (SLT), Abastumani (70 cm), Skinakas, Rozhen (60 cm), Vidojevica (60 cm), Perkins, Liverpool, St. Petersburg, West Mountain Observatory (WMO), the robotic telescope network AAVSOnet, the 60 cm and 1 m telescopes at the TUBITAK National Observatory (TUG T60 and TUG T100), and the Fred Lawrence Whipple Observatory (FLWO). Host galaxy estimation for the *R* filter is obtained from Nilsson et al. (2007), with apertures of 7$''$.5 and 5$''$, used for the various instruments. Galactic extinction was accounted for according to the coefficients from Schafly & Finkbeiner (2011). The calibration stars reported in Villata et al. (1998) were used for calibration.

Due to different filter spectral responses and analysis procedures of the various optical data sets (e.g., for signal and background extraction) in combination with the strong host galaxy contribution (∼12 mJy for an aperture of 7$''$.5 in the *R*-band), the reported fluxes required instrument-specific offsets of a few mJy. These offsets are introduced in order to align multi-instrumental light curves, and were determined using several of the GASP-WEBT instruments as reference, and scaling the other instruments using simultaneous observations. The required offsets for each instrument are as follows: Abastumani (70 cm) = 4.8 mJy; Skinakas = 1.2 mJy; Rozhen (60 cm) = −1.3 mJy; Vidojevica (60 cm) = 2.2 mJy; St. Petersburg = 0.3 mJy; Perkins = 0.6 mJy; Liverpool = 0.6 mJy; AAVSOnet = −3.4 mJy; WMO = −0.7 mJy; TUG T60 = 0.5 mJy; TUG T100 = −1.2 mJy. Additionally, a point-wise fluctuation of 0.2 mJy (∼0.01 mag) was added in quadrature to the statistical errors in order to account for potential differences of day-to-day observations within single instruments. Within Figure 5, the *R*-band observations can be seen to remain fairly steady around 4.5 mJy.

3.5. Radio

3.5.1. Metsähovi

The 14-m Metsähovi Radio Observatory also participated in this multi-instrument campaign, as it has been doing since 2008. Metsähovi observed Mrk 501 every few days at 37 GHz. Details of the observing strategy and data reduction can be found at Teräsranta et al. (1998). As can be seen in the bottom panel of Figure 5, there is evidence of a low level of variability at 37 GHz as observed by Metsähovi. This variability is quantified in terms of fractional variability (see Section 5.1).

3.5.2. OVRO

Regular 15 GHz observations of Mrk 501 were carried out using the OVRO 40-m telescope with a nominal bi-weekly cadence (Richards et al. 2011). The instrument consists of off-axis dual-beam optics and a cryogenic high electron mobility transistor low-noise amplifier with a 15 GHz center frequency and 3 GHz bandwidth. The two sky beams were Dicke-switched using the off-source beam as a reference, while the source was alternated between the two beams in an ON–ON mode to remove atmospheric and ground contamination. The total system noise temperature was about 52 K. The typical noise level achieved in a 70-s observation was 3–4 mJy. The flux density uncertainty includes an additional 2% uncertainty mostly due to pointing errors, but does not include the systematic uncertainty in absolute calibration of about 5%. Calibration was performed using a temperature-stable diode noise source to remove receiver gain drifts; the flux density scale is derived from observations of 3C 286 assuming the Baars et al. (1977) value of 3.44 Jy at 15 GHz. Details of the reduction and calibration procedure can be found in Richards et al. (2011).

3.5.3. F-Gamma

The cm/mm radio light curves of Mrk 501 were obtained within the framework of a *Fermi*-related monitoring program of gamma-ray blazars (F-Gamma program; Fuhrmann et al. 2007; Angelakis et al. 2008). The millimeter observations were closely coordinated with the more general flux monitoring conducted by IRAM, and data from both programs are included here. The overall frequency range spans from 2.64 to 142 GHz using the Effelsberg 100-m and IRAM 30-m telescopes.

The Effelsberg measurements were conducted with the secondary focus heterodyne receivers at 2.64, 4.85, 8.35, 10.45, 14.60, 23.05, 32.00, and 43.00 GHz. The observations were performed quasi-simultaneously with cross-scans; that is, slewing over the source position, in azimuth and elevation direction with an adaptive number of sub-scans for reaching the desired sensitivity (for details, see Angelakis et al. 2008; Fuhrmann et al. 2008). Subsequently, pointing offset correction, gain correction, atmospheric opacity correction and sensitivity correction were applied to the data.

The IRAM 30-m observations were carried out with calibrated cross-scans using the Eight MIxer Receiver horizontal and vertical polarization receivers operating at 86.2 and 142.3 GHz. The opacity-corrected intensities were converted to the standard temperature scale and finally corrected

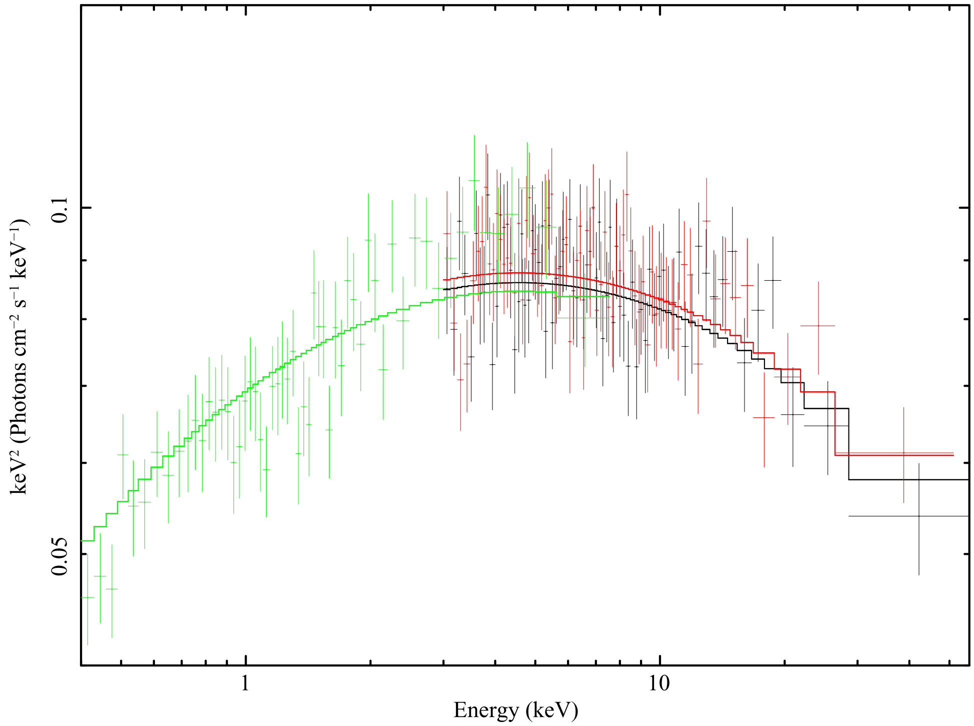

Figure 8. Example of a broadband X-ray spectrum of Mrk 501 in the crucial region where the synchrotron peak (in the $E \times F(E)$ representation) is located. The spectra result from a simultaneous observation with *Swift* (green) and *NuSTAR* (FPMA: red, FPMB: black) on 2013 July 12–13. The spectral fit used a log-parabolic model (see the text) with Galactic column density of 1.55×10^{20} cm^{-2}. For the purpose of illustrating the intrinsic spectrum of the source, the solid lines which represent the fit to the *Swift* and *NuSTAR* data show the spectrum *before* the Galactic absorption. The normalizations of the *Swift* and *NuSTAR* data were allowed to be free, and the offset between them was less than 10%, thus illustrating generally good cross-calibration of the two instruments.

for small remaining pointing offsets and systematic gain-elevation effects. The conversion to the standard flux density scale was done using the instantaneous conversion factors derived from frequently observed primary (Mars, Uranus) and secondary (W3(OH), K3-50A, NGC 7027) calibrators.

4. SIMULTANEOUS *NuSTAR* AND *Swift* EXPOSURES

Since Mrk 501 is highly variable, detailed inferences regarding the broadband SED and its temporal evolution require simultaneous observations of multiple bands. In particular, for the determination of the low-energy peak E_{syn}, and the flux at E_{syn}, $F(E_{syn})$, *Swift* XRT and *NuSTAR* observations must be simultaneous. There are five periods within the campaign for Mrk 501 where the observations by *NuSTAR* and *Swift* occurred within one hour of each other. The *Swift* exposure IDs for these quasi-simultaneous periods are summarized in Table 4. For Mrk 501, E_{syn} is located in the X-ray band and can be determined reliably (except for the first *NuSTAR* observation where E_{syn} is $\leqslant$0.85 keV) since there is no evidence of X-ray variability of Mrk 501 on a timescale shorter than a *NuSTAR* orbit ($\sim$90 minutes).

As a precursor to the joint fitting of XRT and *NuSTAR* data, we confirm agreement between the 3–7 keV flux values derived from the *Swift* XRT and *NuSTAR* fitted models. There is a residual discrepancy (not a uniform offset) at the level of $<$10%. Using XSPEC, we performed simultaneous fitting to the data sets using the absorbed log-parabolic model as done in Section 2 for the *NuSTAR* data alone. During the fitting process, we allowed the normalizations of the data sets to vary, but required the same spectral shape parameters. A representative plot of the simultaneous fit for XRT and *NuSTAR* data collected on MJD 56485 is provided in Figure 8. The model spectrum is shown as a solid line in Figure 8. The agreement between XRT and *NuSTAR* was studied and found to be within the calibration uncertainties.[99]

For the determination of the spectral parameters characterizing the synchrotron peak (namely the energy E_{syn} and $F(E_{syn})$) with the simultaneous *NuSTAR* and *Swift* XRT observations, we apply the log-parabolic model modified by the photoelectric absorption due to our Galaxy, with a (fixed) neutral hydrogen column density of 1.55×10^{20} cm^{-2}, taken from Kalberla et al. (2005). The procedure to search for E_{syn} involves the variation of the "normalization energy" parameter (in the `logpar` model in XSPEC) until the local index Γ returns a value of 2—then E_{syn} corresponds to the peak in the $E \times F(E)$ representation. This procedure correctly accounts for the effect of the soft X-ray absorption by Galactic column density as the absorption is included in the model fitted to the data. For the determination of the error on E_{syn}, we freeze the "local index"—defined at energy E_{syn}—to a value of 2, and then step the value of E_{syn} keeping all other parameters free. We then search for the value of the E'_{syn} which corresponds to the departure of χ^2 from the minimum by $\Delta\chi^2 = 2.7$. The error quoted is the difference between E_{syn} and E'_{syn}. The E_{syn} and curvature parameters (β) for each of the simultaneous data sets are summarized in Table 5. We quote the value of $F(E_{syn})$ inferred from the *NuSTAR* module FPMA (Focal Plane Module A).

The combination of *Swift* XRT and *NuSTAR* observations provides an unprecedented view of the synchrotron peak variability. From Table 5, it is evident that the synchrotron peak

99 http://heasarc.gsfc.nasa.gov/docs/heasarc/caldb/swift/docs/xrt/SWIFT-XRT-CALDB-09v18.pdf

Table 5
Fitting Results for *Swift* XRT and *NuSTAR* Simultaneous Observations

Observation ID	Date (MJD)	Orbit Number	E_{syn} (keV)	$F(E_{syn})$ ($\times 10^{-11}$ erg cm^{-2} s^{-1})	Curvature β	χ^2/dof
60002024002	56395.1	1	<0.85	4.1	0.061	669/673
60002024006	56485.9	1	4.9 ± 0.7	13.8	0.21	596/577
60002024006	56486.0	2	5.1 ± 0.9	13.7	0.22	697/715
60002024006	56486.2	4	7.0 ± 0.8	14.6	0.2	877/848
60002024008	56487.1	4	3.3 ± 0.9	11.2	0.17	832/851

Note. The data were simultaneously fit with a log-parabolic function.

moves by a factor of about ten during this campaign, with the highest synchrotron peak occurring during the elevated X-ray and gamma-ray state.

5. VARIABILITY

5.1. Fractional Variability

In order to quantify the broadband variations we utilize the fractional variability, F_{var}. We follow the description given in Vaughan et al. (2003), where F_{var} is calculated as

$$F_{var} = \sqrt{\frac{S^2 - \langle \sigma^2 \rangle}{\langle F_\gamma \rangle}^2} \qquad (4)$$

where $\langle F_\gamma \rangle$ is the average photon flux, S is the standard deviation of the flux measurements, and $\langle \sigma^2 \rangle$ is the mean squared error of the measurement.

F_{var} was determined for the temporal binning and sampling presented in Figure 5 and Table 3 (for MJD 56485 and 56486, the bold lines in Table 3 are used). The value of F_{var} is known to be dependent on sampling and should be interpreted with caution. For example, a well sampled light curve with small temporal bins will allow us to probe the variability on small timescales (e.g., *NuSTAR*), which could be hidden if the variability is computed with fluxes obtained with relatively coarse temporal bins (e.g., *Fermi* LAT).

The fractional variability for each band (from 15 GHz radio through VHE) is shown in Figure 9. For the period of observations covered in this work, the fractional variability shows a double-peaked shape with the highest variability in the X-ray and VHE bands. A similar broadband variability pattern has recently been reported for Mrk 501 (Doert 2013; Aleksić et al. 2015c), for Mrk 421 (Aleksić et al. 2015b; M. Baloković et al. 2015, in preparation), and for other high-synchrotron-peaked blazars in, for example, Aleksić et al. (2014). This double-peaked shape of F_{var} from radio through VHE can be interpreted as resulting from a correlation between the synchrotron and inverse-Compton peaks.

F_{var} is below $\sim$5% at 15 GHz and optical/UV frequencies, while at 37 GHz the fractional variability is $\sim$20%. The relatively high fractional variability at 37 GHz is not produced by any single flaring event, but rather by a consistent flickering in the radio flux. Such flickering is not typically observed in blazars, but has been reported for Mrk 501 in Aleksić et al. (2015c). At X-ray frequencies, F_{var} gradually increases with energy, reaching the largest value ($\sim$0.6) in the 7–30 keV band measured by *NuSTAR*. The F_{var} computed for the *Swift* XRT 3–7 keV observations is higher than for the *NuSTAR* 3–7 keV fluxes due to the larger temporal coverage of the *Swift*

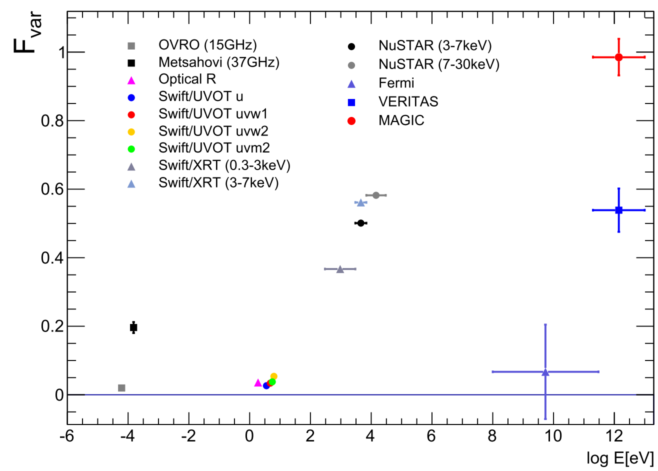

Figure 9. Fractional variability (F_{var}) calculated for each instrument separately.

observations, allowing for observation of Mrk 501 during high activity levels that were not observed with *NuSTAR*.

The *Swift* XRT F_{var} for Mrk 501 published in Stroh & Falcone (2013) was 0.15 or 0.18, depending on the timescale used for calculation, illustrating that the value of F_{var} is dependent on sampling. In Abdo et al. (2011a), *RXTE*-ASM (2–10 keV) and *Swift* BAT (15–50 keV) show F_{var} values between 0.2 and 0.3, although it should be noted that due to the limited sensitivity of *RXTE*-ASM and *Swift* BAT (in comparison with *Swift* XRT and *NuSTAR*), the variability was studied on timescales larger than 30 days.

5.2. Cross Correlations

Cross-correlations between the different energy bands were studied with the Discrete Correlation Function (DCF) described in Edelson & Krolik (1988). The DCF method can be applied to unevenly sampled data, and no interpolation of the data points is necessary. Also, the errors in the individual flux measurements are naturally taken into account when calculating the DCF. One important caveat, however, is that the resulting DCF versus time lag relation is not continuous, and hence the results should only be interpreted with a reasonable balance between the time resolution and the accuracy of the DCF values. It is also important to only consider instruments with similar time coverage. In this study, we considered all the energy bands with a non-zero fractional variability. Among the *Swift* UVOT data, only the UVW2 filter was checked, as it is the filter which has the best time coverage across the *Swift* UVOT observations and also is least contaminated by the host galaxy light. For a better time coverage, MAGIC and

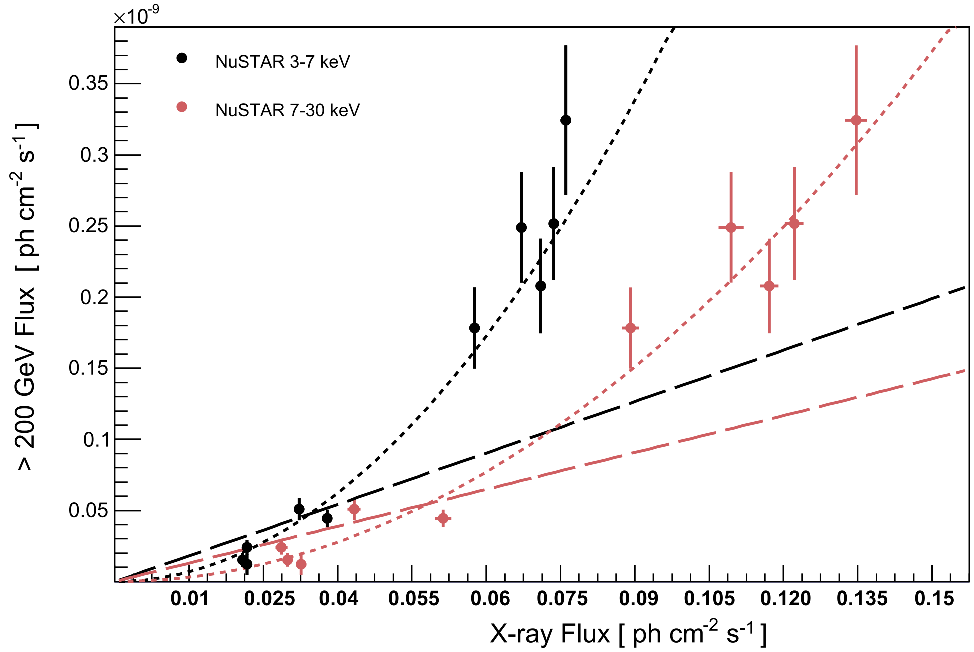

Figure 10. *NuSTAR* X-ray photon flux vs. simultaneous >200 GeV flux from MAGIC and VERITAS. The dotted lines show quadratic fits to the data, while the dashed lines show linear fits to the 3–7 and 7–30 keV bands.

VERITAS data points are combined to make a single data set as the VHE band.

A significant correlation in the DCF was seen only between the VHE data and the 0.3–3 keV and the 3–7 keV *Swift* XRT bands. For both of the combinations, the largest correlation is seen with a time lag of 0 ± 1.5 days. This result does not change if the binning of 3 days is altered. Note that the *NuSTAR* observations covered a relatively short period with a dense sampling, thus we did not see any significant correlation between *NuSTAR* and any other band. Since the observations of *Swift* XRT and *NuSTAR* were made simultaneously (within a few hours) with the VHE observations, correlations between the X-ray and the VHE observations were investigated in more detail (see Section 5.3).

5.3. X-Ray/VHE Correlation

The light curve of the broadband observations is shown in Figure 5, with a zoom of the period showing an elevated X-ray and VHE state in Figure 6. The VERITAS and MAGIC flux points within the light curve are shown with statistical errors only. Correlation studies using the VHE flux values are completed with statistical and systematic errors included, as described below. The radio, optical, and UV observations show relatively steady flux over the campaign period, while the largest amplitude of variability can be seen in the X-ray and VHE gamma-ray bands. An elevated state in both the X-ray and VHE bands can be seen to occur on MJD 56483 (*Swift* Observation ID 00030793232 in Table 4). Zooming in on this epoch (Figure 6), shows that the *NuSTAR* observations occurring on MJD 56485 and 56486 occurred after the highest state observed by MAGIC and *Swift*. The XRT observations show an elevated X-ray flux in both the 0.3–3 and 3–7 keV bands on MJD 56483.

A comparison between the *NuSTAR*-observed X-ray photon flux values (derived from XSPEC) in the 3–7 and 7–30 keV bands and the epochs of simultaneous VHE observations is shown in Figure 10. During this campaign, 10 observations occurred within one hour between either *NuSTAR* and MAGIC (seven observations) or *NuSTAR* and VERITAS (three observations). The simultaneous X-ray and VHE data, where the VHE data include both statistical and systematic errors, were fit with both a linear and a quadratic function.

Within the one-zone SSC emission paradigm, there is a physical motivation for a quadratic relationship between the X-ray and VHE flux values (Marscher & Gear 1985). More specifically, the inverse-Compton flux depends not only on the density of photons, but also on the density of the electron population producing those photons. If, however, the particle population is energetic enough for the inverse-Compton scattering to occur in the Klein–Nishina regime, the relationship between the X-ray and VHE fluxes can be complex and will depend in detail on the energy bands considered, the particle energy loss mechanisms and the magnetic field evolution. In particular, Katarzyński et al. (2005) suggest that a roughly linear relationship may arise during the declining part of a flare when the emitting region expands adiabatically, leading to a decrease of both the particle number density and the magnetic field strength.

A quadratic relationship provides a better fit than the linear fit for the 3–7 keV flux values measured simultaneously by *NuSTAR*, with χ^2 of 11.4 and 87.3, respectively, for 9 dof. The 3–7 keV flux and the >200 GeV flux are highly correlated, with a Pearson correlation coefficient (r) of 0.974. Similarly, for the 7–30 keV band, the quadratic relation fits the data better than the linear relation, with χ^2 of 17.5 and 79.1, respectively, for 9 dof. The r-value for the 7–30 keV flux and the >200 GeV flux is 0.979.

A comparison between the *Swift*-observed X-ray photon flux values (derived from XSPEC) in the 0.3–3 and 3–7 keV bands and the epochs of simultaneous VHE observations is shown in Figure 11. These data are not simultaneous with the *NuSTAR* observations shown in Figure 10 and therefore the results cannot be directly compared. During this campaign, 12

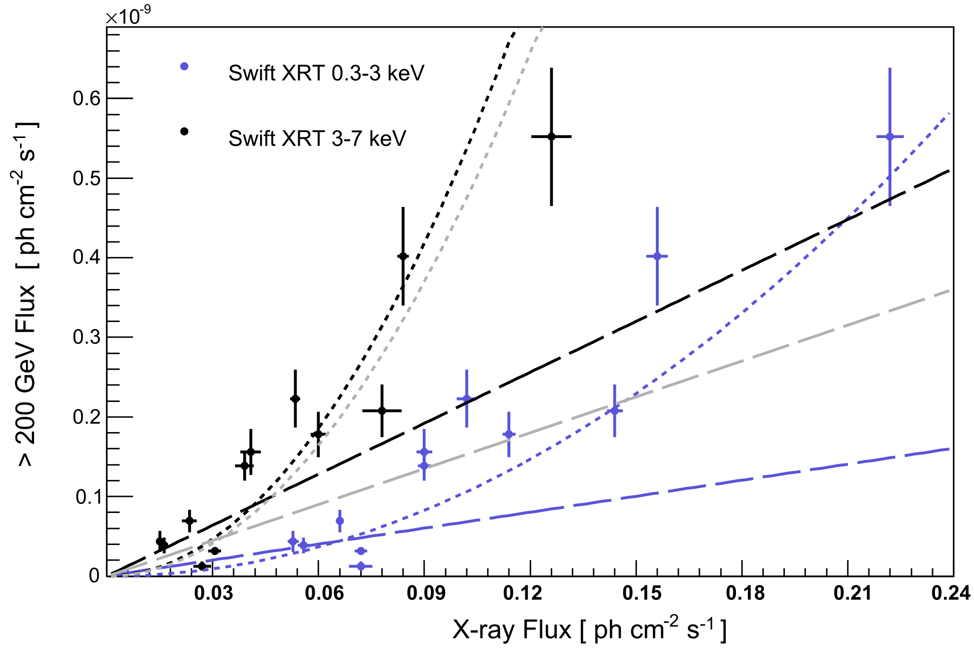

Figure 11. *Swift* 0.3–3 and 3–7 keV X-ray photon flux values vs. simultaneously measured >200 GeV flux from MAGIC and VERITAS. The black and blue dotted lines show quadratic fits to the 3–7 and 0.3–3 keV data, respectively, while the black and blue dashed lines show linear fits to the 0.3–3 and 3–7 keV bands, respectively. For completeness, we also compare the linear and quadratic fits of the simultaneous 3–7 keV *NuSTAR* and >200 GeV flux from MAGIC and VERITAS summarized in Figure 10 (light gray dashed and dotted line).

absolutely simultaneous observations occurred between *Swift* and MAGIC (10) and *Swift* and VERITAS (2), shown in Figure 11. Similarly as done for the *NuSTAR* bands, the simultaneous *Swift* X-ray and VHE data were fit with both a linear and a quadratic function with an offset fixed to zero. For the 0.3–3 keV flux values measured simultaneously by *Swift*, a quadratic relationship provides a better fit than the linear fit, with χ^2 of 81.8 and 162.0, respectively, for 11 dof. The 0.3–3 keV flux and the >200 GeV flux are highly correlated, with a Pearson correlation coefficient (r) of 0.958. For the 3–7 keV band, the quadratic function fits the data better than the linear function, with χ^2 of 58.0 and 114.0, respectively, for 11 dof. The r-value for the 3–7 keV flux as measured with *Swift* and the >200 GeV flux is 0.954.

6. MODELING THE BROADBAND SED

Previous MWL campaigns on Mrk 501 have been sufficiently characterized with a one-zone SSC model (Abdo et al. 2011a; Acciari et al. 2011), although there are a few notable instances where a one-zone SSC model was found not to be appropriate for the broadband emission (Pian et al. 1998; Kataoka et al. 1999). In this study we decided to use the simplest approach, which is provided by a leptonic model with a single emitting region. The broadband spectral data were modeled with an equilibrium version of the single-zone SSC model from Böttcher & Chiang (2002) and Böttcher et al. (2013). This model has been used to describe the broadband emission from various other VHE-detected blazars (e.g., Acciari et al. 2009a; Abdo et al. 2011b; Aliu et al. 2011, 2013).

Within this equilibrium model, the emission originates from a spherical region of relativistic leptons with radius R. This emission region moves down the jet with a Lorentz factor Γ. We set the Doppler factor δ to 15 for all model representations. Notably, it has been shown that when using least-squares fitting of emission models to broadband data of Mrk 501, the Doppler factor can vary widely from state to state (Mankuzhiyil et al. 2012). We do not complete least-squares fitting in this work and instead choose to fix the Doppler factor to 15 for the representation of all states, limiting the number of free parameters of the SSC model. The Doppler factor of 15 is similar to the Doppler factor used in previous studies of Mrk 501 (Abdo et al. 2011a; Acciari et al. 2011; Mankuzhiyil et al. 2012). In order to reduce the number of free parameters, the jet axis is aligned toward the line of sight with the critical angle $\theta = 3\overset{\circ}{.}8$. At the critical angle, the jet Lorentz factor is equal to the Doppler factor ($\Gamma = \delta$).

Within this emission model, relativistic leptons are injected into this emission region continuously according to a power-law distribution $Q = Q_0\gamma^{-q}$ between $\gamma_{\rm min}$ and $\gamma_{\rm max}$. The injected population of particles is allowed to cool. The simulation accounts for synchrotron emission due to a tangled magnetic field B_0, Compton up-scattering of synchrotron photons, $\gamma\,\gamma$ absorption and the corresponding pair production rates (via the general solution in Böttcher & Schlickeiser 1997). The cooling of the injected electrons is dominated by radiative losses, which are balanced by injection and particle escape from the system. This particle escape is characterized with an escape efficiency factor $\eta = 100$, where $t_{\rm esc} = \eta R/c$. The use of $\eta = 100$ is motivated by success in representing SEDs of TeV blazars in previous studies using the same model (e.g., Aliu et al. 2013). The electron cooling rates and photon emissivity and opacity are calculated using similar routines of the code for jet radiation transfer described in Böttcher et al. (1997). Together, the particle injection, cooling and escape mechanisms lead to an equilibrium particle population.

A key result of the equilibrium that occurs between continual particle injection, particle escape, and radiative cooling is a break in the electron distribution γ_b (referred to as γ_c within Böttcher et al. 2013), where $t_{\rm esc} = t_{\rm cool}(\gamma_b)$. As described in Equations (1) and (2) of Böttcher et al. (2013), if γ_b is smaller than $\gamma_{\rm min}$, the system will be in a fast cooling regime. If γ_b is greater than $\gamma_{\rm min}$, the system will be in a slow cooling regime. Within the fast cooling regime, the equilibrium particle distribution is a broken power law, with an index of 2 for particles with Lorentz factors less than $\gamma_{\rm min}$, and an index of (q + 1) for Lorentz factors above $\gamma_{\rm min}$. In the slow cooling regime, the resulting broken power law of the equilibrium particle distribution is equal to the injected spectrum (q) for particles with Lorentz factor below γ_b, and (q + 1) above γ_b. It is known that a hard injected electron spectrum would lead to a small amount of pile-up, followed by a smooth cut-off toward the HE end of the distribution (for details, see, e.g., Kardeshev 1962 and Stawarz et al. 2008). More specifically, the equilibrium electron spectrum slightly deviates from the (q + 1) approximation at the HE end ($\gamma \sim \gamma_{\rm max}$) due to pile-up effects that increase as the injected spectrum becomes harder (i.e., $q < 1.5$). Notably, although scattering in the KN regime is appropriately accounted for within the SSC model, neither the pile-up at the highest energy nor the energy loss (Compton cooling) of the electrons participating in scattering within the KN regime is accounted for within the model. The two aforementioned effects, however, are expected to result in a negligible deviation of the equilibrium electron spectrum from the approximated index of q + 1.

L_e is the kinetic power in the relativistic electrons and L_B is the power in the Poynting flux carried by the magnetic field of the equilibrium particle distribution. The L_e and L_B parameters allow the calculation of the equipartition parameter L_B/L_e. A state with an equipartition near unity minimizes the total (magnetic field + particle) energy requirement to produce a given synchrotron flux. Therefore, from an energetics point of view a situation near equipartition is usually favored. If the jet is powered by a Blandford–Znajek type mechanism, it is expected to be initially Poynting-flux dominated, and this luminosity is then (through an unknown mechanism, possibly magnetic reconnection) converted partially into particle energy. This conversion is expected to stop at an approximately equipartition situation as an equilibrium is reached between the conversion of magnetic energy to particle energy, and vice versa (via turbulent charged-particle motion generating small-scale, turbulent magnetic fields). For examples of blazar modeling based on equipartition, see Cerruti et al. (2013), Dermer et al. (2014). Alternatively, a sub-equipartition magnetic field may be expected in an MHD-driven, initially particle-dominated jet, where magnetic fields could be self-generated (amplified) by, e.g., shocks. The sub-equipartition magnetic fields that are often found in blazar SED modeling might therefore favor this latter scenario. Sub-equipartition states are a common result in the application of single-zone SSC emission scenarios to VHE blazars, as in Aliu et al. (2011, 2012a, 2012b), Acciari et al. (2008b, 2009a, 2009b, 2009c) and Abdo et al. (2011c).

The broadband data and model representations for five days from the MWL observation campaign are shown in Figure 12. The flux resulting from the model simulation (solid line) is corrected for absorption by interaction with the extragalactic background light (EBL) for the redshift of $z = 0.03$, assuming the EBL model outlined in Domínguez et al. (2011). The model thus represents the observed VHE emission as opposed to the intrinsic VHE emission. When applying the model to the data, the radio flux is likely to include a significant portion of extended radio emission and is therefore taken as an upper limit, as done in Abdo et al. (2011a).

The parameters used to represent the data with the equilibrium model are summarized in Table 6. The data in this work are represented with the emission model within the fast cooling regime, where the emitting equilibrium particle population follows $n(e) \propto \gamma^{-2}$ for $\gamma_b < \gamma < \gamma_{\rm min}$ and $n(e) \propto \gamma^{-(q+1)}$ for $\gamma_{\rm min} < \gamma < \gamma_{\rm max}$. A particle population with an injection index of $q = 1.8$–1.9 provides a reasonable representation of the synchrotron emission on MJD 56395 (red; top panel) and 56420 (green; second panel from top). There are no *Swift* data for observations on MJD 56420. Each of these epochs (MJD 56395 and 56420) can be sufficiently described with similar parameters, although the SED on MJD 56420 requires a slightly more energetic electron population and lower magnetic field to account for the marginally elevated X-ray and VHE emission as compared to what is observed on MJD 56395.

Although the highest VHE gamma-ray ($\geqslant$200 GeV) flux during this campaign was observed by MAGIC on MJD 56484, a reliable spectrum from that MAGIC observation could not be reconstructed due to the presence of Calima and the lack of LIDAR data to correct for it. *Swift* XRT also recorded the highest X-ray flux in its observation on the same day. On the other hand, there are sufficient broadband data to model the SED on MJD 56485.0 (turquoise; middle panel Figure 12), which is less than one day later than the MAGIC and *Swift* observation of the highest fluxes occurred.

The light curve in Figure 5 shows that Mrk 501 displayed relatively steady emission in each band between MJD 56420 and the elevated state observed by *Swift* and MAGIC on MJD 56484. In moving from the relatively quiescent SED on MJD 56420 to the elevated state observed on MJD 56485, a hardening of the injection spectrum is required ($q = 1.3$) to match the X-ray spectrum observed by *Swift* XRT. With the injection index responsible for the hardness of the synchrotron emission at X-ray energies, the frequency at which the synchrotron emission peaks, is related to the spectrum of the injected particle population, and the magnetic field (B_0). When moving from the state on MJD 56420 to 56485.0, the strength of the magnetic field decreases, moving the peak of the synchrotron emission to lower energies. The decrease of the synchrotron flux resulting from a lower magnetic field is counteracted with an increase of particle luminosity L_e. Finally, to match the relative magnitudes of the synchrotron and inverse-Compton peak fluxes, the electron and photon density of the emission region was increased with a decrease of the emission region size. The decrease of the emission region size to 5.0×10^{15} cm on MJD 56485.0 provides a higher inverse-Compton flux while maintaining the synchrotron flux.

Following Blumenthal & Gould (1970), the regime at which the up-scattering is occurring can be estimated (in the observer frame) according to $4\, h\nu_{\rm syn\,pk}\gamma/\delta m_e c^2$, where γ represents the energy of the electrons up-scattering $\nu_{\rm syn\,pk}$ photons. If this quantity is less than 1, the inverse-Compton emission is occurring within the Thomson regime, while if it is greater than 1, the emission is occurring in the KN limit. With $\nu_{\rm syn\,pk}$ at approximately 5 keV, $4\, h\nu_{\rm syn\,pk}\gamma_{\rm min}/\delta m_e c^2 \sim 25$, indicating that, according to the model applied within this work, the inverse-Compton scattering of the photons near the synchrotron peak is far into the KN regime. We note that this is not necessarily in conflict with the quadratic relationship between

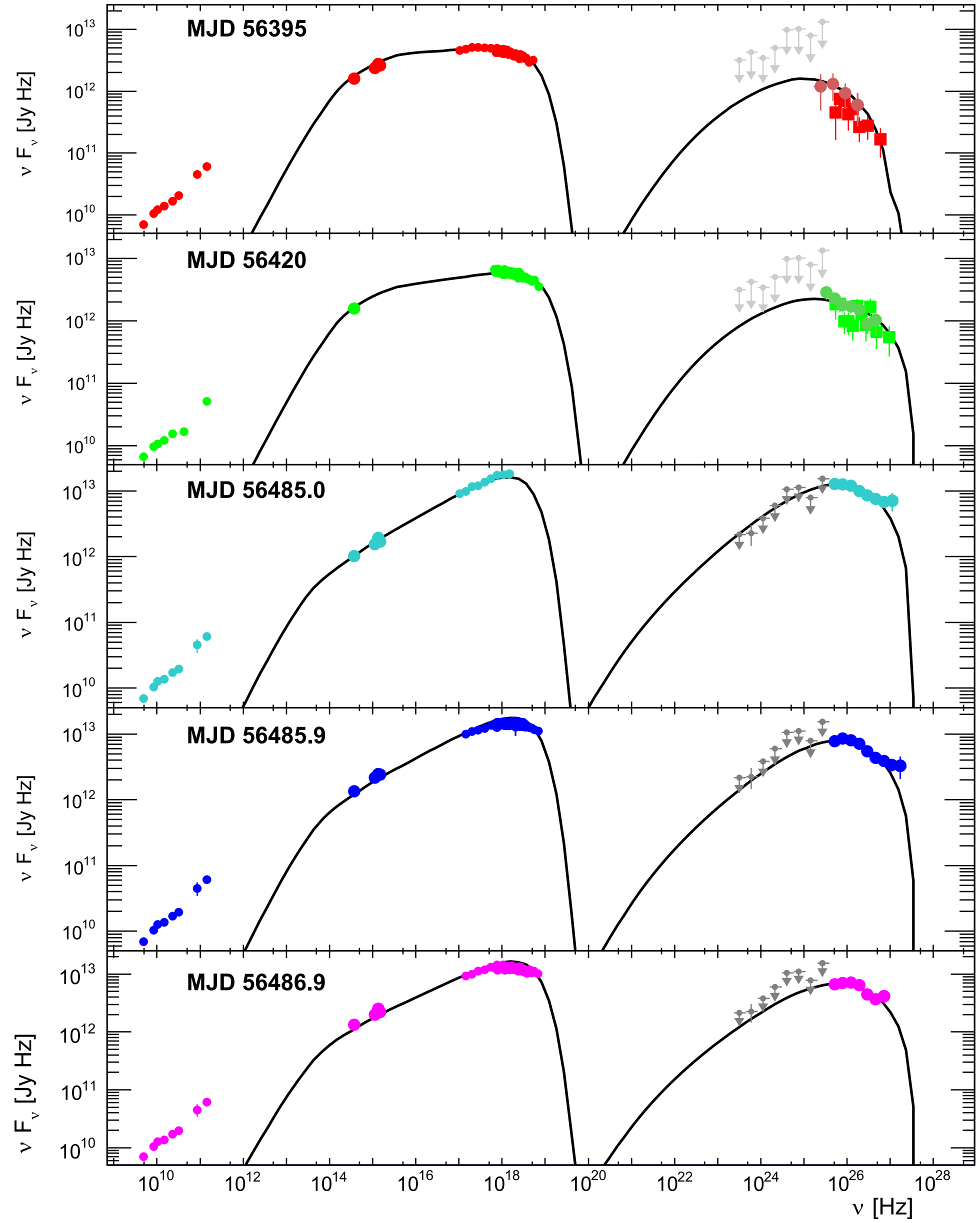

Figure 12. Observed broadband SEDs of Mrk 501 on each of the days where *NuSTAR* observations occurred (red, green, blue, and pink data). Additionally we include observations from MJD 56485.0 (turquoise, center panel), which show the SED one day after the most elevated flux state observed during this campaign. The broadband data are represented with a single-zone SSC model (solid line), with the model parameters summarized in Table 6. The *Fermi* LAT limits shown in the top two panels are taken from analysis of data between MJD 56381 and 56424, while the bottom three panels show *Fermi* results produced from analysis of data between MJD 56471 and 56499.

the simultaneous X-ray and VHE flux measurements, but it implies a reasonably steady value of magnetic field that is supported by our SSC models; see Table 6. For a more extensive discussion, see Katarzyński et al. (2005).

The SEDs on the days MJD 56485.9 and 56486.9 are similar to MJD 56485.0. All model representations explored here result in emission scenarios which are heavily matter dominated (far below equipartition), where the majority of the energy is distributed within the particle population instead of in the magnetic field. Notably, even a single-zone SSC model is difficult to constrain, and the solutions presented here are not applied with the intent of constraining parameter space, but instead to just show that a reasonable representation of the data is possible. There are additional models (e.g., multi-zone or hadronic models) which might alternatively be used to describe the broadband emission from Mrk 501 during these epochs (e.g., Tavecchio et al. 2011; Aleksić et al. 2015b). However, these models have twice as many free parameters as single-zone leptonic models and, in this particular case, there are not strong constraints from MWL flux evolution correlations that point to the necessity of such models.

7. DISCUSSION AND CONCLUSIONS

The inclusion of the hard X-ray telescope *NuSTAR* in this observational campaign has provided unprecedented insight into the temporal evolution of the 3–30 keV X-rays emitted by Mrk 501. Before this campaign, Mrk 501 had not been observed to display hard X-ray variability on timescales of ~7 hr. The fractional variability of Mrk 501 observed during

Table 6
Single-zone SSC Model Parameter Values (See Section 6 for Overview of Model and Parameters)

Parameter	MJD 56395	MJD 56420	MJD 56485.0	MJD 56485.9	MJD 56486.9
$\gamma_{\rm min}$ $(\times 10^4)$	2.0	2.1	2.0	2.0	2.0
$\gamma_{\rm max}$ $(\times 10^6)$	1.0	1.4	1.4	1.7	1.4
$\gamma_{\rm break}$ $(\times 10^3)$	4.1	4.6	2.8	3.3	3.4
q	1.9	1.8	1.3	1.3	1.3
η	100	100	100	100	100
δ	15	15	15	15	15
B_0 (G)	0.06	0.05	0.03	0.03	0.03
Γ	15	15	15	15	15
R $(\times 10^{15}$ cm)	7.0	7.0	5.0	7.0	7.0
θ (degrees)	3.8	3.8	3.8	3.8	3.8
$t_{\rm var}$ (hr)	4.3	4.3	3.1	4.3	4.3
L_e $(\times 10^{42}$ erg s^{-1})	9	12	36	28	26
$\epsilon = L_B/L_e$	1.8×10^{-2}	6.1×10^{-2}	5.3×10^{-4}	1.3×10^{-3}	1.4×10^{-3}

Note. Model representations are shown along with the broadband data in Figure 12.

this campaign was highly significant for the *NuSTAR* 7–30 keV band ($F_{\rm var} = 0.6$).

Investigation of the DCF allows insight into possible leads or lags between the low (0.3–3 keV) and high (3–7 keV) X-ray and VHE emission. The variability between these two bands shows evidence for a zero day lag. Correlation between the X-ray and VHE bands is further supported by the correlated variability inferred from the Pearson coefficients of 0.958 and 0.954 for simultaneous observations (occurring within one hour), respectively. Correlation is also found between the *NuSTAR* X-ray flux values and the simultaneous >200 GeV flux values (with observations occurring within one hour), with Pearson coefficients of 0.974 and 0.979 for the 3–7 keV and 7–30 keV bands, respectively.

Correlation of variability between the X-ray and VHE flux, and more notably direct correlation without any lead or lag time, is a natural signature of SSC emission. Within the single-zone SSC paradigm, the inverse-Compton flux is emerging from the same region as the synchrotron emission, and is fundamentally derived from the same particle and photon populations as the synchrotron emission. In this way, any variability in the synchrotron photon luminosity will immediately be translated into a change in the up-scattered inverse Compton luminosity.

In applying a single-zone equilibrium SSC model to the broadband data of Mrk 501, we find that the data could be reasonably represented in each of the five simultaneous epochs. Notably, the injected particle populations on MJD 56485.0, 56485.9, and 56486.9 are very hard, with an injection index of $q = 1.3$. Such a hard injection index is difficult to produce with standard shock acceleration scenarios alone, but is possible through a magnetic reconnection event (e.g., as explained in Romanova & Lovelace 1992; Guo et al. 2014; Sironi & Spitkovsky 2014). The increase in energy of the particle population (with an additional hardening to the injection index of $q = 1.3$) between the SED derived for MJD 56485.0 as compared to MJD 56420 indicates an introduction of additional energetic particles to the emission region, requiring some source of energy input. The decrease of the magnetic field, similar to what would naturally occur after a magnetic reconnection event, is capable of accelerating particles near the point of reconnection and producing the newly injected $q = 1.3$ particle population. Additionally, the decrease in the emission region size is consistent with a magnetic reconnection event that affects a more localized region as compared to a larger, more steady non-thermal emission region. More information on particle acceleration via magnetic reconnection can be found in Werner et al. (2014) and Guo et al. (2015).

The variability timescale for these model representations, quoted in Table 6, is determined from the light-crossing timescale of the emission region according to $t_{\rm var} = R/c\delta(1 + z)$. For the emission region sizes and Doppler factor of $\delta = 15$ used within the model, the predicted variability timescales of a couple of hours are compatible with the variability timescale observed during the broadband observations. The radiative cooling timescale is approximately equal to the synchrotron cooling timescale, $t_{\rm sync} \sim 1.4 \times 10^4 (B_0/0.06\ G)^{-2} \gamma_6^{-1}$ s, where $\gamma_6 = \gamma/(10^6)$. With a minimum light crossing time, corresponding to the minimum variability timescale of $t_{\rm var} \sim 1.6 \times 10^4$ s (in the observer frame), all but the most energetic electrons within the emitting region cool on timescales that are longer than the crossing timescale, showing that the observed variability is likely a reflection of changes in the particle acceleration and/or injection processes directly.

Notably, faster variability timescales have been observed from Mrk 501 in the past (e.g., Albert et al. 2007) and so the model parameters shown here cannot be generalized to all Mrk 501 flux variability episodes. *NuSTAR* observations show the hard X-ray flux to significantly decrease by more than 10% between its 90-minute orbits. Moreover, on MJD 56420 the source hard X-ray flux was observed to change by a factor of greater than 40% in the 7–30 keV band during a 7 hr exposure.

In an attempt to describe a possible emission scenario which might result in the broadband SED variability observed for Mrk 501 in 2013, the parameter changes were made to the single zone equilibrium SSC model monotonically. With a degeneracy between several of the input parameters, the model applied here cannot be used for conclusive studies regarding which changes occur within the emitting region from one state to the next. Instead, through the study of band-to-band spectral variability, leads and/or lags and fractional variability, as well as broadband modeling of various flaring episodes, we find compelling evidence to support a single zone SSC emission scenario for Mrk 501 during the broadband observations in this campaign.

The collection of simultaneous broadband observations is a necessity for the study of the relativistic emission mechanisms at work within blazars such as Mrk 501. It is known that these sources vary continually, with characteristics that significantly change between different flaring episodes, requiring the continuation of deep broadband observations such as those presented in this work.

This work was supported under NASA Contract No. NNG08FD60C, and made use of data from the *NuSTAR* mission, a project led by the California Institute of Technology, managed by the Jet Propulsion Laboratory, and funded by the National Aeronautics and Space Administration. We thank the *NuSTAR* Operations, Software and Calibration teams for support with the execution and analysis of these observations. This research has made use of the *NuSTAR* Data Analysis Software (NuSTARDAS) jointly developed by the ASI Science Data Center (ASDC, Italy) and the California Institute of Technology (USA).

The MAGIC Collaboration would like to thank the Instituto de Astrofísica de Canarias for the excellent working conditions at the Observatorio del Roque de los Muchachos in La Palma. The financial support of the German BMBF and MPG, the Italian INFN and INAF, the Swiss National Fund SNF, the ERDF under the Spanish MINECO, and the Japanese JSPS and MEXT is gratefully acknowledged. This work was also supported by the Centro de Excelencia Severo Ochoa SEV-2012-0234, CPAN CSD2007-00042, and MultiDark CSD2009-00064 projects of the Spanish Consolider-Ingenio 2010 programme, by grant 268740 of the Academy of Finland, by the Croatian Science Foundation (HrZZ) Project 09/176 and the University of Rijeka Project 13.12.1.3.02, by the DFG Collaborative Research Centers SFB823/C4 and SFB876/C3, and by the Polish MNiSzW grant 745/N-HESS-MAGIC/2010/0.

This research is also supported by grants from the U.S. Department of Energy Office of Science, the U.S. National Science Foundation, and the Smithsonian Institution, by NSERC in Canada, by Science Foundation Ireland (SFI 10/RFP/AST2748), and by STFC in the U.K. We acknowledge the excellent work of the technical support staff at the Fred Lawrence Whipple Observatory and at the collaborating institutions in the construction and operation of the VERITAS instrument. The VERITAS Collaboration is grateful to Trevor Weekes for his seminal contributions and leadership in the field of VHE gamma-ray astrophysics, which made this study possible.

The *Fermi* LAT Collaboration acknowledges generous ongoing support from a number of agencies and institutes that have supported both the development and the operation of the LAT as well as scientific data analysis. These include the National Aeronautics and Space Administration and the Department of Energy in the United States, the Commissariat à l'Energie Atomique and the Centre National de la Recherche Scientifique/Institut National de Physique Nucléaire et de Physique des Particules in France, the Agenzia Spaziale Italiana and the Istituto Nazionale di Fisica Nucleare in Italy, the Ministry of Education, Culture, Sports, Science and Technology (MEXT), High Energy Accelerator Research Organization (KEK) and Japan Aerospace Exploration Agency (JAXA) in Japan, and the K. A. Wallenberg Foundation, the Swedish Research Council and the Swedish National Space Board in Sweden.

Additional support for science analysis during the operations phase is gratefully acknowledged from the Istituto Nazionale di Astrofisica in Italy and the Centre National d'Études Spatiales in France.

We thank the *Swift* team duty scientists and science planners and we acknowledge the use of public data from the *Swift* data archive. This research has made use of the *Swift* XRT Data Analysis Software (XRTDAS) developed under the responsibility of the ASI Science Data Center (ASDC), Italy.

This research is partly based on observations with the 100-m telescope of the MPIfR (Max-Planck-Institut für Radioastronomie) at Effelsberg and with the IRAM 30-m telescope. IRAM is supported by INSU/CNRS (France), MPG (Germany) and IGN (Spain). V. Karamanavis and I. Myserlis are funded by the International Max Planck Research School (IMPRS) for Astronomy and Astrophysics at the Universities of Bonn and Cologne.

The OVRO 40-m monitoring program is supported in part by NASA grants NNX08AW31G and NNX11A043G, and NSF grants AST-0808050 and AST-1109911.

T.G. acknowledges support from Istanbul University (Project numbers 49429 and 48285), Bilim Akademisi (BAGEP program) and TUBITAK (project numbers 13AT100-431, 13AT100-466, and 13AT60-430).

St. Petersburg University team acknowledges support from Russian RFBR grant 15-02-00949 and St. Petersburg University research grant 6.38.335.2015.

The research at Boston University (BU) was funded in part by NASA Fermi Guest Investigator grant NNX14AQ58G and Swift Guest Investigator grant NNX14AI96G. The PRISM camera at Lowell Observatory was developed by K. Janes et al. at BU and Lowell Observatory, with funding from the NSF, BU, and Lowell Observatory.

This research was partially supported by Scientific Research Fund of the Bulgarian Ministry of Education and Sciences under grant DO 02-137 (BIn-13/09). The Skinakas Observatory is a collaborative project of the University of Crete, the Foundation for Research and Technology—Hellas, and the Max-Planck-Institut für Extraterrestrische Physik.

The Abastumani Observatory team acknowledges financial support by the by Shota Rustaveli National Science Foundation under contract FR/577/6-320/13.

We are grateful to the American Association of Variable Star Observers (AAVSO) for assisting us with some of the optical data acquisition.

G. Damljanovic and O. Vince gratefully acknowledge the observing grant support from the Institute of Astronomy and Rozhen National Astronomical Observatory, Bulgarian Academy of Sciences. This work is in accordance with the Projects No 176011 ("Dynamics and kinematics of celestial bodies and systems"), No 176004 ("Stellar physics") and No 176021 ("Visible and invisible matter in nearby galaxies: theory and observations") supported by the Ministry of Education, Science and Technological Development of the Republic of Serbia.

Facilities: NuSTAR, MAGIC, VERITAS, *Fermi* LAT, *Swift* XRT/UVOT, AAVSOnet, FLWO, WEBT, CrAO: 1.25m, Perkins, Rozhen, Skinakas, OVRO, Metsahovi.

REFERENCES

Abdo, A. A., Ackermann, M., Ajello, M., et al. 2011a, ApJ, 727, 129
Abdo, A. A., Ackermann, M., Ajello, M., et al. 2011b, ApJ, 731, 77
Abdo, A. A., Ackermann, M., Ajello, M., et al. 2011c, ApJ, 726, 43
Acciari, V. A., Aliu, E., Aune, T., et al. 2009a, ApJ, 707, 612
Acciari, V. A., Aliu, E., Aune, T., et al. 2009b, ApJL, 690, L126
Acciari, V. A., Aliu, E., Aune, T., et al. 2009c, ApJ, 703, 169
Acciari, V. A., et al. 2011, ApJ, 729, 2
Acciari, V., Aliu, E., Arlen, T., et al. 2008a, ApJ, 679, 1427
Acciari, V., Aliu, E., Arlen, T., et al. 2008b, ApJL, 684, L73
Aharonian, F. A., Belyanin, A. A., Derishev, E. V., Kocharovsky, V. V., & Kocharovski, Vl. V. 2002, PhRvD, 66, 2
Albert, A., Aliu, E., Anderhub, H., et al. 2007, ApJ, 669, 862
Albert, A., Aliu, E., Anderhub, H., et al. 2008, NIMA, 588, 424
Albert, J., Aliu, E., Anderhub, H., et al. 2008, ApJ, 674, 1037
Aleksić, J., Ansoldi, S., Antonelli, L. A., et al. 2015b, A&A, 576, 126
Aleksić, J., Ansoldi, S., Antonelli, L. A., et al. 2015c, A&A, 573, 50
Aleksić, J., Antonelli, L. A., Antoranz, P., et al. 2010, A&A, 524, A77
Aleksić, J., Alvarez, E. A., Antonelli, L. A., et al. 2012, APh, 35, 435
Aleksić, J., Ansoldi, S., Antonelli, L. A., et al. 2014, A&A, 572, 121
Aleksić, J., Ansoldi, S., Antonelli, L. A., et al. 2015a, APh, 02, 005
Aliu, E., Aune, T., Beilicke, M., et al. 2011, ApJ, 742, 127
Aliu, E., Aune, T., Beilicke, M., et al. 2012a, ApJ, 750, 94
Aliu, E., Aune, T., Beilicke, M., et al. 2012b, ApJ, 755, 118
Aliu, E., Aune, T., Beilicke, M., et al. 2013, ApJ, 779, 92
Anderhub, H., Antonelli, L. A., Antoranz, P., et al. 2009, ApJ, 705, 1624
Angelakis, E., Fuhrmann, L., Marchili, N., Krichbaum, T. P., & Zensus, J. A. 2008, arXiv:0809.3912
Atwood, W., Abdo, A., Ackermann, M., et al. 2009, ApJ, 697, 1071
Baars, J. W. M., Genzel, R., Paulini-Toth, I. I. K., & Witzel, A. 1977, A&A, 61, 99
Baloković, M., Paneque, D., Madejski, G. et al., 2015, ApJ submitted
Bednarek, W. 1993, ApJL, 402, 29
Blumenthal, G. R., & Gould, R. J. 1970, RvMP, 42, 237
Borracci, F. 2013, Proc. 33rd ICRC, 33, 0934
Böttcher, M., Reimer, A., Sweeny, K., Prakash, A., et al. 2013, ApJ, 768, 54
Böttcher, M., & Chiang, J. 2002, ApJ, 581, 127
Böttcher, M., Mause, H., Schlickeiser, R., et al. 1997, A&A, 324, 395
Böttcher, M., & Schlickeiser, R. 1997, A&A, 325, 866
Catanese, M., Bradbury, S. M., Breslin, A. C., et al. 1997, ApJL, 487, 143
Cerruti, M., Dermer, C. D., Lott, B., Boisson, C., Zech, A., et al. 2013, ApJL, 771, 4
Cogan, P. 2008, in Proc. 30th ICRC, 30, 1385
Dermer, C. D., et al. 2014, ApJ, 782, 82
Dermer, C., Schlickeiser, R., Mastichiadis, A., et al. 1992, A&A, 256, 27
Doert, M. 2013, in Proc. 33rd ICRC, 33, 762
Domínguez, A., Primack, J., Rosario, D. J., et al. 2011, MNRAS, 410, 2556
Edelson, R., & Krolik, J. 1988, ApJ, 333, 646
Fitzpatrick, E. L. 1999, PASP, 111, 63
Fomin, V. P., Sepanian, A. A., Lamb, R., et al. 1994, APh, 2, 137
Fruck, C. 2013, in Proc. 33rd ICRC, 33, 1054
Fruck, C. 2015, PhD thesis, Technische Univ. München
Fruck, C., & Gaug, M. 2015, in EPJ Web of Conf. 89, Proc. of ATOMHEAD (Padova), 02003, 2015
Fuhrmann, L., Krichbaum, T. P., Witzel, A., et al. 2008, A&A, 490, 1019
Fuhrmann, L., Zensus, J. A., Krichbaum, T. P., Angelakis, E., & Readhead, A. C. S. 2007, The Frst GLAST Symp., 921, 249
Gehrels, N., Chincarini, G., Giommi, P., et al. 2004, ApJ, 611, 1005
Gliozzi, M., Samruna, R. M., Jung, I., et al. 2006, ApJ, 646, 61
Guo, F., Li, H., Daughton, W., & Liu, Y. 2014, arXiv:1405.4040
Guo, F., Liu, Y. H., Daughton, W., & Li, H. 2015, arXiv:1504.02193
Harrison, F. A., Craig, W. W., Christensen, F. E., et al. 2013, ApJ, 770, 103
Hillas, A. M., et al. 1985, Proc. 19th ICRC, 19, 445
Holder, J., Atkins, R. W., Badran, H. M., et al. 2006, APh, 25, 391
Kalberla, P., Burton, W., Hartmann, D., et al. 2005, A&A, 440, 775
Kardeshev, N. 1962, SvA, 6, 317
Kataoka, J., Mattox, J. R., Quinn, J., et al. 1999, ApJ, 514, 138
Katarzyński, K., Ghisellini, G., Tavecchio, F., et al. 2005, A&A, 433, 479
Kieda, D. 2013, Proc. 33rd ICRC, arXiv:1308.4849
Li, T., & Ma, Y. 1983, ApJ, 272, 317
Madhavan, A. 2013, PhD thesis, Iowa State Univ.
Mankuzhiyil, N., Ansoldi, S., Persic, M., et al. 2012, ApJ, 753, 145
Maraschi, L., Ghisellini, G., & Celotti, A. 1992, ApJL, 397, 5
Marscher, A. 2008, ASPC, 386, 437
Marscher, A., & Gear, W. 1985, ApJ, 298, 114
Massaro, E., Perri, M., Giommi, P., Nesci, R., Verrecchia, F., et al. 2004a, A&A, 422, 103
Massaro, E., Perri, M., Giommi, P., Nesci, R., et al. 2004b, A&A, 413, 489
Mattox, J., Bertsch, D., Chiang, J., et al. 1996, ApJ, 461, 396
Nilsson, K., Pasanen, M., Takalo, L. O., et al. 2007, A&A, 475, 199
Nolan, P. L., Abdo, A. A., Ackermann, M., et al. 2012, ApJS, 199, 31
Petry, D., Bötcher, M., Connaughton, V., et al. 2000, APJ, 536, 742
Pian, E., Vacanti, G., Tagliaferri, G., et al. 1998, ApJL, 492, 17
Poole, T. S., Breeveld, A. A., Page, M. J., et al. 2008, MNRAS, 383, 627
Prokoph, H. 2013, PhD thesis, Humboldt Univ. Berlin
Quinn, J., Akerlof, C. W., Biller, S., et al. 1996, ApJL, 456, L83
Richards, J. L., Max-Moerbeck, W., Pavlidou, V., et al. 2011, ApJS, 194, 29
Romanova, M., & Lovelace, R. 1992, A&A, 262, 26
Schafly, E. F., & Finkbeiner, D. P. 2011, ApJ, 737, 103
Schlegel, D. J., Finkbeiner, D. P., & David, M. 1998, ApJ, 500, 525
Sikora, M., Begelman, M. C., Rees, M. J., et al. 1994, ApJ , 421, 153
Sironi, L., & Spitkovsky, A. 2014, ApJL, 783, 21
Snedecor, G., & Cochran, W. 1989, Statistical Methods (8th ed.; Iowa City, IA: Iowa State Univ. Press)
Stawarz, L., Petrosian, V., & Blandford, R. 2008, ApJ, 681, 725
Stroh, M., & Falcone, A. 2013, ApJS, 207, 28
Takahashi, H., Tashiro, M., Madejski, G., et al. 1996, ApJL, 470, L89
Tavecchio, F., Becerra-Gonzalez, J., Ghisellini, G., et al. 2011, A&A, 534, 86
Teräsranta, H., Tornikoski, M., Mujunen, A., et al. 1998, A&AS, 132, 305
Tramacere, A., Giommi, P., Massaro, E., et al. 2007, A&A, 467, 501
Urry, C. M., & Padovani 1995, PASP, 107, 803
Vaughan, S., Edelson, R., Warwick, R. S., Uttley, P., et al. 2003, MNRAS, 345, 1271
Villata, M., Raiteri, C. M., Gurwell, M. A., et al. 2009, A&A, 504, L9
Villata, M., Raiteri, C. M., Lanteri, L., Sobrito, G., & Cavallone, M. 1998, A&AS, 130, 305
Villata, M., Raiteri, C. M., Larionov, V. M., et al. 2008, A&A, 481, L79
Werner, G. R., Uzdensky, D. A., Cerutti, B., Nalewajko, K., & Begelman, M. C. 2014, arXiv:1409.8262
Zanin, R. 2013, in Proc. 33rd ICRC, 33, 773

The Astronomical Journal, 151:170 (8pp), 2016 June
doi:10.3847/0004-6256/151/6/170

DISCOVERY OF AN X-RAY-EMITTING CONTACT BINARY SYSTEM 2MASS J11201034−2201340

Chin-Ping Hu[1,2], Ting-Chang Yang[2], Yi Chou[2], L. Liu[3], S.-B. Qian[3], C. Y. Hui[4], Albert K. H. Kong[5], L. C. C. Lin[6], P. H. T. Tam[7], K. L. Li[8], Chow-Choong Ngeow[2], W. P. Chen[2], and Wing-Huen Ip[2]

[1] Department of Physics, University of Hong Kong, Pokfulam Road, Hong Kong; cphu@hku.hk
[2] Graduate Institute of Astronomy, National Central University, Jhongli 32001, Taiwan; yichou@astro.ncu.edu.tw
[3] Yunnan Observatories, Chinese Academy of Sciences, P.O. Box 110, 650011 Kunming, China
[4] Department of Astronomy and Space Science, Chungnam National University, Daejeon, Korea
[5] Institute of Astronomy and Department of Physics, National Tsing Hua University, Hsinchu, Taiwan
[6] Institute of Astronomy and Astrophysics, Academia Sinica, Taiwan
[7] Institute of Astronomy and Space Science, Sun Yat-Sen University, Guangzhou 510275, China
[8] Department of Physics and Astronomy, Michigan State University, East Lansing, MI 48824-2320, USA
Received 2015 December 2; accepted 2016 April 17; published 2016 June 1

ABSTRACT

We report the detection of orbital modulation, a model solution, and the X-ray properties of a newly discovered contact binary, Two Micron All Sky Survey (2MASS) J11201034−2201340. We serendipitously found this X-ray point source outside the error ellipse when searching for possible X-ray counterparts of γ-ray millisecond pulsars among the unidentified objects detected by the *Fermi Gamma-ray Space Telescope*. The optical counterpart of the X-ray source (unrelated to the γ-ray source) was then identified using archival databases. The long-term Catalina Real-Time Transient Survey detected a precise signal with a period of $P = 0.28876208(56)$ days. A follow-up observation made by the Super Light Telescope of Lulin Observatory revealed the binary nature of the object. Utilizing archived photometric data of multi-band surveys, we construct the spectral energy distribution (SED), which is well fit by a K2V spectral template. The fitting result of the orbital profile using the Wilson–Devinney code suggests that 2MASS J11201034-2201340 is a short-period A-type contact binary and the more massive component has a cool spot. The X-ray emission was first noted in observations made by *Swift*, and then further confirmed and characterized by an *XMM-Newton* observation. The X-ray spectrum can be described by a power law or thermal Bremsstrahlung. Unfortunately, we could not observe significant X-ray orbital modulation. Finally, according to the SED, this system is estimated to be 690 pc from Earth with a calculated X-ray intensity of $(0.7 - 1.5) \times 10^{30}$ erg s^{-1}, which is in the expected range of an X-ray emitting contact binary.

Key words: binaries: close – binaries: eclipsing – stars: individual (2MASS J11201034-2201340) – X-rays: stars

1. INTRODUCTION

A W UMa-type system is a contact binary system where both components share a common envelope and are typical main-sequence stars with similar surface temperatures. Astronomers have been aware of the optical variability of prototypical W UMa-type systems for more than a century (Müller & Kempf 1903). To date, thousands of known W UMa-type variables have been found. The spectral type of this kind of system usually ranges from A to K, with a period that ranges from 0.2 to 1.4 days and variability amplitudes typically less than 1 mag. Contact binaries can be further classified into two major types: A and W (Binnendijk 1970). The primary minimum in the folded light curve of an A-type contact binary is caused by the less massive component transiting the more massive one; otherwise, the contact binary is a W-type. In general, an A-type system has a relatively longer orbital period ($P \gtrsim 0.3$ day), a lower mass ratio ($q \lesssim 0.3$), and an earlier spectral type (typically from A to G). On the other hand, a W-type system usually has a later spectral type. A- and W-type contact binaries are possibly related with respect to their evolution. For example, Hilditch et al. (1988) suggested that a W-type system evolves to an A-type system; however, Gazeas & Niarchos (2006) proposed an opposite evolutionary track.

W UMa-type systems are expected to have high chromospheric activity and coronal emission; hence, some systems are strong X-ray emitters, e.g., VW Cep (Carroll et al. 1980; Huenemoerder et al. 2006). The strength of the X-ray emission is related to the binary orbital period and the spectral type (Stępień et al. 2001; Chen et al. 2006). Chromospheric activity is related to the presence of cool spots, which cause asymmetry, known as the O'Connell effect (O'Connell 1951; Wilsey & Beaky 2009), in the orbital profile. In addition, the variability of the Hα equivalent width along with the orbital phase is an indication of chromospheric activity (Kaszas et al. 1998). A detailed investigation of the X-ray timing and spectral variability, as occurred with the brightest contact binary VW Cep (Huenemoerder et al. 2006), can reveal the position and geometry of the corona.

We present the detection of the contact binary 2MASS J11201034−2201340 in the X-ray, optical, and infrared bands in Section 2. Section 3 presents the results of optical band analysis, including the determination of the orbital period and the spectral energy distribution (SED). We also present the photometric solution to determine the basic physical parameters of this system, utilizing orbital profile fitting. Section 4 presents X-ray timing and spectral behaviors determined from the results of X-ray data analysis, e.g., the non-detection of orbital modulation and the non-thermal spectral nature. We also estimate X-ray intensity and discuss the relationship between X-ray and optical luminosities. Finally, we summarize our results and future aspects in Section 5.

2. SOURCE DETECTION

2.1. *Swift Observations*

After the detection of 1FGL J1119.9−2205 (also named 2FGL J1120.0−2204 and 3FGL J1119.9−2204), the *Swift XRT*

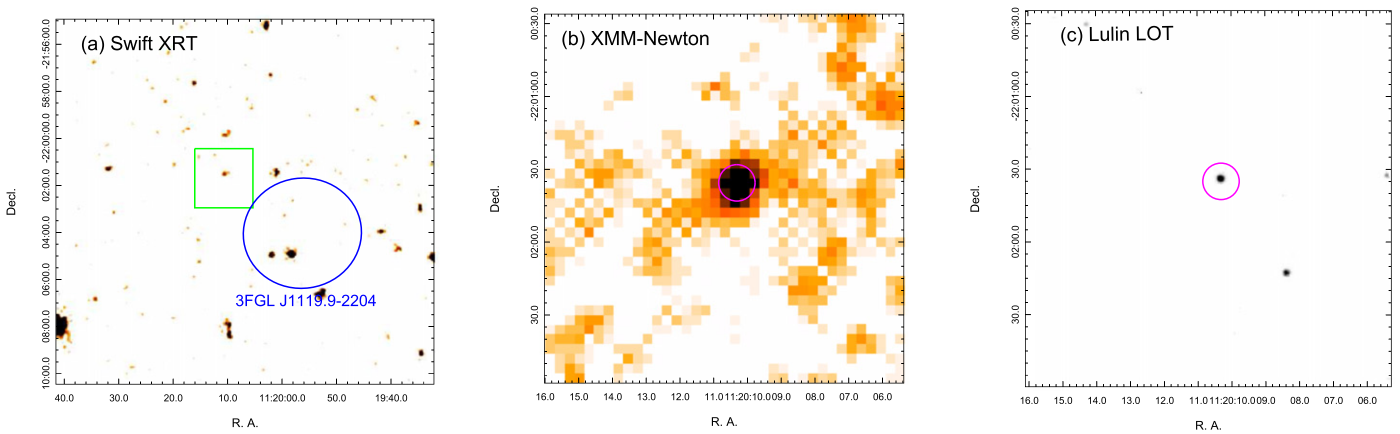

Figure 1. (a) *Swift* image of the field containing 2MASS J11201034−2201340 and 3FGL J1119.9−2204. This image is smoothed with a Gaussian kernel of $\sigma = 3''$ to enhance the visibility of faint sources. The blue circle encompasses the 95% error ellipse of 3FGL J1119.9−2204 and the green box is the region of the cropped *XMM-Newton* and Lulin LOT r'-band images in the center and right panels, respectively. (b) Enlarged view of the *XMM-Newton* image. The center of the cyan circle is located at the *XMM-Newton* determined position, with coordinates R.A. = $11^{\rm h}20^{\rm m}10\overset{\rm s}{.}32$ and decl. = $-22°01'35\overset{''}{.}6$ and the diameter of the circle is the *XMM-Newton* half-energy width. (c) The r'-band image of the same field in the center panel taken by the LOT.

took 27 exposures of this field for a total exposure time of ~67 ks between 2010 and 2013. Hui et al. (2015) studied all of the *Swift* observational data and found two millisecond pulsar candidates within the 95% error ellipse of 3FGL J1119.9−2204. On the other hand, several uncataloged X-ray point sources outside the error ellipse were also detected, but their properties were not further investigated. 2MASS J11201034−2201340, which has relatively faint X-ray emission, is one of the outliers unrelated to the γ-ray source 3FGL J1119.9−2204.

The energy range of *XRT* is 0.2–10 keV, the pixel scale is $2\overset{''}{.}36$, and the FWHM of the point-spread function (PSF) is roughly $7''$ in 1.5 keV (or a half-power diameter of $18''$). All the data, including two target IDs (41371 and 49351), were used to determine the X-ray positions of the point sources. We extracted photon events and X-ray images from the standard products of all the *XRT* observations using *xselect* version 2.4. The point sources were detected using the *detect* task of the multi-mission X-ray image analysis program *XIMAGE*, for which the signal-to-noise threshold was set to 3.0. The position and corresponding uncertainty were determined using the *xrtcentroid* task. We found an X-ray point source located at R.A. = $11^{\rm h}20^{\rm m}10\overset{\rm s}{.}65$ and decl. = $-22°01'30\overset{''}{.}7$ with a 90% uncertainty of $\sim 7\overset{''}{.}6$. Figure 1(a) is the *Swift* image of the field containing 2MASS J11201034−2201340 and 3FGL J1119.9−2204.

2.2. XMM-Newton Observation

2FGL J1120.0−2204 was observed by the *XMM-Newton* observatory on 2014 June 14 for a total exposure time of ~70 ks (ObsID 0742930101). All three detectors of the European Photon Imaging Camera (EPIC) were used in this observation. The MOS1 and MOS2 detectors were operated in full-frame mode with a timing resolution of 2.6 s and an on-axis PSF FWHM of $6''$ (half-energy width $13\overset{''}{.}6$). The pn detector was operated in timing mode with an extreme timing resolution of 0.03 ms. In this mode, all X-ray photons are compressed in one dimension. However, this observation was performed to investigate the timing properties of the millisecond pulsar candidate 2FGL J1120.0-2204. The pn data were useless because the target is far from the aim point of the observation. The optical/UV monitor also was used in this observation but our target was outside the field of view and the optical/UV monitor data were unavailable. We applied the pipeline task *emproc* of the XMM Science Analysis Software (XMMSAS version 15.0.0) program to the MOS data using the latest instrumental calibration database. Events with patterns <12 were adopted in this research, and the flaring background was filtered out when the entire count rate was >3.5 counts s^{-1}. We performed source detection using the maximum likelihood fitting with the aid of the XMMSAS task *edetect_chain* and the signal-to-noise threshold set to 4σ.

We found a source located at R.A. = $11^{\rm h}20^{\rm m}10\overset{\rm s}{.}32$ and decl. = $-22°01'35\overset{''}{.}6$ with a 90% uncertainty of $2''$. The detection likelihood is 34.5, which corresponds to a 8σ significance level. This source is likely a point source because the likelihood of source extent is not determined. Figure 1(b) shows the *XMM-Newton* image of the region containing 2MASS J11201034−2201340 where a point source is clearly seen.

2.3. Optical and Infrared Counterparts

The field around the X-ray source was surveyed in the optical and infrared bands by USNO-B-1.0, the Two Micron All Sky Survey (2MASS), and the *Wide-field Infrared Survey Explorer* (*WISE*). All three catalogs are well organized by the the NASA/IPAC Infrared Science Archive (IRSA). Each catalog has only one source that is within the PSF of the *XMM-Newton*: USNO-B1.0 0679−0311979 at R.A. = $11^{\rm h}20^{\rm m}10\overset{\rm s}{.}36$ and decl. = $-22°01'34\overset{''}{.}14$, 2MASS J11201034−2201340 at R.A. = $11^{\rm h}20^{\rm m}10\overset{\rm s}{.}35$ and decl. = $-22°01'34\overset{''}{.}04$, and WISE J112010.35−220134.1 at R.A. = $11^{\rm h}20^{\rm m}10\overset{\rm s}{.}35$ and decl. = $-22°01'34\overset{''}{.}16$. 2MASS J11201034−2201340 is $5\overset{''}{.}3$ from the *Swift* determined X-ray source and $1\overset{''}{.}5$ from the position determined by *XMM-Newton*. Hence, 2MASS J11201034−2201340 is likely to be the optical counterpart of the X-ray source because the angular separation between the optical and X-ray positions reside well within the uncertainties of *Swift* and *XMM-Newton*.

We also observed the field with the Lulin One-Meter Telescope (LOT), located at Central Taiwan, using the ALTA U42 CCD with SDSS r'-band and g'-band filters. This configuration has a pixel scale of $0\overset{''}{.}32$ and a limiting

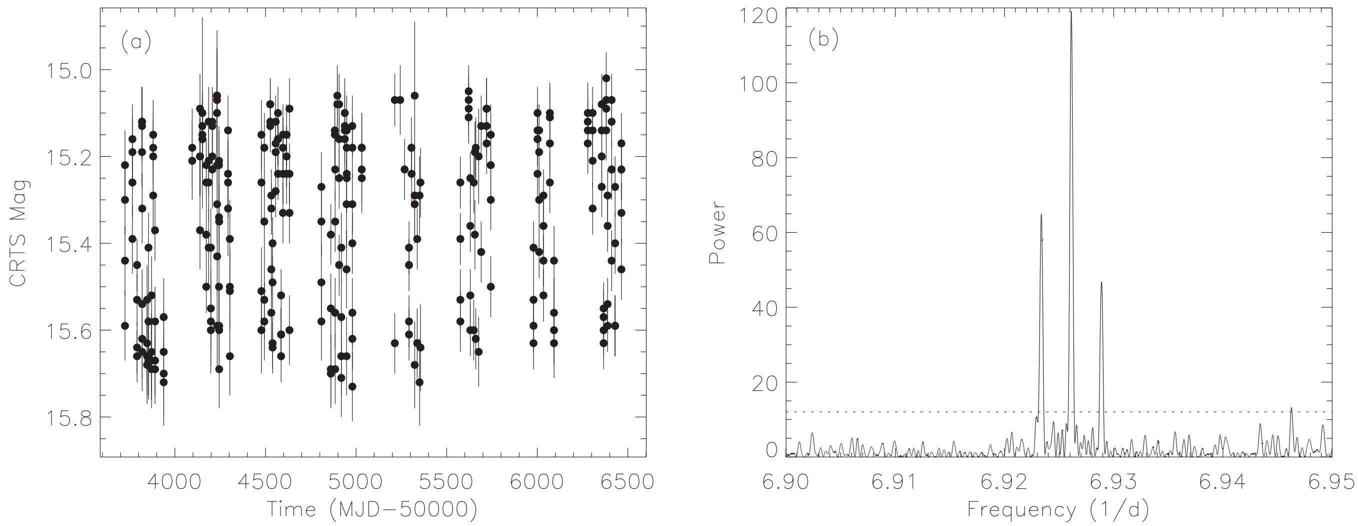

Figure 2. CRTS light curve (a) and the corresponding Lomb–Scargle power spectrum (b) of 2MASS J11201034−2201340. A significant peak located at $f = 6.926$ 1/day and its two associated 1 year aliases are clearly seen. The 3σ white noise level is indicated by the dashed line.

magnitude of ∼19.5 at the detection level of 5 σ. Figure 1(c) shows the cropped r'-band image. Only one source is detected in the region of the PSF of *XMM-Newton*.

3. DETAILED OPTICAL INVESTIGATION

3.1. Timing Analysis

To investigate the temporal variation of 2MASS J11201034−2201340, we first collected the multi-epoch photometric data obtained by the Catalina Real-Time Transient Survey (CRTS) to search for periodicity. The CRTS data set contains the observations made by the Siding Springs Survey 0.5 m Schmidt telescope (218 exposures) and by the Catalina Sky Survey 0.7 m Schmidt telescope (76 exposures). We found a significant periodicity with a period of 0.144 day by applying the Lomb–Scargle periodogram (Scargle 1982; Horne & Baliunas 1986). Figure 2 shows the light curve from the CRTS and the power spectrum. One-year aliases due to the observational window function also were detected in the power spectrum.

To check the robustness of the detected result and the possibility that the true periodicity is twice the detected value, we observed the field using the R and V bands of the 0.4 m Super Light Telescope (SLT) at the Lulin Observatory on 2015 April 24–27. The SLT was equipped with an Andor iKon-L 936 CCD with a field of view of $28 \times 28'$ and a pixel scale of $0\farcs82$. The exposure time for each frame was 5 minute, and the observation lasted ∼5 hr on April 24, 27, and 2.2 hr on April 26. The R band had 117 exposures and the V band had 115. For comparing the phase alignment of the CRTS data, the SLT data, and the data from other wavelengths, the observation times were corrected from the Earth to the solar barycenter. The CCD reduction package of the *Image Reduction and Analysis Facility* was used for standard image reduction, including bias, dark current, and flat-field corrections. We then compared the instrumental magnitude of 2MASS J11201034−2201340 with that of four comparison stars in the same field to obtain differential photometric data. The light curves clearly showed variability on a timescale of several hours. After folding both the light curves and the $B - V$ color curve using 0.144 and 0.288 day, respectively, we found that the color seemed to vary with a period of 0.288 day (see Figure 3). The true period of $0.28876208 \pm 5.6 \times 10^{-7}$ day is twice that detected by the Lomb–Scargle periodogram from the CRTS light curve. The uncertainty was estimated by a combination of the limited time span and photon statistical error. The uncertainty caused by limited time span and the strength of the signal was estimated using Equation (3) in Levine et al. (2011) and the statistical error was estimated using a 10^4 times Monte Carlo simulation.

From the archived multiepoch photometry data of *WISE* observations of this field, we found 52 *W1*-band (3.4 μm) and 42 *W2*-band (4.6 μm) significant detections and folded them with the best-determined periodicity. Figure 3 shows that there is still modulation and it is coherent in the mid-infrared bands.

3.2. Spectral Energy Distribution

We further investigated the physical properties of this system using currently available broadband SED data. For the optical band, we used the photometric B-, R-, and I-band data in the USNO-B 1.0 catalog, where $B1 = 16.4$, $B2 = 16.03$, $R1 = 14.36$, $R2 = 14.96$, and $I = 14.55$. To describe the spectral behavior of a contact binary system, it is better to use one of the flux minimum in the folded light curve that has all of the photons from the primary component. However, the amount of current data is insufficient because only one or two measurements were made for individual bands. Therefore, we took the average of the detected magnitudes for the B and R bands, for which there were two measurements, and applied a typical photometric uncertainty of 0.3 mag (Monet et al. 2003). The near-infrared data were from 2MASS in the J, H, and Ks bands, where $J = 13.875 \pm 0.03$, $H = 13.354 \pm 0.03$, and $Ks = 13.276 \pm 0.04$. The mid-infrared data were from *WISE* in the *W1* and *W2* bands, where $W1 = 13.286 \pm 0.025$ and $W2 = 13.331 \pm 0.031$.

The SLT did not observe standard stars, and so calibration in the V and R bands was not possible. Instead, to estimate the apparent magnitude of 2MASS J11201034−2201340, we used the cataloged star TYC 6090-207-1, which is a bright star with a coordinate of R.A. $= 11^{h}19^{m}56\overset{s}{.}983$ and decl. $= -22°04'43\farcs94$ and magnitudes of $B = 13.09 \pm 0.26$ and a $V = 12.20 \pm 0.16$ (Høg et al. 2000). By scaling of the brightness of 2MASS J11201034−2201340 and TYC 6090-

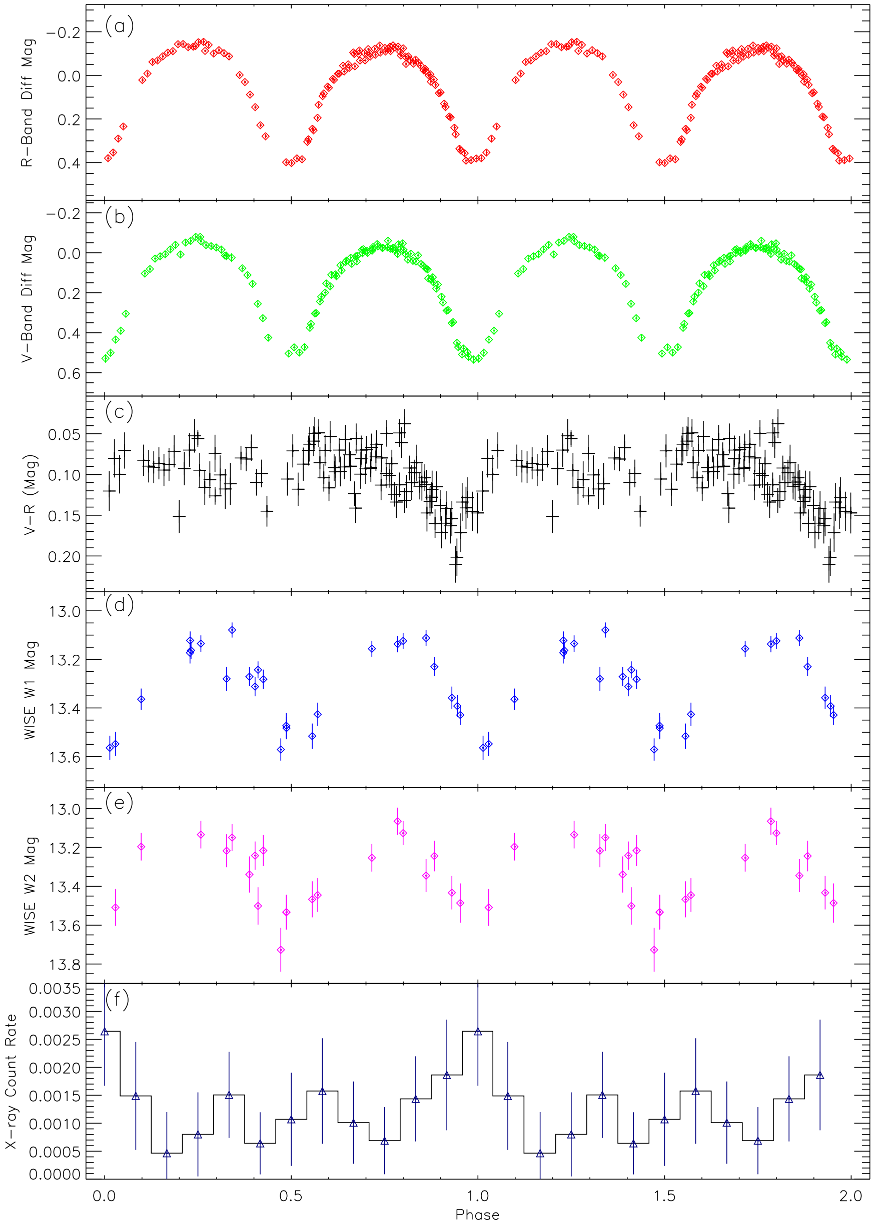

Figure 3. Multi-band light and color curves of 2MASS JJ11201034−2201340 folded according to a period of 0.288 day. (a) and (b) Folded *R*-band and *V*-band light curves obtained by SLT, (c) $V - R$ color variability, (d) and (e) folded *W1*-band and *W2*-band light curves obtained by *WISE*, and (f) folded X-ray light curve obtained by *XMM-Newton* with energy of 0.2–10 keV.

207-1, we estimated the *V*-band magnitude of 2MASS J11201034−2201340 as 15.37 ± 0.16.

Before constructing the SED, the measured magnitudes underwent extinction correction using the online Galactic dust extinction tool provided by IRSA. We assumed that the relationship between the extinction (A_V) and reddening ($E(B-V)$) is $A_V = 3.1E(B-V)$ (Güver & Özel 2009). We estimated the extinction for individual bands according to the latest measurements provided by Schlafly & Finkbeiner (2011). Figure 4 shows the constructed SED of 2MASS J11201034−2201340. We compared the SED with various stellar spectral templates presented in Pickles (1998) and found that our SED fit that of a K2V star that has a typical surface temperature of 4960 K. This indicates that the major component of 2MASS J11201034−2201340 is a late-type star.

3.3. Photometric Solution

To determine the physical nature of this contact binary system using the available data, we fit the observed *V*-band and *R*-band light curves using the Wilson–Devinney code (Wilson & Devinney 1971; Wilson 1979, 1990, 1994) to obtain a photometric solution. The surface temperature of the more massive star (T_1) was fixed at 4960 K as suggested by the SED fitting. The gravity darkening parameters were fixed at $g_1 = g_2 = 0.32$, according to the prediction made by Lucy (1967), and the bolometric albedos were fixed at $A_1 = A_2 = 0.5$ (Ruciński 1969) on the basis of the assumption that both components have convective envelopes. The limb-darkening coefficients for bolometric and individual bands ($x_{1\mathrm{bol}}$, $x_{2\mathrm{bol}}$, $y_{1\mathrm{bol}}$, $y_{2\mathrm{bol}}$, x_{1V}, x_{2V}, y_{1V}, y_{2V}, x_{1R}, x_{2R}, y_{1R}, and y_{2R}) were estimated using the values provided by van Hamme (1993; see Table 1). The remaining free parameters were the

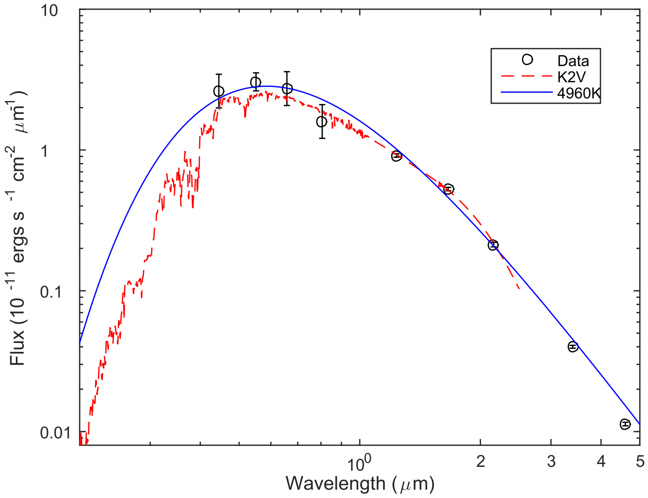

Figure 4. Spectral energy distribution of 2MASS J11201034−2201340. The data points were obtained from the USNO-B 1.0 catalog, the 2MASS catalog, and the *WISE* All-Sky Point Source catalog. The red dashed line is the best-fit K2V spectral template and the blue line is the corresponding blackbody radiation spectrum.

mass ratio (q), the inclination angle of the orbital plane (i), the surface temperature of the less massive component (T_2), the phase shift of the V and R bands, the dimensionless potential of the more massive star ($\Omega_1 = \Omega_2$), and the relative luminosity (L_1 and L_2) of each star in the V and R bands.

Because the spectral mass ratio could not be determined using the radial velocity method, we searched for a proper initial guessing value before fitting the light curves. We estimated the sum of the weighted square deviations (Σ) with respect to different trial values of q, ranging between 0.1 and 6. A minimum of Σ was clearly seen at $q = 0.3$, so we chose that as the initial q values for the fitting. Moreover, the profile seemed to be asymmetric, so we introduced a cool (dark) spot in the fitting to compare against the model without a cool spot. The cool spot model included three additional parameters: the colatitude (θ), longitude (ψ), and radius (Ω) of the spot. The best-fit parameters are given in Table 1 and the model light curves are shown in Figure 5.

The result of the fitting indicates that 2MASS J11201034−2201340 is a short-period A-type contact binary with a nearly edge-on orbital plane. It is necessary that there be a cool spot on the more massive component to explain the O'Connell effect. In this scenario, the best-fit mass ratio is $q = 0.317$ and a fill-out factor is estimated to be $f = 14.8\%$, which suggests a low degree of over contact. From the averaged value of the phase shift, we proposed a linear ephemeris for the primary minimum defined as

$$T_{\rm primary} = \text{MJD (TDB) } 53791.3984(1) + 0.28876208(56) \times N,$$

where N is the number of cycle count.

The magnitude of the secondary minimum (phase ∼0.5), which is not much different from that of the primary in the folded light curve, indicates that the less massive star is completely obscured and only the more massive star contributes to the flux. The V-band magnitude of the secondary minimum is estimated as 15.75 ± 0.16 in this measurement. Therefore, the distance can be roughly estimated as 690 ± 50 pc after considering the extinction and assuming that the more massive component is a K2V star.

Table 1
Photometric Solutions for 2MASS J11201034−2201340

Parameters	Photometric Elements Without Cool Spot	Errors	Photometric Elements Cool Spot Solutions	Errors
$g_1 = g_2$	0.32	assumed	0.32	assumed
$A_1 = A_2$	0.50	assumed	0.50	assumed
$x_{1\rm bol}$, $x_{2\rm bol}$	0.299, 0.299	assumed	0.299, 0.299	assumed
$y_{1\rm bol}$, $y_{2\rm bol}$	0.396, 0.396	assumed	0.396, 0.396	assumed
x_{1V}, x_{2V}	0.581, 0.581	assumed	0.581, 0.581	assumed
y_{1V}, y_{2V}	0.249, 0.249	assumed	0.249, 0.249	assumed
x_{1R}, x_{2R}	0.356, 0.356	assumed	0.356, 0.356	assumed
y_{1R}, y_{2R}	0.413, 0.413	assumed	0.413, 0.413	assumed
T_1	4960K	fixed	4960K	fixed
Phase Shift	−0.0153	±0.0005	−0.0155	±0.0004
q	0.291	±0.006	0.317	±0.004
$\Omega_1 = \Omega_2$	2.4253	±0.0126	2.4735	±0.0111
$\Omega_{\rm in}$	2.4464	…	2.5026	…
$\Omega_{\rm out}$	2.2645	…	2.3060	…
T_2	5125 K	±20 K	5124 K	±16 K
i	89°.4	±3.3	88°.5	±2.7
$L_1/(L_1 + L_2)(V)$	0.7180	±0.0051	0.7019	±0.0046
$L_1/(L_1 + L_2)(R)$	0.7259	±0.0045	0.7100	±0.0042
θ (°)	…	…	86.5	±2.6
ψ (°)	…	…	92.2	±4.7
Ω(°)	…	…	11.9	±1.2
T_s/T_*	…	…	0.80	±0.09
f	11.6%	±6.9%	14.8%	±5.7%

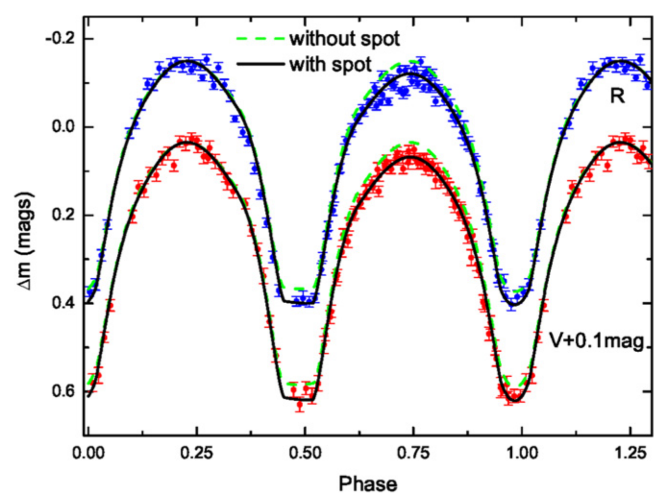

Figure 5. Observed folded R-band light curve (blue), folded V-band light curve (red) with a shift of 0.1 mag, and the corresponding best-fit contact binary model estimated using the Wilson–Devinney code. The green dashed line is the best-fit model without a cool spot and the black line is the best-fit model with a cool spot.

4. RESULTS FROM X-RAY OBSERVATIONS

4.1. X-Ray Profile and Spectrum

Investigation of the timing and spectral properties of the X-ray emission from 2MASS J11201034−2201340 detected by *XMM-Newton* will add to our understanding of the nature of this system. After filtering out the flaring background, the effective exposure time was ∼57 ks. We extracted 238 X-ray photons from a 20 arcsec radius circular region centered at the detected centroid of 2MASS J11201034−2201340 (see Figure 1). Because the effective exposure time encompassed only approximately two orbital cycles of 2MASS J11201034−2201340, we needed to carefully examine background variability. We selected 10 backgrounds with the same area in the source-free region on the same chip and found that the background counts were ∼150. Therefore, only ∼90 X-ray photons that originated from the source were available for use in a marginal investigation of the timing and spectral analysis. First, we individually folded the source and all the backgrounds according to the best period determined in the optical band. Then, we obtained a mean folded light curve by averaging all the folded background light curves to obtain the fluctuation of the background in the phase domain. The clean folded light curve shown in Figure 3(f) was obtained by subtracting the background profile from the folded source light curve. Another way to compute the background contribution is by weighting a larger source-free region, e.g., a circle with an 80 arcsec radius or a large annulus around the source. Both methods yield similar results. The folded light curve showed no detection of significant X-ray variability. We used different bin sizes and applied the χ^2 test to the folded profile and found that the detection significance in all cases was $<1\sigma$. The lack of detection of variability means that the geometry of the X-ray emission area may differ from that of the optical area.

The high-energy emission mechanism can be investigated by X-ray spectral analysis, despite the small number of X-ray photons. The source selection criterion was the same as that for the X-ray timing analysis above, while we used an 80 arcsec radius circle around a source-free region to estimate the background spectrum. The response matrix was created using the XMMSAS task *rmfgen* and the ancillary response file was created using *arfgen*. The X-ray photons were further grouped to have at least 15 counts per spectral bin. No pile-up issue was addressed for this faint source.

The X-ray spectral fitting was achieved using `XSPEC v12.9.0`. The X-ray emission from a contact binary system may come from a hot coronal plasma and may be represented with a thermal or non-thermal model. We tried two typical spectral models: non-thermal power law (`XSPEC` model `power-law`), and the thermal Bremsstrahlung (`XSPEC` model `bremss`) to fit the X-ray spectrum. The spectral fitting was calculated within the energy range 0.2–10 keV. We first set the $N_{\rm H}$ to be a free parameter and yielded a best-fit value of 2.7×10^{-20} cm^{-2}, which is not very far from 3.65×10^{-20} cm^{-2} derived from Leiden/Argentine/Bonn (LAB) Survey (Kalberla et al. 2005). However, the uncertainty is 5×10^{-21} cm^{-2}, which is too large to well constrain the $N_{\rm H}$ value. Therefore, we fixed the $N_{\rm H}$ value at the galactic one of 3.65×10^{-20} cm^{-2} in the following analysis. The power-law model yielded an acceptable fitting with a photon index of 2.4 ± 0.5 and a $\chi^2_\nu = 1.09$. The uncertainties of spectral parameters are estimated within the 90% confidence interval. On the other hand, the thermal Bremsstrahlung model result in an equally good fitting with a slightly larger χ^2_ν of 1.15 and a plasma temperature of $kT = 0.8^{+1.4}_{-0.3}$ keV. Both of the single component model can describe the X-ray spectrum of 2MASS J11201034−2201340 very well and no additional components are required. The best-fit parameters for the two models are given in Table 2, and the spectral data and corresponding best-fit models are shown in Figure 6. The X-ray flux in the 0.3–10 keV energy range was estimated as $1.7^{+0.9}_{-0.5} \times 10^{-14}$ erg cm^{-2} s^{-1}.

Table 2
The Best-fit Parameters of two Different Models for the X-ray Spectrum of 2MASS J11201034−2201340 Obtained with *XMM-Newton*

	Power Law	Bremsstrahlung
Γ	2.4 ± 0.5	⋯
kT (eV)	⋯	$0.8^{+1.4}_{-0.3}$
Normalization	$4.2^{+1.2}_{-1.3} \times 10^{-6}$	$1.1^{+1.0}_{-0.6} \times 10^{-6}$
χ^2_ν (dof)	1.09(12)	1.15 (12)

4.2. Indications from X-Ray Emission

Because the fitting of the optical folded light curve suggested the presence of a cool spot, the existence of X-ray emission suggests chromospheric activity. The result of the X-ray spectral fitting also suggests a possible non-thermal or thermal Bremsstrahlung origin for the X-ray emission. However, the X-ray orbital profile shows no significant variations, but this may be due to an insufficient number of X-ray photons. Considering the stability of star spots, it is possible that their position and size in these two observations are quite different. To investigate the origin of the X-ray emission and its connection to the star spot, simultaneous X-ray and optical observations using an *X-ray telescope* with a large effective area are necessary.

Although only ∼ 30X-ray photons were detected in all the *Swift* observations, we were able to estimate a crude X-ray spectrum and the corresponding X-ray flux by using the online tool provided by UK *Swift* Science Data Centre. The flux of X-rays between 0.3 and 10 keV determined by *Swift* was $1.0^{+0.6}_{-0.5} \times 10^{-14}$ erg cm^{-2} s^{-1}, which is consistent with the value obtained by a single *XMM-Newton* observation ($1.7^{+0.9}_{-0.5} \times 10^{-14}$ erg cm^{-2} s^{-1}). This may indicate that no significant X-ray flare was detected during the *Swift* observations.

Using the distance estimated from the SED, the X-ray intensity was estimated to be $(0.7 - 1.5) \times 10^{30}$ erg s^{-1}. Factoring in the relationship between the X-ray intensity and the orbital period (Chen et al. 2006), 2MASS J11201034−2201340 is within a reasonable range on the X-ray intensity versus orbital period plot (see Figure 7). Stępień et al. (2001) categorized W UMa-type stars into hot $[(B - V)_0 \leqslant 0.6]$ and cool $[(B - V)_0 > 0.6]$ groups. The X-ray flux seems to positively correlate with the color index for the hot group, whereas it reaches a constant value after $(B - V)_0 > 0.6$. Judging from the SED fitting, 2MASS J11201034−2201340 is likely to be in the cool group. The ratio of the X-ray and bolometric fluxes, $\log(L_x/L_{\rm bol})$, is roughly estimated to be between −3 and −3.3, which is reasonably close to the value presented in Stępień et al. (2001). Accurate multi-band photometric observations and standard star calibration are required to investigate the nature of this system in detail.

5. SUMMARY

While searching for the X-ray and optical counterparts of millisecond pulsar candidates, we serendipitously detected the

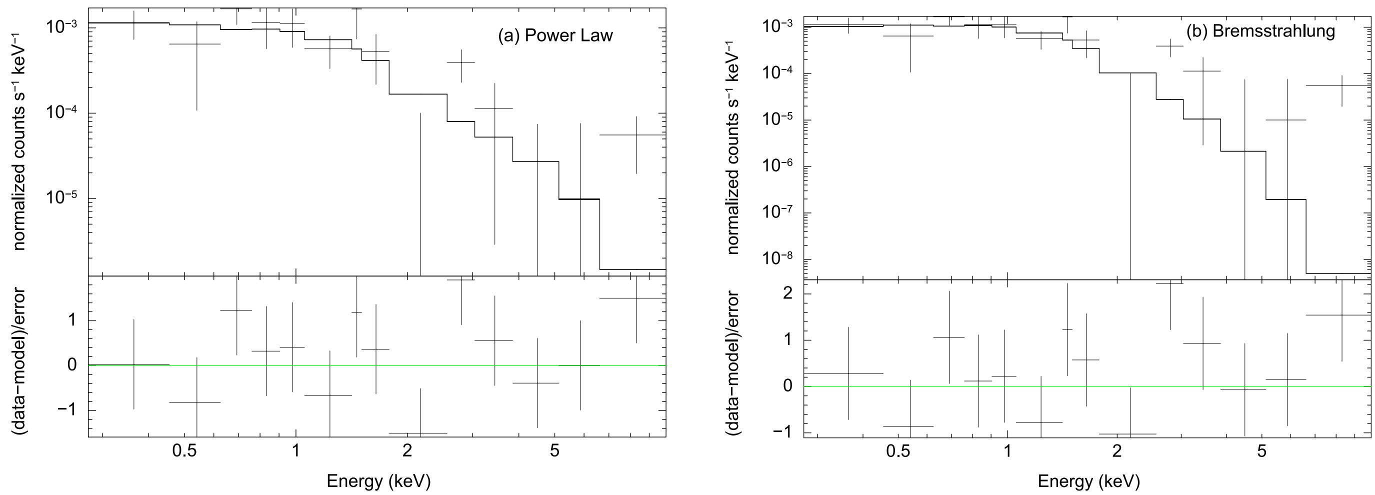

Figure 6. (a) X-ray spectral data (crosses) and the best-fit power-law model (steps) of 2MASS J11201034−2201340 obtained with *XMM-Newton*. The lower panel shows the deviation of each data point from the best-fit model. (b) The same as (a) for the thermal Bremsstrahlung model.

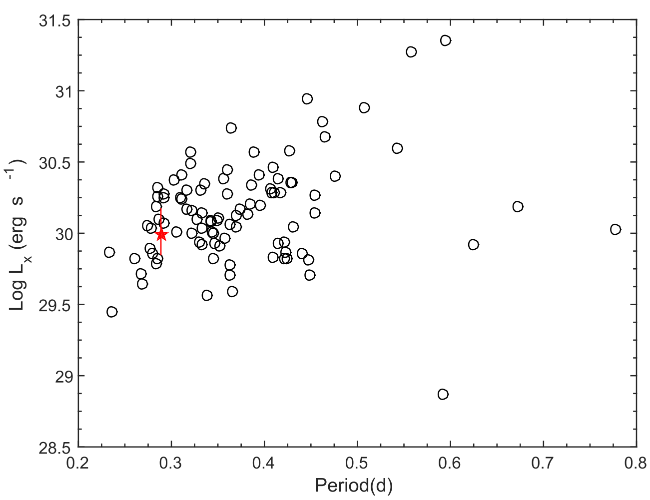

Figure 7. Relation between the X-ray luminosity and orbital period for contact binaries. The red star denotes 2MASS J11201034−2201340 and the open circles are historical data adopted from Chen et al. (2006).

modulation of the uncataloged X-ray-emitting contact binary 2MASS J11201034−2201340. We presented a multi-wavelength investigation of the object because it is detectable from infrared to X-ray bands. We first detected 2MASS J11201034 −2201340 after we combined all of the *Swift* observations of 2FGL J1120.0−2204. The exact X-ray position was further confirmed by an *XMM-Newton* observation. For the optical band, the long-term CRTS light curve and SLT color measurements confirmed that the orbital period of this system is 0.288 day, which is between the values for A-type and W-type contact binaries. Photometric measurement data in the USNO-B 1.0, 2MASS, and *WISE* catalogs indicate that the broadband SED of 2MASS J11201034−2201340 is that of a K-type star. We used the Wilson–Devinney code to fit the orbital profile in the *R*- and *V*-band follow-up light curves observed by the SLT and showed that this system is an A-type contact binary with a mass ratio of ∼0.3. Furthermore, we proposed a cool spot to explain the asymmetric orbital profile. In addition to the optical periodicity, the X-ray emission hints at the X-ray origin of this object. Although the number of X-ray photons was insufficient to obtain a significant X-ray orbital profile, the X-ray spectrum is likely to be nonthermal, and thus can be linked to chromospheric activity and star spots. The X-ray flux, orbital period, and color index of 2MASS J11201034−2201340 all point to it being a typical contact binary. Additional multi-band observations with standard star calibrations and long-time-baseline monitoring should conclusively determine the physical properties of this object in detail.

This work made use of the data collected by *XMM-Newton*, an ESA science mission with instruments and contributions directly funded by ESA Member States and the USA (NASA). The *Swift* data was supplied by the UK *Swift* Science Data Centre at the University of Leicester. The orbital ephemeris is obtained using the data collected by the CRTS survey, which is supported by the U.S. National Science Foundation under grants AST-0909182. The LOT and SLT are maintained by the Graduate Institute of Astronomy, National Central University. The near-infrared data is collected by the 2MASS, which is a joint project of the University of Massachusetts and the Infrared Processing and Analysis Center/California Institute of Technology, funded by the NASA and the National Science Foundation. The mid-infrared data was provided by the *WISE*, which is a joint project of the University of California, Los Angeles, and the Jet Propulsion Laboratory/California Institute of Technology, funded by NASA.

C.-P.H. is supported by the NSC 101-2119-M008-007-MY3 grant from the Ministry of Science and Technology (MOST) of Taiwan and an ECS grant of Hong Kong Government under HKU 709713P. T.-C.Y. and W.-H.I. are supported by the MOST grant NSC 101-2119-M008-007-MY3 and MOST 104-2119-M-008-024. Y.C. is supported by the MOST grant NSC 102-2112-M-008-020-MY3. L.L. and S.-B.Q. is supported by the Science Foundation of Yunnan Province (2012HC011) and the Chinese Natural Science Foundation (No.11133007 and No. 11325315). C.Y.H. is supported by the National Research Foundation of Korea through grant 2014R1A1A2058590. A.K.H.K. is supported by the MOST grant 103-2628-M-007-003-MY3. P.H.T. is supported by the One Hundred Talents Program of the Sun Yat-Sen University. C.-C.N. is supported by the MOST grant NSC 101-2112-M-008-017-MY3 and 104-2112-M-008-012-MY3. W.P.C. is supported by the MOST grants 103-2112-M-008-024-MY3.

REFERENCES

Binnendijk, L. 1970, VA, 12, 217
Carroll, R. W., Cruddace, R. G., Friedman, H., et al. 1980, ApJL, 235, L77
Chen, W. P., Sanchawala, K., & Chiu, M. C. 2006, AJ, 131, 990
Gazeas, K. D., & Niarchos, P. G. 2006, MNRAS, 370, L29
Güver, T., & Özel, F. 2009, MNRAS, 400, 2050
Hilditch, R. W., King, D. J., & McFarlane, T. M. 1988, MNRAS, 231, 341
Høg, E., Fabricius, C., Makarov, V. V., et al. 2000, A&A, 355, L27
Horne, J. H., & Baliunas, S. L. 1986, ApJ, 302, 757
Huenemoerder, D. P., Testa, P., & Buzasi, D. L. 2006, ApJ, 650, 1119
Hui, C. Y., Park, S. M., Hu, C. P., et al. 2015, ApJ, 809, 68
Kalberla, P. M. W., Burton, W. B., Hartmann, D., et al. 2005, A&A, 440, 775
Kaszas, G., Vinko, J., Szatmary, K., et al. 1998, A&A, 331, 231
Levine, A. M., Bradt, H. V., Chakrabarty, D., Corbet, R. H. D., & Harris, R. J. 2011, ApJS, 196, 6
Lucy, L. B. 1967, ZAp, 65, 89
Monet, D. G., Levine, S. E., Canzian, B., et al. 2003, AJ, 125, 984
Müller, G., & Kempf, P. 1903, AN, 161, 141
O'Connell, D. J. K. 1951, PRCO, 2, 85
Pickles, A. J. 1998, PASP, 110, 863
Ruciński, S. M. 1969, AcA, 19, 245
Scargle, J. D. 1982, ApJ, 263, 835
Schlafly, E. F., & Finkbeiner, D. P. 2011, ApJ, 737, 103
Stępień, K., Schmitt, J. H. M. M., & Voges, W. 2001, A&A, 370, 157
van Hamme, W. 1993, AJ, 106, 2096
Wilsey, N. J., & Beaky, M. M. 2009, in Society for Astronomical Sciences Annual Symp. 28 (Rancho Cucamonga, CA: Society for Astronomical Sciences), 107
Wilson, R. E. 1979, ApJ, 234, 1054
Wilson, R. E. 1990, ApJ, 356, 613
Wilson, R. E. 1994, PASP, 106, 921
Wilson, R. E., & Devinney, E. J. 1971, ApJ, 166, 605

The Astronomical Journal, 149:66 (13pp), 2015 February doi:10.1088/0004-6256/149/2/66

VI-BAND FOLLOW-UP OBSERVATIONS OF ULTRA-LONG-PERIOD CEPHEID CANDIDATES IN M31

Chow-Choong Ngeow[1], Chien-Hsiu Lee[2,3], Michael Ting-Chang Yang[1], Chi-Sheng Lin[1], Hsiang-Yao Hsiao[1], Yu-Chi Cheng[1], Zhong-Yi Lin[1], I-Ling Lin[1], Shashi M. Kanbur[4], and Wing-Huen Ip[1]
[1] Graduate Institute of Astronomy, National Central University, Jhongli 32001, Taiwan
[2] Max Planck Institute for Extraterrestrial Physics, D-85748 Garching, Germany
[3] University Observatory Munich, D-81679 Munich, Germany
[4] Department of Physics, SUNY Oswego, Oswego, NY 13126, USA
Received 2014 September 25; accepted 2014 December 2; published 2015 January 19

ABSTRACT

The ultra-long-period Cepheids (ULPCs) are classical Cepheids with pulsation periods exceeding ≈80 days. The intrinsic brightness of ULPCs are ∼1 to ∼3 mag brighter than their shorter period counterparts. This makes them attractive in future distance scale work to derive distances beyond the limit set by the shorter period Cepheids. We have initiated a program to search for ULPCs in M31, using the single-band data taken from the Palomar Transient Factory, and identified eight possible candidates. In this work, we presented the *VI*-band follow-up observations of these eight candidates. Based on our *VI*-band light curves of these candidates and their locations in the color–magnitude diagram and the Period–Wesenheit diagram, we verify two candidates as being truly ULPCs. The six other candidates are most likely other kinds of long-period variables. With the two confirmed M31 ULPCs, we tested the applicability of ULPCs in distance scale work by deriving the distance modulus of M31. It was found to be $\mu_{\rm M31,ULPC} = 24.30 \pm 0.76$ mag. The large error in the derived distance modulus, together with the large intrinsic dispersion of the Period–Wesenheit (PW) relation and the small number of ULPCs in a given host galaxy, means that the question of the suitability of ULPCs as standard candles is still open. Further work is needed to enlarge the sample of calibrating ULPCs and reduce the intrinsic dispersion of the PW relation before re-considering ULPCs as suitable distance indicators.

Key words: distance scale – galaxies: individual (M31) – stars: distances – stars: variables: Cepheids

Supporting material: machine-readable table and VO table

1. INTRODUCTION

Cepheid variables span a class of pulsating stars within the instability strip in the Hertzsprung–Russell diagram. Their well-known period–luminosity (PL) relation (also known as the Leavitt law, as first presented in Leavitt & Pickering 1912) makes Cepheids good standard candles. They constitute the first rung of the extra-galactic distance scale ladder. Previous studies have shown that the Cepheid PL relation can be used to determine distances out to the order of 10–30 Mpc (e.g., Freedman et al. 2001; Riess et al. 2011) using the *Hubble Space Telescope* (*HST*). When coupled with other secondary distance indicators, such as type Ia supernovae and the Tully–Fisher relation, one is able to determine distances to galaxies that are well within the Hubble flow. However, the cosmic distance ladder suffers from several uncertainties at each ladder rung. Thus, Bird et al. (2009) have proposed the use of very luminous Cepheids, the so-called ultra-long-period Cepheids (hereafter ULPCs), to extend distance estimation beyond ≈100 Mpc. Besides the potential to be used as distance indicators, ULPCs can also be used to constrain and enhance our understanding of stellar pulsation and evolution theories for intermediate- to high-mass stars crossing the instability strip (Bird et al. 2009; Fiorentino et al. 2012). Bird et al. (2009) defined ULPCs to be fundamental-mode (FU) Cepheids with periods longer than ∼80 days.

Most studies of extragalactic distance determination use the Large Magellanic Cloud (LMC) as a distance anchor. Since the LMC has irregularity in its three-dimensional shape and low metallicity, many authors suggest instead using M31 as a stepping stone to cosmic-distance determination (see, e.g., Clementini et al. 2001; Vilardell et al. 2010 and references therein). The merits of M31 include the following: it has a simple geometry; potential M31 distance-indicator stars are bright enough to be resolved; it is a local counterpart to the spiral galaxies that are used to determine the extragalactic distance (see, e.g., Freedman et al. 2001); and it is a local benchmark to calibrate the Tully–Fisher relation. Despite its proximity, M31 has not been considered as a distance anchor (see, e.g., Riess et al. 2011), because a distance anchor has to have a precise distance estimate and harbor a fair amount of distance indicators such as Cepheids. M31 has not yet met these two criteria because (1) its current distance estimate has larger uncertainty (~4%, Vilardell et al. 2010) compared to other distance anchors (for example, LMC at ~2% level; see Pietrzyński et al. 2013), and (2) there was no large sample of well studied Cepheids in the literature. Nevertheless, recent studies of M31 eclipsing binaries (Lee et al. 2014b) and Cepheids (Fliri & Valls-Gabaud 2012; Riess et al. 2012; Kodric et al. 2013, 2014) have demonstrated the potential of establishing M31 as a distance anchor in the near future. Given the increasing importance of M31 in future distance scale work, it makes sense to search for and identify ULPCs in M31: such studies could provide a "one-step" calibration of the Hubble constant, similar to the role of NGC 4258 in Riess et al. (2011).

Ground-based CCD observations of Cepheids in M31 originate either from dedicated surveys to search for Cepheids and (detached) eclipsing binaries, or as by-products from intense monitoring of M31 to detect micro-lensing events. Examples of the former case include Freedman & Madore (1990), Magnier et al. (1997), and Vilardell et al. (2006, 2007), as well as the DIRECT project (see Kaluzny

Table 1
Summary of Modern-day Cepheid Observations in M31

Project/Survey[a]	Telescope[b]	Field Center[c]	Field of View	Pix. Scale[d]	Obs. Time Span[e]	Ref.[f]
		Dedicated Surveys to Search for Cepheids (and Eclipsing Binaries)				
Freedman & Madore	3.6 m CFHT	10 fields covering Baade's Field I, III and IV	$2' \times 3'$[g]	⋯	1985–1988	1
Magnier et al.	2.5 m INT	9 fields along spiral arms	$12\overset{\prime}{.}5 \times 12\overset{\prime}{.}5$	0.367	1993 (9)	2
	1.3 m MDM	(same as above)	$10\overset{\prime}{.}9 \times 10\overset{\prime}{.}9$	0.637	1993 (11)	2
Vilardell et al.	2.5 m INT	$\alpha = 00^{h}44^{m}46^{s}$ $\delta = +41°38'20''$	$33\overset{\prime}{.}8 \times 33\overset{\prime}{.}8$	0.33	1999–2003 (21)	3, 4
DIRECT: M31 B	Two Tel.[h]	$\alpha = 11\overset{\circ}{.}20$ $\delta = +41\overset{\circ}{.}59$	$11' \times 11'$	0.32	1996–1997 (~43)	5
DIRECT: M31 A	Two Tel.[h]	$\alpha = 11\overset{\circ}{.}34$ $\delta = +41\overset{\circ}{.}37$	$11' \times 11'$	0.32	1996–1997 (~44)	6
DIRECT: M31 C	Two Tel.[h]	$\alpha = 11\overset{\circ}{.}10$ $\delta = +41\overset{\circ}{.}42$	$11' \times 11'$	0.32	1996–1997 (~53)	7
DIRECT: M31D	Two Tel.[h]	$\alpha = 11\overset{\circ}{.}03$ $\delta = +41\overset{\circ}{.}27$	$11' \times 11'$	0.32	1996–1997 (~58)	8
DIRECT: M31 F	Two Tel.[h]	$\alpha = 10\overset{\circ}{.}10$ $\delta = +40\overset{\circ}{.}72$	$11' \times 11'$	0.32	1996–1997 (~51)	9
DIRECT: M31 Y	1.2 m FLWO	$\alpha = 10\overset{\circ}{.}97$ $\delta = +41\overset{\circ}{.}69$	$11' \times 11'$	0.33	1999–2000 (~25)	10
		By-products from Micro-lensing Experiments				
AGAPE	2.0 m TBL	6 + 1 fields centered at M31, oriented along the main axis	$14' \times 10'$[i]	0.30	1994–1996 (~69)	11
NMS	1.0 m ST	$\alpha = 00^{h}43^{m}38^{s}$ $\delta = +41°09\overset{\prime}{.}1$	$13' \times 13'$	0.37	1998–2002 (>150)	12, 13
POINT-AGAPE	2.5 m INT	$\alpha = 00^{h}43^{m}10^{s}$ $\delta = +40°58'15\overset{\prime\prime}{.}0$	$33' \times 33'$	0.33	1999–2001 (~180)	14
		$\alpha = 00^{h}44^{m}00^{s}$ $\delta = +41°34'00\overset{\prime\prime}{.}0$	$33' \times 33'$	0.33	1999–2001 (~180)	14
WeCAPP	1.2 m CAO	$\alpha = 00^{h}42^{m}44^{s}.3$ $\delta = +41°16'07\overset{\prime\prime}{.}5$	$17\overset{\prime}{.}2 \times 17\overset{\prime}{.}2$	0.50	2000–2001	15
	0.8 m WO	mosaic CAO's FOV with 4 pointings	$8\overset{\prime}{.}3 \times 8\overset{\prime}{.}3$	0.49	1999–2008	15
POMME	3.6 m CFHT	$\alpha = 00^{h}43^{m}50^{s}$ $\delta = +41°45'0''$	$1° \times 1°$	0.187	2004 (~50)	16
		$\alpha = 00^{h}41^{m}50^{s}$ $\delta = +40°44'0''$	$1° \times 1°$	0.187	2005 (~50)	16
		Other Time-series Observations				
Clementini et al.	8.4 m LBT	$\alpha = 00^{h}48^{m}13.11^{s}$ $\delta = +40°19'09\overset{\prime\prime}{.}4$	$23' \times 23'$	0.225	2007 (~8)	17
		$\alpha = 00^{h}49^{m}08.31^{s}$ $\delta = +42°16'09\overset{\prime\prime}{.}4$	$23' \times 23'$	0.225	2007 (~8)	17
PAndromeda	1.8 m PS1	$\alpha = 00^{h}42^{m}44.33^{s}$ $\delta = +41°16'07\overset{\prime\prime}{.}5$	$\sim 2.6° \times \sim 2.6°$	0.258	2010–2011 (~183)	18

[a] AGAPE = Andromeda Gravitational Amplification Pixel Experiment; NMS = Nainital Microlensing Survey; POINT-AGAPE = Pixel-lensing Observations with the Isaac Newton Telescope-Andromeda Galaxy Amplified Pixels Experiment; WeCAPP = Wendelstein Calar Alto Pixellensing Project; POMME = Pixel Observations of M31 with MEgacam.
[b] CFHT = Canada–France–Hawaii Telescope (Hawaii, USA); INT = Issac Newton Telescope (Spain); MDM = McGraw-Hill Telescope at the Michigan-Dartmouth-MIT (MDM) Observatory; FLWO = F. L. Whipple Observatory (Arizona, USA); TBL = Bernard Lyot Telescope (France); WO = Wendelstein Observatory (Germany); CAO = Calar Alto Observatory (Spain); ST = Sampurnanand Telescope (India); LBT = Large Binocular Telescope (Arizona, USA); PS1 = Pan-STARRS1 Telescope (Hawaii, USA).
[c] R.A. and decl. of field center is in *J*2000.
[d] CCD pixel scale in ″/pixel.
[e] Number in the parenthesis is the number of observing nights when available.
[f] Reference: (1) Freedman & Madore (1990), (2) Magnier et al. (1997), (3) Vilardell et al. (2006), (4) Vilardell et al. (2007), (5) Kaluzny et al. (1998), (6) Stanek et al. (1998), (7) Stanek et al. (1999), (8) Kaluzny et al. (1999), (9) Mochejska et al. (1999), (10) Bonanos et al. (2003), (11) Ansari et al. (2004), (12) Joshi et al. (2003), (13) Joshi et al. (2010), (14) An et al. (2004), (15) Fliri et al. (2006), (16) Fliri & Valls-Gabaud (2012), (17) Clementini et al. (2011), (18) Kodric et al. (2013).
[g] The FOV for each of the 10 CCD fields.
[h] The two telescopes used in the DIRECT project are: 1.3 m MDM and 1.2 m FLWO.
[i] This is the total FOV; the FOV for individual fields is $4' \times 4\overset{\prime}{.}5$.

et al. 1998, and subsequent papers in the series). For the micro-lensing experiments, these include the AGAPE (Ansari et al. 2004), the Nainital Microlensing Survey (Joshi et al. 2010), the POINT-AGAPE Survey (An et al. 2004), the WeCAPP survey (Fliri et al. 2006), and the POMME Survey (Fliri & Valls-Gabaud 2012). In addition, time-series observations of two M31 fields, using the Large Binocular Telescope, have also detected a number of short-period Cepheids (Clementini et al. 2011). Recently, Riess et al. (2012) combined data from the POMME Survey and *HST* observations for 68 Cepheids, and derive a true distance of 752 ± 27 kpc to the M31. Kodric et al. (2013) presented a catalog of M31 Cepheids, including fundamental and first overtone Cepheids (as well as Type II Cepheids), based on the first year of the Panoramic Survey Telescope and Rapid Response System (PS1, Pan-STARRS1) PAndromeda Survey. A summary of these surveys and projects is presented in Table 1, and the coverage for some of the surveys is shown in Figure 1. These studies are limited in that most of the observations, with the exception of the POMME Survey and the PAndromeda Survey, cover only part of M31, and most of them concentrate on the disk (see Figure 1). Furthermore, no Cepheids with periods longer than ~80 days were detected in these studies.

Therefore, we have initiated a program to search for ULPCs in M31 by using data from the Palomar Transient Factory (PTF; Law et al. 2009; Rau et al. 2009). This is because the

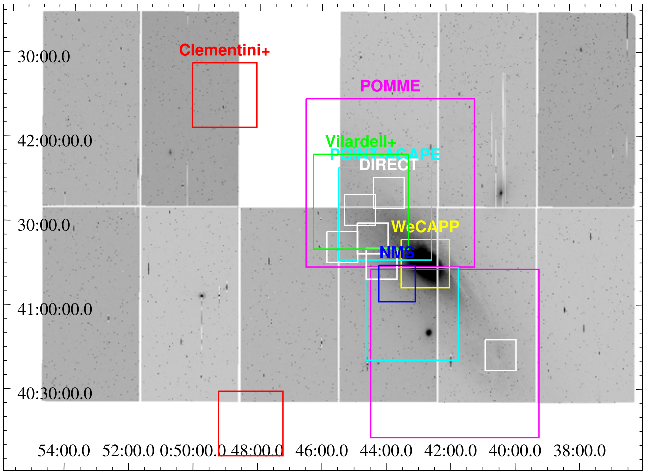

Figure 1. Footprints for some of the previous surveys, as summarized in Table 1, superimposed on a PTF image of M31. Note that one CCD (upper row, third from the left) is inoperable.

PTF data can cover the entire disk of M31, as shown in Figure 1. In addition, PTF observes M31 routinely with cadence up to one day. These two conditions make PTF an ideal data set to search for the ULPCs in M31. Our search results were published in Lee et al. (2013, hereafter Paper I) and Lee et al. (2014a). Using image subtraction techniques, eight ULPC candidates were identified. Figure 2 displays the postage stamp images for these candidates based on PTF data. As mentioned in Paper I, time series *VI*-band data is needed to further confirm or disprove the ULPC nature of these candidates. In this work, we report the *VI*-band follow-up observations for all these eight candidates. Section 2 describes the follow-up observations, data reduction, and the calibration of the light curves. Analysis of these light curves and the results are presented in Section 3, followed by our conclusions in Section 4.

2. THE FOLLOW-UP OBSERVATIONS

The *VI*-band follow-up observations were carried out with the P60 Telescope (P60; Cenko et al. 2006) at the Palomar Observatory and the Lulin 1 m Telescope (LOT; Kinoshita et al. 2005) at the Lulin Observatory. These observations began in 2012 October and ended in 2013 November. P60 is equipped with a 2k × 2k CCD with a pixel scale of 0.379 arcsec per pixel, while LOT used a 1k × 1k CCD with a pixel scale of 0.512 arcsec per pixel. Observations for both telescopes were obtained in queue mode when there was available observing time in suitable weather conditions. Imaging data from P60 was reduced with a dedicated pipeline as described in Cenko et al. (2006). For LOT images, subroutines in IRAF[5] were used to reduce the data in the usual manner (bias and dark subtraction, and flat-fielded with master flat images). The LOT *I*-band images suffered from a fringing problem. To remove the fringe patterns, we median combined the *I*-band images for candidates with an internal ID 4-1047[6] and created a master fringe image. We selected the images for this candidate because it is located far away from the M31 bulge and disk (see Figure 1 in Paper I). Hence, the images do not have a strong background gradient. The master fringe image was smoothed by a "boxcar" averaging algorithm available from IRAF, and then scaled and subtracted from all of the LOT *I*-band images. Astrometric refinement for both P60- and LOT-reduced images were performed using `astrometry.net` (Lang et al. 2010). Figure 3 shows the seeing distributions of all the images taken from both telescopes. It can be seen that some images with large seeing could be affected by bad weather. After visual inspection, images that were affected by bad weather were discarded. This left 568 and 386 images from P60 and LOT, respectively.

Photometry based on point-spread function fitting (hereafter PSF photometry) for the candidates and suitable stars in each frame were obtained from `IRAF/DAOPHOT` subroutines. For each candidate, we first created a "master" catalog (with ∼50 stars) that included: (1) the location of the ULPC candidate itself; (2) faint stars in the vicinity of the candidate star (selected based on the best seeing images); and (3) relatively bright ($V_{\rm LGS} \sim 16.3$ to ∼19.9 mag) and isolated stars taken from the M31 Local Group Survey catalog (LGS; Massey et al. 2006). These LGS stars were visually inspected to ensure they were located within the P60 and LOT images, as well as away from any crowded regions in the images. About ∼15 to ∼25 LGS stars in the "master" catalog were used to construct the PSF model for each image by executing the IRAF subroutines `DAOPHOT.PHOT`, `DAOPHOT.PSTSELECT`, and `DAOPHOT.PSF`. Sky coordinates for all the stars in the "master" catalogs were then converted to pixel coordinates and saved as a coordinate file. Finally, `DAOPHOT.PHOT` and `DAOPHOT.ALLSTAR` were run with the input coordinate file and PSF model to obtain the instrumental PSF photometry for the stars in the "master" catalog.

2.1. Light Curves from Differential Photometry

The *VI*-band light curves for the eight candidates were constructed using differential photometry techniques given in Broeg et al. (2005). Instead of using a single star as a comparison star (cs) to obtain differential photometry, the technique presented in Broeg et al. (2005) used a number of stars (either all stars in the images or a subset of suitable constant stars) to construct an artificial comparison star:

$$\Delta m = m_c - < m >_{\rm cs} = m_c - \sum_i w_i m_i^{\rm cs}, \qquad (1)$$

where m_c was the instrumental magnitudes for our candidates in either the *V* or *I* band, and w_i were the weights for individual comparison stars such that $\sum_i w_i = 1$. At the first stage, we constructed differential photometry light curves for a pair of LGS stars in our "master" catalogs, as mentioned in the previous section, by taking one of them as a comparison star. We then removed those LGS stars that exhibited a large scatter in the differential light curves. This left a subset of good LGS stars before Equation (1) was applied to each of our candidates. Since the calibrated *VI*-band magnitudes were available for these comparison stars from the LGS catalog, light curves constructed from Equation (1) were calibrated via the

[5] IRAF is distributed by the National Optical Astronomy Observatories, which are operated by the Association of Universities for Research in Astronomy, Inc., under cooperative agreement with the National Science Foundation.

[6] See Paper I for the meaning of internal ID.

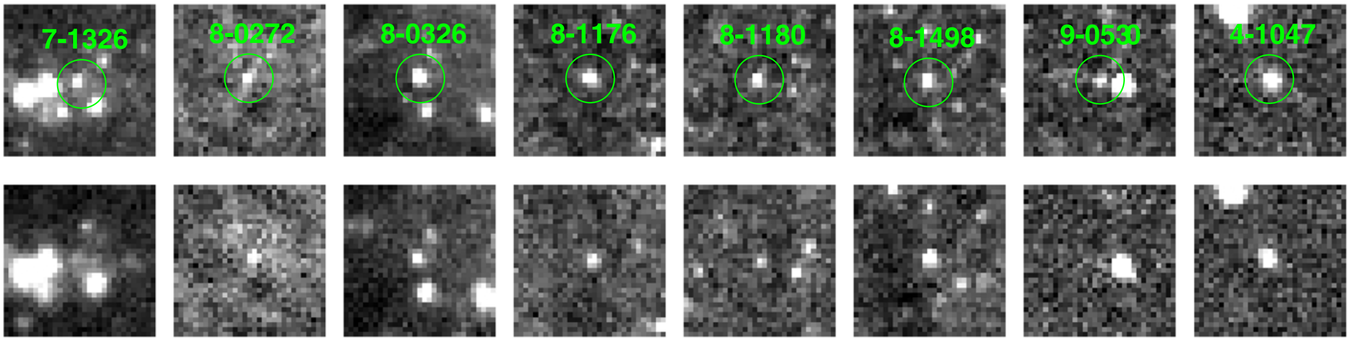

Figure 2. Postage-stamp images of the eight ULPC candidates reported in Paper I. The upper row shows the PTF *R*-band images, while the lower row shows the PTF *g*-band images. Note that the *R*- and *g*-band images are from different epochs. All stamps have a FOV of $30'' \times 30''$. The green circles with a radius of $5''$ indicate the locations of the candidates.

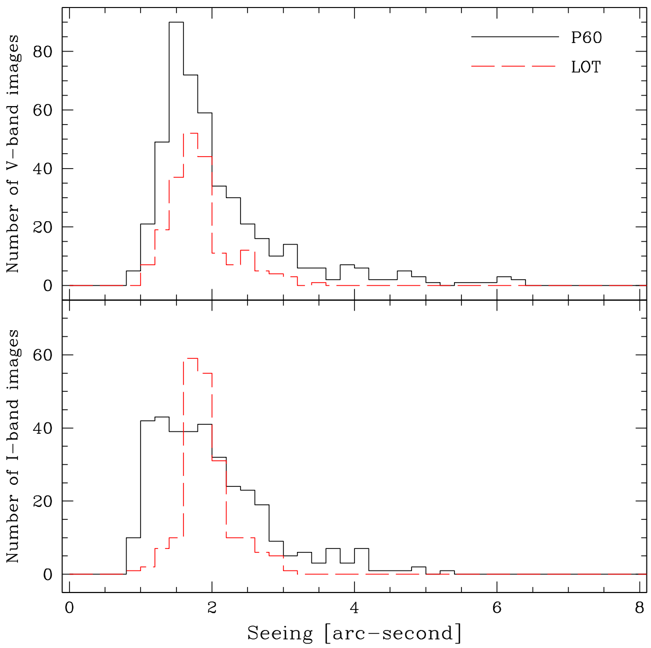

Figure 3. Seeing distributions in the *V* (upper panel) and *I* bands (lower panel) for the P60 and LOT images. For the P60 observations, besides a pair of *VI* -band images, an additional *V*-band image was also taken on the nights between 2012 November and 2013 March.

following equation:

$$m_{\text{calibrate}} = \Delta m + \sum_i w_i m_i^{\text{cs,LGS}}, \qquad (2)$$

where w_i were the same weights as in Equation (1), and $m_i^{\text{cs,LGS}}$ were the *VI*-band magnitudes from the LGS catalog. The calibrated *VI*-band light curves for the eight candidates are given in Table 2 and displayed in panel (a) and (b) of Figures 4–7.

3. ANALYSIS AND RESULTS

3.1. Period Search and Folded Light Curves

The new *VI*-band light curves suggested that periods for the candidates need to be revised from Paper I. For each pair of the *VI*-band light curves, we first subtracted the arithmetic mean of the light curve, followed by normalization of the light curve using the peak-to-peak amplitude. We then applied the well-documented Lomb–Scargle algorithm to search for periodic signals by combining these mean-subtracted and normalized pair of *VI*-band light curves (as shown in panel (c) of Figures 4–7) to each of the candidates. We only searched for periodic signals around $\sim\pm30$ or $\sim\pm50$ days from the periods reported in Paper I (with the exception of candidate 8-0272, for which a shorter period range was searched for periodic signals). The periods corresponding to the highest peaks in the Lomb–Scargle periodogram were taken as the periods for these candidates. They are indicated by a vertical dashed line in panel (d) of Figures 4–7, as well as listed in the second column of Table 3. We also ran a Monte-Carlo simulation to quantify the errors on the corresponding periodic signals. Assuming the photometric errors are Gaussian, about 10,000 simulated light curves were generated using the Box–Muller method for each of the candidates. The Lomb–Scargle algorithm was then applied to these light curves in a similar fashion to the combined *VI*-band light curves. The errors on the derived periods were then estimated as the rms of the corresponding peaks in the power spectra.

Table 2
VI-band Light Curves for the Candidates

Candidate	Telescope	Band	MJD	m	σ_m
8-0326	LOT	V	56218.62510	18.819	0.031
8-0326	LOT	V	56224.71680	18.931	0.034
8-0326	LOT	V	56224.71403	18.935	0.033
8-0326	LOT	V	56235.64163	19.026	0.038

(This table is available in its entirety in machine-readable and Virtual Observatory (VO) forms.)

Using the periods given in Table 3, we folded the *VI*-band light curves for these eight candidates. The folded *VI*-band light curves were then fitted with a low-order Fourier decomposition (for example, see Simon & Lee 1981) in the following form:

$$m(\phi) = m_0 + \sum_{i=1}^{i=2,3,4} A_i \cos\left(2i\pi\phi + \Phi_i\right) \qquad (3)$$

where $\phi \in [0, 1]$ were phases of the pulsating cycles. The fitted light curves, shown as black curves in panels (e) and (f) of Figures 4–7, were used to derive the *VI*-band mean magnitudes (by converting the fitted light curves to intensity, taking the average, and converting back to magnitude), as well as the extinction-free Wesenheit function *W*. In order to be consistent with previous works (Bird et al. 2009; Fiorentino et al. 2012), we adopted the same Wesenheit function in the form of $W = I - 1.55(V - I)$ from Udalski et al. (1999a). The

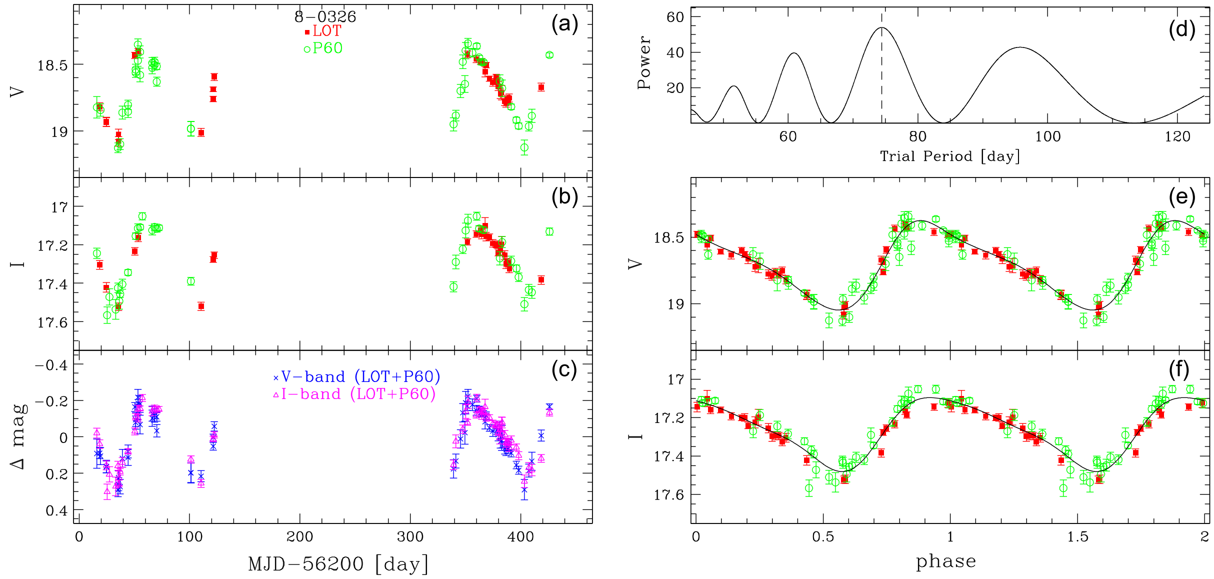

Figure 4. (a) Observed *V*-band light curve for candidate 8-0326, where the green open circles and red filled squares are for the P60 and LOT data, respectively. (b) Observed *I*-band light curve for the same candidate. (c) the combined *VI* band light curve that was used in period search; see the text (Section 3) for details. (d) The Lomb–Scargle periodogram, at which the corresponding period at the peak of the periodogram (indicated by a vertical dashed line) is the adopted period listed in Table 3. (e) The *V*-band folded light curve using the period given in Table 3. (f) The *I*-band folded light curve for the same candidate. The black curves in (e) and (f) represent the fitted light curves based on low-order Fourier decomposition.

Table 3
Revised Periods and Mean Magnitudes for the Candidates

Candidate	Period (days)	$<V>$	$<I>$	W
M31 ULPC Candidates				
8-0326	74.427 ± 0.120	18.684	17.256	15.043
8-1498	83.181 ± 0.178	18.856	17.783	16.120
M31 non-ULPC Candidates				
8-1176	125.313 ± 4.832	19.095	17.367	14.689
7-1326	132.608 ± 4.543	19.357	17.356	14.254
8-0272	169.262 ± 4.461	20.464	18.176	14.630
4-1047	216.169 ± 0.907	18.625	17.548	15.879
9-0530	221.779 ± 17.695	20.218	19.092	17.347
8-1180	222.124 ± 5.959	19.780	17.246	13.318

coefficient of 1.55 in the Wesenheit function is based on the extinction law from Schlegel et al. (1998). The derived mean magnitudes and the values of Wesenheit function are listed in Table 3.

The shape of the ULPC *VI*-band light curves are similar to the classical Cepheids (Bird et al. 2009; Ngeow et al. 2013), for which light curves exhibit the characteristic "saw-tooth" shape with a quick rise to maximum light followed by a slow decline to minimum light. Based on our *VI*-band light curves, only two of the candidates (8-0326 and 8-1498) exhibit Cepheid-like light curves, as shown in Figures 4 and 5, respectively. The *VI*-band light curves for the other six candidates are given in Figures 6 and 7. These curves do not display light curves that are expected for Cepheids. In the following sub-sections, the two candidates with Cepheid-like

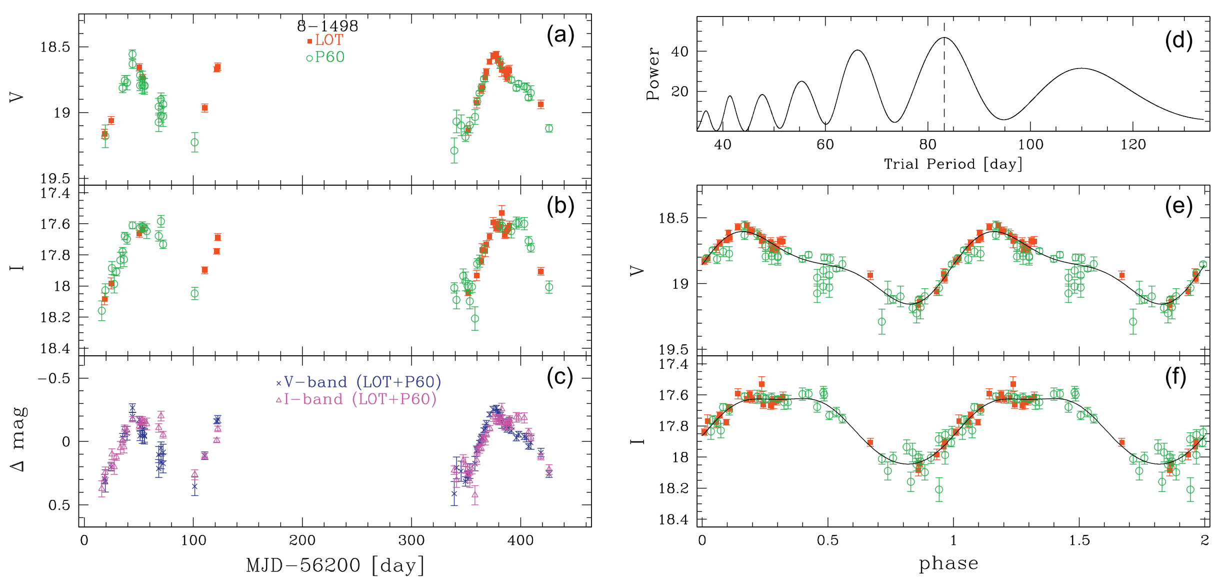

Figure 5. Same as Figure 4, but for candidate 8-1498.

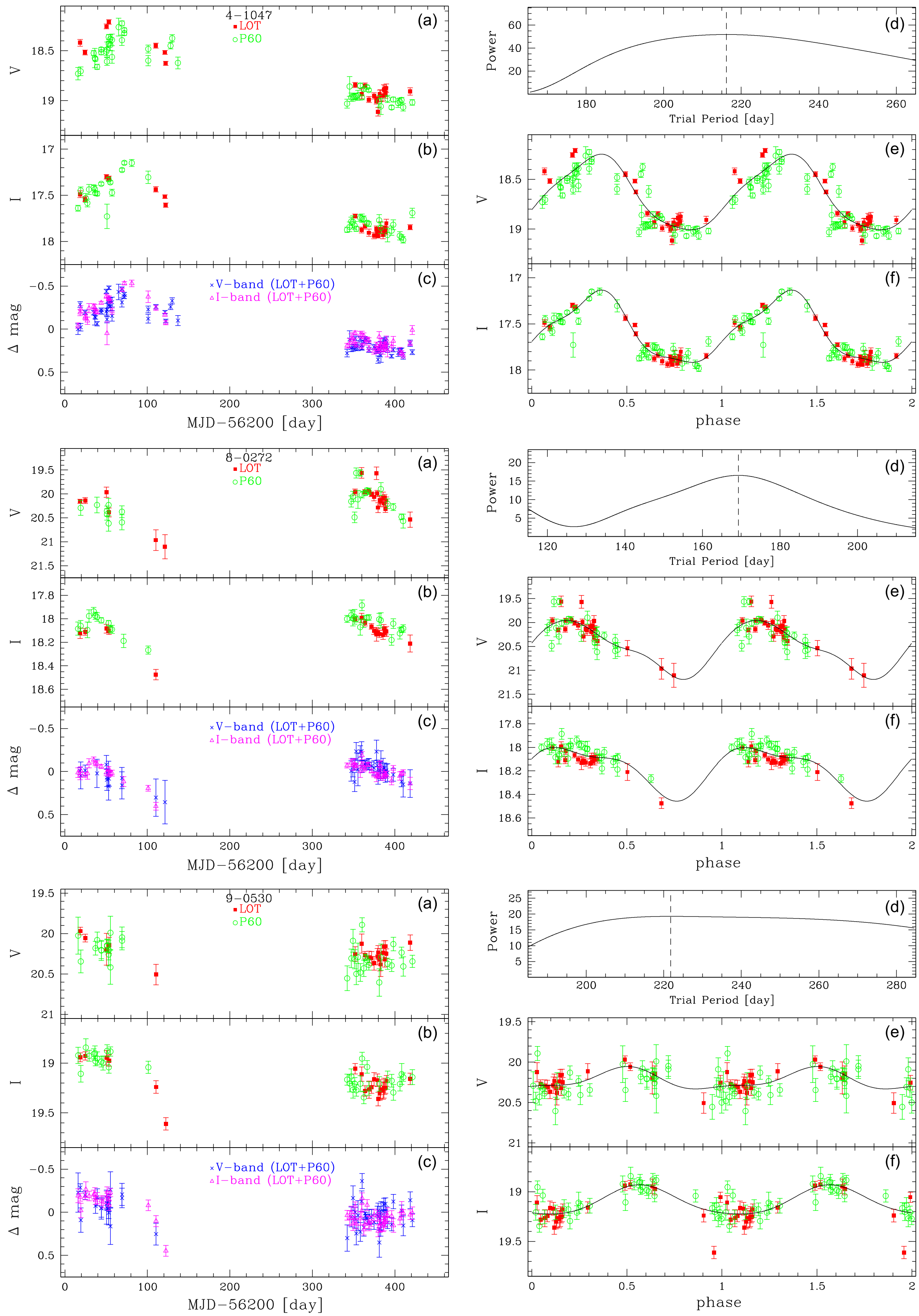

Figure 6. Same as Figure 4, but for candidates 4-1047, 8-0272, and 9-0530.

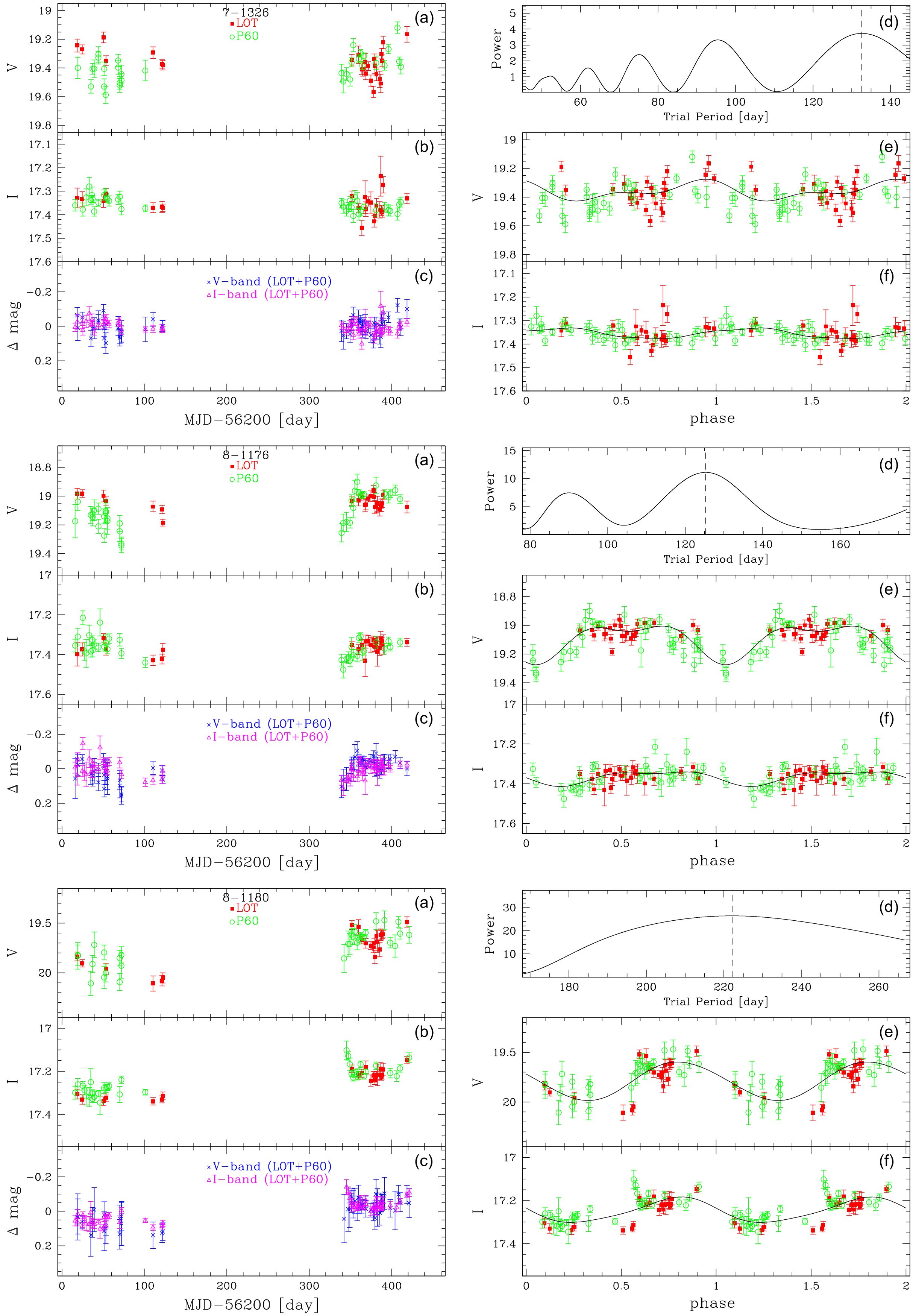

Figure 7. Same as Figure 4, but for candidates 7-1326, 8-1176, and 8-1180. We found that an additional zero-point offset of +0.078, +0.089, and +0.078 is needed to be added to P60 data for these candidates with an internal ID 7-1326, 8-1176, and 8-1180, respectively.

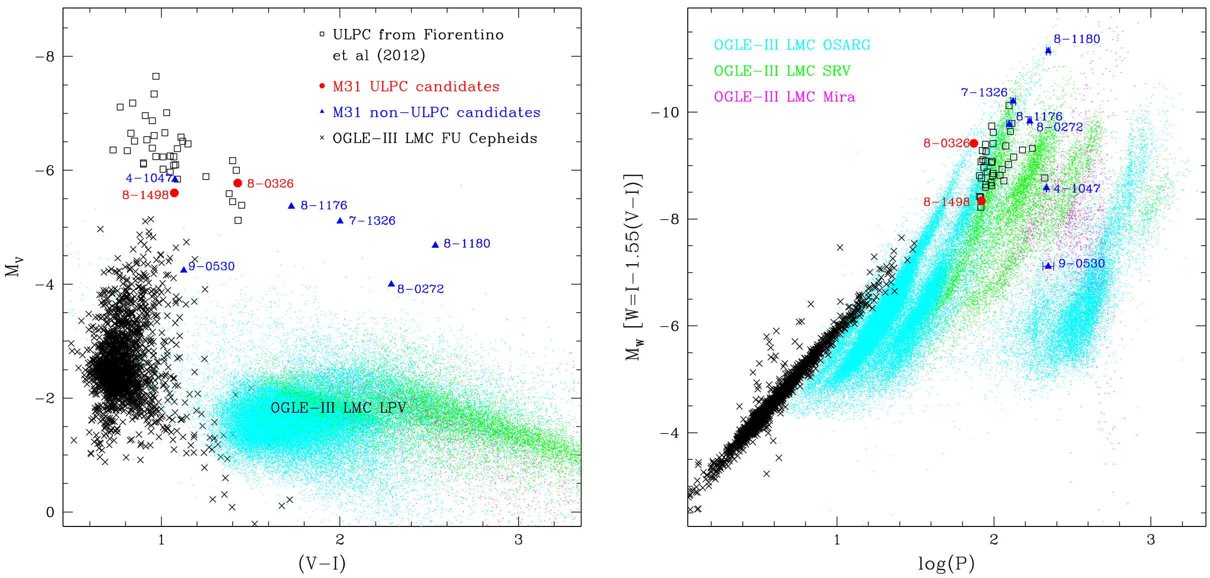

Figure 8. Comparison of our eight candidates to the known ULPCs listed in Fiorentino et al. (2012), as well as the LMC Cepheids and long-period variables (LPV) from the OGLE-III database, in the observed CMD (left panel) and PWD (right panel). We included LPVs to aid in falsifying the ULPC nature of our candidates. The LPVs were classified as small amplitude red giants (OSARG), semi-regular variables (SRV), and Mira by the OGLE team (Soszynski et al. 2009). Note that the saturation limit in OGLE-III data is around ∼13 mag to ∼13.5 mag. This translates to $M_V \sim -5.0$ mag to ~ -5.5 mag.

light curves are referred to as "M31 ULPC candidates," while the other six candidates will be referred to as "M31 non-ULPC candidates." Further confirmation or falsification of their ULPC nature will be detailed in the next sub-section. We note that the two "M31 ULPC candidates" have well-determined periods (with errors of the order of ∼0.2%), while the periods for the "M31 non-ULPC candidates," with the exception of the candidate with an internal ID of 4-1047, have a much larger error (from ∼2.6% to ∼8%). Furthermore, as mentioned in Paper I, these two "M31 ULPC candidates" have previously been classified as Cepheids in the literature (for example, in Magnier et al. 1997, but they have incorrect periods).

The two M31 ULPC candidates have periods of ∼74.4 and ∼83.2 days, respectively. According to the definition by Bird et al. (2009), a ULPC should have a period longer than 80 days. Hence, the ∼74.4 days ULPC found in this work may not be classified as ULPC. However, an 80 day period cut is rather arbitrary, and we prefer to identify the ULPCs based on the discussion given in Section 3.2. Furthermore, initial period detection searches for this candidate gave results in excess of 80 days in Paper I, and was refined to a shorter period with other period-search algorithms and *VI*-band light curve data. Therefore, we retained this candidate in the sample of M31 ULPCs.

3.2. *Verification of the ULPC Candidates*

Besides the shapes of the *VI*-band light curves, we verify/falsify the ULPC nature of our eight candidates by comparing them to the known ULPCs (given in Fiorentino et al. 2012) in the color–magnitude diagram (CMD) and the Period–Wesenheit diagram (PWD), collectively presented in Figure 8. Using the CMD and PWD to identify Cepheids has been done, for example, in Udalski et al. (1999b) and Kodric et al. (2013). Only those Cepheids identified with periods longer than ∼80 days will be re-classified as ULPC (Bird et al. 2009; Fiorentino et al. 2012). When making such comparisons, we have adopted the distance modulus of M31 as $\mu_{M31} = 24.46$ mag, recommended by de Grijs & Bono (2014), to convert the observed magnitudes of these candidates to the absolute magnitudes. We also included the LMC FU Cepheids and long-period variables (LPV) based on the OGLE-III database, taken from Soszynski et al. (2008) and Soszynski et al. (2009), respectively, in these diagrams. Again, we adopted $\mu_{LMC} = 18.49$ mag (de Grijs et al. 2014) when converting the observed magnitudes to absolute magnitudes. We enlarged Figure 8 by only showing the known ULPCs and our eight candidates in Figure 9. Figures 8 and 9 reveal that the two "M31 ULPC candidates" are indeed ULPC, as both of them fall in the parameter spaces defined by the known ULPCs. The remaining six "M31 non-ULPC candidates" are falsified as ULPC based on their location in the CMD and PWD diagrams, even though a few of them may be consistent with ULPCs in either the CMD or PWD diagram, but not in both. For example, candidates 4-1047 and 9-0530 fall within the ULPC instability strip, but they are outside the $\pm 3\sigma$ boundary of the Period–Wesenheit (PW) relation. Similarly, candidates 7-1326, 8-0272, and 8-1176 are located within the $\pm 3\sigma$ boundary of the PW relation, however they are too red in the CMD to be considered as ULPC. Since the main goal of this work is to verify the ULPC nature of our candidates in M31, determining the nature of these six non-ULPC candidates is beyond the scope of this paper, and they will not be discussed further.

It is expected that a galaxy would have small number of ULPCs for two reasons. First, ULPCs are intermediate- to high-mass stars with masses between $\sim 15\,M_\odot$ and $\sim 20\,M_\odot$ (Bird et al. 2009; Fiorentino et al. 2012). Hence, their number should be lower than their shorter period counterparts that have lower mass. Second, these intermediate- to high-mass stars need to cross the instability strip in order to pulsate and the time that they spend inside the instability strip is relatively short as compared to their evolutionary age. Based on the list compiled in Fiorentino et al. (2012), the number of ULPCs in a given galaxy ranges from one (NGC 6822), two (M81 and I Zw 18), three (SMC and NGC 300), four (LMC, NGC 1309 and NGC 3021), five (NGC 55), and nine (NGC 3370). Then, it is not a

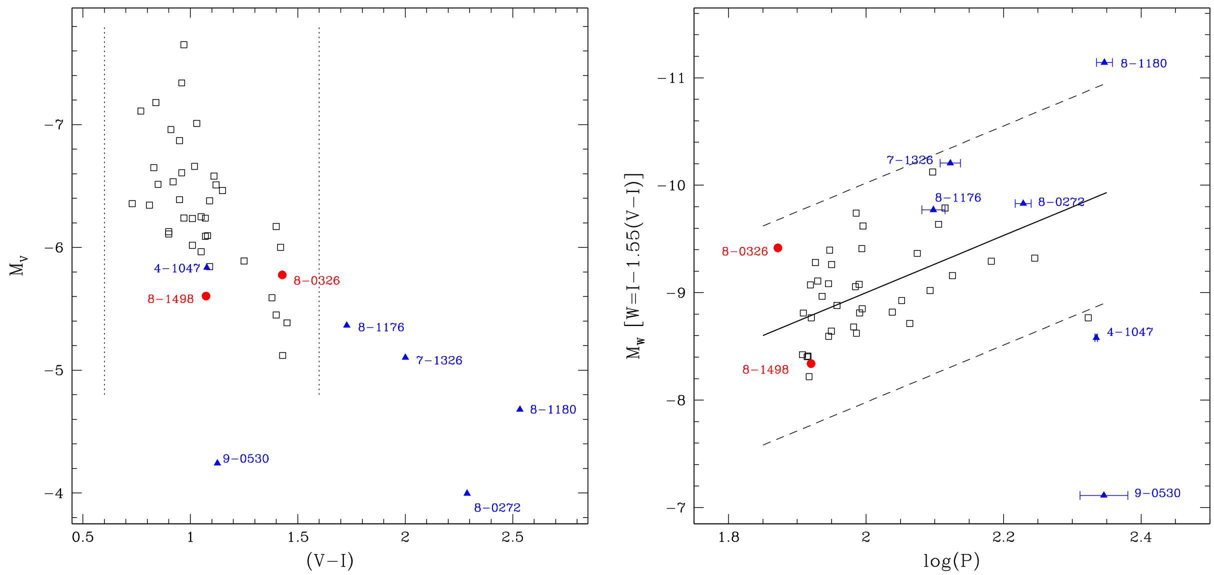

Figure 9. Observed CMD (left panel) and PWD (right panel) only showing the ULPCs. Since the predicted boundary of the ULPC instability strip from theoretical calculations is not yet available, we used the color range available from known ULPCs (Fiorentino et al. 2012), $0.6 < (V - I) < 1.6$, to represent the (crude) boundary of the instability strip (shown as vertical lines in the left panel). The solid line in the right panel is the Period–Wesenheit relation adopted from Fiorentino et al. (2012), and the dashed lines represent the $\pm 3\sigma$ boundary (where $\sigma = 0.34$ mag).

Table 4
M31 Cepheids with Periods Greater than ~75 days but Less than 80 days

Name or ID	Period (days)	α (J2000)	δ (J2000)	Reference
vn.4.2.678	78.00	11.06420	41.56927	Riess et al. (2012)
PSO J010.5806+40.8319	74.79	10.58066	40.83192	Kodric et al.(2013, only for Cepheids classified as "FU")

surprise that only two ULPCs were found in M31. Another reason for detecting a small number of ULPCs in M31 could be due to characteristics of PTF data. For example, the one CCD that is out of commission covers a portion of M31's disk (see Figure 1), and the stars in M31's bulge region are not resolvable in PTF images. Further discussion on the effect of PTF data can be found in Paper I, and will not be repeated here. A few additional ULPCs might be discovered from the three years of the Pan-STARRS1's PAndromeda Survey (M. Kodric et al. 2014, private communication). On the other hand, if the period cut of ~80 days that defines ULPC is lowered to ~75 days, then there are a few more very long-period Cepheids in M31 that could be classified as ULPCs. These are listed in Table 4. They were not reported in Paper I because their periods are lower than the search criterion of $P > 80$ days. Furthermore, there is no *VI*-band photometric data available for these Cepheids currently.

3.3. Distance Scale Application

In the previous sub-section, we adopted a distance modulus for M31 in order to verify the ULPC nature of our candidates. In this sub-section, we reverse the problem by using the two confirmed ULPCs to determine the distance modulus of M31, i.e., $\mu = W - M_W$. The absolute magnitude M_W of the two ULPCs can be determined from the latest PW relation as given in Fiorentino et al. (2012): $M_W = -2.66 \log(P) - 3.68$, with a dispersion of $\sigma = 0.34$. Since the PW relation is a statistical relation, the dispersion of this relation (σ) will dominate the error term of the derived distance modulus for individual ULPCs. Hence, we have adopted the dispersion of the PW relation as the error in the calculated distance moduli for the two M31 ULPCs: $\mu(\text{8-0326}) = 23.70 \pm 0.34$ mag, and $\mu(\text{8-1498}) = 24.91 \pm 0.34$ mag. Since the weights for these two distance moduli are the same, taking an average of them reduces to the case of an unweighted mean. This procedure yielded $\mu_{\rm M31,ULPC} = 24.30 \pm 0.76$ mag, where the error on the averaged distance modulus is calculated using the small number statistics given in Keeping (1962, p. 202). The large error on the determined distance modulus is mainly due to the combination of small number statistics (as there are only two ULPCs found in M31) and the large dispersion of the PW relation for ULPCs.

G. Fiorentino (2014, private communication) suggested using the PW relation derived from ULPCs in metal-rich galaxies (hereafter metal-rich ULPCs). However, the sample of metal-rich ULPCs given in Fiorentino et al. (2012), i.e., those with $12 + \log[\text{O/H}] > 8.4$ dex, only occupied a narrow range in $\log(P)$. This causes the derived PW relation to be unreliable. Instead, we have averaged the absolute Wesenheit magnitudes for this sample of metal-rich ULPCs, yielding $\overline{M_W} = -8.84$ mag. Using this absolute Wesenheit magnitude, the derived distance modulus to M31 with our two ULPCs is $\mu_{\rm M31,ULPC} = 24.42 \pm 0.68$ mag with a (unbiased) standard deviation of 0.76. The value of this distance modulus is almost identical to the value recommended in de Grijs & Bono (2014). Note that the sample of metal-poor ULPCs ($12 + \log[\text{O/H}] < 8.4$ dex) in Fiorentino et al. (2012) is the same as the sample given in Bird et al. (2009). The derived distance modulus is $\mu_{\rm M31,ULPC} = 24.74 \pm 0.68$ mag when using the PW relation given in Bird et al. (2009).

The distance moduli derived using the PW relations given in Fiorentino et al. (2012) and Bird et al. (2009) differed by

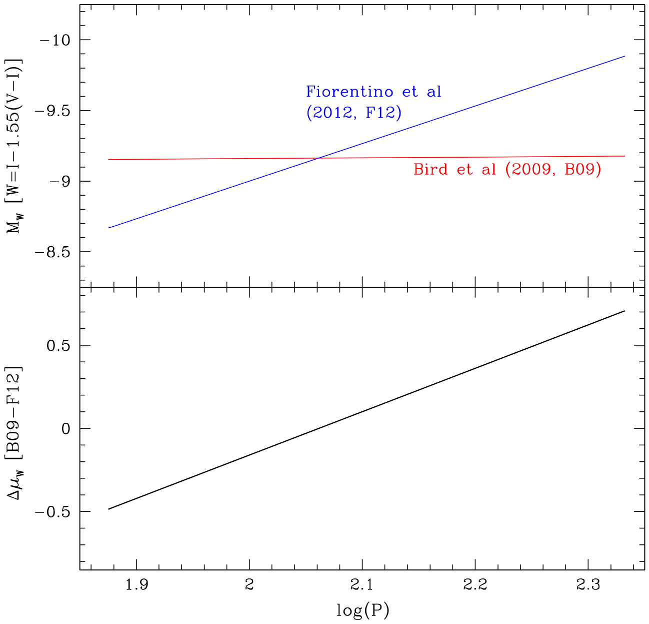

Figure 10. Top: comparison of the two Period–Wesenheit relations adopted from Bird et al. (2009) and Fiorentino et al. (2012); Bottom: difference in the derived distance modulus from these two Period–Wesenheit relations as a function of the ULPC periods.

0.44 mag, albeit with large uncertainties. This reflects one of the current problems in using ULPCs to derive distances: the calibration of the ULPC PW relations is still uncertain with many discrepant results. The slope of the PW relation derived in Bird et al. (2009), based on 18 ULPCs in metal-poor host galaxies, is essentially zero but with a large error (-0.05 ± 0.54). In contrast, the PW slope given in Fiorentino et al. (2012) is -2.66 (though no error on the slope is quoted in their paper). The intercepts of these two PW relations even displayed a larger difference: -9.06 ± 1.12 versus -3.68. The top panel in Figure 10 compares these two PW relations, while the bottom panel shows the difference of the derived distance modulus based on these two PW relations: this can be as large as ~0.5 mag. This disagreement between the two PW relations suggests more work is needed in the future to properly calibrate the ULPC PW relation. Nevertheless, the distance modulus derived from the Fiorentino et al. (2012) PW relation will be adopted in this work, because this PW relation is derived from a larger sample of ULPCs than can be found in the literature. Figure 11 shows a comparison of the adopted distance modulus (based on the two M31 ULPCs) to other distance moduli given in literature. Our calculated distance modulus is consistent with some of recent determinations, including the recommended value of 24.46 ± 0.10 mag (de Grijs & Bono 2014).

We note that the Wesenheit magnitudes and the distance moduli for these two ULPCs differ by ~1 mag. This is not due to the "depth effect," as one ULPC is located at the near-side and another ULPC is located at the far-side of M31 (see Figure 12). Assuming the size of M31 is about 40 kpc, the maximum difference in distance modulus for two stars located at the two extreme edges is ~0.11 mag. This is ~10× smaller than the observed difference. Instead, the observed ~1 mag difference in Wesenheit magnitudes or distance moduli for these two ULPCs is consistent with the spread of M_W at $\log(P) \sim 1.9$, as shown in right panel of Figure 8 (or Figure 2 in Fiorentino et al. 2012), and the expected spread of the PW

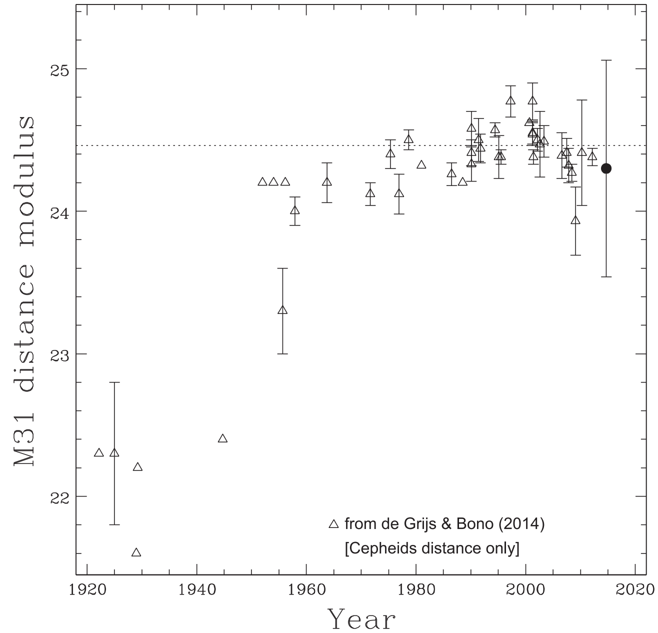

Figure 11. Comparison of the M31 distance modulus based on the two ULPCs in this work ($\mu_{\mathrm{M31,ULPC}} = 24.30 \pm 0.76$ mag, filled circle) to other distance moduli determined using Cepheids (as compiled in de Grijs & Bono 2014, open triangles). Note that some of the distance moduli, especially those in early years, did not include an error estimation. The horizontal dashed line represents the recommended distance modulus of 24.46 mag (de Grijs & Bono 2014).

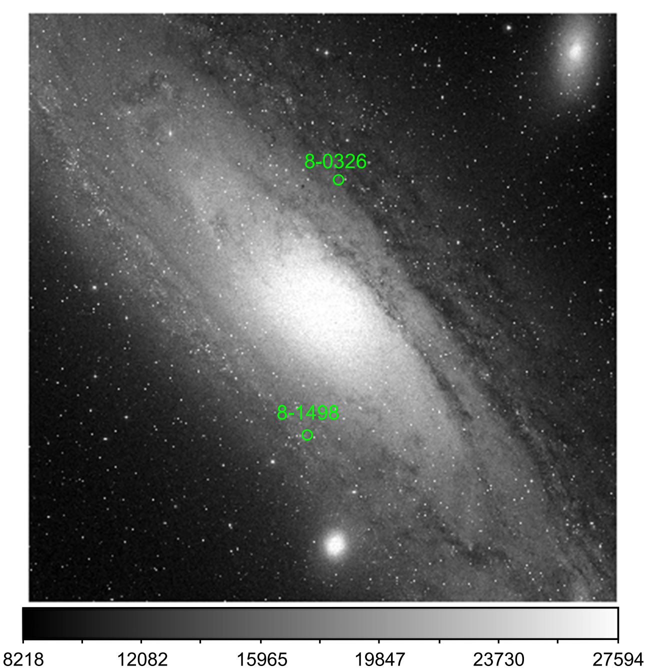

Figure 12. Locations of the two ULPCs in M31. The M31 image, with a size of $60' \times 60'$, was downloaded from the Digitized Sky Surveys (DSS) archive.

relation ($4 \times \sigma = 1.36$ mag). We believe this is due to their relative locations within the instability strip on the CMD, depending on their evolutionary status.[7] Figure 13 compares the locations of the ULPCs in individual galaxies, as listed in Fiorentino et al. (2012), to the locations of the two M31

[7] The evolutionary status of ULPCs could be affected by various physical parameters, such as age, metallicity, mass-loss, etc. However, a detailed investigation of their evolutionary status is beyond the scope of this paper.

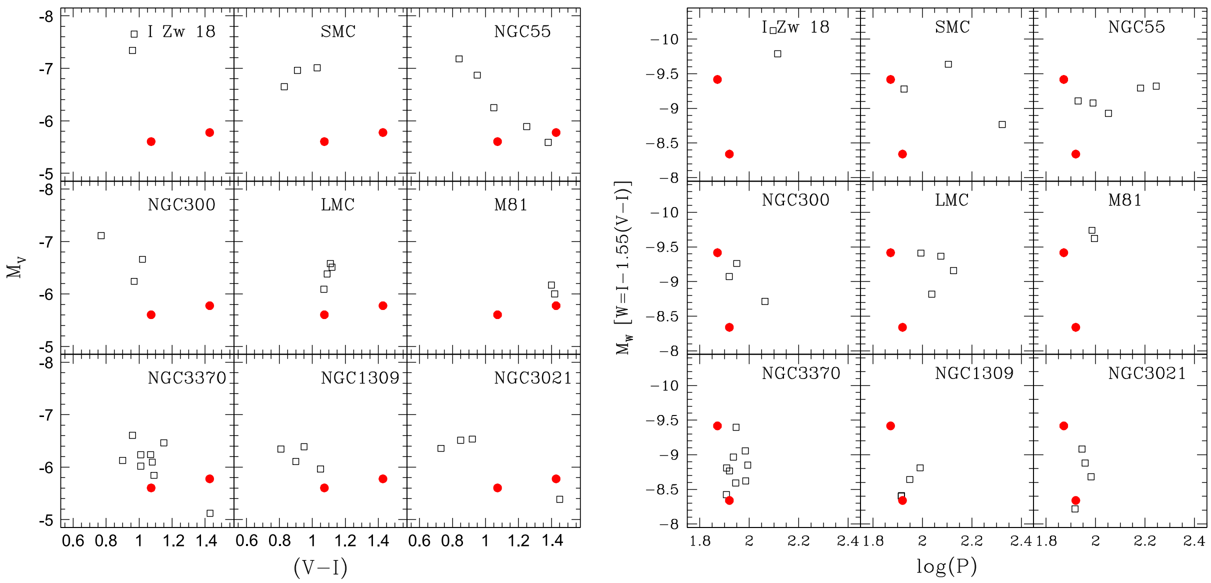

Figure 13. Comparison of the locations of the two M31 ULPCs (red filled circles) with ULPCs in other galaxies (open squares, taken from Fiorentino et al. 2012) in the CMD (left panel) and PWD (right panel). We excluded the ULPC in NGC 6822, as this galaxy has only one ULPC. Note that sub-figures in each panel are ordered according to the metallicity of the host galaxy, which is given in Fiorentino et al. (2012).

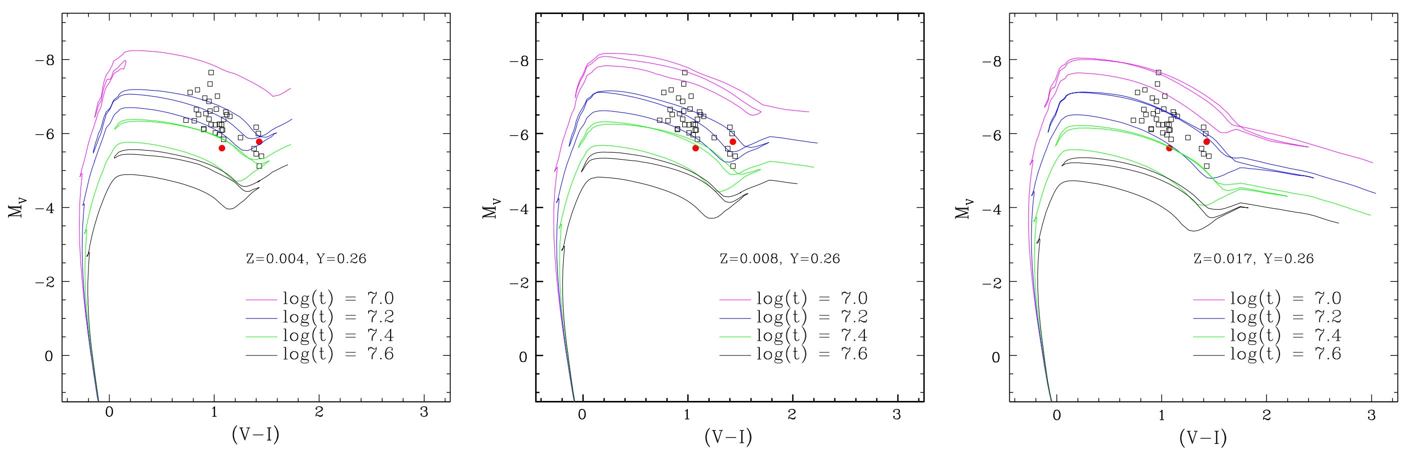

Figure 14. Isochrones at four different ages with three metallicity ($Z = 0.004$ in the left panel; $Z = 0.008$ in the middle panel; and $Z = 0.017$ in the right panel) overplotted on CMD with ULPCs taken from Fiorentino et al. (2012, open squares) and the two M31 ULPCs (red filled circles). These isochrones were taken from Bertelli et al. (2009).

ULPCs in CMD and PWD. This shows that ULPCs in some galaxies (such as NGC 3370 and NGC 3021) exhibit a similar spread in Wesenheit magnitudes as in the case of the M31 ULPCs. The spread of Wesenheit magnitudes, at a given period, can be expressed as $\Delta M_W = \Delta M_I - 1.55\Delta(V - I)$, where ΔM_I and $\Delta(V - I)$ represent the range of magnitudes and colors, respectively, for ULPCs in the same galaxy. Therefore, assuming $\Delta M_I \sim 0$ and a difference of $\Delta(V - I) \sim 0.5$ mag could translate to a difference of $\Delta M_W \sim 0.8$ mag, which is close to the observed spread of M31 ULPCs.[8] This implies that at a given period, the Wesenheit magnitudes or distance moduli for the ULPCs can differ by as much as by $\sim$1 mag. This calls into question the use of ULPCs as standard candles.

[8] To be more specific, using the values give in Table 3, we found that $\Delta I = -0.527$ mag and $\Delta(V - I) = 0.355$ mag for the two M31 ULPCs yielding $\Delta M_W \sim 1.08$ mag as observed.

4. CONCLUSION

In this work, we have presented the *VI*-band follow-up observations of eight ULPC candidates in M31. Based on their light curve shapes and their locations on the CMD and PWD, we verified that two of the candidates are indeed ULPCs, and the remaining six candidates are not ULPCs (and possibly belong to the LPV class). These six non-ULPC candidates also showed that other types of LPV could be misclassified as ULPCs (and vice versa) if they have not had appropriate follow-up observations in the *VI*-bands (see also Ngeow et al. 2013). We then used these two confirmed ULPCs to test their applicability in distance scale work by deriving the distance modulus to M31. Our derived distance modulus is consistent with the recommended value given in the literature, but with a large error of 0.76 mag. We have demonstrated three problems when using ULPCs as a distance indicator.

1. Small number statistics: the number of ULPCs is expected to be small in a host galaxy; hence, the ULPCs do not sample the instability strip well.
2. The discrepancy between PW relations in the literature: the two available PW relations from Bird et al. (2009) and Fiorentino et al. (2012) are in disagreement. As a result, the derived distance moduli can differ by as much as ∼0.5 mag.
3. The large dispersion of the PW relation: the current calibration of PW relation, defined as $W = I - 1.55(V - I)$, for ULPCs still possesses a large dispersion compared to their shorter period counterparts (which is ∼5 × smaller as shown in Ngeow et al. 2009). Furthermore, at a given period, the back-to-back scatter in the PWD can be as large as ∼1 mag.

Combining these three problems with currently available PW relations results in a less precise and accurate distance modulus. As mentioned in Fiorentino's oral presentation[9], ULPCs are not yet ready to be used as a standard candle. Larger samples of ULPCs with well calibrated distance host galaxy distances are needed in order to derive a better PW relation (with smaller σ) before using ULPCs in "one-step" determinations of the Hubble constant in the future.

Regardless of their potential or problems in future distance scale applications, ULPCs represent a unique probe for studies of stellar pulsation and evolution because they occupy the upper part of the instability strip that has attracted little attention to date. Evolutionary tracks based on stellar evolution models appropriate for ULPCs have been explored in Bird et al. (2009) and Fiorentino et al. (2012) and will not be repeated here. In Figure 14, we showed the isochrones adopted from Bertelli et al. (2009)[10] on the CMD, suggesting that ULPCs are young objects as expected. Nevertheless, detailed investigation of the evolutionary status for ULPCs with theoretical evolutionary tracks and isochrones is beyond the scope of this paper and will be addressed in future work.

We thank the referee for valuable input that improved the manuscript. The authors acknowledge funding from the National Science Council of Taiwan under contracts NSC101-2112-M-008-017-MY3 and NSC101-2119-M-008-007-MY3. S.M.K. acknowledges the Indo-U.S. Science and Technology Forum for funding partial work carried out in this project. We also thank C. Broeg for sharing his code to calculate the differential photometry, as well as G. Fiorentino, L. Macri, and J. Mould for valuable discussions. We acknowledge MIAPP (Munich Institute for Astro- and Particle Physics) for organizing the 2014 "Extra-Galactic Distance Scale" Workshop, at which part of this work was conducted.

The Digitized Sky Surveys were produced at the Space Telescope Science Institute under U.S. Government grant NAG W-2166. The images of these surveys are based on photographic data obtained using the Oschin Schmidt Telescope on Palomar Mountain and the UK Schmidt Telescope. The plates were processed into the present compressed digital form with the permission of these institutions.

The National Geographic Society—Palomar Observatory Sky Atlas (POSS-I) was made by the California Institute of Technology with grants from the National Geographic Society.

The Second Palomar Observatory Sky Survey (POSS-II) was made by the California Institute of Technology with funds from the National Science Foundation, the National Geographic Society, the Sloan Foundation, the Samuel Oschin Foundation, and the Eastman Kodak Corporation.

The Oschin Schmidt Telescope is operated by the California Institute of Technology and Palomar Observatory.

The UK Schmidt Telescope was operated by the Royal Observatory Edinburgh, with funding from the UK Science and Engineering Research Council (later the UK Particle Physics and Astronomy Research Council), until 1988 June, and thereafter by the Anglo-Australian Observatory. The blue plates of the southern Sky Atlas and its Equatorial Extension (together known as the SERC-J), as well as the Equatorial Red (ER), and the Second Epoch [red] Survey (SES) were all taken with the UK Schmidt.

Facilities: PO:1.5m

REFERENCES

An, J. H., Evans, N. W., Hewett, P., et al. 2004, MNRAS, 351, 1071
Ansari, R., Aurière, M., Baillon, P., et al. 2004, A&A, 421, 509
Bertelli, G., Nasi, E., Girardi, L., & Marigo, P. 2009, A&A, 508, 355
Bird, J. C., Stanek, K. Z., & Prieto, J. L. 2009, ApJ, 695, 874
Bonanos, A. Z., Stanek, K. Z., Sasselov, D. D., et al. 2003, AJ, 126, 175
Broeg, C., Fernández, M., & Neuhäuser, R. 2005, AN, 326, 134
Cenko, S. B., Fox, D. B., moon, D.-S., et al. 2006, PASP, 118, 1396
Clementini, G., Contreras Ramos, R., Federici, L., et al. 2011, ApJ, 743, 19
Clementini, G., Federici, L., Corsi, C., et al. 2001, ApJL, 559, L109
de Grijs, R., & Bono, G. 2014, AJ, 148, 17
de Grijs, R., Wicker, J. E., & Bono, G. 2014, AJ, 147, 122
Fiorentino, G., Clementini, G., Marconi, M., et al. 2012, Ap&SS, 341, 143
Fliri, J., Riffeser, A., Seitz, S., & Bender, R. 2006, A&A, 445, 423
Fliri, J., & Valls-Gabaud, D. 2012, Ap&SS, 341, 57
Freedman, W. L., & Madore, B. F. 1990, ApJ, 365, 186
Freedman, W. L., Madore, B. F., Gibson, B. K., et al. 2001, ApJ, 553, 47
Joshi, Y. C., Pandey, A. K., Narasimha, D., Sagar, R., & Giraud-Héraud, Y. 2003, A&A, 402, 113
Joshi, Y. C., Narasimha, D., Pandey, A. K., & Sagar, R. 2010, A&A, 512, A66
Kaluzny, J., Stanek, K. Z., Krockenberger, M., et al. 1998, AJ, 115, 1016
Kaluzny, J., Mochejska, B. J., Stanek, K. Z., et al. 1999, AJ, 118, 346
Keeping, E. S. 1962, Introduction to Statistical Inference (Princeton, NJ: Van Nostrand-Reinhold)
Kinoshita, D., Chen, C.-W., Lin, H.-C., et al. 2005, ChJAA, 5, 315
Kodric, M., Riffeser, A., Hopp, U., et al. 2013, AJ, 145, 106
Kodric, M., Riffeser, A., Seitz, S., et al. 2014, arXiv:1405.5218
Lang, D., Hogg, D. W., Mierle, K., Blanton, M., & Roweis, S. 2010, AJ, 139, 1782
Law, N. M., Kulkarni, S. R., Dekany, R. G., et al. 2009, PASP, 121, 1395
Leavitt, H. S., & Pickering, E. C. 1912, HarCi, 173, 1
Lee, C.-H., Ngeow, C.-C., Yang, T.-C., et al. 2013, Proc. 2013 IEEE Int. Conf. on Space Science and Communication (IconSpace2013), ed. M. Abdullah et al. (IEEE Xplore), 1
Lee, C.-H., & Ngeow, C.-C. 2014a, in ASP Conf. Ser. 482, The Tenth Pacific Rim Conference on Stellar Astrophysics, ed. H.-W. Lee, Y. W. Kang, & K.-C. Leung (San Francisco, CA: ASP), 55
Lee, C.-H., Koppenhoefer, J., Seitz, S., et al. 2014b, ApJ, 797, 22
Magnier, E. A., Augusteijn, T., Prins, S., van Paradijs, J., & Lewin, W. H. G. 1997, A&AS, 126, 401
Massey, P., Olsen, K. A. G., Hodge, P. W., et al. 2006, AJ, 131, 2478
Mochejska, B. J., Kaluzny, J., Stanek, K. Z., Krockenberger, M., & Sasselov, D. D. 1999, AJ, 118, 2211
Ngeow, C.-C., Kanbur, S. M., Neilson, H. R., Nanthakumar, A., & Buonaccorsi, J. 2009, ApJ, 693, 691
Ngeow, C.-C., Lucchini, S., Kanbur, S., Barrett, B., & Lin, B. 2013, Proc. 2013 IEEE Int. Conf. on Space Science and Communication (IconSpace2013), ed. M. Abdullah et al. (IEEE Xplore), 7
Pietrzyński, G., Graczyk, D., Gieren, W., et al. 2013, Natur, 495, 76
Rau, A., Kulkarni, S. R., Law, N. M., et al. 2009, PASP, 121, 1334
Riess, A. G., Fliri, J., & Valls-Gabaud, D. 2012, ApJ, 745, 156
Riess, A. G., Macri, L., Casertano, S., et al. 2011, ApJ, 730, 119

[9] At the 2014 "Extra-Galactic Distance Scale" Workshop.
[10] http://stev.oapd.inaf.it/YZVAR/

Schlegel, D. J., Finkbeiner, D. P., & Davis, M. 1998, ApJ, 500, 525
Simon, N. R., & Lee, A. S. 1981, ApJ, 248, 291
Soszynski, I., Poleski, R., Udalski, A., et al. 2008, AcA, 58, 163
Soszynski, I., Udalski, A., Szymañski, M. K., et al. 2009, AcA, 59, 239
Stanek, K. Z., Kaluzny, J., Krockenberger, M., et al. 1998, AJ, 115, 1894
Stanek, K. Z., Kaluzny, J., Krockenberger, M., et al. 1999, AJ, 117, 2810
Udalski, A., Szymanski, M., Kubiak, M., et al. 1999a, AcA, 49, 201
Udalski, A., Soszynski, I., Szymanski, M., et al. 1999b, AcA, 49, 223
Vilardell, F., Jordi, C., & Ribas, I. 2007, A&A, 473, 847
Vilardell, F., Ribas, I., & Jordi, C. 2006, A&A, 459, 321
Vilardell, F., Ribas, I., Jordi, C., Fitzpatrick, E. L., & Guinan, E. F. 2010, A&A, 509, A70

Monthly Notices
of the
ROYAL ASTRONOMICAL SOCIETY

MNRAS **451**, 4060–4072 (2015) doi:10.1093/mnras/stv1187

Ground-based transit observations of the HAT-P-18, HAT-P-19, HAT-P-27/WASP40 and WASP-21 systems

M. Seeliger,[1★] M. Kitze,[1] R. Errmann,[1,2] S. Richter,[1] J. M. Ohlert,[3,4] W. P. Chen,[5] J. K. Guo,[5] E. Göğüş,[6] T. Güver,[7] B. Aydın,[6] S. Mottola,[8] S. Hellmich,[8] M. Fernandez,[9] F. J. Aceituno,[9] D. Dimitrov,[10] D. Kjurkchieva,[11] E. Jensen,[12] D. Cohen,[12] E. Kundra,[13] T. Pribulla,[13] M. Vaňko,[13] J. Budaj,[13,14] M. Mallonn,[15] Z.-Y. Wu,[16] X. Zhou,[16] St. Raetz,[1,17] C. Adam,[1] T. O. B. Schmidt,[1,18] A. Ide,[1] M. Mugrauer,[1] L. Marschall,[19] M. Hackstein,[20] R. Chini,[20,21] M. Haas,[20] T. Ak,[7] E. Güzel,[22] A. Özdönmez,[23] C. Ginski,[1,24] C. Marka,[1] J. G. Schmidt,[1] B. Dincel,[1] K. Werner,[1] A. Dathe,[1] J. Greif,[1] V. Wolf,[1] S. Buder,[1] A. Pannicke,[1] D. Puchalski[25] and R. Neuhäuser[1]

Affiliations are listed at the end of the paper

Accepted 2015 May 22. Received 2015 May 21; in original form 2014 October 7

ABSTRACT

As part of our ongoing effort to investigate transit timing variations (TTVs) of known exoplanets, we monitored transits of the four exoplanets HAT-P-18b, HAT-P-19b, HAT-P-27b/WASP-40b and WASP-21b. All of them are suspected to show TTVs due to the known properties of their host systems based on the respective discovery papers. During the past three years 46 transit observations were carried out, mostly using telescopes of the Young Exoplanet Transit Initiative. The analyses are used to refine the systems' orbital parameters. In all cases we found no hints for significant TTVs, or changes in the system parameters inclination, fractional stellar radius and planet-to-star radius ratio. However, comparing our results with those available in the literature shows that we can confirm the already published values.

Key words: planets and satellites: individual: HAT-P-18b – planets and satellites: individual: HAT-P-19b – planets and satellites: individual: HAT-P-27b/WASP-40b – planets and satellites: individual: WASP-21b.

1 INTRODUCTION

Observing extrasolar planets transiting their host stars has become an important tool for planet detection and is used to obtain and constrain fundamental system parameters: The inclination has to be close to 90°, while the planet-to-star radius ratio is constrained mainly by the transit depth. Also, in combination with spectroscopy, the semimajor axis and the absolute planet and star radii can be obtained.

Several years ago, when the first results of the *Kepler* mission were published (see Borucki et al. 2011 for first scientific results and Koch et al. 2010 for an instrument description), studying the transit timing became one of the standard techniques in the analysis of transit observations. Commonly the mid-time of each transit observation is plotted into an observed minus calculated (O−C) diagram (Ford & Holman 2007), where the difference between the observed transit mid-time and the mid-time obtained using the initial ephemeris is shown versus the observing epoch. In such a diagram, remaining slopes indicate a wrong orbital period, while e.g. periodic deviations from a linear trend indicate perturbing forces. Since space-based missions are able to observe many consecutive transit events with high precision, one can detect even small variations of the transit intervals indicating deviations from a strictly Keplerian motion and thus yet hidden planets in the observed system. Furthermore, with the discovery of multiplanetary systems, transit timing variations (TTVs) are used to find the mass of the companions without the need of radial velocity (RV) measurements due to the influence of planetary interaction on TTVs. Since many planet candidates found in photometric surveys are too faint for RV follow-up even with bigger telescopes, TTV analyses can be considered as a photometric workaround to estimate masses.

Although the existence of TTVs can be shown in already known exoplanetary systems, only a few additional planet candidates have

★ E-mail: martin.seeliger@uni-jena.de

Table 1. The observing telescopes that gathered data within the TTV project for HAT-P-18b, HAT-P-19b, HAT-P-27b/WASP-40b and WASP-21b in order of the number of observed transit events of the Observatory. The table lists the telescopes and corresponding observatories, as well as the telescope diameters ⊘ and number of observed transit events per telescope in this project N_{tr}.

#	Observatory	Telescope (abbreviation)	⊘(*m*)	N_{tr}
1	Michael Adrian Observatory Trebur (Germany)	T1T (Trebur 1.2 m)	1.2	8
2	Graduate Institute of Astronomy Lulin (Taiwan & USA)	Tenagra II (Tenagra 0.8 m)	0.8	5
		RCOS16 (Lulin 0.4 m)	0.4	2
3	University Observatory Jena (Germany)	90/60 Schmidt (Jena 0.6 m)	0.9/0.6	5
		Cassegrain (Jena 0.25 m)	0.25	3
4	TÜBİTAK National Observatory (Turkey)	T100 (Antalya 1.0 m)	1.0	5
5	Calar Alto Astronomical Observatory (Spain)	1.23 m Telescope (CA-DLR 1.2 m)	1.23	4
6	Sierra Nevada Observatory (Spain)	Ritchey-Chrétien (OSN 1.5 m)	1.5	2
7	Peter van de Kamp Observatory Swarthmore (USA)	RCOS (Swarthmore 0.6 m)	0.6	2
8	National Astronomical Observatory Rozhen (Bulgaria)	Ritchey-Chrétien-Coudé (Rozhen 2.0 m)	2.0	1
		Cassegrain (Rozhen 0.6 m)	0.6	1
9	Teide Observatory, Canarian Islands (Spain)	STELLA-I (Stella 1.2 m)	1.2	2
10	University Observatory Bochum (Cerro Armazones, Chile)	VYSOS6 (Chile 0.15 m)	0.15	1
11	Xinglong Observing Station (China)	90/60 Schmidt (Xinglong 0.6 m)	0.9/0.6	1
12	Gettysburg College Observatory (USA)	Cassegrain (Gettysburg 0.4 m)	0.4	1
13	Stará Lesná Observatory (Slovak Rep.)	0.5 m Reflector (StaraLesna 0.5 m)	0.5	1
14	Istanbul University Telescope at Çanakkale (Turkey)	0.6 m Telescope (Çanakkale 0.6 m)	0.6	1
15	Toruń Centre for Astronomy (Poland)	0.6 m Cassegrain Telescope (Torún 0.6 m)	0.6	1

been found using TTVs so far. One of the most prominent examples is the KOI-142 system. By analysing the TTV signals of KOI-142b, Mazeh et al. (2013) suggested the existence of additional planets in the system. Later on, Nesvorný et al. (2013) proposed a non-transiting planet KOI-142c that was confirmed using RV measurements by Barros et al. (2014). Regarding ground-based analyses e.g. Maciejewski et al. (2011a) and von Essen (2013) found indications of TTVs potentially induced by additional planets. The lack of confirmed TTV planets is not surprising, since large bodies often can be found using RV measurements or direct transit detections, while small (e.g. Earth-like) objects result in small TTV amplitudes and therefore high-precision timing measurements are needed. However, these measurements can already be acquired with medium size ground-based telescopes.

Besides the discovery of small planets, the amount of known massive planets on close-in orbits increased as well. First studies on a larger sample of planet candidates detected with *Kepler* suggest that hot giant planets exist in single planet systems only (Steffen et al. 2012). However, Szabó et al. (2013) analysed a larger sample of *Kepler* hot Jupiters and found a few cases where TTVs cannot be explained by other causes (e.g. artificial sampling effects due to the observing cadence) but the existence of perturbers – additional planets or even exomoons – in the respective system. In addition, Szabó et al. (2013) point towards the planet candidates KOI-338, KOI-94 and KOI-1241, who are all hot Jupiters in multiplanetary systems, as well as the WASP-12 system with a proposed companion candidate found by ground-based TTV analysis (Maciejewski et al. 2011a).

The origin of those planets is yet not fully understood. One possible formation scenario shows that close-in giant planets could have migrated inwards after their creation further out (Steffen et al. 2012). In that case, inner and close outer planets would have either been thrown out of the system, or caught in resonance. In the latter case, even small perturbing masses, e.g. Earth-mass objects, can result in TTV amplitudes in the order of several minutes (see Ford & Holman 2007 or Seeliger et al. 2014). Though *Kepler* is surveying many of those systems, it is necessary to look at the most promising candidates among all close-in giant planets discovered so far. Since many of the stars observed with *Kepler* are too faint to perform RV follow-up, investigating stars outside the field of view (FoV) of *Kepler*, e.g. objects found by HATnet (Bakos et al. 2004) or the WASP project (Pollacco et al. 2006), is advisable. In our ongoing study[1] of TTVs in exoplanetary systems we perform photometric follow-up observations of specific promising transiting planets where additional bodies are expected. The targets are selected by the following criteria.

(i) There is an indication for a perturber in the system, e.g. a non-zero eccentricity in the orbital solution of the known transiting planet (though the circularization time-scale is much shorter than the system age) or deviant RV data points.

(ii) The brightness of the host star is $V \leq 13$ mag and the transit depth is at least 10 mmag to ensure sufficient photometric and timing precision at 1–2 m class ground-based telescopes.

(iii) The target is visible from the Northern hemisphere.

(iv) The target has not been studied for TTV signals before.

In the past the transiting exoplanets WASP-12b (Maciejewski et al. 2011a, 2013b), WASP-3b (Maciejewski et al. 2010, 2013a), WASP-10b (Maciejewski et al. 2011b; Maciejewski et al., in preparation) , WASP-14b (Raetz 2012; Raetz et al. 2015), TrES-2 (Raetz et al. 2014) and HAT-P-32b (Seeliger et al. 2014) have been studied by our group in detail. In most cases, except for WASP-12b, no TTVs could be confirmed.

Here, we extend our investigations to search for TTVs in the HAT-P-18, HAT-P-19, HAT-P-27/WASP-40 and WASP-21 planetary systems. In Section 2, we give a short description of the targets analysed within this project. Section 3 explains the principles of data acquisition and reduction and gives an overview of the telescopes used for observation. The modelling procedures are described in Section 4, followed by the results in Section 5. Finally, Section 6 gives a summary of our project.

[1] see http://ttv.astri.umk.pl/doku.php for a project overview.

Table 2. The list of all transit observations gathered within the TTV project sorted by object and date. Though no pre-selections for quality or completeness have been applied to this list, transits used for further analysis have been marked by an asterisk. The filter subscripts B, C and J denote the photometric systems of Bessel, Cousins and Johnson, respectively. The last column lists the number of exposures and the exposure time of each observation.

#	Date	Telescope	Filter	Exposures
		HAT-P-18b		
1*	2011-04-21	Trebur 1.2 m	R_B	189 × 90 s
2	2011-05-02	Trebur 1.2 m	R_B	123 × 45 s
3*	2011-05-24	Trebur 1.2 m	R_B	323 × 60 s
4	2011-06-04	Rozhen 2.0 m	R_C	1000 × 10 s
5*	2012-05-05	Rozhen 0.6 m	I_C	219 × 90 s
6	2012-06-07	CA DLR 1.23 m	B_J	250 × 60 s
7	2013-04-28	Antalya 1.0 m	R	214 × 50 s
8	2014-03-30	Toruń 0.6 m	Clear	297 × 40 s
		HAT-P-19b		
9*	2011-11-23	Jena 0.6 m	R_B	246 × 50 s
10	2011-11-23	Jena 0.25 m	R_B	320 × 50 s
11	2011-11-23	Trebur 1.2 m	R_B	461 × 30 s
12	2011-12-05	Jena 0.6 m	R_B	129 × 60 s
13	2011-12-05	Jena 0.25 m	V_B	28 × 300 s
14*	2011-12-09	Jena 0.6 m	R_B	290 × 50 s
15	2011-12-09	Jena 0.25 m	V_B	118 × 150 s
16	2011-12-09	Trebur 1.2 m	R_B	380 × 35 s
17*	2011-12-17	CA DLR 1.23 m	R_J	273 × 60 s
18	2014-08-01	Antalya 1.0 m	R	148 × 60 s
19	2014-08-05	Antalya 1.0 m	R	196 × 40 s
20	2014-08-21	Jena 0.6 m	R_B	152 × 50 s
21*	2014-10-04	Jena 0.6 m	R_B	280 × 50 s
		HAT-P-27b		
22*	2011-04-05	Lulin 0.4 m	R_B	166 × 40 s
23*	2011-04-08	Lulin 0.4 m	R_B	250 × 40 s
24	2011-05-03	Stella 1.2 m	Hα	180 × 100 s
25*	2011-05-05	Trebur 1.2 m	R_B	162 × 70 s
26	2011-05-08	Stella 1.2 m	Hα	190 × 100 s
27	2011-05-21	Tenagra 0.8 m	R	141 × 40 s
28	2012-03-07	StaraLesna 0.5 m	R	361 × 30 s
29	2012-03-29	Tenagra 0.8 m	R	240 × 30 s
30	2012-04-01	Tenagra 0.8 m	R	329 × 20 s
31	2012-04-04	Tenagra 0.8 m	R	333 × 20 s
32	2012-04-25	Xinglong 0.6 m	R	154 × 40 s
33	2012-05-16	Trebur 1.2 m	R_B	231 × 70 s
34	2012-05-25	Chile 0.15 m	I_J/R_J	220 × 80 s
35	2012-06-13	Tenagra 0.8 m	R	223 × 15 s
36*	2013-06-03	Antalya 1.0 m	R	156 × 60 s
37*	2013-06-03	OSN 1.5 m	R	435 × 30 s
38	2013-06-06	CA DLR 1.23 m	R_J	172 × 60 s
39*	2014-06-18	Antalya 1.0 m	R	146 × 50 s
		WASP-21b		
40*	2011-08-24	Swarthmore 0.6 m	R_B	545 × 45 s
41	2011-08-24	Gettysburg 0.4 m	R	230 × 60 s
42*	2012-08-16	Trebur 1.2 m	R_B	365 × 40 s
43	2012-10-20	Antalya 1.0 m	R	242 × 40 s
44*	2013-09-18	CA DLR 1.23 m	R_J	584 × 30 s
45	2013-09-22	Antalya 1.0 m	R	208 × 50 s
46	2013-09-22	Ulupinar 0.6 m	R_B	163 × 110 s

2 TARGETS

2.1 HAT-P-18b and HAT-P-19b

Hartman et al. (2011) reported on the discovery of the exoplanets HAT-P-18b and HAT-P-19b. The two Saturn-mass planets orbit their early K-type host stars with periods of 5.51 and 4.01 d, respectively.

In the case of HAT-P-18b, Hartman et al. (2011) found the eccentricity to be slightly non-zero ($e = 0.084 \pm 0.048$). Recent studies of Esposito et al. (2014) found the eccentricity to be consistent with a non-eccentric retrograde orbit by analysing the Rossiter–McLaughlin effect. Knutson et al. (2014) also analysed the RV signal and found a jitter of the order of 17.5 m s^{-1} that remains unexplained. Ginski et al. (2012) presented the results of the lucky imaging campaign with AstraLux at the Calar Alto 2.2 m Telescope to search for additional low-mass stellar companions in the system. With the data gathered in this previous study objects down to a mass of $0.140 \pm 0.022\,M_\odot$ at angular separations as small as 0.5 arcsec and objects down to $0.099 \pm 0.008\,M_\odot$ outside of 2 arcsec could already be excluded. In addition to this study, we performed follow-up observations of HAT-P-18b planetary transits, as well as a monitoring project of the planet host star over a longer time span to possibly find overall brightness variations.

For HAT-P-19b, a small eccentricity of $e = 0.067 \pm 0.042$ was determined by Hartman et al. (2011). They also found a linear trend in the RV residuals pointing towards the existence of a long-period perturber in the system. Within this project we want to address the problem of the proposed perturber using photometric methods, i.e. follow-up transit events to find planetary induced TTV signals.

2.2 HAT-P-27b/WASP-40b

HAT-P-27b (Béky et al. 2011), independently discovered as WASP-40b by Anderson et al. (2011) within the WASP-survey (Pollacco et al. 2006), is a typical hot Jupiter with a period of 3.04 d. While the eccentricity was found to be $e = 0.078 \pm 0.047$ by Béky et al. (2011), Anderson et al. (2011) adopted a non-eccentric orbit. However, the latter authors found a huge spread in the RV data with up to 40 m s^{-1} deviation from the circular single planet solution. According to Anderson et al. (2011) one possible explanation, despite a changing activity of the K-type host star, is the existence of a perturber that might not be seen in the Béky et al. (2011) data due to the limited data set. However, the authors suggest further monitoring to clarify the nature of the system. One possibility is to study the companion hypothesis from the TTV point of view.

Another interesting aspect is the transit shape of HAT-P-27b. With an increasing impact parameter $b = a/R_s \cos i$, the typical flat bottom phase of the box-shaped transit becomes shorter and even vanished completely for grazing transit events (V-shaped transit). The data of Béky et al. (2011) show a flat bottom phase, while the best-fitting solutions of Anderson et al. (2011) and Sada et al. (2012) point towards a V-shape. The latter ones found that there is a high probability that the system is grazing using the grazing criterion (Smalley et al. 2011). Though this would explain the unusual shape of the transit, the impact parameter of the U-shaped transit seen by Béky et al. (2011) ($b = 0.89$) lies between the one derived by Anderson et al. (2011) and Sada et al. (2012) ($b = 0.86$ and $b = 0.92$, respectively). New high-quality observations of HAT-P-27b planetary transits could be used to further constrain the real system configuration.

Table 3. The input parameters for the JKTEBOP and TAP runs for all objects listed in Section 2. All values have been obtained from the original discovery papers. LD coefficients are taken from Claret & Bloemen (2011) linear interpolated in terms of T_{eff}, log *g* and [Fe/H] using the EXOFAST/QUADLD code (Eastman et al. 2013). Free parameters are marked by an asterisk. At the bottom the duration of ingress and egress according to Winn (2010) has been added.

Object	HAT-P-18b	HAT-P-19b	HAT-P-27b	WASP-21b
$r_p + r_s$*	0.0575(19)	0.0709(33)	0.1159(65)	0.0959(44)
R_p/R_s*	0.1365(15)	0.1418(20)	0.1186(31)	0.1040(35)
i (°)*	88.8(3)	88.2(4)	84.7(7)	88.75(84)
a/R_s*	16.04(75)	12.24(67)	9.65(54)	10.54(48)
M_p/M_s	0.000 243(26)	0.000 329(37)	0.000 663(58)	0.000 282(19)
e	0.084(48)	0.067(42)	0.078(47)	0
P (d)	5.508 0023(06)	4.008 778(06)	3.039 586(12)	4.322 482(24)
R (mag)	12.61	12.82	11.98	11.52
T_{eff} (K)	4803(80)	4990(130)	5300(90)	5800(100)
log *g* (cgs)	4.57(04)	4.54(05)	4.51(04)	4.2(1)
[Fe/H] (dex)	+0.10(08)	+0.23(08)	+0.29(10)	– 0.46(11)
$v\sin i$ (km s^{-1})	0.5(5)	0.7(5)	0.4(4)	1.5(6)
LD law of the star	Quadratic	Quadratic	Quadratic	Quadratic
R band linear*	0.5736	0.5433	0.4808	0.3228
R band non-linear*	0.1474	0.1710	0.2128	0.2982
V band linear*	0.7180	0.6783	0.6002	0.4055
V band non-linear*	0.0697	0.1039	0.1643	0.2892
$\tau_{\mathrm{egress/ingress}}$ (min)	22.8	23.1	37.8	20.1

2.3 WASP-21b

The planetary host star WASP-21, with its Saturn-mass planet on a 4.32 d orbit discovered by Bouchy et al. (2010), is one the most metal-poor planet hosts accompanied by one of the least dense planets discovered by ground-based transit searches to date. Bouchy et al. (2010) found that including a small non-zero eccentricity to the fit does not improve the results. Hence, they concluded that the eccentricity is consistent with zero.

In a later study, Barros et al. (2011) found the G3V star to be in the process of moving off the main sequence. Hence, though the WASP-21 system does not match our criteria concerning the expectations for additional bodies in the system, we included further observations of WASP-21b planetary transits to improve the knowledge on this system.

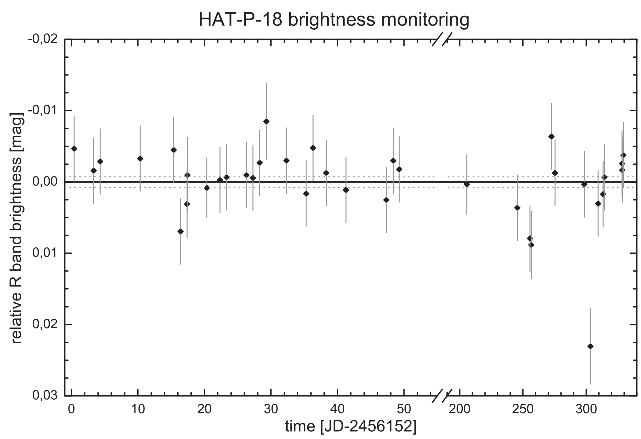

Figure 1. Relative *R*-band brightness of the star HAT-P-18 over a time span of 12 months. The dotted line represents the rms of a constant fit.

3 DATA ACQUISITION AND REDUCTION

Our observations make use of YETI network telescopes (Young Exoplanet Transit Initiative; Neuhäuser et al. 2011), a worldwide network of small- to medium-size telescopes mostly on the Northern hemisphere established to explore transiting planets in young open clusters.

A summary of all participating telescopes and the number of performed observations can be found in Table 1. Most of the observing telescopes are part of the YETI network. This includes telescopes at Cerro Armazones (Chile, operated by the University of Bochum), Gettysburg (USA), Jena (Germany), Lulin (Taiwan), Rozhen (Bulgaria), Sierra Nevada (Spain), Stará Lesná (Slovak Republic), Swarthmore (USA), Tenagra (USA, operated by the National Central University of Taiwan) and Xinglong (China). For details about location, mirror and chip, see Neuhäuser et al. (2011).

In addition to the contribution of the YETI telescopes, we obtained data using the following telescopes:

(i) the 1.2 m telescope of the German–Spanish Astronomical Center on Calar Alto (Spain), which is operated by German Aerospace Center (DLR);

(ii) the 1.2 m robotic telescope STELLA-I, situated at Teide Observatory on Tenerife (Spain) and operated by the Leibnitz-Institut für Astrophysik Potsdam;

(iii) the Trebur 1 Meter Telescope operated at the Michael Adrian Observatory Trebur (Germany);

(iv) the T100 telescope of the TÜBITAK National Observatory (Turkey);

(v) the 0.6 m telescope (CIST60) at Ulupınar Observatory operated by Istanbul University (Turkey);

(vi) the 0.6 m Cassegrain telescope of the Toruń Centre for Astronomy (Poland).

Besides the transit observations, the Jena 0.6 m telescope with its Schmidt Teleskop Kamera (Mugrauer & Berthold 2010) was used to perform a long term monitoring of HAT-P-18 as described in Sections 2.1 and 5.1.

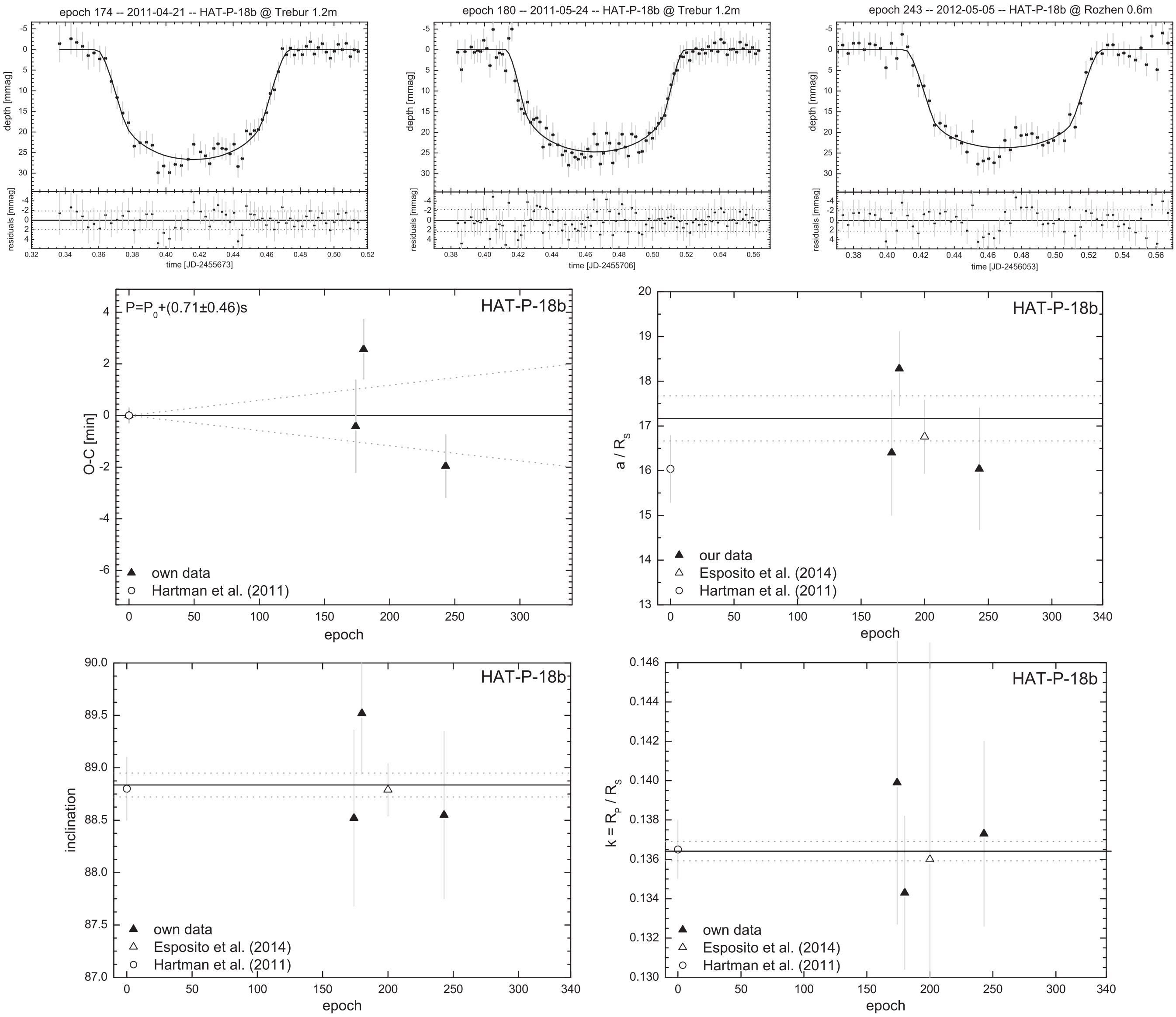

Figure 2. Top: the threefold binned transit light curves of the three complete transit observations of HAT-P-18b. The upper panels show the light curve, the lower panels show the residuals. The rms of the fit of the threefold binned light curves (dotted lines) are shown as well. Bottom: the present result for the HAT-P-18b observing campaign, including the O−C diagram, as well as the results for the reverse fractional stellar radius a/R_s, the inclination i and the planet-to-star radius ratio k. The open circle denotes literature data from Hartman et al. (2011) and the open triangles denote data from Esposito et al. (2014). Filled triangles denote our data (from Trebur and Rozhen). The dotted line shows the 1σ error bar of the constant fit .

Between 2011 April and 2013 June our group observed 46 transit events (see Table 2) using 18 different telescopes (see Table 1). 16 observations could be used for further analysis, while 30 observations had to be rejected due to several reasons, e.g. no full transit event has been observed or bad weather conditions and hence low signal to noise. For example, Southworth et al. (2009a, 2009b) showed that defocusing the telescope allows us to reduce flat fielding effects. Since the light of a star is spread over a larger amount of pixels and more light is gathered due to a longer exposure time, seeing effects are reduced as well as photon noise. Since a defocused image spreads the light over several CCD pixel, one can increase the exposure time and hence the effective duty cycle of the CCD assuming a constant read out time (as mentioned also in the conclusions of Barros et al. 2011). Thus we tried to defocus the telescope and increase the exposure time during all our observations. Table 3 lists the ingress/egress durations τ derived using the formulas (18) and (19) given in Winn (2010). With our strategy we obtain at least one data point within 90 s. This ensures to have at least 10 data points during ingress/egress phase which is required to fit the transit model to the data and get precise transit mid-times.

All data have been reduced in a standard way by applying dark/bias and flat-field corrections using IRAF.[2] The respective calibration images have been obtained in the same night and

[2] IRAF is distributed by the National Optical Astronomy Observatories, which are operated by the Association of Universities for Research in Astronomy, Inc., under cooperative agreement with the National Science Foundation.

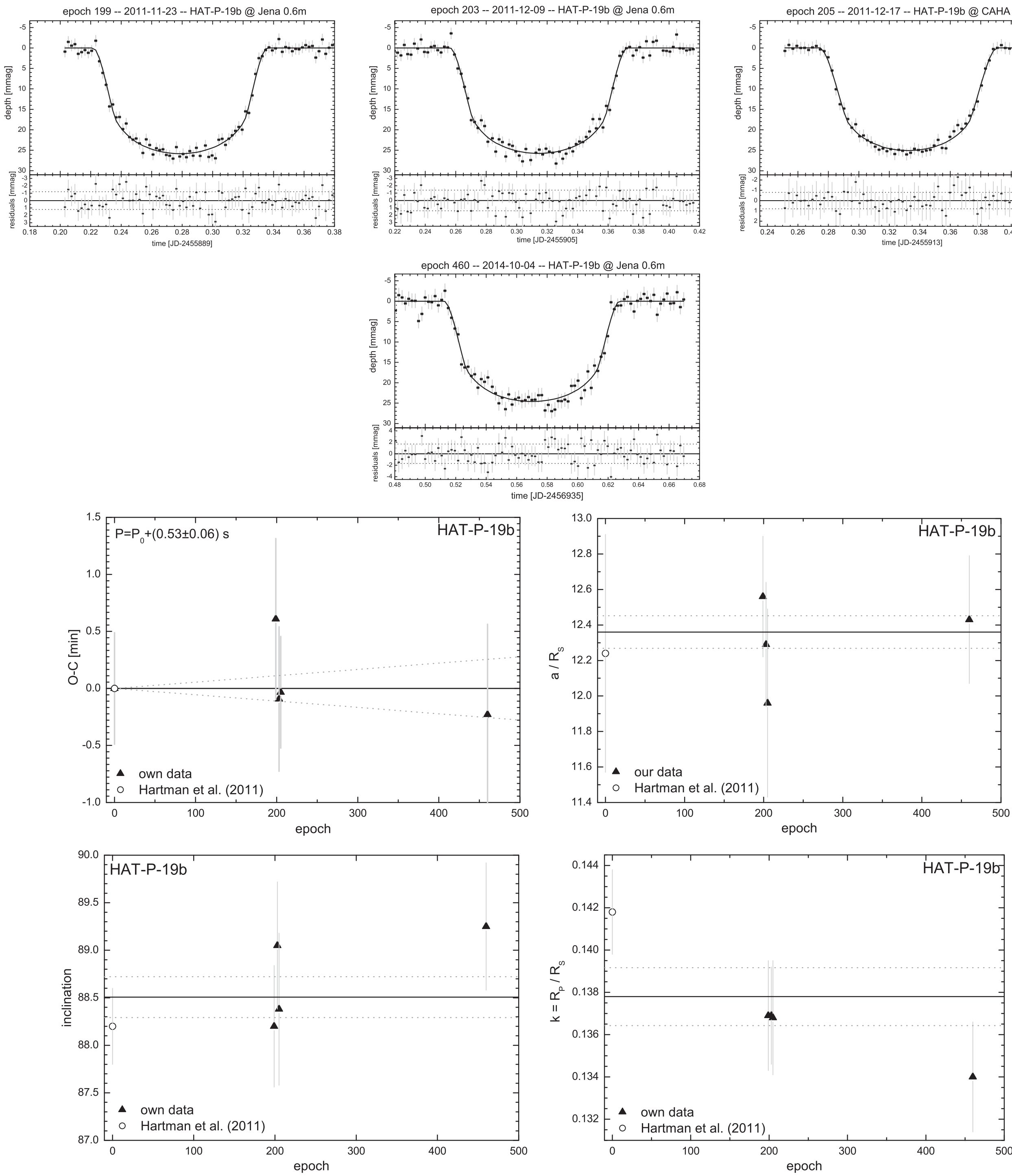

Figure 3. Top: the transit light curves obtained for HAT-P-19b. Bottom: the present result for the HAT-P-19b observing campaign. All explanations are equal to Fig. 2. The open circle denotes literature data from Hartman et al. (2011) and filled triangles denote our data (from Jena and Calar Alto).

with the same focus as the scientific observations. This is necessary especially if the pointing of the telescope is not stable. When using calibration images obtained with different foci, patterns remain in the images that lead to distortions in the light curve.

Besides our own observations, we also use literature data. This involves data from the respective discovery papers mentioned in Section 2, as well as data from Esposito et al. (2014) in the case of HAT-P-18b, Sada et al. (2012) in the case of HAT-P-27b, Barros et al. (2011) and Ciceri et al. (2013) for WASP-21b, and Simpson et al. (2010) for WASP-38b.

4 ANALYSES

The light-curve extraction and modelling is performed analogous to the procedure described in detail in Seeliger et al. (2014).

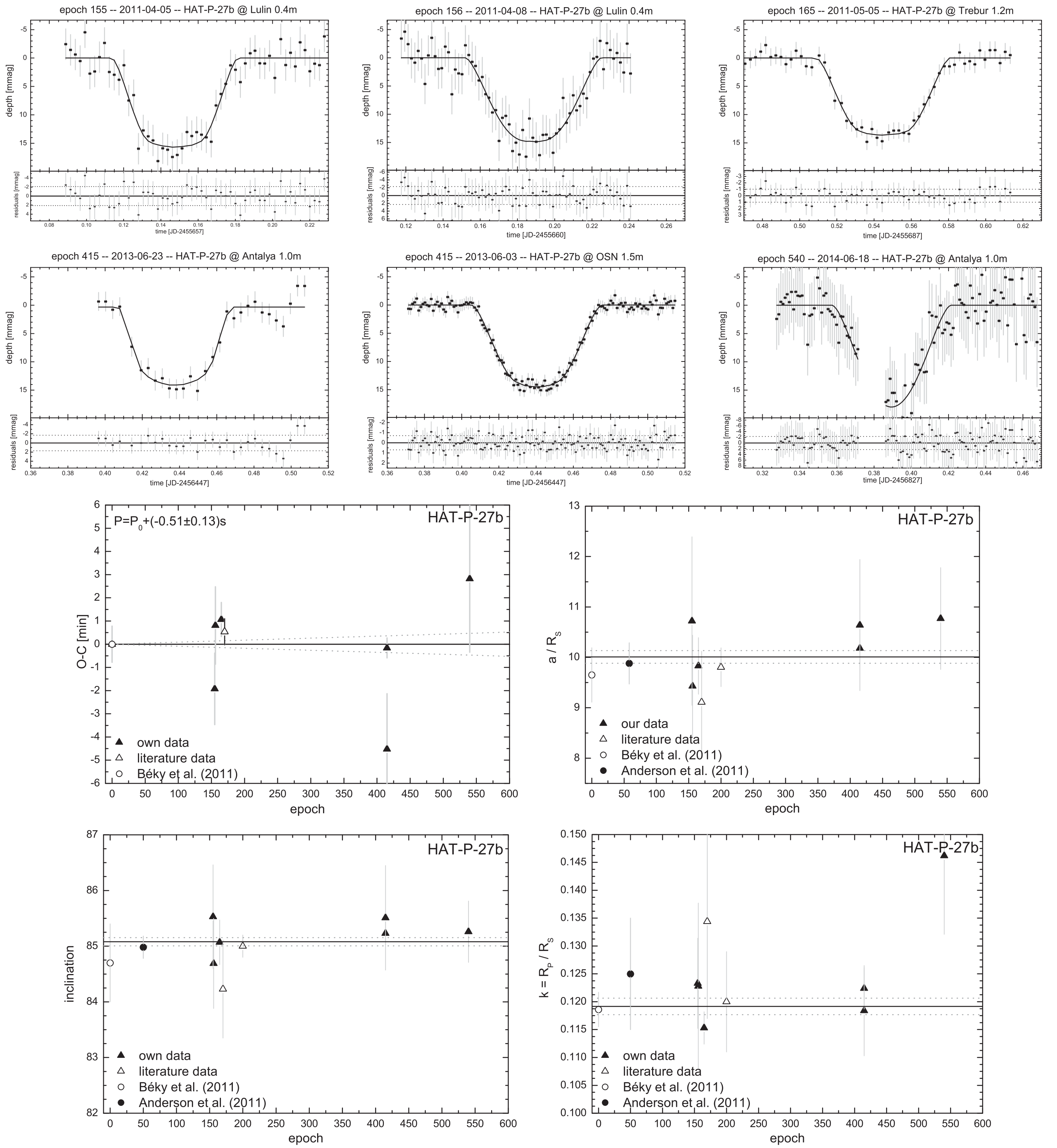

Figure 4. Top: the transit light curves obtained for HAT-P-27b. Bottom: the present result for the HAT-P-27b observing campaign. All explanations are equal to Fig. 2. The open circles denote data from the discovery papers of Béky et al. (2011) and Anderson et al. (2011), open triangles denote literature data from Sada et al. (2012) and Brown et al. (2012) (the latter one set to epoch 200 artificially), filled triangles denote our data (from Lulin, Trebur, Xinglong and Antalya).

4.1 Light-curve extraction

The Julian date of each image is calculated from the header information of the start of the exposure and the exposure time. To precisely determine the mid-time of the transit event, these pieces of information have to be stored most accurate. The reliability of the final light-curve model thus also depends on a precise time synchronization of the telescope computer system. Since all data are obtained using JD_{UTC} as time base, we transform the fitted mid-transit times to BJD_{TDB} afterwards using the online converter[3] provided by

[3] http://astroutils.astronomy.ohio-state.edu/time/utc2bjd.html

Table 4. Impact parameters of HAT-P-27b planetary transits.

Observation epoch	Impact parameter
155 – Lulin 0.4 m	0.84 ± 0.30
156 – Lulin 0.4 m	0.87 ± 0.23
165 – Trebur 1.2 m	0.84 ± 0.12
415 – Antalya 1.0 m	0.81 ± 0.27
415 – OSN 1.5 m	0.85 ± 0.06
540 – Antalya 1.0 m	0.89 ± 0.19
Our analysis combined	0.859 ± 0.023
Béky et al. (2011)	0.89 ± 0.17
Anderson et al. (2011)	0.86 ± 0.07
Sada et al. (2012)	0.92 ± 0.24
Brown et al. (2012)	0.85 ± 0.07

Jason Eastman (for a detailed description of the barycentric dynamical time see Eastman, Siverd & Gaudi 2010).

We use differential aperture photometry to extract the light curve from the reduced images by measuring the brightness of all bright stars in the field with routines provided by IRAF. The typical aperture radius is ≈1.5 times the mean full width half-maximum of all stars in the FoV. The best-fitting aperture is found by manually varying the aperture radius by a few pixels to minimize the photometric scatter. The final light curve is created by comparing the star of interest against an artificial standard star composed of the (typically 15–30) brightest stars in the FoV weighted by their respective constantness as introduced by Broeg, Fernández & Neuhäuser (2005).

The final photometric errors are based on the instrumental IRAF measurement errors. The error of the constant comparison stars are rescaled by their photometric scatter using shared scaling factors in order to achieve a mean $\chi^2_{\rm red} \approx 1$ for all comparison stars. The error bars of the transit star are rescaled afterwards using the same scaling factors (for further details on the procedure, see Broeg et al. 2005).

Trends in light curves induced by atmospheric effects can impact the determination of transit parameters. To eliminate such effects we start the observation about 1 h before and finish about 1 h after the transit itself. Thus we can detrend the observations by fitting a second-order polynomial to the out-of-transit data.

4.2 Modelling with TAP and JKTEBOP

To model the light curves we used the Transit Analysis Package (TAP, version v2.104; Gazak et al. 2012). The modelling of the transit light curve is done by using the EXOFAST routines (Eastman, Gaudi & Agol 2013) with the light-curve model of Mandel & Agol (2002). For error estimation TAP uses Markov Chain Monte Carlo simulations (in our case 10 times 10^5 MCMC chains) together with wavelet-based likelihood functions (Carter & Winn 2009). The coefficients for the quadratic limb-darkening (LD) law used by TAP are taken from the EXOFAST/QUADLD-routine of Eastman et al. (2013)[4] that linearly interpolates the LD tables of Claret & Bloemen (2011).

For comparison we also use JKTEBOP (version 25, see Southworth 2008, and references therein) which is based on the EBOP code for eclipsing binaries (Etzel 1981; Popper & Etzel 1981). To compare the results with those obtained with TAP, we only use a quadratic LD law which is sufficient for ground-based data. For error estimation we used Monte Carlo simulations (task #7, 10^4 runs), bootstrapping (task #8, 10^4 data sets) and a residual shift method (task #9) as provided by JKTEBOP.

As input values for the modelling we take the system properties presented in the respective discovery papers (see Table 3 for a summary). As free parameters we use the mid-transit time $T_{\rm mid}$, inclination i, and planet-to-star radius ratio $k = r_{\rm p}/r_{\rm s}$ (with $r_{\rm p}$ and $r_{\rm s}$ being the planet and stellar radius scaled by the semimajor axis, respectively). In the case of TAP, the inverse fractional stellar radius $a/R_{\rm s} = 1/r_{\rm s}$, in the case of JKTEBOP the sum of the fractional radii $(r_{\rm p} + r_{\rm s})$ is fitted as well. Both quantities are an expression of the transit duration and can be transformed into each other according to the following equation:

$$a/R_{\rm s} = \left(1 + r_{\rm p}/r_{\rm s}\right) / \left(r_{\rm p} + r_{\rm s}\right) .$$

The fitting procedure is applied two times. First, keeping the LD coefficients fixed at their theoretical values, and afterwards letting them vary. For TAP we set the fitting interval to ±0.2. In the case of JKTEBOP, we use the option to set the LD coefficients fixed for the initial model, but let them being perturbed for the error estimation. Thus the fitted model does not change, but the error bars are increased. The eccentricity was fixed to zero for all our analyses.

Finally, we derive the photometric noise rate (pnr; Fulton et al. 2011) as a quality marker for all light curves, which is defined as the ratio between the root mean square of the model fit and the number of data points per minute. For further analysis, we took data with pnr $\lesssim$4.5 into account which corresponds to a timing precision of $\Delta T_{\rm mid} \approx 90$ s.

5 RESULTS

For every light curve, we get three different models, two from TAP (for the model with the LD coefficients fixed and free, respectively) and one from JKTEBOP (LD coefficients set free for error estimation only). To get one final result for every transit event, we averaged those three results. As for the errors, we got two different estimations from TAP and six from JKTEBOP. As final error value, we took the maximum of either the largest of the error estimates, or the spread of the model fit results to use a conservative error estimate. It has to be noted, though, that the spread between the different models has always been below size of the error bars.

The same counts for the differences between the TAP models obtained with fixed LD values and those obtained with the LD coefficients set free to fit. For a detailed discussion of the influence of the LD model on transit light curves, see e.g. Raetz et al. (2014).

The redetermination of the system parameters is performed with ORIGIN 6.0 (OriginLab, Northampton, MA). In order to find possible deviations from a constant value, we use the internally provided linear fitting function with a fixed slope of zero on all single results obtained for a given target and property. The individual model errors are taken as instrumental weights during the χ^2-minimization fitting procedure.

5.1 HAT-P-18b

Over a timespan of 12 months, we obtained three images in four bands (B, V, R, I) in each clear night using the Jena 0.6 m telescope in order to look at the long-term variability of the parent star. As shown in Fig. 1, the mean variation of the R-band brightness is ≈0.9 mmag taking the individual error bar of the measurements into account. The result is in agreement with no variation.

[4] The LD calculator is available online at http://astroutils.astronomy.ohio-state.edu/exofast/limbdark.shtml.

Table 5. A comparison between the results obtained in Our analysis and the literature data. All epochs T_0 are converted to BJD_{TDB}.

	T_0 (d)	P (d)	a/R_s	$k = R_p/R_s$	i (°)
		HAT-P-18b			
Our analysis	$2454\,715.022\,54 \pm 0.000\,39$	$5.508\,0291 \pm 0.000\,0042$	17.09 ± 0.71	0.1362 ± 0.0011	88.79 ± 0.21
Hartman et al. (2011)	$2454\,715.022\,51 \pm 0.000\,20$	$5.508\,023 \pm 0.000\,006$	16.04 ± 0.75	0.1365 ± 0.0015	88.3 ± 0.3
Esposito et al. (2014)	$2455\,706.7 \pm 0.7$	$5.507\,978 \pm 0.000\,043$	16.76 ± 0.82	0.136 ± 0.011	88.79 ± 0.25
		HAT-P-19b			
Our analysis	$2455\,091.535\,00 \pm 0.000\,15$	$4.008\,7842 \pm 0.000\,0007$	12.36 ± 0.09	0.1378 ± 0.0014	88.51 ± 0.22
Hartman et al. (2011)	$2455\,091.534\,94 \pm 0.000\,34$	$4.008\,778 \pm 0.000\,006$	12.24 ± 0.67	0.1418 ± 0.0020	88.2 ± 0.4
		HAT-P-27b			
Our analysis	$2455\,186.019\,91 \pm 0.000\,44$	$3.039\,5803 \pm 0.000\,0015$	10.01 ± 0.13	0.1192 ± 0.0015	85.08 ± 0.07
Béky et al. (2011)	$2455\,186.019\,55 \pm 0.000\,54$	$3.039\,486 \pm 0.000\,012$	$9.65^{+0.54}_{-0.40}$	0.1186 ± 0.0031	$84.7^{+0.7}_{-0.4}$
Anderson et al. (2011)	$2455\,368.394\,76 \pm 0.000\,18$	$3.039\,5721 \pm 0.000\,0078$	9.88 ± 0.39	0.1250 ± 0.0015	$84.98^{+0.20}_{-0.14}$
Sada et al. (2012)	$2455\,186.198\,22 \pm 0.000\,32$	$3.039\,5824 \pm 0.000\,0035$	$9.11^{+0.71}_{-1.01}$	$0.1344^{+0.0174}_{-0.0389}$	84.23 ± 0.88
Brown et al. (2012)	–	$3.039\,577 \pm 0.000\,006$	$9.80^{+0.38}_{-0.29}$	$0.120^{+0.009}_{-0.007}$	85.0 ± 0.2
		WASP-21b			
Our analysis	$2454\,743.042\,17 \pm 0.000\,65$	$4.322\,5126 \pm 0.000\,0022$	9.62 ± 0.17	0.1030 ± 0.0008	87.12 ± 0.24
Bouchy et al. (2010)	$2454\,743.0426 \pm 0.0022$	$4.322\,482^{+0.000\,024}_{-0.000\,019}$	10.54 ± 0.49	$0.1040^{+0.0017}_{-0.0018}$	$88.75^{+0.70}_{-0.84}$
Barros et al. (2011)	$2455\,084.520\,48 \pm 0.000\,20$	$4.322\,5060 \pm 0.000\,0031$	$9.68^{+0.30}_{-0.19}$	$0.1071^{+0.0009}_{-0.0008}$	87.34 ± 0.29
Ciceri et al. (2013)	$2454\,743.040\,54 \pm 0.000\,71$	$4.322\,5186 \pm 0.000\,0030$	9.46 ± 0.27	0.1055 ± 0.0023	86.97 ± 0.33
Southworth (2012)	$2455\,084.520\,40 \pm 0.000\,16$	$4.322\,5060 \pm 0.000\,0031$	9.35 ± 0.34	0.1095 ± 0.0013	86.77 ± 0.45

Looking at the Exoplanet Transit Database (ETD; Poddaný, Brát & Pejcha 2010) one can see that the values for the transit depth reported there vary by several tens of mmag. Such variations can be caused by close variable stellar companions placed within the aperture due to the pixel scale of the detectors and the telescope defocusing. However, our results together with the data of Hartman et al. (2011) and Esposito et al. (2014) neither show a variation in the transit depth, i.e. the k-value, nor the overall stellar brightness. Thus, the data provided by ETD in the case of HAT-P-27b should be treated with caution.

For HAT-P-18b, we obtained three useful transit observations (see Fig. 2). However, due to the size of the used telescopes, the relatively faint planet host star and the small amount of suitable comparison stars available in the respective FoV of each observation, the resultant light curves are dominated by a large scatter.

Except for one – but not significant – outlier the differences in the O−C diagram (see Fig. 2) can be explained by redetermining the published period by (0.53 ± 0.36) s. Hence, our result is in good agreement with the originally published period of Hartman et al. (2011).

Despite a spread in the data, which can be explained by the quality of the light curves, we do not see any significant differences for k, i and a/R_s between the respective observations. A summary of all obtained parameters can be found in Table 5, as well as a comparison with literature values.

5.2 HAT-P-19b

For HAT-P-19b, we got two light curves using the Jena 0.6 m and one light curve from the CAHA 1.2 m telescope (Fig. 3). In all three cases, we obtained high-precision data. The light curves show no artefacts that could be ascribed to e.g. spots on the stellar surface. Plotting the mid-transit times into the O−C diagram, we can redetermine the period by (0.53 ± 0.06) s. As for the inclination and the reverse fractional stellar radius, we can confirm the values reported in Hartman et al. (2011). The radius ratio of $k = 0.1378 \pm 0.0014$, however, seems to be smaller than assumed by Hartman et al. (2011) ($k = 0.1418 \pm 0.0020$).

5.3 HAT-P-27b

HAT-P-27b planetary transits were observed six times (see Fig. 4). Unfortunately, due to the observing conditions and sizes of the telescopes used for the observations most light curves are of lower quality. An advantage of a network such as the YETI network lies within the possibility of simultaneous observations using different telescopes. This enables us to independently check whether the data are reliable. For HAT-P-27b, simultaneous observations could be achieved at epoch 415 using two different telescopes (Antalya 1.0 m and OSN 1.5 m).

In addition to our own data, we added data from Sada et al. (2012) and Brown et al. (2012). The latter one only lists system parameters without giving an epoch of observation, thus we artificially put them to epoch 200. The system parameters i, a/R_s and k can be determined more precisely than before taking the errors of the individual measurements into account. All three parameters are in good agreement with the results of previous authors. Furthermore, we do not see any significant variation. The larger k-value of the epoch 540 observations are due to the quality of the corresponding light curve.

Looking at the mid-transit time we see that a period change of (-0.51 ± 0.12) s explains the data quite well. The mid-transit time of one of the epoch 415 observations was found to be ≈4.5 min ahead of time, while the other one is as predicted. This way we could identify a synchronization error during one of the observations. This example shows the importance of simultaneous transit observations. Unfortunately, this was the only successful observation of that kind within this project (for a larger set of double and threefold observations, see e.g. Seeliger et al. 2014).

As mentioned before, one of the previous discussions in the case of HAT-P-27b planetary transits has been the transit shape. Table 4 lists the derived impact parameters for our single observations,

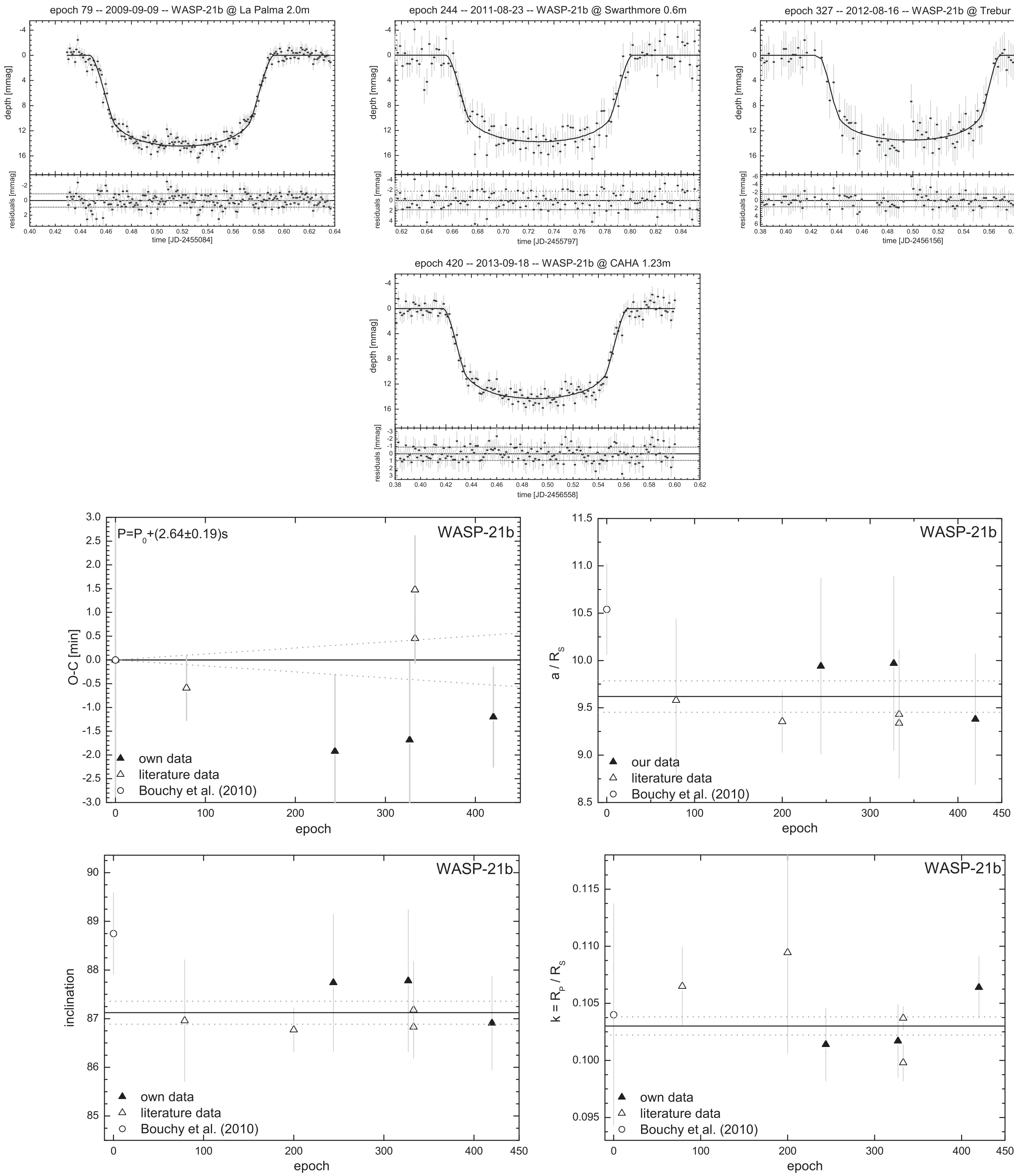

Figure 5. Top: the transit light curves obtained for WASP-21b. Bottom: the present result for the WASP-21b observing campaign. All explanations are equal to Fig. 2. The open circle denotes data from the discovery paper of Bouchy et al. (2010), open triangles denote literature data from Barros et al. (2011), Ciceri et al. (2013) and Southworth (2012) (the latter one artificially set to epoch 200), filled triangles denote our data (from Swarthmore, Trebur and Calar Alto).

as well as the weighted mean and the literature results. Though there are small deviations between the different transit events, no significant difference can be seen. Our observations point towards $b = 0.86$ and thus confirm the results of Anderson et al. (2011) and Béky et al. (2011). One has to state, though, that the error bars of the individual results are quite large. With $b > 0.8$ the HAT-P-27 system shows one of the largest known impact parameter of all known transiting exoplanets in combination with a very high probability that the transit is indeed gracing.

5.4 WASP-21b

Four transit light curves of WASP-21b are available, including one light curve from Barros et al. (2011) (see Fig. 5). In addition, the

Table 6. The results of the individual fits of the observed complete transit event. The rms of the fit and the resultant pnr are given in the last column. The table also shows the result for the transits with pnr > 4.5 that are not used for redetermining the system properties.

Date	Epoch	Telescope	$T_{\mathrm{mid}} - 245\,0000$ d	a/R_{s}	$k = R_{\mathrm{p}}/R_{\mathrm{s}}$	i (°)	rms/pnr (mmag)
			HAT-P-18b				
2011-04-21	174	Trebur 1.2 m	5673.419 67 ± 0.001 24	16.4 ± 1.4	0.1399 ± 0.0072	88.52 ± 0.84	3.0 / 3.3
2011-05-24	180	Trebur 1.2 m	5706.469 93 ± 0.000 80	18.28 ± 0.83	0.1343 ± 0.0039	89.52 ± 0.58	3.7 / 4.0
2012-05-05	243	Rozhen 0.6 m	6053.472 76 ± 0.000 84	16.04 ± 1.36	0.1373 ± 0.0047	88.55 ± 0.79	3.5 / 4.4
2012-06-07	249	CA-DLR 1.2 m	6086.518 56 ± 0.001 25	–	–	–	4.1 / 4.5
2013-04-28	308	Antalya 1.0 m	6411.496 38 ± 0.000 84	15.22 ± 1.52	0.1464 ± 0.0068	87.89 ± 0.75	3.9 / 5.0
			HAT-P-19b				
2011-11-23	199	Jena 0.6 m	5899.283 45 ± 0.000 49	12.56 ± 0.34	0.1369 ± 0.0026	88.20 ± 0.64	2.1 / 2.2
2011-12-09	203	Jena 0.6 m	5905.318 10 ± 0.000 44	12.29 ± 0.35	0.1369 ± 0.0023	89.05 ± 0.67	2.3 / 2.4
2011-12-17	205	CA-DLR 1.2 m	5913.335 71 ± 0.000 34	11.96 ± 0.53	0.1368 ± 0.0027	88.38 ± 0.80	1.2 / 1.3
2014-10-04	460	Jena 0.6 m	6935.575 59 ± 0.000 55	12.43 ± 0.36	0.1340 ± 0.0026	89.25 ± 0.67	2.8 / 3.0
			HAT-P-27b				
2011-04-05	155	Lulin 0.4 m	5657.153 33 ± 0.001 07	10.72 ± 1.67	0.1233 ± 0.0081	85.53 ± 0.93	3.4 / 3.8
2011-04-08	156	Lulin 0.4 m	5660.194 81 ± 0.001 16	9.43 ± 1.01	0.1228 ± 0.0149	84.69 ± 0.81	3.4 / 3.2
2011-05-05	165	Trebur 1.2 m	5687.551 22 ± 0.000 51	9.83 ± 0.56	0.1153 ± 0.0029	85.07 ± 0.40	1.6 / 1.8
2012-04-01	274	Tenagra 0.8 m	6018.864 57 ± 0.002 32	9.65 ± 1.63	0.1199 ± 0.0126	84.13 ± 1.63	5.7 / 5.8
2012-04-25	282	Xinglong 0.6 m	6043.180 95 ± 0.001 35	9.89 ± 1.67	0.1186 ± 0.0067	84.83 ± 1.24	4.3 / 5.1
2013-06-03	415	Antalya 1.0 m	6447.442 68 ± 0.001 66	10.64 ± 1.30	0.1184 ± 0.0081	85.51 ± 0.94	2.6 / 3.5
2013-06-03	415	OSN 1.5 m	6447.445 71 ± 0.000 30	10.18 ± 0.29	0.1224 ± 0.0037	85.23 ± 0.21	1.2 / 0.9
2013-06-18	540	Antalya 1.0 m	6827.395 45 ± 0.002 20	10.77 ± 1.01	0.1462 ± 0.0141	85.26 ± 0.55	3.1 / 4.0
			WASP-21b				
2011-08-24	244	Swarthmore 0.6 m	5797.734 00 ± 0.001 12	9.94 ± 0.93	0.1014 ± 0.0032	87.74 ± 1.41	3.3 / 3.1
2012-08-16	327	Trebur 1.2 m	6156.502 60 ± 0.001 15	9.97 ± 0.92	0.1017 ± 0.0032	87.78 ± 1.46	2.9 / 2.6
2013-09-18	420	CA-DLR 1.2 m	6558.496 48 ± 0.000 73	9.38 ± 0.69	0.1064 ± 0.0027	86.91 ± 0.96	1.6 / 1.4

results of the analysis of two transit events of Ciceri et al. (2013) and one transit observation of Southworth (2012) are also taken into account. Concerning the O−C diagram, we found that a period change of (2.63 ± 0.17) s removes the linear trend which is present in the data fitted with the initial ephemeris. As in the previous analyses, no trend or sinusoidal variation in the system parameters can be seen.

However, regarding inclination and reverse fractional stellar radius we do see a significant difference between our results and the initial values published by Bouchy et al. (2010). This was also found by other authors before. As discussed in Barros et al. (2011), this result is a consequence of the assumption of Bouchy et al. (2010) that the planet host star is a main-sequence star, while Barros et al. (2011) found that the star starts evolving off the main sequence and thus its radius increases. This in turn leads to corrections of the stellar and hence planetary properties.

6 SUMMARY

We presented the results of the transit observations of the extra-solar planets HAT-P-18b, HAT-P-19b, HAT-P-27b/WASP-40b and WASP-21b which are part of our ongoing project on ground-based follow-up observations of exoplanetary transits using small- to medium-size telescopes with the help of YETI network telescopes. During the past three years we followed these well-chosen objects to refine their orbital parameters as well as to find TTVs indicating yet unknown planetary companions. Table 5 contains an overview of the redetermined properties, as well as the available literature values, while Table 6 lists the results of the individual light-curve fits.

In all cases we could redetermine the orbital parameters. Especially, the period could be determined more precise than before. So far, we cannot rule out the existence of TTV signals for the planets investigated within this study due to the limited number of available high-quality data. Also the parameters a/R_{s}, $r_{\mathrm{p}}/r_{\mathrm{s}}$ and inclination have been obtained and compared to the available literature data. Despite some corrections to the literature data, we found no significant variations within these parameters. To distinguish between a real astrophysical source of the remaining scatter and random noise as a result of the quality of our data more high-precision transit observations would be needed.

HAT-P-18b was also part of an out-of-transit monitoring for a spread in the transit depth was reported in the literature that could be due to a significant variability of the transit host star. Regarding our transit data we cannot confirm the spread in transit depth. Looking at the quality of the literature data showing the transit depth variation, it is very likely that this spread is of artificial nature. Thus it is not surprising that we did not find stellar variability larger than ≈3.8 mmag. However, we do see some structures in the light curves that could be caused by spot activity on the stellar surface.

ACKNOWLEDGEMENTS

All the participating observatories appreciate the logistic and financial support of their institutions and in particular their technical workshops. MS would like to thank all participating YETI telescopes for their observations, as well as G. Maciejewski and the anonymous referee for helpful comments on this work. JGS, AP, and RN would like to thank the Deutsche Forschungsgemeinschaft (DFG) for support in the Collaborative Research Center Sonderforschungsbereich SFB TR 7 'Gravitationswellenastronomie'. RE, MK, SR and RN would like to thank the DFG for support in the Priority Programme SPP 1385 on the First ten Million years of the Solar system in projects NE 515/34-1 and -2. RN would like to acknowledge financial support from the Thuringian government (B 515-07010) for the STK CCD camera (Jena 0.6 m) used in this project. MM and CG thank DFG in project MU 2695/13-1. The research of DD and DK was supported partly by funds of projects DO 02-362, DO 02-85 and DDVU 02/40-2010 of the Bulgarian Scientific Foundation, as well as project RD-08-261 of Shumen University. Z-YU was supported by the Chinese National Natural Science Foundation grant no. 11373033. The research of RC, MH and MH is supported as a project of the Nordrhein-Westfälische Akademie der Wissenschaften und Künste in the framework of the academy programme by the Federal Republic of Germany and the state Nordrhein-Westfalen. MF acknowledges financial support from grants AYA2011-30147-C03-01 of the Spanish Ministry of Economy and Competitiveness (MINECO), cofunded with EU FEDER funds, and 2011 FQM 7363 of the Consejería de Economía, Innovación, Ciencia y Empleo (Junta de Andalucía, Spain). We also wish to thank the TÜBİTAK National Observatory (TUG) for supporting this work through project numbers 12BT100-324-0 and 12CT100-388 using the T100 telescope. MS thanks D. Keeley, M. M. Hohle and H. Gilbert for supporting the observations at the University Observatory Jena. This research has made use of NASA's Astrophysics Data System. This research is based on observations obtained with telescopes of the University Observatory Jena, which is operated by the Astrophysical Institute of the Friedrich-Schiller-University. This work has been supported in part by Istanbul University under project number 39742, by a VEGA Grant 2/0143/14 of the Slovak Academy of Sciences and by the joint fund of Astronomy of the National Science Foundation of China and the Chinese Academy of Science under grants U1231113.

REFERENCES

Anderson D. R. et al., 2011, PASP, 123, 555
Bakos G., Noyes R. W., Kovács G., Stanek K. Z., Sasselov D. D., Domsa I., 2004, PASP, 116, 266
Barros S. C. C., Pollacco D. L., Gibson N. P., Howarth I. D., Keenan F. P., Simpson E. K., Skillen I., Steele I. A., 2011, MNRAS, 416, 2593
Barros S. C. C. et al., 2014, A&A, 561, L1
Béky B. et al., 2011, ApJ, 734, 109
Borucki W. J. et al., 2011, ApJ, 728, 117
Bouchy F. et al., 2010, A&A, 519, A98
Broeg C., Fernández M., Neuhäuser R., 2005, Astron. Nachr., 326, 134
Brown D. J. A. et al., 2012, ApJ, 760, 139
Carter J. A., Winn J. N., 2009, ApJ, 704, 51
Ciceri S. et al., 2013, A&A, 557, A30
Claret A., Bloemen S., 2011, A&A, 529, A75
Eastman J., Siverd R., Gaudi B. S., 2010, PASP, 122, 935
Eastman J., Gaudi B. S., Agol E., 2013, PASP, 125, 83
Esposito M. et al., 2014, A&A, 564, L13
Etzel P. B., 1981, in Carling E. B., Kopal Z., eds, Proc. NATO ASI, Photometric and Spectroscopic Binary Systems. Reidel, Dordrecht, p. 111
Ford E. B., Holman M. J., 2007, ApJ, 664, L51
Fulton B. J., Shporer A., Winn J. N., Holman M. J., Pál A., Gazak J. Z., 2011, AJ, 142, 84
Gazak J. Z., Johnson J. A., Tonry J., Dragomir D., Eastman J., Mann A. W., Agol E., 2012, Adv. Astron., 2012, 30
Ginski C., Mugrauer M., Seeliger M., Eisenbeiss T., 2012, MNRAS, 421, 2498
Hartman J. D. et al., 2011, ApJ, 726, 52
Knutson H. A. et al., 2014, ApJ, 785, 126
Koch D. G. et al., 2010, ApJ, 713, L79
Maciejewski G. et al., 2010, MNRAS, 407, 2625
Maciejewski G. et al., 2011a, MNRAS, 411, 1204
Maciejewski G., Errmann R., Raetz St., Seeliger M., Spaleniak I., Neuhäuser R., 2011b, A&A, 528, A65
Maciejewski G. et al., 2013a, AJ, 146, 147
Maciejewski G. et al., 2013b, A&A, 551, A108
Mandel K., Agol E., 2002, ApJ, 580, L171
Mazeh T. et al., 2013, ApJS, 208, 16
Mugrauer M., Berthold T., 2010, Astron. Nachr., 331, 449
Nesvorný D., Kipping D., Terrell D., Hartman J., Bakos G. Á., Buchhave L. A., 2013, ApJ, 777, 3
Neuhäuser R. et al., 2011, Astron. Nachr., 332, 547
Poddaný S., Brát L., Pejcha O., 2010, New Astron., 15, 297
Pollacco D. L. et al., 2006, PASP, 118, 1407
Popper D. M., Etzel P. B., 1981, AJ, 86, 102
Raetz St., 2012, PhD thesis, University Jena
Raetz St. et al., 2014, MNRAS, 444, 1351
Raetz St. et al., 2015, MNRAS, 000, 00
Sada P. V. et al., 2012, PASP, 124, 212
Seeliger M. et al., 2014, MNRAS, 441, 304
Simpson E. K. et al., 2010, MNRAS, 405, 1867
Smalley B. et al., 2011, A&A, 526, A130
Southworth J., 2008, MNRAS, 386, 1644
Southworth J., 2012, MNRAS, 426, 1291
Southworth J. et al., 2009a, MNRAS, 396, 1023
Southworth J. et al., 2009b, MNRAS, 399, 287
Steffen J. H. et al., 2012, PNAS, 109, 7982
Szabó R., Szabó G. M., Dálya G., Simon A. E., Hodosán G., Kiss L. L., 2013, A&A, 553, A17
von Essen C., Schröter S., Agol E., Schmitt J. H. M. M., 2013, A&A, 555, A92
Winn J. N., 2010, preprint (arXiv:1001.2010)

[1] *Astrophysical Institute and University Observatory Jena, Schillergäßchen 2-3, D-07745 Jena, Germany*
[2] *Abbe Center of Photonics, Friedrich Schiller Universität, Max-Wien-Platz 1, D-07743 Jena, Germany*
[3] *Astronomie Stiftung Trebur, Michael Adrian Observatorium, Fichtenstraße 7, D-65468 Trebur, Germany*
[4] *University of Applied Sciences, Technische Hochschule Mittelhessen, D-61169 Friedberg, Germany*
[5] *Graduate Institute of Astronomy, National Central University, Jhongli City, Taoyuan County 32001, Taiwan, Republic of China*
[6] *Sabanci University, Orhanli-Tuzla 34956, Istanbul, Turkey*
[7] *Department of Astronomy and Space Sciences, Faculty of Sciences, Istanbul University, 34119 İstanbul, Turkey*
[8] *Deutsches Zentrum für Luft- und Raumfahrt e.V., Institut für Planetenforschung, Rutherfordstr. 2, D-12489 Berlin, Germany*
[9] *Instituto de Astrofisica de Andalucia, CSIC, Apdo. 3004, E-18080 Granada, Spain*
[10] *Institute of Astronomy and NAO, Bulgarian Academy of Sciences, 72 Tsarigradsko Chaussee Blvd, 1784 Sofia, Bulgaria*
[11] *Shumen University, 115 Universitetska str., 9700 Shumen, Bulgaria*
[12] *Department of Physics and Astronomy, Swarthmore College, Swarthmore, PA 19081, USA*
[13] *Astronomical Institute, Slovak Academy of Sciences, 059 60 Tatranská Lomnica, Slovakia*
[14] *Research School of Astronomy and Astrophysics, Australian National University, Canberra, ACT 2611, Australia*
[15] *Leibnitz-Institut für Astrophysik Potsdam, An der Sternwarte 16, D-14482 Potsdam, Germany*
[16] *Key Laboratory of Optical Astronomy, NAO, Chinese Academy of Sciences, 20A Datun Road, Beijing 100012, China*
[17] *European Space Agency, ESTEC, SRE-S, Keplerlaan 1, NL-2201 AZ Noordwijk, the Netherlands*
[18] *Hamburger Sternwarte, Gojenbergsweg 112, D-21029 Hamburg, Germany*
[19] *Gettysburg College Observatory, Department of Physics, 300 North Washington St, Gettysburg, PA 17325, USA*

[20] *Astronomisches Institut, Ruhr-Universität Bochum, Universitätsstraße 150, D-44780 Bochum, Germany*
[21] *Instituto de Astronomía, Universidad Católica del Norte, Avenida Angamos 0610, Casilla 1280 Antofagasta, Chile*
[22] *Department of Astronomy and Space Sciences, Faculty of Science, University of Ege, Bornova, 35100 İzmir, Turkey*
[23] *Graduate School of Science and Engineering, Department of Astronomy and Space Sciences, Istanbul University, 34116 Istanbul, Turkey*
[24] *Sterrewacht Leiden, PO Box 9513, Niels Bohrweg 2, NL-2300 RA Leiden, the Netherlands*
[25] *Centre for Astronomy, Faculty of Physics, Astronomy and Informatics, N. Copernicus University, Grudziadzka 5, PL-87-100 Toruń, Poland*

This paper has been typeset from a TEX/LATEX file prepared by the author.

Monthly Notices
of the
ROYAL ASTRONOMICAL SOCIETY

MNRAS **450,** 2677–2691 (2015) doi:10.1093/mnras/stv823

Multiwavelength behaviour of the blazar OJ 248 from radio to γ-rays*

M. I. Carnerero,[1,2,3]† C. M. Raiteri,[1] M. Villata,[1] J. A. Acosta-Pulido,[2,3] F. D'Ammando,[4,5] P. S. Smith,[6] V. M. Larionov,[7,8,9] I. Agudo,[10,11] M. J. Arévalo,[2,3] A. A. Arkharov,[8] U. Bach,[12] R. Bachev,[13] E. Benítez,[14] D. A. Blinov,[7,15] V. Bozhilov,[16] C. S. Buemi,[17] A. Bueno Bueno,[2,3] D. Carosati,[18,19] C. Casadio,[10] W. P. Chen,[20] G. Damljanovic,[21] A. Di Paola,[22] N. V. Efimova,[8] Sh. A. Ehgamberdiev,[23] M. Giroletti,[5] J. L. Gómez,[10] P. A. González-Morales,[2,3] A. B. Grinon-Marin,[2,3] T. S. Grishina,[7] M. A. Gurwell,[24] D. Hiriart,[25] H. Y. Hsiao,[20] S. Ibryamov,[13] S. G. Jorstad,[7,26] M. Joshi,[26] E. N. Kopatskaya,[7] O. M. Kurtanidze,[27,28,29,30] S. O. Kurtanidze,[27] A. Lähteenmäki,[31,32] E. G. Larionova,[7] L. V. Larionova,[7] C. Lázaro,[2,3] P. Leto,[17] C. S. Lin,[20] H. C. Lin,[20] A. I. Manilla-Robles,[33] A. P. Marscher,[26] I. M. McHardy,[34] Y. Metodieva,[35] D. O. Mirzaqulov,[23] A. A. Mokrushina,[7,8] S. N. Molina,[10] D. A. Morozova,[7] M. G. Nikolashvili,[27] M. Orienti,[5] E. Ovcharov,[16] N. Panwar,[20] A. Pastor Yabar,[2,3] I. Puerto Giménez,[2,3] V. Ramakrishnan,[31] G. M. Richter,[36] M. Rossini,[4] L. A. Sigua,[27] A. Strigachev,[13] B. Taylor,[26,37] M. Tornikoski,[31] C. Trigilio,[17] Yu. V. Troitskaya,[7] I. S. Troitsky,[7] G. Umana,[17] A. Valcheva,[16] S. Velasco,[2,3] O. Vince,[21] A. E. Wehrle[38] and H. Wiesemeyer[12]

Affiliations are listed at the end of the paper

Accepted 2015 April 10. Received 2015 April 10; in original form 2014 December 18

ABSTRACT

We present an analysis of the multiwavelength behaviour of the blazar OJ 248 at $z = 0.939$ in the period 2006–2013. We use low-energy data (optical, near-infrared, and radio) obtained by 21 observatories participating in the Gamma-Ray Large Area Space Telescope (GLAST)-*AGILE* Support Program of the Whole Earth Blazar Telescope, as well as data from the *Swift* (optical–UV and X-rays) and *Fermi* (γ-rays) satellites, to study flux and spectral variability and correlations among emissions in different bands. We take into account the effect of absorption by the Damped Lyman α intervening system at $z = 0.525$. Two major outbursts were observed in 2006–2007 and in 2012–2013 at optical and near-IR wavelengths, while in the high-frequency radio light curves prominent radio outbursts are visible peaking at the end of 2010 and beginning of 2013, revealing a complex radio–optical correlation. Cross-correlation analysis suggests a delay of the optical variations after the γ-ray ones of about a month, which is a peculiar behaviour in blazars. We also analyse optical polarimetric and spectroscopic data. The average polarization percentage P is less than 3 per cent, but it reaches ∼19 per cent during the early stage of the 2012–2013 outburst. A vague correlation of P with brightness is observed. There is no preferred electric vector polarization angle and during

*The data collected by the GASP-WEBT collaboration are stored in the GASP-WEBT archive; for questions regarding their availability, please contact the WEBT President Massimo Villata (villata@oato.inaf.it).

†E-mail: maribel@oato.inaf.it

the outburst the linear polarization vector shows wide rotations in both directions, suggesting a complex behaviour/structure of the jet and possible turbulence. The analysis of 140 optical spectra acquired at the Steward Observatory reveals a strong Mg II broad emission line with an essentially stable flux of 6.2×10^{-15} erg cm^{-2} s^{-1} and a full width at half-maximum of 2053 km s^{-1}.

Key words: galaxies: active – galaxies: jets – quasars: general – quasars: individual: OJ 248.

1 INTRODUCTION

The emission of active galactic nuclei (AGNs) is explained by the existence of a supermassive black hole (SMBH) at the centre of the host galaxy, which converts gravitational energy of material located in the surroundings into electromagnetic energy. This material forms a disc and loses angular momentum due to the viscosity in the disc, finally falling on to the black hole. In general, the AGN spectra may show broad and narrow emission lines produced in regions close to the nucleus. Sometimes they can also show lines from the host galaxy. In radio-loud AGNs two plasma jets are ejected in direction perpendicular to the disc.

Among the different types of radio-loud AGNs, the objects called 'blazars' (BL Lacs and flat spectrum radio quasars, FSRQs) are powerful emitters from radio wavelengths up to γ-ray energies. They present strong flux variability and high and variable polarization (e.g. Smith 1996). The most accepted scenario to explain these features suggests that we are observing the emission from a jet of material accelerated to relativistic velocities in the vicinity of the SMBH, and oriented very close to our line of sight. Thus, the jet radiation is Doppler boosted and dominates over the other emission components from the nucleus (disc, broad line region – BLR, narrow line region) or host galaxy. The origin of the low-frequency radiation (radio to UV or X-ray band) from the jet is attributed to synchrotron emission and the high-energy radiation (X- to γ-rays) to an inverse-Compton process by the same relativistic electrons producing the synchrotron photons. After the launch of satellites for high-energy observations such as the *Astrorivelatore Gamma ad Immagini Leggero* (*AGILE*; Tavani et al. 2009) and *Fermi* (Abdo et al. 2009; Atwood et al. 2009), the number of sources detected at γ-rays has increased significantly, allowing a more detailed investigation of the high-energy processes occurring in blazars.

Among blazars, in general BL Lacs are objects of lower luminosity with featureless spectra or very weak emission lines. In contrast, FSRQs have higher luminosities and stronger emission lines.

In this paper, we present multifrequency observations of the FSRQ OJ 248 (0827+243) in 2006–2013 performed in the framework of a campaign led by the Whole Earth Blazar Telescope[1] (WEBT). The WEBT radio–optical observations are complemented by high-energy data from the *Swift* and *Fermi* satellites.

In the Roma BZCAT multifrequency catalogue of blazars[2] (Massaro et al. 2009) OJ 248 appears with a redshift $z = 0.939$ flagged as uncertain. Mg II and Fe II absorption lines at $z = 0.525$ were detected by Ulrich & Owen (1977) in the source optical spectrum. This intervening Damped Lyman α (DLA) system was subsequently studied by Rao & Turnshek (2000), who estimated a hydrogen column density $N_{\rm H} = (2.0 \pm 0.2) \times 10^{20}$ cm^{-2}. The DLA system is likely a disc galaxy with ongoing star formation (Steidel et al. 2002; Rao et al. 2003). Although it does not affect the blazar photometry because of its faintness (Rao et al. 2003), its absorption of the source radiation must be taken into account.

OJ 248 was detected by the Energetic Gamma Ray Experiment Telescope (EGRET) instrument on board the *Compton Gamma-ray Observatory* (*CGRO*) with a variable flux. In the third EGRET catalogue of high-energy γ-ray sources (Hartman et al. 1999) it appears with a flux $F(E > 100\,\mathrm{MeV}) = (24.9 \pm 3.9) \times 10^{-8}$ ph cm^{-2} s^{-1}, single measurements ranging from 15.6 to 111.0×10^{-8} ph cm^{-2} s^{-1}. It has $F(E > 100\,\mathrm{MeV}) = (5.3 \pm 0.5) \times 10^{-8}$ ph cm^{-2} s^{-1} and a spectral index 2.67 ± 0.07 in the Second *Fermi*-LAT catalog (2FGL; Nolan et al. 2012). In the Nineties, the source was very active also in the optical band (e.g. Villata et al. 1997; Raiteri et al. 1998).

2 OPTICAL AND NEAR-IR PHOTOMETRY

Optical photometric observations were provided in the R band by several observatories participating in this WEBT project, including the GLAST-*AGILE* Support Program (GASP) of the WEBT collaboration and the Steward Observatory program in support of the *Fermi* γ-ray telescope (Smith et al. 2009). They are: Abastumani (Georgia, FSU), Calar Alto[3] (Spain), Crimean (Ukraine), Lowell (Perkins telescope, USA), Lulin (Taiwan), Mt. Maidanak (Uzbekistan), Roque de los Muchachos (Liverpool telescope, Spain), Rozhen (Bulgaria), San Pedro Martir (Mexico), St. Petersburg (Russia), Steward (USA), Teide (IAC80 telescope, Spain), Tijarafe (Spain), Torino (Italy), Vidojevica (Serbia).

The period of interest goes from 2006 March up to 2013 July. We collected a total of 1356 data points, 1211 of which survived the light curve cleaning process, through which we discarded data with large errors as well as clear outliers.

In the light curve of Fig. 1, we can see two major flaring periods, in 2006–2007 and 2012–2013. The first flare is of similar brightness ($R = 15.6$) as that observed in 1995 November by Raiteri et al. (1998), which was a historical maximum. The second outburst appears more prominent and shows a stronger variability. Two minor events are visible in 2009–2010 and in early 2011.

The 2007 peak was very sharp and was characterized by a brightening of ∼1.3 mag in 11 d and about 1.0 mag fading in 9 d. A noticeable variability also characterises the 2012–2013 outburst, with variations of about 1 mag in less than 6 d. This can be compared with variations of 1.43 mag in 16 d observed by Raiteri et al. (1998), of 1.16 mag in 63 d observed by Villata et al. (1997), and of 1.05 mag in 58 d reported by Fan et al. (2004). But the source also exhibits short-term variability. In particular, we found a couple of changes of ∼0.3 mag in about 7.5 h in late 2012. Intraday variability was previously reported by Raiteri et al. (1998), who observed a brightness decrease of 0.73 mag in 20 h.

The GASP-WEBT near-IR data are collected in the J, H, K bands at the Campo Imperatore (Italy) and Teide (TCS, Spain) observatories. Details on the data acquisition and reduction are given in Raiteri et al. (2014). A comparison between the R band and near-IR

[1] http://www.oato.inaf.it/blazars/webt

[2] Edition 4.1.1, August 2012; http://www.asdc.asi.it/bzcat

[3] Calar Alto data was acquired as part of the MAPCAT project: http://www.iaa.es/∼iagudo/research/MAPCAT

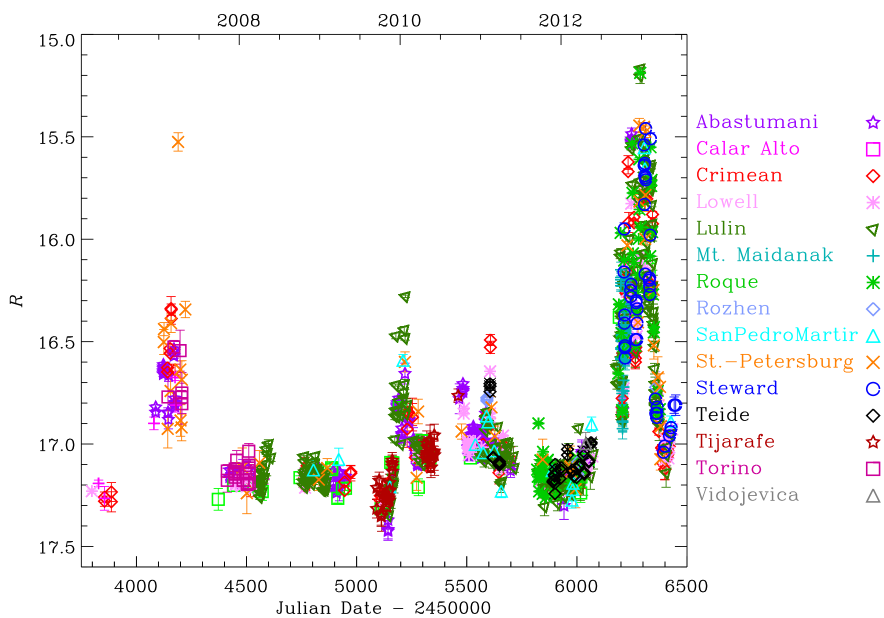

Figure 1. Light curve of OJ 248 in *R* band. It includes 1211 points from 15 observatories, distinguished by different colours and symbols.

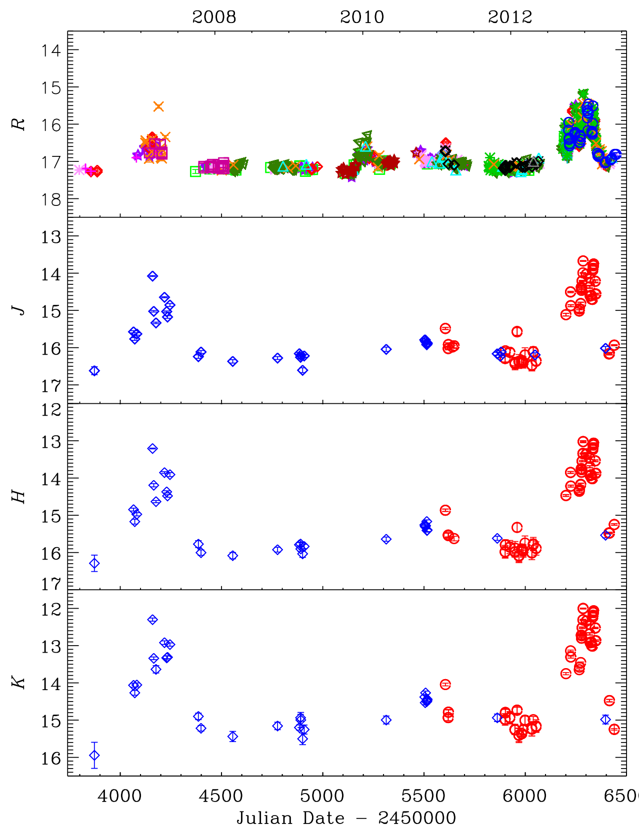

Figure 2. Light curves of OJ 248 in optical (*R* band) and near-IR (*J*, *H*, *K* bands) in 2006–2013 built with GASP-WEBT data. In the near-IR light curves, the blue diamonds are from the Campo Imperatore Observatory and the red points from the Teide Observatory.

source behaviour is shown in Fig. 2. Although the near-IR light curves are less sampled than the optical one, we can recognize the same main features, in particular the two outbursts of 2006–2007 and 2012–2013. The variation amplitude increases with wavelength, as it is usually observed in FSRQs (e.g. Raiteri et al. 2012), suggesting the presence of a 'stable' blue emission component, likely thermal radiation from the accretion disc.

3 OPTICAL POLARIMETRY

Blazars are known to show variable polarization in both polarized flux percentage (*P*) and electric vector polarization angle (EVPA; e.g. Smith 1996). In particular, wide rotations of the linear polarization vector have been detected in a number of cases (Marscher et al. 2008, 2010; Larionov et al. 2013; Sorcia et al. 2014), which have been interpreted as the effect of motion along spiral trajectories.

Optical polarization data for this paper were provided by the Calar Alto, Crimean, Lowell, San Pedro Martir, St. Petersburg, and Steward observatories. In Fig. 3, we show the time evolution of the

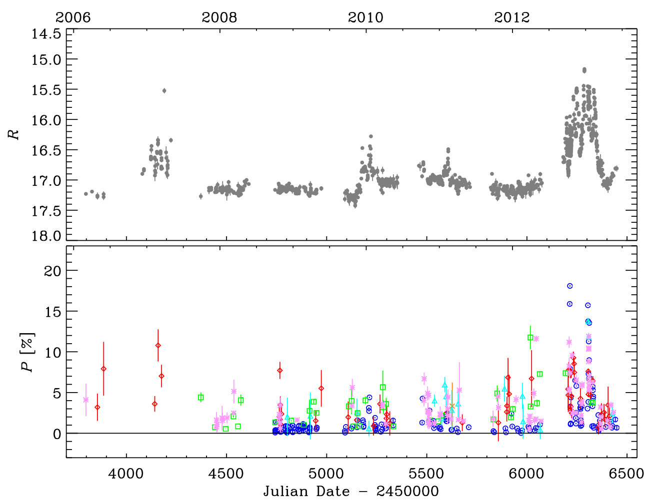

Figure 3. Time evolution of the optical magnitude in *R* band (top panel) and of the percentage of polarized flux (bottom panel). The data are from different observatories: Calar Alto (green squares), Crimean (red diamonds), Lowell (pink asterisks), San Pedro Martir (cyan triangles), Steward (blue circles), and St. Petersburg (orange crosses).

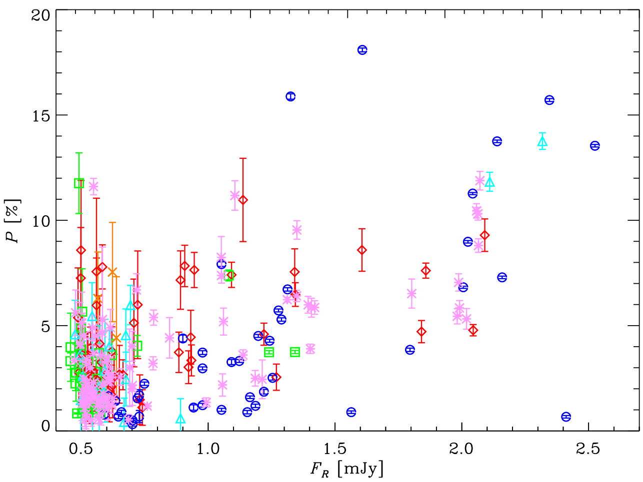

Figure 4. Optical polarization percentage P plotted against the de-absorbed flux density in the R band. The data are from different observatories: Calar Alto (green), Crimean (red), Lowell (pink), San Pedro Martir (cyan), Steward (blue), and St. Petersburg (orange).

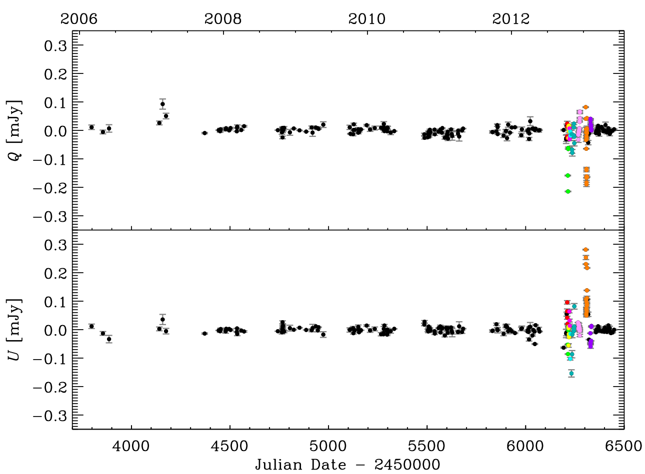

Figure 5. The evolution of the Q and U Stokes' parameters as a function of time. Different colours during the 2012–2013 outburst highlight the data of the selected periods indicated in Fig. 6.

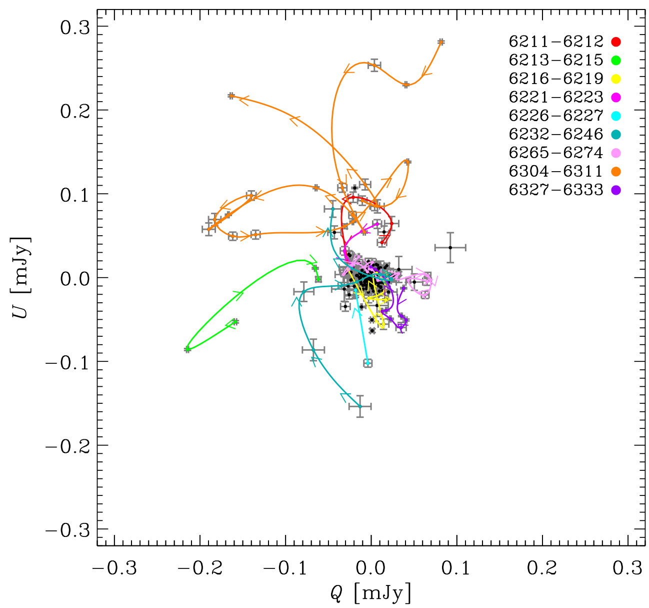

Figure 6. Q versus U for all the data shown in Fig. 5. Coloured lines connect subsequent data belonging to the periods listed in the legend (JD-245 0000). The direction is indicated by the arrows.

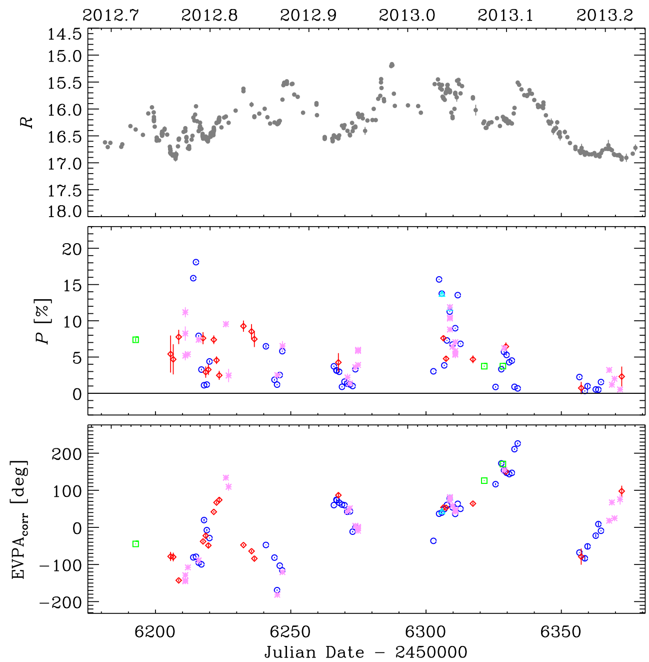

Figure 7. Time evolution of the optical magnitude in R band (top panel), of the percentage of polarized flux (middle panel) and of the EVPA 'corrected' for the $\pm n\pi$ ambiguity (bottom panel, see text for explanation) during the 2012–2013 outburst. Data are from different observatories: Calar Alto (green squares), Crimean (red diamonds), Lowell (pink asterisks), San Pedro Martir (cyan triangles), Steward (blue circles), and St. Petersburg (orange crosses).

polarization percentage P compared with the R-band light curve. For most of the time, the source showed low P (average value of ∼3 per cent), but during the brightening phase of the 2012–2013 outburst P reached ∼19 per cent, suggesting a correlation between P and brightness typical of FSRQs (e.g. Smith 1996; Raiteri et al. 2013). Fig. 4 shows P versus the de-absorbed flux density in the R band (see Section 8). For any value of F_R there is a large dispersion of P, but the highest values of P (>13 per cent) are reached when the source is bright ($F_R > 1.3$ mJy). The linear Pearson's correlation coefficient is 0.60, indicating a marginal correlation.

In order to investigate whether possible rotations of the linear polarization vector occurred, we first examine the behaviour of the Q and U Stokes' parameters. Fig. 5 shows that OJ 248 spent most of the time with Q and U being close to zero. With this being the case, even small variations in Q and U necessarily lead to large EVPA rotations that are difficult to accurately follow unless the observations are very dense. The problem is mitigated during the 2012–2013 outburst, when Q and U exhibit large variations. This appears clearer in the Q versus U plot in Fig. 6, where subsequent data belonging to short time periods with good sampling have been connected to show the time evolution during the 2012–2013 outburst. With this in mind, in Fig. 7 we finally plot the EVPA as a function of time during the outburst. The $\pm n\pi$ ambiguity was fixed by assuming that the most likely value is that minimizing the angle variation, i.e. we added/subtracted 180° when needed to minimize the difference between subsequent points separated by less than 5 d. It seems that there is not a preferable EVPA value and that the linear polarization

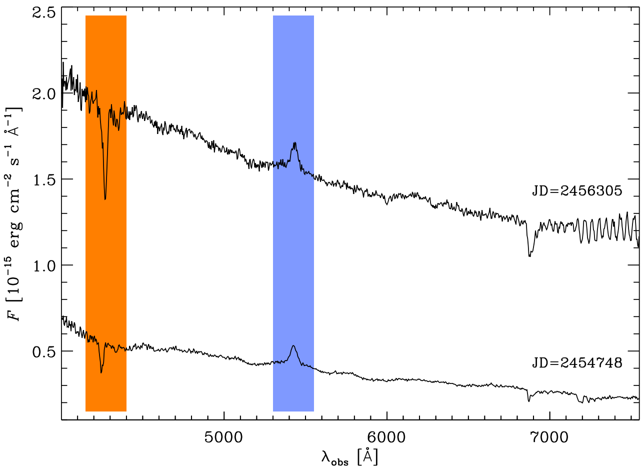

Figure 8. Optical spectra of OJ 248 during different brightness states obtained at the Steward Observatory, showing the Mg II emission line at $z = 0.939$ (blue) and the Mg II absorption line at $z = 0.525$ (orange).

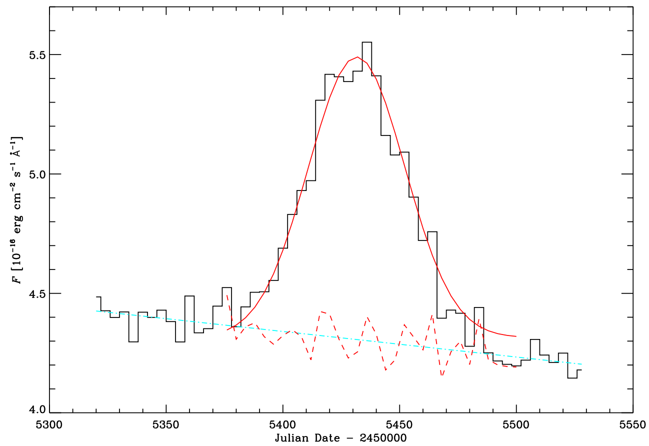

Figure 9. Gaussian fit (red solid line) to the Mg II emission line of the spectrum taken on 2008 October 30 and shown in Fig. 8. The cyan line indicates the linear fit to the continuum; the red dashed line represents the residuals.

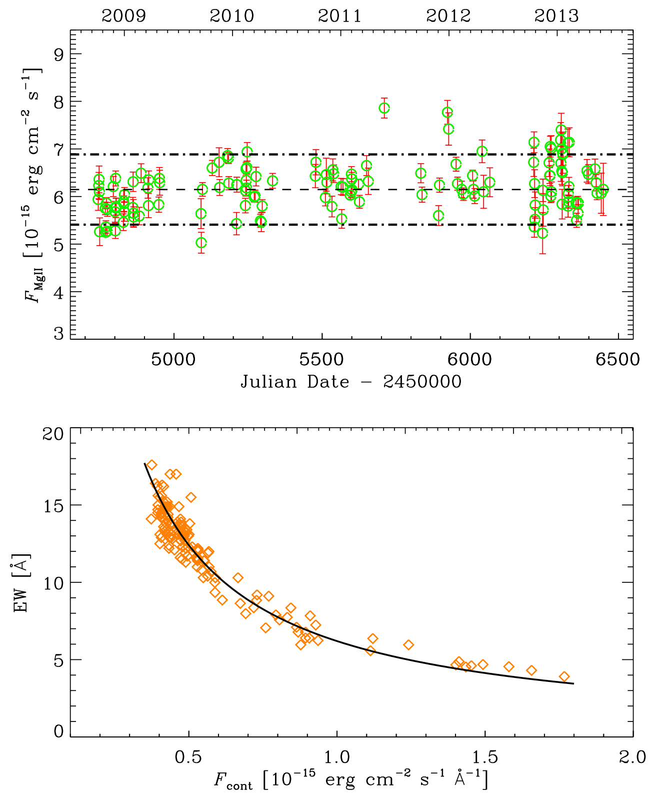

Figure 10. Top: time evolution of the Mg II broad emission line flux; the dashed line represents the average value and the dotted-dashed line the standard deviation around the mean. Bottom: EW of Mg II versus the continuum flux density; the solid line displays the behaviour of the EW assuming a constant line flux equal to its average value.

vector underwent wide rotations in both directions and with different ranges of angles. All this suggests a complex behaviour/structure of the magnetic field in the jet as is expected e.g. from a turbulent plasma flowing at a relativistic speed down the jet (Marscher 2014).

4 OPTICAL SPECTROSCOPY

Several previous studies found that there is no correlation between the jet activity and the behaviour of the broad emission lines in blazars (see e.g. Corbett et al. 2000; Raiteri et al. 2007). Indeed, the BLR gas is likely ionized by the accretion disc radiation, whose variability is weaker and occurs on longer time-scales than the variability of the beamed jet emission (see e.g. Kaspi et al. 2000). However, León-Tavares et al. (2013) detected a flare-like variability of the Mg II emission line in the blazar 3C 454.3 during an outburst and claimed that the broad emission line fluctuations are linked to the non-thermal continuum emission from the jet. With this in mind, we analyse the spectroscopic behaviour of OJ 248 during our monitoring period.

Optical spectra were taken at the Steward Observatory of the University of Arizona for the 'Ground-based Observational Support of the *Fermi* Gamma-ray Space Telescope' program.[4] Data for this program are taken at the 2.3 m Bok telescope and 1.54 m Kuiper telescope (Smith et al. 2009); 140 spectra of OJ 248 were acquired during the first five cycles of the *Fermi* mission, from 2008 October to 2013 June.

All spectra show a prominent Mg II $\lambda\lambda$2796, 2803 broad emission line, which was measured by fitting a Gaussian model with a single component, after subtracting a linear fit to the continuum. We used ad hoc routines developed in IDL and based on the MPFIT[5] libraries (Markwardt 2009). The continuum region was selected from adjacent regions to the emission line, which are free of features. The uncertainty of the measured flux was estimated from the average of the residuals obtained after the continuum fitting and was then used to determine the parameter confidence limits applying the routines in the MPFIT library.

In Fig. 8, we show two of the spectra corresponding to different brightness states and in Fig. 9 the line and continuum fits as well as the residuals. The results of the Mg II analysis are shown in Fig. 10. The line flux presents some dispersion around a mean value of 6.2×10^{-15} erg cm^{-2} s^{-1} with standard deviation of 0.5×10^{-15} erg cm^{-2} s^{-1}. The possible presence of line variability can be checked e.g. by calculating the mean fractional variation $f = \sqrt{\sigma^2 - \delta^2}/\langle F \rangle$, where σ is the standard deviation, δ the mean square uncertainty of the fluxes, and $\langle F \rangle$ the average flux (Peterson 2001). The result is $f = 0.08$, which means that the line

[4] http://james.as.arizona.edu/~psmith/Fermi/
[5] http://www.physics.wisc.edu/~craigm/idl/fitting.html

flux is basically stable, and this is true also during the 2012–2013 outburst period, when the continuum flux increased by a factor ∼6. Moreover, no delayed line flux increase was detected also after the outburst. Hence, the enhanced jet activity responsible for the outburst does not affect the BLR.

We measured the line full width at half-maximum[6] (FWHM), from which one can derive the velocity of the gas clouds in the BLR. The average value is $v_{\rm FWHM} = 2053\,{\rm km\,s^{-1}}$ with a standard deviation of $\sim 310\,{\rm km\,s^{-1}}$. The corresponding de-projected gas velocity, of course, depends on the geometry and orientation of the BLR (see e.g. Decarli, Dotti & Treves 2011). In the blazar model, the BLR should be nearly face on, so measurements of FWHM are likely to be underestimated, since the measurement of the radial velocity will likely miss most of the orbital component.

In the bottom panel of Fig. 10, we finally plot the equivalent width (EW) versus the continuum flux density. The EW decreases when the source brightens, which confirms that the jet is not the ionizing source of the BLR. We notice that, according to the classical definition (Stickel et al. 1991), blazars with rest-frame EW less than 5 Å are classified as BL Lacs; in the case of OJ 248, this happens when the observed EW goes below $5\,\text{Å} \times (1 + z) \sim 9.7\,\text{Å}$, which occurs when the source continuum flux density around the Mg II line[7] exceeds $\sim 0.6 \times 10^{-15}\,{\rm erg\,cm^{-2}\,s^{-1}\,Å^{-1}}$. This underlines the limit of the classical distinction between BL Lacs and FSRQs based on the EW, which depends on the source brightness.

Fig. 8 shows a strong absorption line at $\lambda = 4270$ Å due to Mg II absorption in the intervening DLA system at $z = 0.525$ mentioned in the Introduction. We cannot perform a more detailed analysis of this line because the resolution of our spectra is about 20 Å, implying a velocity resolution of $\sim 1400\,{\rm km\,s^{-1}}$, while the FWHM of the Mg II absorption line is $\simeq 270\,{\rm km\,s^{-1}}$ (Steidel et al. 2002).

5 OBSERVATIONS AT RADIO AND MILLIMETRE WAVELENGTHS

Radio and mm observations were performed with the Medicina (5, 8, and 22 GHz), Metsähovi (37 GHz), Noto (43 GHz), Instituto de Radioastronomía Milimétrica (IRAM) (86 and 230 GHz), and Submillimeter Array (SMA, 230 and 345 GHz) telescopes.

A detailed description of the 43 GHz measurements performed with the Noto Radiotelescope can be found in Leto et al. (2009). For the Medicina observations, see e.g. Bach et al. (2007).

The 37 GHz observations were made with the 13.7 m diameter Metsähovi radio telescope. The flux density scale is set by observations of DR 21. Sources NGC 7027, 3C 274, and 3C 84 are used as secondary calibrators. The error estimate in the flux density includes the contribution from the measurement root mean square and the uncertainty of the absolute calibration. A detailed description of the data reduction and analysis is given in Teräsranta et al. (1998).

IRAM 30 m Telescope data were acquired as part of the POLAMI (Polarimetric AGN Monitoring with the IRAM 30 m Telescope) and MAPI (Monitoring AGN with Polarimetry at the IRAM 30 m Telescope) programs. Data reduction was performed following the procedures described in Agudo et al. (2006, 2010).

Millimetre and submillimetre data were also obtained at the SMA near the summit of Mauna Kea (Hawaii). OJ 248 is included in an ongoing monitoring program at the SMA to determine the fluxes of compact extragalactic radio sources that can be used as calibrators at mm wavelengths (Gurwell et al. 2007). OJ 248 was also observed as part of a dedicated program to follow sources on the *Fermi* LAT Monitored Source List (PI: A. Wehrle) in 2009 and 2010. In the ongoing monitoring sessions, available potential calibrators are observed for 3–5 min, and the measured source signal strength calibrated against known standards, typically Solar system objects (Titan, Uranus, Neptune, or Callisto). In addition, from time to time calibrator data obtained during regular science observations are also used to obtain flux density measurements. Data from this program are updated regularly and are available at the SMA website.[8]

As one can see in Fig. 11, the mm data (230 and 86 GHz) show two prominent outbursts of the same strength peaking in late 2010 and early 2013. Going to lower frequency (37 GHz), the second outburst becomes fainter than the first, and it completely disappears at 8 GHz. A comparison with the optical light curve suggests that the 2013 mm–radio outburst is the time delayed counterpart of the 2012–2013 optical event, while a possible correlation between the optical and radio variations in correspondence of the 2010–2011 mm–radio outburst is more difficult to establish. Indeed, there are no visible optical flares either contemporaneous or slightly preceding the lower frequency outburst, but just one event about one year before, which however is more likely connected with the pre-outburst bumps visible at 230 and 37 GHz. In fact, there is a definite rise in the 230 GHz light curve that starts at essentially the same time as the late 2009–early 2010 optical event. Most likely the more or less prominent optical counterpart of the main mm–radio outburst remained unobserved due to the 2010 seasonal gap: indeed, some residual activity can be seen at the start of the subsequent observing season. The 2006–2007 optical outburst might be correlated with a minor radio event observed a few months later at 86 (and 230) GHz. We used the discrete correlation function (DCF; Edelson & Krolik 1988; Hufnagel & Bregman 1992) to analyse cross-correlations among light curves. Fig. 12 shows the DCF between the optical de-absorbed (see Section 8) and 230 GHz flux densities. The peak value is 0.8, which implies good correlation, and the time delay corresponding to the peak is 28 d, which would be the time lag of the mm variations after the optical ones. However, this result is dominated by the last outburst and the DCF run on the pre-outburst period gives no significant signal.

Flares can be produced by shocks propagating downstream the jet and/or by variations of the Doppler factor δ, which depends on both the bulk Lorentz factor of the relativistic plasma, $\Gamma_{\rm b}$, and the viewing angle θ, $\delta = [\Gamma_{\rm b}(1 - \beta\cos\theta)]^{-1}$, where β is the velocity in units of the light speed. The different behaviour of OJ 248 in various epochs, i.e. different correlation between optical and radio variations, can be explained in terms of a misalignment of the region emitting the bulk of the optical radiation with respect to the zone emitting the bulk of radio photons (see e.g. Villata et al. 2007, 2009b, 2009a; Raiteri et al. 2011). The radiation coming from the jet region with a smaller viewing angle will in fact be more Doppler boosted. According to this interpretation, in 2010–2011 the radio emitting region was more aligned with the line of sight than the optical zone, while in 2012–2013 the most external jet regions, emitting the low-frequency radio photons, had a larger viewing angle, and the strong optical outburst was the effect of a viewing angle smaller than ever.

We finally notice that there is a time delay of the radio flux variations going towards longer wavelengths; in particular, by means of the DCF we could estimate the time lag between the 230 and

[6] Corrected for the instrumental broadening of the line.

[7] We estimated the continuum flux density in the spectral regions 5320–5360 and 5500–5530 Å and then took the mean value.

[8] http://sma1.sma.hawaii.edu/callist/callist.html

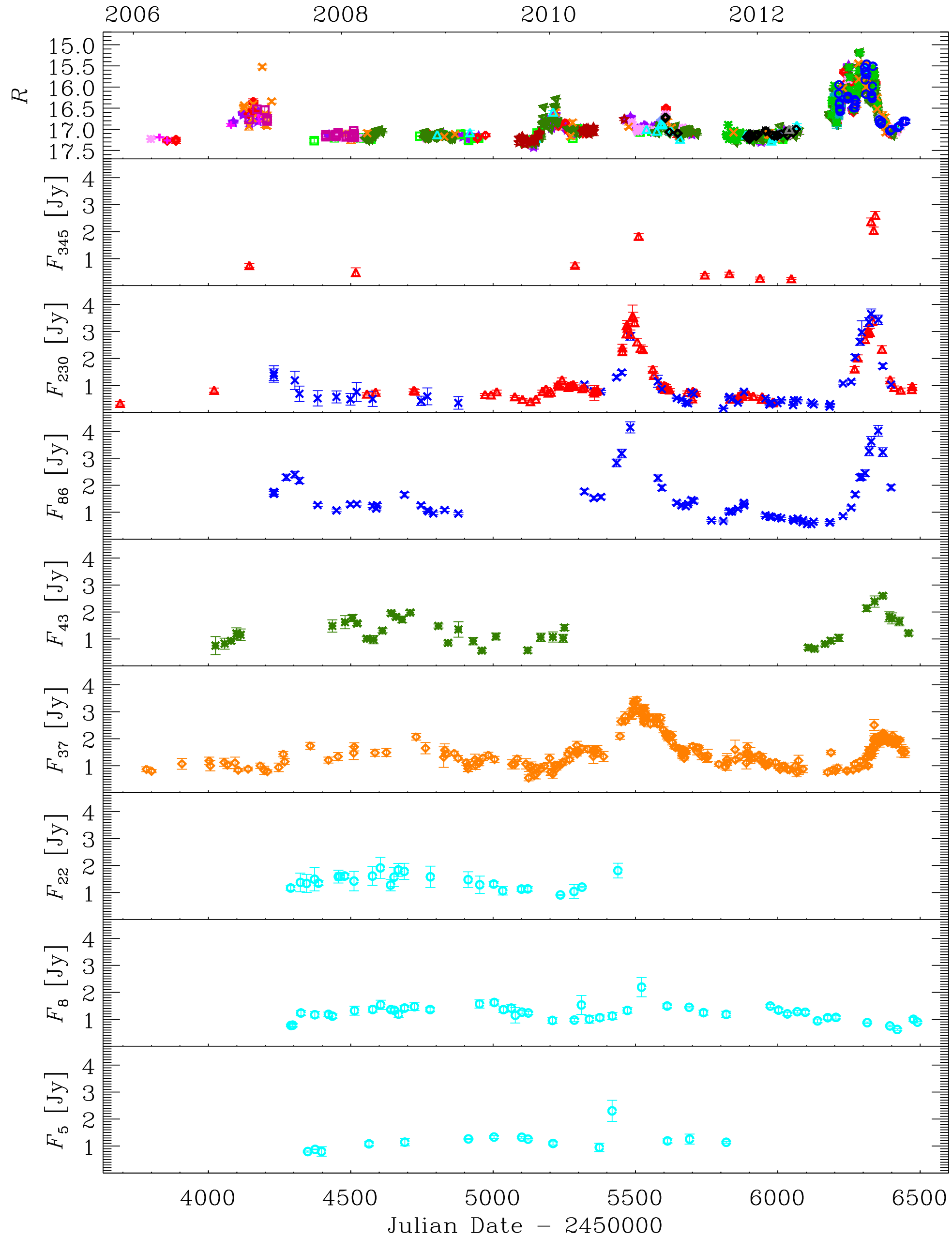

Figure 11. Light curves of OJ 248 at different frequencies in 2006–2013. From top to bottom: *R*-band optical magnitudes (see also Fig. 1), 345 GHz data from SMA, 230 GHz data from SMA (red triangles) and IRAM (blue crosses), 86 GHz data from IRAM, 43 GHz data from Noto, 37 GHz data from Metsähovi, 22, 8, and 5 GHz data from Medicina.

37 GHz flux changes (see Fig. 12). The peak of the DCF is strongly asymmetric, so that a better estimate of the delay in this case is given by the centroid of the distribution (Peterson et al. 1998), which indicates a value of 40–50 d. Moreover, the amplitude of the flux variations decreases at lower frequencies (the ratio between the maximum and minimum flux density is ∼24 at 230 GHz, 7.4 at 86 GHz, and 6.3 at 37 GHz), and the light curves become smoother with longer lasting events. This is what we expect if the radio emission at longer wavelengths comes from more external (because of synchrotron self-absorption) and more extended regions of the jet.

An alternative picture to explain the radio–optical variability is in terms of a disturbance, e.g. shock wave, propagating downstream the jet where the delay from high radio frequencies towards low radio frequencies is naturally caused by opacity effects. In case the optical and mm emitting regions are co-spatial, the reason why the mm peak is time delayed may be due to a rather high lower energy cutoff to the electron energy distribution in the early stages of the outburst.

6 *SWIFT* OBSERVATIONS

The *Swift* satellite (Gehrels et al. 2004) carries three instruments that work simultaneously in different frequency ranges: the X-Ray Telescope (XRT), observing between 0.3 and 10 keV (Burrows et al. 2005), the Ultraviolet-Optical Telescope (UVOT), between 170 and 600 nm (Roming et al. 2005), and the Burst Alert Telescope,

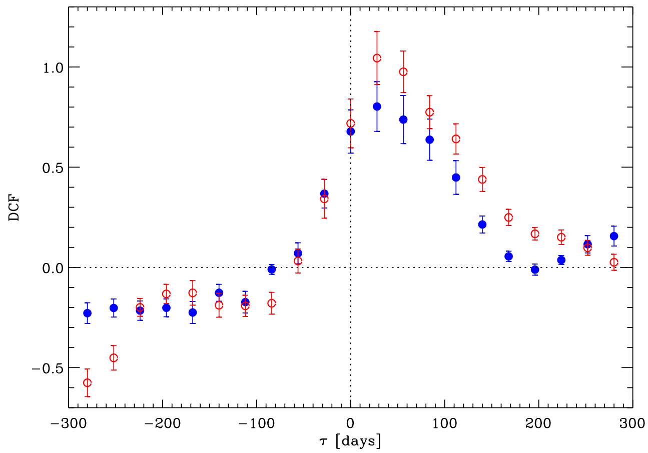

Figure 12. DCFs between the *R* band de-absorbed and 230 GHz flux densities (blue filled circles) and between the 230 and 37 light curves (red empty circles).

between 14 and 195 keV (Barthelmy et al. 2005). OJ 248 was observed by *Swift* 86 times between 2008 January and 2013 May.

6.1 UVOT observations

The UVOT telescope can acquire data in optical (v, b, u) and UV ($w1$, $m2$, $w2$) bands (Poole et al. 2008). The data reduction was performed with the HEASOFT package version 6.13 and the Calibration Database 20130118 of the NASA's High Energy Astrophysics Science Archive Research Center[9] (HEASARC). We extracted the source counts within a 5 arcsec radius aperture and the background counts from a nearby circular region with 15 arcsec radius. We summed multiple observations in the same filter with the `uvotimsum` task and then processed them with `uvotsource`.

The resulting light curves are shown in Fig. 13. No observations were available in the b band. After 2010.0 the difference between the maximum and minimum magnitudes in the different bands is 1.12 in $w2$, 1.05 in $m2$, 1.15 in $w1$, 1.25 in u. It is 0.67 in v, but in this case we have only four points. We can see that the variability in general decreases when the frequency increases, extending the trend we noticed in Section 2 for the optical and near-IR light curves.

6.2 XRT observations

Reduction of the XRT data was performed with the HEASOFT package version 6.13 with the calibration file 20130313. There are 83 observations in photon-counting mode. We ran the task `xrtpipeline` with standard screening criteria. For further analysis, we only kept the 64 observations with more than 50 counts. Source counts were extracted with the `xselect` task from a circular region of 30 pixel radius centred on the source and the background counts were derived from a surrounding annular region of 50 and 70 pixel radii. No correction for pile-up was needed since the count rate is always lower than 0.5 counts s^{-1}. We performed spectral fits with the XSPEC package in the 0.3–10 keV energy range, using the Cash statistics because of the low count number. We modelled the spectra with a power law with photoelectric absorption, adopting a hydrogen

[9] http://heasarc.gsfc.nasa.gov

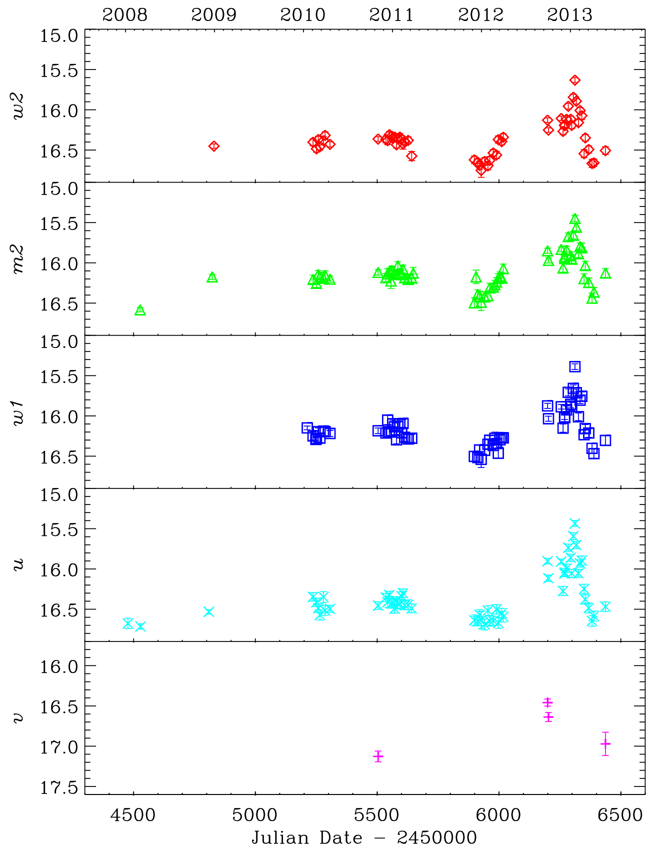

Figure 13. Light curves of OJ 248 built with *Swift*-UVOT data in optical and UV.

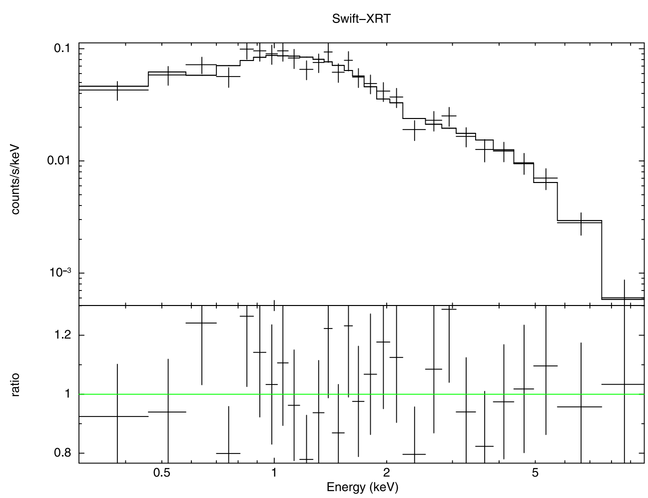

Figure 14. The XRT spectrum of OJ 248 on 2012 October 2. The best fit was obtained with a power law with fixed absorption given by the sum of the Galactic and intervening DLA $N_{\rm H}$ values. The bottom panel shows the ratio of the data to the folded model.

atomic column density $N_{\rm H} = 4.6 \times 10^{20}\,{\rm cm}^{-2}$ obtained by summing the Galactic value $2.6 \times 10^{20}\,{\rm cm}^{-2}$ (Kalberla et al. 2005) to that of the intervening DLA system at $z = 0.525$ (Rao & Turnshek 2000).

The X-ray spectrum acquired on 2012 October 2 is shown in Fig. 14 as an example. It was best-fitted with a power law with photon index $\Gamma = 1.49 \pm 0.10$.

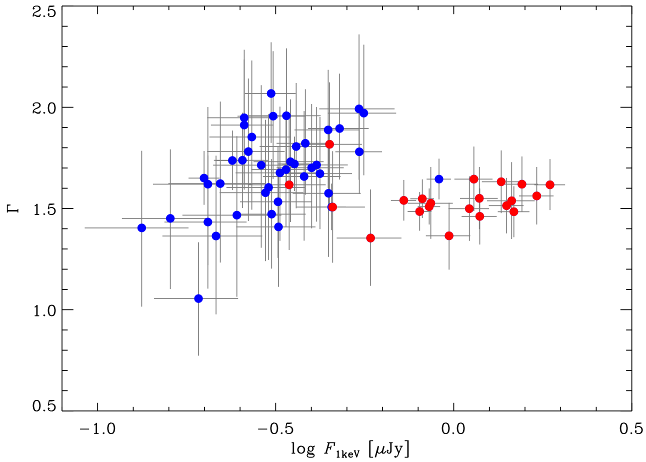

Figure 15. The X-ray photon index Γ as a function of the unabsorbed flux density at 1 keV. Only data with error less than 30 per cent of the flux are shown. Red points correspond to data acquired after JD = 2456100, i.e. during the 2012–2013 outburst.

In Fig. 15, we plotted Γ as a function of the flux density at 1 keV for the 58 observations with error less than 30 per cent of the flux. The values of Γ range between 1.06 and 2.07, with an average value of 1.65 and no significant trend of Γ with flux, in contrast to the harder-when-brighter trend sometimes found in FSRQs (e.g. Vercellone et al. 2010). The smaller dispersion of the data points corresponding to the 2012–2013 outburst (standard deviation $\sigma = 0.09$) with respect to the pre-outburst data ($\sigma = 0.24$) is likely due to their higher precision because of the larger count number. In both cases the standard deviation is less than the average error (0.16 and 0.29, respectively), indicating that the data are consistent with a constant value.

Note that Jorstad & Marscher (2004) analysed *Chandra* data using $N_H = 3.62 \times 10^{20}\,\mathrm{cm}^{-2}$, i.e. the Galactic value according to Dickey & Lockman (1990), and that Stroh & Falcone (2013) found a value of $N_H = (7 \pm 2) \times 10^{20}\,\mathrm{cm}^{-2}$ when analysing XRT data with an absorbed power law with freely varying N_H.

The resulting X-ray light curve (flux densities at 1 keV) is shown in Fig. 16, where it is compared to the source behaviour at other frequencies.

7 *FERMI* OBSERVATIONS

The *Fermi* satellite was launched on 2008 June 11. Its aim is to perform a daily mapping of the γ-ray sources in the Universe. The primary instrument of *Fermi* is the Large Area Telescope (LAT; Atwood et al. 2009). The energy range covered is approximately from 20 MeV to more than 300 GeV. The field of view of the LAT covers about 20 per cent of the sky, and maps all the sky every three hours.

The data in this paper were collected from 2008 August 4 (JD = 245 4683) to 2013 November 8 (JD = 245 6605). We performed the analysis with the SCIENCETOOLS software package version v9r32p5. The data were extracted within a Region of Interest (ROI) of 10° radius and a maximum zenith angle of 100° to reduce contamination from the Earth limb γ-rays, which are produced by cosmic rays interacting with the upper atmosphere. Only events belonging to the 'Source' class were used. The time intervals when the rocking angle of the LAT was greater than 52° were rejected. For the spectral analysis we used the science tool `gtlike` with the response function `P7REP_SOURCE_V15`. Isotropic (iso_source_v05.txt) and Galactic diffuse emission (gll_iem_v05.fit) components were used to model the background.[10]

We evaluated the significance of the γ-ray signal from the sources within the ROI by means of the Test Statistics $\mathrm{TS} = 2\,(\log L_1 - \log L_0)$, where L_1 and L_0 are the likelihood of the data given the model with or without the source, respectively (Mattox et al. 1996). As was done in the 2FGL catalogue (Nolan et al. 2012), for the spectral modelling of OJ 248 we adopted a power law, $N(E) = N_0\,(E/E_0)^{-\Gamma}$, where $E_0 = 392.1$ MeV is the reference energy between 0.1 and 100 GeV. We first ran `gtlike` with the `DRMNFB` optimizer, including all point sources of the catalogue within 15° from our target, and using power-law fits to model the spectra of these sources. We then ran `gtlike` a second time with `NEWMINUIT` as optimizer, after selecting the sources with TS > 10 and the predicted number of counts $N_{\mathrm{pred}} > 3$.

The results of the analysis are reported in Table 1 for time bins of about six months. The average photon index is 2.68, and its standard deviation is 0.22. This value is essentially the same as that reported in the 2FGL catalogue (2.67 ± 0.07), while an analysis over the whole period considered in this paper yields $\Gamma = 2.56 \pm 0.03$ and a flux of $(8.6 \pm 0.3) \times 10^{-8}\,\mathrm{ph\,cm^{-2}\,s^{-1}}$. The photon index variability is dominated by errors, since the variance σ^2 is smaller than the mean square uncertainty δ^2 (see Section 4). In Fig. 16, we can see the corresponding γ-ray light curve (red points). We also plotted a monthly binned light curve (blue points) that includes many upper limits (cyan points) because of the source faintness. Finally, during the 2013 outburst we performed weekly bins when there was a good count number to detail the flux variations (green points).

8 CORRECTION FOR GALACTIC AND DLA EXTINCTION

In the previous sections, we presented light curves of OJ 248 as observed magnitudes. But the near-IR, optical, and UV radiation from the source suffers absorption by both the Galaxy dust and the dust contained in the intervening DLA system at $z = 0.525$ mentioned in the Introduction. This is a problem similar to that met when analysing data from another well-known blazar, AO 0235+16 (Raiteri et al. 2005).

We estimated the Galactic reddening in the *UBVRIJHK* optical and near-IR bands by using the Cardelli, Clayton & Mathis (1989) extinction law, with $R_V = A_V/E(B-V) = 3.1$, which is the standard value for the diffuse interstellar medium. The results are reported in Table 2 (Column 2). An estimate of the extinction due to the DLA system can be calculated starting from the hydrogen column density $N_H = (2.0 \pm 0.2) \times 10^{20}\,\mathrm{cm}^{-2}$ obtained by Rao & Turnshek (2000) and adopting a gas-to-dust ratio equal to the average value in the Milky Way: $N_H = 4.93 \times 10^{21}\,\mathrm{cm^{-2}\,mag^{-1}} \times E(B-V)$ (Diplas & Savage 1994). This yields $E(B-V) = 0.04$, and assuming again $R_V = 3.1$, we obtain $A_V = 0.124$ at $z = 0.525$. Then, by applying the same Cardelli et al. (1989) law properly blueshifted, we get the values reported in Table 2 (Column 3). We note that the DLA system is a more important absorber than the Galaxy. The assumption that the DLA system has the same absorbing characteristics of the Milky Way is justified by its being a spiral galaxy (Rao et al. 2003). The values of the total extinction that we must apply to correct our data

[10] http://fermi.gsfc.nasa.gov/ssc/data/access/lat/ BackgroundModels.html

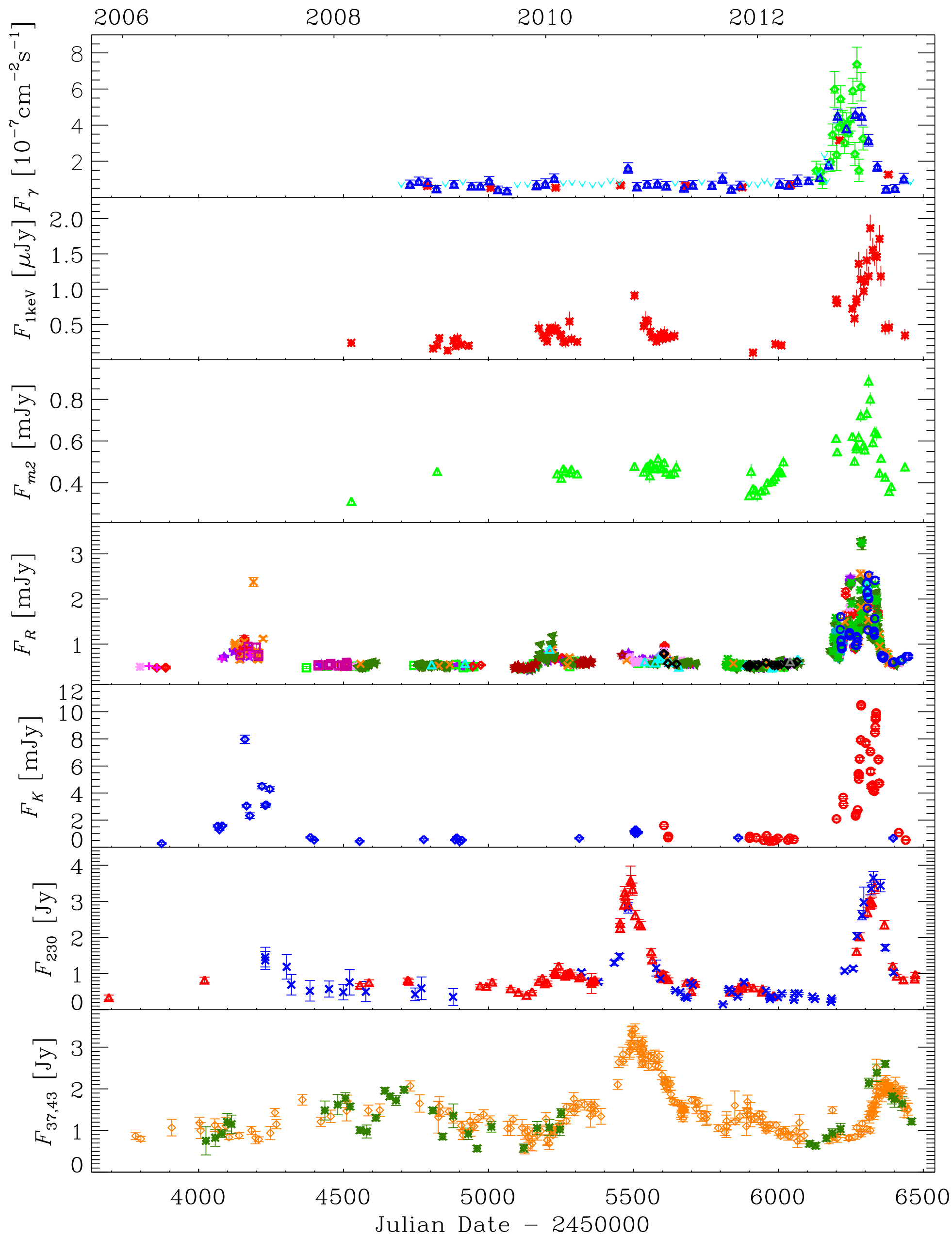

Figure 16. Light curves of OJ 248 at different frequencies in 2006–2013. From top to bottom: the *Fermi*-LAT 0.1–100 GeV fluxes (10^{-8} ph cm^{-2} s^{-1}) derived with different time bins (red symbols refer to data binned over roughly six-month time intervals, blue ones to monthly binned data, and green symbols to weekly binned data in the outburst period; cyan arrows indicate upper limits); the 1-keV *Swift*-XRT flux densities (μJy); the *Swift*-UVOT *m*2 flux densities (mJy); the GASP-WEBT *R*-band flux densities (mJy); the GASP-WEBT *K*-band flux densities (mJy); the 230 GHz flux densities (Jy); the 37 GHz (orange points); and 43 GHz (green points) flux densities (Jy). The X-ray, UV, optical, and near-IR light curves were corrected by both Galactic and DLA absorption.

for absorption in both the Galaxy and the DLA system are given in Column 4.

In the case of the *Swift*-UVOT bands, because of the asymmetric shape of the filter responses and of the bumped shape of the extinction law in the UV, we calculated the absorption in the various bands by integrating the Cardelli et al. (1989) law with the filter effective areas (see e.g. Raiteri et al. 2010). The results are shown in Table 2.

9 CROSS-CORRELATION BETWEEN VARIABILITY AT HIGH AND LOW ENERGIES

In order to better investigate the relationship between the source behaviour in γ-rays and that in the optical band, we show in Fig. 17 the corresponding whole light curves as well as an enlargement of the 2012–2013 outburst period, where the correlation is easier to study. The start of the γ-ray outburst is not covered in the optical band because of the solar conjunction, but the first point after the

Table 1. Results of the spectral analysis of the *Fermi*-LAT data of OJ 248 in the 0.1–100 GeV energy range. The reference energy E_0 was fixed to 392.1 MeV. The fitted model was a power law with photon index Γ.

Date	$N_{\rm pred}$	TS	Γ	$F_{0.1-100\,\rm GeV}$ [10^{-8} ph cm^{-2} s^{-1}]
2008 Aug 04–2009 Mar 05	539	125	2.77 ± 0.12	6.2 ± 0.8
2009 Mar 05–2009 Oct 15	465	131	2.55 ± 0.11	5.2 ± 0.8
2009 Oct 15–2010 May 27	406	104	2.60 ± 0.12	5.3 ± 0.8
2010 May 27–2011 Jan 05	466	100	2.83 ± 0.12	6.6 ± 0.9
2011 Jan 06–2011 Aug 18	439	97	2.81 ± 0.13	6.4 ± 1.0
2011 Aug 18–2012 Feb 02	283	43	3.13 ± 0.23	5.5 ± 1.0
2012 Feb 02–2012 Jul 19	392	107	2.66 ± 0.13	6.9 ± 1.0
2012 Jul 19–2013 Jan 03	1975	2106	2.38 ± 0.03	31.5 ± 1.3
2013 Jan 03–2013 Jun 20	730	401	2.48 ± 0.07	12.6 ± 1.1
2013 Jun 20–2013 Nov 08	313	103	2.56 ± 0.13	6.5 ± 1.1

Table 2. Extinction [mag] in the various Bessel (Bessell, Castelli & Plez 1998) and *Swift*-UVOT bands towards OJ 248. Both the Galactic absorption and that by the DLA system at $z = 0.525$ are given. The value of the total extinction suffered by the source radiation is the sum of the two.

Band	A_λ(Gal)	A_λ(DLA)	Total
	Swift-UVOT bands		
$w2$	0.249	0.397	0.646
$m2$	0.261	0.343	0.604
$w1$	0.211	0.331	0.542
u	0.150	0.349	0.499
b	0.125	0.240	0.365
v	0.095	0.196	0.291
	Bessel bands		
U	0.142	0.316	0.458
B	0.122	0.235	0.357
V	0.093	0.195	0.288
R	0.077	0.173	0.250
I	0.055	0.131	0.186
J	0.027	0.074	0.101
H	0.017	0.045	0.062
K	0.011	0.028	0.039

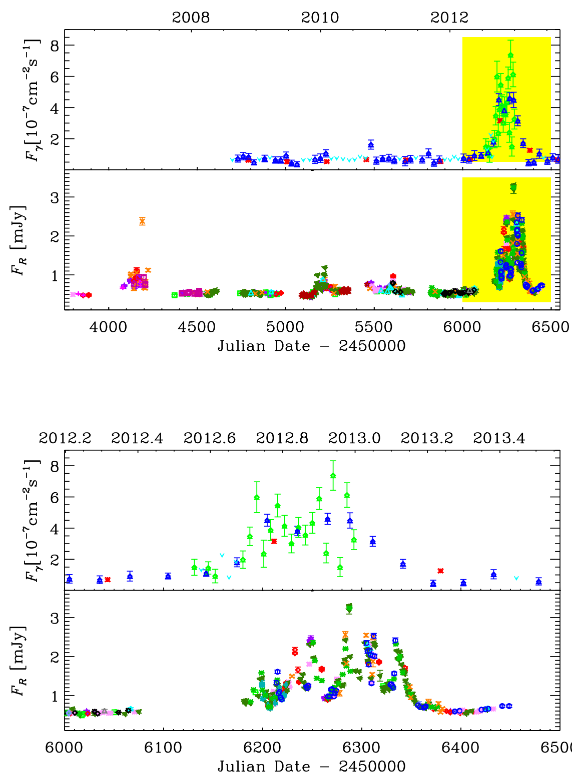

Figure 17. Light curves in the γ-ray and optical (R) bands over the whole period (top), and during the 2012–2013 outburst period indicated by the yellow stripe (bottom).

seasonal gap is about 0.3 mag brighter than before, suggesting that the outburst has already begun. In contrast, the optical light curve is very well sampled in the outburst decline phase, where the γ-ray curve has a worst time resolution because of the low flux. It seems that the γ and optical fluxes may well have risen and declined together, but that the period of major γ activity preceded the phase of strongest optical activity.

To get a quantitative estimate of this time shift, we calculate the DCF (see Section 5) between the γ-ray fluxes and the R-band flux densities corrected for the total absorption reported in Table 2.[11] The DCF is displayed in Fig. 18. It shows a peak at a lag of $\tau_{\rm p} = 28$ d with $\rm DCF_p = 1.3$ that indicates strong correlation with the optical variations following the γ-ray ones after four weeks. The delay is 29 d if we take the centroid instead of the peak. The figure inset displays the result of 2000 Monte Carlo simulations according to the 'flux randomization-random subset selection' method (Peterson et al. 1998; Raiteri et al. 2003). From these simulations it is possible to estimate the uncertainty on the delay. We obtained that 88 per cent of the realizations led to a centroid value between 22 and 36 d. Hence, we infer that the optical flux variations follow the γ flux changes with a delay of 29 ± 7 d.

However, if the γ emission is due to inverse-Compton scattering of soft photons off the same electrons producing the optical radiation, then its variations are expected to be simultaneous or delayed with respect to those characterizing the optical radiation, as resulting from modelling non-thermal flares with shocks in a jet (e.g. Sikora et al. 2001; Sokolov, Marscher & McHardy 2004; Sokolov & Marscher 2005). This was observed in several blazars, in particular

[11] We considered the weekly γ fluxes during the outburst period, and the monthly fluxes before and after that (see Fig. 17), while we binned the optical data in seven-day bins.

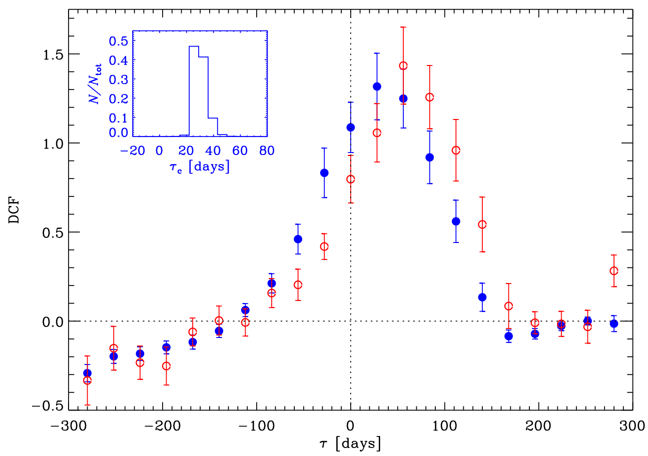

Figure 18. DCFs between the γ-ray fluxes and the *R*-band de-absorbed flux densities (blue filled circles) and between the γ-ray fluxes and the X-ray flux densities at 1 keV (red empty circles). The inset shows the results of Monte Carlo simulations of the γ–optical correlation (see text for details).

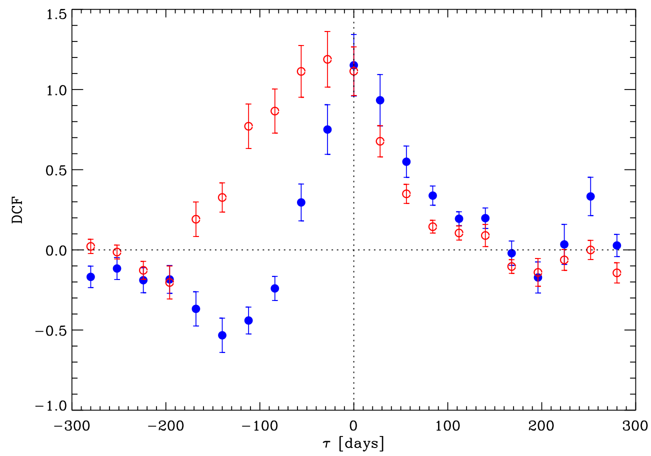

Figure 19. DCFs between the X-ray and 230 GHz flux densities (blue filled circles) and between the X-ray and *R*-band de-absorbed flux densities (red empty circles).

in the FSRQs 4C 38.41 (Raiteri et al. 2012), 3C 345 (Schinzel et al. 2012), and 3C 454.3 (Bonning et al. 2009; Vercellone et al. 2010; Raiteri et al. 2011). In contrast, γ variations leading the optical ones were observed e.g. in the FSRQs PKS 1510−09 by Abdo et al. (2010) and D'Ammando et al. (2011), and 3C 279 by Hayashida et al. (2012). The latter authors found a lag of about 10 d and explained it by assuming that the energy density of the external seed photons for the inverse-Compton process decreases faster along the jet than the energy density of the magnetic field causing the synchrotron optical emission (see also Janiak et al. 2012). Analogous interpretations may also hold for OJ 248.

Alternatively, the complex optical/γ-ray correlation may be explained by considering the effects of turbulence in the jet (Marscher 2014). The fluctuating magnitude and direction of a turbulent magnetic field affects mostly the synchrotron radiation, and therefore adds a component to the optical variability that is not present in the gamma-ray light curve.

Fig. 18 also displays the DCF between the γ-ray fluxes and the X-ray flux densities at 1 keV, suggesting a delay of the X-ray variations of about 2 months. We finally investigated the γ–mm correlation, finding a strong signal and a ∼70 d delay of the mm variations.

Another interesting correlation holds between the X-ray and mm flux densities. Indeed, beside the 2012–2013 outburst, the X-ray light curve also shows a peak during the maximum of the mm light curve at the end of 2010 (see Fig. 16). The DCF in Fig. 19 displays a strong correlation with no time lag, which suggests that the X-ray and mm radiation are produced in the same region, with the X-ray emission likely due to inverse-Compton on the mm photons. A correlation between the X-ray and mm variability has already been found, e.g. in BL Lacertae (Raiteri et al. 2013).

In Fig. 19, we also show the DCF between the X-ray and optical flux densities, indicating that the optical variations precede those in the X-rays by about one month.

Cross-correlations of the γ-ray, X-ray, and *R*-band data with the 37 GHz data only led to weak and somewhat confused signals. This is due to the different behaviour of the corresponding light curves, in particular to the dominance of the 2010–2011 outburst with respect to the 2013 one at 37 GHz.

10 BROAD-BAND SED

Three broad-band Spectral energy distributions (SEDs) of OJ 248 are plotted in Fig. 20. They correspond to the peak of the γ-ray emission (JD = 245 6284), to the peak of the X-ray emission (JD = 245 6317), and to a faint post-outburst epoch (JD = 245 6368). The SEDs are built with simultaneous near-IR, optical, UV, X-ray, and γ-ray data. Because of the smoother radio variability, we gave a tolerance of a few days to the radio data.

Emission in the optical–UV receives an important contribution from the accretion disc radiation, whose signature is more evident in the faint, post-outburst SED. The concave shape of the near-IR spectrum is due to the intersection between the disc contribution and the non-thermal jet emission. These two components have been modelled by Raiteri et al. (2014), who found that the OJ 248 disc is more luminous than a typical type 1 quasi-stellar object (QSO) disc.

Note that the faintest SED at high energies has also the lowest radio flux at 230 GHz, but it exceeds the fluxes of the other SEDs at longer radio wavelengths.

11 SUMMARY AND CONCLUSIONS

In this paper, we have presented the results of a huge multiwavelength observing effort led by the GASP-WEBT Collaboration on the blazar OJ 248. Data were collected starting from 2006 and up to 2013, including two optical–NIR outbursts in 2006–2007 and 2012–2013 and two major radio outbursts in 2010–2011 and 2012–2013. The 2012–2013 outburst was also detected at high energies by the *Swift* and *Fermi* satellites. The correlation between the optical and radio outbursts is clear in 2012–2013, while the optical counterpart of the 2010–2011 radio outburst is difficult to identify. Something likely changed in the source in the period between the two outbursts, one possibility being a slightly better alignment of the optical emitting region with the line of sight with the consequent increase of the Doppler beaming. A strong correlation between the flux variations at γ-rays and those in the optical band is found, but with the optical variations delayed by about one month, which is a peculiar behaviour already found in other blazars. Strong correlation with no time delay has also been found between the X-ray and millimetre flux changes, supporting a common emission region in the jet.

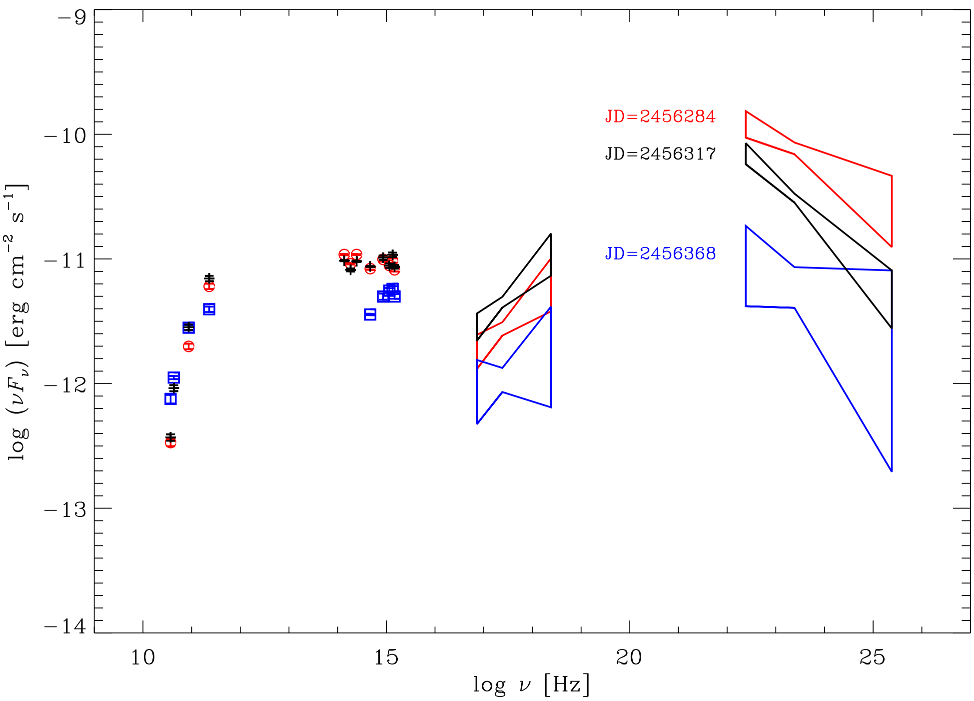

Figure 20. SEDs of OJ 248 from the radio to the γ-ray frequencies during three epochs characterized by different brightness states.

We have analysed the polarimetric behaviour of the source. The fraction of polarized flux remained low for most of time but during the 2012–2013 outburst, when *P* reached ∼19 per cent. Wide rotations of the linear polarization vector can reliably be detected only during the outburst and they occur in both directions, suggesting a complex behaviour of the magnetic field in the jet possibly due to turbulence, and/or a complex jet structure involving spiral paths.

Optical spectra show Mg II lines both in absorption and emission. The absorption line is due to an intervening system at $z = 0.525$ whose reddening effects on the NIR, optical, and UV source emission have been estimated and taken into account. The presence of the intervening system must be considered also when analysing the X-ray radiation. As for the Mg II emission line from the source BLR, we estimated a mean velocity of $(2053 \pm 310)\,\mathrm{km\,s^{-1}}$. The line flux is essentially stable around a mean value of $(6.2 \pm 0.5) \times 10^{-15}\,\mathrm{erg\,cm^{-2}\,s^{-1}}$ also during the 2012–2013 outburst and after, confirming that the jet emission did not affect the BLR, even when considering up to a few months of possible time delay.

ACKNOWLEDGEMENTS

We thank the referee, Vasiliki Pavlidou, for useful comments and suggestions. This article is partly based on observations made with the telescopes IAC80 and TCS operated by the Instituto de Astrofisica de Canarias in the Spanish Observatorio del Teide on the island of Tenerife. Most of the observations were taken under the rutinary observation program. The IAC team acknowledges the support from the group of support astronomers and telescope operators of the Observatorio del Teide. St. Petersburg University team acknowledges support from Russian RFBR grant 15-02-00949 and St. Petersburg University research grant 6.38.335.2015. AZT-24 observations are made within an agreement between Pulkovo, Rome, and Teramo observatories. The Abastumani team acknowledges financial support of the project FR/638/6-320/12 by the Shota Rustaveli National Science Foundation under contract 31/77. This paper is partly based on observations carried out at the German-Spanish Calar Alto Observatory, which is jointly operated by the MPIA and the IAA-CSIC. Acquisition and reduction of the MAPCAT and IRAM 30 m data is supported in part by MINECO (Spain) grant and AYA2010-14844, and by CEIC (Andalucía) grant P09-FQM-4784. This paper is partly based on observations carried out at the IRAM 30 m Telescope, which is supported by INSU/CNRS (France), MPG (Germany), and IGN (Spain). The SMA is a joint project between the Smithsonian Astrophysical Observatory and the Academia Sinica Institute of Astronomy and Astrophysics and is funded by the Smithsonian Institution and the Academia Sinica. The Steward Observatory spectropolarimetric monitoring project is supported by the *Fermi* Guest Investigator grants NNX08AW56G and NNX09AU10G. The research at Boston University (BU) was funded in part by NASA Fermi Guest Investigator grants NNX11AQ03G and NNX13AO99G. The PRISM camera at Lowell Observatory was developed by K. Janes et al. at BU and Lowell Observatory, with funding from the NSF, BU, and Lowell Observatory. The Liverpool Telescope is operated on the island of La Palma by Liverpool John Moores University in the Spanish Observatorio del Roque de los Muchachos of the Instituto de Astrofisica de Canarias, with funding from the UK Science and Technology Facilities Council. The Metsähovi team acknowledges the support from the Academy of Finland to our observing projects (numbers 212656, 210338, 121148, and others). Partly based on observations with the Medicina and Noto telescopes operated by INAF – Istituto di Radioastronomia. EB acknowledge financial support from UNAM-DGAPA-PAPIIT through grant IN111514. GD and OV did the observations/investigations in line with Projects No. 176011 (Dynamics and Kinematics of Celestial Bodies and Systems), 176021 (Visible and Invisible Matter in Nearby Galaxies: Theory and Observations), and 176004 (Stellar Physics) which are supported by the Ministry of Education, Science and Technological Development of the Republic of Serbia. The Torino team acknowledges financial support by INAF through contract PRIN-INAF 2011.

REFERENCES

Abdo A. A. et al., 2009, Astropart. Phys., 32, 193
Abdo A. A. et al., 2010, ApJ, 721, 1425
Agudo I. et al., 2006, A&A, 456, 117
Agudo I., Thum C., Wiesemeyer H., Krichbaum T. P., 2010, ApJS, 189, 1
Atwood W. B. et al., 2009, ApJ, 697, 1071
Bach U. et al., 2007, A&A, 464, 175
Barthelmy S. D. et al., 2005, Space Sci. Rev., 120, 143
Bessell M. S., Castelli F., Plez B., 1998, A&A, 333, 231
Bonning E. W. et al., 2009, ApJ, 697, L81
Burrows D. N. et al., 2005, Space Sci. Rev., 120, 165
Cardelli J. A., Clayton G. C., Mathis J. S., 1989, ApJ, 345, 245
Corbett E. A., Robinson A., Axon D. J., Hough J. H., 2000, MNRAS, 311, 485
D'Ammando F. et al., 2011, A&A, 529, A145
Decarli R., Dotti M., Treves A., 2011, MNRAS, 413, 39
Dickey J. M., Lockman F. J., 1990, ARA&A, 28, 215
Diplas A., Savage B. D., 1994, ApJ, 427, 274
Edelson R. A., Krolik J. H., 1988, ApJ, 333, 646
Fan J.-H., Kurtanidze O. M., Nikolashvili M. G., Gupta A. C., Zhang J.-S., Yuan Y.-H., 2004, Chin. J. Astron. Astrophys., 4, 133
Gehrels N. et al., 2004, ApJ, 611, 1005
Gurwell M. A., Peck A. B., Hostler S. R., Darrah M. R., Katz C. A., 2007, in Baker A. J., Glenn J., Harris A. I., Mangum J. G., Yun M. S., eds, ASP Conf. Ser. Vol. 375, From Z-Machines to ALMA: (Sub)Millimeter Spectroscopy of Galaxies. Astron. Soc. Pac., San Francisco, p. 234
Hartman R. C. et al., 1999, ApJS, 123, 79
Hayashida M. et al., 2012, ApJ, 754, 114
Hufnagel B. R., Bregman J. N., 1992, ApJ, 386, 473
Janiak M., Sikora M., Nalewajko K., Moderski R., Madejski G. M., 2012, ApJ, 760, 129
Jorstad S. G., Marscher A. P., 2004, ApJ, 614, 615
Kalberla P. M. W., Burton W. B., Hartmann D., Arnal E. M., Bajaja E., Morras R., Pöppel W. G. L., 2005, A&A, 440, 775
Kaspi S., Smith P. S., Netzer H., Maoz D., Jannuzi B. T., Giveon U., 2000, ApJ, 533, 631
Larionov V. M. et al., 2013, ApJ, 768, 40
León-Tavares J. et al., 2013, ApJ, 763, L36
Leto P., Umana G., Trigilio C., Buemi C. S., Dolei S., Manzitto P., Cerrigone L., Siringo C., 2009, A&A, 507, 1467
Markwardt C. B., 2009, in Bohlender D. A., Durand D., Dowler P., eds, ASP Conf. Ser. Vol. 411, Astronomical Data Analysis Software and Systems XVIII. Astron. Soc. Pac., San Francisco, p. 251
Marscher A. P., 2014, ApJ, 780, 87
Marscher A. P. et al., 2008, Nature, 452, 966
Marscher A. P. et al., 2010, ApJ, 710, L126
Massaro E., Giommi P., Leto C., Marchegiani P., Maselli A., Perri M., Piranomonte S., Sclavi S., 2009, A&A, 495, 691
Mattox J. R. et al., 1996, ApJ, 461, 396
Nolan P. L. et al., 2012, ApJS, 199, 31
Peterson B. M., 2001, in Aretxaga I., Kunth D., Mújica R., eds, Advanced Lectures on the Starburst-AGN Connection. World Scientific Press, Singapore, p. 3
Peterson B. M., Wanders I., Horne K., Collier S., Alexander T., Kaspi S., Maoz D., 1998, PASP, 110, 660
Poole T. S. et al., 2008, MNRAS, 383, 627
Raiteri C. M., Ghisellini G., Villata M., de Francesco G., Lanteri L., Chiaberge M., Peila A., Antico G., 1998, A&AS, 127, 445
Raiteri C. M. et al., 2003, A&A, 402, 151
Raiteri C. M. et al., 2005, A&A, 438, 39
Raiteri C. M., Villata M., Capetti A., Heidt J., Arnaboldi M., Magazzù A., 2007, A&A, 464, 871
Raiteri C. M. et al., 2010, A&A, 524, A43
Raiteri C. M. et al., 2011, A&A, 534, A87
Raiteri C. M. et al., 2012, A&A, 545, A48
Raiteri C. M. et al., 2013, MNRAS, 436, 1530
Raiteri C. M. et al., 2014, MNRAS, 442, 629
Rao S. M., Turnshek D. A., 2000, ApJS, 130, 1
Rao S. M., Nestor D. B., Turnshek D. A., Lane W. M., Monier E. M., Bergeron J., 2003, ApJ, 595, 94
Roming P. W. A. et al., 2005, Space Sci. Rev., 120, 95
Schinzel F. K., Lobanov A. P., Taylor G. B., Jorstad S. G., Marscher A. P., Zensus J. A., 2012, A&A, 537, A70
Sikora M., Błażejowski M., Begelman M. C., Moderski R., 2001, ApJ, 554, 1
Smith A. G., 1996, in Miller H. R., Webb J. R., Noble J. C., eds, ASP Conf. Ser. Vol. 110, Blazar Continuum Variability. Astron. Soc. Pac., San Francisco, p. 3
Smith P. S., Montiel E., Rightley S., Turner J., Schmidt G. D., Jannuzi B. T., 2009, preprint (arXiv:0912.3621)
Sokolov A., Marscher A. P., 2005, ApJ, 629, 52
Sokolov A., Marscher A. P., McHardy I. M., 2004, ApJ, 613, 725
Sorcia M., Benítez E., Hiriart D., López J. M., Cabrera J. I., Mújica R., 2014, ApJ, 794, 54
Steidel C. C., Kollmeier J. A., Shapley A. E., Churchill C. W., Dickinson M., Pettini M., 2002, ApJ, 570, 526
Stickel M., Fried J. W., Kuehr H., Padovani P., Urry C. M., 1991, ApJ, 374, 431
Stroh M. C., Falcone A. D., 2013, ApJS, 207, 28
Tavani M. et al., 2009, A&A, 502, 995
Teräsranta H. et al., 1998, A&AS, 132, 305
Ulrich M.-H., Owen F. N., 1977, Nature, 269, 673
Vercellone S. et al., 2010, ApJ, 712, 405
Villata M. et al., 1997, A&AS, 121, 119
Villata M. et al., 2007, A&A, 464, L5
Villata M. et al., 2009a, A&A, 501, 455
Villata M. et al., 2009b, A&A, 504, L9

[1] *INAF, Osservatorio Astrofisico di Torino, via Osservatorio 20, I-10025 Pino Torinese, Italy*
[2] *Instituto de Astrofisica de Canarias (IAC), E-38205 La Laguna, Tenerife, Spain*
[3] *Departamento de Astrofisica, Universidad de La Laguna, E-38206 La Laguna, Tenerife, Spain*
[4] *Dip. Fisica e Astronomia, Università degli Studi di Bologna, Via Ranzani 1, I-40127 Bologna, Italy*
[5] *INAF – Istituto di Radioastronomia, Via Gobetti 101, I-40129 Bologna, Italy*
[6] *Steward Observatory, University of Arizona, Tucson, AZ 85721, USA*
[7] *Astronomical Institute, St.-Petersburg State University, 198504 St.-Petersburg, Russia*
[8] *Pulkovo Observatory, 196140 St.-Petersburg, Russia*
[9] *Isaac Newton Institute of Chile, St.-Petersburg Branch*
[10] *Instituto de Astrofísica de Andalucía (CSIC), Apartado 3004, E-18080 Granada, Spain*
[11] *Current Address: Joint Institute for VLBI in Europe, Postbus 2, NL-7990 AA Dwingeloo, the Netherlands*
[12] *Max-Planck-Institut für Radioastronomie, Auf dem Hügel, 69, D-53121 Bonn, Germany*
[13] *Institute of Astronomy, Bulgarian Academy of Sciences, 1784 Sofia, Bulgaria*
[14] *Instituto de Astronomía, Universidad Nacional Autónoma de México, Apdo. Postal 70-264, México, Mexico*
[15] *Physics Department, University of Crete, PO Box 2208, GR-71003 Heraklion, Greece*
[16] *Department of Astronomy, University of Sofia "St. Kliment Ohrisdski", BG-1164 Sofia, Bulgaria*
[17] *INAF, Osservatorio Astrofisico di Catania, Via S. Sofia 78, I-95123 Catania, Italy*
[18] *EPT Observatories, Tijarafe, La Palma, Spain*
[19] *INAF, TNG Fundación Galileo Galilei, E-38712 La Palma, Spain*

[20] *Graduate Inst. of Astronomy, National Central University, 300 Zhongda Road, 32001 Zhongli, Taiwan*
[21] *Astronomical Observatory, Volgina 7, 11060 Belgrade, Serbia*
[22] *INAF, Osservatorio Astronomico di Roma, I-00136 Roma, Italy*
[23] *Maidanak Observatory of the Ulugh Beg Astronomical Institute, 100052 Uzbekistan*
[24] *Harvard–Smithsonian Center for Astrophysics, Cambridge, MA 02138, USA*
[25] *Instituto de Astronomía, Universidad Nacional Autónoma de México, Ensenada, B.C. 22800, Mexico*
[26] *Institute for Astrophysical Research, Boston University, 725 Commonwealth Avenue, Boston, MA 02215, USA*
[27] *Abastumani Observatory, Mt. Kanobili, 0301 Abastumani, Georgia*
[28] *ZAH, Landessternwarte Heidelberg, Knigstuhl 12, D-69117 Heidelberg, Germany*
[29] *Engelhardt Astronomical Observatory, Kazan Federal University, 422526 Tatarstan, Russia*
[30] *Center for Astrophysics, Guangzhou University, Guangzhou 510006, China*
[31] *Aalto University Metsähovi Radio Observatory, Metsähovintie 114, FI-02540 Kylmälä, Finland*
[32] *Aalto University Department of Radio Science and Engineering, PO BOX 13000, FI-00076 AALTO, Finland*
[33] *Department of Physics & Astronomy, University of Canterbury, Private Bag 4800, Christchurch 8140, New Zealand*
[34] *Department of Physics and Astronomy, Univ. of Southampton, Southampton SO17 1BJ, UK*
[35] *Armagh Observatory, College Hill, Armagh BT61 9DG, UK*
[36] *Astrophysikalisches Institut Potsdam, An der Sternwarte 16, D-14482 Potsdam, Germany*
[37] *Lowell Observatory, Flagstaff, AZ 86001, USA*
[38] *Space Science Institute, Boulder, CO 80301, USA*

This paper has been typeset from a TEX/LATEX file prepared by the author.

Planetary and Space Science 118 (2015) 127–137

Contents lists available at ScienceDirect

Planetary and Space Science

journal homepage: www.elsevier.com/locate/pss

Results from the worldwide coma morphology campaign for comet ISON (C/2012 S1)☆

Nalin H. Samarasinha[a,*], Beatrice E.A. Mueller[a], Matthew M. Knight[b], Tony L. Farnham[c], John Briol[d], Noah Brosch[e], John Caruso[f], Xing Gao[g], Edward Gomez[h], Tim Lister[h], Carl Hergenrother[i], Susan Hoban[j], Roy Prouty[j], Mike Holloway[k], Nick Howes[l], Ernesto Guido[l], Man-To Hui[m], Joseph H. Jones[n], Tyler B. Penland[n], Samuel R. Thomas[n], Jim Wyrosdick[n], Nikolai Kiselev[o], Aleksandra V. Ivanova[o], Thomas G. Kaye[p], Jean-Baptist Kikwaya Eluo[q], Betty P.S. Lau[r], Zhong-Yi Lin[s], José Luis Martin[t], Alexander S. Moskvitin[u], Martino Nicolini[v], Brian D. Ottum[w], Chris Pruzenski[x], David C. Vogel[x], Leo Kellett[x], Valerie Rapson[x], Joel Schmid[x], Brandon Doyle[x], Frank Dimino[x], Stephanie Carlino[x], Margarita Safonova[y], Jayant Murthy[y], Firoza Sutaria[y], David G. Schleicher[b], Colin Snodgrass[z], Cihan T. Tezcan[aa], Onur Yorukoglu[aa], David Trowbridge[bb], Dennis Whitmer[cc], Quan-Zhi Ye[dd]

[a] *Planetary Science Institute, USA*
[b] *Lowell Observatory, USA*
[c] *University of Maryland, College Park, USA*
[d] *Spirit Marsh Observatory, USA*
[e] *Wise Observatory, Tel Aviv University, Israel*
[f] *Temecula, CA, USA*
[g] *No 1 Senior High School, Urumqi, China*
[h] *Las Cumbres Observatory Global Telescope Network, USA*
[i] *University of Arizona, USA*
[j] *University of Maryland, Baltimore County, USA*
[k] *Holloway Comet Observatory, USA*
[l] *Remanzacco Observatory, Italy*
[m] *University of California, Los Angeles, USA*
[n] *University of North Georgia, USA*
[o] *Main Astronomical Observatory, National Academy of Sciences, Ukraine*
[p] *Raemor Vista Observatory, USA*
[q] *Vatican Observatory, USA*
[r] *Hong Kong*
[s] *National Central University, Taiwan*
[t] *Carpe Noctem Observatory, Spain*
[u] *Special Astrophysical Observatory, Russian Academy of Sciences, Russia*
[v] *Cavezzo Observatory, Italy*
[w] *Saline, MI, USA*
[x] *Astronomy Section, Rochester Academy of Science, USA*
[y] *Indian Institute of Astrophysics, India*
[z] *The Open University, UK*
[aa] *Ankara University, Kreiken Observatory, Turkey*
[bb] *Tinyblue Observatory, USA*
[cc] *Eagle Nest Digital Observatory, USA*
[dd] *University of Western Ontario, Canada*

☆We dedicate this paper to our colleague and friend Martino Nicolini who on the 29th January 2015 passed away after a long fight against cancer. Martino, who was a nuclear engineer by profession, was an avid amateur astronomer and he collaborated with us as well as with many other organizations. He epitomized what the professional–amateur collaborations could accomplish and will be sorely missed by all.

* Correspondence to: Planetary Science Institute, 1700 E Ft Lowell Road, Suite 106, Tucson, AZ 85719, USA. Tel.: +1 520 547 3952.
E-mail address: nalin@psi.edu (N.H. Samarasinha).

http://dx.doi.org/10.1016/j.pss.2015.10.006

ARTICLE INFO

Article history:
Received 4 March 2015
Received in revised form
27 September 2015
Accepted 9 October 2015
Available online 23 October 2015

Keywords:
Comet C/2012 S1 (ISON)
Coma morphology
Cometary dust
Cometary dynamics

ABSTRACT

We present the results of a global coma morphology campaign for comet C/2012 S1 (ISON), which was organized to involve both professional and amateur observers. In response to the campaign, many hundreds of images, from nearly two dozen groups were collected. Images were taken primarily in the continuum, which help to characterize the behavior of dust in the coma of comet ISON. The campaign received images from January 12 through November 22, 2013 (an interval over which the heliocentric distance decreased from 5.1 AU to 0.35 AU), allowing monitoring of the long-term evolution of coma morphology during comet ISON's pre-perihelion leg. Data were contributed by observers spread around the world, resulting in particularly good temporal coverage during November when comet ISON was brightest but its visibility was limited from any one location due to the small solar elongation. We analyze the northwestern sunward continuum coma feature observed in comet ISON during the first half of 2013, finding that it was likely present from at least February through May and did not show variations on diurnal time scales. From these images we constrain the grain velocities to $\sim 10\ \mathrm{m\ s^{-1}}$, and we find that the grains spent 2–4 weeks in the sunward side prior to merging with the dust tail. We present a rationale for the lack of continuum coma features from September until mid-November 2013, determining that if the feature from the first half of 2013 was present, it was likely too small to be clearly detected. We also analyze the continuum coma morphology observed subsequent to the November 12 outburst, and constrain the first appearance of new features in the continuum to later than November 13.99 UT.

1. Introduction

Comet C/2012 S1 (ISON) (hereafter comet ISON) was discovered on September 21, 2012 at a heliocentric distance, r_h, of 6.3 AU (Novski and Novichonok, 2012). Soon it attracted worldwide interest because of its extremely small perihelion distance (0.0125 AU $=$2.7 solar radii) and the prediction that it may become a bright naked eye object based on its brightness behavior soon after discovery. The discovery of comet ISON at a large heliocentric distance and the favorable observing geometry during most of the apparition, partially facilitated by the comparatively high orbital inclination (61.9°), made it the first instance that the behavior of cometary activity of a sungrazer[1] was monitored for a large range of heliocentric distances. This range included the large distances (i.e., $>$2–3 AU) where the nuclear activity is dominated by super volatiles (e.g., CO, CO_2), the region where water is the primary driver of activity, as well as the extremely small heliocentric distances when the sublimation of refractory material, including metallic species that are present in the dust grains, could occur. In other words, the heliocentric distances covered a range over which the incident solar flux increased by a factor of about 2.5×10^5 making this the first time that the effects due to such a large range of solar fluxes on the nucleus were monitored for any comet. Anticipating these extreme conditions, there were many predictions on what might happen to the nucleus as it approached perihelion. The predictions included those pertaining to cometary activity and nuclear rotational state, as well as the ultimate fate of the nucleus (e.g., Samarasinha and Mueller, 2013; Knight and Walsh, 2013; Ferrín, 2014).

Past work on morphological studies of cometary comae has demonstrated the value for inferring properties of the nucleus such as rotation period, seasonal activity changes, and pole orientation (e.g., Schleicher et al., 2003; Farnham et al., 2007; Farnham, 2009; Knight et al., 2012 and references therein). With the goal of temporal monitoring of comet ISON's coma features, the campaign organizers[2] coordinated a Worldwide Campaign of Coma Morphology (see http://www.psi.edu/ison for the call for images). This effort was also carried out in coordination with the NASA Comet ISON Observing Campaign (CIOC) but was independent of the CIOC activities (see http://www.isoncampaign.org for additional information on CIOC). After May 2013, comet ISON was not observable for more than a few hours from any geographic location due to the relatively small solar elongation, so a global effort, incorporating images from both professionals and amateurs, was necessary to carry out a detailed analysis of the coma morphology and its temporal and spatial evolution. Although the relatively large geocentric distances to the comet during the apparition ($>$0.85 AU during the pre-perihelion leg and $>$0.43 AU during the post-perihelion leg) would not provide the ideal circumstances needed for producing high-resolution detailed coma features, the large range of heliocentric distances over which comet ISON might be studied and the resulting possibility of observing a variety of interesting coma morphologies motivated us to organize this coordinated worldwide campaign. The campaign solicited both continuum (dust) images as well as gas images of the near-nucleus region of the comet. We are happy to note that a large number of images were collected from observers spread around the world at different longitudes.

Monitoring of comet ISON was encouraged for both before and after its perihelion passage, with an emphasis on the time around perigee (December 26, 2013) when it was expected to experience rapid changes and would have been observable for many hours per night in the northern hemisphere. However, the comet started to disintegrate just prior to its perihelion passage (cf. Knight and Battams, 2014; Sekanina and Kracht, 2014) leaving us with images only from the pre-perihelion leg.

In Section 2 of this paper, we provide a description of the images collected by the campaign. In Sections 3 and 4, we discuss the analyses of these images during the pre-water dominated phase and the water-dominated phase, respectively. Section 5 provides the summary and conclusions of this paper.

2. Observations

Images were collected from both amateur and professional observers, with diverse ranges of telescope apertures, observing conditions, filters, and data collection methodologies. These data are far from uniform, but such an approach was necessary in order

[1] A formal definition for the sungrazer comets is provided in Knight and Walsh (2013) in terms of the Roche limit.

[2] The campaign was organized by N.H. Samarasinha, B.E.A. Mueller, M.M. Knight, and T.L. Farnham.

Table 1
Summary of observations corresponding to different observers.

Observers	Longitude, Latitude	Range of UT dates (2013)	Filters	r_h [AU]	Δ [AU]	α [deg]	ε [deg]	$PA_{\odot}$ [deg]
Z.-Y. Lin, H.-Y. Hsiao, C.-S. Lin, H.-C. Lin	120.87° E, 23.47° N	Oct 4–6, 8–10, 12, 14, 17–24, 26–28 Nov 5–8, 11, 13–14, 16, 22	R R	1.6–1.1 0.9–0.4	2.1–1.3 1.1–0.9	28–48 57–101	49–53 50–21	112–113 114–101
Q.-Z. Ye, M.-T. Hui, X. Gao	87.01° E, 43.05° N	Oct 14, 20–21, 26, 31 Nov 1, 6, 13–16	Open Open	1.4–1.0 1.0–0.6	1.8–1.2 1.2–0.9	34–51 52–83	52–52 52–35	112–113 114–110
M. Safonova, J. Murthy, F. Sutaria, N. Brosch	78.96° E, 32.78° N	Jan 22 Feb 19, 21–22 May 1, 4 Sep 8 Oct 1, 3 Nov 10	V, R, I R, I V, R, open I B, R R	5.0 4.7–4.7 3.9–3.9 2.1 1.7–1.6 0.8	4.1 4.0–4.0 4.3–4.3 2.8 2.2–2.1 1.0	3 9–10 13–13 17 27–28 67	164 132–128 59–56 36 48–48 45	315 284–283 270–270 111 111–112 113
N. Kiselev, A. Ivanova, A. Moskvitin	41.44° E, 43.65° N	Nov 11	B, V, R, I	0.7	1.0	69	44	113
C. Tezcan, O. Yorukoglu	32.77° E, 39.84° N	Oct 27	V, R, I	1.1	1.4	46	53	113
P.S. Lau	2.30° W, 38.15° N	Sep 28, 30 Oct 2, 19, 25, 31 Nov 1, 6, 14	R R R	1.7–1.7 1.6–1.0 1.0–0.6	2.2–2.2 2.1–1.2 1.2–0.9	25–26 27–51 52–78	46–48 48–52 52–38	111–111 112–114 114–112
J. Martin	3.68° W, 40.40° N	Sep 24 Oct 6–8, 11–12, 16, 31 Nov 12, 14	V, R V, R, open V, R	1.8 1.6–1.0 0.7–0.6	2.4 2.0–1.2 1.0–0.9	23 29–51 71–78	44 50–52 43–38	111 112–114 113–112
J. Caruso	16.51º W, 28.30° N	Oct 6	R	1.6	2.0	29	50	112
N. Howes, E. Guido, M. Nicolini	17.88° W, 28.76° N	May 1–3, 5–7 Oct 1, 4–11, 17, 20–23 Nov 4, 6–10, 12–13	R R R	3.9–3.8 1.7–1.2 0.9–0.7	4.3–4.3 2.2–1.5 1.1–0.9	13–12 27–42 56–74	59–53 48–54 50–41	270–270 111–113 114–112
S. Hoban, R. Prouty	76.71° W, 39.25° N	Nov 4, 8–10	CN, GC, C_2, H_2O^+, open	0.9–0.7	1.1–1.0	56–68	50–44	114–113
D. Vogel	77.40° W, 42.93° N	Nov 14, 16	Open	0.7–0.6	0.9–0.9	77–78	40–38	112–111
C. Pruzenski, L. Kellett, V. Rapson, J. Schmid, B. Doyle, F. Dimino, D. Vogel, S. Carlino	77.50° W, 42.93° N	Nov 8, 11, 14, 16	Open	0.8–0.6	1.0–0.9	63–83	47–35	114–110
B. Ottum	83.71° W, 42.19° N	Oct 8, 18, 25, 30 Nov 8, 12	Open Open	1.5–1.0 0.8–0.7	1.9–1.3 1.0–0.9	31–50 63–73	50–52 47–42	112–114 114–112
J. Jones, T. Penland, J. Wyrosdick, S. Thomas	84.05° W, 34.52° N	Nov 2, 14	V	1.0–0.6	1.2–0.9	53–78	52–38	114–111
M. Holloway	94.40° W, 35.54° N	Sep 3, 6, 26 Oct 7, 11, 24–25 Nov 1, 7	Open Open Open	2.1–1.7 1.5–1.1 1.0–0.8	2.9–2.3 2.0–1.4 1.2–1.1	15–25 30–44 52–62	33–46 50–53 52–48	111–111 112–113 114–114
J. Briol	94.89° W, 45.66° N	Oct 13, 18, 25, 27 Nov 3, 12, 15	Open Open	1.4–1.1 0.9–0.6	1.8–1.4 1.2–0.9	34–46 54–80	52–53 51–37	112–114 114–111
E. Gomez, Z-Y. Lin, T. Lister	104.02° W, 30.68° N	Nov 2, 10-11, 15, 17	B, V, I	1.0–0.6	1.2–0.9	53–84	52–34	114–110
J-B. Kikwaya Eluo	109.89° W, 32.70° N	Sep 28–30 Nov 6–8	B, V, R B, V, R	1.7–1.7 0.9–0.8	2.2–2.2 1.1–1.0	25–26 59–64	46–48 49–47	111–111 114–114
C. Hergenrother	109.89° W, 32.70° N	Jan 15, 20–21 Feb 8, 15 Mar 16–17 Apr 21–22 May 19–21	V, R V, R V, R V, R V, R	5.1–5.0 4.9–4.8 4.4–4.4 4.0–4.0 3.7–3.6	4.1–4.1 4.0–4.0 4.1–4.1 4.3–4.3 4.3–4.3	2–3 7–8 13–13 13–13 11–11	170–165 145–136 104–101 68–66 43–41	346–316 290–286 276–276 271–271 269–269

Table 1 (*continued*)

Observers	Longitude, Latitude	Range of UT dates (2013)	Filters	r_h [AU]	Δ [AU]	α [deg]	ε [deg]	$PA_{\odot}$ [deg]
B. Gary	110.23° W, 31.45° N	Oct 8, 31	R, open	1.5–1.0	1.9–1.3	31–50	50–52	112–114
D. Whitmer, B. Gary	110.25° W, 31.42° N	Oct 16, 31 Nov 1–2, 4, 6, 9	R V, R	1.4–1.0 1.0–0.8	1.7–1.3 1.2–1.0	34–50 52–66	53–52 52–45	113–114 114–113
T. Kaye, B. Gary	110.65° W, 31.67° N	Oct 20, 28 Nov 2	V, R R	1.3–1.1 1.0	1.6–1.3 1.2	39–48 53	53–53 52	113–114 114
M. Knight, D. Schleicher	111.42° W, 34.74° N	Jan 12, 13 Mar 11 Apr 4, 6, 7, 8 May 1, 3 June 11 Sep 12–13, 30 Oct 1-6, 8–9, 15 Nov 1–4, 6–12	R B, V, R B, V, R, I, CN, BC B, V, R, I V, R, I V, R, OH, CN, C_3, CO^+, BC, C_2, GC, RC B, V, R, I, CN, C_3, CO^+, BC, C_2, GC, RC R, CN	5.1–5.1 4.5 4.2–4.2 3.9–3.9 3.4 2.0–1.7 1.7–1.4 1.0–0.7	4.2–4.2 4.1 4.2–4.2 4.3–4.3 4.3 2.7–2.2 2.2–1.7 1.2–1.0	2–2 12 14–14 13–13 7 18–26 27–36 52–72	170–170 109 84–80 59–56 25 38–48 48–53 52–42	355–8 277 273–272 270–270 265 111–111 111–113 114–113
D. Trowbridge	122.60° W, 48.08° N	Oct 6, 29	V, R	1.6–1.1	2.0–1.3	29–49	50–53	112–114
T. Lister, C. Snodgrass, M. Knight	156.26° W, 20.71° N	Oct 22–25 Nov 3–4, 8–9	G, R, I R, OH, CN, C_3, C_2, NH_2	1.2–1.2 0.9–0.8	1.5–1.4 1.2–1.0	41–44 54–65	54–54 51–46	113–113 114–113

Notes:
1. The symbols for the parameters are defined in Fig. 1.
2. "Open" filter refers to either "no filter" or "clear filter".
3. B, V, G, R, and I are broadband filters (could be of different photometric systems) while all others are narrowband filters.
4. Not all filters were used during every night of a given month.

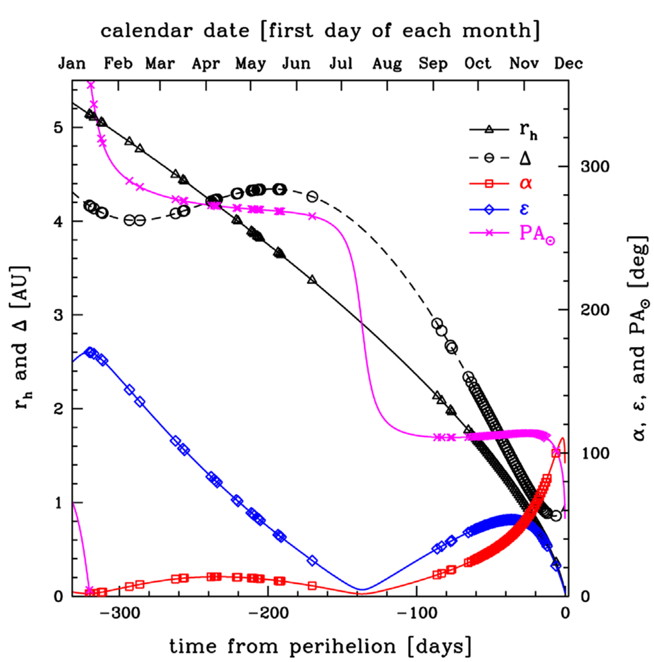

Fig. 1. Behavior of heliocentric distance r_h, geocentric distance Δ, solar phase angle α, solar elongation (Sun–Earth–comet angle) ε, and position angle PA of the skyplane-projected Sun direction $PA_{\odot}$ (measured from north through east) as a function of time. The symbols depict the UT dates when observations are available from this global campaign. The parameters corresponding to each symbol are identified in the legend.

to obtain as much longitudinal coverage as possible. Observers were asked to reduce (remove bias and correct for flat fielding) their own images prior to submitting them to the campaign. The campaign organizers, using these reduced images, carried out all image enhancements. The relevant enhancement techniques are described in Samarasinha and Larson (2014). The coma images we received cover a large interval from January 12, 2013 ($r_h \sim 5.14$ AU) to November 22, 2013 ($r_h \sim$ 0.35 AU). Table 1 lists a summary of information on the images provided by different groups of observers ordered based on the geographic longitude of the observations. Fig. 1 shows the observational circumstances for all the images received by the campaign. The symbols for different parameters listed in Table 1 and Fig. 1 are identified in the legend of Fig. 1. Most observations listed in Table 1 were not published elsewhere and are presented here for the first time. Observers submitted different sized images; however, the pixel scales for all the images were smaller than the respective astronomical seeing.

As can be seen from Table 1 and Fig. 1, the majority of the images were obtained between September and mid-November, 2013, when the comet was bright and the solar elongation was $> 30°$. However, as we will discuss in detail in Section 4, the images from this time interval showed no clearly identifiable coma features in the continuum until the outburst that started around November 12 (e.g., Opitom et al., 2013a). In contrast, when the comet's solar elongation was favorable early in the apparition (i.e., before June, 2013), there were many clearly identifiable coma features in the continuum. In images of the gas coma, features appeared by November 1, nearly a month prior to the perihelion of November 28.779 UT (e.g., Opitom et al., 2013b; Knight and Schleicher, 2015). In the following sections, we analyze the continuum images and provide a rationale for the morphological behavior.

3. Results from the pre-water-dominated phase

The pre-water-dominated phase (i.e., when the surface temperature of a comet is too low for water to be the dominant or the most productive volatile, where super-volatiles such as CO or CO_2 could be the primary driver of cometary activity) occurs when a comet is further than about 2–3 AU from the Sun (e.g., Bockelée-Morvan et al., 2004). The time when comet ISON was at small solar elongations (i.e., approximately $< 30°$ from June through August

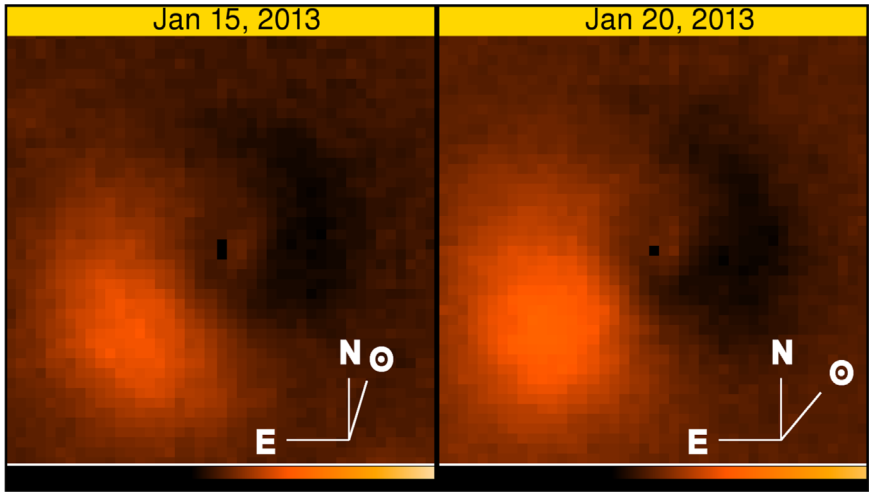

Fig. 2. Inner coma region of two R-band images taken at the Vatican Advanced Technology Telescope in mid-January ($r_h \sim 5$ AU). The images are enhanced using division by azimuthal median technique (e.g., Samarasinha and Larson, 2014). Orange represents brighter regions while black denotes the dimmer regions. Each panel is approximately 48,000 km across with the nucleus located at the center. The skyplane-projected PA of the Sun direction was rapidly moving clockwise from 343° to 320° (respective values are for January 15 and 20). The bright feature in the southeast quadrant is attributed to dust emitted from the nucleus that was subsequently swept away in the respective anti-sunward directions over a few weeks. Low spatial resolution and S/N due to the large geocentric distance prevent unambiguous detection of coma features close to the nucleus.

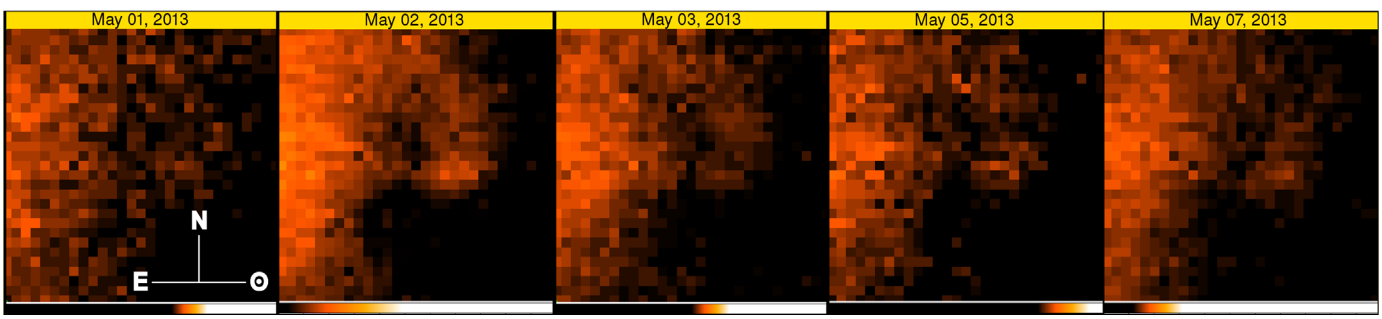

Fig. 3. The near nucleus region of R-band images taken at the Liverpool Telescope on May 1, 2, 3, 5, and 7 (left to right). Images are enhanced using the division by azimuthal average technique, which is nearly identical to the division by azimuthal median (e.g., Samarasinha and Larson, 2014). Each panel is approximately 25,000 km across with the nucleus located at the center. The skyplane-projected PA of the Sun direction is 270°. The sunward feature originates in an approximately westerly direction (to the right) and then moves northward and finally merges with the dust tail which is to the left (East) as a consequence of the radiation pressure effects. No clearly discernable temporal variations of the sunward feature are detected at this spatial resolution and scale. The minor changes from one panel to another are due to low brightness of the comet at this heliocentric distance.

2013; also Fig. 1) coincides with the transition to water-dominated gas production, providing a natural boundary for the observations. Therefore, we designate observations prior to July 2013 (i.e., $r_h > \sim 3.1$ AU) as representing the pre-water-dominated phase, while images after August 2013 (i.e., $r_h < \sim 2.2$ AU) as coinciding with the water-dominated phase. In this section, we analyze and discuss the coma morphology and its evolution in the pre-water dominated phase.

Despite the fact that the comet was discovered at 6.3 AU from the Sun, the large geocentric distance coupled with the low surface brightness of the coma prevented the acquisition of high signal-to-noise (S/N) images with good spatial resolution. In addition, observational manifestation of radiation pressure is the combined effect of the large heliocentric distance and the small solar phase angle (< 10° until late-February with a minimum of 1.8° on January 11). This impeded any immediate detection of unambiguous coma morphology other than the dust tail in the earliest images (Fig. 2). However, as the comet moved towards the inner solar system it underwent a rapid increase in its brightness prior to 5 AU (e.g., Figure 2 of Meech et al., 2013) that provided the first realistic opportunity for coma morphological studies.

3.1. *Sunward feature in the continuum images*

The first announcement of the presence of a coma feature in the continuum was based on enhanced Hubble Space Telescope (HST) images taken on April 10, 2013 (Li et al., 2013). The HST images showed a northwest sunward feature starting at a westerly direction and curving towards north and then merging with the tail due to radiation pressure. Then, Howes and Guido (2013) announced the presence of the same sunward feature in ground-based images taken in early-May ($r_h \sim 3.9$ AU) from the 2 m Liverpool Telescope (LT). Fig. 3 shows the entire set of the LT images from this epoch indicating that there are no clearly discernible changes in the morphology on a daily timescale. Image enhancement of comet ISON images taken at the 4.3 m Discovery Channel Telescope (DCT) by Knight and Schleicher (2015) provides clear evidence that the same sunward feature was present from March through mid-May, and HST observations by Hines and et al.

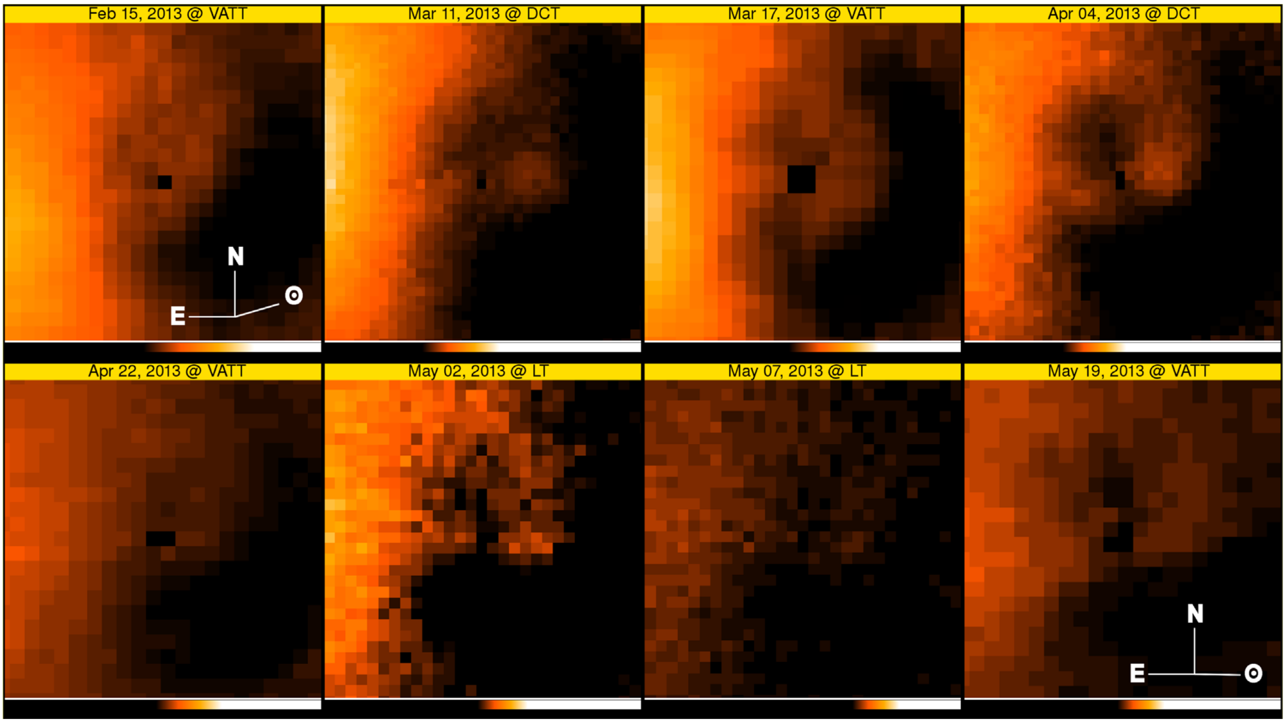

Fig. 4. Images from February to May (r_h decreasing from ~4.8 AU to ~3.7 AU) showing the evolution of the sunward feature. The date and telescope are given at the top of each panel, and the corresponding geometric circumstances can be determined from Fig. 1 and Table 1. All images are enhanced with division by azimuthal median. Each panel is approximately 25,000 km across. The PA of the Sun direction gradually varies from 286° (February 15) to 269° (May 19). The sunward feature in the northwest quadrant was morphologically very similar during the entire time frame.

(2014) in early May confirm that it was relatively unchanged since April even at higher spatial scales. Images of comet ISON taken at the 1.8 m Vatican Advanced Technology Telescope (VATT) by Carl Hergenrother in mid-February show the same sunward feature[3] albeit at a lower S/N. Therefore, we infer that this sunward feature is present at least in the images spanning an interval from mid-February to mid-May 2013. As June approached, the decreasing solar elongation prevented continued monitoring of this feature[4]. Fig. 4 shows the temporal evolution of the feature in the February–May time frame.

For activity originating from a fixed source region away from the poles, one expects to see morphological variations on rotational timescales. No photometric variations in the brightness of comet ISON were detected in January by the Deep Impact spacecraft (Farnham et al., 2013), by the HST in April (Li et al., 2013), or by the Spitzer Space Telescope in June (Lisse and et al., 2013) suggesting any rotational variation should be small. Despite that, observations taken on November 1, 2013 by the HST, when the comet was much closer to us ($r_h = 1.00$ AU, $\Delta = 1.23$ AU), show a single-peak photometric variation of nearly a factor two with a period of ~10.4 h which was attributed to the rotation of the nucleus (Lamy et al., 2014).

However, no variations in the morphology were detected at rotational timescales either based on the ground-based images or on the HST images. Due to this fact, Li et al. (2013) attribute the origin of the sunward feature observed by HST in April to a source region near comet ISON's rotational pole. Another possibility is that this feature is due to the cumulative grain outflow from the sunward side of the nucleus as a response to insolation and not necessarily from a fixed source region on the nucleus (cf. Belton, 2013).

3.2. *Characterization of grains in the sunward feature*

The measured sunward extension of the feature projected onto the skyplane, d, is 4×10^3 – 6×10^3 km. Therefore, for this d, $V^2/\beta > 10^{-3}$ km^2 s^{-2} where V is the outflow velocity of grains and β is the radiation pressure parameter (cf. Eq. (5) of Mueller et al., 2013). For dominant micron-size grains (i.e., $\beta \sim 0.1$; Burns et al., 1979), V should be ~10 m s^{-1}. Grain outflow velocities for micron sized grains that are of the order of ten or a few tens of m s^{-1} are not uncommon and were observed in other comets (e.g., comet Siding Spring (C/2013 A1): Li et al. (2014), Tricarico et al. (2014), Kelley et al. (2014); comet 9P/Tempel 1: Meech et al. (2011), Vasundhara (2009)).

Considering that the corresponding geocentric distance during this interval is approximately 4.0–4.3 AU and assuming a typical ground-based astronomical seeing of 1 arcsec, the spatial resolution at the comet is ~3×10^3 km (for HST, the corresponding spatial resolution is an order of magnitude smaller). During a time interval corresponding to the single peak rotational period near 10.4 h suggested by Lamy et al. (2014), grains would have moved of the order of $4 \times 10^2 \times \cos\gamma$ km in the skyplane where γ is the angle between the skyplane and the initial direction of the feature. This distance is an order of magnitude smaller than the ground-based seeing disk, so it is not surprising that we do not see any fine structure of the sunward feature in the ground-based images. The angular resolution of the HST images is comparable to the spatial

[3] Generally, we are extremely reluctant to trust the reality of the sunward feature present in these mid-February images (and to an extent in some March images), as the spatial location of the feature is extremely sensitive to a single pixel offset of the nucleus position. However, the fact that the PA of the feature and the general morphology are consistent with subsequent April through May images provide confidence that the feature is indeed real.

[4] Knight and Schleicher (2015) have images from June 11; however, these images were taken at extremely high airmass and have S/N too low to detect coma features.

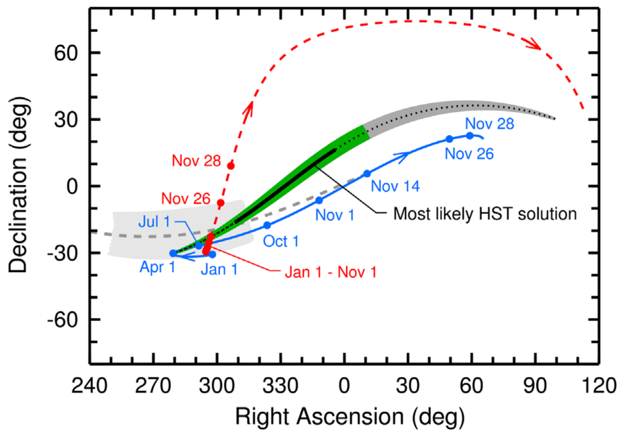

Fig. 5. The family of pole solutions based on Li et al. (2013) is shown by the half-great circle (with its width corresponding to the error in the determination of the PAs). The Earth and Sun directions as seen from the comet from January 1, 2013 up to perihelion are represented by blue solid and red dashed lines, respectively. The dots denote the respective directions at 0 UT on January 1, April 1, July 1, October 1, November 1, November 26, and November 28 while the direction of arrows denote the change in directions with time. The dots for the Sun direction partially overlap from January 1 through November 1 indicating that the Sun motion is minimal during this time; the huge change in Sun direction from November 28 (0 UT) until perihelion corresponds to <19 h. The green and dark gray parts of the half-great circle denote the portions in sunlight and darkness respectively during the HST observations. The Earth direction during the HST observations is nearly the same as that for April 1. The rightmost end of the solid black line (which depicts the "most likely HST solution") represents the pole solution that is in the skyplane. The dashed gray line represents the great circle solution from the November outburst observation (Section 4.3) with the light gray envelope on the left indicating the range for the pole solution for a 10° uncertainty in the PA and 30° uncertainty with respect to the skyplane. For all the pole solutions in the figure, the diametrically opposite solutions are also valid but are not shown.

displacement of grains in the sunward feature over a diurnal cycle. Therefore, despite the better angular resolution, even for HST images, we do not have sufficient spatial resolution to detect any diurnal scale variations in the coma structure.

On the other hand, the long-term variations over timescales of months in the sunward feature during the mid-February to mid-May interval are generally consistent with the evolution of the Earth–comet–Sun geometry and in particular the projected solar direction with respect to the comet in the skyplane (Figs. 1 and 5). Based on the derived grain outflow velocity and the fact that we can observe the ultimate merging of the sunward feature with the tail due to radiation pressure, we estimate that by the time the grains reach the tail, they must have spent 2–4 weeks in the coma after being ejected from the nucleus (cf. Eq. (7) of Mueller et al., 2013).

3.3. Dynamical constraints based on the sunward feature

In general, if a coma feature originates at or near a pole, the pole direction should lie in a half-great circle defined by the PA of that feature. When the Earth direction as seen from the comet changes due to orbital motions, the PA of the feature may also change. One can use a range of PAs corresponding to observations made at different times to determine a pole solution by considering the intersection of these half-great circles.

In the case of comet ISON, the Earth direction changed less than 8° from mid-February to mid-May (cf. Fig. 5). In addition, the lack of good spatial resolution of the sunward feature due to the comparatively large geocentric distances to the comet resulted in large error bars for the PAs for the sunward feature (cf. Fig. 4). Therefore, from these observations, the determination of a robust pole direction based on intersections of multiple half-great circles corresponding to respective PAs is not feasible. In this case, most half-great circles appear to intersect near the Earth's direction, which are confined close to each other. This result is simply a manifestation of the inadequacy of this technique to yield reliable results when the Earth direction has not changed significantly with time, and our data provide no additional constraints to the solution defined by Li et al. (2013) in their Figure 4. This result was based on the higher resolution HST observations (see Fig. 5) with the assumption that the feature originated from a fixed source region at or near the pole. As commented earlier in Section 3.1 (and also as favored by Knight and Schleicher, 2015), the feature could simply be the cumulative dust outflow from the sunward side (with a significant contribution coming from regions near the sub-solar point) and in that case the sunward feature cannot be used to constrain the pole. Detailed modeling of this scenario is beyond the scope of this paper.

4. Results during the water-dominated phase

The coma campaign during the water-dominated phase focused on both continuum as well as gas images. However, there were only a few observers who had access to narrowband gas filters: Hoban and Prouty (Telescope at University of Maryland, Baltimore County), Lister et al. (Faulkes Telescope North as part of the Las Cumbres Observatory Telescope Network), and Knight and Schleicher (using various telescopes at Lowell Observatory). The gas images of Knight and Schleicher were the only images received by the campaign that had sufficient S/N to detect unambiguous coma features. As these images are already discussed in detail in Knight and Schleicher (2015), we will not consider them further. However, we point out that unambiguous gas coma features were seen starting nearly a month prior to the perihelion (cf. Opitom et al., 2013b, Knight and

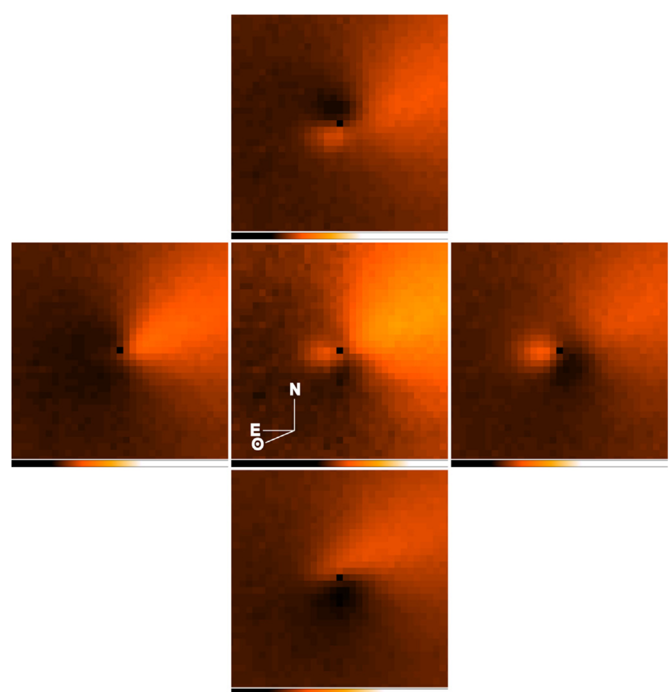

Fig. 6. A high S/N continuum image of comet ISON taken on October 17 ($r_h \sim 1.3$ AU) at the Liverpool Telescope. The image is enhanced using the division by azimuthal average technique. In the center panel, the optocenter is taken to represent the nucleus. In the other panels, the center is shifted by one pixel in the respective directions. Each panel is approximately 12,000 km across. The Sun is at a PA of 113°. The dust tail is at a westerly/northwesterly direction. Note that the apparent sunward feature in the center panel cannot be seen in all the panels at the same orientation.

Schleicher, 2015). In the remainder of this section, we will concentrate on the behavior of the continuum features.

4.1. Searching for coma features in the continuum

As September 2013 approached, the solar elongation increased sufficiently (to $\sim 30°$) for ground-based observations despite the observing window on any given night being short and the comet being at high airmass. Observations from September through November were also facilitated by the decreasing heliocentric and geocentric distances (Fig. 1) and the resultant increase in the comet's apparent brightness (e.g., Meech et al., 2013). However, up until about two weeks prior to the perihelion (i.e., $r_h \sim 0.65$ AU), we could not detect any unambiguous evidence of continuum features, except for the dust tail, even with image enhancements. To illustrate that an unambiguous continuum feature was not detected, we show in Fig. 6, a high S/N image from October 17 ($r_h \sim 1.3$ AU) representative of the middle of the observing window when water was the dominant volatile. This figure demonstrates the dependency of the "sunward feature" on the assumed nucleus (center) location. As shown elsewhere using numerically simulated images (Figure 9 of Samarasinha and Larson, 2014), in the absence of any corroborating evidence, one should be extremely cautious to trust the reality of an apparent coma structure after image enhancement if that structure is sensitive to minute changes in the chosen nucleus location such as a one-pixel offset. We carried out a similar test for the September 12 images taken at the DCT by Knight and Schleicher (2015) and in that case the feature is more stable even though the PA of the feature is still sensitive to the chosen nucleus location. We attribute this behavior to the relatively high S/N as well as the smaller pixel size of the DCT images. Even if the sunward feature is real in early-September, we assert that its skyplane extent must be much smaller than in the February to May time frame, i.e., at best, it can only be marginally detectable.

4.2. Why were no features detected in the continuum?

What happened to the sunward feature observed during the pre-water-dominated phase? Did it disappear, as water became the dominant volatile responsible for cometary outgassing? Since the change in the Sun direction as seen from the comet from May to September is only about 3° (cf. Fig. 5), it is unlikely that the lack of a feature was caused due to a change in the insolation geometry.

If one assumes that (a) the sunward feature during the pre-water-dominated phase retained the same character as during the water-dominated phase, (b) the change in the dust outflow velocity V in the intervening period is small, and (c) the change in the projection effects can be ignored[5], then the sunward extent of the feature d should decrease as $r_h^2/\sin\alpha$ (cf. Eq. (4) of Mueller et al., 2013). In late-September when r_h is nearly half of that in mid-May and α has nearly doubled, d should be ~ 700 km. As $\Delta \sim 2.3$ AU, the angular extent of the sunward feature should be ~ 0.4 arcsec which is smaller than the typical astronomical seeing. Therefore, it is not surprising that we cannot make a clear identification of the sunward feature in late-September even if it indeed existed. In October and November, α increases further while r_h decreases, making the skyplane extent of the feature even smaller. HST images taken in the continuum on October 9 ($r_h \sim 1.5$ AU) and November 1 ($r_h \sim 1.0$ AU) do not show a sunward feature, or another feature for that matter, other than the dust tail (Li; personal communications, 2013). This suggests that, at least around the times when these HST images were taken, the skyplane extent of a sunward feature was extremely small (< 100 km). Another possibility is that such a feature was absent.

If the direction of the sunward feature was close to the skyplane during the mid-February to mid-May time frame, then during late-September, the feature could still maintain a PA approximately in the same general westerly to north-westerly direction as that during the pre-water dominated phase. To illustrate this, in Fig. 5, we show that the family of solutions suggested for the pole in Li et al. (2013) as well as the Sun and Earth directions as a function of time. However, as seen from Fig. 1, the PA of the solar direction in the skyplane changed dramatically in July and by late-September the PA of the Sun was around 110°. That means the February–May sunward feature would be essentially in the tailward direction in late-September, thus effectively precluding its detection. We emphasize that this argument is relevant only if the feature is due to a fixed source region near the pole, the pole direction is close to the skyplane during the mid-February to mid-May interval, and this direction was nearly the same in September.

4.3. Behavior of the coma in the month before perihelion

A series of observations indicating rapid increases in activity and outburst events were reported in the month before perihelion. By November 5 ($r_h \sim 0.9$ AU), water production rate increased by $\sim 50\%$ from two days earlier, and that of other gas species increased by twice the corresponding amount, but no change was observed in the dust production (Opitom et al. 2013b). On November 12 ($r_h \sim 0.7$ AU), water production rate was $\sim 50\%$ higher than the previous night, and continued to increase by nearly an order of magnitude over the next two days. Dust production also increased by an order of magnitude by November 14 (Opitom et al., 2013a). Likely associated with this outburst, two arclet-like "wings" were detected (Boehnhardt et al., 2013) in the coma for the first time around November 14.2 UT, and confirmed on November 14.37 (Opitom; personal communications, 2015) and November 14.99 (Ye et al., 2013). These "wings", which originate from the nucleus at PAs nearly perpendicular to the tail and curve back in the tailward direction, are likely to be associated with fragmentation[6] of the nucleus (e.g., Harris et al., 1997; Tozzi et al., 1997; Farnham et al., 2001, Jehin and et al., 2002; Hadamcik and Levasseur-Regourd, 2003; Boehnhardt, 2004; Farnham, 2009). A third increase in the gas production was reported (Opitom et al., 2013c) to have started between November 18 and 19 ($r_h \sim 0.5$ AU). These observations reveal behavior that is remarkably similar to that of comet D/1999 S4 (LINEAR) before its complete breakup. One of the LINEAR outbursts was connected to a fragmentation event, with associated "wings" in the coma, that may have been related to the final disintegration of the nucleus (e.g., Farnham et al., 2001; Tozzi and Licandro, 2002). The existence of "wings" in comet ISON, after a long period of quiescence, may have foreshadowed the comet's ultimate fate.

Our global coma morphology campaign, which contains at least one set of images every day from November 1–17, provides an opportunity to explore this outburst timeframe in more detail. This task is challenging due to the non-uniformity of the data sets, but the temporal coverage is of value. During and after the reported increase in gas production on November 5, we see no changes in the dust coma morphology. However, the total gas

[5] For many of the "most likely solutions" suggested for the jet/pole direction in Figure 4 of Li et al. (2013) (also Fig. 5), the projection effects tend to make d even smaller during the September to October time frame (compared with the February to May time frame) based on the corresponding Earth directions if the feature is caused by a fixed source region on the nucleus.

[6] Fragmentation here is referred to small pieces breaking away from the nucleus and not to the complete disruption/breakup of the nucleus.

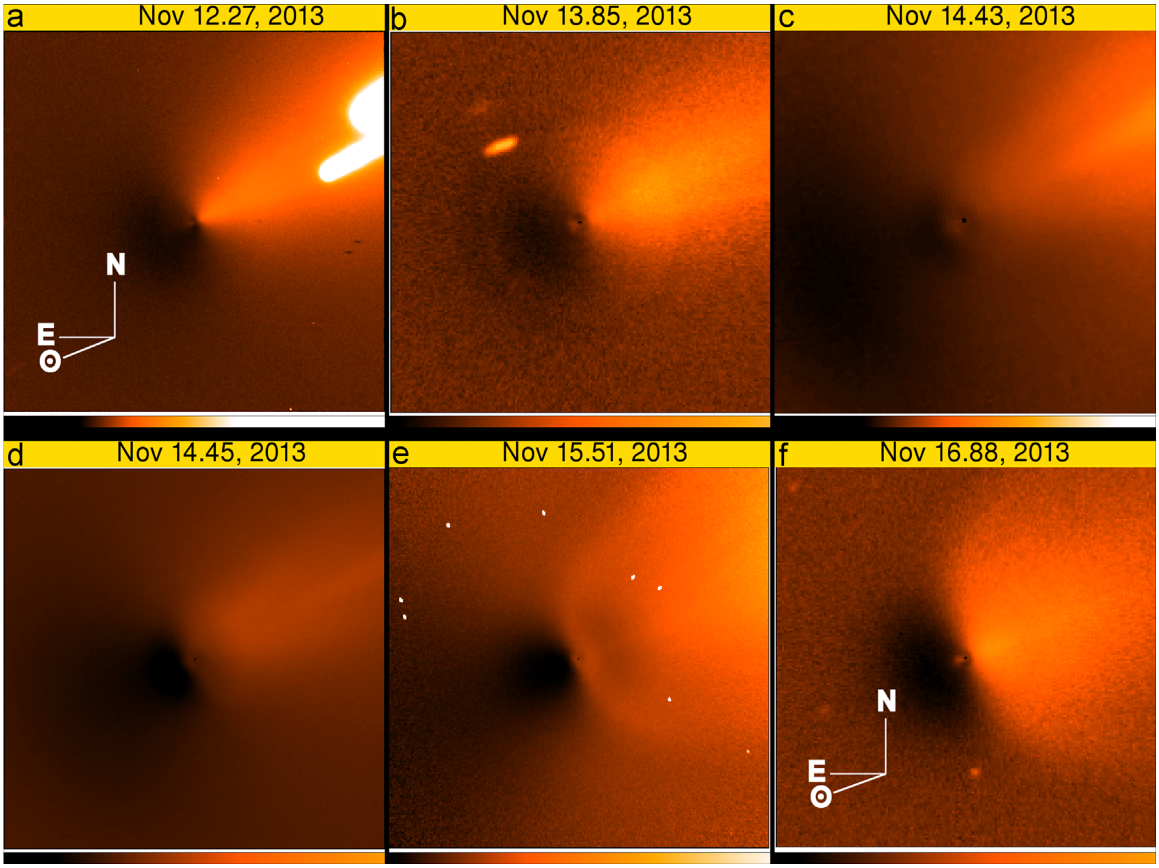

Fig. 7. Images of comet ISON from November 12 ($r_h \sim 0.70$ AU) to November 16 ($r_h \sim 0.56$ AU) showing the development of the coma "wings" in comet ISON subsequent to the outburst of November 12. The time of observation is indicated at the top of each image and the time sequence is from left to right in the top row followed by left to right in the bottom row. The nucleus is at the center of each panel. Each panel is approximately 96,000 km across. The position angle of the Sun varies from 112° to 110° during this interval. All images were enhanced using the division by azimuthal median technique. The streaks present in some images are star trails. The observers were: (a) Howes and colleagues, (b) Lin and colleagues, (c) Vogel, (d) Pruzenski and colleagues, (e) Gomez and colleagues, and (f) Lin and colleagues.

production in this event increased by only ~50%, and it was noted that the dust production remained flat.

The November 12 outburst, on the other hand, showed an order of magnitude increase in both gas and dust productions, indicating a significantly more energetic event that is likely associated with the observed "wings". Our campaign includes two sets of images, obtained at the appropriate time and with sufficient S/N to investigate this timeframe. Neither images acquired by Lin and colleagues on November 13.85 nor images from Ye and colleagues on November 13.99 show any identifiable "wing" structure, but images acquired by the same groups on November 14.86 and November 14.99, respectively, do show features similar to those reported by Boehnhardt et al. (2013). Based on this, we suggest that the faint "wings" reported by Boehnhardt et al. from images on November 14.2, first appeared in the coma sometime between November 13.99 and November 14.2 UT. In Fig. 7, we show a sequence of images bracketing this time interval, showing the coma with no "wings", the initial stage of their formation during November 14, and well developed "wings" lasting for at least three days.

The "wing" structure, as noted above signifies that a fragmentation event has occurred, and its timing corresponds to the (measured) "peak" in the production rates around November 14 (Opitom et al., 2013a; Combi et al., 2014), rather than to the start of the outburst on November 12. This indicates that the fragmentation is the result of the increased gas production, rather than the cause of the outburst. The morphology of the "wings" in both comet LINEAR and comet ISON, with nearly identical lobes in opposing directions, suggests that the source region is near the equator of a rapidly rotating nucleus, and the Earth is at low latitudes. These characteristics, combined with the timing of the events, allow us to propose a possible mechanism to explain these observations. As the nucleus approaches the Sun, heat penetrates into a pocket of volatiles, dramatically increasing the gas production. The higher gas drag, aided by erosion and centripetal acceleration near the equator, cause a piece of the surface to break off, revealing fresh ices. Material from this new active area, rotating with the nucleus, produces nearly axisymmetric lobes that appear as the "wings" seen in Fig. 7, while contributing additional gas and dust to the peak of the outburst.

By November 15 and 16, the "wing" structure was mature and well established. The dust in the "wings" further away from the nucleus was clearly affected by radiation pressure, being pushed significantly towards the anti-sunward direction. Unfortunately, we do not have sufficient observations to allow us to determine how long the "wings" persisted past November 16. Nor can we evaluate the effects of the weaker outburst reported by Opitom et al. (2013c) around November 18. They note the presence of "wings", though it is not known if these are newly generated in the outburst or if they are simply the remaining vestiges of the November 14 features.

The equator being nearly edge-on around November 14 suggests that at that time the pole solution should lie close to the great circle defined by the sunward and anti-sunward directions as well as nearly in the skyplane, yielding a pole in the general direction of (RA=285°, Dec=−20°). Fig. 5 shows the great circle solution for the sunward PA (dashed gray line) with a light gray envelope that denotes an uncertainty of 10° in the measured PA and an allowance for the pole being up to 30° out of the skyplane. Although this solution overlaps the HST solution discussed earlier, they are not required to be consistent because the pole could have changed due to the torques caused by outgassing in the intervening period between April and mid-November (cf. Samarasinha and Mueller, 2013).

Many of our images from November 14 do not exhibit the "wings" seen in the high-resolution data. This is likely due to a combination of differences in astronomical seeing and S/N between images as well as the enhancement techniques being employed. However, the overlap of these data represents a means of connecting the signature from higher-resolution images to the lower-resolution images and for exploring the effects of enhancing those images. The data taken at the TRAPPIST Telescope at the La Silla Observatory in Chile around the same time as our observations show sharper "wings" if all images are enhanced with the same technique (C. Opitom; personal communications, 2015), which we attributed to the better seeing at the TRAPPIST location. As for enhancements, Boehnhardt et al. (2013) used Laplace filtering which is optimized for identifying spatial discontinuities. As a result, the strong sunward edge of the coma seen for images from November 14 in Fig. 7, where we have enhanced the images by the more benign division of azimuthal median technique, may look like "wings" if enhanced with a Laplace filter (e.g., see Figure 6 in Farnham, 2009). (For a detailed comparison of differences between enhancement techniques, the reader is directed to Samarasinha and Larson (2014).) A comparison of different images indicates that the same structure that shows well-developed "wings" in some observations, appears as a flattening or squashing of the sunward side coma in others (e.g., images acquired by D. Vogel on November 14.43 and C. Pruzenski and colleagues on November 14.45). This type of behavior can be used as a signature of a potential fragmentation event in future observations, when only low-resolution data are available.

An increase in polarization was observed for comet D/1999 S4 (LINEAR), which was tied to its fragmentation (Hadamcik and Levasseur-Regourd, 2003). However, to our knowledge, no polarimetric observations are available from around mid-November until ISON's demise although studies were conducted by comparing coma colors (e.g., Li et al., 2013) and polarization properties (e.g., Hines et al., 2014; Zubko et al., in press) for comet ISON during the first half of 2013.

5. Summary and conclusions

We collected many hundreds of images from nearly two dozen groups of amateur and professional observers, spanning nearly the entire time comet ISON was observable from the ground. During November 2013, when ISON was brightest but its visibility was severely restricted due to a small solar elongation, this allowed much better temporal coverage than would have been possible from a single location. For most of the apparition, comet ISON displayed no prominent morphological features. We attribute this partially to the relatively large geocentric distances to the comet. The main results based on this study are summarized below.

- A distinctive northwesterly sunward feature in the continuum marked the coma morphology during the pre-water dominated phase. This feature did not vary on diurnal timescales. We derive grain velocities of the order of 10 m s^{-1} and the grains must have spent 2–4 weeks in the sunward side prior to merging with the dust tail.
- During the water-dominated phase, either the earlier continuum feature was absent or if it actually existed, it did not present itself prominently in the images, i.e., its skyplane-projected extent was of the order of the astronomical seeing or smaller and we provide an explanation for that based on the radiation pressure effects and the ground-based observational capabilities.
- Nearly two weeks prior to the perihelion, the comet started to display a variety of continuum features. The onset of this is related to the November 12 outburst reported by other authors. We constrain the "wing"-like features to have appeared between November 13.99 and 14.2 UT.
- This study shows that organized observing campaigns such as this one can collect observations from numerous observers, both professional and amateur, and assemble them into useful datasets. These campaigns may be most valuable in situations where any single observer can only obtain data during a small window of time, but contributions from many such observers provide coverage that leads to a more complete understanding of the spatial and temporal evolution of the comet.

Acknowledgments

The NASA Planetary Astronomy Program with Grant NNX14AG73G supported NHS and BEAM. MMK thanks NASA Planetary Astronomy Grant NNX14AG81G. We thank the CIOC and many other individuals for providing publicity about this campaign. We thank C. Opitom for discussions related to their observations. MMK thanks Stephen Levine, Brian Skiff, and Larry Wasserman for help obtaining the data from Lowell Observatory. Z-YL thanks the staff of Lulin Observatory, Hsiang-Yao Hsiao, Chi-Sheng Lin, and Hung-Chin Lin, for their assistance with observations. We thank the two anonymous reviewers for their comments to improve the paper. This is PSI Contribution Number 629.

References

Belton, M.J.S., 2013. The sources of the unusual dust jets seen in comet 103P/Hartley 2. Icarus 222, 653–661. http://dx.doi.org/10.1016/j.icarus.2012.12.007.
Bockelée-Morvan, D., Crovisier, J., Mumma, M.J., Weaver, H.A., 2004. The composition of cometary volatiles. In: Festou, M.C., Keller, H.U., Weaver, H.A. (Eds.), Comets II. University of Arizona Press, Tucson, pp. 391–423.
Boehnhardt, H., 2004. Split comets. In: Festou, M.H., Keller, U., Weaver, H. (Eds.), Comets II. University of Arizona Press, Tucson, pp. 301–316.
Boehnhardt, H., Tubiana, C., Oklay, N., Vincent, J.B., Hopp, U., Ries, C., Schmidt, M., Riffeser, A., and Gossel, C., 2013. Comet C/2012 S1 (ISON). CBET 3715.
Burns, J.A., Lamy, P.L., Soter, S., 1979. Radiation forces on small particles in the solar system. Icarus 40, 1–48. http://dx.doi.org/10.1016/0019-1035(79)90050-2.
Combi, M.R., Fougere, N., Makinen, J.T.T., Bertaux, J.-L., Quemerais, E., Ferron, S., 2014. Unusual water production activity of comet C/2012 S1 (ISON): outbursts and continuous fragmentation. Astroph. J. Lett. 788, 5. http://dx.doi.org/10.1088/2041-8205/788/1/L7, article id. L7.
Farnham, T.L., 2009. Coma morphology of Jupiter-family comets. Planet. Sp. Sci. 57, 1192–1217. http://dx.doi.org/10.1016/j.pss.2009.02.008.
Farnham, T.L., Schleicher, D.G., Woodney, L.M., Birch, P.V., Eberhardy, C.L., Levy, L., 2001. Imaging and photometry of comet C/1999 S4 (LINEAR) before perihelion and after breakup. Science 292, 1348.
Farnham, T.L., Samarasinha, N.H., Mueller, B.E.A., Knight, M.M., 2007. Cyanogen jets and the rotation state of comet Machholz (C/2004 Q2). Astron. J. 133, 2001–2007. http://dx.doi.org/10.1086/513186.
Farnham, T., Bodewits, D., Feaga, L.M., A'Hearn, M.F., Sunshine, J.M., Wellnitz, D.D., Klaasen, K.P., Himes, T.W., 2013. Imaging comets ISON and Garradd with the Deep Impact flyby spacecraft. DPS 2013 #45, #407.08 (abstract).
Ferrín, I., 2014. The impending demise of comet C/2012 S1 (ISON). Planet. Sp. Sci. 96, 114–119. http://dx.doi.org/10.1016/j.pss.2014.03.007.
Hadamcik, E., Levasseur-Regourd, A.-C., 2003. Dust coma of comet C/1999 S4 (LINEAR): imaging polarimetry during nucleus disruption. Icarus 166, 188–194.
Harris, W.M., Combi, M.R., Honeycutt, R.K., Mueller, B.E.A., 1997. Evidence for interacting gas flows and an extended volatile source distribution in the coma of comet C/1996 B2 (Hyakutake). Science 277, 676–681.
Hines, D.C., 11 colleagues, 2014. Hubble Space Telescope pre-perihelion ACS/WFC imaging polarimetry of comet ISON (C/2012 S1) at 3.81 AU. Astroph. J. Lett. 780, 6. http://dx.doi.org/10.1088/2041-8205/780/2/L32, article id. L32.
Howes, N., Guido, E., 2013. Comet observations. Minor Planet Circ., 81942.

Jehin, E., 14 colleagues, 2002. Split comet C/2001 A2 (LINEAR). Earth Moon Planets 90, 147–151.
Kelley, M.S., Li, J., Mutchler, M.J., Weaver, H.A., Knight, M.M., HST ISON Imaging Science Team, 2014. The pre-perihelion size of the nucleus of comet C/2012 S1 (ISON). In: Proceedings of AAS Meeting #223, #247.15 (abstract).
Knight, M.M., Battams, K., 2014. Preliminary analysis of SOHO/STEREO observations of sungrazing comet ISON (C/2012 S1) around perihelion. Astroph. J. Lett. 782, 5. http://dx.doi.org/10.1088/2041-8205/782/2/L37, article id. L37.
Knight, M.M., Schleicher, D.G., 2015. Observations of comet ISON (C/2012 S1) from Lowell Observatory. Astron. J. 149, 15. http://dx.doi.org/10.1088/0004-6256/149/1/19, article id. 19.
Knight, M.M., Walsh, K.J., 2013. Will comet ISON (C/2012 S1) survive perihelion? Astroph. J. Lett. 776, 5. http://dx.doi.org/10.1088/2041-8205/776/1/L5, article id. L5.
Knight, M.M., Schleicher, D.G., Farnham, T.L., Schwieterman, E.W., Christensen, S.R., 2012. A quarter-century of observations of comet 10P/Tempel 2 at Lowell Observatory: continued spin-down, coma morphology, production rates, and numerical modeling. Astron. J. 144, 25. http://dx.doi.org/10.1088/0004-6256/144/5/153, article id. 153.
Lamy, P.L., Toth, I., Weaver, H.A., 2014. Hubble space telescope observations of the nucleus of comet C/2012 S1 (ISON). Astroph. J. Lett. 794, 6. http://dx.doi.org/10.1088/2041-8205/794/1/L9, article id. L9.
Li, J.-Y., Kelley, M.S., Knight, M.M., Farnham, T.L., Weaver, H.A., A'Hearn, M.F., Mutchler, M.J., Kolokolova, L., Lamy, P., Toth, I., 2013. Characterizing the dust coma of comet C/2012 S1 (ISON) at 4.15 AU from the sun. Astroph. J. Lett. 779, 5. http://dx.doi.org/10.1088/2041-8205/779/1/L3, article id. L3.
Li, J.-Y., Samarasinha, N.H., Kelley, M.S.P., Farnham, T.L., A'Hearn, M.F., Mutchler, M.J., Lisse, C.M., Delamere, W.A., 2014. Constraining the dust coma properties of comet C/Siding Spring (2013 A1) at large heliocentric distances. Astroph. J. Lett. 797, 7, DOI: 0.1088/2041-8205/797/1/L8.
Lisse, C.M., 13 co-authors, 2013. Observing comet C/2012 S1 (ISON) with Spitzer. DPS2013#45, #407.06 (abstract).
Meech, K.J., 57 co-authors, 2011. Deep Impact, Stardust-NExT and the behavior of comet 9P/Tempel 1 from 1997 to 2010. Icarus 213, 323–344. http://dx.doi.org/10.1016/j.icarus.2011.02.016.
Meech, K.J., 28 co-authors, 2013. Outgassing behavior of C/2012 S1 (ISON) from 2011 September to 2013 June. Astroph. J. Lett. 776, 6. http://dx.doi.org/10.1088/2041-8205/776/2/L20, article id. L20.
Mueller, B.E.A., Samarasinha, N.H., Farnham, T.L., A'Hearn, M.F., 2013. Analysis of the sunward continuum features of comet 103P/Hartley 2 from ground-based images. Icarus 222, 799–807. http://dx.doi.org/10.1016/j.icarus.2012.08.014.
Novski, V., Novichonok, A., 2012. Comet C/2012 S1 (ISON). CBET 3238.
Opitom, C., Jehin, E., Manfroid, J., Gillon, M., 2013a. Comet C/2012 S1 (ISON). CBET 3711.
Opitom, C., Jehin, E., Manfroid, J., Gillon, M., 2013b. Comet C/2012 S1 (ISON). CBET 3693.
Opitom, C., Jehin, E., Manfroid, J., Gillon, M., 2013c. Comet C/2012 S1 (ISON). CBET 3719.
Samarasinha, N.H., Larson, S.M., 2014. Image enhancement techniques for quantitative investigations of morphological features in cometary comae: a comparative study. Icarus 239, 168–185. http://dx.doi.org/10.1016/j.icarus.2014.05.028.
Samarasinha, N.H., Mueller, B.E.A., 2013. Relating changes in cometary rotation to activity: current status and applications to comet C/2012 S1 (ISON). Astroph. J. Lett. 775, 6. http://dx.doi.org/10.1088/2041-8205/775/1/L10, article id. L10.
Schleicher, D.G., Woodney, L.M., Millis, R.L., 2003. Comet 19P/Borrelly at multiple apparitions: seasonal variations in gas production and dust morphology. Icarus 162, 415–442. http://dx.doi.org/10.1016/S0019-1035(02)00072-6.
Sekanina, Z., Kracht, R., 2014. Disintegration of Comet C/2012 S1 (ISON) shortly before perihelion: Evidence from independent data sets. arXiv:1404.5968.
Tozzi, G.-P., Cimatti, A., di Serego Alighieri, S., Cellino, A., 1997. Imaging polarimetry of comet C/1996 B2 (Hyakutake) at the perigee. Planet. Sp. Sci. 45, 535–540.
Tozzi, G.P., Licandro, J., 2002. Visible and infrared images of C/1999 S4 (LINEAR) during the disruption of its nucleus. Icarus 157, 187–192.
Tricarico, P., Samarasinha, N.H., Sykes, M.V., Li, J.-Y., Farnham, T.L., Kelley, M.S.P., Farnocchia, D., Stevenson, R., Bauer, J.M., Lock, R.E., 2014. Delivery of dust grains from comet C/2013 A1 (Siding Spring) to Mars. Astroph. J. Lett. 787, 5. http://dx.doi.org/10.1088/2041-8205/787/2/L35, article id. L35.
Vasundhara, R., 2009. Investigations of the pre-Deep Impact morphology of the dust coma of Comet Tempel 1. Icarus 204, 194–208. http://dx.doi.org/10.1016/j.icarus.2009.06.001.
Ye, Q.-Z., Hui, M-T., Gao, X., 2013. Comet C/2012 S1 (ISON). CBET 3718.
Zubko, E., 12 co-authors, 2015. Comet C/2012 S1 (ISON) coma composition at $\sim$4 AU from HST observations. Planet. Sp. Sci., in press, http://dx.doi.org/10.1016/j.pss.2015.08.002

EPJ Web of Conferences **101**, 06034 (2015)
DOI: 10.1051/epjconf/201510106034

Ground-Based *BVRI* Time-Series Follow-Up Observations for the RR Lyrae stars in *Kepler* Field

Young-Beom Jeon[1,a], Chow-Choong Ngeow[2], and James M. Nemec[3]

[1] Korea Astronomy and Space Science Institute, Daejeon 305-348, Korea
[2] Graduate Institute of Astronomy, National Central University, Jhongli 32001, Taiwan
[3] Department of Physics & Astronomy, Camosun College, Victoria, British Columbia, Canada

Abstract. Time series observations for the 41 RR Lyrae stars in *Kepler*'s fields were carried out in 2010 to 2013 using a number of meter class (or smaller) telescopes. These telescopes include the 1-m and 41-cm telescopes of Lulin Observatory (LOT and SLT respectively, Taiwan), the 81-cm telescope of Tenagra-II Observatory (TNG, Arizona, USA), the 1-m telescope at the Mt. Lemmon Optical Astronomy Observatory (LOAO, Arizona, USA), the 1.8-m and 15-cm telescopes at the Bohyunsan Optical Astronomy Observatory (BOAO, Korea), and the 61-cm telescope at the Sobaeksan Optical Astronomy Observatory (SOAO, Korea). All of these telescopes were equipped with commercial available CCD imagers, and the observations were done in standard *BVRI* filters. Photometric calibration of the RR Lyrae light curves was done with standard stars listed in Landolt standard stars [1]. Observations of selected Landolt standard stars (centered on SA 107-456 & SA 110-232) in Johnson-Kron-Cousins *BVRI* filters, spanning three distinct airmasses, were done with the 81-cm Tenagra II telescope on 25 June 2011. Raw imaging data were reduced with IRAF in the same manner as in the case of the RR Lyrae, and astrometric calibrated with astrometry.net [2]. We calibrated *BVRI* magnitudes for 40 RR Lyrae stars.

1 Photometric Calibration and Results

Photometric calibration of the RR Lyrae light curves was done with standard stars listed in [1] (hereafter Landolt standard stars). Observations of selected Landolt standard stars (centered on SA 107-456 & SA 110-232) in Johnson-Kron-Cousins *BVRI* filters, spanning three distinct airmasses, were done with the 81-cm Tenagra II telescope on 25 June 2011. Raw imaging data were reduced with `IRAF` in the same manner as in the case of the RR Lyrae, and astrometric calibrated with `astrometry.net` [2]. Aperture photometry of the Landolt standard stars were obtained using an aperture of 7-arcsecond radius. These instrumental magnitudes (normalized with exposure time) were then used to solve for the following two sets of transformation equations:

$$b = B + ZP_B + \kappa_B X_B + C_B(B-V), \quad v = V + ZP_V + \kappa_V X_V + C_V(B-V), \tag{1}$$

$$r = R + ZP_R + \kappa_R X_R + C_R(R-I), \quad i = I + ZP_I + \kappa_I X_I + C_I(R-I), \tag{2}$$

where the lower case letters (b, v, r & i) represent the instrumental magnitudes, the upper case letters (B, V, R & I) are standard magnitudes adopted from [1], and X is the airmass. Coefficients that need to be solved are ZP, κ and C: represent the zero-point, extinction-coefficient and color-coefficient in a given filter, respectively. The solutions of these coefficients are summarized in Table 1.

Derived V magnitude and colors for 40 RR Lyrae stars are presented in Table 2.

[a] e-mail: `ybjeon@kasi.re.kr`

Table 1. Solutions of the transformation equations.

Band	ZP	κ	C	σ
B	2.993 ± 0.084	0.520 ± 0.061	-0.079 ± 0.022	0.031
V	2.787 ± 0.055	0.325 ± 0.040	0.052 ± 0.014	0.019
R	2.488 ± 0.103	0.233 ± 0.060	0.431 ± 0.118	0.023
I	3.653 ± 0.104	0.153 ± 0.059	0.053 ± 0.120	0.023

Table 2. Derived V magnitude and colors.

KIC	V	$(B-V)$	$(V-R)$	$(V-I)$	KIC	V	$(B-V)$	$(V-R)$	$(V-I)$
3733346	12.822	0.416	0.323	0.676	7742534	16.594	0.388	0.263	0.490
3864443	15.790	0.492	0.523	0.784	7988343	14.879	0.800	0.458	0.982
3866709	16.717	0.482	0.325	0.677	8344381	17.043	0.280	0.260	0.621
4064484	14.635	0.345	0.253	0.569	8832417	13.195	0.429	0.300	0.648
4484128	15.614	0.506	0.368	0.799	9001926	17.309	0.392	0.320	0.584
5299596	15.677	0.723	0.523	1.055	9453114	13.513	0.208	0.172	0.491
5520878	14.245	0.295	0.223	0.490	9508655	15.966	0.357	0.271	0.592
5559631	15.045	0.672	0.466	0.933	9578833	16.743	0.383	0.282	0.588
6070714	16.016	0.748	0.502	1.002	9591503	13.330	0.366	0.263	0.623
6100702	13.802	0.520	0.323	0.689	9658012	16.067	0.433	0.335	0.706
6183128	16.422	0.413	0.309	0.651	9697825	16.278	0.366	0.293	0.631
6186029	17.519	0.395	0.307	0.638	9717032	17.178	0.424	0.292	0.701
6763132	13.538	0.338	0.275	0.618	9947026	13.583	0.446	0.288	0.621
6936115	12.959	0.342	0.280	0.628	9973633	17.731	0.604	0.499	1.004
7021124	15.879	0.405	0.345	0.691	10136240	16.223	0.420	0.267	0.593
7030715	13.392	0.392	0.338	0.712	10136603	14.668	0.401	0.290	0.603
7176080	17.372	0.360	0.279	0.615	10789273	14.252	0.382	0.258	0.539
7257008	16.674	0.312	0.233	0.572	11125706	11.920	0.425	0.276	0.590
7505345	14.434	0.355	0.278	0.541	11802860	12.892	0.421	0.264	0.522
7671081	16.997	0.349	0.292	0.633	12155928	14.853	0.290	0.264	0.540

References

1. Landolt, A. U., AJ **137**, (2009) 4186
2. Lang, D., Hogg, D. W., Mierle, K., Blanton, M., & Roweis, S., AJ **139**, (2010) 1782

工作報告

CCD Reduction of LOT/U42 Data using IRAF

Kinoshita Daisuke
Institute of Astronomy, National Central University

31 March 2016

This document first describes the basic usage of IRAF (Image Reduction and Analysis Facility), and then shows a way to reduce the data produced by Apogee U42 CCD camera attached on Lulin 1-m Telescope (LOT).
この文書では、まず IRAF (Image Reduction and Analysis Facility) の基本 的な使い方を説明し、そして、鹿林天文台の 1-m 望遠鏡に取り付けられた Apogee 社製 U42 CCD カメラのデータの整約の一例を示す。

1 Basic Usage of IRAF

1.1 Installation and Set-up

1.1.1 Installation of IRAF

About the installation of IRAF (Image Reduction and Analysis Facility), see the documentation on IRAF website `http://iraf.noao.edu/`. (Fig. 1)
IRAF (Image Reduction and Analysis Facility) のインストールに関しては、 `http://iraf.noao.edu/` を参照のこと。 (Fig. 1)

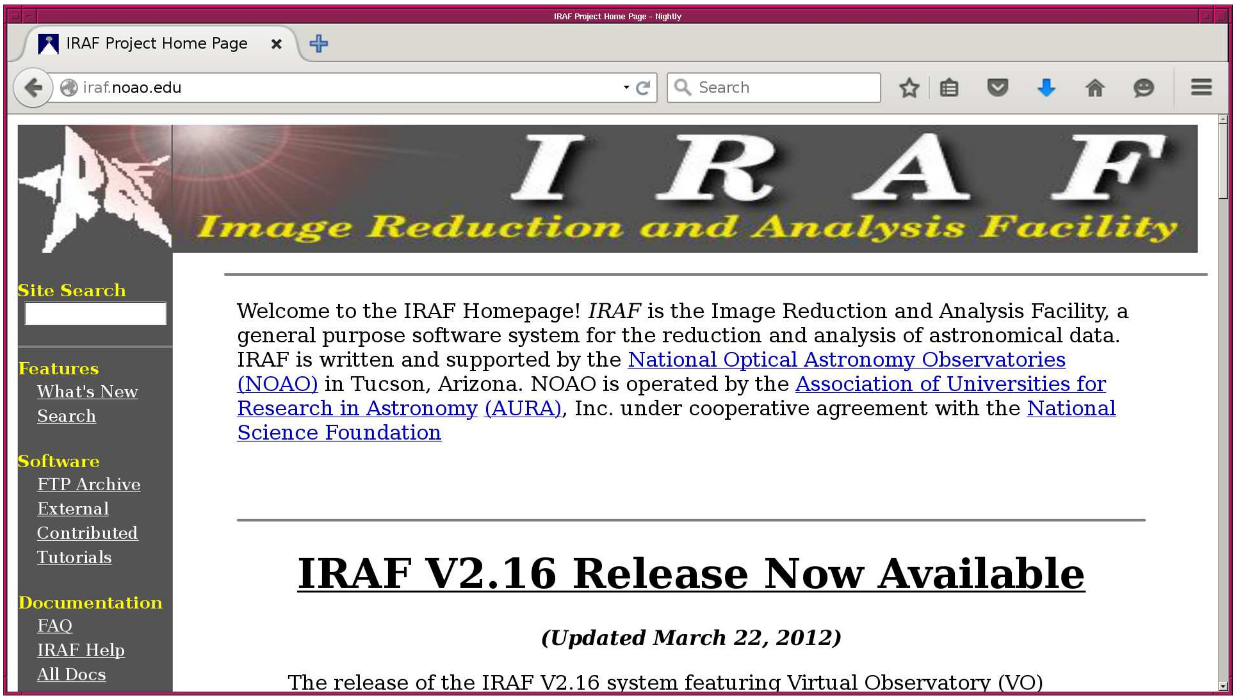

Figure 1: The IRAF website. `http://iraf.noao.edu/`

1.1.2 Installation of X11IRAF

The terminal emulator `xgterm` is often used in conjunction with IRAF, and `xgterm` is included in the X11IRAF package. Download the relevant file from `http://iraf.noao.edu/projects/x11iraf/` and install it.

IRAF と共に端末エミュレータ xgterm がよく用いられる。 xgterm は X11IRAF パッケージに付属する。 http://iraf.noao.edu/projects/x11iraf/ より X11IRAF をダウンロードし、 インストールすることが望ましい。

1.1.3 Installation of SAOimage DS9

The SAOimage DS9 is usually needed for the visualization of the image and interactive sessions during the data reduction and analysis using IRAF. About the installation of SAOimage DS9, see the documentation on SAOimage DS9 website http://ds9.si.edu/. (Fig. 2)

IRAF によるデータリダクションおよびデータ解析にあたっては、画像の表示 や対話的な操作において SAOimage DS9 がよく用いられる。 SAOimage DS9 の インストールに関しては http://ds9.si.edu/ (Fig. 2) を参照のこと。

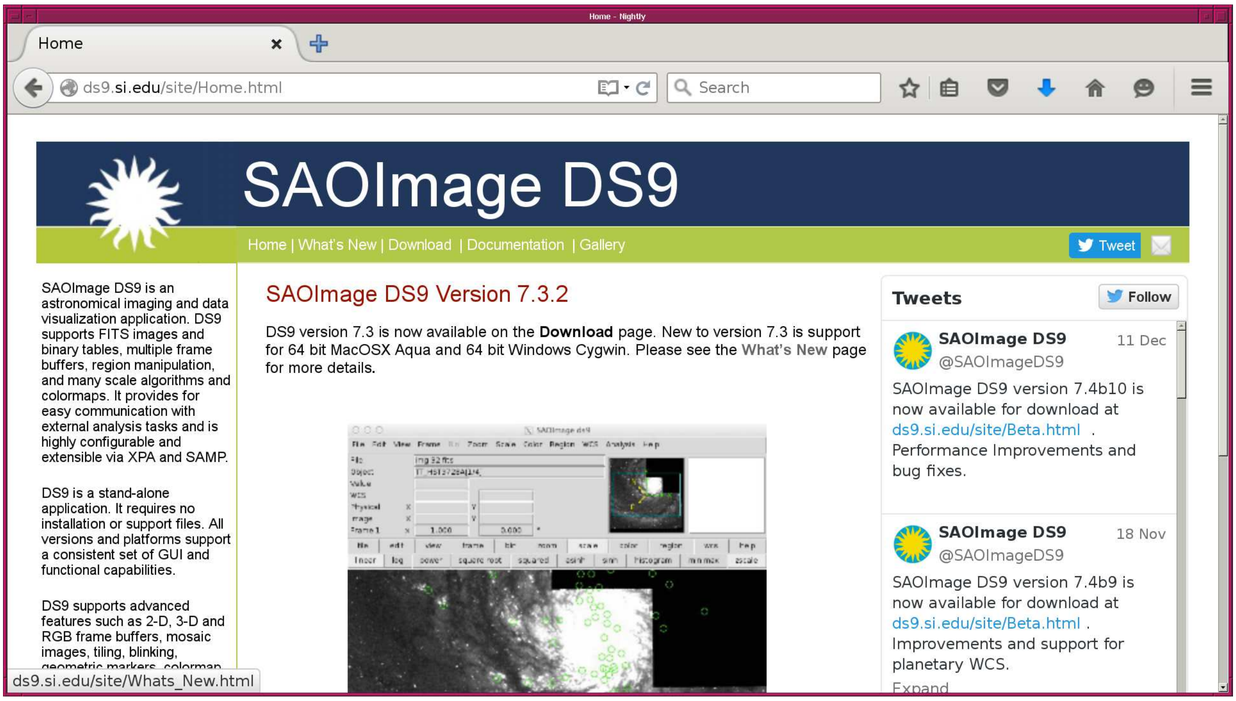

Figure 2: The SAOimage DS9 website. http://ds9.si.edu/

After the installation of SAOimage DS9, the communication method between IRAF and SAOimage DS9 must be properly set. Either, FIFO, Unix domain socket, and TCP/IP can be used for the communication between two software. A way to define the communication method is to set an environmental variable IMTDEV. If you are using tcsh, try following.

SAOimage DS9 のインストールが完了したら、 IRAF と SAOimage DS9 の間の 通信方法を正しく設定する必要がある。名前付きパイプ、 Unix ソケット、 TCP/IP の三つのうちの一つを使って通信することができる。通信方法の設定 は環境変数 IMTDEV を設定することで行う。もしもシェルに tcsh を使っている場合は、例えば以下のようにすればよい。

```
% setenv IMTDEV inet:5137:localhost
```

1.1.4 Set-up of IRAF

For the first to use the IRAF, the command mkiraf must be invoked before starting IRAF. This is usually done at your home directory. The terminal emulator to be used in conjunction with IRAF must be specified. The choice of xgterm is recommended. The command mkiraf generates the file login.cl.

IRAF を初めて使う際、 IRAF を起動する前にまず mkiraf という コマンドを実行する必要がある。これは、通常、ホームディレクトリで行わ れる。 IRAF と共に用いられる端末エミュレータを指定するように促される。 xgterm を選択するとよい。 mkiraf というコマンドは login.cl というファイルを生成する。

```
% mkiraf
-- creating a new uparm directory
Terminal types: xgterm,xtermjh,xterm,etc.
Enter terminal type (xgterm):
A new LOGIN.CL file has been created in the current directory.
You may wish to review and edit this file to change the defaults.
```

You may edit `login.cl` file in order to change the behaviour of IRAF at the start-up. If you prefer Emacs-like key bindings rather than vi-like key bindings, then you need to edit the variable `editor`. If you use images larger than 800 × 800 pixels, you need to edit the variable `stdimage`. See Fig. 3.
起動時の IRAF の設定を変えるために、必要に応じてファイル `login.cl` を編集するとよい。 vi エディター風のキーバインディングよ りも、 Emacs エディター風のキーバインディングが好みであれば、変数 `editor` を変更すればよい。 800 × 800 ピクセルよりも大 きな画像を扱う場合には、変数 `stdimage` を変更する必要がある。 Fig. 3 を参照のこと。

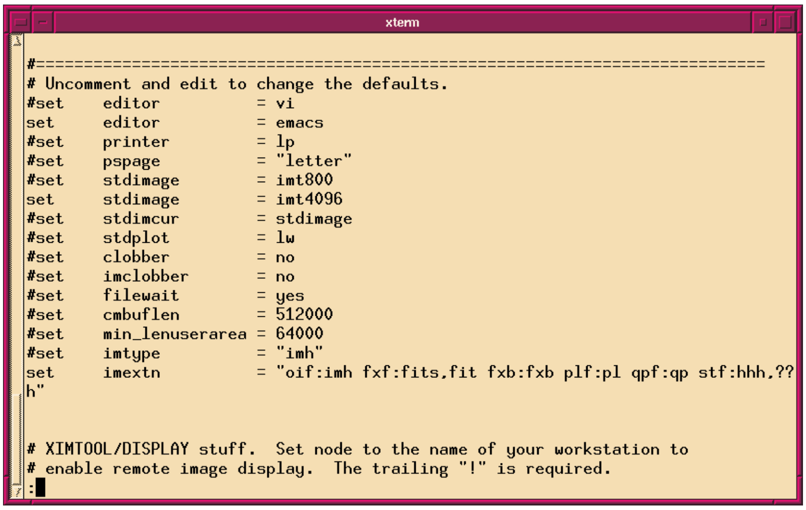

Figure 3: An example of the part of `login.cl` file.

It is useful to register the information of the observatory. The observatory information is stored in `obsdb.dat` file. Add following information if it is not in `obsdb.dat` yet.
観測所の位置情報などを登録しておくと便利である。観測所情報は `obsdb.dat` というファイルに格納されている。まだ書き込まれていない場合 は、以下の情報を `obsdb.dat` ファイルに追加しておく。

```
observatory = "lulin"
        name = "Lulin Observatory"
        longitude = -120:52:25
        latitude = 23:28:07
        altitude = 2862.
        timezone = -8
```

1.1.5 Starting IRAF

To use IRAF, you first need to start the terminal emulator `xgterm`.
IRAF を利用するためには、まず端末エミュレータ `xgterm` を起動 する。

```
% xgterm &
```

Then, type the command `cl` on xgterm.
そして、 `cl` コマンドを使う。

```
% cl
```

Now, you should see the command prompt. (Fig. 4)
うまくいけば、コマンドプロンプトが現れるはずである。 (Fig. 4)
Also, you need to start SAOimage DS9.
また、 SAOimage DS9 も起動しておく。

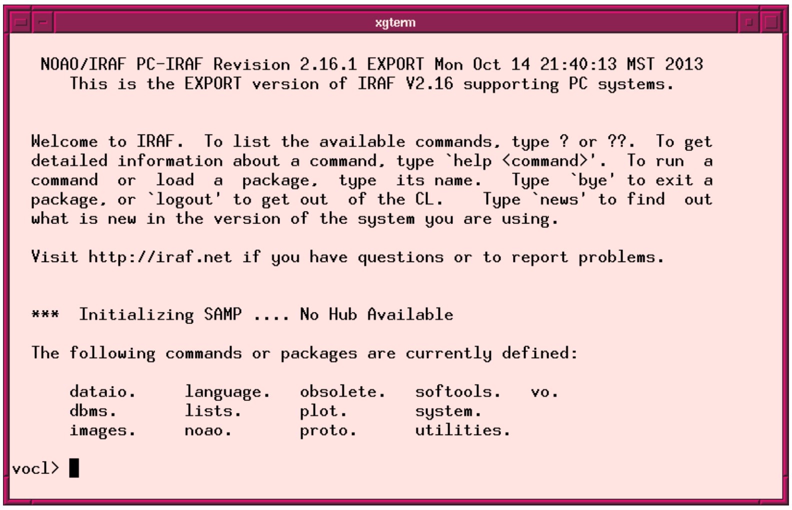

Figure 4: The welcome message and command prompt shown by IRAF just after the start-up.

```
% ds9 &
```

Started SAOimage DS9 is shown in Fig. 5.
起動したばかりの SAOimage DS9 を Fig. 5 に示す。

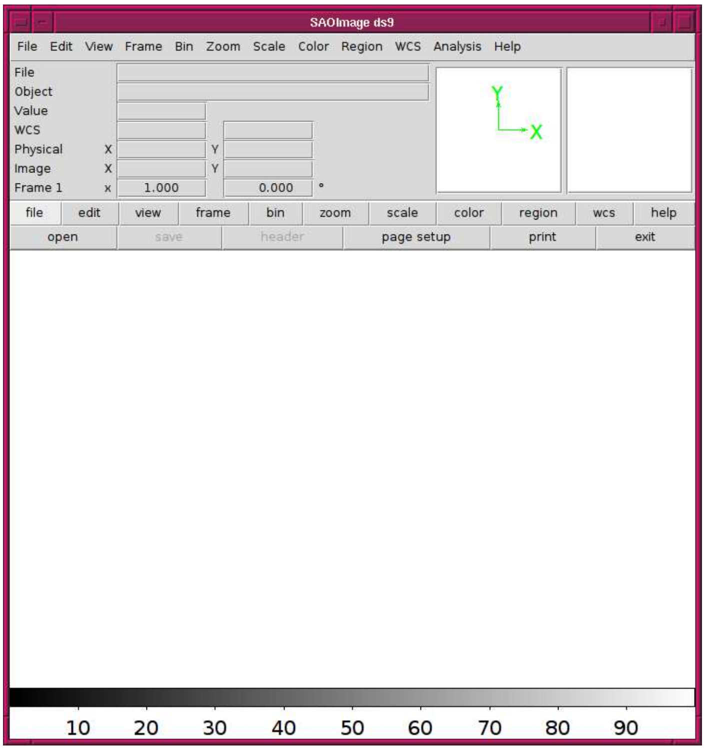

Figure 5: The window of SAOimage DS9 just after the start-up.

1.1.6 Installation of WCSTools

WCSTools is a colletion of command which manipulate FITS files and catalogues. It is also useful for CCD data reduction. Visit WCSTools website `http://tdc-www.harvard.edu/wcstools/` (Fig. 6), and download the software. Compile the codes, and install it.

WCSTools は FITS ファイルやカタログを取り扱ういくつものコマンドから構 成されている。 CCD データリダクションにも有用である。 WCSTools のウェ ブページ `http://tdc-www.harvard.edu/wcstools/`

(Fig. 6) からソフトウェアをダウンロードし、ソースコー ドをコンパイルし、インストールしておくとよい。

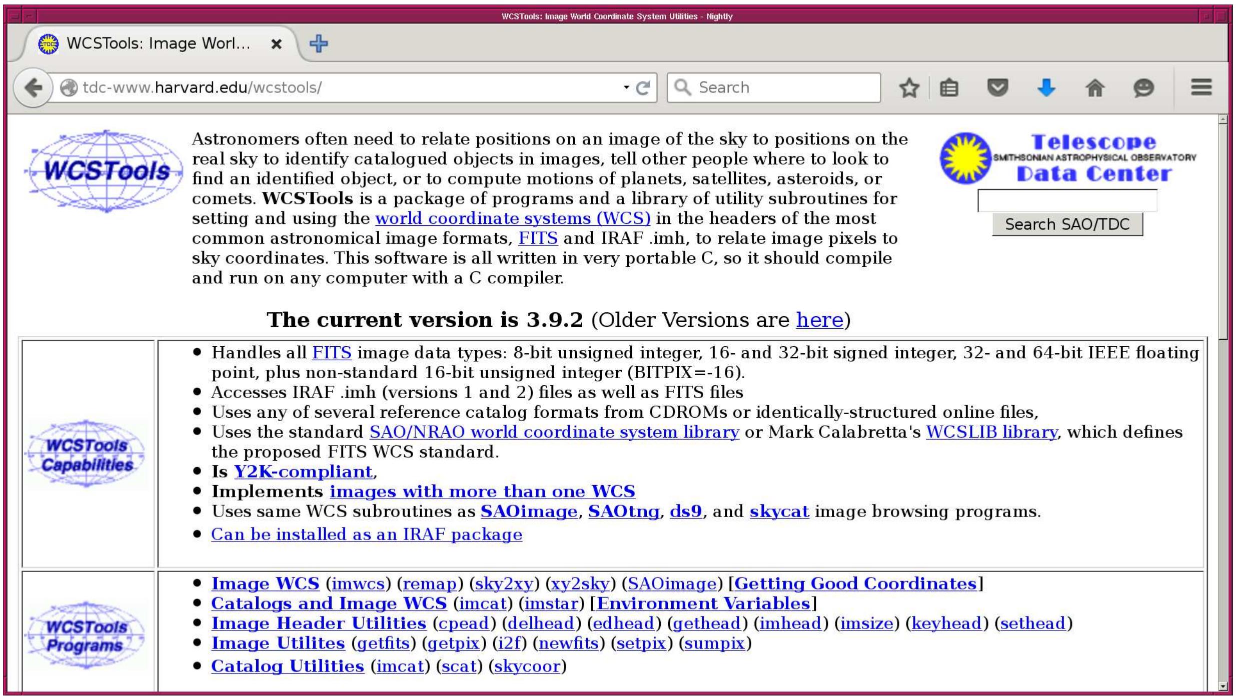

Figure 6: The WCSTools website. `http://tdc-www.harvard.edu/wcstools/`

1.1.7 Installation of Gnuplot

Gnuplot is a easy-to-use and versatile plotting program. It is very useful to visualize numerical data and do model fitting by least square fit.

Gnuplot は、簡単に使えて機能も豊富な作図プログラムである。数値データ の可視化や最小二乗法によるモデルフィッティングなどに便利である。

Visit the official website of Gnuplot (Fig. 7), and install it.

Gnuplot の公式ウェブサイト (Fig. 7) を参照し、プログ ラムをインストールしておくと便利である。

1.2 Basic and Commonly Used Tasks of IRAF

1.2.1 Finding a task of your interest

Use the task `references` to find a task of your interest. Here is an example.

`references` というタスクを用いて興味のあるタスクを探すことが できる。以下に例を示す。

```
vocl> references statistics
searching the help database...
bitcount - Accumulate the bit statistics for a list of images  [obsutil]
imstatistics - Compute and print statistics for a list of images  [imutil]
mimstatistics - Do image statistics through a mask  [proto]
nlerrors - Compute the fits statistics and errors in the parameters  [nlfit]
oimstatistics - IMSTATISTICS from V2.11.3  [obsolete]
qstatistics - Calculate image statistics for multi-amplifier CCD images  [quadred]
vocl>
```

Here is another example. The task name can be abbreviated as long as the task is specified uniquely. `refer` is enough for the task `references`.

また、別の例を示す。タスクの名前はユニークさが保証される範囲において省 略して書くことができる。 `references` の場合、 `refer` で十分である。

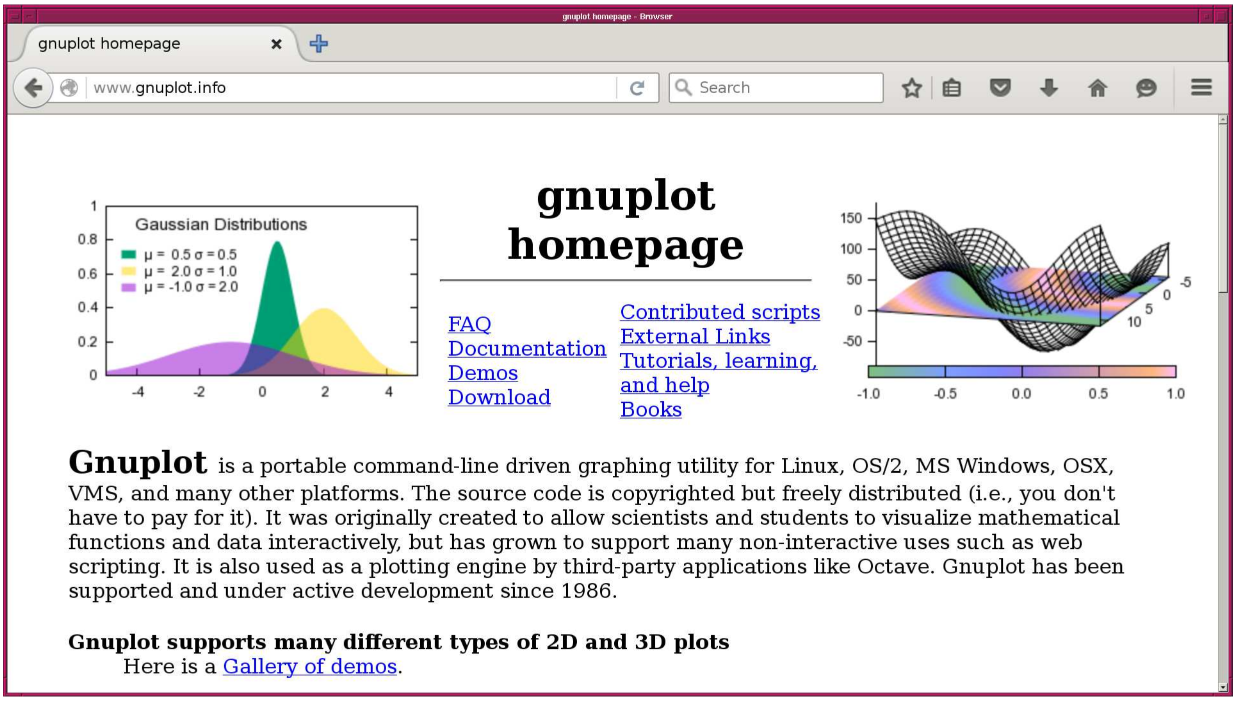

Figure 7: The Gnuplot website. `http://www.gnuplot.info/`

```
vocl> refer bias
searching the help database...
bias - General bias subtraction tools  [imred]
colbias - Fit and subtract an average column bias  [bias]
linebias - Fit and subtract an average line bias  [bias]
vocl>
```

1.2.2 Reading online documentation of a specific task

Try to use the task `phelp` to read the online documentation of a task.
タスク phelp を使って、指定したタスクの解説を表示させてみよ う。

```
vocl> phelp refer
```

Above command will provide you the online documentation of the task `references`. (Fig. 8)
上記のタスクを実行すると、タスク references の解説を読むこ とができる。 (Fig. 8)

1.2.3 Copying a FITS file

The task `imcopy` can be used to copy FITS files. The image of M51 (Whirlpool Galaxy) is included in IRAF package. Copy the image of M51 to the currently working directory using the task `imcopy`.
タスク imcopy を使って FITS ファイルをコピーすることができ る。 IRAF パッケージには M51 (子持ち銀河) の画像が含まれている。タス ク imcopy を使って M51 の画像を現在いるディレクトリにコピー し てみよう。

```
vocl> imcopy dev$pix m51.fits
dev$pix -> m51.fits
vocl> ls -l m51.fits
-rw-r--r-- 1 daisuke taiwan 532800 Dec 15 23:59 m51.fits
```

For copying a part of the image into a new file, you may try following.
画像の一部分のみをコピーする場合、以下のようにすればよい。

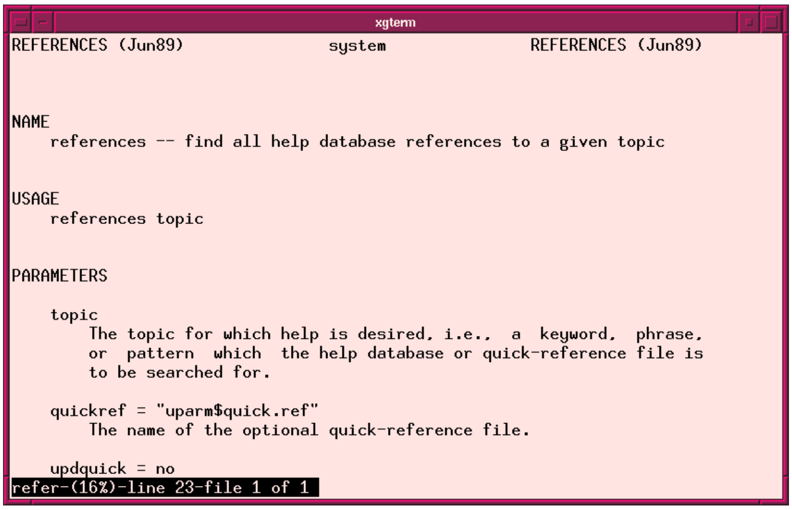

```
REFERENCES (Jun89)              system              REFERENCES (Jun89)


NAME
    references -- find all help database references to a given topic


USAGE
    references topic


PARAMETERS

    topic
        The topic for which help is desired, i.e.,  a  keyword,  phrase,
        or  pattern  which  the help database or quick-reference file is
        to be searched for.

    quickref = "uparm$quick.ref"
        The name of the optional quick-reference file.

    updquick = no
refer-(16%)-line 23-file 1 of 1
```

Figure 8: The online documentation of the task `references`.

```
vocl> imheader dev$pix
dev$pix[512,512][short]: m51  B  600s
vocl> imcopy dev$pix[200:299,200:299] m51_center.fits
dev$pix[200:299,200:299] -> m51_center.fits
vocl> imheader dev$pix,m51_center
dev$pix[512,512][short]: m51  B  600s
m51_center[100,100][short]: m51  B  600s
```

1.2.4 Deleting a FITS file

The task `imdelete` can be used to delete FITS files. Delete the file `m51.fits` that you just created using the task `imdelete`.
タスク `imdelete` を使って FITS ファイルを消去することができ る。タスク `imdelete` を使って、さきほど作ったファイル `m51.fits` を消去してみよう。

```
vocl> imdelete m51.fits
vocl> ls -l m51.fits
ls: cannot access m51.fits: No such file or directory
```

1.2.5 Checking the header of a FITS file

The task `imheader` is used to show the header of FITS files.
タスク `imheader` は FITS ファイルのヘッダー部分の情報を表示する のに用いられる。

```
vocl> imheader m51
m51[512,512][short]: m51  B  600s
```

More information is shown with the option `longheader=yes`.
`longheader=yes` というオプションを付けることで、より多くの情報が 表示される。

```
vocl> imheader m51 longheader=yes | head
m51[512,512][short]: m51  B  600s
No bad pixels, min=0., max=0. (old)
Line storage mode, physdim [512,512], length of user area 2673 s.u.
Created Fri 12:20:10 18-Dec-2015, Last modified Fri 12:20:10 18-Dec-2015
Pixel file "m51.fits" [ok]
EXTEND  =                    F / File may contain extensions
ORIGIN  = 'NOAO-IRAF FITS Image Kernel July 2003' / FITS file originator
DATE    = '2015-12-18T04:20:10' / Date FITS file was generated
IRAF-TLM= '2015-12-18T04:20:10' / Time of last modification
OBJECT  = 'm51  B  600s'       / Name of the object observed
IRAF-MAX=          1.993600E4  /  DATA MAX
IRAF-MIN=         -1.000000E0  /  DATA MIN
```

1.2.6 Extracting FITS keywords

We occasionally need to check a value of the FITS keyword. The task hselect can be used for this.
FITS ヘッダーのなかに格納されているキーワードの値を参照したい場合があ る。 hselect を使うことでキーワードの値を表示させせることができる。

```
vocl> hselect m51.fits OBJECT yes
"m51  B  600s"
```

We get the same result by using small letters for the name of the keyword.
キーワードの指定には小文字を使っても、同じ結果が得られる。

```
vocl> hselect m51.fits object yes
"m51  B  600s"
```

The task hselect is also used for showing values of multiple keywords.
hselect は、複数のキーワードの値を表示させせるのに使うこともでき る。

```
vocl> hselect m51.fits ra,dec yes
13:29:24.00     47:15:34.00
```

In case that the image file name should also be printed, then add $I.
画像のファイル名も出力させたい場合には、 $I を追加すればよい。

```
vocl> hselect m51.fits $I,ra,dec yes
m51.fits        13:29:24.00     47:15:34.00
```

1.2.7 Editing FITS header

To edit FITS header, the task hedit is used. The value for the keyword DATA-TYP in the file m51.fits is OBJECT (0).
FITS ヘッダーを編集するには hedit というタスクを用いる。 m51.fits のヘッダーのなかのキーワード DATA-TYP の値は OBJECT (0) となっている。

```
vocl> hselect m51 data-typ yes
"OBJECT (0)"
```

Now, we modify the value of the keyword DATA-TYP.
キーワード DATA-TYP の値を変更してみる。

```
vocl> hedit m51 data-typ OBJECT
m51,DATA-TYP ("OBJECT (0)" -> OBJECT):
m51,DATA-TYP: "OBJECT (0)" -> OBJECT
update m51 ? (yes):
m51 updated
```

The value of the keyword DATA-TYP has been changed.
これで、キーワード DATA-TYP の値が変更された。

```
vocl> hselect m51 data-typ yes
OBJECT
```

To turn off the verification, add the option `verify=no`.
確認を無効にしたい場合には、 `verify=no` オプションを追加すればよ い。

```
vocl> imdel m51
vocl> imcopy dev$pix m51.fits
dev$pix -> m51.fits
vocl> hselect m51 date-obs,ut yes
05/04/87        " 9:27:27.00"
vocl> hedit m51 date-obs "1987-04-05T09:27:27.00" verify=no
m51,DATE-OBS: 05/04/87 -> 1987-04-05T09:27:27.00
m51 updated
vocl> hselect m51 date-obs yes
1987-04-05T09:27:27.00
```

Next, we add a new keyword `EXPTIME` to `m51.fits`.
次に、 `m51.fits` に新たなキーワード `EXPTIME` を追加してみる。

```
vocl> imdel m51
vocl> imcopy dev$pix m51.fits
dev$pix -> m51.fits
vocl> hselect m51 exptime yes

vocl> hselect m51 otime yes
600
vocl> hedit m51 exptime 600 add=yes verify=no
add m51,exptime = 600
m51 updated
vocl> hselect m51 exptime yes
600
```

1.2.8 Displaying a FITS file on SAOimage DS9

A FITS file can be displayed on SAOimage DS9 using the task `display`. Try following command.
タスク `display` を使うと、 SAOimage 上に FITS ファイルを表示 させることができる。以下の例を試してみよう。

```
vocl> imcopy dev$pix m51.fits
dev$pix -> m51.fits
vocl> display m51.fits 1
z1=35. z2=346.0218
vocl>
```

Now, you should see the image of M51 on the SAOimage DS9. (See Fig. 9.)
これで、 SAOimage DS9 上に M51 の画像が表示されているはずである。 (Fig. 9. を参照のこと。)
You may sometimes want to adjust the minimum and maximum intensity to be displayed on SAOimage DS9 by adding `z1` and `z2` options. When you specify the FITS file, you can omit the extension `.fits`.
`z1` と `z1` の二つのオプションを与えることで、 SAOimage DS9 上に表示される輝度範囲を調整することができる。また、 FITS を指定する際、拡張子 `.fits` は省略することができる。

```
vocl> display m51 1 zs- zr- z1=40 z2=200
z1=40. z2=200.
```

1.2.9 Simple image examination

The task `imexamine` can be used to examine images. For examining the FITS file `m51.fits`, try following command. Then, the image of `m51.fits` is now displayed on SAOimage DS9.
`imexamine` というタスクを使って、画像の特徴を調べることができる。 `m51.fits` という名前の FITS ファイルの素性を調べるためには、以下 のようにする。すると、 `m51.fits` の画像が SAOimage DS9 上に表示 される。

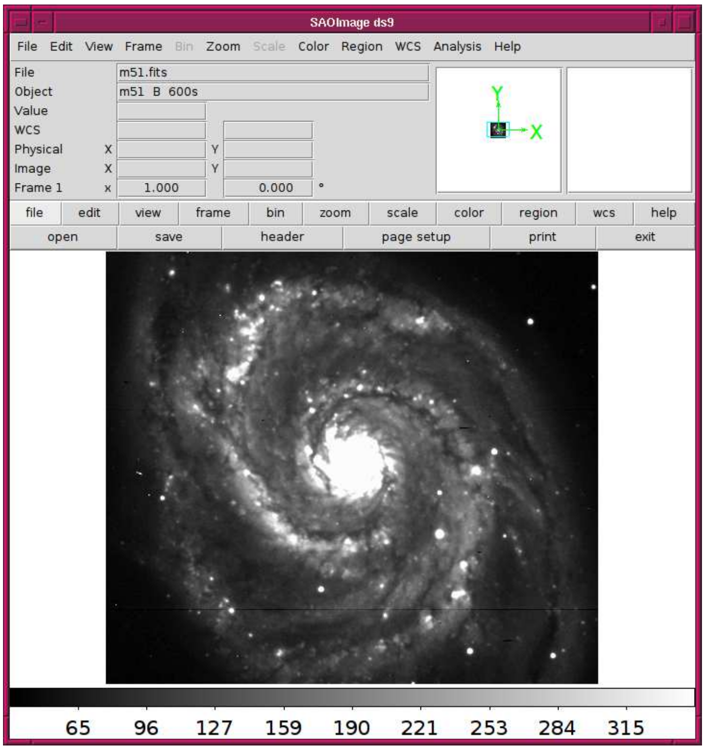

Figure 9: The image of M51 displayed on SAOimage DS9.

```
vocl> imexamine m51 1
```

Move the cursor to somewhere on the image, and press “c” key. Then, a Tektronix window showing the column profile appears. (Fig. 10) Pressing “l” key shows the line profile. We can also make a brightness profile between arbitrary two points. Move the cursor to the start point and press “v” key. Then, move the cursor to the end point and press “v” key again. This will show you a profile between those two point. (Fig. 11)

マウスのカーソルを画像上のどこかへ移動させ、 “c” キーを押してみる。 すると、テクトロニクスウィンドウが表示され、 そこにカーソルで指定され たピクセルを含むカラムのプロファイルが表示される。(Fig. 10) カラム (縦) ではなく、ライン (横) 方向のプロ ファイルが見たい場合には “l” キーを押せばよい。また、任意の二点間の プロファイルも表示させることができる。カーソルを起点まで持っていき、 そこで “v” キーを押す。次に、カーソルを終点まで持っていき、そこでま た “v” キーを押す。こうするとその二点間を結ぶ直線上のプロファイルが 表示される。 (Fig. 11)

For displaying a contour map of the region of the interest, move the cursor to the region of your interest and press “e” key. Fig. 12 is an example of contour map by `imexamine`.

画像のなかの興味ある領域のコンターマップを表示させるには、カーソルを その興味のある領域に持っていき、 “e” キーを押せばよい。 Fig. 12 に一例を示す。

The task `imexamine` is also used to make a histogram for a small region of the interest. Move the cursor to the region of your interest, and press “h” key. A histogram like Fig. 13 appears.

`imexamine` タスクは、画像のなかの興味のある小さな領域について、 ヒストグラムを表示させることもできる。カーソルを興味のある領域に移動 させ、 “h” キーを押す。すると、 Fig. 13 のような図が 表示されるはずである。

For making a radial profile of an object, move the cursor to a specific object and press “r” key. Then, a plot of the radial profile is shown. Fig. 14 is an example.

画像上の天体のラディアルプロファイルを表示させるには、カーソルを特定 の天体の上に持っていき、そこで “r” キーを押す。すると、ラディアルプ ロファイルの図が表示される。 Fig. 14 に例を示す。

To show the results of Gaussian fitting of an object along the line direction , move the cursor to the object of your interest and press “j” key. Fig. 15 is an example. For the Gaussian fitting along the column direction, use “k” key, instead.

星像のガウシアンフィッティングの結果を見る場合には、カーソルを興味の ある天体の上に持ってい き、そこで “j” キーを押す。すると、その天体の ライン方向のプロファイルとガウシアンフィッティングの 結果が表示される。 ライン方向ではなく、カラム方向にフィッティングしたい場合には、 “k” キーを使えばよい。

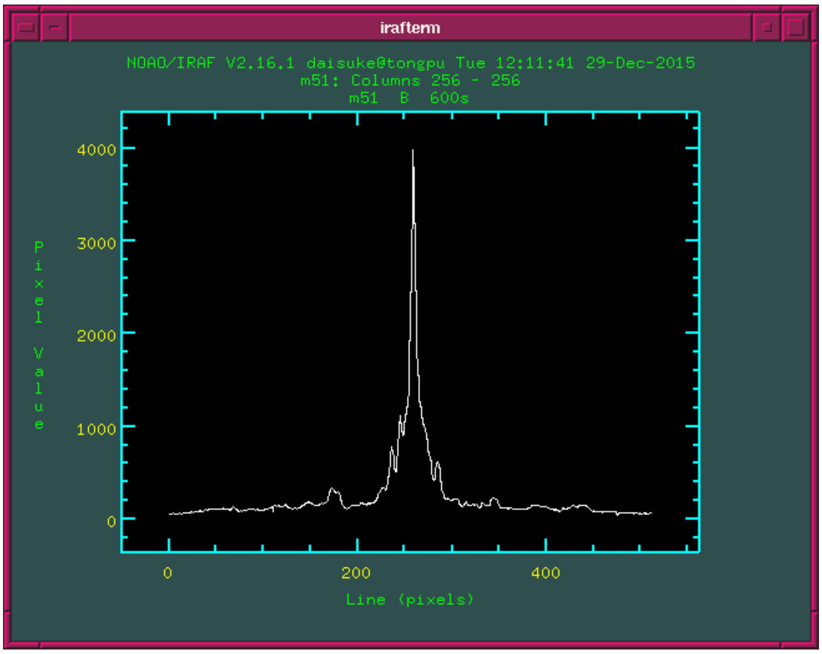

Figure 10: An example of the column profile produced by the task `imexamine`.

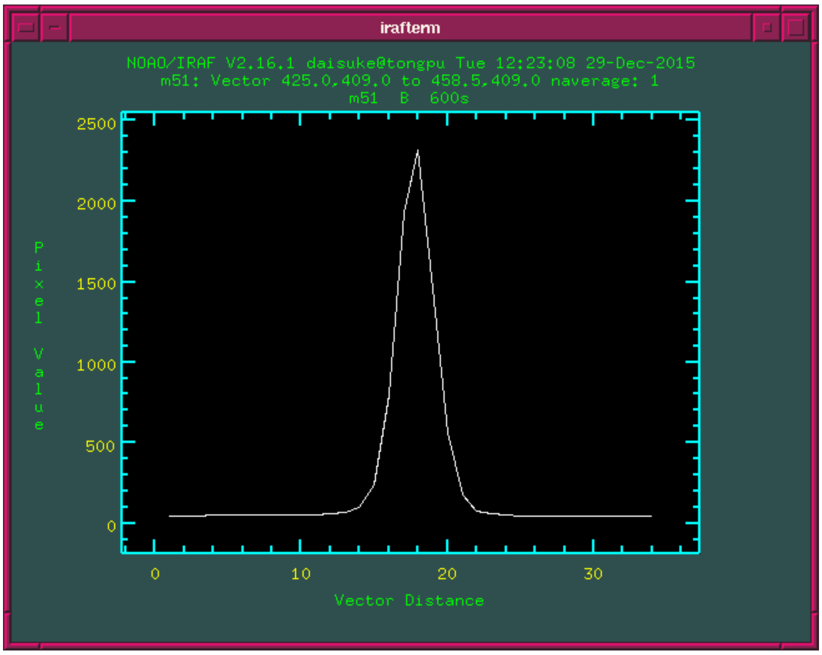

Figure 11: An example of the vector profile produced by the task `imexamine`.

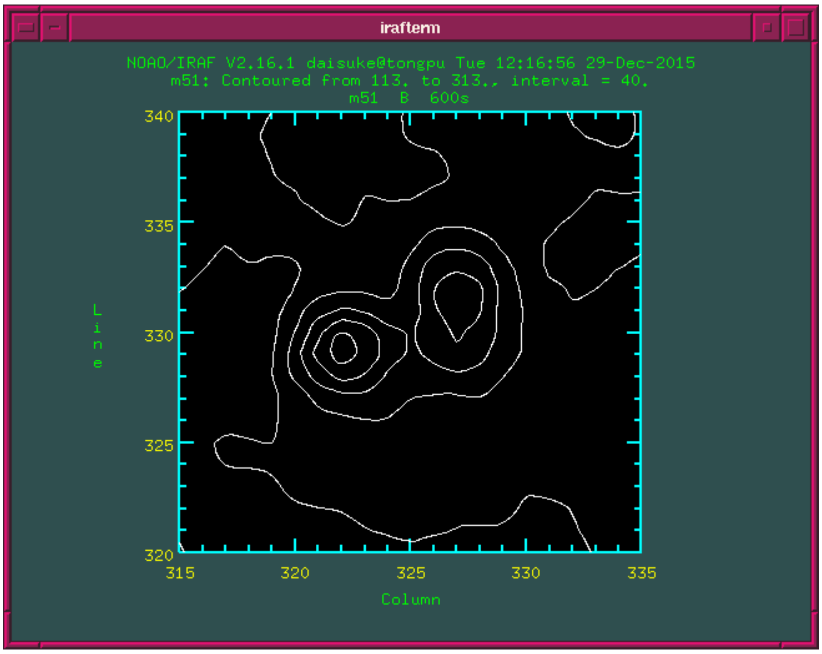

Figure 12: An example of the contour map produced by the task `imexamine`.

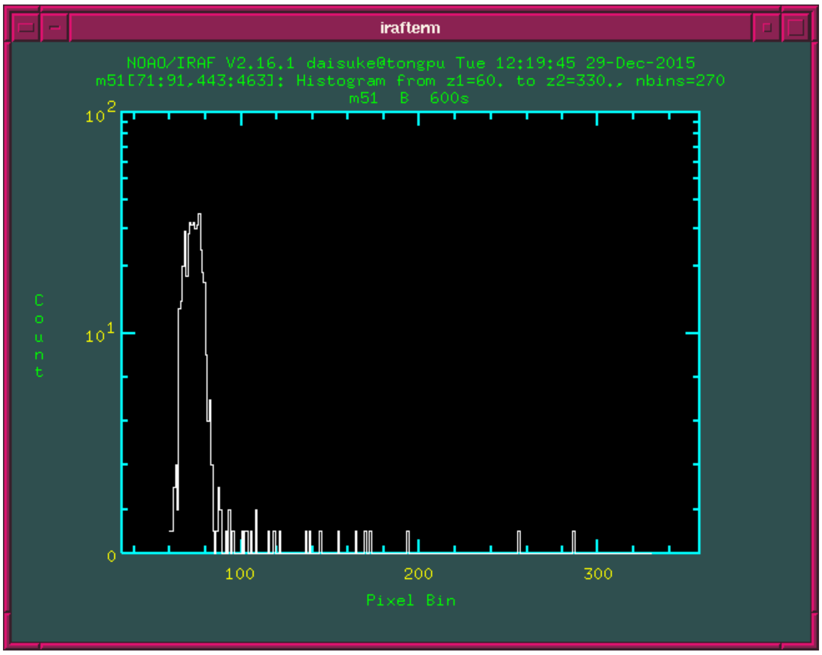

Figure 13: An example of the histogram produced by the task `imexamine`.

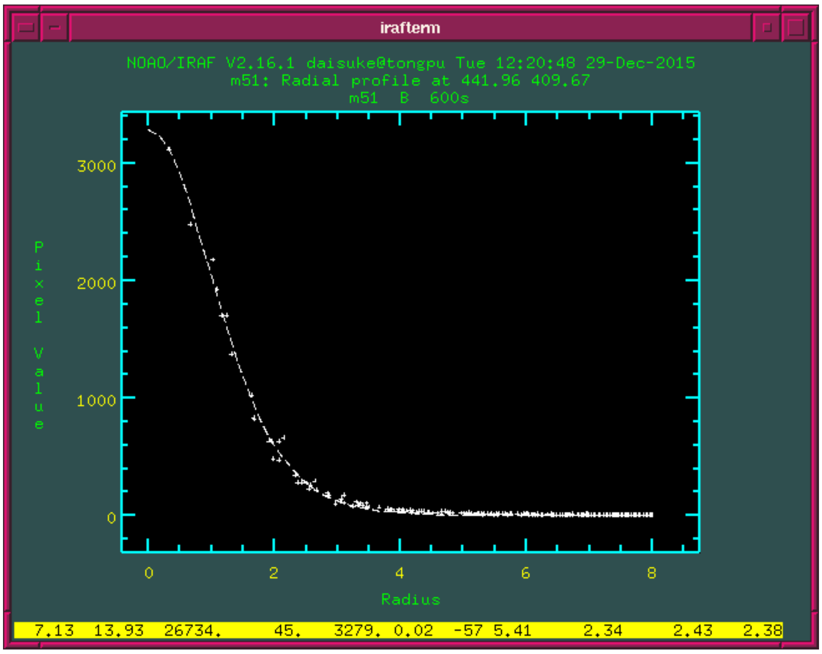

Figure 14: An example of the radial profile produced by the task `imexamine`.

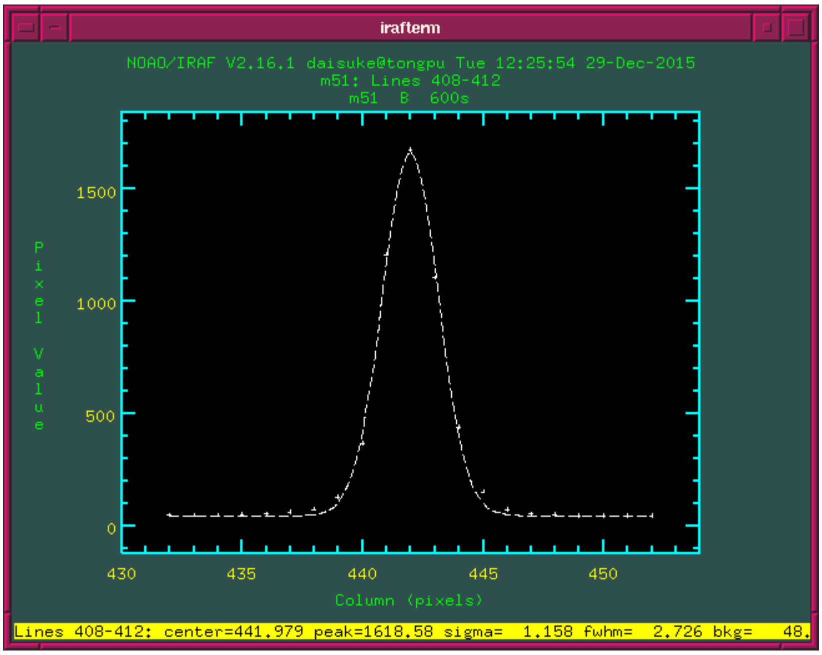

Figure 15: An example of the results of Gaussian fitting by the task `imexamine`.

The task imexamine also has some functions to make text outputs. Move the cursor to an object on the image, and press “a” key. You will get the results of the aperture photometry.
imexamine タスクは、グラフを作成するだけでなく、文字列として結 果を出力する機能も備えている。カーソルを画像上の天体の上に移動させ “a” キーを押すと、その天体のアパーチャー測光を行い、結果を出力して くれる。

```
#   COL     LINE    COORDINATES
#      R     MAG     FLUX      SKY     PEAK     E    PA BETA ENCLOSED    MOFFAT DIRECT
 441.96  409.67 441.96 409.67
   7.13  13.93  26734.      45.    3279. 0.02  -57 5.41      2.34      2.43   2.38
```

Move the cursor to the region of your interest, and press “m” key. The statistical information of pixel values of the region around the cursor is shown.
カーソルを興味のある領域に移動させ、そこで “m” キーを押すと、その領 域のピクセル値の統計情報が表示される。

```
#             SECTION      NPIX      MEAN    MEDIAN    STDDEV       MIN       MAX
   [467:471,374:378]        25      44.2       44.     1.756       42.       49.
   [440:444,408:412]        25     959.4      673.      821.      152.     3164.
   [254:258,257:261]        25     3625.     3510.     1778.     1770.     7734.
```

The task imexamine has many more functions. Also, many parameters can be adjusted. For further details, check the online documentation by typing following command.
imexamine タスクは、さらに多くの機能を持っている。また、さまざ まなパラメータが調整可能である。より詳しい使い方については、以下のコ マンドを使ってオンラインのマニュアルを参照すること。

```
vocl> phelp imexamine
```

To quit the task imexamine, press “q” key.
imexamine タスクを終了させるには “q” キーを押す。

1.2.10 Calculating statistics of pixel data

Try to use the task imstatistics to calculate the statistics of pixel data of a FITS file.
タスク imstatistics を使って FITS ファイルのピクセルデータ の統計情報を計算させてみよう。

```
vocl> imstat m51
#                IMAGE      NPIX      MEAN    STDDEV       MIN       MAX
                   m51    262144     108.3     131.3       -1.    19936.
```

If you need more information, then specify what you want using fields option.
より多くの情報が必要であれば、 fields オプションで指定すれ ばよい。

```
vocl> imstat m51 fields="image,npix,mean,midpt,stddev,min,max"
#                IMAGE      NPIX      MEAN     MIDPT    STDDEV       MIN       MAX
                   m51    262144     108.3     88.75     131.3       -1.    19936.
```

If you deal with many FITS files, then consider to use a list file. Prepare a file containing names of FITS files line by line. Specify the list file with preceding @, when executing the task. Many FITS files can be processed easily in this way.
多数の FITS ファイルを一度に扱うには、リストファイルを使うと便利であ る。一行に一つずつのファイル名を記述したファイルを用意し、タスク実行 の際に @ を前につけてリストファイルを指定すると、複数のファイル を一括して処理することができる。

```
vocl> imcopy dev$pix m51_0.fits
dev$pix -> m51_0.fits
vocl> imcopy dev$pix m51_1.fits
dev$pix -> m51_1.fits
vocl> imcopy dev$pix m51_2.fits
dev$pix -> m51_2.fits
vocl> ls m51*
m51_0.fits  m51_1.fits  m51_2.fits
vocl> print m51_0 > list
vocl> print m51_1 >> list
vocl> print m51_2 >> list
vocl> cat list
m51_0
m51_1
m51_2
vocl> imstat @list
#               IMAGE      NPIX      MEAN    STDDEV       MIN       MAX
                m51_0    262144     108.3     131.3       -1.    19936.
                m51_1    262144     108.3     131.3       -1.    19936.
                m51_2    262144     108.3     131.3       -1.    19936.
```

1.2.11 Making a histogram of an image

The task `imhistogram` is used to make a histogram of an image. Following command generates and shows a histogram. An example of histograms generated by `imhistogram` is shown in Fig. 16.

`imhistogram` というタスクを使って、画像のヒストグラムを作成する ことができる。以下のコマンドにより、ヒストグラムが作成され、表示され る。 `imhistogram` で作成されたヒストグラムの例を Fig. 16 に示す。

```
vocl> imhistogram m51
```

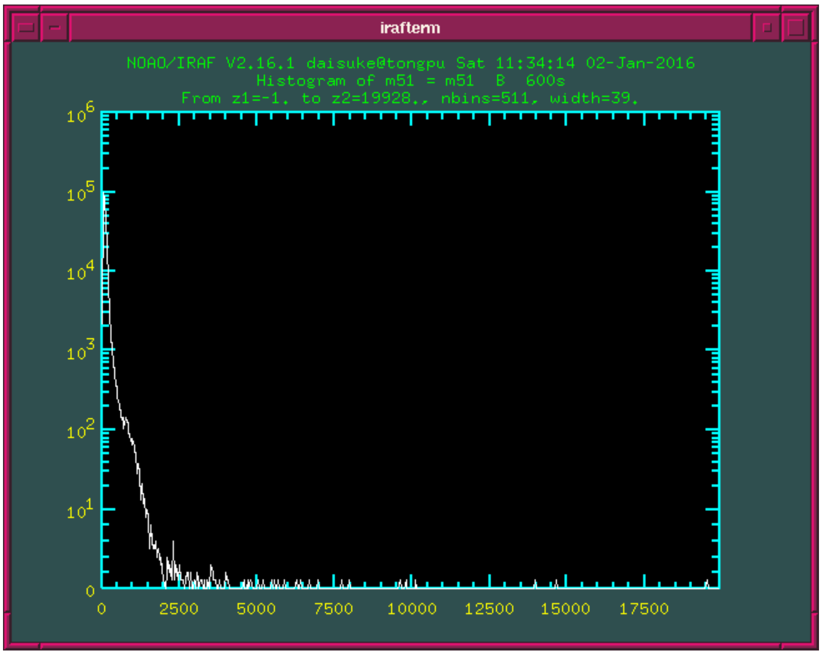

Figure 16: An example of the histogram generated by the task `imhistogram`.

We can adjust the range of pixel values to be plotted with `z1` and `z2` options. Following is an example. (Fig. 17)

`z1` および `z2` オプションを指定することで、表示するピクセル 値の範囲を調整することができる。以下に例を示す。 (Fig. 17)

```
vocl> imhistogram m51 z1=0 z2=1500
```

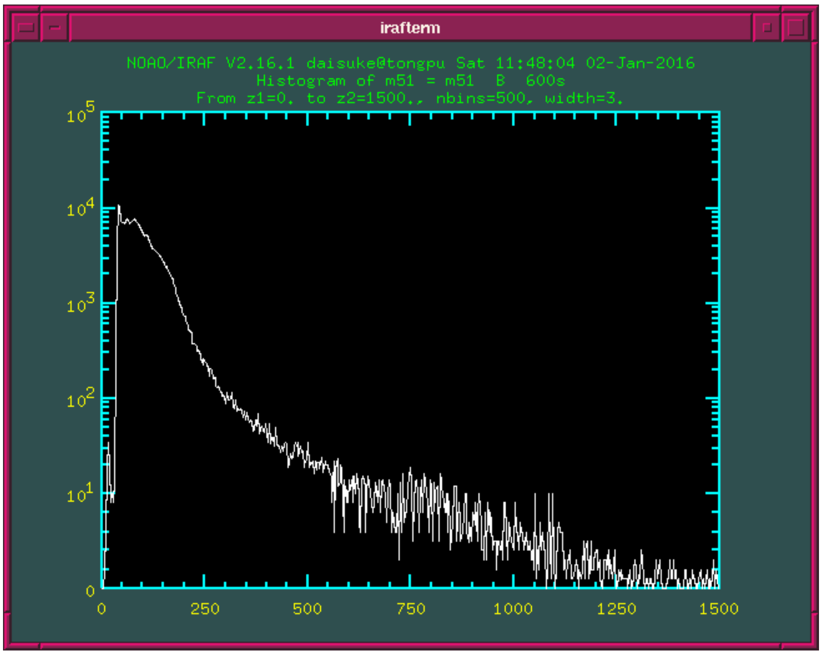

Figure 17: The histogram generated by the task `imhistogram` with `z1` and `z2` options.

The width of the bin can also be adjusted by using `binwidth` option. (Fig. 18)
`binwidth` オプションを使うことで、ヒストグラムのビンの幅を調整す ることができる。 (Fig. 18)

```
vocl> imhistogram m51 z1=0 z2=1500 binwidth=10 plot_type=box
```

Sometimes, we need outputs of numerical data for further analyses. We get the text output by adding `listout=yes` option.
さらなる解析のために、グラフではなく数値データを出力させたいこともあ る。 `listout=yes` というオプションをつけることで、テキストとして 結果を出力することができる。

```
vocl> imhistogram m51 z1=0 z2=1500 binwidth=10 listout=yes > m51_hist.data
vocl> head m51_hist.data nlines=5
5. 3
15. 74
25. 31
35. 7427
45. 30169
```

1.2.12 Editing parameters of a task

The task `eparam` is used to edit parameters of a task. Try following, then you will see the page for editing parameters of the task `imstatistics`. (Fig. 19)
タスク `eparam` は、タスクのパラメータの預設値を変更するのに使わ れる。次の例を実行することで、タスク `imstatistics` のパラメータ の預設値を変更するためのページが現れる。 (Fig. 19)

```
vocl> eparam imstatistics
```

You may change some parameters as needed. An example of parameters setting is shown in Fig. 20. Type `:wq` when finishing editing. If you discard changes, then type `:q`.
必要に応じて、パラメータを変更するとよい。変更後の例を Fig. 20 に示す。編集を終了する際には `:wq` と入力すればよい。変更を破棄したい場合には `:q` と入力する。
Now, the task `imstatistics` gives the mode of pixel values without adding `fields` options.
これで、タスク `imstatistics` は `fields` オプションで指定し なくても最頻値を表示してくれるように なる。

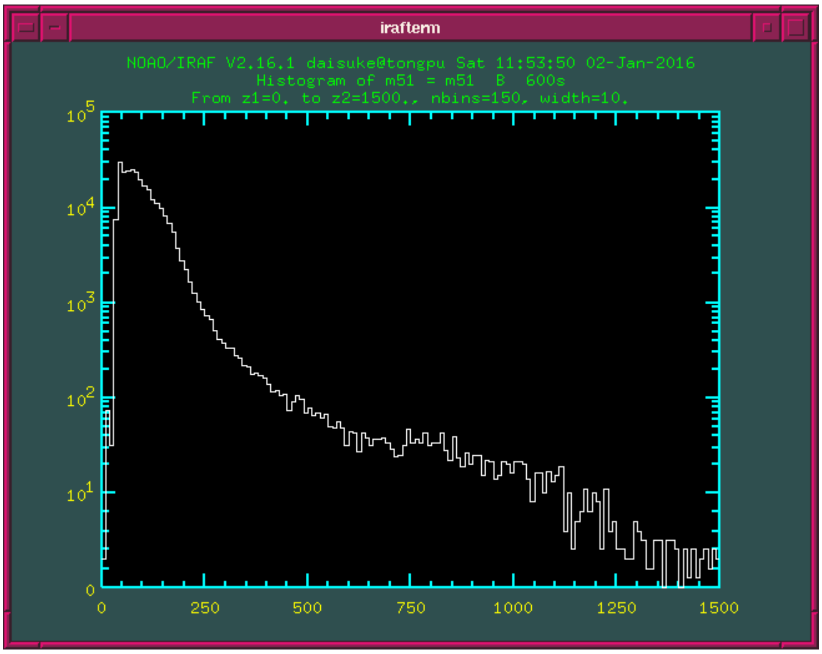

Figure 18: The histogram generated by the task **imhistogram** with **binwidth** option.

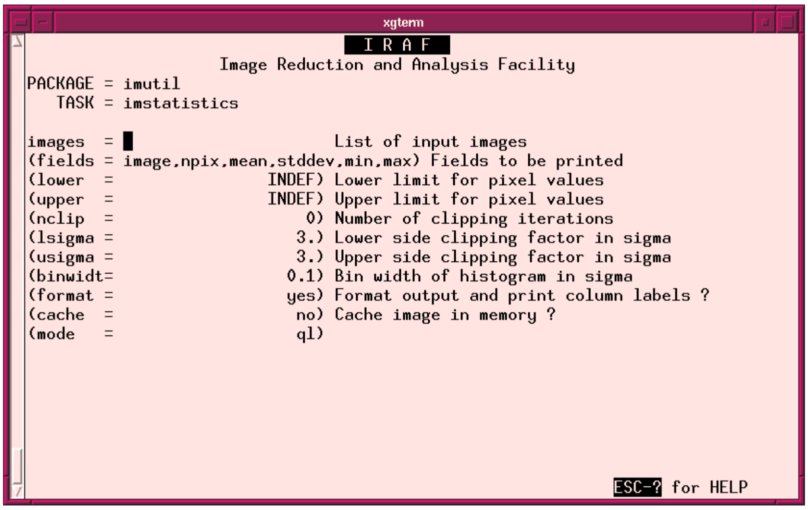

Figure 19: The page for editing task's parameters.

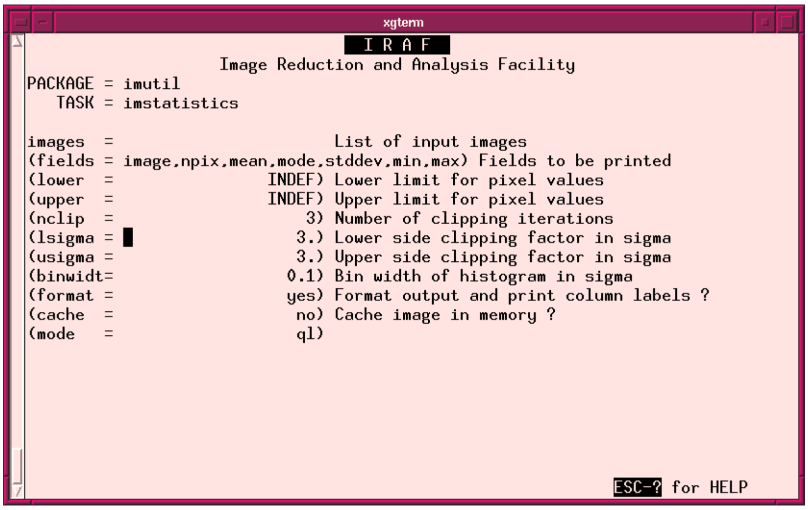

Figure 20: The page for editing task's parameters after changing some parameters.

```
vocl> imstat @list
#            IMAGE      NPIX      MEAN      MODE     STDDEV       MIN       MAX
             m51_0    252591     94.99     41.97       43.4       -1.      235.
             m51_1    252591     94.99     41.97       43.4       -1.      235.
             m51_2    252591     94.99     41.97       43.4       -1.      235.
```

The task `lparam` can be used to show the current settings of parameters.
タスク `lparam` は現在のパラメータの設定値を表示してくれる。

```
vocl> lparam imstatistics
       images = "@list"         List of input images
      (fields = "image,npix,mean,mode,stddev,min,max") Fields to be printed
       (lower = INDEF)          Lower limit for pixel values
       (upper = INDEF)          Upper limit for pixel values
       (nclip = 3)              Number of clipping iterations
      (lsigma = 3.)             Lower side clipping factor in sigma
      (usigma = 3.)             Upper side clipping factor in sigma
    (binwidth = 0.1)            Bin width of histogram in sigma
      (format = yes)            Format output and print column labels ?
       (cache = no)             Cache image in memory ?
        (mode = "ql")
```

The task `unlearn` can be used to reset the parameters back into the default values.
パラメータを初期値に戻したいときは、タスク `unlearn` を用いればよ い。

```
vocl> unlearn imstatistics
vocl> lparam imstatistics
       images =                 List of input images
      (fields = "image,npix,mean,stddev,min,max") Fields to be printed
       (lower = INDEF)          Lower limit for pixel values
       (upper = INDEF)          Upper limit for pixel values
       (nclip = 0)              Number of clipping iterations
      (lsigma = 3.)             Lower side clipping factor in sigma
      (usigma = 3.)             Upper side clipping factor in sigma
    (binwidth = 0.1)            Bin width of histogram in sigma
      (format = yes)            Format output and print column labels ?
       (cache = no)             Cache image in memory ?
        (mode = "ql")
```

1.2.13 Executing a CL script

Sometimes, it is painful to type many commands one by one, but it is rather convenient to run a number of tasks sequentially. Try following example.
いくつものタスクを一つずつ実行していくのは時に面倒でかつ苦痛であり、 複数のタスクをまとめて連続的に実行したいこともある。以下を試してみる。

```
vocl> !perl -e 'for($el=90;$el>=30;$el-=15){ print "airmass $el\n"; }' \
>>> > calc_airmass.cl
```

A very simple CL script `airmass.cl` is generated.
非常に簡単な CL スクリプト `airmass.cl` ができた。

```
vocl> cat calc_airmass.cl
airmass 90
airmass 75
airmass 60
airmass 45
airmass 30
```

To define a new task, use the task `task`.
新たなタスクを定義するには、 `task` というタスクを使う。

```
vocl> task $calc_airmass = calc_airmass.cl
```

Type `calc_airmass` to execute the newly defined task for this case.
新たに定義したタスクを実行するには、この場合 `calc_airmass` とコ マンドを打てばよい。

```
vocl> calc_airmass
airmass 1. at an elevation of 90. degrees (1.5708 radians) above horizon
airmass 1.0352 at an elevation of 75. degrees (1.309 radians) above horizon
airmass 1.1544 at an elevation of 60. degrees (1.0472 radians) above horizon
airmass 1.4133 at an elevation of 45. degrees (0.7854 radians) above horizon
airmass 1.996 at an elevation of 30. degrees (0.5236 radians) above horizon
```

1.2.14 Some astronomical calculations

Here are some examples of astronomical calculations using the task `astcalc`.
`astcalc` というタスクを用いた天文の計算の例を以下に挙げる。
First, we calculate the JD corresponding to 19 December 2015.
まず、 2015 年 12 月 19 日に対応するユリウス日を計算してみる。

```
vocl> astcalc
astcalc> date = "2015-12-19"
astcalc> ut = 12:00:00
astcalc> jd = julday(date,ut)
astcalc> print (jd)
2457376.
astcalc> quit
vocl>
```

Next, we calculate the airmass of SA101 326 at Lulin Observatory at 19:11:37 (UT) on 10 December 2015. RA and Dec of SA101 326 are 09:56:08.101 and -00:27:10.94, respectively. The integration time of the image is 30 sec. The airmass is found to be 1.1746 at the start of the exposure, and the effective airmass is found to be 1.1741.
次に、 SA101 326 の鹿林天文台での 2015 年 12 月 10 日 19:11:37 (UT) におけるエアマスを計算する。SA101 326 の赤経赤緯は、それぞれ 09:56:08.101 と -00:27:10.94 である。積分時間は 30 秒だった。積分開始時のエアマスは 1.1746 であり、積分中の実効的なエアマスは 1.1741 であ ることが分かった。

```
vocl> astcalc
astcalc> observatory = "lulin"
astcalc> date = "2015-12-10"
astcalc> ut = 19:11:37
astcalc> exptime = 30
astcalc> ra = 09:56:08.101
astcalc> dec = -00:27:10.94
astcalc> epoch = epoch(date, ut)
astcalc> print (epoch)
2015.940587909093
astcalc> mst = mst(date, ut, obsdb(observatory, "longitude"))
astcalc> print (mst)
8:31:53.47
astcalc> ra_current = ra_precess(ra, dec, 2000, epoch)
astcalc> dec_current = dec_precess(ra, dec, 2000, epoch)
astcalc> print (ra_current)
9:56:57.03
astcalc> print (dec_current)
-0:31:45.18
astcalc> airmass_start = airmass(ra_current, dec_current, mst, \
>>> obsdb(observatory, "latitude"))
astcalc> print (airmass_start)
1.174639150549566
astcalc> airmass_eff = eairmass(ra_current, dec_current, mst, exptime, \
>>> obsdb(observatory, "latitude"))
astcalc> print (airmass_eff)
1.174139104730688
astcalc> quit
vocl>
```

2 Basic CCD Data Reduction using IRAF

In this section, basic data reduction procedure for astronomical CCD images using IRAF is described.
この章では、 IRAF による CCD 観測データの基本的な整約手法について説明す る。

2.1 Bias subtraction using overscan region

The bias level of Apogee U42 CCD imager seems to have time variation. It may be a good idea to subtract the bias using the overscan region. To do so, the task `colbias` can be used.

Apogee 社の U42 CCD カメラのバイアスレベルは時間変動しているようである。 オーバースキャン領域を利用してバイアスを差し引きするのがよい方法かもし れない。そのためには、 `colbias` というタスクを使う。

First of all, we need to examine the regions of imaging area and overscan area. The information of imaging area and overscan area is not shown in FITS header, but it is clear when looking at flatfield images. An example of the twilight flatfield image is shown in Fig. 21. A black vertical stripe region is recognized at the right hand side of the image. This is the overscan region, and it is from the column 2049 to the column 2098.

まず初めに、画像が記録されている領域とオーバースキャンの領域の範囲を把 握する必要がある。残念ながら、これらの情報は FITS ヘッダーに含まれてい ないが、フラットフィールドの画像を見れば一目瞭然である。 Fig. 21 に薄明中に得られたフラットフィールドの一例を示す。画 像の一番右側に、縦の黒い帯状の領域が認められる。これがオーバースキャン 領域であり、その範囲は 2049 列から 2098 列までである。

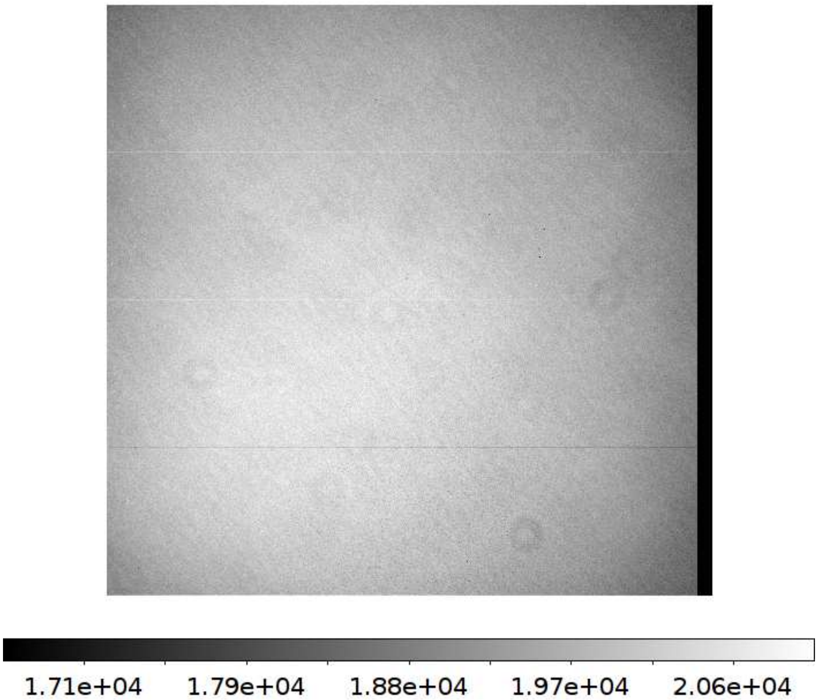

Figure 21: A sample of R-band flatfield image. The image was taken during the twilight in the evening on 12 December 2015.

An example is shown below to subtract the bias using the task `colbias`. Note that the task `colbias` is in the package `noao.imred.bias`. You need to load `noao.imred.bias` package before using `colbias`. If you prefer that `noao.imred.bias` package is automatically loaded at the start-up of IRAF, then you need to add two lines (`imred` and `bias`) in `login.cl` file. See Fig. 22.

以下に `colbias` を使ったバイアスの差し引きの一例を示す。 `colbias` は `noao.imred.bias` パッケージ内にある。もしもまだこの パッケージがロードされていない場合には、 `colbias` を使う前にパッ ケージをロードする必要があることに注意しなければならない。 IRAF の起 動時に `noao.imred.bias` が自動的にロードされるようにするためには、 `login.cl` に二行 (`imred` と `bias`) を追加すればよい。 Fig. 22 を参照のこと。

```
vocl> noao
      artdata.      digiphot.     nobsolete.    onedspec.
      astcat.       focas.        nproto.       rv.
      astrometry.   imred.        observatory   surfphot.
      astutil.      mtlocal.      obsutil.      twodspec.

noao> imred
      argus.      crutil.     echelle.    iids.       kpnocoude.  specred.
      bias.       ctioslit.   generic.    irred.      kpnoslit.   vtel.
      ccdred.     dtoi.       hydra.      irs.        quadred.

imred> bias
      colbias   linebias

bias> colbias 20151212_flat-007R.fits flat_R_007_o.fits bias="[2049:2098,*]" \
>>> trim="[1:2048,*]" function=spline3 order=3 niterate=5 interactive=no
```

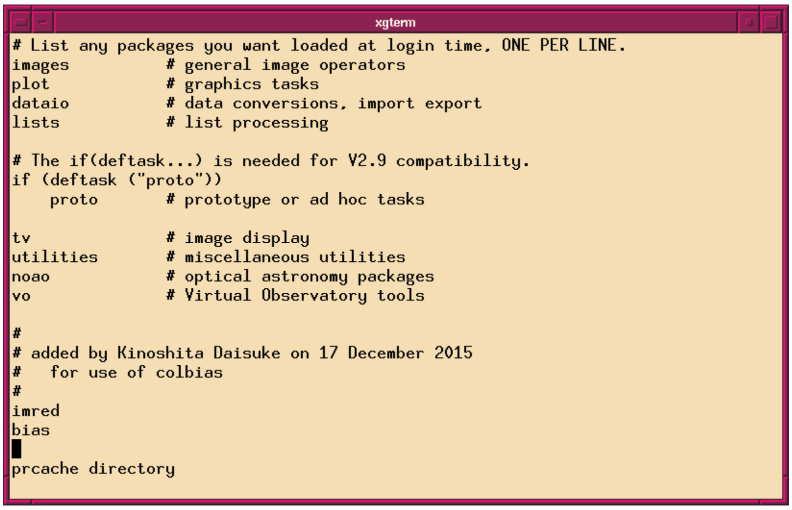

Figure 22: A sample setting of `login.cl` for loading packages at the start-up of IRAF.

We check the sizes of images before and after the bias subtraction. While the image before the bias subtraction has 2098 × 2048 pixels, the image after the bias subtraction has 2048 × 2048 pixels.
バイアスの差し引きの前後の画像の大きさを比べてみる。バイアスを引く前 は 2098 × 2048 ピクセルだったが、引いた後には 2048 × 2048 ピクセルになっていることが確認できる。

```
bias> imheader 20151212_flat-007R,flat_R_007_o
20151212_flat-007R[2098,2048][ushort]: evening twilight flatfield
flat_R_007_o[2048,2048][real]: evening twilight flatfield
```

We can also check the mean value of flatfield image before and after the bias subtraction. The mean value is about 1000 ADUs lower after the subtraction. The difference of mean values corresponds to the mean value of the overscan region of the raw data.
バイアスを引く前後でのピクセル値の平均も見てみる。バイアスを引いた後、 平均値がおよそ 1000 ADUs ほど小さくなっていることが分かる。この差はも ともとの生データのオーバースキャン領域の平均値に対応する。

```
bias> imstat 20151212_flat-007R,flat_R_007_o nclip=5
#               IMAGE      NPIX      MEAN    STDDEV       MIN       MAX
   20151212_flat-007R   4183698    19809.     540.1    18189.    21260.
         flat_R_007_o   4183556    18751.     539.6    17132.    20201.
bias> imstat 20151212_flat-007R[2049:2098,*] nclip=5
#               IMAGE      NPIX      MEAN    STDDEV       MIN       MAX
 20151212_flat-007R[2049:2098,*]      97146     1054.     5.557     1038.      1070.
```

Hundreds of CCD images are taken on a night, and we need to process many FITS files efficiently. In order to process multiple files in a convenient manner, you may consider to use list files. Following is an example.

一晩の観測では何百枚もの画像が得られるため、多数のファイルを効率よく 処理することが求められる。複数のファイルを手際よく処理するためにはリ ストファイルを活用するとよい。以下に一例を示す。

```
bias> ls *flat*R.fits
20151212_flat-001R.fits  20151212_flat-012R.fits  20151212_flat-020R.fits
20151212_flat-002R.fits  20151212_flat-013R.fits  20151212_flat-021R.fits
20151212_flat-006R.fits  20151212_flat-014R.fits  20151212_flat-022R.fits
20151212_flat-007R.fits  20151212_flat-015R.fits  20151212_flat-023R.fits
20151212_flat-008R.fits  20151212_flat-016R.fits  20151212_flat-024R.fits
20151212_flat-009R.fits  20151212_flat-017R.fits  20151212_flat-025R.fits
20151212_flat-010R.fits  20151212_flat-018R.fits  20151212_flat-026R.fits
20151212_flat-011R.fits  20151212_flat-019R.fits  20151212_flat-027R.fits
bias> ls *flat*R.fits > flat_R_raw.list
bias> !sed s/.fits/_o.fits/g flat_R_raw.list > flat_R_os.list
bias> colbias.bias = "[2049:2098,*]"
bias> colbias.trim = "[1:2048,*]"
bias> colbias @flat_R_raw.list @flat_R_os.list function=spline3 order=3 \
>>> niterate=5
bias> ls *flat*R_o.fits
20151212_flat-001R_o.fits  20151212_flat-012R_o.fits  20151212_flat-020R_o.fits
20151212_flat-002R_o.fits  20151212_flat-013R_o.fits  20151212_flat-021R_o.fits
20151212_flat-006R_o.fits  20151212_flat-014R_o.fits  20151212_flat-022R_o.fits
20151212_flat-007R_o.fits  20151212_flat-015R_o.fits  20151212_flat-023R_o.fits
20151212_flat-008R_o.fits  20151212_flat-016R_o.fits  20151212_flat-024R_o.fits
20151212_flat-009R_o.fits  20151212_flat-017R_o.fits  20151212_flat-025R_o.fits
20151212_flat-010R_o.fits  20151212_flat-018R_o.fits  20151212_flat-026R_o.fits
20151212_flat-011R_o.fits  20151212_flat-019R_o.fits  20151212_flat-027R_o.fits
```

The command `sed` is a stream editor. It is useful for simple text processing. For more about `sed`, you may go through the online documentation of `sed` by typing following command.

コマンド `sed` は、ストリームエディターである。簡単な文字列操作に おいて非常に便利である。 `sed` についてのより詳しい使い方は、以下 のようにして調べること。

```
% man sed
```

2.2 Combining dark frames

We usually take 10 or more dark frames, and combine them into a single frame for later use. Here, a way to combine multiple FITS file into a single FITS file using `imcombine` is described.

通常、 10 あるいはそれ以上のダークフレームが取得され、そして、それら は合成され、合成されたものがのちに利用される。ここでは、タスク `imcombine` を用いて、複数の FITS ファイルを合成することについて説明す る。

We combine 10 dark frames of 10-sec exposure. First, we make sure that dark frames of the same integration time are selected.

ここでは 10 枚の 10 秒積分のダークフレームを合成する。まず、同じ積分 時間で得られたダークフレームであることを確認する。

```
vocl> hselect *dark*d02.fits date-obs,imagetyp,exptime yes
2015-12-12T10:01:13     DARK    10.000000000000000
2015-12-12T10:01:32     DARK    10.000000000000000
2015-12-12T10:01:52     DARK    10.000000000000000
2015-12-12T10:02:11     DARK    10.000000000000000
2015-12-12T10:02:30     DARK    10.000000000000000
2015-12-12T10:02:50     DARK    10.000000000000000
2015-12-12T10:03:09     DARK    10.000000000000000
2015-12-12T10:03:29     DARK    10.000000000000000
2015-12-12T10:03:48     DARK    10.000000000000000
2015-12-12T10:04:08     DARK    10.000000000000000
```

Then, we subtract bias using overscan region.
そして、オーバースキャン領域を使ってバイアスを差し引く。

```
bias> ls *dark*d02.fits
20151212_dark-001d02.fits  20151212_dark-005d02.fits  20151212_dark-009d02.fits
20151212_dark-002d02.fits  20151212_dark-006d02.fits  20151212_dark-010d02.fits
20151212_dark-003d02.fits  20151212_dark-007d02.fits
20151212_dark-004d02.fits  20151212_dark-008d02.fits
bias> ls *dark*d02*.fits > dark_010_raw.list
bias> !sed s/.fits/_o.fits/g dark_010_raw.list > dark_010_os.list
bias> colbias.bias = "[2049:2098,*]"
bias> colbias.trim = "[1:2048,*]"
bias> colbias @dark_010_raw.list @dark_010_os.list order=3 niterate=5
bias> ls *dark*d02*_o.fits
20151212_dark-001d02_o.fits  20151212_dark-006d02_o.fits
20151212_dark-002d02_o.fits  20151212_dark-007d02_o.fits
20151212_dark-003d02_o.fits  20151212_dark-008d02_o.fits
20151212_dark-004d02_o.fits  20151212_dark-009d02_o.fits
20151212_dark-005d02_o.fits  20151212_dark-010d02_o.fits
```

Then, we combine 10 dark frames into a single frame.
そして、 10 枚のダークフレームを合成し、一枚の画像にする。

```
vocl> imcombine *dark*d02_o.fits dark_010.fits

Dec 18 10:47: IMCOMBINE
  combine = average, scale = none, zero = none, weight = none
  blank = 0.
                Images
  20151212_dark-001d02_o.fits
  20151212_dark-002d02_o.fits
  20151212_dark-003d02_o.fits
  20151212_dark-004d02_o.fits
  20151212_dark-005d02_o.fits
  20151212_dark-006d02_o.fits
  20151212_dark-007d02_o.fits
  20151212_dark-008d02_o.fits
  20151212_dark-009d02_o.fits
  20151212_dark-010d02_o.fits

  Output image = dark_010.fits, ncombine = 10
```

Without any options, `imcombine` takes simple averages. This probably does not always produce what we want. Some pixels may have comic ray hits and have significantly higher values. Sometimes, we may consider to take median to generate combined dark frames. In that case, we give `combine=median` option.

オプションなしだと、 `imcombine` は単純な平均を取る。これだと、い つも期待通りの結果を出してくれるとは限らない。宇宙線により非常に高い 値を持つピクセルがあるかもしれず、そうしたピクセルがあると平均値は大 きく影響を受ける。平均ではなく、メジアンを使いたい場合もあるかもしれ ない。そのような場合、 `combine=median` オプションを使えばよい。

```
vocl> imcombine *dark*d02_o.fits dark_010.fits combine=median

Dec 18 10:58: IMCOMBINE
  combine = median, scale = none, zero = none, weight = none
  blank = 0.
                Images
  20151212_dark-001d02_o.fits
  20151212_dark-002d02_o.fits
  20151212_dark-003d02_o.fits
  20151212_dark-004d02_o.fits
  20151212_dark-005d02_o.fits
  20151212_dark-006d02_o.fits
  20151212_dark-007d02_o.fits
  20151212_dark-008d02_o.fits
  20151212_dark-009d02_o.fits
  20151212_dark-010d02_o.fits

  Output image = dark_010.fits, ncombine = 10
```

Or, we may still use average, but with rejection operations. Following example will reject the highest value and the lowest value, and take averages.
あるいは、一部のデータを除外して平均を取るという方法もある。以下の例 では、最も大きな値を持つデータと最も小さな値を持つデータを除外した上 で平均を取っている。

```
vocl> imcombine *dark*d02_o.fits dark_010.fits combine=average reject=minmax \
>>> nhigh=1 nlow=1

Dec 18 11:01: IMCOMBINE
  combine = average, scale = none, zero = none, weight = none
  reject = minmax, nlow = 1, nhigh = 1
  blank = 0.
                Images
  20151212_dark-001d02_o.fits
  20151212_dark-002d02_o.fits
  20151212_dark-003d02_o.fits
  20151212_dark-004d02_o.fits
  20151212_dark-005d02_o.fits
  20151212_dark-006d02_o.fits
  20151212_dark-007d02_o.fits
  20151212_dark-008d02_o.fits
  20151212_dark-009d02_o.fits
  20151212_dark-010d02_o.fits

  Output image = dark_010.fits, ncombine = 10
```

The sigma clipping algorithm can also be used to combine images. Following example rejects values outside $median \pm 3\sigma$, and takes averages.
標準偏差 σ を使って除外するピクセルを決めるという方法もある。 以下の例では、メジアン $\pm 3\sigma$ の範囲外のデータを除外してか ら平均を取っている。

```
vocl> imcombine *dark*d02_o.fits dark_010.fits combine=average reject=sigclip \
>>> mclip=yes

Dec 18 11:12: IMCOMBINE
  combine = average, scale = none, zero = none, weight = none
  reject = sigclip, mclip = yes, nkeep = 1
  lsigma = 3., hsigma = 3.
  blank = 0.
                Images
  20151212_dark-001d02_o.fits
  20151212_dark-002d02_o.fits
  20151212_dark-003d02_o.fits
  20151212_dark-004d02_o.fits
  20151212_dark-005d02_o.fits
  20151212_dark-006d02_o.fits
  20151212_dark-007d02_o.fits
  20151212_dark-008d02_o.fits
  20151212_dark-009d02_o.fits
  20151212_dark-010d02_o.fits

  Output image = dark_010.fits, ncombine = 10
```

2.3 Subtracting combined dark from individual flatfields

The combined dark frame has to be subtracted from individual flatfield frames of the same integration time.
それぞれのフラットフィールドフレームから同じ積分時間の合成したダーク フレームを差し引く必要がある。

We first make sure that we have bias subtracted flatfield frame and a combined dark frame of the same integration time.
まず、バイアスを引き去ったあとのフラットフィールドフレームと、それと 同じ積分時間の合成済みのダークフレームであることを確認する。

```
vocl> ls -l 20151212_flat-010R_o.fits dark_010.fits
-rw-r--r-- 1 daisuke root 16784640 Dec 18 12:47 20151212_flat-010R_o.fits
-rw-r--r-- 1 daisuke root 16787520 Dec 18 12:36 dark_010.fits
vocl> hselect 20151212_flat-010R_o,dark_010 imagetyp,exptime yes
FLAT    10.000000000000000
DARK    10.000000000000000
```

Then, the dark frame is subtracted from the flatfield frame using the task `imarith`.
そして、 imarith を使いフラットフィールドフレームからダークフレー ムを引く。

```
vocl> imarith 20151212_flat-010R_o - dark_010 20151212_flat-010R_od.fits
```

2.4 An example of dark subtraction from flatfields

Here are FITS files of evening twilight flatfields taken on 12 December 2015. There are also corresponding dark frames.
これらのファイルは 2015 年 12 月 12 日の夕方の薄明時に得られたフラッ トフィールドである。また、対応するダークフレームも用意した。

```
vocl> ls
20151212_dark-001d01.fits  20151212_dark-005d03.fits  20151212_dark-010d01.fits
20151212_dark-001d02.fits  20151212_dark-005d04.fits  20151212_dark-010d02.fits
20151212_dark-001d03.fits  20151212_dark-006d01.fits  20151212_dark-010d03.fits
20151212_dark-001d04.fits  20151212_dark-006d02.fits  20151212_dark-010d04.fits
20151212_dark-002d01.fits  20151212_dark-006d03.fits  20151212_flat-001R.fits
20151212_dark-002d02.fits  20151212_dark-006d04.fits  20151212_flat-002R.fits
20151212_dark-002d03.fits  20151212_dark-007d01.fits  20151212_flat-006R.fits
20151212_dark-002d04.fits  20151212_dark-007d02.fits  20151212_flat-007R.fits
20151212_dark-003d01.fits  20151212_dark-007d03.fits  20151212_flat-008R.fits
20151212_dark-003d02.fits  20151212_dark-007d04.fits  20151212_flat-009R.fits
20151212_dark-003d03.fits  20151212_dark-008d01.fits  20151212_flat-010R.fits
20151212_dark-003d04.fits  20151212_dark-008d02.fits  20151212_flat-011R.fits
20151212_dark-004d01.fits  20151212_dark-008d03.fits  20151212_flat-012R.fits
20151212_dark-004d02.fits  20151212_dark-008d04.fits  20151212_flat-013R.fits
20151212_dark-004d03.fits  20151212_dark-009d01.fits  20151212_flat-014R.fits
20151212_dark-004d04.fits  20151212_dark-009d02.fits  20151212_flat-015R.fits
20151212_dark-005d01.fits  20151212_dark-009d03.fits  20151212_flat-016R.fits
20151212_dark-005d02.fits  20151212_dark-009d04.fits
```

First of all, we check the integration time of flatfield frames. We have 5, 10, 20, and 30 sec exposures.
まず、フラットフィールドフレームの積分時間を確認する。 5, 10, 20, 30 秒のデータがあることが分かる。

```
vocl> hselect *flat*R.fits $I,imagetyp,exptime yes
20151212_flat-001R.fits FLAT    5.0000000000000000
20151212_flat-002R.fits FLAT    5.0000000000000000
20151212_flat-006R.fits FLAT    5.0000000000000000
20151212_flat-007R.fits FLAT    5.0000000000000000
20151212_flat-008R.fits FLAT    5.0000000000000000
20151212_flat-009R.fits FLAT    10.000000000000000
20151212_flat-010R.fits FLAT    10.000000000000000
20151212_flat-011R.fits FLAT    20.000000000000000
20151212_flat-012R.fits FLAT    20.000000000000000
20151212_flat-013R.fits FLAT    30.000000000000000
20151212_flat-014R.fits FLAT    30.000000000000000
20151212_flat-015R.fits FLAT    30.000000000000000
20151212_flat-016R.fits FLAT    30.000000000000000
```

The bias is subtracted using the overscan region using `colbias` for all the FITS files.
`colbias` によりオーバースキャン領域を使ってすべての FITS ファイ ルについて、バイアスを引き去る。

```
vocl> ls *.fits > all.list
vocl> !sed s/.fits/_o.fits/g all.list  > all_os.list
vocl> colbias.bias = "[2049:2098,*]"
vocl> colbias.trim = "[1:2048,*]"
vocl> colbias @all.list @all_os.list order=3 niterate=5 interactive=no
```

We check which files are 5-sec dark frames.
どのファイルが 5 秒積分のダークフレームなのか調べる。

```
vocl> hselect *_o.fits $I,imagetyp,exptime yes | grep DARK | grep 5\.000000
20151212_dark-001d01_o.fits     DARK    5.0000000000000000
20151212_dark-002d01_o.fits     DARK    5.0000000000000000
20151212_dark-003d01_o.fits     DARK    5.0000000000000000
20151212_dark-004d01_o.fits     DARK    5.0000000000000000
20151212_dark-005d01_o.fits     DARK    5.0000000000000000
20151212_dark-006d01_o.fits     DARK    5.0000000000000000
20151212_dark-007d01_o.fits     DARK    5.0000000000000000
20151212_dark-008d01_o.fits     DARK    5.0000000000000000
20151212_dark-009d01_o.fits     DARK    5.0000000000000000
20151212_dark-010d01_o.fits     DARK    5.0000000000000000
```

We combine 10 dark frames of 5-sec integration time.
5 秒積分のダークフレームを合成する。

```
vocl> imcombine *d01_o.fits dark_005.fits combine=average reject=sigclip mclip=yes

Dec 18 13:12: IMCOMBINE
  combine = average, scale = none, zero = none, weight = none
  reject = sigclip, mclip = yes, nkeep = 1
  lsigma = 3., hsigma = 3.
  blank = 0.
                Images
  20151212_dark-001d01_o.fits
  20151212_dark-002d01_o.fits
  20151212_dark-003d01_o.fits
  20151212_dark-004d01_o.fits
  20151212_dark-005d01_o.fits
  20151212_dark-006d01_o.fits
  20151212_dark-007d01_o.fits
  20151212_dark-008d01_o.fits
  20151212_dark-009d01_o.fits
  20151212_dark-010d01_o.fits

  Output image = dark_005.fits, ncombine = 10
```

We also make combined dark frames of 10, 20, and 30 sec integration times.
10, 20, 30 秒積分のダークフレームも合成する。

```
vocl> imcombine *d02_o.fits dark_010.fits combine=average reject=sigclip mclip=yes
vocl> imcombine *d03_o.fits dark_020.fits combine=average reject=sigclip mclip=yes
vocl> imcombine *d04_o.fits dark_030.fits combine=average reject=sigclip mclip=yes
```

Now, we have combined dark frames of 5, 10, 20, and 30 sec integration times.
これで、 5, 10, 20, 30 秒の合成済みのダークフレームが得られた。

```
vocl> ls dark*.fits
dark_005.fits  dark_010.fits  dark_020.fits  dark_030.fits
vocl> hselect dark*.fits $I,imagetyp,exptime yes
dark_005.fits   DARK    5.0000000000000000
dark_010.fits   DARK    10.000000000000000
dark_020.fits   DARK    20.000000000000000
dark_030.fits   DARK    30.000000000000000
```

Type following command to generate a CL script for dark subtraction.
以下のコマンドを実行し、ダークの差し引きに用いるために用いる CL スク リプトを実行する。

```
vocl> hselect *flat*_o.fits $I,exptime yes > flat_exp.list
vocl> !perl -ne 'chop; ($file,$exp)=split; \
>>> $new=$file; $new=~s/_o.fits/_od.fits/; \
>>> printf("imarith %s - dark_%03d.fits %s\n", $file, $exp, $new);' \
>>> < flat_exp.list > darksub.cl
```

Now, you have a file `darksub.cl`.
これで `darksub.cl` というファイルが作られた。

```
vocl> cat darksub.cl
imarith 20151212_flat-001R_o.fits - dark_005.fits 20151212_flat-001R_od.fits
imarith 20151212_flat-002R_o.fits - dark_005.fits 20151212_flat-002R_od.fits
imarith 20151212_flat-006R_o.fits - dark_005.fits 20151212_flat-006R_od.fits
imarith 20151212_flat-007R_o.fits - dark_005.fits 20151212_flat-007R_od.fits
imarith 20151212_flat-008R_o.fits - dark_005.fits 20151212_flat-008R_od.fits
imarith 20151212_flat-009R_o.fits - dark_010.fits 20151212_flat-009R_od.fits
imarith 20151212_flat-010R_o.fits - dark_010.fits 20151212_flat-010R_od.fits
imarith 20151212_flat-011R_o.fits - dark_020.fits 20151212_flat-011R_od.fits
imarith 20151212_flat-012R_o.fits - dark_020.fits 20151212_flat-012R_od.fits
imarith 20151212_flat-013R_o.fits - dark_030.fits 20151212_flat-013R_od.fits
imarith 20151212_flat-014R_o.fits - dark_030.fits 20151212_flat-014R_od.fits
imarith 20151212_flat-015R_o.fits - dark_030.fits 20151212_flat-015R_od.fits
imarith 20151212_flat-016R_o.fits - dark_030.fits 20151212_flat-016R_od.fits
```

We carry out the dark subtraction for flatfield frames by executing `darksub.cl`.
`darksub.cl` を実行することで、フラットフィールドフレームからダー クフレームを引く。

```
vocl> task $darksub = darksub.cl
vocl> darksub
```

Finally, we have dark subtracted flatfields.
ダークフレームを引いたフラットフィールドフレームが得られた。

```
vocl> ls *_od.fits
20151212_flat-001R_od.fits  20151212_flat-011R_od.fits
20151212_flat-002R_od.fits  20151212_flat-012R_od.fits
20151212_flat-006R_od.fits  20151212_flat-013R_od.fits
20151212_flat-007R_od.fits  20151212_flat-014R_od.fits
20151212_flat-008R_od.fits  20151212_flat-015R_od.fits
20151212_flat-009R_od.fits  20151212_flat-016R_od.fits
20151212_flat-010R_od.fits
```

2.5 Combining flatfields

We combine dark subtracted flatfields. The task `imcombine` is used for this.
ダークを引いたフラットフィールドを合成する。ここでも `imcombine` を使えばよい。

We first check the statistics of pixel data of dark subtracted flatfields. For first two files, the signals are saturated. We decide not to use these two files.
まず、ピクセルデータの統計情報を得る。最初の二枚のデータはシグナルが 飽和しているので、使わないこととする。

```
vocl> imstat *flat*R_od.fits
#               IMAGE      NPIX      MEAN    STDDEV       MIN       MAX
 20151212_flat-001R_od.fits   4194304    64440.     3.189    63248.    64457.
 20151212_flat-002R_od.fits   4194304    64442.      4.05    63249.    64465.
 20151212_flat-006R_od.fits   4194304    33802.     933.3    21119.    36806.
 20151212_flat-007R_od.fits   4194304    18738.      546.    11614.    21312.
 20151212_flat-008R_od.fits   4194304    14126.     415.1     8638.    15609.
 20151212_flat-009R_od.fits   4194304    15736.     458.6     9645.    17445.
 20151212_flat-010R_od.fits   4194304     9198.     276.1     5650.    11453.
 20151212_flat-011R_od.fits   4194304    11444.     332.6     5140.    16872.
 20151212_flat-012R_od.fits   4194304     7226.     220.8     852.1     8806.
 20151212_flat-013R_od.fits   4194304     8728.      257.     5255.    15647.
 20151212_flat-014R_od.fits   4194304     7988.     236.8     5090.     9902.
 20151212_flat-015R_od.fits   4194304     6786.     201.3     4170.    14733.
 20151212_flat-016R_od.fits   4194304     3777.     119.6     2173.     9272.
```

Then, we make a list file for combining.
そして、合成のためにリストファイルを作成する。

```
vocl> ls 20151212_flat-00[6-9]R_od.fits 20151212_flat-01*R_od.fits
20151212_flat-006R_od.fits  20151212_flat-012R_od.fits
20151212_flat-007R_od.fits  20151212_flat-013R_od.fits
20151212_flat-008R_od.fits  20151212_flat-014R_od.fits
20151212_flat-009R_od.fits  20151212_flat-015R_od.fits
20151212_flat-010R_od.fits  20151212_flat-016R_od.fits
20151212_flat-011R_od.fits
vocl> ls 20151212_flat-00[6-9]R_od.fits 20151212_flat-01*R_od.fits \
>>> > flat_R_evening.list
```

In the list file, the names of files to be combined are listed.
リストファイルには、合成されるファイルの名前が格納されている。

```
vocl> cat flat_R_evening.list
20151212_flat-006R_od.fits
20151212_flat-007R_od.fits
20151212_flat-008R_od.fits
20151212_flat-009R_od.fits
20151212_flat-010R_od.fits
20151212_flat-011R_od.fits
20151212_flat-012R_od.fits
20151212_flat-013R_od.fits
20151212_flat-014R_od.fits
20151212_flat-015R_od.fits
20151212_flat-016R_od.fits
```

We combine flatfield frames using the task `imcombine`. Note that mean level of each flatfield frame differs for twilight flatfield. It is essential to do scaling before combining and take weighted average for combining. With the option `scale=median`, scaling is carried out before combining. With the option `weight=median`, the weighted averaging is used for combining.

`imcombine` を使ってフラットフィールドフレームを合成する。薄明の 空で得たフラットフィールドの場合、各データの平均レベルが大きくことな ることに注意が必要である。合成の前にスケーリングを行い平均レベルを合 わせることと、合成の際に重み付き平均を使うことはおそらく必須である。 `scale=median` オプションを付けると、合成の前に各フレームをスケー リングしてくれる。 `weight=median` オプションを付けると、合成の際 に重み付き平均が計算される。

```
vocl> imcombine @flat_R_evening.list flat_R_evening.fits reject=sigclip mclip=yes \
>>> scale=median weight=median

Dec 18 13:51: IMCOMBINE
  combine = average, scale = median, zero = none, weight = median
  reject = sigclip, mclip = yes, nkeep = 1
  lsigma = 3., hsigma = 3.
  blank = 0.
              Images   Median  Scale Weight
  20151212_flat-006R_od.fits  33878.  1.000  0.246
  20151212_flat-007R_od.fits  18787.  1.803  0.136
  20151212_flat-008R_od.fits  14160.  2.392  0.103
  20151212_flat-009R_od.fits  15779.  2.147  0.114
  20151212_flat-010R_od.fits  9219.5  3.675  0.067
  20151212_flat-011R_od.fits  11472.  2.953  0.083
  20151212_flat-012R_od.fits  7243.5  4.677  0.053
  20151212_flat-013R_od.fits  8747.2  3.873  0.063
  20151212_flat-014R_od.fits  8007.1  4.231  0.058
  20151212_flat-015R_od.fits   6801.  4.981  0.049
  20151212_flat-016R_od.fits  3784.4  8.952  0.027

  Output image = flat_R_evening.fits, ncombine = 11
```

Combined flatfield is shown in Fig. 23. It is clearly recognized that the combined flatfield looks more smooth than the individual flatfield.

合成したフラットフィールドを Fig. 23 に示す。単一 のフラットフィールドフレームと比べると、合成したフラットフィールドは 非常になめらかになっていることが見て取れる。

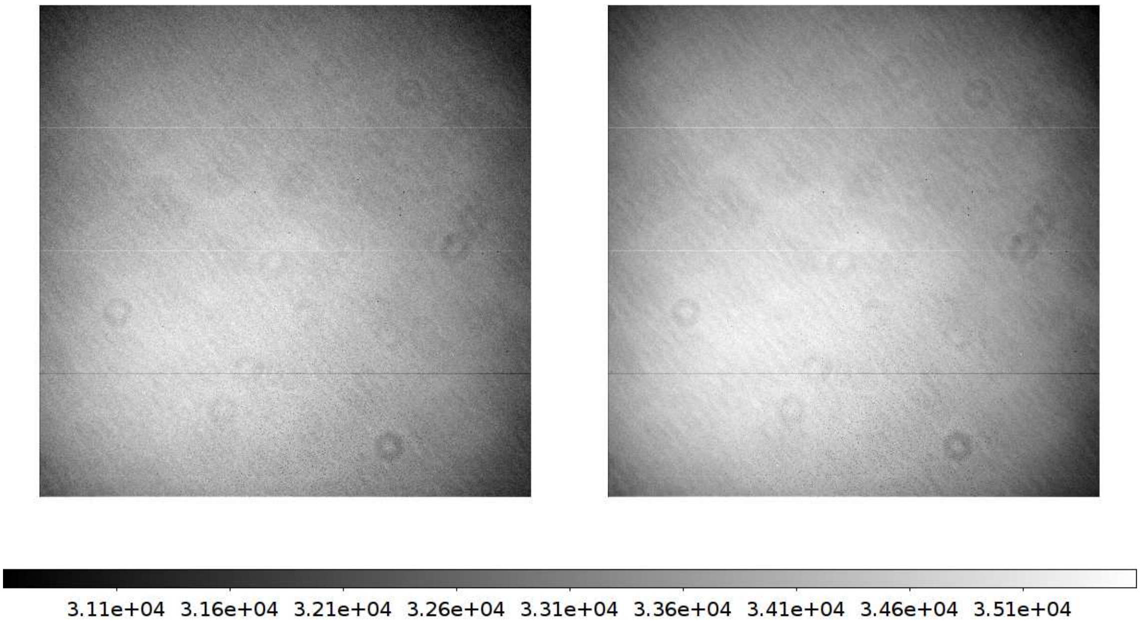

Figure 23: A comparison of single flatfield and combined flatfield. The left panel shows an individual flatfield in R-band taken during the evening twilight on 12 December 2015. The right panel shows the combined flatfield in R-band using 11 exposures taken on the same day.

Finally, we normalize the combined flatfield.
最後に、合成したフラットフィールドを規格化する。

```
vocl> imstat flat_R_evening.fits
#                IMAGE      NPIX      MEAN    STDDEV       MIN       MAX
  flat_R_evening.fits   4194304    33797.     942.2    20897.    37134.
vocl> imarith flat_R_evening / 33797.0 normflat_R_evening.fits
vocl> imstat normflat_R_evening.fits
#                IMAGE      NPIX      MEAN    STDDEV       MIN       MAX
 normflat_R_evening.fits   4194304        1.   0.02788    0.6183     1.099
```

Or, the task `normalize` is used to noamalize the flatfield. The task `normalize` is in the package `generic` under `noao.imred`. Load the package `noao.imred.generic` before using the task `normalize`.
または、 `normalize` というタスクでも規格化を行うことができる。 `normalize` は `noao.imred` のなかの `generic` パッケージ に含まれている。使う前にこのパッケージをロードしておく必要がある。

```
vocl> generic
      background  darksub     flat1d      flatten     normalize   normflat

generic>
```

Note that the task `normalize` overrides existing files. It may be a good idea to copy the file first, and then apply the normalization.
`normalize` はファイルを上書きしてしまうことに注意が必要である。 まずもともとのファイルをコピーし、その上で `normalize` を使い規格 化するのがよいかもしれない。

```
generic> imcopy flat_R_evening.fits nflat_R_evening.fits
flat_R_evening.fits -> nflat_R_evening.fits
generic> imstat nflat_R_evening.fits
#               IMAGE      NPIX      MEAN    STDDEV       MIN       MAX
 nflat_R_evening.fits   4194304    33797.     942.2    20897.    37134.
generic> normalize nflat_R_evening.fits sample=[*,*]
generic> imstat nflat_R_evening.fits
#               IMAGE      NPIX      MEAN    STDDEV       MIN       MAX
 nflat_R_evening.fits   4194304        1.   0.02788    0.6183     1.099
```

2.6 Processing object frames

Suppose we have an object frame named `20151212_asteroid_001R.fits`. The integration time and filter used for this frame are checked by following task.
今 `20151212_asteroid_001R.fits` という目標天体を観測したオブジェ クトフレームがあるとする。このデータの積分時間および使われたフィルター は以下のタスクで確認できる。

```
vocl> hselect 20151212_asteroid_001R.fits $I,imagetyp,exptime,filter yes
20151212_asteroid_001R.fits     LIGHT   60.000000000000000       R_Asahi_2007
```

The integration time was 60 sec and R-band filter was used to obtain this data. We need a combined dark frame of 60 sec exposure and a normalized combined flatfield of R-band filter. The file `dark_00060.fits` is the combined dark frame of 60 sec exposure, and the file `normflat_R.fits` is the normalized combined R-band flatfield.
積分時間は 60 秒で、 R バンドフィルターが用いられたことが分かった。つ まり、積分時間 60 秒の合成済みのダークフレームと、規格化された合成済 みの R バンドのフラットフィールドフレームが必要となる。 `dark_00060.fits` が 60 秒積分のダークフレームであり、 `normflat_R.fits` が規格化された R-band のフラットフィールドである。

```
vocl> hselect dark_00060.fits $I,imagetyp,exptime yes
dark_00060.fits DARK    60.000000000000000
vocl> hselect normflat_R.fits $I,imagetyp,exptime,filter yes
normflat_R.fits FLAT    5.0000000000000000       R_Asahi_2007
```

First, we subtract bias from the raw data `20151212_asteroid_001R.fits` using the overscan region.
まず最初に、オーバースキャン領域を使って `20151212_asteroid_001R.fits` からバイアスを引き去る。

```
vocl> colbias 20151212_asteroid_001R.fits 20151212_asteroid_001R_o.fits \
>>> bias="[2049:2098,*]" trim="[1:2048,*]" order=3 niterate=5 median=yes
```

Next, we subtract dark from `20151212_asteroid_001R_o.fits`.
次に、 `20151212_asteroid_001R_o.fits` からダークを引く。

```
vocl> imarith 20151212_asteroid_001R_o.fits - dark_00060.fits \
>>> 20151212_asteroid_001R_od.fits
```

Finally, we devide `20151212_asteroid_001R_od.fits` by the nofrmalized flatfield.
最後に、 `20151212_asteroid_001R_od.fits` を規格化されたフラット フィールドで割る。

```
vocl> imarith 20151212_asteroid_001R_od.fits / normflat_R.fits \
>>> 20151212_asteroid_001R_odf.fits
```

The file `20151212_asteroid_001R_odf.fits` is the reduced object frame.
`20151212_asteroid_001R_odf.fits` が整約済みのオブジェクトフレー ムである。

2.7 An example of reducing CCD data

Here, an example of CCD data reduction for the data obtained on 10 December 2015 is shown.
ここでは、例として、 2015 年 12 月 10 日に得られたデータの整約の流れ を紹介する。
First, we extract the data files from the archived file.
まず最初に、圧縮結合されたファイルから、観測データを取り出す。

```
vocl> !unzip lot20151210.zip
```

Then, we make a new directory for reducing the data, and move to newly created directory.
そして、データの整約のための新たなディレクトリを作成し、そのディレク トリに移動する。

```
vocl> mkdir lot20151210red
vocl> cd lot20151210red/
```

For each FITS file, we subtract the bias component using overscan region.
それぞれの FITS ファイルについて、オーバースキャン領域を使ってバイア スを引き去る。

```
vocl> !ls ../lot20151210 | head -3
20151210_catalina-001B.fits
20151210_catalina-001bias.fits
20151210_catalina-002B.fits
vocl> ls ../lot20151210/*.fits > all_raw.list
vocl> !sed s%../lot20151210/20151210_%% all_raw.list | sed s/-/_/g | \
>>> sed s/.fits/_o.fits/ > all_os.list
vocl> colbias.bias = "[2049:2098,*]"
vocl> colbias.trim = "[1:2048,*]"
vocl> colbias @all_raw.list @all_os.list function=spline3 order=3 \
>>> niterate=5 median=yes interactive=no
```

For the convenience of further processing, we now make a list of FITS file name, time of data acquisition, data type, exposure time, and filter used.

今後の処理に便利なように、 FITS ファイル名、データ取得の時間、データ の種類、積分時間、使われたフィルターの情報をまとめておく。

```
vocl> hselect *.fits $I,date-obs,imagetyp,exptime,filter yes > datatype.list
```

We combine dark frames.
ダークフレームの合成を行う。

```
vocl> !grep DARK datatype.list  | perl -ne 'chop; (@data)=split; \
>>> printf("echo %s >> dark%05d.list\n", $data[0], $data[3]);' | sh
vocl> !ls dark*.list | perl -ne 'chop; $list=$_; s/.list/.fits/; \
>>> printf("imcombine \@%s %s combine=average reject=sigclip\n", $list,$_);' \
>>> > dark_comb.cl
vocl> cat dark_comb.cl
imcombine @dark00005.list dark00005.fits combine=average reject=sigclip
imcombine @dark00010.list dark00010.fits combine=average reject=sigclip
imcombine @dark00020.list dark00020.fits combine=average reject=sigclip
imcombine @dark00030.list dark00030.fits combine=average reject=sigclip
imcombine @dark00040.list dark00040.fits combine=average reject=sigclip
imcombine @dark00060.list dark00060.fits combine=average reject=sigclip
imcombine @dark00090.list dark00090.fits combine=average reject=sigclip
imcombine @dark00180.list dark00180.fits combine=average reject=sigclip
imcombine @dark00300.list dark00300.fits combine=average reject=sigclip
imcombine @dark03600.list dark03600.fits combine=average reject=sigclip
vocl> task $dark_comb = dark_comb.cl
vocl> dark_comb
```

Now, we start to process the flatfield frames. We subtract the corresponding combined dark frame from each flatfield frame.

ここからフラットフィールドフレームの処理を始める。まず、それぞれのフ ラットフィールドフレームから対応する合成済みのダークフレームを差し引 く。

```
vocl> !grep FLAT datatype.list | perl -ne 'chop; (@data)=split; $new=$data[0]; \
>>> $new=~s/_o.fits/_od.fits/; printf("imarith %s - dark%05d.fits %s\n", \
>>> $data[0], $data[3], $new);' > darksub_flat.cl
vocl> !head -5 darksub_flat.cl
imarith flat_001B_o.fits - dark00060.fits flat_001B_od.fits
imarith flat_001I_o.fits - dark00060.fits flat_001I_od.fits
imarith flat_001R_o.fits - dark00060.fits flat_001R_od.fits
imarith flat_001V_o.fits - dark00060.fits flat_001V_od.fits
imarith flat_002B_o.fits - dark00060.fits flat_002B_od.fits
vocl> task $darksub_flat = darksub_flat.cl
vocl> darksub_flat
```

We make list files containing names of flatfield frames for each pass band.
それぞれのバンドについて、フラットフィールドフレームのファイル名を含 んだリストファイルを作成する。

```
vocl> !grep FLAT datatype.list  | perl -ne 'chop; (@data)=split; \
>>> $data[0]=~s/_o.fits/_od.fits/; \
>>> printf("echo %s >> flat_%s.list\n", $data[0], $data[4]);' | sh
vocl> ls flat*.list
flat_B_Asahi_2007.list  flat_R_Asahi_2007.list
flat_I_Asahi_2007.list  flat_V_Asahi_2007.list
vocl> !head -5 flat_R_Asahi_2007.list
flat_001R_od.fits
flat_002R_od.fits
flat_003R_od.fits
flat_004R_od.fits
flat_005R_od.fits
```

We examine the mean count level of each flatfield using `imstatistics`.
それぞれのフラットフィールドの平均カウント値を `imstatistics` を 使って調べる。

```
vocl> imstat @flat_R_Asahi_2007.list
#               IMAGE      NPIX      MEAN    STDDEV       MIN       MAX
    flat_001R_od.fits   4194304     1956.     795.9     518.7    64475.
    flat_002R_od.fits   4194304     2484.     287.2     984.7    64468.
    flat_003R_od.fits   4194304     3531.     138.6     1833.    37360.
    flat_004R_od.fits   4194304     3829.     413.9     2138.    64479.
    flat_005R_od.fits   4194304     4362.     227.4     2581.    64471.
    flat_006R_od.fits   4194304     4735.     165.1     2877.    29504.
    flat_007R_od.fits   4194304    13250.     389.2     8243.    21293.
    flat_008R_od.fits   4194304    14416.      449.     8718.    64469.
    flat_009R_od.fits   4194304    17142.     510.7    10600.    62008.
    flat_010R_od.fits   4194304    30042.     864.5    18268.    33380.
    flat_011R_od.fits   4194304    55557.     1578.    34456.    64456.
```

One of R-band flatfield is found to have the mean count more than 50,000 ADUs. We decide not to use this file.
R バンドのフラットフィールドのうちの一枚は、平均カウント値が 50,000 ADUs を超えていることが分かったので、それは使わないことにする。

```
vocl> !head -10 flat_R_Asahi_2007.list  > tmp.list
vocl> cat tmp.list
flat_001R_od.fits
flat_002R_od.fits
flat_003R_od.fits
flat_004R_od.fits
flat_005R_od.fits
flat_006R_od.fits
flat_007R_od.fits
flat_008R_od.fits
flat_009R_od.fits
flat_010R_od.fits
vocl> !mv -i tmp.list flat_R_Asahi_2007.list
mv: overwrite ‘flat_R_Asahi_2007.list’? y
```

We combine flatfields.
フラットフィールドの合成を行う。

```
vocl> !ls flat*.list | perl -ne 'chop; $list=$_; s/.list/.fits/; \\
>>> printf("imcombine \@%s %s combine=average reject=sigclip scale=median \
>>> weight=median mclip=yes lsigma=2.0 hsigma=2.0\n", $list, $_);' > flat_comb.cl
vocl> cat flat_comb.cl
imcombine @flat_B_Asahi_2007.list flat_B_Asahi_2007.fits combine=average reject=sigcl
imcombine @flat_I_Asahi_2007.list flat_I_Asahi_2007.fits combine=average reject=sigcl
imcombine @flat_R_Asahi_2007.list flat_R_Asahi_2007.fits combine=average reject=sigcl
imcombine @flat_V_Asahi_2007.list flat_V_Asahi_2007.fits combine=average reject=sigcl
vocl> task $flat_comb = flat_comb.cl
vocl> flat_comb
```

We normalize combined flatfields.
合成されたフラットフィールドを規格化する。

```
vocl> !ls flat_[BVRI]*.fits | perl -ne 'chop; \
>>> printf("imcopy %s norm%s\nnormalize norm%s sample=[*,*]\n", $_, $_, $_);' \
>>> > norm_flat.cl
vocl> cat norm_flat.cl
imcopy flat_B_Asahi_2007.fits normflat_B_Asahi_2007.fits
normalize normflat_B_Asahi_2007.fits sample=[*,*]
imcopy flat_I_Asahi_2007.fits normflat_I_Asahi_2007.fits
normalize normflat_I_Asahi_2007.fits sample=[*,*]
imcopy flat_R_Asahi_2007.fits normflat_R_Asahi_2007.fits
normalize normflat_R_Asahi_2007.fits sample=[*,*]
imcopy flat_V_Asahi_2007.fits normflat_V_Asahi_2007.fits
normalize normflat_V_Asahi_2007.fits sample=[*,*]
vocl> task $norm_flat = norm_flat.cl
vocl> norm_flat
```

Now, we have normalized flatfields for BVRI bands. The flatfield images for BVRI bands are shown in Fig. 24.

これで、B, V, R, I バンドのそれぞれについて、規格化されたフラットフィー ルドが得られた。作成された B, V, R, I バンドのそれぞれのフラットフィー ルドを Fig. 24 に示す。

```
vocl> imstat normflat_*
#                IMAGE      NPIX      MEAN    STDDEV       MIN       MAX
 normflat_B_Asahi_2007.fits   4194304        1.    0.02522    0.2327     1.121
 normflat_I_Asahi_2007.fits   4194304        1.    0.03218    0.6387     1.175
 normflat_R_Asahi_2007.fits   4194304        1.    0.02854    0.6125     1.093
 normflat_V_Asahi_2007.fits   4194304        1.    0.02486    0.4029     1.085
```

The normalized flatfields are ready, and we now process the object frames.
規格化されたフラットフィールドが準備できたので、オブジェクトフレーム の処理を行う。

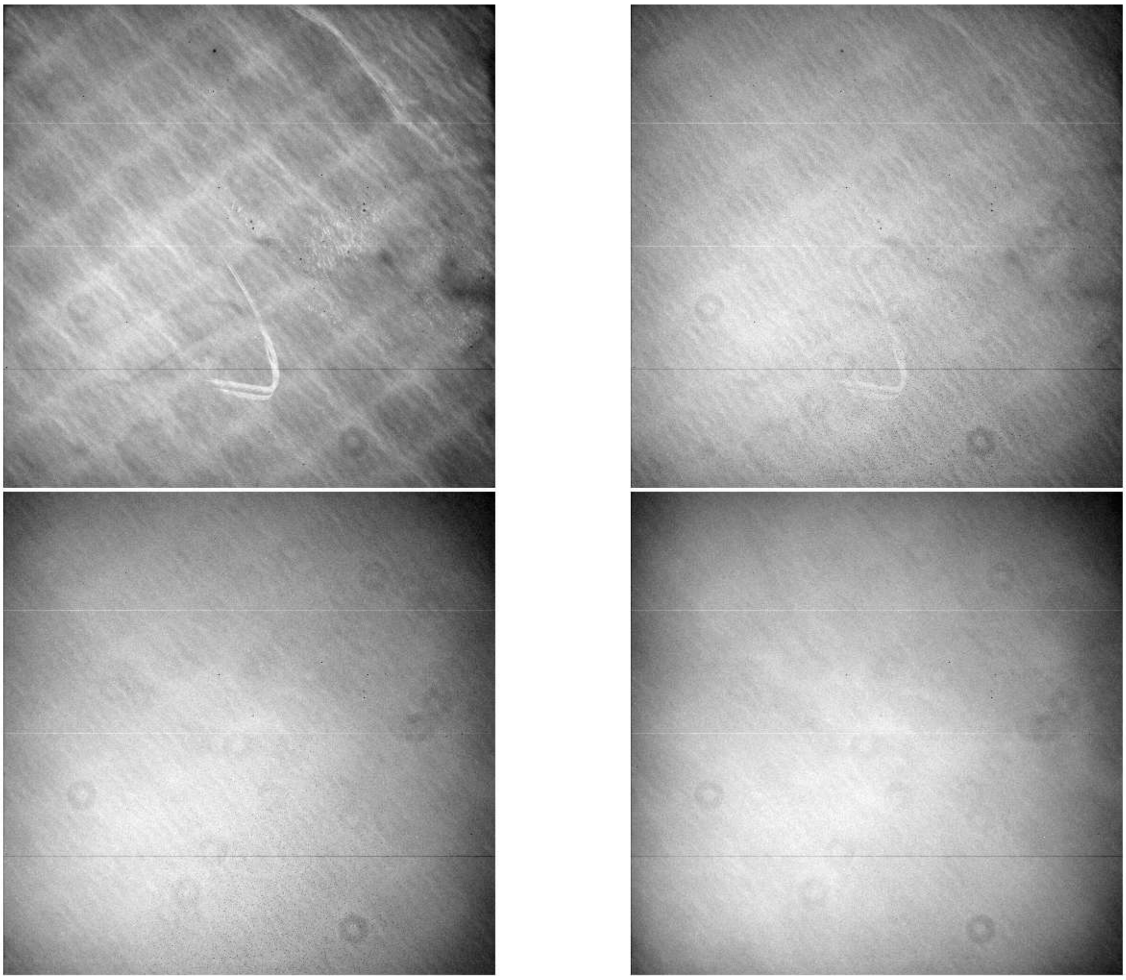

Figure 24: The normalized flatfields images of BVRI bands. The top-left, top-right, bottom-left, and bottom-right images are B, V, R, and I flatfield images, respectively. The ring shaped patterns are recognized at same positions for all the BVRI images. These are probably due to dust particles on the glass window of the CCD cameras.

```
vocl> !grep LIGHT datatype.list | perl -ne 'chop; (@data)=split; $o=$data[0]; \
>>> $d=$o; $d=~s/_o.fits/_od.fits/; $f=$d; $f=~s/_od.fits/_odf.fits/; \
>>> printf("imarith %s - dark%05d.fits %s\nimarith %s / normflat_%s.fits %s\n", \
>>> $o, $data[3], $d, $d, $data[4], $f);' > red.cl
vocl> !head -6 red.cl
imarith catalina_001B_o.fits - dark00060.fits catalina_001B_od.fits
imarith catalina_001B_od.fits / normflat_B_Asahi_2007.fits catalina_001B_odf.fits
imarith catalina_002B_o.fits - dark00060.fits catalina_002B_od.fits
imarith catalina_002B_od.fits / normflat_B_Asahi_2007.fits catalina_002B_odf.fits
imarith catalina_003B_o.fits - dark00060.fits catalina_003B_od.fits
imarith catalina_003B_od.fits / normflat_B_Asahi_2007.fits catalina_003B_odf.fits
vocl> task $red = red.cl
vocl> red
```

The data reduction of CCD images obtained on 10 December 2015 is now finished.

これで、 2015 年 12 月 10 日に得られたデータの整約が完了した。

Fig. 25 shows the comparison of raw data, bias subtracted data, dark subtracted data, and flatfielded data of B-band image of the comet C/2013 US10 (Catalina) taken at 21:09:35 (UT) on 10 December 2015.

2015 年 12 月 10 日の世界時 21:09:35 に得られたカタリーナ彗星 (C/2013 US10) の B バンド画像の生データ、バイアスを引いた画像、ダークを引いた 画像、フラットフィールドで割った画像を例として Fig. 25 に 示す。

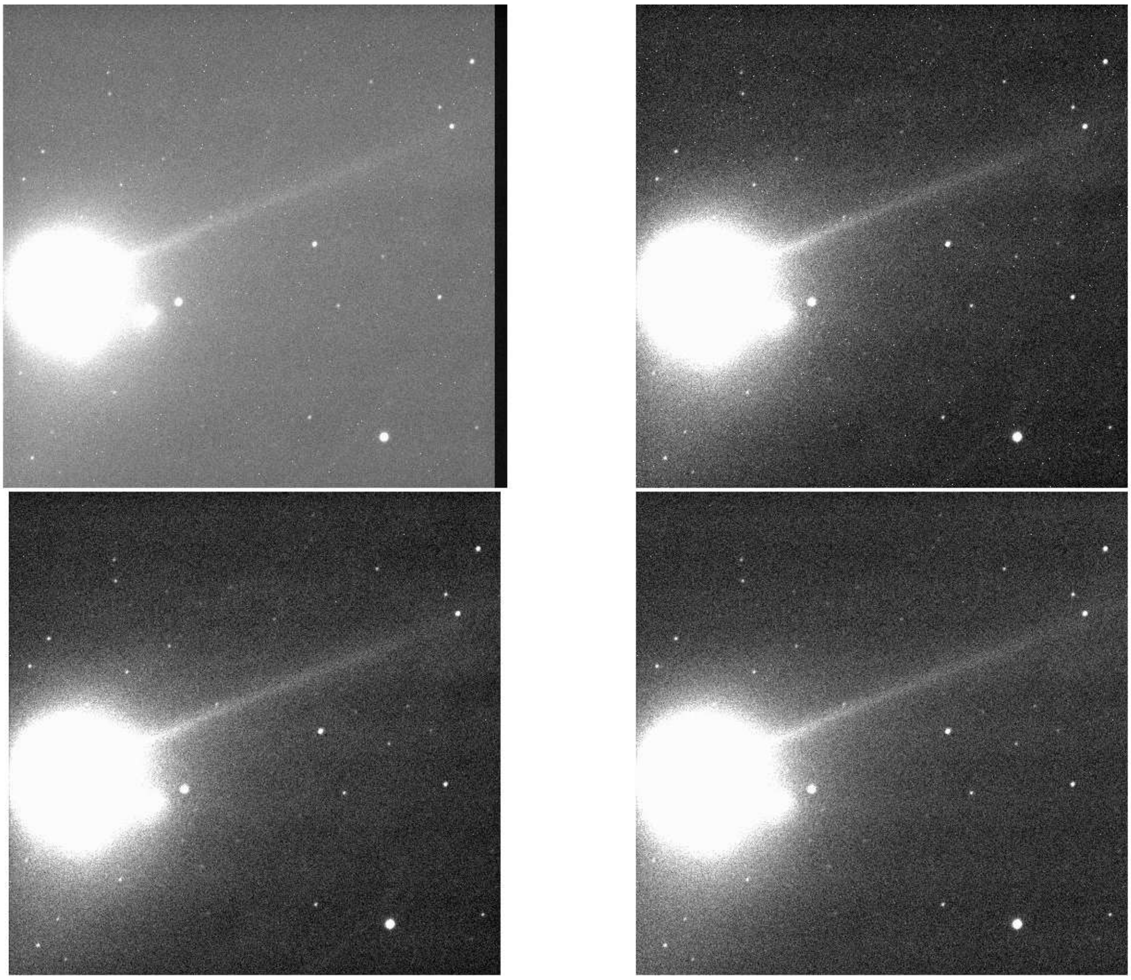

Figure 25: A comparison of raw data, bias subtracted data, dark subtracted data, and flatfielded data of B-band image of the comet C/2013 US10 (Catalina) taken at 21:09:35 (UT) on 10 December. The top-left panel is the raw data. The top-right, bottom-left, and bottom-right images are bias sutracted, dark subtracted, and flatfielded images, respectively.

3 Further Data Analyses

In this section, number of frequently used astronomical data analysis techniques are introduced.
ここでは、よく用いられるデータ解析手法を紹介する。

3.1 Astrometry

Knowing coordinates (e.g. RA and Dec) of the object of interest is essential in astronomy. For the measurements of astrometric positions, one needs to add WCS (World Coordinate System) related keywords into the header part of the FITS file.
興味のある天体の位置 (例えば、赤経赤緯) を知ることは、天文観測では非常 に基本的で重要なことである。位置測定のためには、 WCS (World Coordinate System) 関連のキーワードをFITS ファイルのヘッダーに書き込む必要がある。

3.1.1 Preparation of the astrometric catalogue

The USNO-B1.0 catalog is the most recent version of astrometric catalog released by USNO (US Naval Observatory). It contains positions of more than 1 billion stars. The total size of the catalog is more than 80 GB. The catalog is not distributed online, and you may need to get a copy of USNO-B1.0 catalog from someone who has it.
USNO-B1.0 カタログは、アメリカ海軍天文台が作成した最新の位置星表であ る。このカタログには 10 億個以上の星の位置が登録されていて、そのサイ ズは全体で 80 GB 以上になる。カタログデータはオンラインでは公開されて いないので、誰かすでに持っている人からコピーさせてもらうしかない。
Once you get a full set of the copy of USNO-B1.0, then you place those files on your computer. Then, set the environmental variable `UB1_PATH` properly. For example, if the catalog is located at `/data/usnob1` and `tcsh` is used, then type following command. The value of the environmental variable `UB1_PATH` should point to the directory where we find directories `000`, `001`, `002`, etc.
USNO-B1.0 カタログのデータが手に入ったら、それをコンピュータのディス ク上のどこかに配置する。そして、環境変数 `UB1_PATH` を適切に設定 する必要がある。 USNO-B1.0 カタログが `/data/usnob1` にあり `tcsh` を使っている場合、以下のコマンドで環境変数の設定ができる。環境 変数 `UB1_PATH` で指定するディレクトリは、 `000`, `001`, `002` などのディレクトリがある場所である。

```
% setenv UB1_PATH /data/usnob1
```

For those who does not need a full set of the catalog, following website is useful to download a part of the catalog.
カタログ全体が必要ない場合、必要な小さな領域のデータのみ切り出してダ ウンロードできるので以下のウェブページが有用かもしれない。

- `http://www.nofs.navy.mil/data/fchpix/`

3.1.2 Trying WCSTools

To check whether USNO-B1.0 catalog is properly prepared, we use the command `scat` of WCSTools. Try following command.
USNO-B1.0 カタログが適切に準備されたかどうか確認するために、 WCSTools に含まれる `scat` というコマンドを使ってみる。以下を試してみよ。

```
% scat -c ub1 3:32:55.8 -9:27:30 J2000
```

If you see following output, then USNO-B1.0 catalog is properly configured.
以下の出力が見られたら、 UBNO-B1.0 カタログはおそらく適切に設定されて いる。

```
0805.0034857 03:32:55.844 -09:27:29.75    4.73    3.22    4.19    3.16    2.74 10  0 12
```

3.1.3 Adding WCS related keywords into a FITS file

Suppose we have a reduced object frame `ast_003R_odf.fits`, and add WCS related FITS keywords into this file.
ここでは、整約済みの `ast_003R_odf.fits` というファイルがあると し、このファイルに WCS 関連の FITS キーワードを追加することを考える。

The task ccsetwcs that we use later will modify original FITS file. It may be a good idea to copy the file before we start the astrometric calibration and position measurements.
後で用いる ccsetwcs というタスクは、元々の FITS ファイルに変更 を加えてしまう。位置較正や位置測定などの作業を始める前に、元々のファ イルをコピーしておくとよいかもしれない。

```
vocl> imcopy ast_003R_odf.fits ast_003R_odfw.fits
ast_003R_odf.fits -> ast_003R_odfw.fits
vocl> ls -l ast_003R_odf*
-rw-r--r-- 1 daisuke root 16784640 Dec 23 22:00 ast_003R_odf.fits
-rw-r--r-- 1 daisuke root 16784640 Dec 23 22:01 ast_003R_odfw.fits
```

First, we check the RA and Dec of the center of the image. Rough values of RA and Dec are recorded in the raw data.
まず最初に、画像の視野中心の赤経赤緯を確認する。おおよその赤経赤緯の 値が生データのなかに記録されている。

```
vocl> hselect ast_003R_odfw.fits $I,objctra,objctdec yes
ast_003R_odfw.fits      "07 07 44"      "+13 48 01"
```

The rough values of RA and Dec of the image center are 07:07:44 and +13:48:01, respectively.
おおよその視野中心の赤経赤緯は 07:07:44 および +13:48:01 であることが 分かった。
Second, we obtain positions of stars around this point. For this purpose, scat command of WCSTools is useful. Following command searches the brightest 500 stars within the radius of 600 arcsec ranging between 10 mag and 20 mag centered at RA = 07:07:44 and Dec = +13:48:01.
次に、この付近の星の位置を取得する。そのためには、 WCSTools に含まれ る scat コマンドを用いるのが便利である。以下のコマンドは、赤経 07:07:44 、赤緯 +13:48:01 を中心とした半径 600 秒角内にある 10 等から 20 等の範囲内の星のうち明るい 500 個を探してくれる。

```
vocl> !scat -c ub1 -r 600 -mx 10,20 -n 500 07:07:44 +13:48:01 > ub1.cat
```

We need to extract RA and Dec of stars for later use.
あとで使いやすいように赤経赤緯のみを取り出しておく。

```
vocl> fields ub1.cat 2,3 > ub1.list
```

Pick one star near the center of the image. Check DSS (Digitized Sky Survey) image and record RA and Dec of the star. For example, a star near the center of the image ast_003R_odfw.fits has RA = 07:07:47.8 and Dec = 13:47:57, and it is located at x = 917 and y = 1081 on the image. Type following command to match stars on the catalog and stars on the image. The pixel scales of the image have to be provided using xmag and ymag options. The Lulin One-meter Telescope has the focal length of 8-m and the pixel size of the CCD camera Apogee U42 is 13.5 μm. Therefore, the rough value of the pixel scale is 0.348 arcsec/pix. If the east is left hand side on the image, then we give a rough value of the pixel scale for xmag option. If the north is up on the image, then we give a positive value for ymag option.
画像の視野中心付近の星を一つ選び、 DSS (Digitized Sky Survey) の画像 を参照しその星の赤経赤緯を記録しておく。例えば、 ast_003R_odfw.fits の中心付近の x = 917, y = 1081 にある星の赤経赤 緯は RA = 07:07:47.8, Dec = 13:47:57 である。次のコマンドでカタログ上 の星と画像上の星のマッチングを行う。 xmag と ymag という オプションを使っておおよそのピクセルスケールを与える必要がある。鹿林 の 1-m 望遠鏡の焦点距離は 8-m であり、 Apogee 社製の U42 CCD カメラの ピクセルサイズは 13.5 μm なので、おおよそのピクセルスケールは 0.348 arcsec/pix となる。画像上で東が左側になっている場合、 xmag オプションに与えるピクセルスケールの値は負にしなければならない ことに注意する必要がある。画像上で北が上側である場合、 ymag オ プションには正の値を使う。

```
vocl> ccfind ub1.list ast_003R_odfw.match ast_003R_odfw.fits xref=917 yref=1081 \
>>> lngref=07:07:47.8 latref=13:47:57 xmag=-0.348 ymag=-0.348 tolerance=2
```

Examine the result of the matching by typing following command.
マッチングの結果の良し悪しを以下のコマンドで確認する。

```
vocl> display ast_003R_odfw.fits 1
z1=39.78941 z2=146.5096
vocl> fields ast_003R_odfw.match 3,4 | tvmark 1 STDIN col=204 mark=circle radii=20
```

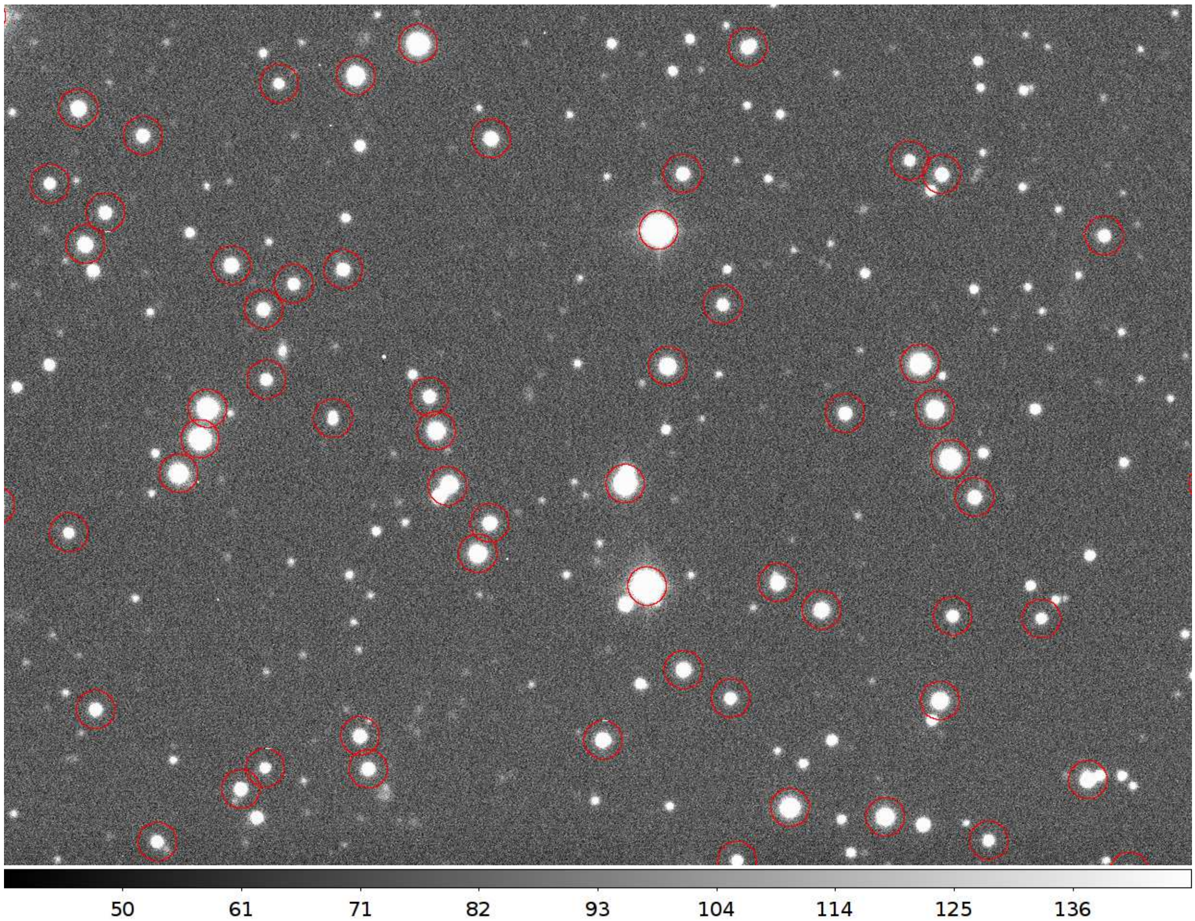

Figure 26: A example of the result of star matching using the task `ccfind`. The matching seems to be successful.

Fig. 26 shows an example of the result of the matching.
Fig. 26 にマッチングの結果の例を示す。

Then, we use the task `ccmap` to calculate the plate constants. A Tektronix window (Fig. 27) appears after invoking the task `ccmap`. Type “x”, “y”, “r”, and “s” keys to see the goodness of the fitting (Fig. 28). Type the key “d” near the data points of large residuals. Type the key “f” to check the result of refined fitting. Type “q” to finish.

次に、 `ccmap` を使い乾板定数を計算する。 `ccmap` を実行する と、テクトロニクスウィンドウ (Fig. 27) が現れる。 “x”, “y”, “r”, “s” キーを押してフィッティングの良し悪しを確認する (Fig. 28) 。残差の大きなデータ点がある場合には、その点の付 近で “d” キーを押し、そのデータ点を除外する。“f” キーを押し、改良 されたフィッティングの結果を確認する。納得がいったら、 “q” キーを押 して終了する。

```
vocl> ccmap ast_003R_odfw.match ast_003R_odfw.db image=ast_003R_odfw.fits \
xcol=3 ycol=4 lngcol=1 latcol=2
Refsystem: j2000  Coordinates: equatorial FK5
    Equinox: J2000.000 Epoch: J2000.00000000 MJD: 51544.50000
Insystem: j2000  Coordinates: equatorial FK5
    Equinox: J2000.000 Epoch: J2000.00000000 MJD: 51544.50000

Coords File: ast_003R_odfw.match  Image: ast_003R_odfw.fits
    Database: ast_003R_odfw.db  Solution: ast_003R_odfw.fits
Coordinate mapping status
    Ra/Dec or Long/Lat fit rms: 0.175  0.162   (arcsec  arcsec)
Coordinate mapping parameters
    Sky projection geometry: tan
    Reference point: 7:07:46.631  13:48:44.12  (hours  degrees)
    Reference point: 969.626  946.065  (pixels  pixels)
    X and Y scale: 0.346  0.347  (arcsec/pixel  arcsec/pixel)
    X and Y axis rotation: 180.728  180.731  (degrees  degrees)
Wcs mapping status
    Ra/Dec or Long/Lat wcs rms: 0.175  0.162   (arcsec  arcsec)
```

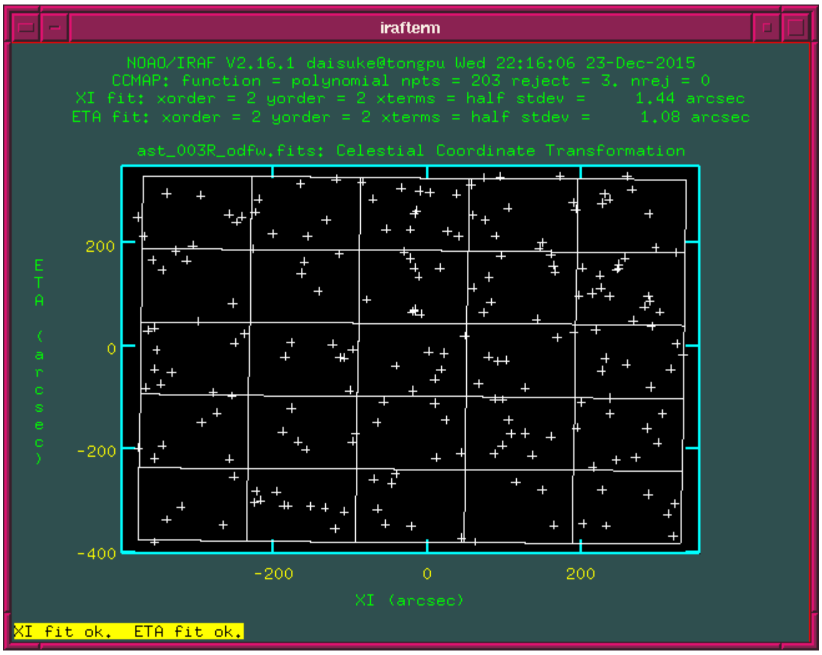

Figure 27: A Tektronix window shown after invoking the task `ccmap`.

Plate constants are successfully obtained, and now we write those plate constants into the FITS file `ast_003R_odfw.fits`. The task `ccsetwcs` is used for this.

乾板定数が求まったので、それらを FITS ファイル `ast_003R_odfw.fits` に書き込む。 `ccsetwcs` というタスクを使え ばよい。

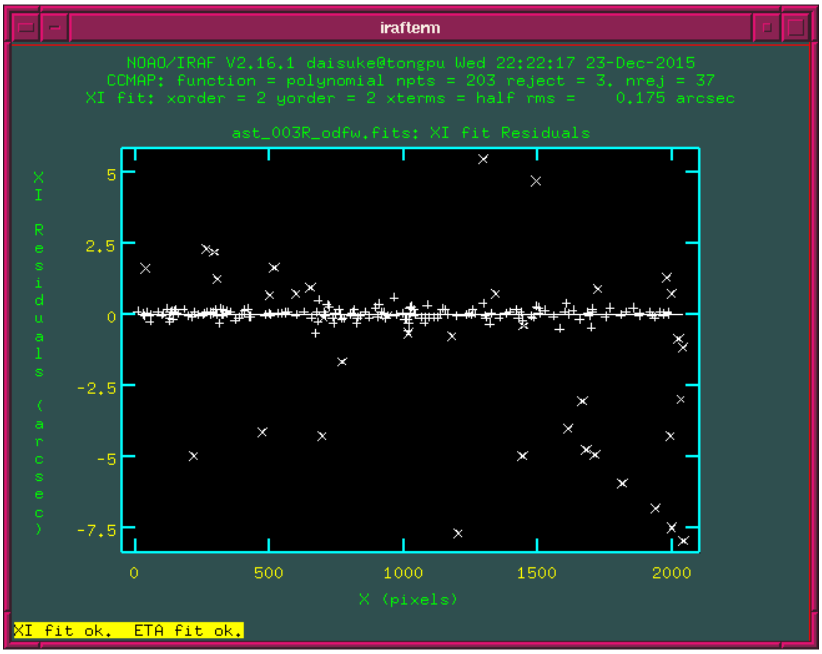

Figure 28: Residuals of fitting by the task ccmap.

```
vocl> ccsetwcs ast_003R_odfw.fits ast_003R_odfw.db ast_003R_odfw.fits
Image: ast_003R_odfw.fits  Database: ast_003R_odfw.db  Solution: ast_003R_odfw.fits
Coordinate mapping parameters
    Sky projection geometry: tan
    Reference point: 7:07:46.631  13:48:44.12  (hours   degrees)
    Ra/Dec logical image axes: 1  2
    Reference point: 969.626  946.065  (pixels  pixels)
    X and Y scale: 0.346  0.347  (arcsec/pixel  arcsec/pixel)
    X and Y coordinate rotation: 180.728  180.731  (degrees  degrees)
Updating image header wcs
```

Following information is added to the header of the FITS file.
以下の情報が FITS ファイルのヘッダー部分に追加された。

```
WCSDIM  =                    2
LTM1_1  =                   1.
LTM2_2  =                   1.
WAT0_001= 'system=image'
WAT1_001= 'wtype=tan axtype=ra'
WAT2_001= 'wtype=tan axtype=dec'
EQUINOX =                2000.
CTYPE1  = 'RA---TAN'
CTYPE2  = 'DEC--TAN'
CRVAL1  =     106.944294740994
CRVAL2  =     13.8122560688788
CRPIX1  =     969.625714557085
CRPIX2  =     946.065375125484
CD1_1   =  -9.6233984315548E-5
CD1_2   =  -1.2285060149875E-6
CD2_1   =  1.22288081638130E-6
CD2_2   =  -9.6275133062677E-5
```

3.1.4 Astrometric measurements

Here, the procedure to measure (RA, Dec) from the image coordinate (x, y) is described.
ここでは、画像上の座標 (x, y) から、赤経赤緯 (RA, Dec) を求める方法を 述べる。

First, we measure the position (x, y) of the object of the interest on the image using the task `center`. The results of the measurements are stored in the file `ast_003R_odfw.ctr.1`.

まず、位置を測定したい天体の画像上の座標 (x, y) を `center` を使っ て求める。測定結果は `ast_003R_odf.ctr.1` というファイルの なかに記録される。

```
vocl> display ast_003R_odfw.fits 1
z1=39.78941 z2=146.5096
vocl> center ast_003R_odfw
Warning: Graphics overlay not available for display device.
ast_003R_odfw   704.00 1030.00   704.52 1030.26    0.00    0.00  ok
ast_003R_odfw  1935.00 1934.00  1934.95 1933.16    0.00    0.00  ok
ast_003R_odfw   257.00  482.00   257.64  482.74    0.00    0.00  ok
```

Second, we extract (x, y) coordinate from the file `ast_003R_odf.ctr.1`.

次に X 座標と Y 座標を `ast_003R_odf.ctr.1` から取り出す。

```
vocl> txdump ast_003R_odfw.ctr.1 XCENTER,YCENTER yes > ast_003R_odfw.coo
vocl> cat ast_003R_odfw.coo
704.520  1030.262
1934.949  1933.163
257.644  482.737
```

Finally, the task `skyctran` is used to convert (x, y) into (RA, Dec).

最後に、 `skyctran` を使って (x, y) を (RA, Dec) に変換する。

```
vocl> skyctran ast_003R_odfw.coo ast_003R_odfw.radec ast_003R_odfw.fits j2000.0

Insystem: ast_003R_odfw.fits logical  Projection: TAN  Ra/Dec axes: 1/2
    Coordinates: equatorial FK5 Equinox: J2000.000
    Epoch: J2015.94578295 MJD: 57368.69722
Outsystem: j2000.0  Coordinates: equatorial FK5
    Equinox: J2000.000 Epoch: J2000.00000000 MJD: 51544.50000

Input file: ast_003R_odfw.coo  Output file: ast_003R_odfw.radec
```

Obtained (RA, Dec) is in the file `ast_003R_odfw.radec`.

得られた (RA, Dec) は `ast_003R_odf.radec` というファイルのなか に書き込まれている。

```
vocl> cat ast_003R_odfw.radec

# Insystem: ast_003R_odfw.fits logical  Projection: TAN  Ra/Dec axes: 1/2
#     Coordinates: equatorial FK5 Equinox: J2000.000
#     Epoch: J2015.94578295 MJD: 57368.69722
# Outsystem: j2000.0  Coordinates: equatorial FK5
#     Equinox: J2000.000 Epoch: J2000.00000000 MJD: 51544.50000

# Input file: ast_003R_odfw.coo  Output file: ast_003R_odfw.radec

704.520  1030.262   7:07:52.910  13:48:13.77
1934.949  1933.163   7:07:23.381  13:43:06.19
257.644  482.737   7:08:03.708  13:51:21.54
```

We compare the results obtained from the image with the positions of the stars in the USNO-B1.0 catalog. The difference is about 0.1 arcsec for both RA and Dec.

得られた測定結果を、 USNO-B1.0 カタログのなかの値とを比べてみる。測定 値とカタログのなかの値との差は、赤経赤緯ともに 0.1 秒角程度であること が分かる。

```
vocl> !scat -c ub1 07:07:52.910 13:48:13.77
1038.0128664 07:07:52.915 +13:48:13.75   14.34  12.76  13.98  12.89  12.60  9  5  8
vocl> !scat -c ub1 07:07:23.381 13:43:06.19
1037.0129564 07:07:23.371 +13:43:06.28   14.60  13.09  14.10  12.75  11.46  0  5  3
vocl> !scat -c ub1 07:08:03.708 13:51:21.54
1038.0128773 07:08:03.711 +13:51:21.08   14.60  13.91  14.53  13.78  13.62  0  5  4
1038.0128772 07:08:03.671 +13:51:15.51   20.41  99.99  13.54  17.98  99.99  7  3  2
```

3.1.5 Adding WCS related keywords to a FITS file using WCStools

It is more convenient to add WCS related keywords into a FITS file using WCSTools.
WCSTools を使うとより簡便に WCS 関連キーワードを FITS ファイルに追加 することができる。
As usual, we copy the file before starting the analysis.
作業を始める前に、取り扱うファイルをコピーしておく。

```
vocl> imcopy ast_003R_odf.fits ast_003R_odfw2.fits
ast_003R_odf.fits -> ast_003R_odfw2.fits
```

First, we add some keywords into the header part of the FITS file for the later use of `imwcs` command of WCSTools. We add three keywords (`RA`, `DEC`, and `SECPIX`).
まず最初に、あとで WCSTools の `imwcs` コマンドを使うために、いく つかのキーワードを FITS ファイルのヘッダー部分に追加しておく必要があ る。三つのキーワード `RA`, `DEC`, `SECPIX` を追加する。

```
vocl> hselect ast_003R_odfw2.fits objctra,objctdec yes
"07 07 44"      "+13 48 01"
vocl> !sethead ast_003R_odfw2.fits ra=07:07:44 dec=13:48:01 secpix=0.348
vocl> hselect ast_003R_odfw2.fits ra,dec,secpix yes
07:07:44        13:48:01        0.348
```

Second, use the task `imexamine` to measure the standard deviation of sky background level. Type following command and move the cursor into the blank sky region on the image. Then, type “m” key. The statistical information is shown. You may check the standard deviation of several points on the image.
次に、 `imexamine` タスクを使って背景の空の明るさの標準偏差を求め ておく。以下のコマンドを実行し、マウスのカーソルを星のない領域に持っ ていき、 “m” キーを押す。すると、統計情報が表示される。画像上のいく つかの点について調べておくとよい。

```
vocl> display ast_003R_odfw2.fits 1
vocl> imexamine ast_003R_odfw2.fits 1
#            SECTION     NPIX     MEAN   MEDIAN   STDDEV      MIN      MAX
 [549:553,1310:1314]       25    79.75    79.94    9.636    66.12     100.
[1579:1583,1091:1095]       25    72.04    73.42    10.02    53.65    89.53
 [1433:1437,686:690]       25    77.45    76.16    9.657    54.21    94.54
   [687:691,784:788]       25    75.72    75.44    11.39    56.15    99.29
 [972:976,1027:1031]       25    79.33    81.44    10.84     63.7    96.15
```

The standard deviation of the sky background is found to be about 10 ADUs.
背景の空の明るさの標準偏差はおよそ 10 ADUs 程度であることが分かった。
We also examine the stellar PSF (Point Spread Function) using the task `imexamine`. Choose a few stars. Move the cursor to the center of the star, and type “r” key or “a” key. By typing “r” key, we will see the viewgraph of radial profile of the star on Tektronix window, and the FWHM (Full Width at Half Maximum) of the stellar PSF can be found at the bottom of the window. (Fig. 29) By typing “a” key, results of the aperture photometry is shown on the terminal, and the FWHM of stellar PSF is included in the results.
同じく `imexamine` を使って、恒星の PSF (Point Spread Function)も 調べておく。いくつかの星を選び、マウスのカーソルをその星の中心にもっ ていき、 “r” または “a” キーを押す。 “r” キーを押すと、その星の ラディアルプロファイルの図が表示される。星の PSF の半値幅はウィンドウ の一番下に表示される。(Fig. 29) “a” キーを押すと、アパー チャ測光の結果がターミナル上に表示され、星の PSF の半値幅も結果に含ま れている。

```
vocl> display ast_003R_odfw2.fits 1
vocl> imexamine ast_003R_odfw2.fits 1
#   COL    LINE    COORDINATES
#     R     MAG     FLUX      SKY    PEAK     E   PA BETA ENCLOSED   MOFFAT DIRECT
 658.78 1358.97 658.78 1358.97
  17.03  10.56 595617.    81.77  13000. 0.03  -36 4.63     5.77     5.72   5.68
 484.53  893.88  484.53 893.88
  17.69  10.83 464206.    81.42   9628. 0.02  -75 7.53     5.93     5.94   5.90
1154.52 1379.20 1154.52 1379.20
  16.20  11.31 300258.    80.73   6935. 0.04  -47 5.19     5.51     5.57   5.40
1296.74 1015.87 1296.74 1015.87
  16.90  10.81 476081.    84.25  10556. 0.04  -46 5.87     5.72     5.72   5.63
1258.58 1201.81 1258.58 1201.81
  16.43  12.30 120284.    78.05   2732. 0.04  -50 5.21     5.58     5.61   5.48
```

The FWHM of stellar PSF is found to be about 5.6 pixels.
星の PSF の半値幅はおよそ 5.6 ピクセルであることがわかった。

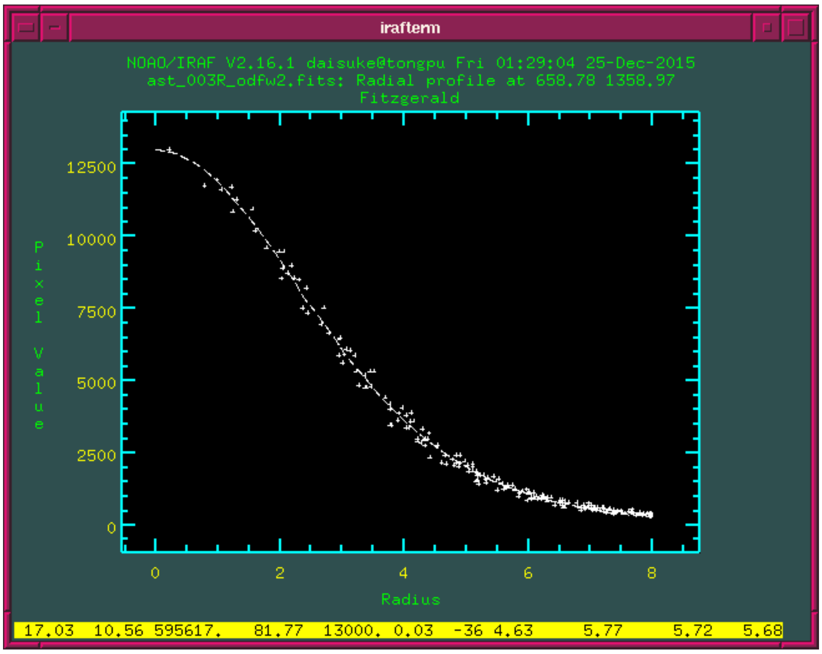

Figure 29: Result of the radial profile fitting by the task `imexamine`.

Third, we invoke the task `daofind` to extract sources on the image. We do not want to deal with fainter stars, and set the detection threshold of S/N = 15 by specifying `datapars.sigma` option. The file `ast_003R_odfw2.coo.1` is created by following command.
さらに、 `daofind` というタスクを用いて画像上の天体を検出する。暗 い星を無理に取り扱う必要はないので、 `datapars.sigma` オプション を使って検出限界を S/N = 15 と指定する。次のコマンドを実行すると `ast_003R_odfw2.coo.1` というファイルが作られる。

```
vocl> datapars.fwhmpsf = 5.6
vocl> datapars.sigma = 10
vocl> findpars.threshold = 15
vocl> centerpars.cbox = 15
vocl> daofind ast_003R_odfw2 verify=no
```

For the later use of WCStools, we extract necessary information from the file `ast_003R_odw2.coo.1`.
あとで WCStools を使うのに便利なように、 `ast_003R_odw2.coo.1` から必要な情報を抽出しておく。

```
vocl> txdump ast_003R_odfw2.coo.1 XCENTER,YCENTER,MAG yes > ast_003R_odfw2.cat
vocl> !head -5 ast_003R_odfw2.cat
1333.925  3.769  -0.229
771.246  5.339  -6.402
1748.411  4.656  -2.489
117.809  20.086  -0.225
1323.204  20.888  -5.493
```

We check the result of the source extraction by the task `daofind`. The result of the following command is shown in Fig. 30.
`daofind` による天体検出の結果を確認しておく。以下のコマンドによ り表示される図を Fig. 30 に示す。

```
vocl> display ast_003R_odfw2.fits 1
z1=39.78941 z2=146.5096
vocl> fields ast_003R_odfw2.cat 1,2 | tvmark 1 STDIN col=204 mark=circle radii=20
```

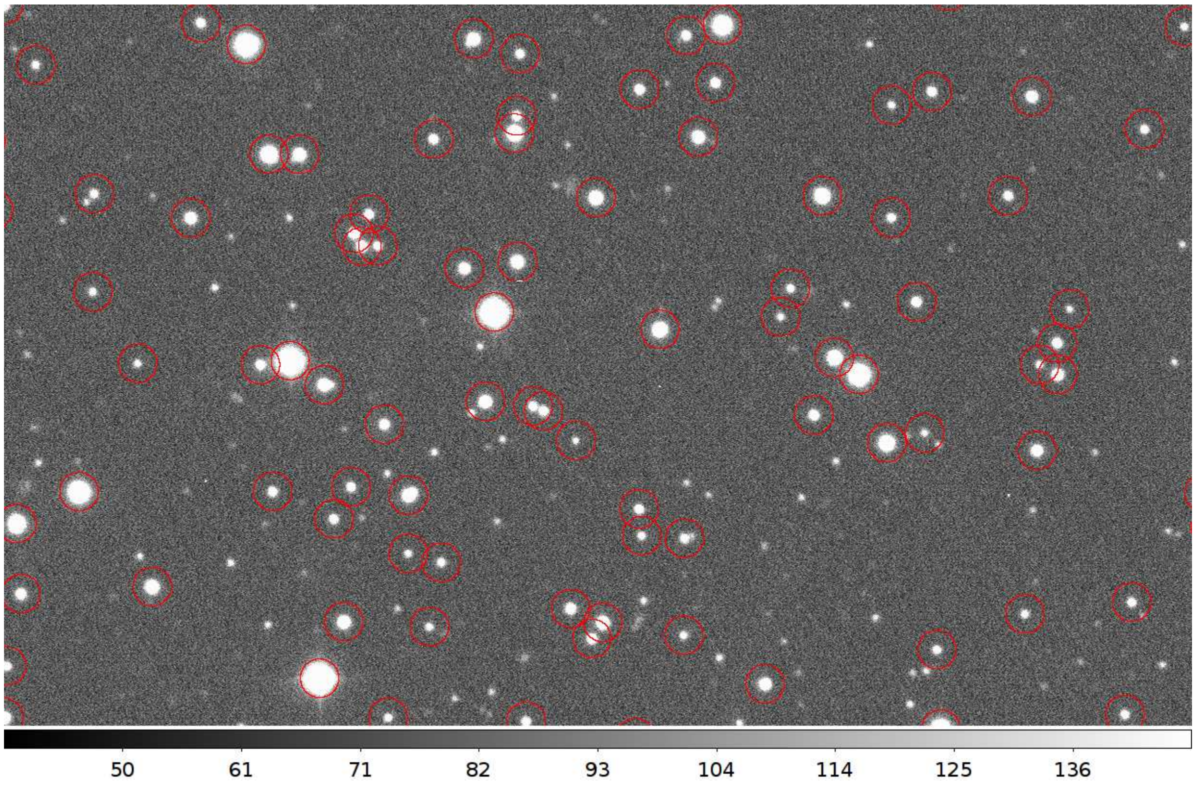

Figure 30: Result of the source extraction by the task `daofind`.

Now, the command `imwcs` is used to calculate the plate constants and write WCS related keywords into the header of the FITS file.
準備が整ったので、 `imwcs` コマンドを用いて乾板定数を求め、それを FITS ファイルのヘッダーに書き込む。

```
vocl> !imwcs -v -c ub1 -r 180 -l -n 8 -h 200 -t 3 -q irst -o \
>>> -d ast_003R_odfw2.cat ast_003R_odfw2.fits

.....

# Mean  dx= -0.0266/0.4239  dy= 0.0016/0.4494  dxy= 0.5097
# Mean dra= 0.0092/0.1470  ddec= 0.0004/0.1556 sep= 0.1766/0.2141
# nmatch= 151 nstars= 200 between ub1 and ast_003R_odfw2.cat  niter= 4
CTYPE1 = RA---TAN
CRVAL1 = 106.93873531
CRPIX1 = 1024.72310000
CTYPE2 = DEC--TAN
CRVAL2 = 13.80499561
CRPIX2 = 1024.91780000
CD1_1 = -9.6232068e-05
CD1_2 = 1.228476e-06
CD2_1 = 1.218934e-06
CD2_2 = 9.6272668e-05
ast_003R_odfw2.fits: rewritten successfully.
```

To calculate (RA, Dec) for corresponding (x, y), the command `xy2sky` is used.
画像上の座標 (x, y) に対応する赤経赤緯 (RA, Dec) を求めるには、 `xy2sky` を用いればよい。

```
vocl> display ast_003R_odfw2.fits 1
z1=47.80875 z2=145.8657
vocl> center ast_003R_odfw2
Warning: Graphics overlay not available for display device.
ast_003R_odfw2   704.00 1018.00   704.45 1018.89    0.00    0.00   ok
ast_003R_odfw2  1935.00  116.00  1935.04  115.79    0.00    0.00   ok
ast_003R_odfw2   257.00 1566.00   257.51 1566.43    0.01    0.01   ok

vocl> txdump ast_003R_odfw2.ctr.1 XCENTER,YCENTER yes
704.455  1018.890
1935.040  115.794
257.512  1566.434
vocl> !xy2sky ast_003R_odfw2.fits 704.455 1018.890 1935.040 115.794 257.512 1566.434
07:07:52.911 +13:48:14.48 J2000  704.455 1018.890
07:07:23.379 +13:43:06.83 J2000 1935.040  115.794
07:08:03.711 +13:51:22.25 J2000  257.512 1566.434
```

3.1.6 Reporting asteroid positions to MPC

The format of optical astrometric observations of minor planet for reporting to the Minor Planet Center of IAU is described at following web page.
可視光の観測による小惑星の位置測定の結果を小惑星中央局に報告する際の フォーマットは以下のウェブページで説明されている。

- http://www.minorplanetcenter.net/iau/info/OpticalObs.html

The observatory code of Lulin Observatory is “D35”.
鹿林天文台の観測所コードは “D35” である。
For other observatories, check following web page.
その他の天文台については、以下のウェブページを参照のこと。

- http://www.minorplanetcenter.net/iau/lists/ObsCodesF.html

3.2 Co-adding multiple frames to get higher S/N

Here, we process following 10 FITS files. These files are reduced images of an asteroid.
ここでは、以下の 10 枚の FITS ファイルを取り扱う。これらのファイルは、 小惑星を撮像したもので、整約済みのデータである。

```
vocl> ls ast_*.fits
ast_003R_odf.fits  ast_006R_odf.fits  ast_009R_odf.fits  ast_012R_odf.fits
ast_004R_odf.fits  ast_007R_odf.fits  ast_010R_odf.fits
ast_005R_odf.fits  ast_008R_odf.fits  ast_011R_odf.fits
```

3.2.1 Sky subtraction

We subtract the sky background level to adjust the background to be zero ADUs for later analyses. Here, we assume the sky background level is spatially uniform within the entire field-of-view of the image. We calculate the median value for all the pixel and subtract the median value from the reduced image.
あとの解析のためにまず背景のスカイレベルを引き去り、背景レベルをゼロ に合わせる。ここでは、簡単のため、視野内でスカイレベルは空間的に一様 であると仮定する。すべてのピクセル値の中央値を求め、整約済みの画像か ら中央値を引く。

```
vocl> ls ast_*.fits > ast_reduced.list
vocl> imstat @ast_reduced.list fields="image,midpt"
#               IMAGE     MIDPT
    ast_003R_odf.fits     367.2
    ast_004R_odf.fits     358.3
    ast_005R_odf.fits     346.3
    ast_006R_odf.fits     339.3
    ast_007R_odf.fits     350.6
    ast_008R_odf.fits     328.1
    ast_009R_odf.fits     342.6
    ast_010R_odf.fits     335.6
    ast_011R_odf.fits     325.9
    ast_012R_odf.fits     320.7
vocl> imstat @ast_reduced.list fields="image,midpt"  > ast_sky.list
vocl> !grep -v # ast_sky.list | perl -ne 'chop; ($file,$median)=split; $ss=$file; \
>>> $ss=~s/_odf/_odfs/; print "imarith $file - $median $ss\n";' > skysub.cl
vocl> task $skysub = skysub.cl
vocl> skysub
```

Now, sky subtracted images are obtained.
スカイレベルを引き去った画像が得られた。

```
vocl> ls ast_*_odfs.fits
ast_003R_odfs.fits  ast_006R_odfs.fits  ast_009R_odfs.fits  ast_012R_odfs.fits
ast_004R_odfs.fits  ast_007R_odfs.fits  ast_010R_odfs.fits
ast_005R_odfs.fits  ast_008R_odfs.fits  ast_011R_odfs.fits
vocl> imstat ast_*_odfs.fits fields="image,midpt"
#               IMAGE     MIDPT
   ast_003R_odfs.fits  0.009095
   ast_004R_odfs.fits  -0.01254
   ast_005R_odfs.fits  -0.04242
   ast_006R_odfs.fits  -0.02295
   ast_007R_odfs.fits  -0.01681
   ast_008R_odfs.fits  -0.04371
   ast_009R_odfs.fits  1.523E-4
   ast_010R_odfs.fits   0.04284
   ast_011R_odfs.fits  -0.02844
   ast_012R_odfs.fits   0.00194
```

3.2.2 PSF measurements

We use the task psfmeasure to measure the PSF (Point Spread Function). The task psfmeasure is in the package obsutil. We need to load the package obsutil before using the task psfmeasure.

天体の PSF を測定するため psfmeasure というタスクを使う。このタ スクは obsutil というパッケージに含まれている。 psfmeasure を使う前に、 obsutil パッケージをロードしておく必要 がある。

```
vocl> obsutil
      bitcount    cgiparse    kpno.       psfmeasure  specfocus   sptime
      ccdtime     findgain    pairmass    shutcor     specpars@   starfocus

obsutil>
```

Type following command to measure the PSF of the target object. The image is shown on the SAOimage DS9. Move the cursor to the target object, and press "m" key. Then, press "q" key to proceed to next image. Do this for all the images. Finally, a Tektronix window appears (Fig. 31). Press "q" key to finish.

以下のコマンドを実行して、 PSF を測定する。画像が SAOimage DS9 上に表 示されるので、カーソルを目的天体の場所にもっていき、 "m" キーを押す。 次に "q" キーを押すと、次の画像に進む。すべての画像で天体の場所を指 定すると、最後にグラフが表示される (Fig. 31) 。 "q" キーを押すと終了する。

```
obsutil> ls ast_*_odfs.fits > ast_skysub.list
obsutil> psfmeasure @ast_skysub.list size=GFWHM radius=10 iterations=5 \
>>> > ast_fwhm.list
```

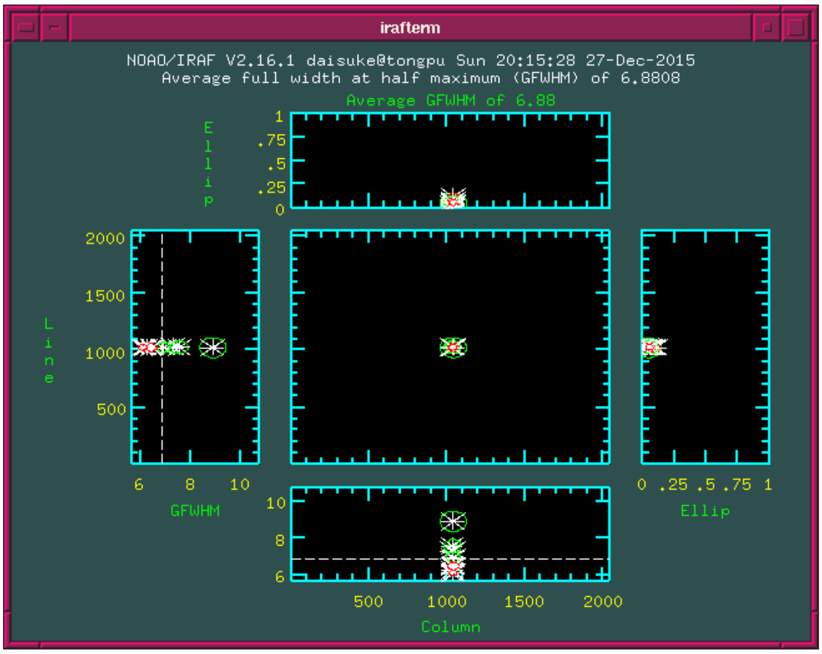

Figure 31: Results of PSF measurements by the task `psfmeasure`.

We examine the results of the PSF measurements. There is one image (`ast_008R_odfs.fits`) which has much poorer PSF than others. We decide not to use this image. For other 9 images, the poorest PSF has the Gaussian FWHM of 7.553 pixels.

PSF 測定の結果を見てみる。他よりもだいぶ PSF が悪いデータが一つある (`ast_008R_odfs.fits`) ので、そのデータは使わないことにする。そ の他の九枚の画像では、最も PSF がよくないのは半値幅 7.553 ピクセルの ものである。

```
obsutil> !tail -15 ast_fwhm.list
NOAO/IRAF V2.16.1 daisuke@tongpu Sun 20:15:35 27-Dec-2015

          Image  Column     Line     Mag   GFWHM   Ellip      PA SAT
ast_003R_odfs.f 1041.45 1024.01    0.23   6.453    0.01     -74
ast_004R_odfs.f 1040.49 1024.03    0.08   6.950    0.01      83
ast_005R_odfs.f 1039.68 1023.98    0.16   6.252    0.06     -18
ast_006R_odfs.f 1039.64 1023.73    0.12   6.463    0.11     -42
ast_007R_odfs.f 1039.90 1023.81    0.11   6.127    0.08     -82
ast_008R_odfs.f 1040.10 1024.56    0.09   8.896    0.05     -75
ast_009R_odfs.f 1039.57 1025.10    0.18   6.480    0.07      75
ast_010R_odfs.f 1038.42 1025.70    0.26   6.093    0.05       6
ast_011R_odfs.f 1037.73 1025.90    0.00   7.304    0.03     -47
ast_012R_odfs.f 1036.53 1026.66    0.21   7.553    0.05     -70

  Average full width at half maximum (GFWHM) of 6.8808
```

3.2.3 Convolution

For co-adding images, we need to smooth the images to have a uniform PSF. We apply Gaussian convolution to the images, so that all the images have the PSF equals to that of the poorest PSF image.

画像を足し合わせるためには、個々の画像の PSF をそろえておく必要がある。 畳み込みを行い、画像を平滑化し、それぞれの画像の PSF を最も悪い PSF に合わせる作業を行う。

The FWHM of a Gaussian distribution is

$$FWHM = 2\sqrt{2\ln 2}\sigma \sim 2.3548\sigma, \tag{1}$$

where σ is the standard deviation of the distribution.

Suppose σ_i is the standard deviation of the original distribution, σ_o is the standard deviation of the distribution after the convolution, and σ_k is the Gaussian convolution kernel. Then, we have the relationship

$$\sigma_o^2 = \sigma_i^2 + \sigma_k^2. \tag{2}$$

Therefore, σ_k is

$$\sigma_k = \sqrt{\sigma_o^2 - \sigma_i^2} = \frac{\sqrt{FWHM_o^2 - FWHM_i^2}}{2.3548}, \tag{3}$$

where $FWHM_i$ is the FWHM of the input image, and $FWHM_o$ is the FWHM of the image after the convolution.
ガウス分布の半値幅 $FWHM$ と標準偏差 σ との関係は以下の通りで ある。

$$FWHM = 2\sqrt{2\ln 2}\sigma \sim 2.3548\sigma, \tag{4}$$

ここで、 σ_i がもともとのガウス分布の標準偏差だとする。また、 σ_o は畳み込みを行ったあとの分布の標準偏差で、 σ_k は畳 み込みのカーネルとする。この三つの量には以下の関係がある。

$$\sigma_o^2 = \sigma_i^2 + \sigma_k^2. \tag{5}$$

したがって、半値幅が $FWHM_i$ の画像を、半値幅が $FWHM_o$ である画像 になるようにガウシアンフィルターで平滑化しようとすると、使うべきカー ネルは以下のようになる。

$$\sigma_k = \sqrt{\sigma_o^2 - \sigma_i^2} = \frac{\sqrt{FWHM_o^2 - FWHM_i^2}}{2.3548}, \tag{6}$$

Now, we apply the Gaussian convolution to the images. The task `gauss` is used for the Gaussian convolution.
ここで、画像の平滑化を行う。画像の平滑化には gauss というタスク を用いる。

```
obsutil> !grep ast_ ast_fwhm.list | grep -v 008R | perl -ne 'chop; (@data)=split; \
>>> $sigma_k = sqrt(7.553**2-$data[4]**2)/2.3548; \
>>> printf("%5.3f\n", $sigma_k);' > ast_sigma.list
obsutil> ls ast_*_odfs.fits | grep -v 008R > ast_beforeconv.list
obsutil> !sed s/_odfs/_odfsc/ ast_beforeconv.list > ast_afterconv.list
obsutil> !sed s/ast_/"gauss ast_"/ ast_beforeconv.list > ast_gauss.list
obsutil> !paste ast_gauss.list ast_afterconv.list ast_sigma.list \
>>> | grep -v 0.000  > gauss.cl
obsutil> task $conv = gauss.cl
obsutil> conv
obsutil> imcopy ast_012R_odfs.fits ast_012R_odfsc.fits
ast_012R_odfs.fits -> ast_012R_odfsc.fits
```

3.2.4 Image alignment

We align the images. Here, we apply the linear transformation only. First, we measure the centroid of the target object using the task `center`. Move the cursor to the target object, and press space key, "q" key, and "w" key.
画像の位置合わせを行う。ここでは、簡単のため、平行移動のみで十分な位 置合わせができると仮定する。まず、 center というタスクを使って、 天体の重心を計算する。カーソルを天体の場所に移動させ、スペースキーを 押す。さらに、 "q" キーを押し、最後に "w" キーを押す。

```
obsutil> !ls ast_*_odfsc.fits | perl -ne 'chop; s/.fits//; \
>>> print "display $_ 1\ncenter $_ cbox=15\n";' > ast_center.cl
obsutil> task $ast_center = ast_center.cl
obsutil> ast_center
obsutil> ls ast_*.ctr.1
ast_003R_odfsc.ctr.1  ast_006R_odfsc.ctr.1  ast_010R_odfsc.ctr.1
ast_004R_odfsc.ctr.1  ast_007R_odfsc.ctr.1  ast_011R_odfsc.ctr.1
ast_005R_odfsc.ctr.1  ast_009R_odfsc.ctr.1  ast_012R_odfsc.ctr.1
```

We then calculate the amount of shifts which should be applied to the images.
次に、それぞれの画像について、平行移動の移動量を計算する。

```
obsutil> txdump ast_*.ctr.1 XCENTER,YCENTER yes
1041.398  1024.036
1040.543  1024.047
1039.635  1024.012
1039.631  1023.675
1039.926  1023.831
1039.500  1025.105
1038.339  1025.718
1037.765  1025.863
1036.621  1026.521
obsutil> txdump ast_*.ctr.1 XCENTER,YCENTER yes > ast_center.list
obsutil> !cat ast_center.list | perl -ne 'chop; ($x,$y)=split; \
>>> printf("%8.3f %8.3f\n", 1041.398-$x, 1024.036-$y);' > ast_shift.list
obsutil> cat ast_shift.list
   0.000    0.000
   0.855   -0.011
   1.763    0.024
   1.767    0.361
   1.472    0.205
   1.898   -1.069
   3.059   -1.682
   3.633   -1.827
   4.777   -2.485
```

Now, we shift the images.
画像を平行移動させる。

```
obsutil> !sed s/ast_/"imshift ast_"/ ast_afterconv.list  > ast_imshift.list
obsutil> !sed s/_odfsc/_odfsca/ ast_afterconv.list > ast_shifted.list
obsutil> !paste ast_imshift.list ast_shifted.list ast_shift.list > ast_shift.cl
obsutil> cat ast_shift.cl
imshift ast_003R_odfsc.fits     ast_003R_odfsca.fits       0.000    0.000
imshift ast_004R_odfsc.fits     ast_004R_odfsca.fits       0.855   -0.011
imshift ast_005R_odfsc.fits     ast_005R_odfsca.fits       1.763    0.024
imshift ast_006R_odfsc.fits     ast_006R_odfsca.fits       1.767    0.361
imshift ast_007R_odfsc.fits     ast_007R_odfsca.fits       1.472    0.205
imshift ast_009R_odfsc.fits     ast_009R_odfsca.fits       1.898   -1.069
imshift ast_010R_odfsc.fits     ast_010R_odfsca.fits       3.059   -1.682
imshift ast_011R_odfsc.fits     ast_011R_odfsca.fits       3.633   -1.827
imshift ast_012R_odfsc.fits     ast_012R_odfsca.fits       4.777   -2.485
obsutil> task $ast_shift = ast_shift.cl
obsutil> ast_shift
```

3.2.5 Co-add

We combine sky subtracted, smoothed, and aligned images into a single image. The task `imcombine` is used to combine the images.

スカイレベルを差し引き、最も PSF の悪い画像に合わせるよう平滑化させ、 そして、位置合わせを行った画像を足し合わせて合成する。画像の合成には `imcombine` を用いる。

```
obsutil> ls ast_*_odfsca.fits > ast_aligned.list
obsutil> imcombine @ast_aligned.list ast_combined.fits combine=average \
>>> reject=sigclip mclip=yes

Dec 27 21:39: IMCOMBINE
  combine = average, scale = none, zero = none, weight = none
  reject = sigclip, mclip = yes, nkeep = 1
  lsigma = 3., hsigma = 3.
  blank = 0.
                Images
   ast_003R_odfsca.fits
   ast_004R_odfsca.fits
   ast_005R_odfsca.fits
   ast_006R_odfsca.fits
   ast_007R_odfsca.fits
   ast_009R_odfsca.fits
   ast_010R_odfsca.fits
   ast_011R_odfsca.fits
   ast_012R_odfsca.fits

  Output image = ast_combined.fits, ncombine = 9
```

The combined image is shown in Fig. 32. The radial profile of an asteroid measured from the combined image is shown in Fig. 33.

合成された画像を Fig. 32 に示す。また、合成された画像 を使って測ったラディアルプロファイルを Fig. 33 に 示す。

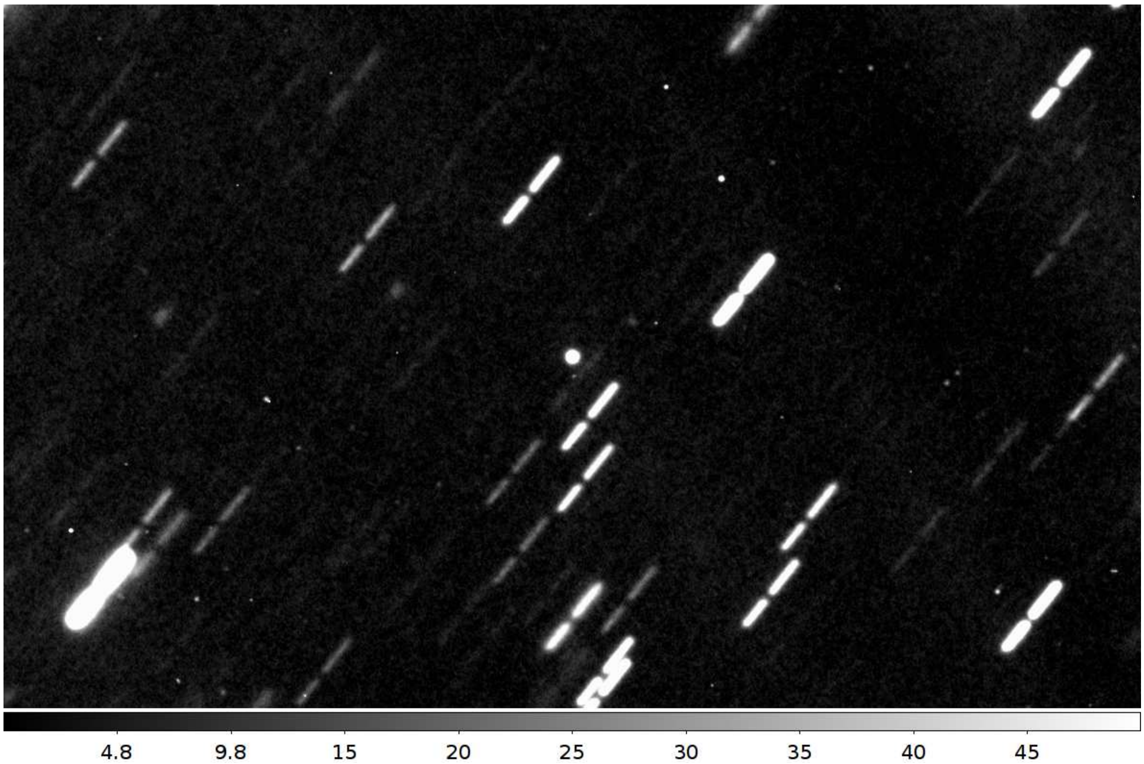

Figure 32: Combined image of an asteroid.

Similarly, we can shift the images according to the positions of a field star and combine the shifted images. Then, we obtain the combined static-sky image of higher signal-to-noise ratio. Fig 34 shows such an example.

同様に、恒星の位置を使って位置合わせを行い、画像を合成することもでき る。その場合、高い S/N 比の恒星や銀河の画像が得られる。 Fig. 34 に一例を示す。

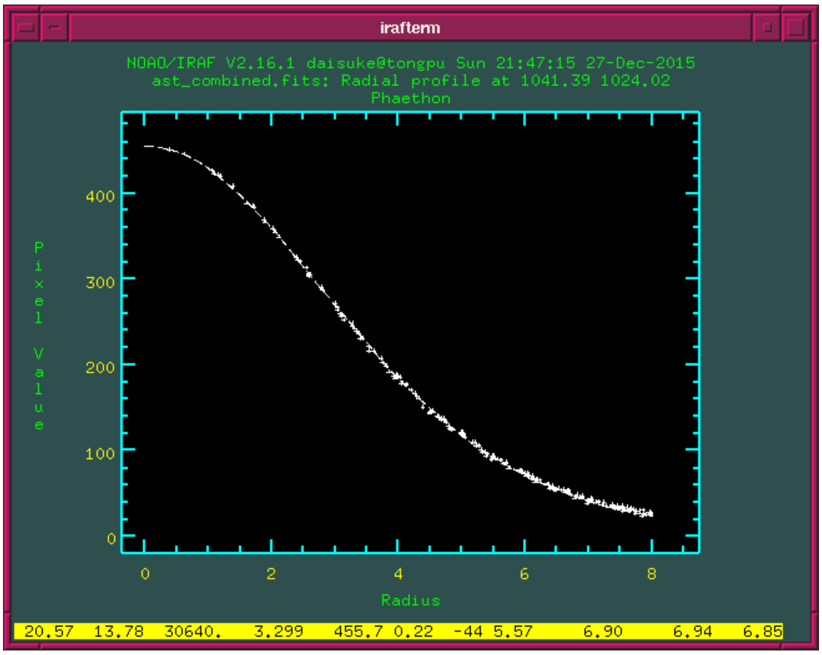

Figure 33: The radial profile of an asteroid measured from the Combined image.

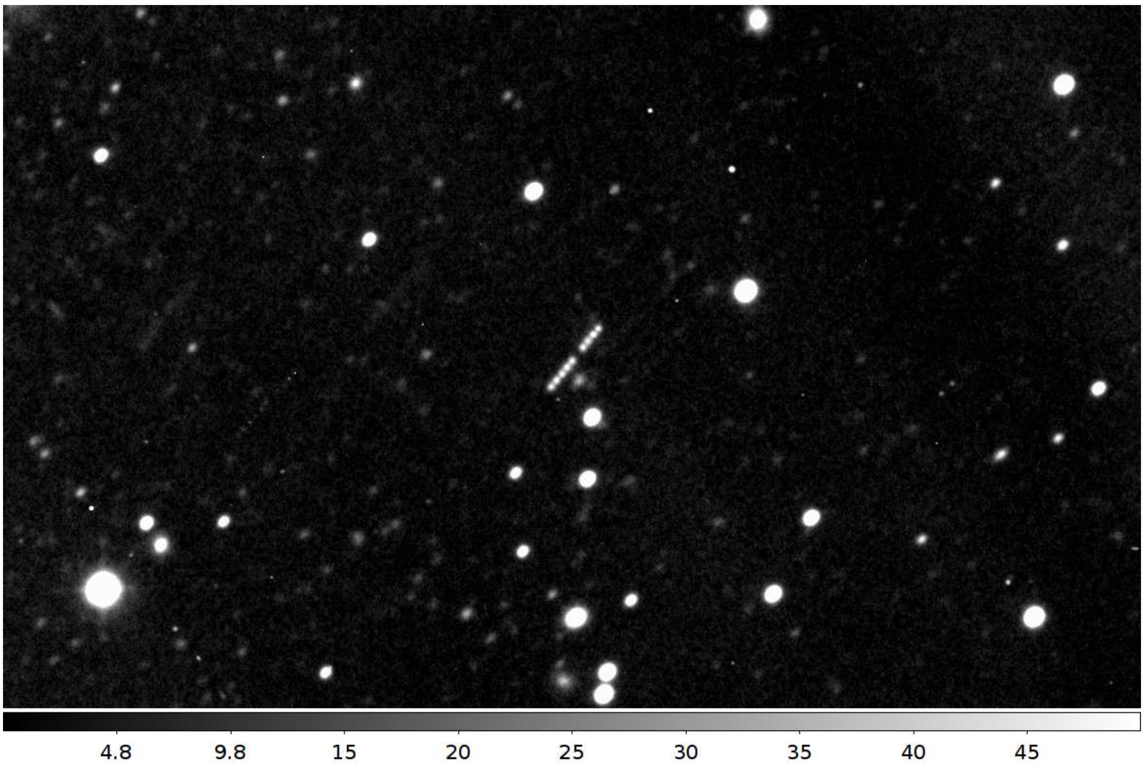

Figure 34: Combined image of the static sky.

3.3 Checking the existence of coma around an asteroidal object

Here, we examine the combined asteroid image and check the existence/non-existence of the coma around the asteroid. Following paper is useful to understand the method described here.
ここでは、合成された小惑星の画像を用いて、彗星活動によるコマの存在の有 無を調べる。その手法を理解するのに、次の論文が有用であると思われる。

- Hsieh and Jewitt, 2005, ApJ, 624, 1093.

We use two images. One is the combined image aligned to the field star. The other is the combined image aligned to the target asteroid.
二つの画像を用いる。一つは、視野内の恒星で位置合わせをして、合成を行っ た画像で、もう一つは、小惑星で位置合わせをして、合成を行った画像である。

3.3.1 Measuring the field star PSF

We first use the combined image aligned to the field star. Choose a relatively bright field star near the target asteroid. We use the task `psfmeasure` to measure the position angle of elongated stellar image.
まず、恒星で位置合わせをして合成した画像を使う。小惑星の近くの比較的 明るい恒星を一つ選ぶ。`psfmeasure` を使って、小惑星追尾のために 伸びた恒星の像が、どの方向に伸びているのかを調べる。

```
obsutil> display ast_combined_fs.fits 1
obsutil> psfmeasure ast_combined_fs.fits size=GFWHM radius=21 iterations=5
** Select stars to measure with 'm' and finish with 'q'.
** Additional options are '?', 'g', and :show.
NOAO/IRAF V2.16.1 daisuke@tongpu Sun 22:18:24 27-Dec-2015

          Image  Column    Line     Mag   GFWHM   Ellip      PA SAT
ast_combined_fs 1244.15 1124.04    0.00   8.843    0.12      47

  Full width at half maximum (GFWHM) of 8.8432
```

The position angle is found to be 47 deg. Using the image acquired by the non-sidereal tracking, we should measure the brightness profile of the star perpendicular to the elongation. (Fig. 35) Hence, we measure the profile along the direction of the position angle 137 deg.
恒星像の伸びている方向の位置角は 47 度であることが分かった。小惑星追 尾のために、恒星の像がある方向に伸びてしまった画像から、恒星の PSF を 測定するためには、伸びたその方向とは 90 度の方向に輝度分布を調べる必 要がある。(Fig. 35) つまり、位置角 137 度の方向の輝 度分布を測る。
Type following command to measure the brightness profile along the direction of position angle of 137 deg centered at (x,y)=(1244.15,1124.04). Fig. 36 is the result of the measurement.
以下のコマンドにより、 (x,y)=(1244.15,1124.04) を起点とした位置角 137 度の方向の輝度分布が得られる。 Fig. 36 が測定の結果であ る。

```
obsutil> pvector ast_combined_fs.fits 0 0 0 0 1244.15 1124.04 theta=137 width=5 \
>>> length=60
```

We also need numerical data of the measurements. Try following command.
この後の解析のため、数値データが必要となる。以下のコマンドにより、測 定した数値がファイルに出力される。

```
obsutil> pvector ast_combined_fs.fits 0 0 0 0 1244.15 1124.04 theta=137 width=5 \
>>> length=60 vec_output="profile_fieldstar.data"
```

3.3.2 Measuring the asteroid PSF

Now, we measure the brightness profile of the target asteroid from the combined image aligned to the asteroid. The center of the asteroid on the image is (x,y)=(1041.45,1024.01).
小惑星に位置合わせして合成した画像から、小惑星の輝度分布を抽出する。 小惑星の像の中心は (x,y)=(1041.45,1024.01) である。

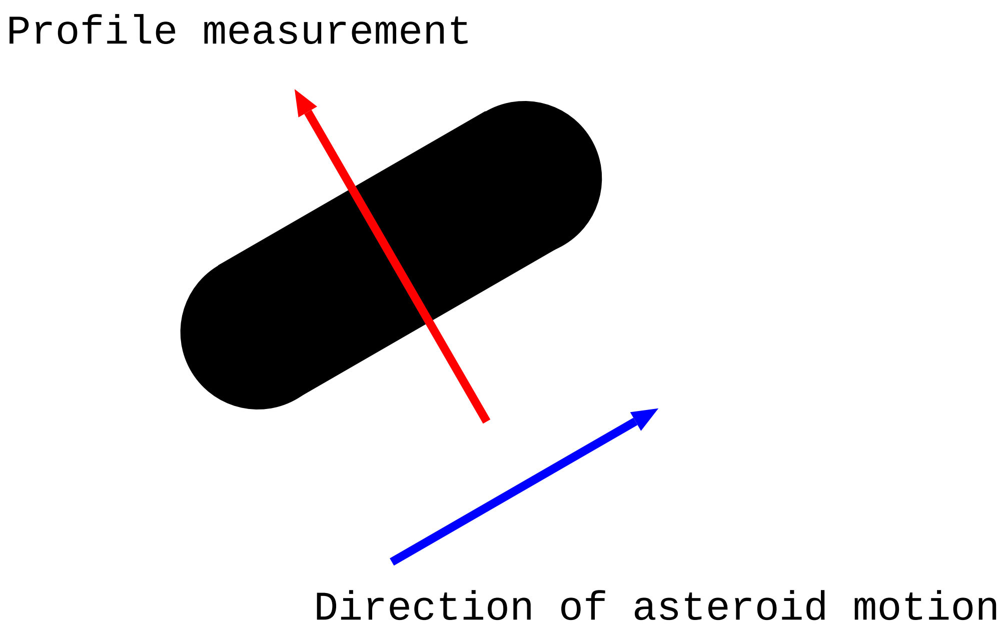

Figure 35: Stars are elongated on the image when the telescope tracks an asteroid. If PSF is measured from such data, the brightness profile must be measured along the direction perpendicular to the direction of the asteroid motion.

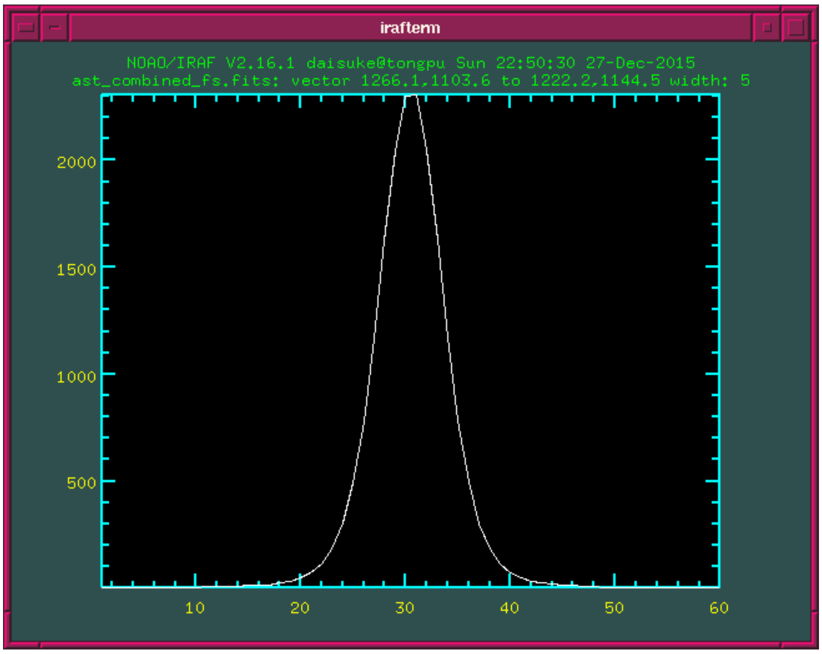

Figure 36: The brightness profile of a field star from asteroid-tracked image.

```
obsutil> psfmeasure ast_combined.fits size=GFWHM radius=21 iterations=5
** Select stars to measure with 'm' and finish with 'q'.
** Additional options are '?', 'g', and :show.
NOAO/IRAF V2.16.1 daisuke@tongpu Sun 22:55:34 27-Dec-2015

          Image  Column    Line     Mag   GFWHM   Ellip      PA SAT
ast_combined.fi 1041.45 1024.01    0.00   8.009    0.18     -47

  Full width at half maximum (GFWHM) of 8.0087
```

We measure the brightness profile of the asteroid using the task pvector.
pvector を使って小惑星の輝度分布を調べる。

```
obsutil> pvector ast_combined.fits 0 0 0 0 1041.45 1024.01 theta=137 width=5 \
>>> length=60 vec_output="profile_asteroid.data"
```

3.3.3 Comparison of star and asteroid

We now compare the brightness profiles of the field star and asteroid. Start gnuplot on the xterm.
恒星と小惑星の輝度分布を比較する。 xterm 上で gnuplot を 起動する。

```
% gnuplot

        G N U P L O T
        Version 5.0 patchlevel 0    last modified 2015-01-01

        Copyright (C) 1986-1993, 1998, 2004, 2007-2015
        Thomas Williams, Colin Kelley and many others

        gnuplot home:     http://www.gnuplot.info
        faq, bugs, etc:   type "help FAQ"
        immediate help:   type "help"  (plot window: hit 'h')

Terminal type set to 'x11'
gnuplot>
```

First, we perform the Gaussian fitting to the brightness profile of the asteroid. Try following on the gnuplot to execute the least square fitting.
まず、小惑星の輝度分布を正規分布でフィッティングしてみる。以下のコマ ンドを gnuplot 上で入力してみる。最小二乗法によるフィッティング が行われる。

```
gnuplot> ra(x) = c_a*exp(-(x-m_a)**2/(2*s_a**2))/sqrt(2*pi*s_a**2)
gnuplot> pi = 3.1415926535
gnuplot> c_a = 400
gnuplot> m_a = 30
gnuplot> s_a = 10
gnuplot> fit ra(x) 'profile_asteroid.data' using 1:2 via c_a,m_a,s_a
```

Then, the results of the fitting are shown.
すると、フィッティングの結果が表示されるはずである。

```
After 22 iterations the fit converged.
final sum of squares of residuals : 3031.81
rel. change during last iteration : -1.85441e-06

degrees of freedom    (FIT_NDF)                        : 58
rms of residuals      (FIT_STDFIT) = sqrt(WSSR/ndf)    : 7.22998
variance of residuals (reduced chisquare) = WSSR/ndf   : 52.2726

Final set of parameters            Asymptotic Standard Error
=======================            ==========================
c_a             = 3136.03          +/- 29.7         (0.9472%)
m_a             = 31.0473          +/- 0.0347       (0.1118%)
s_a             = 3.17295          +/- 0.03473      (1.095%)

correlation matrix of the fit parameters:
                c_a    m_a    s_a
c_a             1.000
m_a            -0.000  1.000
s_a             0.578 -0.005  1.000
```

Next, we perform the Gaissuain fitting to the brightness profile of the field star.
次に、恒星の輝度分布も正規分布でフィッティングしてみる。

```
gnuplot> rs(x) = c_s*exp(-(x-m_s)**2/(2*s_s**2))/sqrt(2*pi*s_s**2)
gnuplot> c_s = 2000
gnuplot> m_s = 30
gnuplot> s_s = 10
gnuplot> fit rs(x) 'profile_fieldstar.data' using 1:2 via c_s,m_s,s_s
```

We also obtain the results of the fitting for the field star.
恒星についても、フィッティングの結果が得られる。

```
After 15 iterations the fit converged.
final sum of squares of residuals : 40934.9
rel. change during last iteration : 0

degrees of freedom    (FIT_NDF)                        : 57
rms of residuals      (FIT_STDFIT) = sqrt(WSSR/ndf)    : 26.7984
variance of residuals (reduced chisquare) = WSSR/ndf   : 718.157

Final set of parameters            Asymptotic Standard Error
=======================            ==========================
c_s             = 17894.5          +/- 109.1        (0.6099%)
m_s             = 30.5064          +/- 0.02195      (0.07196%)
s_s             = -3.11784         +/- 0.02197      (0.7048%)

correlation matrix of the fit parameters:
                c_s    m_s    s_s
c_s             1.000
m_s            -0.000  1.000
s_s            -0.578  0.005  1.000
```

Then, we compare those two. The result of the comparison is shown in Fig. 37. For this case, we do not see significant difference between two.
二つの輝度分布を比較してみる。比較の結果を Fig. 37 に示す。この場合、有意な差は認められない。

```
gnuplot> set xlabel 'Distance from the object center [pix]'
gnuplot> set ylabel 'Brightness [ADUs]'
gnuplot> plot [-20:20] 'profile_asteroid.data' using ($1-31.0473):2 \
>title 'asteroid' with points pt 7 ps 2, 'profile_fieldstar.data' \
>using ($1-30.5064):($2/17894.6*3136.03) title 'field star' with point \
>pt 9 ps 2, ra(x+31.0473) title 'Gaussian fit to the asteroid profile' \
>with lines lt 3 lw 2
```

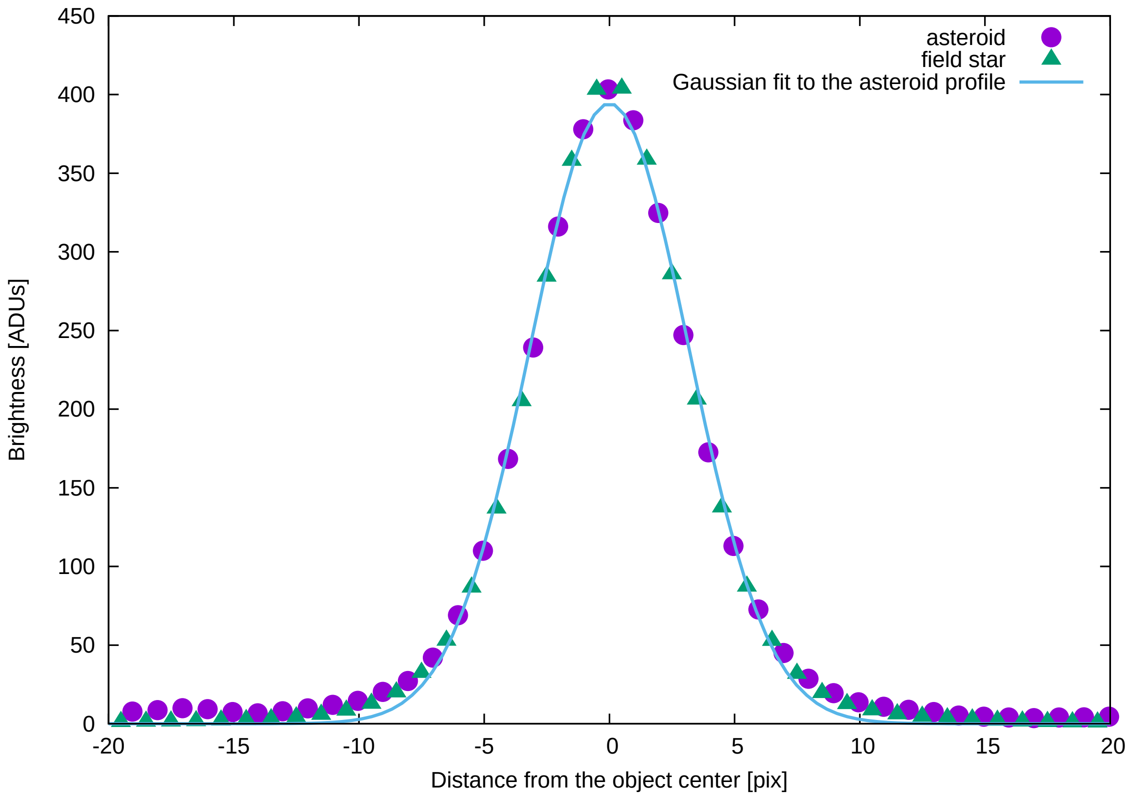

Figure 37: The comparison of PSF of the asteroid and a field star. The brightness profile of the star is scaled for comparison purpose.

Comparisons of the Sky Darkness in Taiwan
臺灣地區天空亮度比較

Kuei-Lan Chang1, Yeah-Chun Yang1, Albert Kong2, Hun-Chin Lin3,
Chu-Wing So4, Chun Shing Jason Pun4, and Sze Leung Cheung5

1 Taipei Astronomical Museum
2 National Tsing Hua University
3 Lulin Observatory, National Central University
4 Department of Physics, The University of Hong Kong
5 IAU Office of Astronomy Outreach, National Astronomical Observatory of Japan, Tokyo, Japan

Abstract

Taipei Astronomical Museum (TAM) is one of 15 monitoring stations of the Globe at Night - Sky Brightness Monitoring Network (GaN-MN). This is an international cooperation project which is supported by Department of Physics at the University of Hong Kong and IAU Office of Astronomy Outreach, and has been continued for more than one year. There are 3 stations in Taiwan, including TAM, National Tsing Hua University and Lulin Observatory of National Central University. Interestingly, these 3 stations are located separately at big city, medium-sized city and countryside in a high mountain. In this article, we compare the sky brightness conditions collecting by naked eyes and Sky Quality Meter - Lensed Ethernet (SQM-LE) at TAM last year. Besides, we also simply compare the darkest sky brightness of the 3 stations in Taiwan to see how the lights pollute the sky at these stations. The GaN-MN is supported by the Knowledge Exchange fund of The University of Hong Kong.

一、前言：

光污染是一種環境污染，成因是室外照明，如街燈、廣告招牌和大廈外牆燈光布置等，將光線直接或間接照射上天空並散射，照亮夜空，令我們失去美麗的星空，甚至影響生態系統和人體健康，但光污染問題卻長期受到大眾的忽視。

國際性光污染監測網絡「Globe at Night - Sky Brightness Monitoring Network」(GaN-MN)獲香港大學知識交流計劃支持，並由國際天文聯合會（International Astronomy Union，IAU）天文推廣辦公室（ Office of Astronomy Outreach，OAO）

推動，於 2015 年做為聯合國教科文組織「國際光之年(International Year of light)」其中一項全球推動項目開始啟動後，到 2016 年 3 月底為止，已有亞歐非等地區 15 個測站加入 GaN-MN 長期監測夜空光度特性的工作。其中臺北市立天文科學教育館為最早加入 GaN-MN 並開始運作的機構，而臺灣地區另有位在新竹的國立清華大學天文所與位在嘉義與南投交界山區的國立中央大學鹿林天文臺也在此列，是 GaN-MN 計畫中測站最多的地區。

本篇報告採用臺北市立天文科學教育館(TAM)、清華大學天文所(NTHU)與中央大學鹿林天文臺(Lulin)2015 年全年監測資料，排除異常資料後，挑選儀器亮度 NSB≧13.7(相當於裸眼極限星等 NELM≧0 等) 進行分析比較。由這些比較可見光污染程度在大都會區、一般都會區與高山地區有明顯差異，類似臺北市這樣的大都會地區受到城市燈光的影響程度非常大，高山地區的觀星條件遠較城市地區好。不過由於 GaN-MN 監測時間迄今僅 1 年多，因此對於季節氣候與月光等因素的影響程度尚無法分離評估，須待累積更多資料後，或許可以剔除這部分影響而看到真正的結果。

圖與表說明：2016 年 3 月 31 日前的 GaN-MN 於全球各地及臺灣之測站分佈概況（引用自 GaN-MN 網站）

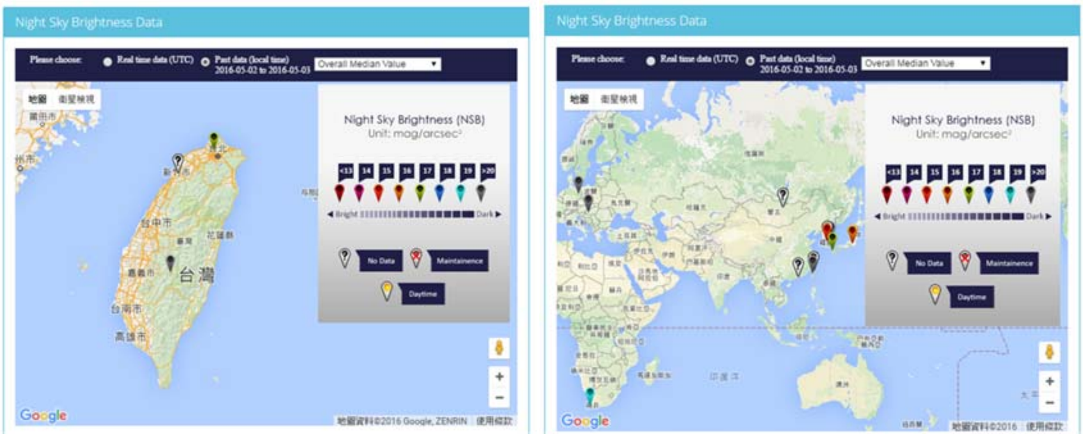

機構名稱	位置	開始運作日期
Taipei Astronomical Museum	Taipei, Taiwan	19 Nov 2014
National Astronomical Observatory of Japan	Tokyo, Japan	19 Dec 2014
The University of Hong Kong	Pokfulam, Hong Kong	26 Dec 2014
National Tsing Hua University	Hsinchu, Taiwan	30 Dec 2014
Yeongyang Firefly Astronomical Observatory	Yeongyang, Korea	24 Jan 2015
Chungbuk National University Observatory	Cheongju, Korea	27 Jan 2015
Lulin Observatory	Lulin, Taiwan	27 Mar 2015
Ho Koon Nature Education cum Astronomical Centre	Tsuen Wan, Hong Kong	18 Apr 2015
South African Astronomical Observatory (Cape Town, SAAO)	Cape Town, South Africa	28 Jul 2015
Kuzuha Observatory	Kanagawa, Japan	1 Aug 2015
National University of Mongolia	Ulaanbaatar, Mongolia	5 Aug 2015
Hungarian Astronomical Association	Zselic Starry Sky Park, Hungary	24 Aug 2015
Hungarian Astronomical Association	Bárduvarnok, Hungary	11 Sept 2015
Elsterland-Observatory	South-Brandenburg, Germany	25 Sept 2015
Nagasaki Nishiyama Observatory	Nagasaki, Japan	19 Mar 2016
Daejeon Astronomical Observatory	Daejeon, Korea	20 Mar 2016

二、觀測儀器基本資料：

1. 觀測儀器：由 IAU OAO 提供之 SQM-LE（Sky Quality Meter -Lensed Ethernet）
2. 觀測時間間隔與資料傳輸：每日 24 小時運作，每 30 秒讀取 1 次資料天空背景輻射資料，即時觀測資料透過網路彙整至設置在香港大學物理系的伺服器中。
3. 儀器視野：約 20 度，朝向天頂。
4. 儀器測量單位：每平方角秒之星等（magnuitude per square arcsec (MPASS)）或夜空亮度（night sky brightness(NSB)），標記為為 B 星等

5. 本報告使用單位：裸眼極限星等（naked eye limiting magnitude (NELM)），近似 V 星等）
6. 儀器測量星等與裸眼極限星等兩者關連(ASP 102:212-229)：經驗公式 $NELM=7.93-5\times\log(10^{(4.316-(Bmpsas/5))}+1)$


圖說：設置在臺北天文館頂樓的 SQM-LE 偵測器外觀，未免雨水損害儀器，SQM-LE 偵測器裝置在有透明天窗的外罩中。


圖說：SQM-LE 偵測器

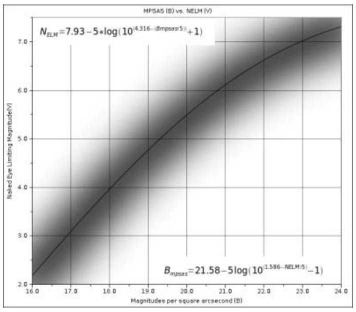

圖說：儀器測量星等與裸眼極限星等轉換圖（取自 SQM-LE 製造商 Unihedron 網站 http://www.unihedron.com/projects/sqm-le/）

三、資料分析比較

1.全年最暗星等概況

經彙整臺北天文館（TAM）、清華大學天文所（NTHU）與中央大學鹿林天文臺（Lulin）三地 2015 全年資料後，得出三地在 2015 年內的最暗亮度概況如下表，其中臺北天文館與清華大學最暗星等發生日期8/20-8/22，恰在颱風來臨前數天，推測應是受到颱風外圍下沈氣流的影響所致。而鹿林天文臺為在臺灣中部山區，可從下列第 3 點見到該地秋冬季氣候較穩定的情況。

位置	資料筆數	最暗 NSB	最暗 NELM	最暗星等發生日期與時間
TAM	437105	18.44	4.33	2015/8/20 3:30~4:30 AM
NTHU	432558	20.23	5.65	2015/8/22 3:00~4:00 AM
Lulin	304045	24.55	7.44	2015/12/10 2:30~3:30 AM

2.全年可見星等統計比較

由下圖中可見位在高山地區的鹿林天文臺有約 50%的 NELM 背景亮度可達 6 等以內，其中還有 1%為裸眼極限以上的 7 等，顯示該地觀測條件良好，不僅背景天空亮度暗，而且空氣中的水汽與霧霾偏低，的確具有設置專業天文臺的優勢。

位在一般都會區的清華大學以 1-3 等為主，大都會區的臺北天文館大多落在 1 等左右，與鹿林天文臺相較之下，可明顯看出都市燈光的影響程度。其中清華大學的儀器設置於該校物理系所與天文所所在的樓頂，比校園內的路燈高度高許多，且新竹地區號稱風城，該地區的空氣污染程度較臺北盆地低許多。

位在大都會中的臺北天文館，周邊大樓的高度均比 SQM-LE 偵測器還高，且鄰近士林夜市、天母、兒童新樂園等光污染嚴重區域，燈光關閉時間也不統一，再加上臺北盆地的地形效應，都會區因空氣污染產生的霧霾累積於地表附近很難散開，極易反射或散射商家、住戶大樓的燈光或路燈，所以光污染影響程度比清華大學還高許多。

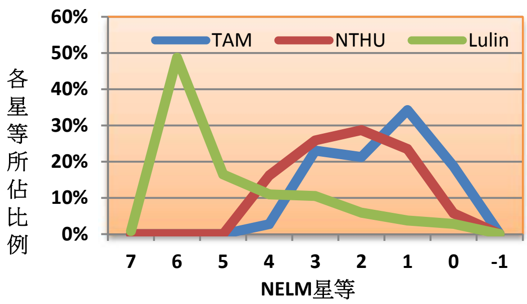

3. NELM 大於 4 等以上者落在各月份的比例

在臺北天文館觀測點，除了進行 SQM-LE 儀器，另有每月挑選幾日進行目視觀測。兩種觀測方式配合之下，發現 NELM 在 1 等左右的記錄，通常天氣不佳，空中雲量較高，所以經由天空中的雲或霧霾漫射的光量也比較高所致。而 NELM 在 3 等以上的記錄，雖可能仍有雲或霧霾影響，但通常是天空中可見星星的夜晚。因此，為確保進行比較的資料是非雲雨天氣狀況下的真正天空背景亮度，因而挑選 NELM 大於 4 等以上的記錄來進行統計比較。

下圖為 NELM 大於 4 等的記錄落在各月份的比例。由圖中明顯可見臺北天文館和鹿林天文臺背景亮度比較暗的月份大都落在下半年度，這與臺灣地區所在氣候帶有關，上半年度的春雨季和梅雨季明顯會影響監測結果。而清華大學所在的新竹地區雖然較佳的月份落在下半年度，但年中的表現比其他兩地好，可能是受到所在地理位置與地形遮蔽的結果。

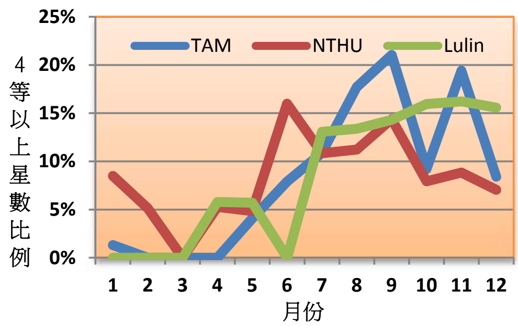

4. NELM 大於 4 等以上者在夜間時段的統計結果

下圖為取三地 NELM 大於 4 等以上的記錄進行所在夜間時段統計的結果，總軸為資料筆數，可見高山區的鹿林天文臺在天文暮光(~19:30)後至天文曙光(~4:30)前的整個夜間狀況相差不多，可能是因為偵測方向朝向天頂，受到山腳下的城市燈光影響非常少的緣故。

而一般都會區的清華大學資料開始增加的時間為子夜前的 22:00 至天文曙光，大都會區的臺北天文館則在近午夜的 23:30 以後至天文曙光，顯見城市內燈光隨夜深而逐漸關閉後，天空亮度才能逐漸變暗，而且清大校園內的作息時間與都會區內的商業作息不同，校園內的燈光關閉時間比臺北天文館所在之處還要早一些，所以 4 等以上記錄增加的時間比臺北天文館早，增加速度也比較快。

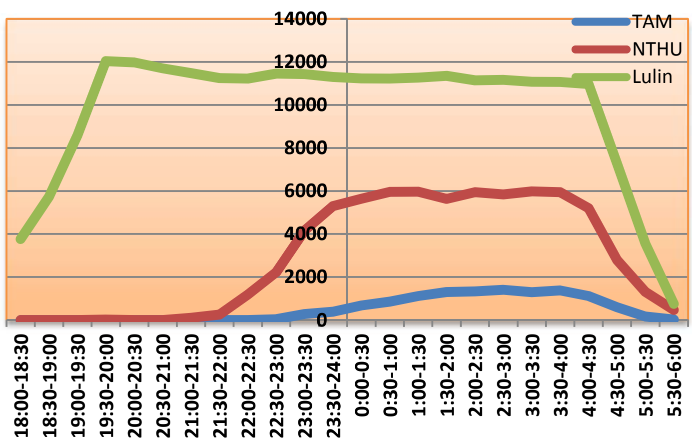

四、結論

從上述統計比較結果，可得出光污染程度在大都會區、一般都會區與高山地區有明顯差異，城市燈光向上漫射和空氣污染、天氣狀況等的影響程度非常大，當然由此可知高山地區的觀星條件遠較城市地區好。

不過由於 GaN-MN 監測時間迄今僅 1 年多，在這份統計分析中並未將針對季節氣候與月光等因素的影響程度進行深入探討，須待累積更多資料後，比較每年同一季節的狀況，或許可以剔除這部分影響而看到真正的結果。

此外，這幾個測站也都有設置雲量感測器（Cloud Sensor），未來可將 SQM-LE 偵測資料與雲量感測器偵測資料結合，或許可以從中瞭解天氣概況與天空背景亮度的關係。

Search for P-mode oscillation in White Dwarfs

Chih-Yuan Liu[1], Jie-Rou Shang[1], Wen-Cheng Huang[2], Hsiang-Kuang Chang[1,2] and Yi-Shan Wu[1]

1. Institute of Astronomy, National Tsing Hua University, Hsinchu 30013 Taiwan
2. Department of Physics, National Tsing Hua University, Hsinchu 30013 Taiwan

Up to now, we have 5 LOT observations with our CMOS camera system:

- **2014Feb16**
- **2014May29 - May31**
  - PI: Yi-Shan Wu, for the above 2 campaigns
  - Scientific products:
    - ASROC2014, Poster presentation PS33, "Search for p-mode oscillations in white dwarfs by using high speed photometry cameras" by Yi-Shan Wu et al.
    - Master Thesis, Yi-Shan Wu, "Search for p-mode oscillations in DAV white dwarf G226-29", 2014July
- **2016Jan11 - Jan14**
- **2016Feb29 - Mar03**
- **2016Apr06 - Apr10**
  - PI: Chih-Yuan Liu, for the above 3 campaigns
  - Scientific products:
    - two possible ASROC2016 presentations, abstracts are submitted

P-mode oscillation of a white dwarf has pressure as the restoring force and frequencies higher than those of g-modes. Probably because of high frequencies and small amplitudes, p-mode oscillation has not been observed in white dwarfs. In our work, we chose several bright white dwarfs as targets to observe with a commercial CMOS camera, Hamamatsu ORCA-Flash4.0V2, mounted on LOT. This work will be part of Mr. Wen-Cheng Huang and Ms. Jie-Rou Shang's Master/PhD thesis researches. For 2015BIII campaign, we got 4 nights from Jan 11 to Jan 14. We are still working on the data reduction and Timing analysis using discrete Fourier transform. We hope we can get some preliminary results as soon as possible. We will keep applying observations for monitoring our other targets for 2016 campaigns. We also mentioned here that this is the 3rd time we used our CMOS camera system at LOT. The first two observations were carried out in 2014, and are the works of Ms. Yi-Shan

Wu's Master thesis: from the results of discrete Fourier transform, there is no feature detected above 3σ confidence level in 1-10Hz, and a 3σ confidence level upper limit is estimated.

  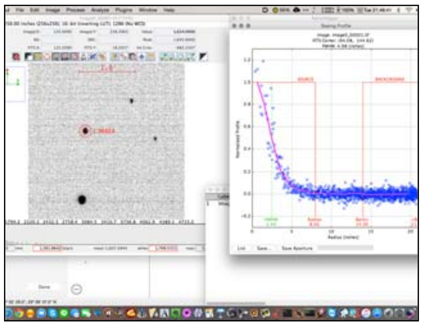

The CMOS camera system consists of Hamamatsu ORCA-Flash4.0V2 (the left image above) and Dell T5600 Desktop (the central image above) that owns large memory capacity (128Gb) and abundant hard disk storage space. The following is the specification of ORCA-Flash4.0V2: the active pixels are 2048×2048 (13.3×13.3 mm), the QE (600 nm) is 70%, the cooling temperature (air cooling) is -10°C, the dark current at -10°C is 0.5 electron/pixel/second, and the readout noise is 1.9 electron rms at readout rate 680MHz.

Take advantage of CMOS's fast readout, ORCA-Flash4.0V2's highest frame rate at frame size 1024x1024 can achieve 200fps. To save the great amount of captured data without interruption, the back-end computer has been enhanced to have ability of quick writing data into hard disks and its' capacity can afford all the captured data. The operation of capturing frames is using 1024x1024 pixels ROI with 4x4 binning and exposure time 50ms. The ROI and binning are settled to reduce the file size so that we can continuously capture data last more than 10 hours. The FOV of ROI is 2.86′×2.86′. The right image above shows one of the targets, WD0501+527, we observed in this January, and the comparison stars within FOV of ROI. We estimated the seeing profile by using AstroImageJ.

Report on TRIPOL performance and magnetic field structure of NGC1893

By
Eswaraiah Chakali (Postdoc, Institute of Astronomy, National Tsing Hua University)
(previously postdoc at Institute of Astronomy, National Central University)

TRIPOL performance: To test the performance of TRIOPL, the tricolor (g'r'i') polarimeter, mounted on 1-meter Lulin Optical Telescope (LOT), we have observed several polarized and unpolarized standard stars taken from Schmidt et al. (1992). This test run was conducted during 17-28 February 2015. The results on observed several polarized and unpolarized standards stars are tabulated in left panel of Fig 1. And the comparison between TRIPOL (SDSS g'r'i'-bands) and standard results (in Johnson-Cousin BRI-bands) from Schmidt et al. (1992) is depicted in the right panel of Fig 2. Detailed results based on the performance of TRIPOL is in preparation (Sato, Chen, Eswaraiah et al. 2016).

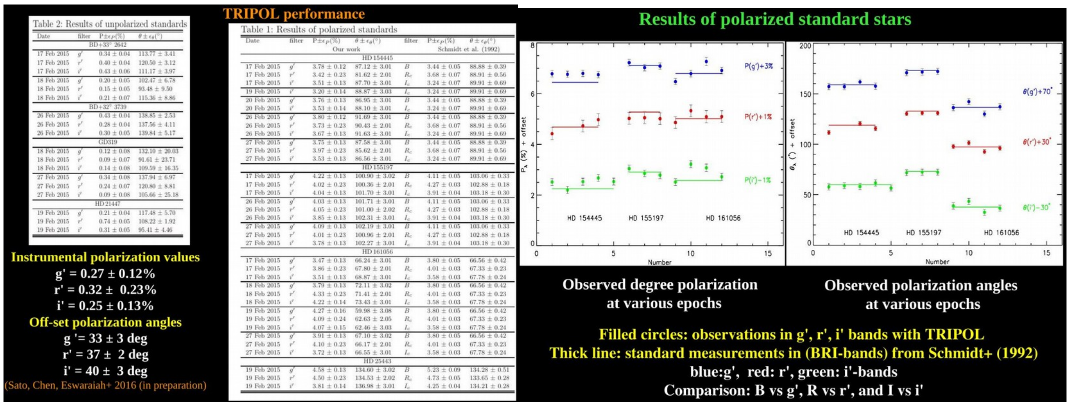

Table 2: Results of unpolarized standards

Date	filter	$P \pm \epsilon_P$(%)	$\theta \pm \epsilon_\theta$(°)
		BD+33° 2642	
17 Feb 2015	g'	0.34 ± 0.04	113.77 ± 3.41
17 Feb 2015	r'	0.40 ± 0.04	120.50 ± 3.12
17 Feb 2015	i'	0.43 ± 0.06	111.17 ± 3.97
18 Feb 2015	g'	0.20 ± 0.05	102.47 ± 6.78
18 Feb 2015	r'	0.15 ± 0.05	93.48 ± 9.50
18 Feb 2015	i'	0.21 ± 0.07	115.36 ± 8.86
		BD+32° 3739	
26 Feb 2015	g'	0.43 ± 0.04	138.85 ± 2.53
26 Feb 2015	r'	0.28 ± 0.04	137.56 ± 4.11
26 Feb 2015	i'	0.30 ± 0.05	139.84 ± 5.17
		GD319	
18 Feb 2015	g'	0.12 ± 0.08	132.10 ± 20.03
18 Feb 2015	r'	0.09 ± 0.07	91.61 ± 23.71
18 Feb 2015	i'	0.14 ± 0.08	109.59 ± 16.35
27 Feb 2015	g'	0.34 ± 0.08	137.94 ± 6.97
27 Feb 2015	r'	0.24 ± 0.07	120.80 ± 8.81
27 Feb 2015	i'	0.09 ± 0.08	105.66 ± 25.18
		HD 21447	
19 Feb 2015	g'	0.21 ± 0.04	117.48 ± 5.70
19 Feb 2015	r'	0.74 ± 0.05	108.22 ± 1.92
19 Feb 2015	i'	0.31 ± 0.05	95.41 ± 4.46

Table 1: Results of polarized standards

Date	filter	$P \pm \epsilon_P$(%)	$\theta \pm \epsilon_\theta$(°)	filter	$P \pm \epsilon_P$(%)	$\theta \pm \epsilon_\theta$(°)
		Our work			Schmidt et al. (1992)	
			HD 154445			
17 Feb 2015	g'	3.78 ± 0.12	87.12 ± 3.01	B	3.44 ± 0.05	88.88 ± 0.39
17 Feb 2015	r'	3.42 ± 0.23	81.62 ± 2.01	R_c	3.68 ± 0.07	88.91 ± 0.56
17 Feb 2015	i'	3.51 ± 0.13	87.70 ± 3.01	I_c	3.24 ± 0.07	89.91 ± 0.69
19 Feb 2015	i'	3.20 ± 0.14	88.87 ± 3.03	I_c	3.24 ± 0.07	89.91 ± 0.69
20 Feb 2015	g'	3.76 ± 0.13	86.95 ± 3.01	B	3.44 ± 0.05	88.88 ± 0.39
20 Feb 2015	i'	3.53 ± 0.14	88.10 ± 3.01	I_c	3.24 ± 0.07	89.91 ± 0.69
26 Feb 2015	g'	3.80 ± 0.12	91.69 ± 3.01	B	3.44 ± 0.05	88.88 ± 0.39
26 Feb 2015	r'	3.73 ± 0.23	90.43 ± 2.01	R_c	3.68 ± 0.07	88.91 ± 0.56
26 Feb 2015	i'	3.67 ± 0.13	91.63 ± 3.01	I_c	3.24 ± 0.07	89.91 ± 0.69
27 Feb 2015	g'	3.75 ± 0.13	87.58 ± 3.01	B	3.44 ± 0.05	88.88 ± 0.39
27 Feb 2015	r'	3.97 ± 0.23	85.62 ± 2.01	R_c	3.68 ± 0.07	88.91 ± 0.56
27 Feb 2015	i'	3.53 ± 0.13	86.56 ± 3.01	I_c	3.24 ± 0.07	89.91 ± 0.69
			HD 155197			
17 Feb 2015	g'	4.22 ± 0.13	100.90 ± 3.02	B	4.11 ± 0.05	103.06 ± 0.33
17 Feb 2015	r'	4.02 ± 0.23	100.36 ± 2.01	R_c	4.27 ± 0.03	102.88 ± 0.18
17 Feb 2015	i'	4.04 ± 0.13	101.70 ± 3.01	I_c	3.91 ± 0.04	103.18 ± 0.30
26 Feb 2015	g'	4.03 ± 0.13	101.71 ± 3.01	B	4.11 ± 0.05	103.06 ± 0.33
26 Feb 2015	r'	4.05 ± 0.23	101.00 ± 2.02	R_c	4.27 ± 0.03	102.88 ± 0.18
26 Feb 2015	i'	3.85 ± 0.13	102.31 ± 3.01	I_c	3.91 ± 0.04	103.18 ± 0.30
27 Feb 2015	g'	4.09 ± 0.13	102.19 ± 3.01	B	4.11 ± 0.05	103.06 ± 0.33
27 Feb 2015	r'	4.01 ± 0.23	100.96 ± 2.01	R_c	4.27 ± 0.03	102.88 ± 0.18
27 Feb 2015	i'	3.78 ± 0.13	102.27 ± 3.01	I_c	3.91 ± 0.04	103.18 ± 0.30
			HD 161056			
17 Feb 2015	g'	3.47 ± 0.13	66.24 ± 3.01	B	3.80 ± 0.05	66.56 ± 0.42
17 Feb 2015	r'	3.86 ± 0.23	67.80 ± 2.01	R_c	4.01 ± 0.03	67.33 ± 0.23
17 Feb 2015	i'	3.51 ± 0.13	68.87 ± 3.01	I_c	3.58 ± 0.03	67.78 ± 0.24
18 Feb 2015	g'	3.79 ± 0.13	72.11 ± 3.02	B	3.80 ± 0.05	66.56 ± 0.42
18 Feb 2015	r'	4.33 ± 0.23	71.41 ± 2.01	R_c	4.01 ± 0.03	67.33 ± 0.23
18 Feb 2015	i'	4.22 ± 0.14	73.43 ± 3.01	I_c	3.58 ± 0.03	67.78 ± 0.24
19 Feb 2015	g'	4.27 ± 0.16	59.98 ± 3.08	B	3.80 ± 0.05	66.56 ± 0.42
19 Feb 2015	r'	4.09 ± 0.24	62.63 ± 2.05	R_c	4.01 ± 0.03	67.33 ± 0.23
19 Feb 2015	i'	4.07 ± 0.15	62.46 ± 3.03	I_c	3.58 ± 0.03	67.78 ± 0.24
27 Feb 2015	g'	3.91 ± 0.13	67.10 ± 3.02	B	3.80 ± 0.05	66.56 ± 0.42
27 Feb 2015	r'	4.10 ± 0.23	66.17 ± 2.01	R_c	4.01 ± 0.03	67.33 ± 0.23
27 Feb 2015	i'	3.72 ± 0.13	66.55 ± 3.01	I_c	3.58 ± 0.03	67.78 ± 0.24
			HD 25443			
19 Feb 2015	g'	4.58 ± 0.13	134.60 ± 3.02	B	5.23 ± 0.09	134.28 ± 0.51
19 Feb 2015	r'	4.50 ± 0.23	134.53 ± 2.02	R_c	4.73 ± 0.05	133.65 ± 0.28
19 Feb 2015	i'	3.81 ± 0.14	136.98 ± 3.01	I_c	4.25 ± 0.04	134.21 ± 0.28

Figure 1. Left panel *show the polarization measurements of both polarized (table 1) and un-polarized (table 2) standard stars obtained with TRIPOL in g'r'i'-bands along with the results from Schmidt et al. (1992).* ***Right panel*** *show depicts the comparison between the TRIPOL (filled circles with different colors) and known standard results (thick lines with different colors) for three polarized standards over multi-epochs. X-axis is the running number (or measurements number). Offset is applied to distinguish the results between g', r' and I'-bands.*

Magnetic field structure towards NGC1893: Four fields (with 5'x5' area) were observed with TRIPOL in g'r'i'-bands during 17-28 February 2015. The magnetic field structure inferred using I'-band polarimetry of TRIPOL is shown with white vectors in Fig 2. Length of the vectors is proportional to the percentage of polarization and orientation depicts the orientation of magnetic field. To compare the results obtained from TRIPOL with those of AIMPOL (ARIES IMaging POLarimeter) we also plotted I-band polarization vectors on tricolor image containing NGC1893. Though, two instruments observed different parts of the region, the mean magnetic field orientation inferred using I-band polarimetry of AIMPOL and i'-band polarimetry of TRIPOL are closely matching with each other. These results suggest that B-fields have not modified during and after the star-formation processes as the B-fields at the cluster center (yellow vectors) and B-fields along the bubble (white vectors) seems to be organized without following the bubble. These results may hint that B-fields, though changed during star-formation activity, could have come to their original configuration that is parallel to the Galactic plane (thick white line).

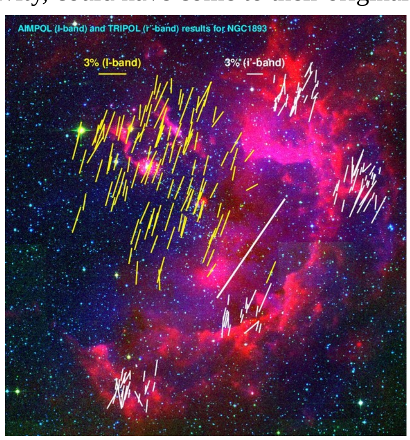

Fig 2. TRIPOL i'-band (white vectors) and AIMPOL I-band (yellow vectors) are overlaid on the tricolor (WISE 4.6 (red), 2MASS K (green), and DSS R-band (blue)) image of NGC 1893. Reference vectors with 3% of polarization are shown. Galactic plane is shown with a thick white line. The draft based on the results of this target is in advanced stage.

東亞天文台 合歡山選址 簡介

張永欣

地理位置

台灣位於中國大陸的東南沿海，南北長約 350km、東西寬約 120km，擁有許多高於海拔 3000m 以上的高山，但大多無道路可以抵達，唯獨只有合歡山，大型車輛可以輕易抵達海拔 3275m 的武嶺，更高的合歡山主峰(海拔 3417m)還有軍方所遺留下的水泥戰備道路可以抵達，為全台灣車輛可抵達的最高點，這裡就是我們這次選址的地點。

交通狀況與周邊資源

合歡山區由台 14 甲線通過，往西最近的城市為 55km 遠的埔里市，往東則為 120km 外的花蓮市。距離台中市區約為 110km，由台中市出發至此約需 3.5 小時車程；其他各點距離如下：

13.5km 8km 10km 6.3km 5.1km 2.1km 1.5km 3.6km 5.1km

埔里 → 霧社 → 清境農場 → 翠峰 → 鳶峰 → 昆陽 → 武嶺 → 合歡山莊 ← 小風口 ←大禹嶺

最近的運補點為霧社，有生鮮超市、郵局以及瓦斯行；清境農場為國內知名的旅遊地點，住宿及餐廳相當多，可提供觀測人員相當好的居住條件，但大型運補仍以埔里為佳。 下面這張照片是位於海拔 1700m 的清境農場。

氣候

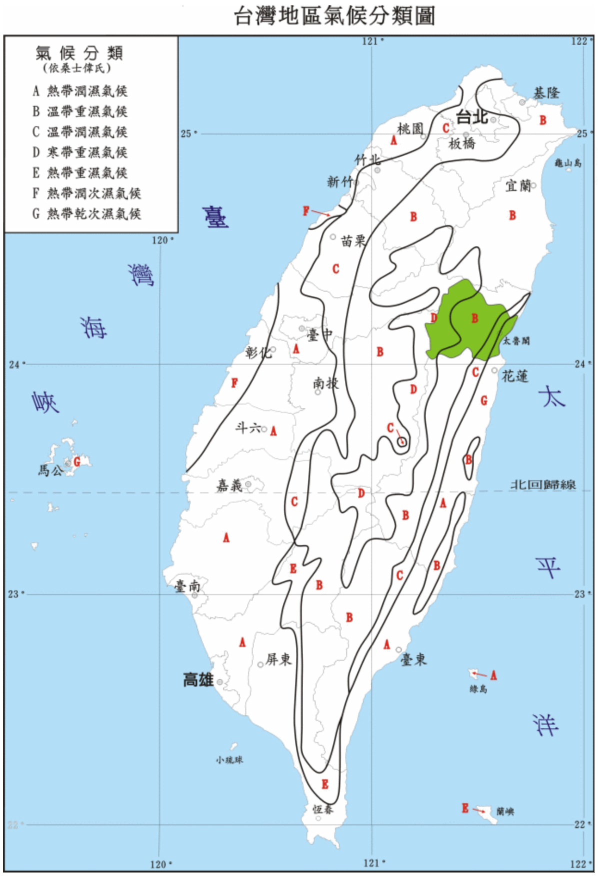

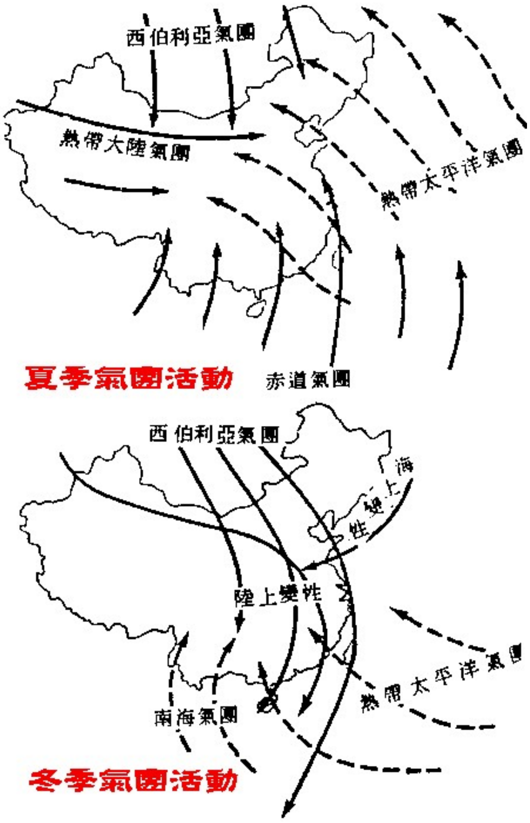

合歡群峰海拔高度皆在 3200m 以上，屬於寒帶重濕氣候區，東方及東北方完全沒有高山屏障，所以易受東北季風的影響，且風勢強勁；南方及西南方為同一高度的中央山脈區域，加上地處偏東，所以西南氣流影響較小。

夏季時逆溫層在海拔 3000m 以上，天氣多半是午後積雲的型態，約在中午前後中低海拔的雲便開始上升，此時山頭便處在雲霧當中，到了傍晚氣溫下降，雲霧也就跟著散去。

冬季逆溫層多半停留在海拔 2000m 以下，此時合歡山區通常是晴朗的天氣，當冬季強大的寒流南下加上水氣又十分充裕時便會開始下雪，但是必須這兩項條件共同成立時才有機會；當高壓一出東海，隨即轉變為晴朗乾燥的天氣。

春季延續冬季的濕冷季節，天氣較不穩定。

秋季是乾燥且晴天率最高的季節。

光害影響

- 東方最大城市為花蓮市(直線距離約為 30km)，市區燈光不多，光害影響不大。
- 南方為中央山脈區域，幾乎無燈光影響。
- 西南方最近城市為埔里(直線距離約為 35km)，以及著名觀光景點清境農場(直線距離約為 19km)，由於直視無阻擋，光害影響待評估；更遠的高雄市(直線距離約為 180km)，及嘉南地區亦有顯著的光害影響，但是比鹿林天文台輕微。
- 西方最大城市為台中市(直線距離約為 55km)，為該區光害最強之方向。
- 北方為台北地區(直線距離約為 90km)，為光害第 2 嚴重之方向。

合歡山主峰地形

由等高線圖可知主峰的西南方為陡坡，僅有東北方、西北方及南方分別為稜線上有緩坡，尤其是南方的稜線比較有足夠的面積可以放置多個圓頂，且南北方向的分佈彼此

之間的干擾較小，下列照片可以提供較為精細的現場狀況。

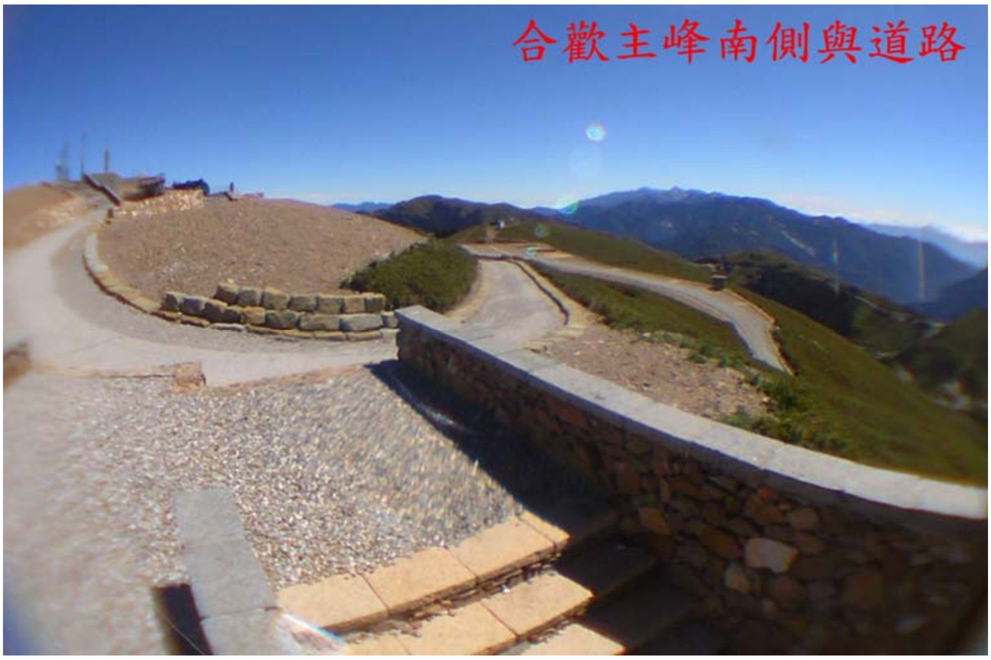

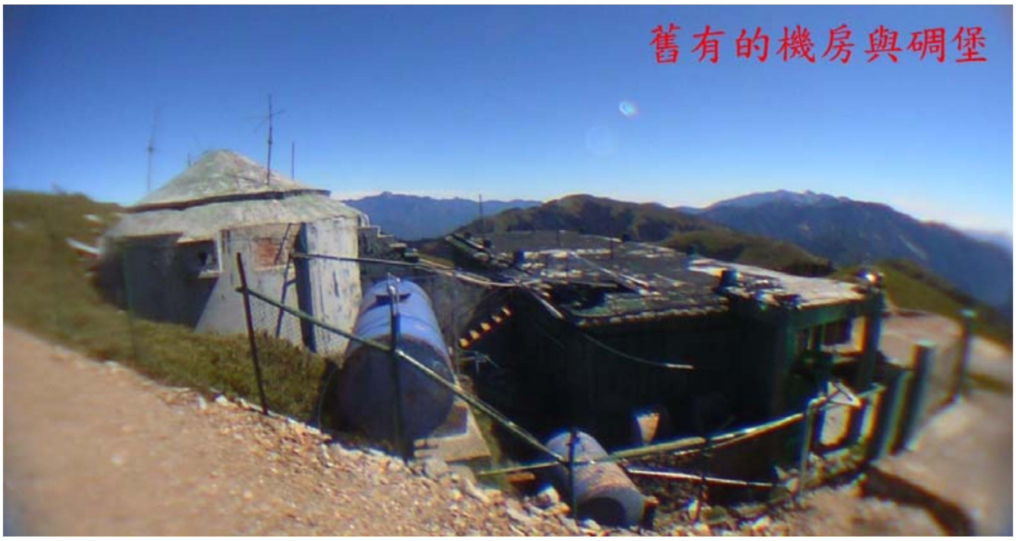

圖中蒙古包形的碉堡直徑約 6m，下方的機房長寬約 15m×6m，若拆除整地之後，加上碉堡旁至主峰頂的空地全部約 20m×18m 的可建築空間，是此山頭上最佳的天文台地點；另外南稜上有兩處碉堡以及瞭望台，空間約 6m×6m，亦可建立單獨圓頂。


合歡主峰南稜

鹿林天文台觀測時數統計(2003-2015)

林宏欽、蕭翔耀、林啟生

鹿林天文台自 2002 年 9 月開始人員常駐，2003 年 LOT 一米望遠鏡上線，開始有正式觀測時數紀錄，可供瞭解鹿林長期的天氣狀況。依 2003-2015 共 13 年的統計結果，鹿林天文台年平均觀測時數為 1456 小時。一年約可分為四個觀測季，

- 最佳觀測季：10-12 月。
- 次佳觀測季：1-3 月。
- 最差觀測季：4-6 月。4 月開始進入雨季，5-6 月受梅雨影響，天氣最差。
- 次差觀測季：7-9 月。主要受颱風及西南氣流影響，天氣變化大。此外夏季晝長夜短，每晚可觀測時間比冬季為短。

詳細統計資料及統計圖如下，

表 1 每月觀測時數統計 (2003-2015)

Month	2003	2004	2005	2006	2007	2008	2009	2010	2011	2012	2013	2014	2015	Average**
1	78.75	125	163.25	129	127.32	179	234.52	206.9	90.8	113.42	153.58	269.62	188.55	155.58
2	142.5	145.98	94.75	149	128.55	118.25	165.7	100.6	123.8	64.88	183.63	109.8	131.65	128.23
3	147.5	163	143	126.05	116.4	138.5	146.75	181.3	75.9	168.23	134.26	78.7	111.1	133.95
4	126.5	110.5	144.75	86.8	53.75	85.25	71.8	75.8	151.45	32.75	55.83	135.95	124	97.36
5	129.75	106.25	136.25	59.5	106.6	98.25	167.4	86.05	56.6	74.3	41.02	32.4	64.2	87.16
6	24	133	45	39.3	54	37	81.75	26.5	61.5	35.15	80.14	33.7	146.9	57.00
7	222.5	48	167.75	91.57	128.88	88.4	76.6	99.85	81.75	106.4	88.05	114.65	87.45	102.85
8	137.75	142	76	111.65	56.6	118.95	6.8	98.3	97.9	35.7	72.2	110.9	45.1	87.37
9	142	116	129.25	60.05	69.55	59.8	0	109.95	90.1	117.35	107.84	134.39	93.25	98.87
10	149.25	219.75	210.25	150.6	172.63	191.38	175.6	139.8	136.95	214.51	200.57	232.33	145.4	179.07
11	166.5	214.5	216.25	71.75	160.55	152.55	175.8	163.65	87.2	93.81	136.1	166.15	197.05	155.81
12	271.5	232.45	129	132	261.09	211.17	169.8	169.65	115.25	132.21	86	137.3	161.2	168.28
Total	1738.5	1756.43	1655.5	1207.27	1435.92	1478.5	1472.52	1458.35	1169.2	1188.71	1339.22	1555.89	1495.85	1456.93

* 2009 年因受莫拉克颱風八八風災影響，自八月八日起至十月初約 2 個月期間道路中斷並停電，無法觀測。所以 2009 年之八、九月觀測時數很少，甚至為 0。
**Average 值為扣除最高及最低值後取平均。

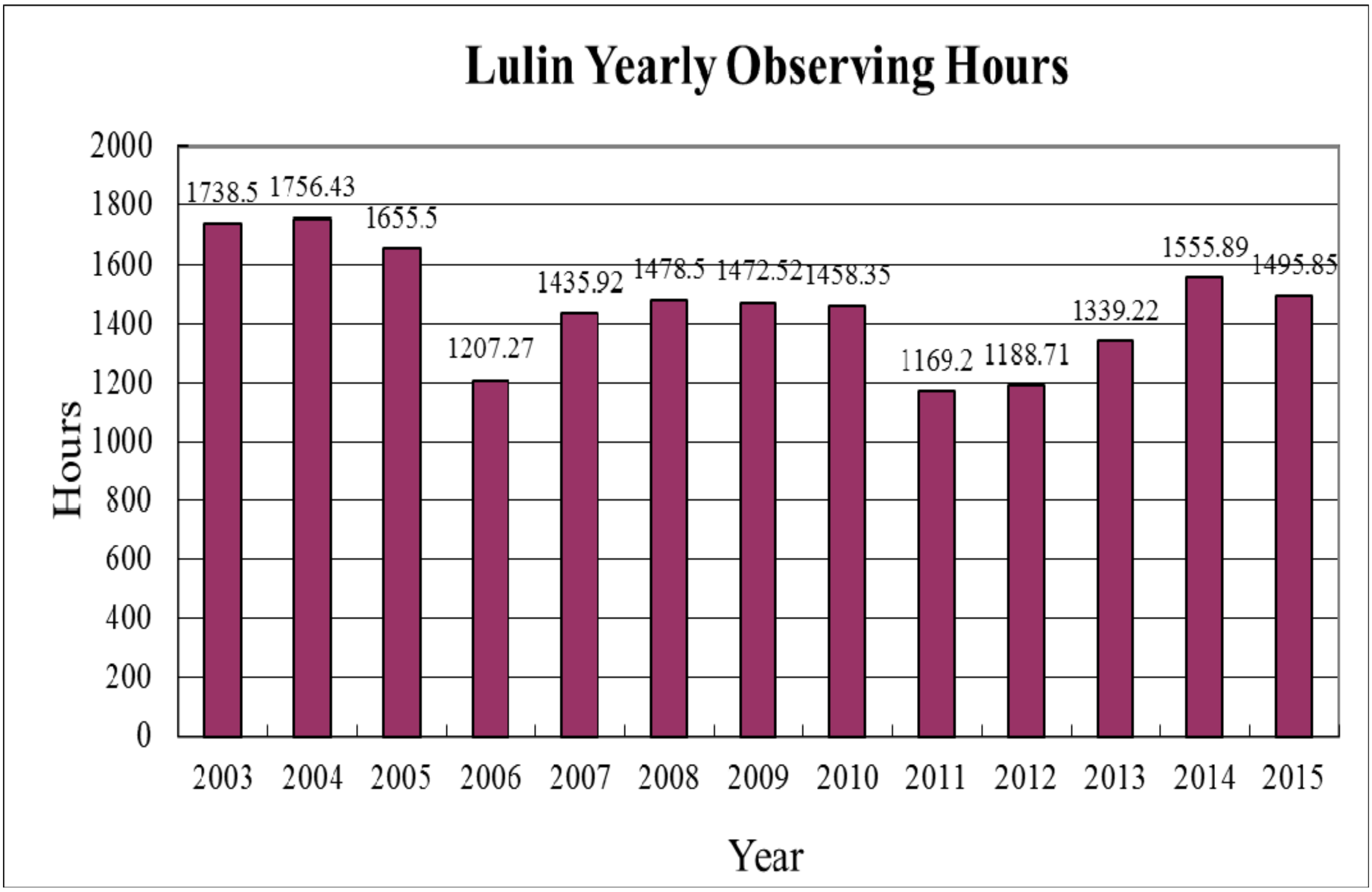

圖 1　鹿林天文台年平均觀測時數統計圖(2003-2015)

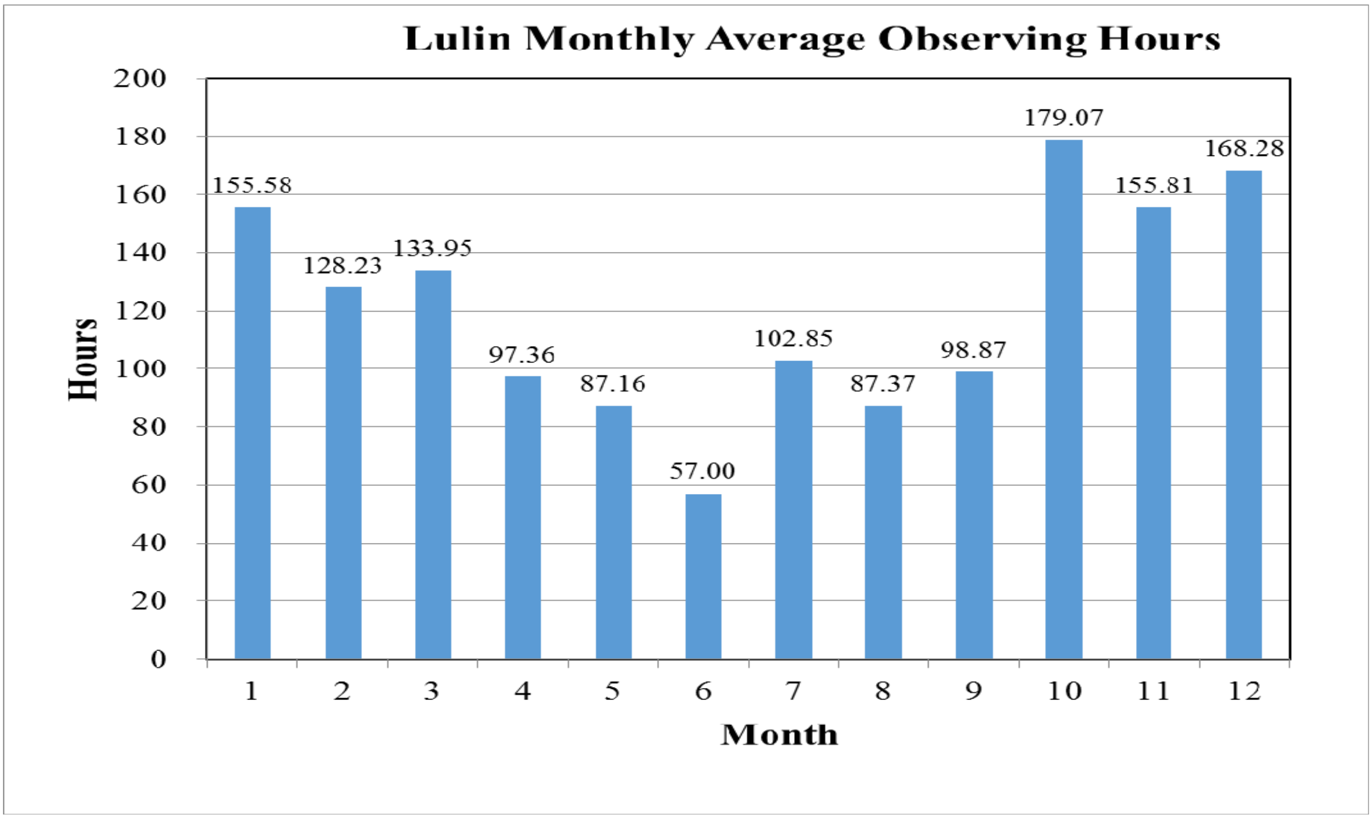

圖 2　鹿林天文台月平均觀測時數統計圖 (2003-2015)

新聞報導

太空研究巨擘 葉永烜榮獲國家講座

【台灣醒報記者黃捷台北報導】「台灣過去能成功發展，是因保有多元文化寬容的價值，未來更應如此。」研究天文學 30 年的葉永烜教授獲 19 屆國家講座主持人獎致詞時，將相對論公式「E=mc2」另類地解釋成「Earth=Multiple Cultures and Civilizations」，說明地球因多種不同文化和文明和諧相處，才能夠永續發展，期許台灣珍惜多元價值而變得更為強大。

第 19 屆國家講座暨第 59 屆學術獎頒獎典禮 21 日於國家圖書館舉行，國家講座主持人從 33 件申請中選出 7 名，學術獎從 130 件申請中選出 12 名，其中葉永烜與季昀教授都是第二次獲獎，獲頒終身榮譽國家講座。教育部長吳思華致詞時提到，評選門檻嚴格，獲選的都是經層層審查後脫穎而出的優秀學者。

代表國家講座主持人獎致詞的葉永烜教授，出生澳門、臺灣長大，赴美求學離臺 50 年後再度落腳臺灣，鑽研天文已 30 年，獲美國太空總署頒發榮譽勳章的他，曾利用鹿林天文臺望遠鏡，進行大型巡天觀察，讓臺灣在時域天文研究也佔一席之地。

葉教授致詞時將相對論的公式解釋為「 Earth = Multiple Cultures and Civilizations」，他說，地球必須讓多種不同的文化和文明和諧相處、寬容待人，才得以永續發展；他也引述 2015 年諾貝爾文學獎得主斯維拉娜·亞歷塞維的發言，「有些國家為了選擇變得強大而拋棄自身價值。」藉此勉勵台灣能堅持自身價值而變得強大。

「成功的教育不是只讓前 10%能發揮所長，而是後面 10%也能夠發揮所長。」曾任中央大學副校長的葉教授也十分關心教育，他認為少子化不一定是危機，將其視為轉機，反而能藉此提高台灣高教品質。

國家講座主持人獲獎者為國立中央大學葉永烜教授、清華大學季昀教授、宋信文教授、江安世教授及國立臺灣大學郭光宇教授、高嘉宏教授及陳銘憲教授。

學術獎得獎人 12 名為中央研究院林滿紅研究員、吳素幸研究員、陳瑞華研究員及黃柏壽研究員，國立交通大學馮品佳教授、國立中央大學阮啟弘教授、國

立臺灣大學李瑩英教授、傅立成教授及廖婉君教授，國立清華大學果尚志教授及陳信龍教授，國防醫學院司徒惠康教授。

原文轉載自【2015-12-21/台灣醒報】

相關連結 / https://anntw.com/articles/20151221-90eR

2015/12/21 【聯合晚報】

葉永烜：成功教育，是讓後 10%的人也能發揮所長

記者鄭語謙／台北報導

教育部今天頒發國家講座及學術獎，馬英九總統致詞時表示表示，政府一向重視學術研究，除了邁頂計畫等多項補助，也積極推動人才培育等；學術研究是國家生存命脈，未來會繼續提供經費、人力等資源給學者，讓國家不斷向前。

由於日前馬總統在視察生技園區工程時因當著中研院長翁啟惠的面批評工程落後，引發各界不少正反意見，馬總統上午的談話，格外受人注意。

馬總統、行政院長毛治國今天出席頒獎，教育部長吳思華表示，國家講座主持人為國內學術界最高榮譽，今年有七人獲得，包括清大教授季昀、江安世、宋世文，台大教授郭光宇、高嘉宏、陳銘憲，及中央大學教授葉永烜，每人每年有 100 萬元連續三年共 300 萬元，季昀、葉永烜都是二度獲國家講座。

二度獲得國家講座的中央大學天文所教授葉永烜，大學就投入物理基礎研究的他，對時下不少年輕人只想念有社會競爭力的科系，忽視基礎科學感到憂心；他認為，研究還是要和興趣結合，不因大環境影響就放棄初衷；他強調成功的教育，不是讓前 10%的人發揮所長，而是讓後面 10%的人也能發揮所長。

葉永烜是國際聞名的天文學家，他 1982 年向歐洲太空總署（ESA）、美國太空總署（NASA）提出的「卡西尼探測土星」計畫，總預算高達 30 億美元，成功將探測船送上土星，當時是美國太空史上最貴的計畫之一，他擔任共同主持

人。這項原本不被大家看好的太空計畫，發現土星最大衛星土衛六「泰坦」存在生命跡象，NASA 還主動將研究從 2008 年延至 2017 年。

葉永烜大學讀的是物理，看了太空研究書籍後傾心天文，研究所改研究太陽系起源當初說。他說，自己肩負全人類的夢想，連晚上也不浪費時間，總是看著星空推敲理論。

對教育部舉辦的高中職青年論壇中，有高中生說，因為社會組被認為就業缺乏競爭力，即使有興趣也不敢選，只能硬著頭皮念自然組。葉永烜表示，想念社會組是非常好的選擇，「有興趣比較重要」，就像他當初大學念物理，研究所時發現天文更有吸引力，扎實的基礎研究讓他有了後來的成果。

來自澳門的葉永烜有感而發說，2030 年台灣 25 歲的年輕人中，將有 13%是新住民第二代，大學國際化也會大幅改變高教面貌，這是社會進步的主要動力，教育若要成功，就要利用這波少子化促進教育品質，讓新一代成為精英中的精英。

他強調，「成功的教育，不是使前面 10%的學生發揮所長，而是讓也要讓後面 10%的學生也能發揮所長」，不管大學排名提升多少，台灣教育應培養年輕一代，讓多元文化和諧相處。

原文轉載自【2015-12-21/聯合晚報】

相關連結 / http://udn.com/news/story/6886/1391403-%E8%91%89%E6%B0%B8%E7%83%9C%EF%BC%9A%E6%88%90%E5%8A%9F%E6%95%99%E8%82%B2%EF%BC%8C%E6%98%AF%E8%AE%93%E5%BE%8C10%EF%BC%85%E7%9A%84%E4%BA%BA%E4%B9%9F%E8%83%BD%E7%99%BC%E6%8F%AE%E6%89%80%E9%95%B7

2015/11/27 【中央社】

天文迷注意 卡塔利納彗星 12 月肉眼看得到

（中央社記者黃麗芸台北 27 日電）台北市立天文館今天表示，卡塔利納（Catalina）彗星從今年底到明年初將成為肉眼可見彗星，日前還被中央大學鹿林天文台團隊捕捉到其身影，天文迷 12 月上旬後可把握機會。

天文館說，卡塔利納彗星目前於日出前會出現在東方低空，亮度接近 6 星等；同時，中央大學鹿林天文台團隊日前也捕捉到其身影，從畫面中間可看到彗髮及朝向左下方的彗尾。

天文館指出，到 12 月上旬後，彗星位置將漸高且較易觀察，亮度預計將達到 4 至 5 星等，成為肉眼可見的彗星，12 月底到達牧夫座，之後朝向大熊、小熊座方向前進。

此外，有興趣的民眾不妨早起用雙筒望遠鏡找尋彗星身影，在無光害處肉眼可見，彗星亮度將維持到明年 1 月中旬後才逐漸下降。

天文館表示，C/2013 US10 卡塔利納（Catalina）彗星是 2013 年 10 月 31 日被卡塔利納巡天計畫的 0.68 公尺望遠鏡所發現，屬於非週期彗星。其在今年 11 月 15 日以距離 1 億 2000 萬公里通過近日點後，於 2016 年 1 月 17 日將以 1 億 1000 萬公里距離掠過地球。

原文轉載自【2015-11-27/中央通訊社】

相關連結 / http://www.cna.com.tw/news/aloc/201511270209-1.aspx

2015/11/10 【聯合報】

季昀、葉永烜 獲終身榮譽國家講座

教育部昨公布第 19 屆國家講座主持人得主，清大特聘講座教授季昀和中央大學天文所教授葉永烜兩度得獎，晉升為終身榮譽講座。

季昀自稱「笨牛型學者」，運用有機分子作為發光材料及研究染敏太陽能電池，不斷失敗換得成功。國際知名天文學家葉永烜，研究之餘也很會畫畫，作品一、兩百幅，還曾賣出一、兩幅。

季昀研究有機發光二極體（OLED）和染敏太陽電池。他表示，現在的日光燈發光效率不佳，且具有不環保的材料如水銀，因此研究如何用有機分子作為發光材料。經上百次失敗，才找到更適合的有機分子，可提升現有的 OLED 效能，目前已運用在智慧型手機螢幕。

發表近 300 篇學術論文的季昀，總論文引用次數破萬次；OLED 等 3 項技術領域獲多項國內外新發明專利；OLED 材料研發也已成功讓售台灣、及美加共 13 件，在化學領域具領先地位。

葉永烜在太空及行星科學領域，是華人世界登上國際頂尖期刊「Nature」、「Science」論文篇數最多的學者。他參與露西達彗星探測計畫，同時也是卡西尼土星計畫的共同主持人；並和加州理工學院天文台合作，利用鹿林天文台望遠鏡，研究太陽系中小物體及變星。

葉永烜從小愛畫畫，30 歲到德國工作時又重新學畫，至今「一手做研究，另一手畫畫。」他表示，研究和畫畫不衝突，有空就會畫油畫，以風景和人文為主。

原文轉載自【2015-11-10/聯合新聞網/聯合報】

相關連結 / http://udn.com/news/story/6886/1303759-%E5%AD%A3%E6%98%80%E3%80%81%E8%91%89%E6%B0%B8%E7%83%9C-%E7%8D%B2%E7%B5%82%E8%BA%AB%E6%A6%AE%E8%AD%BD%E5%9C%8B%E5%AE%B6%E8%AC%9B%E5%BA%A7

2015/11/09 【聯合晚報】

探索星空夜不眠　葉永烜晉升終身榮譽講座

教育部今天公布第 19 屆國家講座得主，中央大學教授葉永烜二度得獎，晉升終身榮譽講座。葉永烜是國際聞名的天文學家，他說自己肩負人類的夢想，即使晚上睡覺，也仰望星空推敲理論。

葉永烜研究外太空 30 年。他大學讀的是物理，看了太空研究書籍後傾心天文，研究所改研究太陽系起源，有逾 40 篇研究論文登《Nature》和《Science》期刊，為華人之最。

1982 年，葉永烜年向歐洲太空總署（ESA）與美國太空總署（NASA）提出名為「卡西尼探測土星」送探測船上土星的計畫，總預算高達 30 億美元，是美國太空史上最貴的計畫之一，他是共同主持人。原不被大家看好的計畫，憑葉永烜的膽識與遠見，才發現土星最大衛星土衛六，也就是「泰坦」存在生命跡象，因卡西尼號成功發射且成效顯著，NASA 主動將研究從 2008 年延至 2017 年。

葉永烜說，人類一直希望了解在宇宙間存在的價值，以及其他星球是否有生命；他肩負全人類的夢想，晚上睡覺也不浪費時間，總是看著星空推敲理論。

出生澳門，在台灣長大，後來赴美求學，娶台灣太太的葉永烜說，對台灣有割捨不了的情感，決定在離台 50 年後回台任教。

原文轉載自【2015-11-09/聯合新聞網/聯合報】

相關連結 / http://udn.com/news/story/6886/1302831-%E6%8E%A2%E7%B4%A2%E6%98%9F%E7%A9%BA%E5%A4%9C%E4%B8%8D%E7%9C%A0-%E5%A4%AE%E5%A4%A7%E8%91%89%E6%B0%B8%E7%83%9C%E6%99%89%E5%8D%87%E7%B5%82%E8%BA%AB%E6%A6%AE%E8%AD%BD%E8%AC%9B%E5%BA%A7

2015/11/09 【中央社】

7 學者獲國家講座　2 人晉終身榮譽講座

（中央社記者許秩維台北 9 日電）教育部今天公布第 19 屆國家講座主持人名單，共 7 位學者獲選，而第 2 度獲獎的中央大學教授葉永烜和清華大學教授季昀則晉升為終身榮譽國家講座。

為獎勵學術研究，教育部設置國家講座及學術獎，包括人文及藝術、社會科學、數學及自然科學、生物及醫農科學、工程及應用科學等 5 類科，國家講座設置期限為 3 年，教育部每年獎助新台幣 100 萬元，學術獎得獎人則獲頒榮譽證書及 60 萬元，第二次獲任國家講座者為終身榮譽國家講座。

教育部今天公布第 19 屆國家講座主持人暨第 59 屆學術獎得獎人名單，共有 7 人獲選國家講座，其中中央大學教授葉永烜和清華大學教授季昀都是第 2 度獲獎，因此晉升為終身榮譽國家講座。

中央大學天文所教授葉永烜在彗星、行星、太空物理等研究有傑出貢獻，他因為參與露西達彗星探測計畫，同時也是卡西尼土星計畫的共同主持人，因此能直接獲得新觀測資料，他也和加州理工學院（Caltech）天文台合作，利用鹿林天文台望遠鏡，針對太陽系中小物體以及變星做研究。

澳門出生長大的葉永烜，大學念物理系，某天晚間到書店看書，被書上的太空研究吸引，開始對太空產生興趣。前往美國攻讀學位時，原本研究所要念電漿物理，最後跟著指導教授研究太陽系起源。葉永烜笑說，「是無意中走進太空世界」。

葉永烜表示，過去一、二十年天文研究發展神速，已從哲學變成科學，現在科學家對太陽系結構有更多瞭解，還希望進一步認識和地球相似的太陽系外行星，而從事天文研究的科學家就像背負全人類的夢想，目標就是瞭解人類的起源和過去。

清華大學化學系教授季昀致力於研究有機發光二極體和染敏太陽電池。季昀表示，全球都在研究如何用有機分子取代汞、水銀等做為發光材料，自己歷經一次次失敗，才找到更適合的有機分子，助現有有機發光二極體提升效能，未來可運用在智慧型手機螢幕。

季昀表示，自己是笨牛型學者，總是一步一腳印做研究，雖然付出未必一定會成功，但若能從中得到經驗，作為下一次研究的改善基礎，經過不斷地努力，就有機會成功。

原文轉載自【2015-11-09/中央通訊社】

相關連結 http://www.cna.com.tw/news/ahel/201511090124-1.aspx

2015/11/09 【中央日報】

台灣/七學者獲國家講座　二人晉終身榮譽講座

教育部今天公布第 19 屆國家講座主持人名單，共 7 位學者獲選，而第 2 度獲獎的中央大學教授葉永烜和清華大學教授季昀則晉升為終身榮譽國家講座。

為獎勵學術研究，教育部設置國家講座及學術獎，包括人文及藝術、社會科學、數學及自然科學、生物及醫農科學、工程及應用科學等 5 類科，國家講座設置期限為 3 年，教育部每年獎助新台幣 100 萬元，學術獎得獎人則獲頒榮譽證書及 60 萬元，第二次獲任國家講座者為終身榮譽國家講座。

中央社台北 9 日電，教育部今天公布第 19 屆國家講座主持人暨第 59 屆學術獎得獎人名單，共有 7 人獲選國家講座，其中中央大學教授葉永烜和清華大學教授季昀都是第 2 度獲獎，因此晉升為終身榮譽國家講座。

中央大學天文所教授葉永烜在彗星、行星、太空物理等研究有傑出貢獻，他因為參與露西達彗星探測計畫，同時也是卡西尼土星計畫的共同主持人，因此能直接獲得新觀測資料，他也和加州理工學院（Caltech）天文台合作，利用鹿林天文台望遠鏡，針對太陽系中小物體以及變星做研究。

澳門出生長大的葉永烜，大學念物理系，某天晚間到書店看書，被書上的太空研究吸引，開始對太空產生興趣。前往美國攻讀學位時，原本研究所要念電漿物理，最後跟著指導教授研究太陽系起源。葉永烜笑說，「是無意中走進太空世界」。

葉永烜表示，過去一、二十年天文研究發展神速，已從哲學變成科學，現在科學家對太陽系結構有更多瞭解，還希望進一步認識和地球相似的太陽系外行星，而從事天文研究的科學家就像背負全人類的夢想，目標就是瞭解人類的起源和過去。

清華大學化學系教授季昀致力於研究有機發光二極體和染敏太陽電池。季昀表示，全球都在研究如何用有機分子取代汞、水銀等做為發光材料，自己歷經一次次失敗，才找到更適合的有機分子，助現有有機發光二極體提升效能，未來可運用在智慧型手機螢幕。

季昀表示，自己是笨牛型學者，總是一步一腳印做研究，雖然付出未必一定會成功，但若能從中得到經驗，作為下一次研究的改善基礎，經過不斷地努力，就有機會成功。

原文轉載自【2015-11-09/中央日報】

相關連結
http://www.cdnews.com.tw/cdnews_site/docDetail.jsp?coluid=121&docid=103446264

2015/10/01 【ETtoday 東森新聞雲】

中央大學團隊發現最年輕的棕矮星！距離太陽 400 光年

生活中心／綜合報導

中央大學天文所博士後研究員姜博識和指導教授陳文屏，利用大型紅外線望遠鏡，在距離太陽 400 光年之處，發現了年齡僅百萬年，而表面溫度不到攝氏 600 度的「棕矮星」！研究登上國際期刊「天文物理通訊（Astrophysical Journal Letters）」。

研究團隊表示，目前已知的數百個棕矮星，都位於距離太陽數十光年之內，最年輕者也已經形成一億年。棕矮星能點燃氘（氫的同位素）或是鋰元素，但短暫發光後，就如行星般逐漸冷卻，亮度變暗，只有在太陽附近才能被大型望遠鏡觀測到。由於棕矮星的亮度不高，觀測困難，直到近十幾年內因為儀器技術進步，得以發現此類天體，但仍然不清楚它是如何形成。理論上，剛誕生的棕矮星比較溫熱而明亮，但是太陽周圍卻沒有觀測到這樣年輕的星體。

姜博識表示，棕矮星的溫度低，所以它的大氣當中可以存在水與一氧化碳等分子，而溫度最冷的棕矮星以及行星則有甲烷，我們研究如何能有效挑選出有甲烷而低溫的天體。

研究搜尋的區域鎖定在蛇夫座方向的恆星形成區域（ρ Ophiuchi），距離太陽約 400 光年處，當中的恆星大約在一、兩百萬年前形成。陳文屏解釋，「我們在恆星形成區裡面找，就能確定找到的棕矮星很年輕，以便比較不同質量的天體剛誕生的情形」，而這次找到的兩顆星體，編號分別為 Oph-T03 以及 Oph-T17。

中大天文所的團隊與其他國家學者合作，利用位於美國夏威夷、口徑四公尺的「加法夏望遠鏡」取得紅外波段影像，在數萬個天體中去蕪存菁，挑選出具有甲烷特性的候選星。接著使用位於智利、口徑八公尺的「雙子星望遠鏡」取得驗證光譜，成功發現目前最年輕、溫度最低的棕矮星。

原文轉載自【2015-10-01/ETtoday 東森新聞雲>生活>校園】

相關連結 http://www.ettoday.net/news/20151001/573062.htm

2015/10/01 【Nownews 今日新聞】

中央大學科學家　發現最年輕棕矮星

天體「棕矮星（brown dwarf）」的質量介於恆星與行星之間，但由於光度黯淡較難發現。中央大學天文所博士後研究員姜博識以及指導教授陳文屏，利用大型紅外線望遠鏡，在距離太陽 400 光年之處，發現了年齡僅百萬年，而表面溫度不到攝氏 600 度的棕矮星！

中大天文所團隊與其他國家學者合作，利用位於美國夏威夷、口徑 4 公尺的「加法夏望遠鏡」取得紅外波段影像，在數萬個天體中去蕪存菁，挑選出具有甲烷特性的候選星。接著使用位於智利、口徑 8 公尺的「雙子星望遠鏡」取得驗證光譜，成功發現目前最年輕、溫度最低的棕矮星，這次找到的 2 顆星體，編號分別為 Oph-T03 以及 Oph-T17。

目前已知的數百個棕矮星，都位於距離太陽數 10 光年內，最年輕者也已經形成 1 億年，棕矮星能點燃氘或鋰元素，但短暫發光後，就如行星般逐漸冷卻，亮度變暗，只有在太陽附近才能被大型望遠鏡觀測到。

相關研究論文刊載於最新一期《天文物理通訊（Astrophysical Journal Letters）》期刊，陳文屏表示這是很有影響力的發現成果，對於這種既非恆星、也不是典型行星的神秘天體，棕矮星提供有關天體誕生與早期演化的關鍵樣本，甚至能幫助科學家推測系外行星的神秘面貌。

原文轉載自【2015-10-01/Nownews 今日新聞】

相關連結 http://www.nownews.com/n/2015/10/01/1831420

2015/10/01 【中央日報】

台灣/中央大學發現最年輕棕矮星　登國際期刊

中央大學天文所團隊利用大型紅外線望遠鏡，在距太陽 400 光年之處，發現最年輕的棕矮星，有助於科學家推測系外行星的神秘面貌，研究登上國期刊。

中央大學天文研究所博士後研究員姜博識和指導教授陳文屏，利用大型紅外線望遠鏡發現年齡僅百萬年，表面溫度不到攝氏 600 度的棕矮星，研究論文刊載於最新一期「天文物理通訊（Astrophysical Journal Letters）」國際期刊。

研究團隊表示，目前已知的數百個棕矮星，都位於距離太陽數十光年內，最年輕者也已形成一億年，由於棕矮星能點燃氘（氫的同位素）或鋰元素，但短暫發光後，就如行星般逐漸冷卻，亮度變暗，只有在太陽附近才能被大型望遠鏡觀測到。

根據中央社 1 日報導，姜博識表示，棕矮星的溫度低，所以它的大氣當中，可以存在水與一氧化碳等分子，而溫度最冷的棕矮星和行星則有甲烷，因此團隊

也針對如何有效挑選出有甲烷而低溫的天體進行研究，並鎖定在蛇夫座方向的恆星形成區域。

研究團隊和其他國家學者合作，利用位於美國夏威夷的「加法夏望遠鏡」取得紅外波段影像，從數萬個天體中挑選具甲烷特性的候選星，再使用位於智利的「雙子星望遠鏡」取得驗證光譜，成功在距離太陽約 400 光年處，發現目前最年輕、溫度最低的棕矮星。

陳文屏說，對於既非恆星、也不是典型行星的神秘天體，棕矮星能提供有關天體誕生與早期演化的關鍵樣本，甚至有助於幫助科學家推測系外行星的神秘面貌。（李漢揚編）

原文轉載自【2015-10-01/中央日報】

相關連結

http://www.cdnews.com.tw/cdnews_site/docDetail.jsp?coluid=121&docid=103395435

2015/10/01 【中央社】

中大發現最年輕棕矮星 助揭外行星面貌

（中央社記者許秩維台北 1 日電）

中央大學天文所團隊利用大型紅外線望遠鏡，在距太陽 400 光年之處，發現最年輕的棕矮星，有助於科學家推測系外行星的神秘面貌，研究登上國際期刊。

中央大學天文研究所博士後研究員姜博識和指導教授陳文屏，利用大型紅外線望遠鏡發現年齡僅百萬年，表面溫度不到攝氏 600 度的棕矮星，研究論文刊載於最新一期「天文物理通訊（Astrophysical Journal Letters）」國際期刊。

研究團隊表示，目前已知的數百個棕矮星，都位於距離太陽數十光年內，最年輕者也已形成一億年，由於棕矮星能點燃氘（氫的同位素）或鋰元素，但短暫

發光後，就如行星般逐漸冷卻，亮度變暗，只有在太陽附近才能被大型望遠鏡觀測到。

姜博識表示，棕矮星的溫度低，所以它的大氣當中，可以存在水與一氧化碳等分子，而溫度最冷的棕矮星和行星則有甲烷，因此團隊也針對如何有效挑選出有甲烷而低溫的天體進行研究，並鎖定在蛇夫座方向的恆星形成區域。

研究團隊和其他國家學者合作，利用位於美國夏威夷的「加法夏望遠鏡」取得紅外波段影像，從數萬個天體中挑選具甲烷特性的候選星，再使用位於智利的「雙子星望遠鏡」取得驗證光譜，成功在距離太陽約 400 光年處，發現目前最年輕、溫度最低的棕矮星。

陳文屏說，對於既非恆星、也不是典型行星的神秘天體，棕矮星能提供有關天體誕生與早期演化的關鍵樣本，甚至有助於幫助科學家推測系外行星的神秘面貌。

原文轉載自【2015-10-01/中央通訊社】

相關連結 / http://www.cna.com.tw/news/aedu/201510010254-1.aspx

2015/10/01 【自由時報】

中央大學發現最年輕棕矮星 距離太陽 **400** 光年

〔記者湯佳玲／台北報導〕

質量介於恆星與行星之間的「棕矮星」由於光度黯淡難以發現，國立中央大學天文所姜博識博士後研究員與指導教授陳文屏，利用大型紅外線望遠鏡找出甲烷候選星，進一步在距離太陽 400 光年之處，發現了年齡僅百萬年，而表面溫度不到攝氏 600 度的棕矮星！

中大天文所所長陳文屏表示，棕矮星是一團氣體，無法自行發光，只能在太陽附近看得到，觀測相當困難。目前已知數百個棕矮星都位於距離太陽數十光年之內，最年輕者也已經形成一億年。

姜博識表示，棕矮星的溫度低，所以它的大氣當中可以存在水與一氧化碳等分子，而溫度最冷的棕矮星則有甲烷，因此先挑選出具甲烷特性的天體再進一步驗證。

陳文屏表示，中大天文所團隊與其他國家學者合作，先利用位於美國夏威夷、口徑四公尺的「加法夏望遠鏡」取得紅外波段影像，利用光譜差別在數萬個天體中挑選出三十個具有甲烷特性的候選星，再使用位於智利、口徑八公尺的「雙子星望遠鏡」取得驗證光譜，成功發現蛇夫座方向的恆星形成區域（ρ Ophiuchi），距離太陽約 400 光年處最年輕的兩顆棕矮星，編號分別為 Oph-T03 以及 Oph-T17。

這篇研究論文刊載於最新一期《天文物理通訊（Astrophysical Journal Letters）》期刊，提供有關天體誕生與早期演化的關鍵樣本，甚至能幫助科學家推測系外行星的神秘面貌。

原文轉載自【2015-10-01/自由時報】

相關連結 / http://news.ltn.com.tw/news/life/breakingnews/1462234

2015/09/12 【蓄新聞】

王思元教授訪台演講　探索太陽系外的行星世界

記者葉志成／桃園報導

由國立中央大學與台達電子文教基金會共同頒發的「年輕天文學者講座」，2015 年秋季獲獎者為瑞士伯恩大學（University of Bern）的王思元（Kevin Heng）教授。九月八日由中央大學周景揚校長頒贈獎座，表彰其在天文學領域

的卓越表現。訪台期間，王教授將分別於中央大學、台達電子公司、中央研究院，以及台中一中演講，介紹太陽系外的行星世界。

王思元教授為生於新加坡之華人，大學畢業後前往美國，獲得科羅拉多天文物理博士學位，目前為伯恩大學教授，任職於該校 Center for Space and Habitability（太空和適居性中心），專長為行星大氣。

「年輕天文學者講座」旨在表彰國際上在天文學領域有卓越表現之年輕學者，邀請具潛力的學術菁英來台與國內學界互動，並啟發年輕心靈。講座獎金由台達電子文教基金會提供，國際甄選委員會推薦候選人，並由中央大學天文所執行邀訪活動。獲獎者除了發表學術演講，與國內學者進行交流，另進行科普演講，讓民眾與學生接觸最前端的天文課題，且能透過與講者互動景仰學術風範。

今年秋季的「年輕天文學者講座」主題將介紹系外行星的世界，尤其是這些天體的大氣層。太空中的雲氣與塵埃聚集，萬有引力壓擠造成中央區域溫度升高而形成太陽，環繞在周圍的物質則凝聚成行星。太陽系當中的八顆行星各有風貌，其中地球的體積以及與太陽的距離皆適中，提供適合生命蓬勃發展的環境。太陽系當中，也有別的行星或衛星擁有各式地質、大氣層，或海洋。地球科學不再侷限於地球，我們要瞭解火星的地質、金星的大氣，或是木衛三地層之下可能的海洋是什麼模樣。地球依然特殊，但不再唯一。

十幾年前雖然理論上認為很多恆星周圍應該有行星，但囿於觀測技術，沒有偵測到太陽系以外的行星，當時提到行星，不必畫蛇添足，說「太陽系的行星」。時至今日，已經在超過數千顆恆星周圍發現行星，這些「系外行星」有些像木星般，為氣體組成的龐然大物；有些如地球般，有岩石的表面。天外的世界，充滿各式可能。

王思元教授在台演講：（1）9 月 10 日（週四）14：00，中央大學天文所（健雄館 1013 室）學術演講，講題為”Exoplanetary Atmospheres in Eras”，同樣題目另將於 9 月 14 日 14：20 於中央研究院天文與天文物理研究所（ASMAB 1203 室）舉行；（2）9 月 11 日（週五）14：00，在台達電子台北總公司（台北市內湖路陽光街 256 號），講題”The Next Great Exoplanet Hunt”，介紹下一代系外行星搜尋；（3）9 月 12 日（週六）9：00，在台中一中（台中市育才街 2 號）演講”Exoplanets and the Search for Life Elsewhere”，並分享其治學態度和理念，以期開啟青年學子寬廣的視野；（4）9 月 15 日（週二）

13:00，中央研究院天文與天文物理所學術演講"The Exoclimates Simulation Platform"。所有演講將以英文進行，其中兩場科普演講現場提供中文講解。

原文轉載自【2015/09/12 蕃新聞/即時/台灣好新聞/地方/桃竹苗】

相關連結 http://n.yam.com/taiwanhot/place/20150911/20150911271239.html

---

2015/07/29 【東網】

中央大學發現小行星　命名「台中」

來自星星的榮耀！國立中央大學鹿林天文台觀測員林啟生與葉泉志，2008 年合作執行「鹿林巡天計畫」觀測任務，找到未被發現的一顆小行星，確認繞日運行軌道特性，小行星擁有永久編號 300892，林啟生今天（28 日）將這顆命名為「台中」的小行星捐給台中市，市長林佳龍欣喜的說，要讓台中成為「星球城市」。

投入天文觀察 30 多年的林啟生表示，「台中」小行星於 2012 年 2 月正式獲得國際天文聯合會小天體命名委員會（IAU CSBN）審核通過，「台中」小行星位在火星與木星之間的主帶小行星內，大小粗估約 4 公里左右，屬於低亮度，無法透過一般用的望遠鏡看見，必須使用鹿林天文台的 1 公尺望遠鏡加上相機才能勉強拍到它的蹤影，相當珍貴。

「台中」小行星由林啟生和 2008 年在廣州就讀中山大學的學生葉泉志一起發現，2011 年由林啟生提出命名，2012 年初獲國際天文聯合會小天體命名委員會，從此天空中多了一顆「台中」的小行星。

林啟生說，中央大學鹿林天文台共發現 800 多顆行星，他發現其中的 200 多顆，目前有 40 顆行星通過命名，「台中」小行星從每 14 到 16 個月離地球接近，可以利用高倍望遠鏡觀測到，觀測月份以 2、3 月到 11 月底。

林佳龍稱讚林啟生的觀星成果，讓台中人同享榮耀，在浩瀚的天空，每顆星星都很渺少，卻能發光發亮，今天晚間 8 點「台中」小行星將出現在台中市東南方天空的人馬座方向，接近冬至點的銀河中，這是它近期最接近台灣的距離。「台中市是星球城市、宇宙城市！」林佳龍向市民正式介紹這顆與台中連接的小星星，期待引發市民探索天文學的興趣，也會在各級學校推廣天文教育。

台中市天文學會理事長呂其潤說，「台中」行星，讓台中的榮耀飛上太空，登入宇宙的一部份，21 世紀人類勢必要往太空發展，「台中」不會在「太空」缺席。

「台中」行星發現者林啟生今天致贈小行星模型給台中市，呂其潤也頒贈命名贈書，由林佳龍代表接受。

目前依台灣城市命名的小行星已有台北、高雄、台南、桃園、嘉義、南投、苗栗等，「台中」小行星的發現，讓台中市加入也「星星」行列。

原文轉載自【2015-07-29/東網/】

相關連結 http://tw.on.cc/tw/bkn/cnt/news/

2015/07/29 【公視新聞】

"台中"不只是城市 也是顆小行星名字

(記者邱植培 彭煥群/ 台中報導)

有一顆新的星取名「台中」！有一名鹿林天文台觀測員 2008 年在太陽系，發現一顆小行星，在確認後，將他命名為「台中」，主要是發現者長期住在台中，對台中很有感情

「台中」現在不只是個台灣的城市，還是顆太陽系小行星，中央大學鹿林天文台觀測員在 2008 年 1 月 28 日，發現太陽系火星與木星之間的小行星群，有顆從未被發現的小行星，發現者將它命名為"台中"。

==中央大學鹿林天文台 觀測員 林啟生==
1984 年來逢甲讀書之後
基本上就長住台中
人是有感情的動物
所以這個是很榮幸
有機會把這個石頭
把它命名台中
這是我命名的動機

小行星"台中"確定軌道取得國際編號後，在 2012 年 2 月通過命名的審核，獲得國際認證，它是一顆直徑約 4 公里、不規則狀的小行星，距離太陽最近距離有 4.1 億公里，而發現人也將它贈送給台中市政府。

==台中市長 林佳龍==
台中可以躍上宇宙
不只是一個國際的城市
而且是在宇宙群星當中
佔有一席之地
這個對於我們推廣天文教育
是很有意義

鹿林天文台表示，這顆小行星每 14~16 個月會繞行地球一周，從現在到 11 月底，將會出現在台中市南方天空的人馬座方向，但因為小行星的體積太小，亮度低，必需要使用專業的天文望遠鏡才能觀察到。

原文轉載自【2015-07-29/公視新聞網 /科技】

相關連結 http://news.pts.org.tw/

2015/07/29 【東森新聞雲】

台中躍上宇宙 新發現小行星名為「台中」

中央大學天文台觀測員林啟生與葉泉志，合作執行「鹿林巡天計畫」觀測任務中，找到過去從未被發現的一顆小行星，確認繞日運行軌道和國際認定後，小行星有了永久編號「300892」，由於林啟生長年住在台中，因此將這顆小行星命名為「台中」，希望和所有市民一同分享「來自星星的榮耀」。

位在火星木星之間大小大約只有 4 公里，因為屬於低亮度無法透過一般望遠鏡看見，必須使用鹿林天文台的望遠鏡加上相機才能勉強拍到它的蹤影，相當珍貴更稀奇的是這顆編號 300892 的小行星它的名字就叫做「台中」。中央大學鹿林天文台觀測員林啟生：「因為我自從 1984 年來逢甲讀書之後，基本上就常駐台中，人是有感情的動物，所以很榮幸把這顆石頭命名為台中，也是我命名的動機。」

林啟生和葉泉志 7 年前合作執行「鹿林巡天計畫」觀測任務，找到過去從沒被發現的一顆小行星，發現這顆從不曾問是的小行星到底要怎麼命名，林啟生說因為自己長年待在台中，很喜歡這片土地因此用「台中」來向國際天文聯合會申請，現在審核通過台中從此在天文學留名。台中市長林佳龍：「讓台中可以躍上宇宙，不只是一個國際城市，也是在宇宙群星當中占有一席之地。」

「台中」留名天文學界，台中人都覺得驕傲從 7 月份到 11 月底，透過專業的高倍數望遠鏡觀測民眾可以在台中市南方天空的人馬座方向，接近冬至點的銀河中發現這顆名為台中的小行星，目前依台灣城市命名小行星偶台北、高雄、南投和苗栗，現在右多了「台中」讓台中人也一起加入這個行列。

原文轉載自【2015-07-29/東森新聞雲】

相關連結 http://news.ebc.net.tw/apps/news

2015/07/29 【新唐人】

台灣天文家發現小行星 命名「臺中」

(記者王媛、詹詠茹/臺灣臺中報導)

很多民眾到晚上會賞月看星星，不過，你知道天上有一顆叫做「臺中」的星星嗎？台灣中央大學鹿林天文觀測家林啟生，因為對臺中的熱愛，將他發現的一顆小行星命名為「臺中」，並且通過了國際天文聯合會的認可。

浩瀚的宇宙，無數的星空，這顆小行星出現在人馬座，南方的夜空裡，而發現他的是，鹿林天文臺觀測員林啟生與葉泉志，並將這顆小行星命名為「臺中」。

中央大學鹿林天文臺觀測員林啟生：「1984 年來逢甲讀書之後，基本上就長住臺中，那人是有感情的動物，所以這個是很榮幸，這顆石頭把它命名為臺中，這是我命名的動機」

居住臺中 30 年，對臺中有一份情感，因此將小行星命名臺中。

中央大學鹿林天文臺觀測員林啟生：「軌道確認了，知道他怎麼跑，我們終於拿到編號，編號就是 300892」

有了自己的永久編號，「臺中」小行星正式獲得國際天文聯合會認可。約 4 公里的直徑，繞太陽一圈需五年半的時間，今天跟明天，晚上六點四十分，將離台灣最近，出現在月亮南邊，林啟生表示，臺中小行星亮度很低，需使用一公尺望遠鏡加上相機，才能捕捉得到。

中央大學鹿林天文臺觀測員林啟生：「這個小行星，對我們望遠鏡是非常暗的，那就是我們一般望遠鏡是沒辦法去觀測到跟拍到」

目前依台灣城市命名的小行星，包括臺北、高雄、臺南、桃園、嘉義、南投，苗栗，「臺中」小行星的發現，讓臺中群星當中占有一席之地。

臺中市長林佳龍：「這對我們推廣天文教育是很有意義，所以我們會把這樣一個命名。今天受贈，我會把他，把它反映到我們未來的教育的課程，也希望跟天文學多多合作」

林佳龍開心表示，相信「臺中」小行星的發現，引發更多市民探索天文的興趣。

原文轉載自【2015-07-29/ 新唐人/首頁 / 視頻節目 / 新聞視頻 / 環球直擊 / 環球直擊新聞】

相關連結 http://www.ntdtv.com/xtr/b5/2015/07/28/a1213619.html

2015/07/29 【新浪新聞】

小行星命名台中 林佳龍：讓台中躍上宇宙

(記者寇世菁/台北報導)

國立中央大學鹿林天文台觀測員林啟生和學生葉泉志，2008 年發現一顆全新小行星，經過軌道確認，獲得永久編號 300892。因為長住台中，決定將小行星命名為台中，市長林佳龍代表接受並感謝讓台中躍上宇宙，在群星中佔有一席之地，11 月前，每晚 6 點 40 分太陽下山後，星星台中就會出現在台中南方天空人馬座方向。

繼台北，高雄，台南等縣市有自己城市名字的小行星後，台中市也加入天文行列。國立中央大學鹿林天文台觀測員林啟生和學生葉泉志，2008 年發現一顆全新小行星，經過幾年軌道確認，獲得永久編號 300892。因為林啟生長住台中，決定將小行星命名為台中，並致贈台中市政府。市長林佳龍代表接受，他說，在浩瀚的天空裡，每顆星星雖然看似渺小卻相當重要，總是努力發光發亮，能在一片雲海裡面找到全新的星球，他感謝林啟生老師發現小行星，還命名為台中，讓台中可以躍上宇宙，在群星中佔有一席之地。

林佳龍指出，未來市府會努力將這份榮耀反映到天文課程中，並和天文學會合作，鼓勵市民探索奧秘的天文領域。他說，到今年 11 月底前，台中小行星約在每晚 6 點 40 分太陽西沉後，出現在台中市南方天空的人馬座方向，歡迎民眾利用天文設備觀賞。

台中小行星的發現者林啟生表示，長住台中超過 30 年，對台中有份感情，因此將小行星命名為台中，並在 2012 年初獲得國際天文聯合會小天體命名委員會（IAU CSBN）審核通過，現在送給台中市政府，希望和大家一起分享這份榮耀。他並與天文協會理事長呂其潤一同將這顆小行星的命名證書及縮小版模型贈予台中市政府，由林佳龍市長代表台中市民接受這份榮耀。

台中小行星位在火星與木星之間的主帶小行星內，直徑約 4 公里，目前亮度只有 21 等多，屬低亮度，無法透過一般用的望遠鏡看見，必須使用鹿林天文台的 1 公尺望遠鏡加上相機，才能勉強拍到它的蹤影，相當珍貴。

原文轉載自【2015-07-29/ 新浪新聞/ 生活消費新聞/ 中廣新聞網】

相關連結 http://news.sina.com.tw/article/20150728/14857023.html

2015/07/29 【聯合新聞網】

他把小行星「台中」 送給台中

(記者程遠/台北報導)

國立中央大學鹿林天文台觀測員林啟生、葉泉志二○○八年發現一顆小行星，林啟生將這顆編號三○○八九二的小行星命名「台中」，獲國際天文聯合會小天體命名委員會認可。昨在台中市府舉行記者會，由市長林佳龍宣布這喜訊。

小行星「台中」的發現，是林啟生團隊在中央大學「鹿林巡天計畫」的成果之一。鹿林巡天計畫至今發現八百多顆小行星，但多數只有編號沒通過命名。

林啟生的團隊在鹿野巡天計畫扮演重要角色，原因是巡天發現的八百多顆小行星，他的團隊就占四分之一有二百多顆；其中兩顆獲國際認可，以「台南」、「歸仁」命名，「台中」是第三顆。

五十二歲的林啟生追星卅多年，拍下破萬張夜空照，到處奔波的追星生活，使他沒時間找對象至今單身；有人笑他根本是把星星當女友，在和星星談戀愛，他笑著承認，「這麼講也對啦。」

林啟生表示，小學時就愛上星空，有時會看這些小光點發呆，感覺不用說話就能交流。大學畢業就開始追星，台灣的高山幾乎都有他觀星足跡；國外最遠曾到澳洲。

「發現一顆星，就是在宇宙中寫下註腳」，林啟生表示，觀測員要在漫長等待中拍下大量照片，並花許多心力整理，但能接近最愛星空「再累也願意」。

台中市天文學會指出，「台中」小行星位於火星和木星間的小行星帶，屬低亮度小行星，能夠看到「機率非常低」；林啟生表示，發現那年剛好離地球最近二億六千萬公里，才捕捉到其身影。

林啟生在二○一一年向國際天文聯合會小天體命名委員會（IAU CSBN）提出命名申請，理由提到「台中是台灣的第三大城市、被稱為文化之都」，審核通過後，遙遠夜空又多了一顆和台灣有連結的小行星。

原文轉載自【2015-07-29/ 聯合新聞網/ 要聞/ 綜合】

相關連結 http://udn.com/news/story/7314/1085588

2015/07/29 【中央廣播電台】

小行星名「台中」 林佳龍：躍上宇宙

中央大學鹿林天文台觀測員林啟生將發現的一顆小行星命名為「台中」，台中市長林佳龍今天(28 日)表示，台中將因此躍上宇宙，在群星之間佔有一席之地。

林啟生與當時在廣州就讀中山大學的學生葉泉志，在 2008 年 1 月 28 日合作執行鹿林巡天的觀測任務中發現這顆小行星，發現時的臨時編號為 2008 BT15，經過幾年的軌道確認，才獲得 300892 的正式編號。

林啟生於 2011 年提出命名「台中」，並於 2012 年初獲得國際天文聯合會小天體命名委員會審核通過，林啟生今天將這顆命名為「台中」的小行星贈送給台中市政府，由林佳龍代表受贈。

林啟生指出，台中小行星位於火星與木星之間的主帶小行星內，大小粗估約直徑 4 公里，屬於低亮度，無法透過一般用的望遠鏡看見，必須使用鹿林天文台的 1 公尺望遠鏡加上相機才能勉強拍到蹤影，到今年 11 月底前，台中小行星在每晚 6 時 40 分太陽下山後，出現在台中市南方天空的人馬座方向。

林佳龍指出，感謝林啟生將小行星命名為台中，讓台中躍上宇宙，在群星之間佔有一席之地，台中很重視天文教育，將反映在教育課程，並鼓勵市民多多接觸天文領域。

目前依台灣城市命名的小行星已有台北、高雄、台南、桃園、嘉義、南投、苗栗等，「台中」小行星的命名，也讓台中市加入宇宙群星行列。

原文轉載自【2015-07-29/中央廣播電台/首頁/新聞頻道/臺灣生活/新聞內頁】

相關連結 http://news.rti.org.tw/news/detail/?recordId=206407

2015/07/28 【聯合財經網】

奧比・薩克思小行星 普照世人 揚名宇宙

(記者曹松清／報導)

為感念唐獎第一屆法治獎得主、前南非憲法法院大法官奧比・薩克思（Albie Sachs）對人權與民治的卓越貢獻，國立中央大學特別將 2006 年所發現的編號 175419 小行星，經國際天文學聯合會(IAU)通過，正式命名為「奧比・薩克思(Albiesachs)」。

奧比・薩克思為國際知名的法學教授、南非解放運動的領袖之一。1988 年因反對種族隔離政策遭到南非政府炸彈攻擊，失去一條手臂和一隻眼睛，他以悲天憫人的胸懷，在斷臂上開出堅毅的花朵，為世人所景仰。

奧比・薩克思一生致力於建立南非的民主和法治，他是南非人權憲章的主要起草人，也是憲法法院的首任大法官之一，15 年的大法官生涯，寫下許多經典的

判決和意見書，並為社會底層人物發聲，在南非憲法法院成就了許多「憲法奇蹟」。

2014 年唐獎首屆法治獎特別授予他，以表彰他對人權及正義做出的重要貢獻。2015 年中央大學歡慶一百週年校慶，在「台灣聯大溫世仁卓越學術講座」經費支持下，邀請到奧比・薩克思蒞校演講，並在其紀錄片「溫柔的復仇」亞洲首映會後舉行座談會。

為感念奧比・薩克思一生的偉大貢獻，中央大學特別將 2006 年發現的編號 175419 小行星命名為「奧比・薩克思」。該小行星由中央大學天文所鹿林天文台觀測助理林啟生與廣東中山大學葉泉志共同發現。發現時在寶瓶座，目前則位在獅子座。初步估計大小約 2~4 公里，繞太陽公轉一圈需時 5.55 年。

中央大學天文所所長高仲明教授表示，要在宇宙蒼穹間發現新星體，一如大海撈針般，誠屬不易，須有專業的判斷和毅力，再經長時間的軌道確認，才能確認是新發現的小行星。台灣中央大學鹿林天文台目前已發現了數百顆小行星，確認軌道的小行星，分別以傑出的科學家、藝術家、音樂家公眾人物來命名，以彰顯其偉大的貢獻。

原文轉載自【2015-07-28/聯合財經網 / 商情 / 產學研訓】

相關連結 http://money.udn.com/money/story/5723/1082354

2015/07/28 【大紀元】

中大感念奧比薩克思 小行星命名通過

(記者徐乃義／桃園報導)

中央大學 2006 年所發現的編號 175419 小行星，經國際天文學聯合會（IAU）通過，正式命名為「奧比・薩克思」（Albiesachs），以感念唐獎第一屆法治獎得主、前南非憲法法院大法官奧比・薩克思（Albie Sachs）對人權與民治之卓越貢獻。

奧比・薩克思是國際知名的法學教授及南非解放運動的領袖之一，1988 年因反對種族隔離政策遭到南非政府炸彈攻擊，失去一條手臂和一隻眼睛。他一生致力於建立南非的民主和法治，是南非人權憲章的主要起草人及憲法法院的首任大法官之一，在南非憲法法院成就許多「憲法奇蹟」。

「奧比・薩克思」小行星是由中央大學天文所鹿林天文台觀測助理林啟生與廣東中山大學葉泉志共同發現，初步估計大小約 2~4 公里，繞太陽公轉一圈需時 5.55 年。

原文轉載自【2015-07-28/大紀元/首頁/要聞】

相關連結 http://www.epochtimes.com.tw/n135322/

2015/07/28 【新浪新聞】

表彰唐獎法治獎得主 中大命名小行星

(記者許秩維／台北報導)

中央大學今天表示，為感念唐獎首屆法治獎得主、前南非憲法法院大法官奧比•薩克思的貢獻，因此將 2006 年發現的編號 175419 小行星，命名為「奧比•薩克思」。

奧比•薩克思（Albie Sachs）為國際知名的法學教授、南非解放運動的領袖之一。1988 年因反對種族隔離政策遭南非政府炸彈攻擊，失去一條手臂和一隻眼睛。他一生致力於建立南非的民主和法治，是南非人權憲章的主要起草人、憲法法院的首任大法官之一，成就許多「憲法奇蹟」。

中央大學表示，2014 年首屆唐獎特別頒授法治獎給奧比•薩克思，表彰他對人權及正義做出的重要貢獻，今年中大歡慶 100 週年校慶，在「台灣聯大溫世仁卓越學術講座」經費支持下，也邀請奧比•薩克思到校演講。

為感念奧比•薩克思的偉大貢獻，中央大學特別將 2006 年發現的編號 175419 小行星命名為「奧比•薩克思」，該小行星是由中央大學天文所鹿林天文台觀測助理林啟生與當時就讀廣東中山大學的學生葉泉志共同發現。

中央大學天文所長高仲明表示，要在宇宙蒼穹間發現新星體，一如大海撈針般，誠屬不易，須有專業的判斷和毅力，再經長時間的軌道確認，才能確認是新發現的小行星。台灣中央大學鹿林天文台目前已發現數百顆小行星，並以傑出的科學家、藝術家、音樂家等人物命名，以彰顯其貢獻。

唐獎教育基金會執行長陳振川也代表中大天文學研究所，在南非開普敦舉行編號 175419 小行星命名為「奧比•薩克思」的贈牌儀式。與會的南非貴賓，也都知道這是相當不尋常的肯定。

駐南非共和國代表處陳忠大使也表示，奧比•薩克思的貢獻，將與以他為名的小行星在宇宙永遠閃爍、恆久，和世界相互輝映。

原文轉載自【2015-07-28/新浪新聞/生活消費新聞/中央社】

相關連結 http://news.sina.com.tw/article/20150727/14849185.html

2015/07/26 【大紀元】

台中央大學發現新行星 取南非大法官名

(大紀元報導)

台灣中央大學 2006 年發現的行星 2006 PN17，決定取名薩克斯，他是唐獎得主及南非首任首席大法官，並請唐獎基金會執行長陳振川 22 日代表中央大學，頒證書給薩克斯。

薩克斯（Albie Sachs）1935 年出生，幼年時隨父母由立陶宛移民南非，1956 年畢業於開普敦大學法律系，隨後留學多國，鑽研法學。

17 歲時，他開始立志為人權奮鬥。1963 至 1964 年間遭到白人政府警察拘留，嚴刑拷打；1966 年遭到羈押收監，被關 5 個多月，釋放後被迫流亡海外，流亡於英國與莫三比克。

1988 年流亡莫三比克時，他因反對南非種族隔離政策，而遭到白人政府派遣特務在他的汽車安置炸彈。所幸躲過死劫，但卻因此失去右手，1 隻眼睛幾乎全盲。

雖遭此不幸，他卻從未放棄為南非人民追求人權的願望。

1994 年新南非誕生，他成為新憲法起草委員會一員。首任總統曼德拉指派他為憲法法庭首任首席大法官。在 15 年大法官生涯中，他與同僚為南非制訂許多獨到且具前瞻性的法律判例。

大法官卸任後，他經常到世界各大學演講，分享南非民主的成就，並希望幫助曾經在歷史中受創的國家癒合傷口。

傑出的法學貢獻讓薩克斯成為台灣唐獎基金會首屆法治獎得主。中央大學為更進一步表彰他讓世人瞭解民主價值、多樣性尊重、社會公正與伸張基本人權的貢獻，特以「175419 艾比薩克斯」（175419 Albiesachs）命名行星。

薩克斯妻子凡妮莎（Vanessa）致詞時表示，她一直都知道丈夫是顆星，並以身為他的妻子為榮，但直到此刻才知道這顆星名字的由來。幽默風趣的話語，充分體現夫妻鶼鰈情深。

原文轉載自【2015-07-26/大紀元/首頁/新聞/科技新聞】

相關連結 http://www.epochtimes.com/b5/15/7/25/n4488530.htm

2015/07/26 【中央社】

中央大學發現新行星 取南非大法官名

(記者徐梅玉/約翰尼斯堡報導)

台灣中央大學 2006 年發現的行星 2006 PN17，決定取名薩克斯，他是唐獎得主及南非首任首席大法官，並請唐獎基金會執行長陳振川 22 日代表中央大學，頒證書給薩克斯。

薩克斯（Albie Sachs）1935 年出生，幼年時隨父母由立陶宛移民南非，1956 年畢業於開普敦大學法律系，隨後留學多國，鑽研法學。

17 歲時，他開始立志為人權奮鬥。1963 至 1964 年間遭到白人政府警察拘留，嚴刑拷打；1966 年遭到羈押收監，被關 5 個多月，釋放後被迫流亡海外，流亡於英國與莫三比克。

1988 年流亡莫三比克時，他因反對南非種族隔離政策，而遭到白人政府派遣特務在他的汽車安置炸彈。所幸躲過死劫，但卻因此失去右手，1 隻眼睛幾乎全盲。

雖遭此不幸，他卻從未放棄為南非人民追求人權的願望。

1994 年新南非誕生，他成為新憲法起草委員會一員。首任總統曼德拉指派他為憲法法庭首任首席大法官。在 15 年大法官生涯中，他與同僚為南非制訂許多獨到且具前瞻性的法律判例。

大法官卸任後，他經常到世界各大學演講，分享南非民主的成就，並希望幫助曾經在歷史中受創的國家癒合傷口。

傑出的法學貢獻讓薩克斯成為台灣唐獎基金會首屆法治獎得主。中央大學為更進一步表彰他讓世人瞭解民主價值、多樣性尊重、社會公正與伸張基本人權的貢獻，特以「175419 艾比薩克斯」（175419 Albiesachs）命名行星。

薩克斯妻子凡妮莎（Vanessa）致詞時表示，她一直都知道丈夫是顆星，並以身為他的妻子為榮，但直到此刻才知道這顆星名字的由來。幽默風趣的話語，充分體現夫妻鶼鰈情深。

原文轉載自【2015-07-26/中央社/首頁/國際焦點】

相關連結 http://www.cna.com.tw/news/aopl/201507250072-1.aspx

2015/07/04 【自由時報】

羅賽塔號彗星研究　中大成果登最新《自然》期刊

〔記者湯佳玲／台北報導〕歐洲太空總署歷經十年飛行的太空船羅賽塔號，去年 8 月順利進入彗星 67P 的軌道。亞洲唯一參與的中央大學，計畫協同主持人天文所葉永烜教授共參與三個科學實驗，他與天文所林忠義博士和地球科學系李睿綺和國際團隊就首批回傳觀測資料作分析，發表彗星凹坑和噴流研究，有助於探索太陽系的生命起源。成果刊登在 7 月 2 日最新一期《Nature》「自然」期刊。

研究發現，遍佈在 67P 彗星表面上的凹坑，與一般小行星上所發現的隕石坑不同，其坑壁陡峭，但底部卻似平坦，直徑從幾十公尺到數百公尺皆有，經拍攝到的高解析影像發現，其深度與直徑大小比值高出一般彗星許多，這可能意謂不同彗星其生成演化的歷史仍有相當程度的差異性。

部分凹坑內有活躍的灰塵噴流噴出，這部分可能與凹坑的形成演化有關。這些凹坑來自於沉洞塌縮，塌縮後所形成凹坑的坑壁，有著初次顯露於地表的水冰物質，這些物質受到太陽加熱揮發，所帶起的灰塵便成為噴流。

中央大學天文所助理研究員林忠義博士表示，彗星是太陽系形成後所留下來的遺跡之一，也是太陽系中改變最少的天體，藉由研究彗星結構中的物理特性，可還原當時原始太陽系形成區域的環境，並且得知太陽系形成的一些線索，有助於探索太陽系的生命起源。

拜羅賽塔號計畫之賜，葉永烜和國際合作團隊今年另有五篇相關論文在「科學《Science》」刊出，主要有關羅塞塔任務的首批影像和光譜觀測結果，其中包括對彗星地形、結構、自轉週期、密度、質量、大小，以及周遭塵埃與氣體環境的測量分析等。

葉永烜表示，彗星 67P 形狀可分為各稱為「頭」和「身體」的二大塊，中間較窄處叫做「頸」部。有趣的是，「頭」和「身體」的紋理方向截然不同，初步地質結構分析指出可能有不同的來源，但仍需進一步的研究。

另外，林忠義博士研究的「彗星初期的噴流與其物理特性」，以及地科系李睿綺研究之「彗星表面上大小石塊分佈與統計」等論文也被國際期刊《天文學及天文物理學》（Astronomy & Astrophysics）所接受。

原文轉載自【2015/07/04 自由時報/生活】

相關連結 http://news.ltn.com.tw/news/life/breakingnews/1367614

2015/02/11 【澳門日報】

培正邀天文學家講星空奧秘

由中國科學技術協會、澳門特區政府主辦，澳門科學技術協進會承辦之“科學家走進校園”活動，邀請到中國著名天文學家、國際宇航科學院院士、台灣中央大學天文所及太空所、澳門科技大學太空科學所葉永烜教授，引領培正師生展開一場精彩的星空探索之旅。

仰望星際，漫步太空，尋找外星人，幾乎是每個人童年時代的夢，總為那玄奧的宇宙而着迷。銀髮滿頭的葉教授，也是在這種與生俱來的好奇心下，孜孜以求星空奧秘。他以“尋找系外行星”為題，與大家談“天”說“地”：介紹了天文學最新的研究趨勢，是探尋“生物圈適居帶”，為人類的永續生存，尋找“第二個地球”。可是，要到太陽系外找行星，談何容易？以如今太空船的運行速度，實在是天方夜譚。所以很多天文學家轉而思考蟲洞理論——蟲洞是宇宙中可能存在的連接兩個不同時空的狹窄隧道。愛因斯坦等科學家在研究引力場方程時假設，認為透過蟲洞可以做瞬間的空間轉移或者做時間旅行。迄今為止，科學家們還沒有觀察到蟲洞存在的證據，一般認為這是由於很難和黑洞相區別。

雖然探索還是起步階段，卻已為人類帶來無限的想象空間，葉教授推薦大家觀看去年拍攝的《星際效應》這部電影，雖有誇張失實的地方，但瑕不掩瑜，這部科幻電影以星際探險的形式，引入不少太空研究前沿的理論，不僅可以擴闊視野、啟發興趣，也誘發我們思考人類的未來。

講座結束，學生圍繞黑洞、霍金、外星人等，踴躍發問，葉教授認真而幽默地解答了大家的疑惑，勉勵大家保持好奇心和求知慾，勇於探尋人類未知的領域。是次出席講座者，還包括中國科學技術協會代表楊書宣、李偉元、宋寧及吳小林。【2015-02-11/澳門日報】

相關連結

https://www.cyberctm.com/newsNote.php?cpid=4&cid=1&nid=86895#.VNqbkvmUeK8

PanSci 科學新聞網
說這專頁讚 · 2013年5月7日 ·

應該有不少朋友們喜歡看 The Big Bang Theory 影集。前幾天有一位眼尖的網友瞄到其中一幕裡，Raj 身後的白板上面有幾個歪歪扭扭的手寫中文字，仔細一看以後發現竟然是我們台灣的中央大學「鹿林天文台」！

關於「鹿林天文台」：http://www.astro.ncu.edu.tw/index.shtml?p=iancu%2Fobsvat%2Flulin%2Findex.html
…… 更多

讚　留言　分享

1,256　人氣留言

901個分享　27則留言

PanSci 科學新聞網 噹噹噹!!! 解謎的時間到啦！根據來自國立中央大學天文研究所的線報指出，他們向 TBBT 節目的科學顧問詢問到黑板上出現鹿林天文台的原因是：由葉泉志先生與鹿林天文台的林宏欽台長發現了一顆小行星，他們將

留言……

瞄到其中一幕裡，Raj 身後的白板上面有幾個歪歪扭扭的手寫中文字，仔細一看以後發現竟然是我們台灣的中央大學「鹿林天文台」<261>

聊天室(10)

天文，追尋真理的浪漫

天文所陳文屏教授專訪

採訪 / 撰文：鍾佳玲、黃思閔

天文，追尋真理的浪漫—天文所陳文屏教授專訪
現職：國立中央大學天文所特聘教授兼天文所所長
學歷：紐約州立大學石溪分校天文博士
專長：觀測天文學、恆星形成
榮譽：97、100、103學年度中央大學特聘教授獎
連結：陳文屏教授個人網頁

從古至今，天文學家常走在時代最前沿。天文學（astronomy）是從人類對宇宙和大自然的好奇心中所誕生的最古老的科學，不僅與天象觀測、物理及幾何等知識緊密相連，也是諸多古文明的文化核心，在每個時代裡扮演著推動人類智慧向前邁進的重要角色，既浪漫又極具挑戰性的特質，正是天文學的魅力所在。

陳文屏教授是臺灣參與國際天文觀測計畫的主持人之一，從1998年起，帶領我國研究團隊接連參與中美掩星計畫及國際泛星計畫，除讓臺灣在國際天文合作中佔有一席之地，也為本校鹿林天文台的發展奠定基礎，也藉此與國外學術單位建立交換學生機制，積極為我國天文領域培養下一代人才菁英。

中美掩星計畫 尋找小行星及彗星的故鄉

中美掩星計畫（Taiwanese American Occultation Survey; 簡稱TAOS）是1992年陳文屏教授至中大任教後，首次的國際合作計畫，由臺灣、美國、韓國共同參與，目的在於利用掩星技術及小型望遠鏡，偵測並清點包含古柏帶天體（Kuiper Belt Objects）以及更遠處的直徑約1公里的小型天體。

在太陽系的內圍，天體成分以金屬及氧化物為主；太陽系外圍天體的成分則以冰體為主，目前的假說認為被大行星拋出的小型冰體，分佈在太陽系以外的廣大球狀區域中，稱為「歐特雲」，Edgeworth及Kuiper兩位學者認為，歐特雲的內層另有扁平的結構，大約與行星所在的黃道面平行，是短週期（小於兩百年）彗星的發源地，這個區域稱為「古柏帶」。

在1990年代，天文學家利用大型光學望遠鏡，陸續在古柏帶區域發現新的天體，證實古柏帶確實存在，成為行星科學近年來的重大突破，原先一些奇特的天體也有了新的認定，例如冥王星被發現其實是個古柏帶天體，因而在2006年被國際天文聯合會從太陽系九大行星中除名的重大天文事件，引發全球的熱烈討論。陳教授表示，這些小天體由於直徑小、亮度低，因此非常不易被偵測，然而其不但保存了早年太陽系生成的訊息，也對早期行星的演化，包括大氣與海洋的形成、生物的起源以及急遽的環境變遷，有極關鍵的影響。

那麼要如何偵測這些小天體呢？陳教授指出，目前唯一的方式就是透過掩星技術，「當彗星掩過恆星時，恆星的亮度瞬間會變暗，稱為掩星現象。藉由監測彗星發生掩星的機率，便能夠推測彗星的數量及大小。」TAOS計畫的內容就是清點這些小型天體的數量，同時進一步估計它們的大小分佈及空間分佈。陳教授坦言，這是一項非常困難的工作，因為掩星現象發生的時間很短，甚至比眨眼的時間還要短，而且發生機率很低，因此必須同時監測上千顆星星，持續數年，才可能有機會偵測到位於古柏帶之小天體對遠處背景恆星造成的掩星現象。

TAOS計畫由我國中央研究院、中央大學，以及美國、韓國等單位參與，一共建置了四座口徑50公分的超廣角望遠鏡，安裝於嘉義鹿林山上的鹿林天文台，也為天文台的系統建置打下基礎。TAOS計畫自2005年開始收集資料，結果並沒有偵測到任何的掩星事件，一方面表示太陽系外圍天體的數量，沒有某些學說估計來得多；另一方面也由於受限於望遠鏡性能及臺灣天氣不佳等因素，因此觀測結果不如預期。

雖然TAOS計畫沒有獲得預期的成果，但陳教授樂觀表示，這項計畫所發展的各項前瞻性技術都是世界第一，在科學上仍深具意義，目前TAOS二期正在墨西哥興建三座口徑1.3公尺的望遠鏡，希望能藉由口徑更大的望遠鏡、速度更快的相機、觀測條件更理想的位址，觀測到足夠的掩星事件，揭開太陽系如何形成的歷史之謎。

國際泛星計畫 提升臺灣天文實力

天文學家所研究的天體及宇宙現象，不論時間或空間，都距離現在的地球十分遙遠，和人們日常生活的關聯性可說是微乎其微，但1994年發生的一件重大天文事件，卻從此改變了這項認知。

1994年7月，被天文學家稱做「珠鍊」的彗星（Shoemaker-Levy9）碎塊陸續地撞上木星，這一撞的威力等同於數百萬噸黃色炸藥，不僅在木星表面造成巨大破壞，也撞出了人類對於彗星不知何時來襲的憂慮，人們意識到，即使宇宙浩瀚無邊，「彗星撞地球」的情節仍有可能真實上演。由於此事攸關人類文明的延續，2005年美國布希總統簽署法案，要求NASA提出可行的規劃，以清點軌道可能與地球相交的近地小行星。

「泛星計畫」（Panoramic Survey Telescope And Rapid Response System; Pan-STARRS）便由此而生，英文名稱直譯為「全天域觀測望遠鏡及快速反應系統」，由夏威夷大學負責建構，口徑1.8 公尺的超廣角望遠鏡，配備新技術開發具備14億個像元之電子數位相機，針對整個天空觀測，單個天區每個月循環好幾次，藉由比對前後的影像，找出亮度或位置有變化的天體，以進行各項科學課題的探討。

泛星計畫為美、德、英與台灣等國參與之大型國際合作，陳文屏教授為我國計畫主持人之一，除了中央大學，其他還有清華大學、台灣大學、台灣師範大學、成功大學，以及中央研究院的學者，主要研究宇宙時變現象。陳教授表示，泛星望遠鏡的最大功能在標認出可能撞擊地球的小行星，該成果與人類文明的延續息息相關，為發現近地小行星最成功的計畫。泛星計畫產生極大資料量，所涵蓋的天空深度、廣度以及時間覆蓋面都前所未有，對觀測天文學產生革命性影響，對象包括古柏帶天體、變星、系外行星、超新星、迦瑪射線源，以及宇宙大尺度研究。

由於事前已預期到巡天觀測的影像拍攝會產生龐大資料，計畫一開始台灣團隊就結合天文與資訊工程學者一同加入國際團隊，針對此計畫之巨量資料建立資料庫，結果十分成功，是成功的跨國且跨領域的合作。暨數位革命後，巨量資料的強大功能在世界上開啟各領域的新紀元，尤其是天文研究，觀測設備隨時都在蒐集宇宙中的各種數據，而要如何在這龐大的資料裡去蕪存菁分析星際間的各種新發現，跨領域的整合顯得格外重要。「計畫整合很重要。」陳教授說，「大量的數據如何儲存、分配、傳輸，要事先規劃好。例如一開始就要與統計學家討論實驗設計，而不是等到數據收集完畢，再找他們商量如何分析。」

泛星計畫成果 全民共享

目前泛星第一期計畫已於2014年執行完畢，所產生的龐大資料預料將會有許多新發現，。令人期待的是，並非只有研究團隊才能拿到第一手資料，陳教授表示，泛星計畫的成果將在2015年底，由美國馬里蘭州的太空望遠鏡研究中心向全世界公開資料，由於資料量非常龐大，要以何種方式公開，成了一項艱鉅的挑戰。

陳教授解釋，美國天文學界對於使用公家經費取得的觀測數據，常規定取得一年後必須對外公開。有些人覺得自己國家花了很多錢，或是團隊費了很多時間建造了儀器，這樣不公平，但長期觀察發現這對整個領域的發展很有幫助，讓學界在更開放的環境中相互競爭，反而有助成長。「相較於其他領域，天文在科教這方面做得比較出色，主要因為宇宙本身吸引人，又有迷人的照片。例如哈伯太空望遠鏡，以及很多大型望遠鏡的影像提供免費使用，結果並沒有讓科學家少做研究，反而在良性競爭當中得到更好的成果，一般民眾也輕易能在網路下載美麗的宇宙天體圖像。」

雖然所有人未來都可使用泛星計畫的資料，但陳教授指出，真正的本事是如何使用數據。台灣的研究團隊從中美掩星計畫，有處理大量資料的經驗，再加上泛星計畫的數據，探討近地天體、超新星，天體運動等，也順勢與加州理工學院合作另一項名為 PTF 的國際計畫，一樣是探討宇宙天體隨時間變化的現象。陳教授的團隊利用泛星計畫尋找銀河系中尚未發現的星團，或是在已知星團中指認出低質量恆星，甚至棕矮星成員，以研究其特性。今年陳教授與博士後研究員姜博識就利用大型紅外線望遠鏡在距離太陽400光年之處，發現了年齡僅百萬年，而表面溫度不到攝氏600度的棕矮星，為天體誕生與早期演化提供了關鍵樣本，也幫助科學家推測系外行星的神秘面貌。

※註：中大天文所團隊發現棕矮星之研究論文刊載於最新一期《天文物理通訊（Astrophysical Journal Letters）》期刊（請參閱中央大學首頁校園新聞：http://www.ncu.edu.tw/campus/article/1729）。

打破疆界 國際合作經驗談

「國際合作在學術界很常見，天文學這個領域更是非常自然，幾乎沒有不合作的。」地球公轉讓大家日夜輪替，有些天文現象需要不同經度的天文台接力觀測。也因為天文是門觀測的學科，需要把觀測設備放在條件好的地點，除了太空，就是地球上高海拔、氣候晴朗的地方，而現代大型設備更需要在資金與技術方面跨國合作，造就了國際合作的必要。

面對國際合作，陳教授表示團隊間的彼此信任非常重要。科學發現當然有其獨享性（只有第一），頂尖的成果常源自激烈的競爭，「一將功成萬骨枯」在科學團隊裡面也是一樣。我們不希望永遠當科學代工，但也不該幻想可以一蹴可及成為超級英雄。陳教授回想合作經驗當中，曾經剛開始小心謹慎，彼此深怕被搶先發表的顧慮，事後發現其實可以探討的課題非常多，關鍵在於如何與同伴既競爭又合作，反而要注意專精而不要貪多。國際合作還能體驗不同文化，尤其需要保持開放的態度。合作需要隊友之間互補，首重溝通，常需要電話會議，來自不同時區的合作者，根本約不到大家都方便的時間，有時候這裡半夜三點鐘，已經精神不濟了，還要費能量解讀不同口音的英文，很是辛苦。

既浪漫又富挑戰性的工作─天文學家

成為天文學家是陳文屏教授從小就確立的目標。他認為天文學家和化學家、物理學家一樣都是科學家，只是研究場域是宇宙，雖然可以研究的題目很多，但因為距離遙遠，常有別於其他領域的挑戰，但樂此不疲。

陳教授坦言，因為天文研究不賺錢，所以一定要有興趣。做為職業天文學家的工作不多，但是跟

其他國家比起來，我國的天文學家數量還是相當不足。一般的物理系，應該都要有天文學家，因為宇宙是個好大的實驗室，有好多值得研究的問題。要成為天文學家，除了在數學、物理、英文等基礎訓練上必須紮實，也要學習與人合作、溝通，培養尋找問題、思索答案的能力。天文所的學生常有機會到國外接受訓練，一方面學習如何做研究，也藉由告訴別人自己的研究內容，來釐清自己的觀念。一定要透過國際合作的舞台，讓學者有實力和全世界競爭。

2002年中央大學安裝在鹿林天文台的一米望遠鏡，是目前台灣最大口徑，提供了師生基本的研究與教學的工具。陳教授認為，受限於台灣的研究社群規模以及天氣條件，不適合建構大型觀測設備，但是可以利用我國現有的望遠鏡，和國際上其他天文台合作觀察具有時間變化的天文現象，另外目前我國中央研究院也透過在夏威夷、智利等地與他國合資設置望遠鏡，以換取望遠鏡的觀測機會，如果未來能再配合臺灣自建的兩米望遠鏡，想必能夠大大提升臺灣在國際天文領域的競爭力，並促進天文領域在我國的發展。

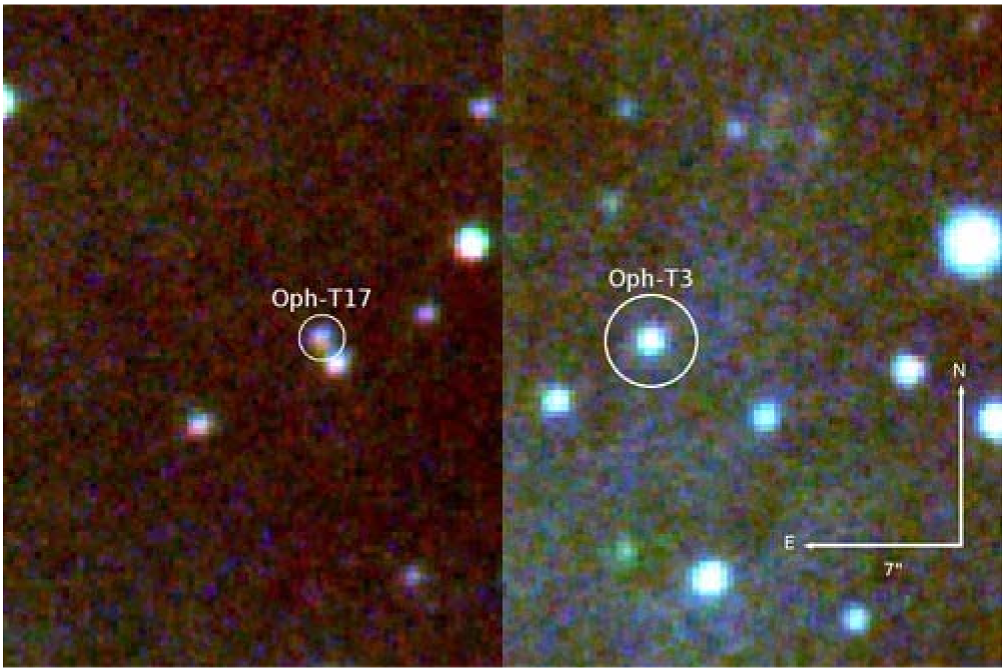

蛇夫座恆星形成區發現兩顆最年輕的棕矮星，編號Oph-T03、Oph-T17。中大天文所姜博識提供。

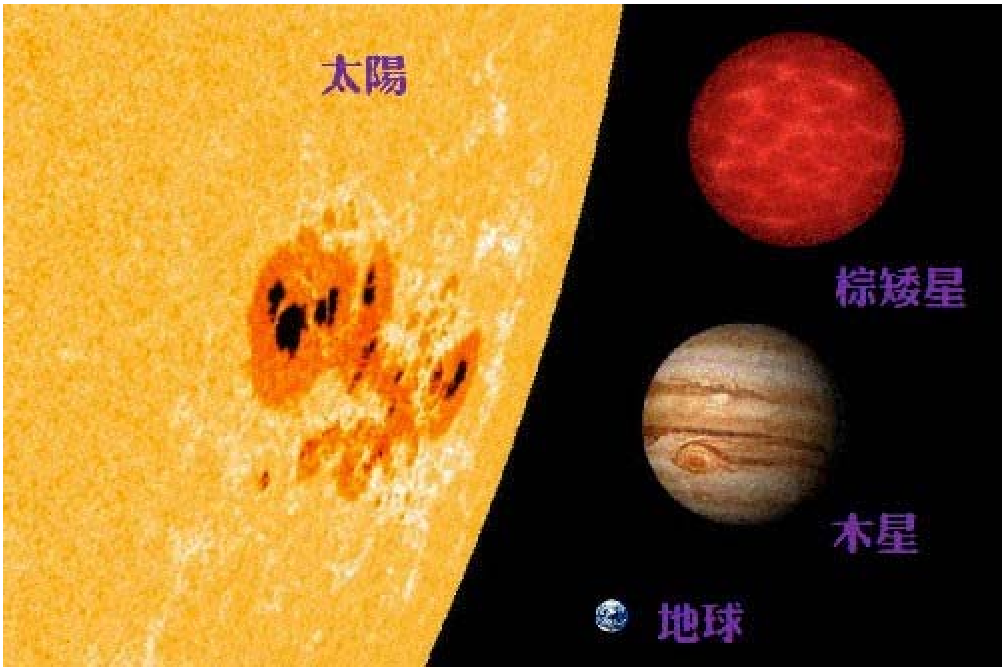

棕矮星與太陽、行星的大小示意圖，本次發現的棕矮星約1到2個木星質量。中大天文所陳文屏教授提供。

【回目錄】

太空研究巨擘 葉永烜榮獲國家講座

黃捷 (/author/jessiewww)　2015/12/21 16:28　點閱 457 次

第19屆國家講座暨第59屆學術獎頒獎典禮21日於國家圖書館舉行，總統馬英九到場頒獎。（photo by 黃捷/台灣醒報）

【台灣醒報記者黃捷台北報導】「台灣過去能成功發展，是因保有多元文化寬容的價值，未來更應如此。」研究天文學30年的葉永烜教授獲19屆國家講座主持人獎致詞時，將相對論公式「E=mc2」另類地解釋成「Earth=Multiple Cultures and Civilizations」，說明地球因多種不同文化和文明和諧相處，才能夠永續發展，期許台灣珍惜多元價值而變得更為強大。

第19屆國家講座暨第59屆學術獎頒獎典禮21日於國家圖書館舉行，國家講座主持人從33件申請中選出7名，學術獎從130件申請中選出12名，其中葉永烜與季昀教授都是第二次獲獎，獲頒終身榮譽國家講座。教育部長吳思華致詞時提到，評選門檻嚴格，獲選的都是經層層審查後脫穎而出的優秀學者。

代表國家講座主持人獎致詞的葉永烜教授，出生澳門、臺灣長大，赴美求學離臺50年後再度落腳臺灣，鑽研天文已30年，獲美國太空總署頒發榮譽勳章的他，曾利用鹿林天文臺望遠鏡，進行大型巡天觀察，讓臺灣在時域天文研究也佔一席之地。

葉教授致詞時將相對論的公式解釋為「 Earth = Multiple Cultures and Civilizations」，他說，地球必須讓多種不同的文化和文明和諧相處、寬容待人，才得以永續發展；他也引述2015年諾貝爾文學獎得主斯維拉娜·亞歷塞維的發言，「有些國家為了選擇變得強大而拋棄自身價值。」藉此勉勵台灣能堅持自身價值而變得強大。

「成功的教育不是只讓前10%能發揮所長，而是後面10%也能夠發揮所長。」曾任中央大學副校長的葉教授也十分關心教育，他認為少子化不一定是危機，將其視為轉機，反而能藉此提高台灣高教品質。

國家講座主持人獲獎者為國立中央大學葉永烜教授、清華大學季昀教授、宋信文教授、江安世教授及國立臺灣大學郭光宇教授、高嘉宏教授及陳銘憲教授。

學術獎得獎人12名為中央研究院林滿紅研究員、吳素幸研究員、陳瑞華研究員及黃柏壽研究員，國立交通大學馮品佳教授、國立中央大學阮啟弘教授、國立臺灣大學李瑩英教授、傅立成教授及廖婉君教授，國立清華大學果尚志教授及陳信龍教授，國防醫學院司徒惠康教授。

聯合晚報 United Evening News 中華民國104年12月21日 星期一

二度獲獎國家講座 葉永烜談教育：「後10%的人也能發揮所長」

「馬總統：學術研究是國家生存命脈，未來會繼續提供經費、人力等資源給學者，讓國家不斷向前。」

國家講座暨學術獎頒獎上午舉行，馬英九總統（左）頒獎給中央大學特聘教授葉永烜（右）。 記者陳正興／攝影

【記者鄭語謙／台北報導】教育部今天頒發國家講座及學術獎，馬英九總統致詞時表示表示，政府一向重視學術研究，除了邁頂計畫等多項補助，也積極推動人才培育等；學術研究是國家生存命脈，未來會繼續提供經費、人力等資源給學者，讓國家不斷向前。

由於日前馬總統在視察生技園區工程時因當著中研院長翁啟惠的面批評工程落後，引發各界不少正反意見，馬總統上午的談話，格外受人注意。

馬總統、行政院長毛治國今天出席頒獎，教育部長吳思華表示，國家講座主持人為國內學術界最高榮譽，今年有七人獲得，包括清大教授季昀、江安世、宋世文，台大教授郭光宇、高嘉宏、陳銘憲，及中央大學教授葉永烜，每人每年有100萬元連續三年共300萬元，季昀、葉永烜都是二度獲國家講座。

二度獲得國家講座的中央大學天文所教授葉永烜，大學就投入物理基礎研究的他，對時下不少年輕人只想念有社會競爭力的科系，忽視基礎科學感到憂心；他認為，研究還是要和興趣結合，不因大環境影響就放棄初衷；他強調成功的教育，不是讓前10%的人發揮所長，而是讓後面10%的人也能發揮所長。

葉永烜是國際聞名的天文學家，他1982年向歐洲太空總署（ESA）、美國太空總署（NASA）提出的「卡西尼探測土星」計畫，總預算高達30億美元，成功將探測船送上土星，當時是美國太空史上最貴的計畫之一，他擔任共同主持人。這項原本不被大家看好的太空計畫，發現土星最大衛星土衛六「泰坦」存在生命跡象，NASA還主動將研究從2008年延至2017年。

葉永烜大學讀的是物理，看了太空研究書籍後傾心天文，研究所改研究太陽系起源當初說。他說，自己肩負全人類的夢想，連晚上也不浪費時間，總是看著星空推敲理論。

對教育部舉辦的高中職青年論壇中，有高中生說，因為社會組被認為就業缺乏競爭力，即使有興趣也不敢選，只能硬著頭皮念自然組。葉永烜表示，想念社會組是非常好的選擇，「有興趣比較重要」，就像他當初大學念物理，研究所時發現天文更有吸引力，扎實的基礎研究讓他有了後來的成果。

來自澳門的葉永烜有感而發說，2030年台灣25歲的年輕人中，將有13%是新住民第二代，大學國際化也會大幅改變高教面貌，這是社會進步的主要動力，教育若要成功，就要利用這波少子化促進教育品質，讓新一代成為精英中的精英。

他強調，「成功的教育，不是使前面10%的學生發揮所長，而是讓也要讓後面10%的學生也能發揮所長」，不管大學排名提升多少，台灣教育應培養年輕一代，讓多元文化和諧相處。

◎文／張光祥

何處是天時、地利、人和而久美

探索星空是與生俱來的天性

有眼睛就能仰望浩瀚星空，能用心更可感受星空至大無外。

在星空下我們就立即擁有了一片天空，沒有光害，星空完全屬於你的，我們立足地球航向宇宙。你有多久沒看星星呢？抬起頭吧！你會發現月亮對你微笑，星星在與你眨眨眼傳達訊息！

西藏的藏族人有句諺語：

一滴水如何不讓它乾涸蒸發，把它放到大海去吧！

一個人如何不使他心靈孤寂，把他投入大自然吧！

大自然裡，浩瀚星空孕藏遠古至今的故事，帶給人類無窮盡的希望……

近期有一部影片在天文愛好者間流傳，內容是有關鹿林天文臺的紀錄片，影片名稱為「高山之眼－鹿林天文臺」，48 分鐘的影片，起頭是臺灣在天文觀測中與世界同步，掌握了我們自己的一方天空，後段介紹葉永烜教授提供自己的畫作，為臺灣 2 公尺望遠鏡籌募不足款項，當畫面呈現了今年四月份，在雪霸國家公園舉辦的「江山萬里行之何處是人間－葉永烜油畫創作個展」時的畫作，一般人會對「何處是人間」產生想像。畫展結束至今已半年，此畫展曾經受到畫壇與媒體關注並獲多位畫家好評，收視後，令我感到最有賣點的也是「何處是人間」這個語詞。因為我將「何處是人間」延伸引用到「布農族小行星發表與頒贈會」的籌劃思考，突然在腦海中聯想出這樣一幅畫面「何處是天時、地利、人和而久美」。

為了十二月將舉行「布農族小行星發表與頒贈會」，也是以鹿林天文臺發現小行星的故事當主軸，來邀集相關單位支持、響應辦理。當然天文臺現地的環境最好的承辦伙伴有南投縣政府、玉管處、人和國小、久美國小等，可運用玉管處水里遊客中心的空間，來促成天時、地利、人和而久美的小行星發表會，一般在企劃活動時，會先在媒體上作宣傳，以加強活動效果。所以就以此散文篇名「何處是天時、地利、人和而久美」來發揮，宣傳本活動。我們的活動已邀請到人和國小表演話劇及久美國小表演踢踏舞蹈，希望能受到媒體關注。經過幾次小行星頒贈活動，已在臺灣繞了一回，是相當吸引媒體關注的活動，其吸引社

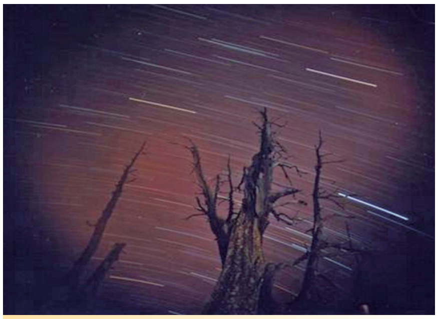

↑玉山國家公園塔塔加夫妻樹星跡

→南投久美國小和人和國小分別用舞蹈和戲劇，慶祝「布農族小行星」命名通過，並和與會貴賓大合影」(陳如枝攝影)

會大眾的焦點是：天文發現是全球性的新聞，而小行星命名是一件表彰，在臺灣有特色的名號 (人名，地名)，可吸引大家探索宇宙、滿足好奇心。

剛好在上述影片中有一段影片中的談話與旁白如下：

我比較喜歡畫雲
雲因為你畫的不對的話
好像還是像個雲
旁白：
葉永烜教授善於以風趣的語言
傳達深奧的課題
雲不一定是雲
畫也不是只是讓人看到所畫的景物
就如同科學的真理
往往隱於熟見的景物之中
等待人們心靈觸動時
發現它的存在

—葉永烜

我的聯想是，雲不一定是雲……所以說小行星不只是 (一定是) 小行星，它是有生命的「帶著故事，在宇宙運行不停。」並且〈金剛經〉有一段名言「中央即非中央是謂之中央」，有著異曲同工之妙耐人尋味。原來深奧的物理，可在於表面上看似簡易的事物上探索而理解。當對小行星探索愈多愈能理解太陽系起源並可往深奧宇宙前進拓展人類生存空間，就像簡單的炮竹可拓展成火箭，一場活動亦可啟發學童探索未來。下次的小行星活動將到臺東的一個市場，將銘版頒贈給一位善心女士，因為她長年低調行善所以小行星頒贈活動也要低調進行，並讓她知道，她的小行星一樣帶著故事在宇宙運行引領大家行善。

現代部落在天災人禍的沖擊下，部落面臨消亡。布農部落族人感受到，如果是國破山河在的情境只會難過一些歲月，但如果是因天然災害造成的國在山河破將會造成部落消亡連難過的機會都沒有，天災救援最快的是善心組織，政府的救災體制雖在但救災速度仍緩慢。我們回憶天災後布農族村民的談話：最嚴重的是我們飽受「賀伯颱風、九二一地震、桃芝颱風、

八八風災等連續大難，生存的信念已瀕絕望。」「人是沒死，精神已死。」而政府援助尚未到達，我們在全國同胞的鼓勵下期望部落不會消亡。在持續進行救急工作同時。我們向媒體發表以下看法：南投是臺灣的心臟，而原住民部落是世界文化的寶貴資產，現在部落逐漸凋零，很需要政府及全民的力量協助持續救援，不能以部落人數少而忽略了。根據新聞報導部落可能無法獲得政府的太多援助予以全面重建，只想以遷村為救災原則，「但是部落沒了、部落文化也就沒了；部落文化沒了，臺灣的文化將會失去一塊最重要的部分！」廢棄部落將是國家的損失，文化資產的損失是無法挽回的。我們要珍惜部落的存在，因為國在山河穩固，即可走向世界，揚名國際。莫言作家如果寫臺灣南投信義鄉部落的故事一樣有可能獲得諾貝爾文學獎 (二〇一二年諾貝爾文學獎得主莫言，其一著作《紅高粱家族》描述其出生地山東高密東北鄉的故事)。受世界矚目的諾貝爾獎，頒獎盛典在每年十二月於瑞典首都，斯德哥爾摩音樂廳舉行，我們的布農族小行星發表與頒贈，亦擇期在今年十二月，特地於南投縣水里鄉玉管處盛大慶祝。

←南投縣久美國小布農與鄒族踢踏舞蹈團表演「久美踢出希望 踏上未來」(圖片提供：久美國小楊玉珠主任)

↓信義鄉布農族的人和國小合唱團以布農族傳統歌謠歡迎所有與會來賓 (圖片提供：南投家扶中心)

現今部落存活了所以我們有機會參與「布農族小行星發表與頒贈會」可共同欣賞部落國小的表演。人和國小表演的劇本將演出一個布農婦女被敵人擄走的傳說 (巒社)，本以為與活動主題關聯性不大，然而其中精彩劇情是母子在他族部落生活 10 年後，是以星星來導航回到布農部落的故事可見仍與活動主軸連結。久美國小表演「踢出希望，踏上未來」的踢踏舞蹈，踢踏舞團員共25 位。其中布農族 19 位，鄒族 4 位，漢族 2 位。我們真的運氣很好，在天時、地利、人和的情況下，仍然擁有美麗部落，期待部落國小在「布農族小行星發表與頒贈會」上盛大演出。

鹿林天文台地址 ➢ 南投縣信義鄉神木村九鄰鹿林一號
發現布農族小行星的時間 ➢ 2006年3月18日
小行星永久編號 ➢ 268669
地利村位於 ➢ 南投縣信義鄉地利村
人和國小位於 ➢ 南投縣信義鄉人和村民生巷3號
久美國小位於 ➢ 南投縣信義鄉望美村美信巷54號

◎文／張光祥

小行星的搜尋
激盪出科學與人文的創意

其後不久，我就走了──到大陸去。我沒有護照；但我探出一條便道，先搭船到日本，再轉往大連；到了那裡，以後往南往北，一切都隨你的便。我就這樣走了。我沒有給自己定下要做什麼的計劃，祇想離開當時的臺灣；也沒有到重慶去找二哥。我不是愛國主義者，但是原鄉人的血，必須流返原鄉，才會停止沸騰！二哥如此，我亦沒有例外。

《原鄉人・鍾理和》

鄰近阿里山與玉山的鹿林天文臺夜間盡是星海、銀河、動物聲，陪伴觀測員浪漫又寂寞的冷冽時光。鹿林天文臺是鹿的原鄉……天文臺南方是旗山溪上游的楠梓仙溪，在美濃與茎濃溪會合即是高屏溪，天文臺北面是神木溪，往下游匯入陳有蘭溪，再匯入濁水溪，可見鹿林是水、星星、鹿的原鄉。人類在此探索宇宙，觀察星空找到新發現來滿足好奇心。

觀測員與觀測助理的血液裡流著鄒族傳統勇士精神，不眠、不休在觀察天地宇宙的變化。白天片刻的休息時段，便將來自星星的訊息，利用四通八達的電腦網路傳送給各地的天文學家。在科學教育者的眼光下，每個人都在與時間競賽，想為人類提供宇宙的新發現。每年偶有遇到特殊天象時，也就是鹿林山最熱鬧的時候，民眾與媒體記者都聚焦於來自鹿林天文臺的第一手新訊息。

↑鹿林山、阿里山、玉山環繞出來的雲海像極了一個良好港灣，而鹿林天文臺就坐落於雲海之間

↑二〇〇一年獅子座流星雨採訪

為追念臺灣當代文學家鍾理和先生一生為文學的奉獻，中央大學特別將二〇〇八年所發現的編號 237187小行星，經國際天文學聯合會 (IAU)通過，正式命名為「鍾理和」(Zhonglihe)。並於二〇一二年八月四日鍾理和先生逝世的 52 週年紀念日，於臺南的國立臺灣文學館舉行頒贈儀式，感念這位被稱為「倒在血泊中的筆耕者」。鍾理和先生的家人，扶老攜幼共一百廿餘人，遠從各地前來出席這場盛會，包括鍾理和八十歲的姪子，鍾理和第四代的外曾孫女，全家族一起分享榮耀。

然而，鍾理和小行星的發現，只是利用我們鹿林天文臺望遠鏡所看到的一顆石頭而已，此發現並不特別，但是經過大家巧思就能發揮科學與文學的創作，引起人們重新欣賞他的文學鉅作，作品中有著北京、瀋陽、臺灣的故事。看到鍾理和與鍾台妹在北京的足跡，就像搜尋到小行星一樣，令人興奮與陶醉，人們的原鄉，隨祖先的遷移可知，當時的原鄉。而人們想知道宇宙空間的原鄉，可從小行星的探索開始；人類宇宙空間原鄉的探索可以憑藉科

↑鍾理和家族一同前來參與頒獎典禮，分享鍾理和小行星的命名榮耀 (張明新攝影)

↓經國際天文學聯合會 (IAU) 通過，正式命名為「鍾理和」(Zhonglihe)

學與人文的創意發覺宇宙原鄉。鍾理和小行星形如不規則的馬鈴薯，直徑約 2000 公尺左右，與阿里山的海拔高度相當。鍾理和小行星是中大鹿林天文臺發現 800 多顆小行星中的一顆，經世界天文學聯合會小行星命名委員會命名通過的，在國際小行星中心的永久編號是：237187，鹿林巡天計畫 LUSS 的環境、設備與全球五大巡天計畫的設備比較有如小舢舨與航空母艦的懸殊差距，只能算是「小蝦米對大鯨魚」，而且鹿林天文臺沒有路，重要的是，「在這個世界的舞臺上，我們沒有缺席」。根據國際天文學聯合會小行星中心 (IAU：Minor Planet Center) 的統計資料，鹿林天文臺已成為亞洲發現小行星最活躍的地方，全球排名第 48 名。此排名公布於國際天文學聯合會小行星中心的網頁網址如下：http://www.minorplanetcenter.net/iau/lists/MPDiscSites.html

天文臺經過環評的流程後，籌劃人員從過程中理解到，天文臺所在的這塊寶地，潛藏著許多從前所未知的故事；如施工過程中為了不干擾棲息的動植物，所以工程要細心而緩慢，對防火逃生、儀器運送、環境監測、施工時的安全，更是需要嚴加遵守的事項，而且現有觀測團隊的運作，又不能因施工而停擺，這些要求在平地並不困難，但在海拔近 3000 公尺，又沒有正式道路的情況下，2 公尺望遠鏡要能開光使用，甚至比太空探測任務還要艱鉅。一如俗話所說：「比登天還難」。

我們經常從國際新聞聽聞中東情勢的不穩定，以色列與鄰國又有紛爭，可能引發戰爭。如果再從環評報告書仔細端詳，會發覺每次鑑界的過程，為何如此之冗長與繁複，參與的單位與人數眾多，把鹿林山頭擠的滿滿，甚至已無立錐之地這時天文臺助理，最頭痛的是如何在沸點只有 86℃ 的水溫下煮好一大鍋麵條，好讓這次鑑界的人員能夠在工作之後填飽肚

←↓二〇一一年三月四日申請天文臺索道案會勘

子。在此過程中，由於這個山頭是嘉義、南投縣界，土地管轄的單位為臺大實驗林與嘉義林區管理處，再加上玉山國家管理處，建管單位是嘉義縣政府、南投縣政府、水土保持局等，周邊單位是環保署，還有將來營運配合的單位如臺電、通訊公司、消防局……等單位，眾多部會的意見，使得每一次的會勘當下都未必會產出結論，可以說鹿林天文臺要進行一項申請案，必須從位處土石流區域的道路開始，風雨無阻冒險上山的進行聯合會勘，依各單位表述後，才可以進行下一個流程……而每經一個流程都會出現未曾接觸到的陌生的法規。土地界線有很多的不確定性，想起小時後，看見鄰居大吵一架不相往來，其紛爭原因往往是房子土地鑑界而產生，所以把鹿林山的處境想像成以色列是很貼切的。

天文臺每個月都接受三個團體的參觀，有一次一個學童說，中央大學怎麼那麼小，只有兩棟校舍，因為他只看到三角點旁立牌上寫的大字國立中央大學，沒繼續往下方較小的字看完，就很大聲的在山頂上笑著說：「中央大學好小！」，助理聽到急忙出來解釋：這是學校的天文臺，校區在北部的中壢，你不相信再好好看清楚立牌下方的字，亦可上網看，更可以瞭解。我們好辛苦奮鬥了 22 年才有的小基地，2 棟建物：一棟是嘉義阿里山鄉自忠 78 號，另一棟是南投信義鄉鹿林 1 號。往下方看到的鹿林山莊是依我們的門牌號，才申請編定出的鹿林 2 號。兩公尺口徑望遠鏡天文臺完成後的門牌號應該是嘉義縣阿里山鄉中山村六鄰自忠 76 號，與玉山的排雲山莊同樣是中山村。我曾經說過一段話：「要在臺灣的高山上建天文臺要有不怕死、像瘋子的精神，才能安然為望遠鏡開光。」當然此話是喝了會令人陶醉又能壯膽的飲料後才說的。

二〇一二年八月，我們在臺南的臺灣文學館舉行鍾理和小行星頒贈活動，雖然兩公尺望遠鏡在那時尚未建成，希望將來完成時能邀請您的家人前往鹿林天文臺，從兩公尺望遠鏡向您問候天上的鍾理和小行星。

↑兩公尺望遠鏡天文臺的虛擬圖

鹿林天文臺地址➢南投縣信義鄉神木村九鄰鹿林一號
發現鍾理和小行星的時間➢2008年
小行星永久編號➢237187
正式命名時間➢2012年8月4日鍾理和逝世 52 週年紀念日

◎文／張光祥

鱟火星任務

一個人若從臺灣的平原直登上 3000 米以上大山，生態環境的改變就像從北回歸線到北極圈一樣迅速，這也造就了寶島臺灣多變的自然環境與極為豐沛的生物資源。臺灣現存極為古老的一種生物《鱟》，將成為全球太空計畫探索外星生命的重要物種。

鱟 (horseshoe crab) 亦稱馬蹄蟹，屬肢口綱劍尾目的海生節肢動物，主要生長於北美東海岸和亞洲的臺灣、印尼等地，是臺灣現存非常古老的一種潮間帶海棲生物，有鐵甲武士、活化石的稱號，以蠕蟲等軟體動物為食，平均壽命 24～31 年 (圖 1、2)，成鱟因一公一母成對生活，又被稱為鴛鴦魚。

鱟與蟹類並無親緣關係，從動物學的分類上更接近於蠍、蜘蛛和現已絕滅的三葉蟲。從四億多年前出世至今，鱟仍保留著其原始而古老的相貌，故有「活化石」之稱。科學家們發現，鱟之所以能存活如此長久的時間，與它原始但發達的免疫系統息息相關。

臺灣沿海常見的鱟，在生物學分類上屬節肢動物門之三棘鱟 (*Tachypleus tridentatus*，Leach, 1891)，曾經分布廣泛，早年與先民的生活密不可分，包括：鱟卵醃醬、如意鱟殼杓、鱟殼炒蚵麵、虎頭牌……等。鱟的族群數量最能反映出潮間帶受到污染或人為干擾的程

↑圖1. 金門灘地上的三棘鱟成鱟 (陳佳宜攝)

↑圖2. 臺灣屏東海洋生物博物館所飼養展示的成鱟 (鄭宇棋攝)

度。海域中如果能夠發現鱟的棲息，代表該處水域環境純淨。牠們大多生活在沙質的淺水海域，每一隻鱟魚都要經過十餘次的蛻皮才會成體。不過，這些需要十多年才能長成的鱟魚，現在正因為棲息地的人為破壞及水質惡化，族群大量減少當中，已經瀕臨滅種的危機，臺灣農委會因此特別在鱟的棲地之一，澎湖縣成立了一個保育中心，另外在中央研究院的生物多樣性研究中心，亦有專研繁育的實驗室 (圖3、4)。相關當局已訂立了禁捕令，依據連建漁第0920022102 號公告，在「連江縣海域轄區內水產動物採捕體長限制」規定一文中：「中國鱟 *Tachypleus tridendatus*，無論體型大小一律禁捕」。

過去，鱟的族群大量分布於臺灣本島、澎湖、金門的沙泥質海岸，與沿海地區居民的生活息息相關，例如以鱟殼製成的生活用品「鱟杓」，在歷史悠久的臺北艋舺龍山寺室內門柱，也可以發現關於鱟的石刻 (圖 5)。不過由於棲地的破壞、人類捕殺、填海造陸、興建海堤、不當投放消波塊等開發行為，對鱟的棲地 (產卵場等) 產生嚴重破壞，鱟在臺灣本島幾乎已經不見蹤跡，況且民間仍然有吃鱟的傳統習慣，原本曾發現稚鱟的嘉義布袋好美寮濕地，目前幾乎已經觀察不到稚鱟蹤跡，也鮮少成鱟被漁民捕獲的紀錄，現階段成鱟數量較為豐富的地區，僅剩下金門和澎湖海域，也只有這些地區的潮間帶，較容易有稚鱟棲息。(海峽兩岸之

↑圖3. 雉鱟養殖盆

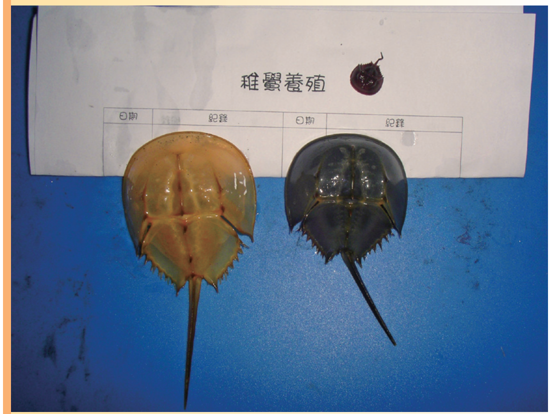

↑圖4. 左為鱟殼，右上為四齡鱟，右下為十齡鱟

↑圖5. 臺北艋舺龍山寺門柱的鱟石刻圖

廈門、金門應合作推動對這種有滅絕之虞的珍稀物種積極複育與保護工作。)

最後，衷心期待在未來，我們能幫鱟保存良好的生存空間，並盼望鱟能協助人類找到可移民外太空的行星，共同延續生命。

移民火星是小學生最感興趣的話題

中央大學天文所經常為國小學童辦理天文科普活動，學童常提問火星生命與移民火星相關問題。有一段對話是很有趣的：如果將來到達火星的第一任務是什麼，童言童語的回答是：要建氧氣倉、儲水倉與種樹，我告知，要記得於農曆春節，打個電話給老師，小學生天真地馬上問，老師的手機號碼是多少？我說是 091……小朋友立刻抄起電話，我最後補上一句，屆時從火星撥出要加星碼 (地球) 910……。

近期英國知名天文物理學家史蒂芬・霍金 (Stephen Hawking) 警告，人類正進入「歷史上越來越危險的時代」，除非在接下來兩個世紀內殖民外太空，不然就會永遠消失。人類能長存的唯一機會就是搬離地球，而本世紀內最可能移民的星球即是火星 (圖 6)。


↑圖6. 小學童參觀中央大學校區天文臺

鱟的血液成分十分特殊，因以銅元素作為內毒螯合酵素而呈現藍色，不像其他動物的血液大都是帶鐵、呈現紅色，其含有一系列對細菌高度敏感的酶，這樣的分子結構遇到細菌中的毒素有螯合現象，可迅速與特定的可溶性蛋白產生凝固反應，進而隔絕入侵的細菌與毒素。此一特性在今日已廣泛使用于葡萄糖、生理食鹽水產品的細菌檢驗上。自從上個世紀六十年代美國麻省 Woods Hole 海洋生物實驗室的弗雷德里克・邦 (Frederik Bang) 博士首次研發出把鱟的血液應用於醫藥業的技術後，如今不少製藥公司都利用這項技術來測試他們生產藥物的藥效，或者檢測產品是否遭受細菌污染。美國太空總署火星探測計畫，也必須仰賴鱟的血液，來做為能夠快速檢驗毒素的生物檢驗試劑。

二○○六年十二月，一種利用鱟的血液特性所開發，掌中寶大小的細菌探測儀 (LOCAD-PTS) 首次搭乘航太飛機 STS – 116 升入太空，科學家們在國際空間站進行了測試 (圖 7)。LOCAD-PTS 的全稱是 Lab-On-a-Chip Application Development-Portable Test System，意為「晶片實驗室應用開發-便攜式測試系統」。LOCAD 以四種由鱟的血液裏提取的酶進行工作，首先，少量的酶被注入測試管，進行烘乾程序；當液體樣本需要被測試時，將液體導入測試管，其水分使原本乾燥的酶再次恢

↑圖7. 宇航員Suni Williams 在國際空間站上使用LOCAD-PTS， 把從空間站內部取得的樣本與水混合後注入儀器，測試空間站內有無細菌存在 (NASA Image - ISS014E18822: A)。

復活性，如果樣本內含有細菌，其毒性會啟動酶的反應，進而改變液體樣本的顏色。顏色變化的程度取決於細菌的菌落數量～細菌數量越多，顏色變化程度越大；反之亦然。由於鱟血液的高度敏感性，單個細菌的出現就足以引發血液內的酶啟動反應，使得 LOCAD 可以被做成這樣小巧又高效率的裝置。

傳統的細菌測試方法是將病人身上取得血液或尿液樣本在實驗室培養皿內的某種培養基中生長，兩到三天後，可以得到結果，判斷感染病源是由病毒、還是一些抗生素可以對付的細菌或真菌引起。但無論是在載人還是無人的太空任務，兩三天的檢測時間太過於冗長。相形之下，LOCAD 只需要 5～15 分鐘就能給出結果，而且非常精確，即使單個細菌也能被測試出來 (圖 8、9)。

早在二〇〇三年，在 NASA 的火星車勇氣號和機遇號從地球發射升空之前，科學家們已經

↑圖8. 二〇〇八年九月一日新疆塔克拉瑪干沙漠西南角模擬火星探測 (張光祥拍攝)

↑圖9. 二〇〇八新疆卡拉蘇站進行西部天文臺選址時模擬火星探測 (張光祥拍攝)

使用鱟血液對火星車進行了無菌檢測，確保這兩輛火星車不會把地球生命帶到火星上，從而對火星環境構成污染。根據《行星保護協定》條約的規定，任何一個國家都不允許發射攜帶有地球微生物的飛行器到外星，對地外星球的原始環境造成污染和破壞。這樣做的目的是確

保未來對宇宙生命的研究具有未被破壞的原始條件。

除了被應用於行星保護和空間環境的細菌測試，鱟的血液還被計畫用於未來的行星生命探測中。比如 NASA 計畫在未來發射的火星車上搭載類似 LOCAD 的儀器，以測試火星土壤中是否有微生物存在。關於火星上可能有生命存在的猜想已經產生了至少好幾百年了。一八七七年，義大利天文學家斯基帕雷利 (Schiaparelli) 觀察到了火星表面有一個明暗錯綜的複雜網路，他認為可能是水道，而這個詞 (Canali) 被翻譯成英文時匆忙中被譯成運河 (Canal)，這個誤解頓時再次在歐美掀起了探討火星上是否有生命的熱潮。後來的事實證明，斯基帕雷利觀察到的不過是火星表面因沙塵暴引起的表面明暗變化罷了。故事雖然如此，關於火星上到底有沒有生命的問題仍然有待解答。

一九七五年發射的兩個「海盜號」火星探測器，攜帶了用於尋找火星生命的探測儀器著陸于火星表面 (圖 10)，分析的結果未能證實火星上有生命。不過「海盜號」的實驗是一次開創性的努力，並不代表尋找火星生命的最終結果。火星有一個稀薄的、主要由二氧化碳組成的大氣層，它的極地有類似于地球的水冰冰蓋；近年來，科學家們又在火星的中、高緯度帶發現了含冰量很高的地下冰存儲帶。種種跡象表明，早期火星表面的條件有可能適於生命的誕生。當然，如果是這樣，並且火星上的原始生命諸如細菌又被保存了下來，他們是否與地球上的細菌類似，又會與鱟的血液中的酶發生怎樣的作用呢？科學家們需要進行進一步的探索。二〇一二年八月六日好奇號火星探測車成功著陸火星。好奇號的任務包括：探測火星氣候、地質，探測蓋爾撞擊坑內的環境是否曾經能夠支援生命，探測火星上的水，及研究日後人類著陸火星進行探索的可行性，期待好奇號後續能探索到火星生命以滿足人類的好奇心。

↑圖10.「海盜號」探測器模擬圖

參考資料

中央研究院生物多樣性研究中心陳章波研究員 陳佳宜助理研究文獻
農委會水產試驗所澎湖海洋生物研究中心文獻

◎文／張光祥

鹿林天文臺鄰近部落的一則故事

鹿林天文臺就位於阿里山部落中，莫拉克八八風災時，駐守在天文臺的工作人員，傳來的求救訊息，開啟了我們一連串的協助救援工作，而過程中我們體驗到了大自然的無情與強大威力，也看到了阿里山部落族人團結同心不畏艱難絕處逢生，愈挫愈勇的精神，更見證了臺灣人民面對天災，不分彼此，真誠協助的暖心救援。

八八水災後的第六天，我被突來的求救簡訊震撼到。

> 「光光你好：目前我們駐站人員有三人在部落家人都平安，有一人留守鹿林天文臺也很安全，目前無法前往天文臺值班，而部落聯外道路都中斷所以我們急需空投民生物資，如米、泡麵、蠟燭、手電筒。
>
> 石俊雄

> 嘉義縣阿里山目前急需米糧、嬰兒用品(奶粉、紙尿褲)、照明設備（蠟燭、手電筒、乾電池、發電機、油料)，電話訊號全鄉不通，光是我們特富野部落就有二百人左右到現在我傳簡訊為止還沒領過空投物資敬請協助，謝謝。
>
> 梁錦德

災後第七天

梁錦德先生再次傳出的簡訊：「請救救我們撐不住了！阿里山鄉特富野部落與鄰近幾個部落一樣危急，請救救阿里山部落，在特富野部落，約有 200 人受困，大部份是孩童與老人。已斷糧 3 天鄰近幾個部落一樣危急急需物資。今日不空投許多孩童會撐不下去。嘉義縣阿里山目前急需米糧泡麵、嬰兒用品 (奶粉、紙尿褲)、照明設備 (蠟燭、手電筒、乾電池、發電機、油料)，電話訊號全鄉不通，敬請協助，謝謝。空投阿里山鄉特富野部落，座標：N 23 度 27 分 51 秒，E 120 度 45 分 32 秒，海拔高度約 1050 米。」

當時因為大家的目光都聚焦在小林村的嚴重災情，且阿里山部落通訊全部失效，無法將災情傳送出。因為特富野部落將到天文臺值班

的同仁都有回報的機制。在八八後的第六天駐站人員石俊雄先生發出簡訊告知部落道路與通訊中斷無法前往天文臺值班，那通簡訊，傳出後，大家才知道阿里山部落很危急，需要急救，最急迫的就是民生物質，而且留守部落駐站人員，發次簡訊都要走到，能有微弱訊號的地方，走到那兒已精疲力盡，還好，一天只有傳送一到二次，因為直升機還未接獲勤務指示空投救災物資，而且里佳部落等區域地處深山老林很難空投，又因地勢環境因素直昇機很難起降載送病患，因而救災任務困難重重。

理學院胡院長曾經到訪特富野部落，親自探望過駐站人員，慰勉其工作的辛勞，當聽到部落救災工作無法進行，立即與立法院聯絡，當天立刻有意想不到的進度。我的手機一度成為像戰情的調度電話，要與部落、嘉義縣災害應變中心及海鷗救難大隊聯繫，因為部落手機訊號不良又無法充電，只有我在學校，可與部落的駐站人員一天連絡兩次，所以就成為救災的訊息中心，急需物品與搶救工作就此正式展開。在這過程中，每戶可以領到的物資仍匱乏，所以部落的人只好採野菜與捕捉蜜蜂來因應食物的不足。並組織伙食團供應基本餐飲，等待救援。

↑快到明隧道了，可以運送物資回部落

↓路經老王溪前往阿里山石桌搬運救災物資

災後第八天

災後第八天，晚上 12：00 前，中央大學理學院胡院長打電話告知，立法院長王金平先生已請海鷗直升機將於明晨空投物資與照明設備，而且是拂曉運補，天剛亮就會送達；請部落準備接收此物資，果然一大早就聽到直昇機達…達…達…的聲音，在部落上空出現，收到物資後，大家驚喜若狂，然而部落對物資不敢一次完全發放完，深怕下一次的物資，不會很快的再空投運送。所以一個家庭只分配到幾包泡麵，還好之前部落曾在賀伯、九二一、桃芝等天災的衝擊，已有克難的經驗，才可以撐過八八風災。部落出動大批人力前往物資集中點，搬運物資，一大早從部落走到物資集中點路程來回需要一天，背負 30 公斤以上的物資

走在崩塌的山路，吃力的慢慢行走，回到部落已天黑。困難的搬運過程可說是披星戴月，篳路藍縷。大家團結合作共體時艱胼手胝足重建部落。部落像是壓不垮的野百合，擁有超強的生命力。

當阿里山公路搶通時車輛仍難以下山，因為部落聯絡道路以里佳的通路損壞最嚴重，可以說是柔腸寸斷，無法搶通，當路臨時搶通時，受困已久的災民，想做的第一件事：想衝到山下看看繁華市區五花八門的燈光。重建過程最遙遙無期的是將中斷已久的電復通到散居的每一戶，最後的辦法是先以部份明線先行接通電路，暫時通電的方式供電，通到塔塔加時，已是災後一個多月了。雖然電力不穩定但大家非常感謝臺電日以繼夜的趕工強修。在通電可大放光明時，大家最想進行的事就是，開燈慶祝，心情比看煙火更興奮，每人臉上露出充滿希望與喜悅的神情。後續臺電在山區克服萬難重新布設電力線路，山區的供電才逐漸穩定。

使命必達

中大感謝嘉義縣災害應變中心與海鷗救難大隊立即救援。經八月十四日至八月十六日三天已運送多次救援物資到達阿里山鄉各部落，唯特富野與里佳部落飛行運送困難，但經〈嘉義縣災害應變中心與海鷗救難大隊〉等單位克服萬難，完成風險極高的運送任務，現部落已有物資可暫時安頓生活。

↑部落降落點都要建立 GPS 的定位資料檔且每年都要更新，不然救災直升機駕駛都不知道精確地點，還要降落到如籃球場大小的山巔空地再來問路定位呢

本校天文臺位於阿里山鄉中山村 6 鄰自忠 78 號，海拔 2862 公尺，目前留守二位工作人員，一位是阿里山鄉里佳村的汪榮進先生，另一是住在高雄的蕭翔耀先生，物資都還充足，每隔二天都能向校方連絡回報。阿里山鄉特富野與里佳部落是天臺駐站人員的家鄉，石俊雄、石皓偉、杜進全先生都住特富野部落，目前在部落都平安，汪榮進家位於里佳部落，現留守鹿林天文臺。

想想自己在鹿林山工作 20 多年，進入部落無數次，在這次的救援工作比任何人，更能感同身受到部落的無奈與即將消亡，從桃芝、賀伯颱風、九二一地震等災害，部落仍安然挺住，此次的八八風災，確實嚴重到要遷村，如來吉部落，算是消亡了一半以上。有一則有趣

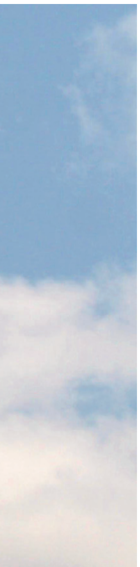

↑搶通臺18 與臺 21 線公路過程，路通後，善心人士捐贈的物資可快速送達災區 (臺 18、臺 21 線公路是通往阿里山部落與鹿林天文臺主要道路)

↓連續大豪雨將高海拔山區的大量土石，瞬間沖刷到山路與河床再流向出海口

精彩的傳說故事：駕駛直昇機要降落問路才能準確送達，因為山區地形複雜，氣候變化萬千能見度不足需要臨時起降探索方位好再飛行前往正確的投送物資點，飛行技術，好到可說是「使命必達」，若未問好方向，容易發生像一般車輛全依 GPS 導航系統指引，不小心就會進入羊腸小徑，產生進退兩難的悶境。假如當時我能現地為直昇機導航，即可增加物資投送的準確性，亦不會發生要降落問路的窘態。另一則新聞報導了救災感人事蹟：有一位原住民飛行員降落後，將物資送達部落後立即起飛執行下一個任務，他的父母親也是災民在直昇機停降點等候領物資，亦無法與他的飛行員兒子見面一下。可見救災工作的黃金時刻不容稍歇片刻與久未見面的父母親打招呼一下。

相呴以濕，相濡以沫

後來的需求品愈來愈多，特富野部落申請了蒼蠅紙、鹹魚等都列入補給品的清單，因為部落聚集非常多的蒼蠅，而鹹魚是為了可長期儲備，因為不知道路何時又不通，我當時非常有信心地回報部落說，此需求品的訊息已向救災中心反應，目前嬰兒奶粉等物資已充足，是否可買一些蒼蠅紙與鹹魚，而且救災人員肯定的說 OK。但是過了兩個星期一直都沒送達特富野部落。而在一個月後手機通話較正常時，從兩個部落間的手機通話才知道有送，只是送到它處。對話是如此：我的里佳部落傳出一件得意的好事，很傳奇的啦！現在救災工作愈來愈貼心會主動送我們好用的物品，我這里佳部落很有意思，有收到蒼蠅紙與鹹魚，駐站人員立即告知，這是特富野部落主動申請的啦，不小心送到里佳部落的啦，如果有用剩，等路通後，再給我一些吧！救災中心真是貼心，沒有想到申請的是特富野部落結果送達到里佳部落。黏蒼蠅紙成了傳奇物品。另一傳奇物品是成堆的礦泉水，部落看到礦泉水就膽戰心驚因為期盼已久的大雨水剛退又面臨再度接受那麼多的礦泉水，要何時才能喝完！

部落民眾於八八風災一個月的共同生活中、大家互相扶助、共體時艱，合作集中食物共同分享，當外援進入時，井然有序的分配食物，當通電、通路後，就各自散居，不再如此凝聚。部落停電的一個月中大家集思廣益的檢討救災進度並建議政府如何進行復健。大家認為若依靠理想的救災、復建 SOP 流程難以順利完善救災，不如發揮人類與生俱來的本性，心存人飢己飢，人溺己溺的善心，並捨棄自掃門前雪的自私心態，應可達到老吾老以及人之老，災民皆有所養的大同世界。二〇〇九年八八風災、二〇一一年日本 311 地震災害及福島核災事件、二〇一四年高雄氣爆事件、二〇一五年六月二十七日，八仙樂園粉塵爆炸事件，救災人員與醫護人員盡全力不眠不休搶救，大家在人間煉獄中，竭力互相幫助來脫離險境，如泉涸時，魚兒相呴以濕，相濡以沫來脫離險境。人類求生的特性如小時候看見池塘乾涸時，魚蝦相聚求生存，魚蝦於泉涸時安然渡過，並在大自然恢復生機時回歸，悠遊相忘於江湖。

人間福地

「經過極度悲苦的人，愈容易滿足」。臺灣的部落原住民都有此特性。可在極端異常的環境下仍安然自在。經過許多自然災害的洗禮從不怨天尤人。部落目前在各界的關懷下，生活已逐漸穩定，而且臺北某基金會在三所部落國小 (阿里山國中小、達邦國小、山美國

↑災區勇士們行經溪床，前往物資集中點運補

小) 正進行音樂拔尖計劃，想發揮原住民部落的音樂天份來安頓大家恐慌許久的心靈。此計劃已成為可輔導部落學童又能飄香久遠的一貼心藥，而計劃資助者被譽為傳承愛心的心醫。期許此計劃能引發拋磚引玉的作用，讓更多人關懷部落，將快消失的部落再延續著。在部落消失前請大家來部落，親自體驗感受茶淳、咖啡香、悅耳音樂滿山的「人間福地」。您會發覺愈簡單的生活愈容易滿足，不會再輕言說出「我是不滿族！」。

作者簡歷

於九二一大地震、桃芝颱風等重大災變，張光祥多次發起「送愛到鹿林」活動，將中大愛心物資送抵原住民部落。看到他們的家園重建緩慢，他更不惜挺身而出，上書陳情九二一重建委員會李遠哲院長。原住民朋友的樂天知命、珍惜所有，讓張光祥體驗到生命韌性。

◎文／張光祥

小行星回娘家

有位詩人曾說過這樣一名句：

「獸類未能完成的，由人類去完成它。人類未能完成的，由渴望去完成它。」中大天文所將持續參與國際型重要天文計劃，共同完成探索宇宙，拓展人類空間領域的夢想。

已退休臺灣知名企業家鄭崇華先生出席中大天文所成立 20 週年慶與小行星回娘家活動時，說過一段故事：他退休後的日子仍每天到大安森林公園當志工，為花草樹木澆水。有一天突然發現，有一大群螞蟻在搬遷，他馬上聯想：螞蟻是否知道要遷移到何處才安全？這個故事不禁讓人有所聯想，人類是不是該先檢視居住在地球的安全性，是否要更保護地球就不用搬遷到外太空的其他星球？亦或是要天文學家加倍努力，找好適合人類搬遷的星球，因為人類要移民外太空已經是刻不容緩的事了！

←圖1.葉永烜教授親筆創作油畫，畫名為「鄭崇華小行星與鹿林彗星喜相逢」，於二〇〇八年贈與臺達電子董事長鄭崇華。國際天文聯合會 (IAU) 通過中央大學發現的 168126 號小行星命名為「鄭崇華(Chengbruce)」於二〇〇八年七月八日頒贈以肯定臺達電子董事長鄭崇華追求環境永續、愛地球具體貢獻，以及善盡綠色公民責任的努力

中大鹿林天文臺發現 800 多顆小行星，長軸大小約 2 公里至 4 公里左右，與阿里山、鹿林山、玉山的海拔高度相當。我們想知道宇宙空間的原鄉，可從小行星的探索開始；亦可偵測其軌道是否成為近地小行星，而產生撞擊地球的可能，造成毀滅性災害。過去就有很多小型天體撞向地球，但大都在穿越大氣層時，燃燒變成流星、最後化成灰燼；或墜落海洋等人煙稀少之處。總有一天，地球會跟直徑達幾公里的小行星發生碰撞危機。

一九九二年中央大學成立天文研究所，開創國內天文學研究與教育的第一個機構，至今已二十三年。好奇號火星探測車在火星上探索人類未來，中大天文所在培育探索人類未來的

↑圖2. 獅子座流星雨
時間：二〇〇一年十一月十九日 A.M 02：00
地點：麟趾山 曝光：8分　　　作者：張光祥

科學家。為了天文觀測的需要，早期中大校園的照明燈都罩上黑色半球的燈罩，目的在於避免光害直接影響星空。現今因光害影響，校內的觀測較少，因此對夜間照明的控制逐漸降低，因而校內的照明燈也就變的五花八門。當初半黑半白設計的照明燈只剩校史館前一盞，保留了校園早期原有照明的風味。如果您在中大校園內看到此類型的燈，或許能喚起您對建校初期校園的記憶。中央大學目前是交通最方便的大學。有國際機場、高鐵，未來中壢市將有捷運經過，所以中大天文所可便利地與國內各學術單位交流，並與國際接軌。

光害造成人們的錯覺
浩瀚銀河看成夜間白雲片片

談起中大天文所師生觀測星空與流星雨的有趣故事：本所前所長蔡文祥老師回憶民國八十一年，帶著首屆天文研究所學生，到玉山國家公園進行天文觀測教學，在燦爛星空下，幾位不曾見過「銀河」的都市小孩，陶然自得的感受宇宙浩瀚，忽然有人迸出一句「為什麼天上那一大片白雲都不動？」他定睛一看，原來那亮麗耀眼的「銀河」，被誤認為「白雲」才發覺需要創造更多機會，讓學生接近大自

↑圖3. 黑色半球的照明比較不會影響夜間星空的觀測

然與浩瀚宇宙。1998年獅子座流星雨引領大家觀測星空的風潮，曾經流傳一則冷笑話：「請問：看流星雨要用雨衣還是雨傘好？」

中大天文所成立於民國八十一年，為國內最早成立的天文研究所。二十年來積極培育研究天文領域方面的菁英人才，並給予完整而嚴格的科學訓練，畢業校友散布海內、外，從事研究、教育、儀器或工業研發等相關行業。本所主導規劃的與國際研究接軌所需之前瞻性基礎建設，已分布在國內，如鹿林山、臺南等地，都設立研究與教學使用之天文臺，供各地民眾或學生教學觀星使用。

中大天文所師生在鹿林山經過多年謹慎規劃、選址、地形地質勘查、氣象資料蒐集、土木興建、儀器設備架設建構等艱辛歷程，於民國九十一年設置了一部購自德國，精度高、集光性佳，並配有自動導星系統、高靈敏度電子相機等設備的一公尺口徑望遠鏡，提供本所師生，以及臺灣其他大學研究與教學需求。鹿林山天文臺另安置了中美掩星計畫的 4 臺 50 公分口徑超廣角望遠鏡。由於臺灣位於低緯度，佔有可見天區大的優勢，鹿林山天文臺已成為國際間小型望遠鏡觀測網的重要成員。鹿林天文臺目前為亞洲發現小行星活躍之處，發現記錄居全球第 47 名。

中央大學鹿林天文臺介紹
有「鹿」而沒「路」的天文臺

前往鹿林山天臺是從臺灣的平原直登上3000 公尺左右的大山，生態環境的改變就像從北回歸線到北極圈一樣，可體驗到豐富的生物多樣性。鹿林山，傳說是群鹿如林的地方，目前為臺灣最高的天文臺，也是國內天文學術的研究重鎮，天文臺規模設備雖小，卻有著全世界極佳的觀測優勢。

其得天獨厚的觀測優勢有三，一是臺灣高山多，鹿林天文臺設於海拔 2,862 公尺的玉山國家公園旁，光害和塵害很少。其次，接近赤道的低緯度，可以觀測較寬廣的天域，尤其是南天球的天體，這是日本、韓國等高緯度國家所觀測不到的。再者，在經度上位於西太平洋重要觀測據點，沿夏威夷的大天文臺群過來，下一次觀測站就是臺灣，國際上扮演著舉足輕重的地位。在國際上沒有一處可以取代它。

披星戴月　篳路藍縷的籌建過程

臺灣天文發展最早可追溯至日據時代，但是一九九〇年代，中央大學在鹿林山開始籌備建立一米望遠鏡的天文臺，才真正起步。相較於國際知名天文臺豐沛的資源，鹿林天文臺籌建過程可說是披星戴月，篳路藍縷，建設十餘年了，由於法規的限制，至今尚未有公路通往鹿林天文臺，是世上少數幾個沒有路的天文臺。車子到不了，即使是諾貝爾獎得主李遠哲前院長也得邊走邊爬上來，建設之困難可以想見。

在鹿林天文臺的背後是許多原住民同胞的付出，鹿林海拔 2800 公尺，一般人很難在這

麼高的地方工作生活。天文臺建設之初，端賴布農族和鄒族原住民披荊斬棘，一磚一瓦揹上山頭。成立迄今，更有四位鄒族同仁全年 365 天 24 小時輪班守候，無論颱風來襲或除夕過年，在鹿林前山之巔堅守著崗位。他們是玉山的子民，守護著鹿林。建設鹿林天文臺的同時，我們亦同步見證臺灣交通建設多處快速公路的完成，使得師生前往鹿林的時程大大縮短，從一天變半天。在賀伯颱風、九二一地震、桃芝颱風、八八風災等天然災害與環境的巨大變遷 (如土石流)，重創山區的環境下我們仍一日又一日，滿懷希望。希望在不久的將來，能在對環境衝擊最小的狀況下完成 2 公尺望遠鏡天文臺與道路設施。

參與許多國際大型計畫
第一個十年與第二個十年

透過天文望遠鏡看到的天空面積只有約月亮大小，用這月亮大小的視野逐一搜索整個天空稱為「巡天」，要從浩瀚星空找出會動的目標是一項大海撈針的工作。而且尋找彗星是跟全世界在競爭，每 1 萬個新發現的移動天體 (小行星) 裡只有一個彗星，機率只有萬分之一；同時也是跟時間在賽跑，只要晚一秒鐘發現就是別人的，唯有堅持到底才能揚名國際。跟全球幾個大型巡天計畫相比，鹿林巡天的規模只是他們的千百分之一，要想以小博大，就必須策略正確，並持之以恆。

鹿林天文臺正是這種策略下的產物，第一個十年：從無到有，完成基礎建設。第二個十年：從一米到二米，布局全球；有了更大更精良的望遠鏡之後，可以看得更多、看得更遠，培養更多的本土天文人才，在全球的天文學術研究上，讓臺灣發光，站上更重要的一席之地。由天文所支撐的鹿林天文臺在師生胼手胝足辛苦經營下，已有豐碩成果是國際上罕見的。因為一般研究型天文臺的創立與營運，大部分屬國家級的直屬機構。

↑圖4. 鹿林天文臺

↑圖5. 第一個十年合影

我們於二〇一二年十月二十日邀集百位以上校友來校 (回娘家)，並邀請中大已命名的22 顆小行星返校 (回娘家) 共襄盛舉；慶祝中大天文所成立二十週年。中大將臺灣推向宇宙的創舉，一步一腳印的將小行星名遍布全臺。中大天文所帶領臺灣人物、地名、山名及少數民族之名神遊宇宙。(中大命名的小行星：中大、鹿林、嘉義、南投、中壢、桃園、苗栗、玉山、小林村、慈濟、雲門、鄒族、溫世仁、鄭崇華、沈君山、李國鼎、吳大猷、鄧雨賢、鍾理和、蔡文祥、陳其寬、馮元楨等)

↑圖6. 中大天文所二十週年慶及小行星回娘家大合影 (攝影：陳澤銓)

中大天文所二十週年慶海報

關於鹿林天文臺➢鹿林前山，海拔2862公尺，
位於逆溫層之上

設立時間➢民國 88 年 (1999～迄今)

經緯度：➢東經 120 度 52 分，北緯 23 度28 分

參與計畫➢1. 中美掩星合作計畫 (TAOS)。
2. 低質量雙星系統X射線源。
3. 彗星與小行星的觀測。
4. 超新星巡天計畫。
5. 伽瑪射線爆可見光餘暉認定。
6. 參與美國夏威夷大學天文所及美國空軍合作的泛星計劃。
7. 紅色精靈地面觀測與極低頻無線電波(ELF) 偵測系統。
8. 亞洲大氣污染物之長程輸送與衝擊研究。
9. 中大太空所的 airglow imager 與華衛二號 ISUA 之聯合觀測。

發現新天體➢1. 二〇〇二年發現臺灣第一顆小行星，迄今累計發現近 800 多顆。
2. 二〇〇七年臺灣本土望遠鏡發現第一顆彗星，名為「鹿林彗星」。
3. 二〇〇七年臺灣第一顆近地小行星。

國際期刊➢自然《Nature》2 篇、科學《Science》6 篇

在臺灣的中心，做臺灣的眼睛

相信你如果在臺灣深山過夜，只要天氣晴朗到戶外去看，一定會被滿天星斗震撼住，覺得那裡的星星特別的大、特別的亮、特別的多，希望對它們有更多、更深入的認識。

但現在我們獲得的天文知識，幾乎都來自歐美，臺灣可有較積極的角色？

國內的天文學家也希望能把握這樣的星空，在國內建立天文臺。尤其臺灣東方是片廣袤海域，缺少天文觀測的據點，如果有什麼重要天象發生，因為地球由西向東自轉的關係，臺灣有很大的機會可以優先觀察到，因此就此角度而言，這兒具很好的戰略位置，但該在哪裡蓋呢？

篳路藍縷，以啟山林

位於中壢的中央大學是國內最早開設天文課程的學校，雖然校內早就設有 61 公分口徑的望遠鏡，但在市區逐漸發展之下，光害日趨嚴重，而且中壢多雨，並不適合觀測。

為此天文所蔡文祥教授從民國 79 年起率領團隊選擇於臺灣中心、海拔 2862 公尺的鹿林前山為探查位址，經過四年的評估，確定在氣候、視相、大氣穩定度、天空透明度等各項條件都達到要求，於是便開始搬土運石，準備興建正式的天文臺。由於那邊是在國家公園境內，不能隨便開闢公路，因此只能請原住民沿著步道，一步步、一項項地運上去，後來才有流籠的設計。但為了降低物重負擔，因此在興建的時候便以輕便與組裝容易為原則，即使會增加成本也在所不惜。

目錄
火箭自造
樹人立言
臺灣眼睛
神祕花園
未來建築
孝易順難
繽紛書語

經過多年辛苦的開墾興建，到了民國 91 年正式完成直徑 1 公尺的望遠鏡天文臺與控制中心，正式開啟本土天文的專業研究。

目前山上不只一臺一公尺望遠鏡，還有兩臺較小的獨立望遠鏡，一臺 45 公分，另一臺 30 公分，還有一套專為找尋海王星外小天體的四臺 50 公分望遠鏡所組成的系統（簡稱 TAOS）。這些望遠鏡形成一個群聚，有趣的是，它們雖然是在同個山頭範圍，但卻分屬不同行政區域，因此望遠鏡群也分屬兩個地址，有的在南投縣信義鄉神木村，另外的則在嘉義縣阿里山鄉。

這些應該很專業吧！一般人可以怎麼來認識它呢？就讓我們從三個方面來談：一、望遠鏡的外觀；二、在天文臺工作者；三、鹿林天文臺觀測的成果。

目錄
火箭自造
樹人立言
臺灣眼睛
神祕花園
未來建築
孝易順難
繽紛書語

沒有圓筒的望遠鏡

這臺 1 公尺望遠鏡的外觀看起來好像跟一般常見的望遠鏡不大一樣，怎麼看不見像大砲一樣的長圓筒呢？

那是因為圓筒的功用是擋住其他方向來的光，但這裡的天文臺在深山裡，夜晚戶外除了星光月光之外，沒有其他光源，包括路燈、汽車燈，全都沒有，控制中心也有厚厚的窗簾擋住，不滲一絲光線出去，因此就省掉了厚重的圓筒，只保留能讓面鏡安放支撐的架構，以固定在精確的位置上，這樣望遠鏡就輕便許多。

再來就是這臺望遠鏡也不採用**透鏡**折射光線，而是用**面鏡**反射光線。這是因為透鏡的光線經過不同介質時，不同波段的折射角會不同，這樣會有色像差。好不容易把望遠鏡做大想看得更清楚，但如果因為色像差而又模糊，那就太可惜了。使用面鏡反射則光線都在同一介質中行進，因此不會有色像差，可以看得更清楚。

天文臺的工作者

在天文臺工作的人，通常是什麼人呢？

這分成兩部份，一個是技術人員，林宏欽臺長介紹說，他們這些同事，包括他，都是對天文有興趣的人。大家高中或大學都曾擔任過學校天文社的社長，雖然大學、研究所有不同專業，但剛好結合起來就可以解決各種資訊、機、電、工業工程等問題，讓天文臺順利運作。

這次採訪時一公尺望遠鏡的圓頂正準備更換旋轉的動力設備，這由具機械背景的張永欣先生來負責，事先張永欣就先估計過圓頂重量、結構、材料力度等諸多事項，設計了一些設備，但實際裝配的時候某些角度不如預期，因此要想辦法解決。看起來讓旁人憂心，但大家都習慣了，一點都不擔心，而是專注在問題上，怎麼在現有條件下去想辦法。

為什麼不請廠商上來呢？

因為這裡交通不便，多數廠商不大願意大老遠跑這一趟，目前雖有一些合作廠商，但很多事情還是得要天文臺的人自己動手解決，大家這方面的能力也就越來越強。他們不會認為這種黑手工作很辛苦，而是了解這些親自動手的工作是讓天文臺正常運作的基礎，這是他們熱切希望看到的事情。

至於觀測現在都自動化，操作很簡單，只要在控制中心根據申請者所提的目標去輸入目標天體的座標資料以及觀測時間、取像波段即可，望遠鏡會自動指向、追蹤、取像。操作雖然容易，但重點是怎麼找到有趣的題目、提出好的假說，然後再來觀察、解讀資料。

通常一米望遠鏡開放給校內外學者申請研究，每半年就有一次申請機會，這方面都已建立制度。另外兩臺小型望遠鏡則提供中大校內師生研究用，較有彈性。而 TAOS 則是有特別任務，全自動、系統性掃描特定天區，尋找太陽系遙遠角落還未現身的成員。

在天文臺還有另外幾位駐站人員協助庶務，總理天文臺生活起居、水電消防與環境維護。這些人的聘用以當地人為主，因此都是住在阿里山的鄒族同胞，有些人在最初探勘的時候就來協助搬運東西；後來天文臺建好，便再去學習水電、消防、廚師等知識與技能，繼續留下來工作。

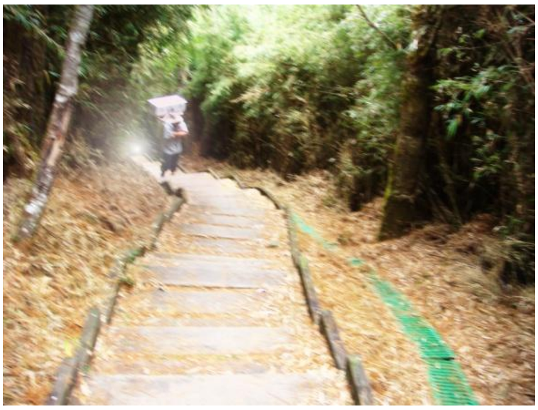

目前搬運東西不再像最初那麼辛苦，但仍相當費力，尤其這裡聯外道路無法直接到達，停好車之後還得爬一個 600 公尺的上升步道，幸好負責人有鄒族特有的大背袋與特殊的背負方式，一切都很穩當，但你如果現場看到，仍會相當敬佩他們的體力與耐力。

鹿林天文臺的成果

鹿林天文臺成立之後，有什麼重要的發現嗎？

這裡的一公尺望遠鏡，在曝光一分鐘的情況下可以看到 19 等暗星，這比人肉眼可見極限還要暗上百萬倍，如果曝光更久，將可看到更暗的天體。而其解析能力也相當精緻，因此可以讓國內外的研究者與天文臺的技術人員一起合作而有豐富的成果。

例如有個巡天計畫，藉由有系統、長時間觀測不同天區，找到了數百顆過去不為人知的小行星，成為東亞在小行星搜尋上最活要的區域。目前已經有超過三百顆經過國際天文聯會確認，此時發現者就有命名權。中央大學通常會藉此表達感謝或紀念，例如有小行星命名為**布農**或**鄒族**，就是為了感謝天文臺創建之初有許多布農族與鄒族的朋友來協助搬土運石；另外命名為**李國鼎**（中大校友、曾任經濟部長與財政部長）、**沈君山**（前清大校長），則是紀念他們在國內的貢獻；還有臺灣的許多地名、文學家，都已成為小行星的名字，留名太陽系。

此二張照片由中大天文所提供，拍攝者：張明新先生。

鹿林天文臺還配合研究學者有其他主題的研究，包括太陽系內的天體、恆星、星雲、星團、星際物質、星系等各類天體。這裡還會積極爭取國際合作，並對重大天文現象進行監測。此外這兒也訓練出基本功紮實的學生與研究人員，有助於參與國際合作計畫。

目錄
火箭自造
樹人立言
臺灣眼睛
神祕花園
未來建築
孝易順難
繽紛書語

由於望遠鏡的鏡頭越大，集光力越強，在相同的曝光時間下可以看到更暗的物體，或者僅需較短的曝光時間，就可觀察到天體。因此若能有更大口徑的望遠鏡就可以讓觀測更有效率，或者看到過去觀察不到的現象。為此未來希望能再建兩公尺望遠鏡的天文臺，讓臺灣的天文研究可以更上層樓。

鹿林天文臺不僅限於天文觀測，也歡迎學校師生前往戶外教學。如果有興趣前往參觀，可參考其參觀辦法，配合規畫。

鹿林天文臺

網頁：http://www.astro.ncu.edu.tw/observatory/index.php

臉書：https://www.facebook.com/LuLinObservatory/?fref=ts